2011

Toward increasing performance and efficiency in gas turbines for power generation and aero-propulsion unsteady simulation of angled discrete-injection coolant in a hot gas path crossflow

Perry L. Johnson
University of Central Florida

TOWARD INCREASING PERFORMANCE AND EFFICIENCY IN GAS TURBINES FOR POWER GENERATION AND AERO-PROPULSION: UNSTEADY SIMULATION OF ANGLED DISCRETE-INJECTION COOLANT IN A HOT GAS PATH CROSSFLOW

by

PERRY L. JOHNSON

A thesis submitted in partial fulfillment of the requirements
for the Honors in the Major Program in Mechanical Engineering
in the College of Engineering and Computer Science
and in The Burnett Honors College
at the University of Central Florida
Orlando, Florida

Fall Term 2011

Thesis Chair: Dr. Jayanta Kapat

ABSTRACT

This thesis describes the numerical predictions of turbine film cooling interactions using Large Eddy Simulations. In most engineering industrial applications, the Reynolds-Averaged Navier-Stokes equations, usually paired with two-equation models such as k-ε or k-ω, are utilized as an inexpensive method for modeling complex turbulent flows. By resolving the larger, more influential scale of turbulent eddies, the Large Eddy Simulation has been shown to yield a significant increase in accuracy over traditional two-equation RANS models for many engineering flows. In addition, Large Eddy Simulations provide insight into the unsteady characteristics and coherent vortex structures of turbulent flows. Discrete hole film cooling is a jet-in-cross-flow phenomenon, which is known to produce complex turbulent interactions and vortex structures. For this reason, the present study investigates the influence of these jet-crossflow interactions in a time-resolved unsteady simulation. Because of the broad spectrum of length scales present in moderate and high Reynolds number flows, such as the present topic, the high computational cost of Direct Numerical Simulation was excluded from possibility.

DEDICATION

To the Authority in Fluid Mechanics, who

“commands the wind and the water, and they obey Him.”

ACKNOWLEDGEMENTS

First of all, I would like to thank Dr. Jay Kapat for igniting my passion for thermo-fluids and turbulence research, the effect of which, I hope, will stretch far beyond this thesis. In a similar manner, I have many thanks for Dr. Vikram Shyam for excellent mentorship at NASA GRC and encouraging my thirst for science and technology in a broad and multi-disciplinary sense. Along the way, I have accrued many reasons for thanking Dr. Mark Ricklick, not only for excellent lab management, but also the ability and willingness to step in and help when the going gets tough. In addition, I would like to thank Dr. Cuong "Jeff" Nguyen for breaking me in at CATER and guiding my first steps into research publication, as well as Dr. Son Ho for introducing me to CFD and dealing with ORC.

I have many fellow students to thank as well. Bryan Bernier and Greg Natsui are much appreciated for leadership in funded projects (Siemens and NASA SBIR respectively). I owe much to Carson Slabaugh for first alerting me to the existence of LES and offering a motivating perspective on research as a whole. I also have deep appreciation for Matthew Golsen for teaching me his masterful ways of pizza creation. In my studies, I want to thank my senior design teammates: Jimmy Kullberg, Roberto Claretti, Matthew Golsen, Lucky Tran; who's co-operation helped lighten my burden in undergraduate academia. Lab mates who helped or inspired me innumerable times that I can't recount specifically for brevity's sake (in alphabetical order): Bryan Bernier, Monica Bonadies, Anthony Brevato, Tim Casey, Roberto Claretti, Matthew Golsen, Jimmy Kullberg, Srikrishna Mahadevan, Greg Natsui, Carson Slabaugh, Michael Torrance, Lucky Tran, Michelle Valentino.

I also extend my thanks to Dr. Marcel Ilie (MMAE) and Dr. Ratan Guha (EECS) for enlightening discussions (LES and GPU, respectively) and for serving on my committee. Dr. Guha was also instrumental in the provision of the Ariel cluster, on which some of the simulations from this thesis were performed.

I would like to thank the Lewis Educational Research Collaborative Internship Program (LERCIP) team for their efforts in making my two summers at NASA GRC possible. In my time at NASA GRC, I have reasons to thank Dr. Ali Ameri for fun discussions and insight into turbine heat transfer. Also I have many thanks for Dr. James Heidmann for his encouragement of my efforts. I also want to thank Dr. Chunill Hah, Dr. T. H. Shih, Dr. H. T. Huynh, and Dr. Tim Bencic for discussions about LES, PRNS, discretization and flux limiters, and TSP/PSP, respectively. Finally, I appreciate Dr. Jeff Moder for his support in Fluent licensing during my first summer at GRC.

Last on my list, but certainly not least, are the system administrators for the clusters on which the simulations in this thesis were run: Steve Dick (UCF-MMAE) – Ariel cluster (provided by Dr. Ratan Guha), Dr. Sergio Tafur (UCF Institute for Simulation and Training) – Stokes cluster (headed by Dr. Randall Shumaker and Dr. Brian Goldiez), and Thaddeus Kollar (NASA Glenn Research Center ACCL) – HX cluster.

TABLE OF CONTENTS

LIST OF FIGURES

LIST OF TABLES

NOMENCLATURE

a	speed of a sound wave through a fluid medium	m/s
B_{ij}	subgrid stress tensor	m^2/s^2
C_D	discrete coolant hole discharge coefficient	dimensionless
D	Discrete coolant hole nominal (inlet) diameter	m
DR	Density ratio	dimensionless
f	frequency	Hz = cycles/s
I	Momentum flux ratio	dimensionless
k	turbulent kinetic energy	m^2/s^2
k_{th}	thermal conductivity	W/m-K
L	Discrete coolant hole length	m
M	Blowing ratio or mass flux ratio	dimensionless
p	Fluid pressure	$Pa = N/m^2 = kg/m\text{-}s^2$
P	discrete film hole row pitch (lateral spacing)	m
P_{ij}	production of turbulent kinetic energy	m^2/s^3
Pr	Prandtl number	dimensionless
Q_{ij}	turbulent heat flux vector	W/m^2
q_{ij}	subgrid heat flux vector	W/m^2
R_u	Universal gas constant	J/mol-K
$R_{(gas)}$	Gas constant	J/kg-K
R_{ij}	Reynolds stress tensor	m^2/s^2
s	Specific entropy	J/kg-K

T	Temperature	K
U,V,W,u,v,w	Fluid velocity	m/s
VR	Velocity ratio	dimensionless
x	streamwise Cartesian coordinate direction	m
y	wall-normal Cartesian coordinate direction	m
z	spanwise Cartesian coordinate direction	m

Greek characters

α	discrete film hole inclination angle	° (degrees)
α_{th}	thermal diffusivity	m^2/s
β	discrete film hole expansion angle	° (degrees)
γ	specific heat ratio	dimensionless
Δ_f	Spatial filter width for large eddy simulation	m
δ	boundary layer 99% disturbance thickness	m
δ^*	boundary layer displacement thickness	m
ε	turbulent dissipation rate	m^2/s^3
η_{adia}	adiabatic film cooling effectiveness	dimensionless
η_{th}	thermal cycle efficiency	dimensionless
θ	boundary layer momentum thickness	m
κ	von Karman log-layer ‘universal’ constant	dimensionless
κ_λ	wave-number ($2\pi/\lambda$)	1/m
λ	characteristic length scale	m
μ	fluid molecular dynamic viscosity	Pa-s = kg/m-s

ν	fluid molecular kinematic viscosity	m^2/s
ξ	molecular mean free path	m
ρ	fluid density	kg/m^3
σ_φ	turbulent ‘Prandtl’ number for any scalar φ	dimensionless
τ	characteristic time scale	s
υ	characteristic velocity scale	m/s
ω	turbulent specific dissipation rate	1/s
ω	angular frequency	rad/s

Subscripts

CL	relating to properties at the centerline
c	relating to coolant properties
K	Kolmogorov microscales
mix	scales relating to Prandtl’s mixing-length hypothesis
o	fixed reference property
SGS	subgrid-scale
T	Taylor microscales
t	turbulent
w	relating to properties at a no-slip wall
∞	relating to freestream properties

Other Symbols

$\langle\ \rangle$	statistical mean
$\square'$	fluctuating quantity

CHAPTER 1 INTRODUCTION

1.1 Gas Turbine Engines

Gas turbine engines are commonly used for aircraft propulsion, land-based electrical power generation, and even marine propulsion. These complex machines convert chemical energy into thermal and flow energy through the combustion process. Turbine blades subsequently convert some or all of this energy into mechanical energy in the rotating machinery. For land-based applications the rotation drives an electrical generator. In the case of aircraft engines, the turbine only recovers enough energy from the hot gas path to drive the compressor and a few auxiliary components. The rest of the energy is nozzled and ejected as a propulsive jet.

The ideal Brayton cycle (Cengel and Boles 2008) describes the basic thermodynamic principles governing the operation of a modern gas turbine engine. The four processes of the Brayton cycle (Figure 1) are as follows: (1→2) isentropic compression, (2→3) heat addition by combustion, (3→4) isentropic expansion, and (4→1) heat rejection to the ambient. The 4→1 heat rejection is an imaginary process in for gas turbine engines, because the intake air at state 1 is taken from the ambient and the air at state 4 is exhausted to the ambient (though sometimes used as heat input for a steam engine in combined cycles for power generation).

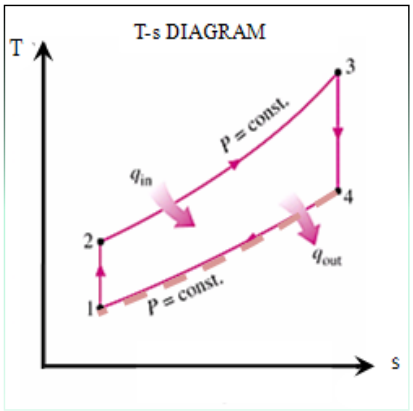

Figure 1 Temperature-entropy diagram of the ideal Brayton cycle

1.2 Turbine Cooling

Simple thermodynamic analysis of the Brayton cycle leads to a thermal efficiency shown in Eq. (1), where T_3 is the turbine inlet temperature for the hot gas path.

$$\eta_{th,Brayton} = 1 - \frac{T_4 - T_1}{T_3 - T_2} \qquad (1)$$

In the development of the gas turbine engine, one of the most successful methods in improving efficiency has been the increase of the turbine inlet temperature. Eventually, this method has led to combustion temperatures exceeding the safe operating temperatures of the metal components. Various areas of research have contributed to pushing combustion temperatures higher, including materials research in super-alloys, ceramics research in thermal barrier coatings, and heat transfer research in various cooling techniques. Figure 2 shows the trends of advancing technology for increasing allowable combustor firing temperatures.

Much more than operating at safe temperature, modern engineering designs strive to perfect a delicate balance of component life and cycle efficiency. The turbine blades are highly loaded with torque and angular speed. In addition to stresses from loading, the blades are also

susceptible to a large amount of thermal stresses. Furthermore, the coolant flow, comprising up to 20% of the total flow through the engine, while allowing for higher firing temperatures, represents a dramatic loss as the work done to compress the cooling flow is simply forfeited.

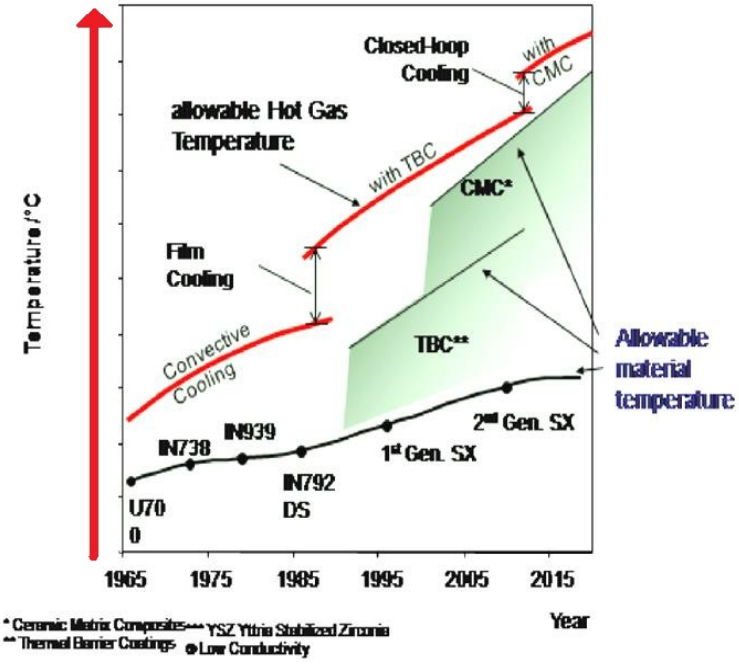

Figure 2 Timeline of technological advances in hot gas path temperatures (Kiesow 2008).

1.3 Film Cooling Basics

For gas turbine cooling, air is bled out of the compressor stage and fed through the engine core into an internal serpentine passage in the interior of the turbine blade and endwalls. After cooling the interior of these metal components, the 'cool' air is injected into the hot gas path through discrete holes. This process creates a film-like covering along the outside surface of the metal component, which acts as a thermal buffer and reduces heat transfer into the component. Initial film cooling research in the 1950s and 1960s investigated the coolant film resulting from injection through various continuous slot geometries (Goldstein 1971). Starting in the late 1960s

and early 1970s, studies were conducted with discrete holes, usually cylindrically-shaped holes inclined at angles around 30 degrees to the surface (Goldstein et al. 1968, 1974, Erikson and Goldstein 1974). The main parameter to measure the benefits of film cooling was defined as the adiabatic effectiveness, Eq.(2). T_r is the recovery temperature (approximately equal to the temperature of the hot gas path for low Mach number flows), T_c is the temperature of the coolant at the hole exit, and T_{aw} is the adiabatic wall temperature downstream of the coolant hole injection. It is common to present film cooling data in terms of spanwise-averaged effectiveness, Eq. (3), and centerline effectiveness, Eq. (4).

$$\eta_{adia}(x,z) = \frac{T_r - T_{aw}(x,z)}{T_r - T_c} \quad (2)$$

$$\bar{\eta}_{adia}(x,z) = \frac{\int \eta_{adia}(x,z)dz}{\int dz} \quad (3)$$

$$\eta_{adia,CL}(x,z) = \eta_{adia}(x,0) \quad (4)$$

Figure 3 shows a simple schematic of the temperatures used in determining film cooling effectiveness. When the temperature of the adiabatic wall becomes equal to the coolant temperature at the exit of the hole, the effectiveness becomes unity, which is the best possible scenario. An adiabatic wall temperature equal to the recovery temperature reduces the effectiveness to zero, because it is as if no film cooling were applied.

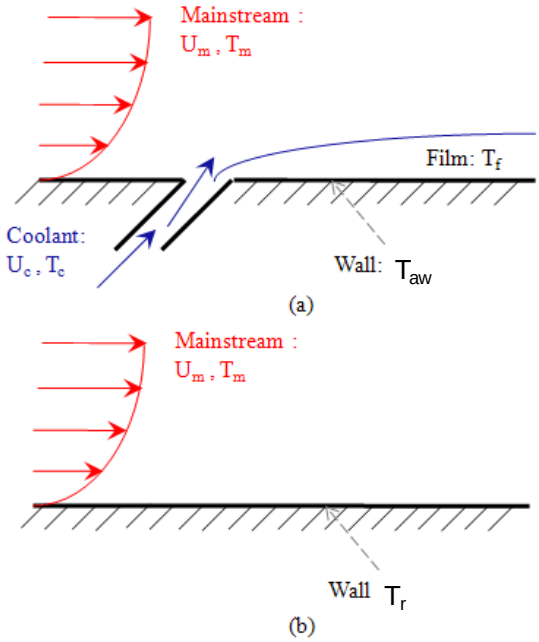

Figure 3 Simple film cooling schematic showing (a) T_c and T_{aw} with coolant applied and (b) T_r with no coolant flow.

Flow parameters used in describing jet conditions include but are not limited to:

Velocity ratio:

$$VR = \frac{U_c}{U_\infty} \tag{5}$$

Density ratio:

$$DR = \frac{\rho_c}{\rho_\infty} \tag{6}$$

Blowing ratio or mass flux ratio:

$$M = \frac{\rho_c U_c}{\rho_\infty U_\infty} = DR * VR \tag{7}$$

Momentum flux ratio:

$$I = \frac{\rho_c {U_c}^2}{\rho_\infty {U_\infty}^2} = VR * M = \frac{M^2}{DR} \tag{8}$$

These ratios represent the quotient of the coolant property at the hole exit divided by the crossflow property in the freestream. Only two of the four parameters are independent. Basic geometric considerations are described in terms of pitch-to-diameter ratio (P/D), length-to-diameter ratio (L/D), and inclination angle (α), illustrated in Figure 4.

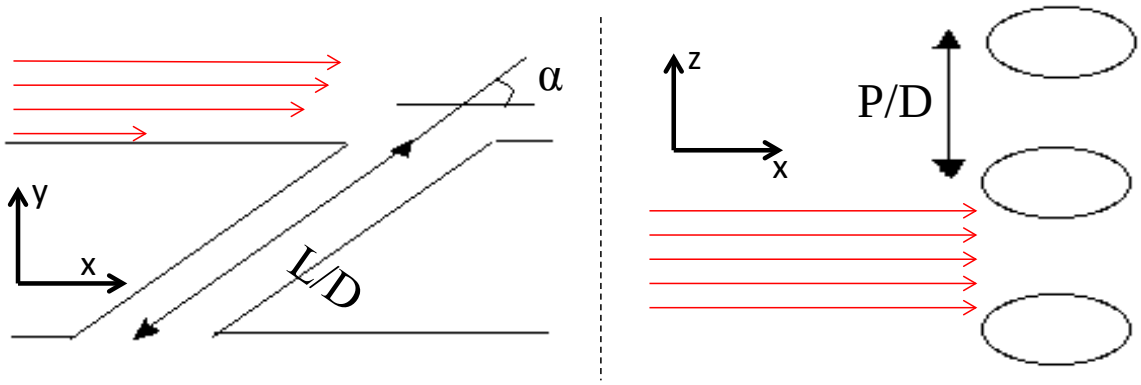

Figure 4 Simple schematic showing basic film cooling geometric parameters for a cylindrical inclined row of cooling holes.

As the state of the art advanced, more complex hole geometries were introduced, including various expansion-shaped holes, (Goldstein et al. 1974, Hay and Lampard 1995, Sen et al. 1996, Schmidt et al. 1996, Thole et al. 1998, Gritsch et al. 1998a,b,c, Cho et al. 1999, Gritsch et al 2000, Bell et al 2000, Yu et al. 2002, Taslim and Ugarte 2004, Bunker 2005, Zuniga 2006, 2009). Figure 5 shows a number of diffusion shaped geometries. In addition to these studies, holes were also embedded in shallow trenches and craters (Bunker 2001, 2002, Lu et al. 2005, Waye and Bogard 2006, Zuniga 2009). Each new geometry introduced its own set of geometrical parameters. For the vast majority of these hole shapes, the more complex geometries led to higher effectiveness values. Increase in complexity of hole geometry, however, generally leads to increase in manufacturing cost. Thus, few of the novel film cooling

designs have been put into widespread use, the notable exception being the fan-shaped expansion (Bunker 2005).

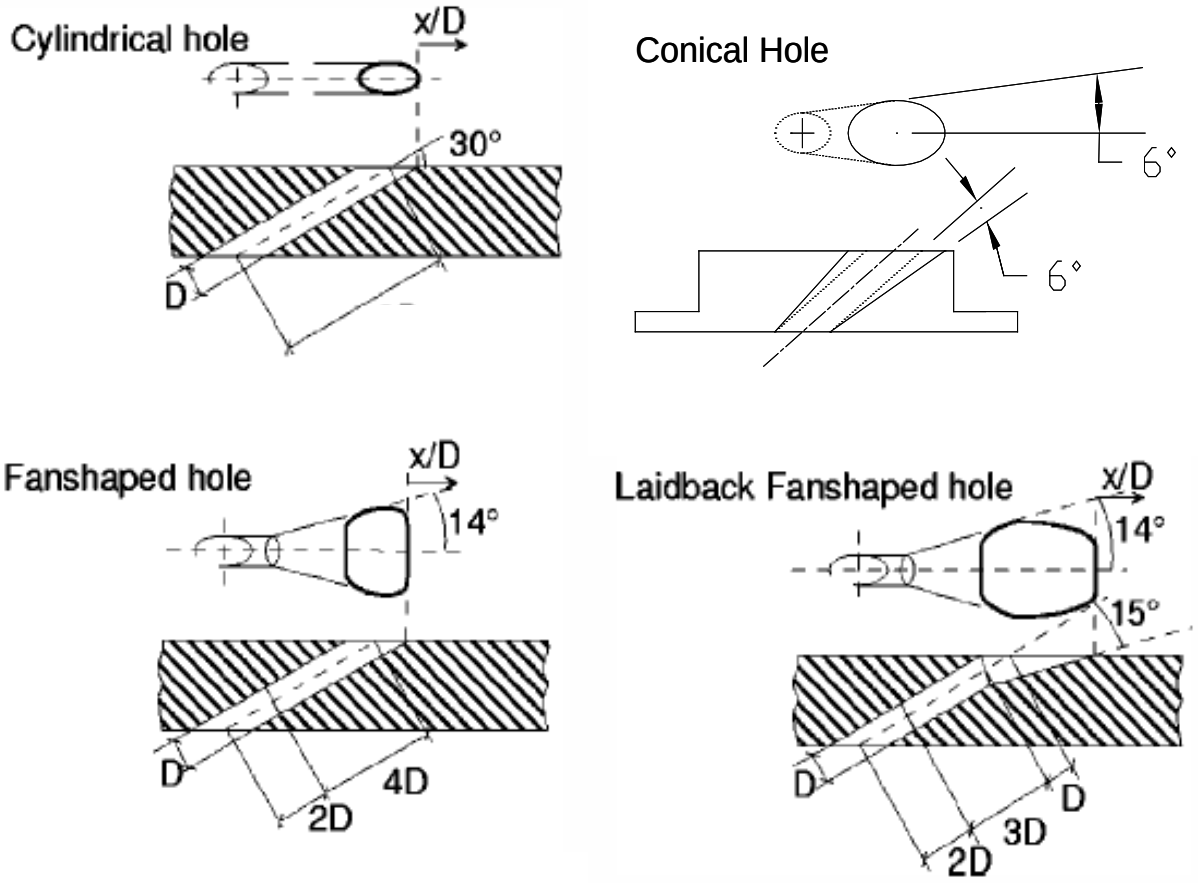

Figure 5 Schematics for various shaped holes (Saumweber et al. 2003, Nguyen 2010)

One of the main concerns in film cooling has proven to be the trajectory of the coolant jet. Early in film cooling research, jets with higher velocity or blowing ratios were noticed to have a tendency to lift off the cooled surface, leading to lower effectiveness. Figure 6 shows three scenarios for film cooling. First, at low mass flux ratios, the coolant will be easily forced along the cooled wall by the mainstream. At median mass flux ratios, the coolant will tend to lift off the wall at the point of injection, incurring a small recirculation region before reattaching

downstream. When the mass flux ratios are increased even higher, the coolant film will lift off at injection and never reattach.

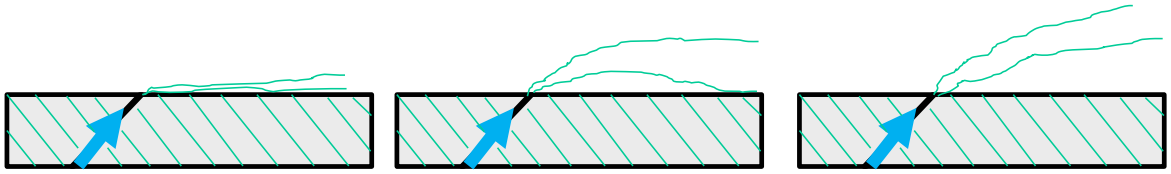

Figure 6 Three regimes for film cooling trajectories: (a) full coverage at low M, (b) lift off and reattachment at median M, and (c) lift-off with no reattachment at high M.

1.4 Turbulence, Modeling, and Simulation

The rapid advance in computer technology over the past four decades has led to the rise of numerical techniques as common prediction tools to compliment experimental tests. Numerical techniques, likewise, have become valuable prediction tools in engineering design, when no experimental data are available. The most difficult, as well as the most researched, element of computational fluid dynamics (CFD) is the modeling and/or simulation of turbulence. Frustrations arising from the 'outstanding difficulty' of this subject (Lamb 1916) have led prominent researches to offer up some amusing remarks, such as Bradshaw's designation of turbulence as the 'invention of the devil on the seventh day of creation' (Bradshaw 1994). Turbulence is the chaotic motion of a fluid resulting from instabilities that arise when viscous forces are too weak to damp out instantaneous disturbances in a fluid flow. Instead, inertial motions overpower the molecular viscosity and disturbances grow, producing the effect of chaos.

1.4.1 Reynolds-Averaged Navier-Stokes (RANS)

For engineering applications, statistical properties of such flows are more useful than detailed, time-resolved data. The basic approach to simulating turbulent flows aims to predict mean and certain second-order statistics while leaving out the details of turbulent motions. A turbulence model is substituted for the effects of these turbulent motions. This statistical approach uses the Reynolds-Averaged Navier-Stokes (RANS) equations coupled with such turbulence models. For engineering design practices, the RANS approach is typically used (film cooling scenarios not being an exception) because of the relative computational ease as compared with more computationally intensive models and simulation techniques.

The complex motions arising from the non-linear geometric, inertial, and viscous interactions over the broad range of length, velocity, and time scales present in turbulent flows have proven the creation of accurate RANS approaches for complex engineering flows to be a difficult challenge. Length scales of turbulence vary from the integral scale, which is comparable to the characteristic dimensions of the flow geometry, down to the so-called Kolmogorov length microscale ($\lambda_K = \nu^{3/4}/\varepsilon^{1/4}$). Velocity scales vary from the root-mean-square velocity down to the Kolmogorov velocity microscale ($\upsilon_K = \nu^{1/2}\varepsilon^{1/2}$). Time scales, likewise, vary from those characteristic of the mean flow velocity gradients down to the Kolmogorov time microscale ($\tau_K = \nu^{1/2}/\varepsilon^{1/2}$). In typical engineering flows, these scales range over many orders of magnitude, not only making the direct simulation of all scales prohibitively costly, but also making the task of developing a universal turbulence model dreadful if not impossible.

1.4.2 Large Eddy Simulation

The development of Large Eddy Simulation (LES) techniques, coupled with the dramatic rise in computational power afforded by modern technology, has opened the door for unsteady analysis of large scale turbulence for fluid dynamic problems in all engineering and scientific disciplines. The theory behind LES rests on the application of a spatial filter to the velocity, pressure, and other fields of interest. In the practice of LES, most often the numerical grid itself is cited as an implicit filter, as it is unable to resolve turbulent motions smaller than the size of the grid at any given point in the flow. In this way, large scale motions are directly resolved in a time-accurate manner, while small scale motions are left to determination by a subgrid-scale model. The opinions of what exactly constitutes a 'large eddy' differs in the context of LES, whether they be those eddies containing 80% of the turbulent kinetic energy (Pope 2000) or eddies larger than the Taylor microscale (λ_T) (Shih 2011). Generally, simulations failing to meet such criteria are referred to as Very Large Eddy Simulations (VLES).

The importance of the difference between the two for practical application in the engineering disciplines is arguable at best. For the purposes of this thesis, these differences will not be highlighted.

The theory supporting VLES and LES is one and the same. The large eddies of a turbulent flow represent the beginning of a cascade of energy from larger to smaller scales. The inherently three-dimensional, inertial (inviscid) effect of vortex stretching provides the main mechanism for breaking turbulent energy-containing motions into smaller and smaller eddies. While the viscous forces may be overpowered at larger scales, eventually the cascade process refines eddies small enough that molecular viscosity dissipates the turbulent kinetic energy (TKE) into thermal

energy. For turbulent flows sufficiently high Reynolds number, the turbulent spectrum is wide enough to facilitate the complete disorientation of turbulent motions from the geometry-dependent processes that supplied the TKE in the first place. This theory gives solid ground for the development of subgrid-scale models with universal applicability.

The second theoretical support for the use of LES is the relative energy content of the different scales. The large geometry-dependent eddies carry the vast majority of the TKE in a turbulent flow at any given time. In this way, they have a higher level of influence over the statistical characteristics of the flow (such as those of interest to engineers). The small scales, being left to a subgrid-scale model in LES, contain much less energy and thus exhibit far lesser ability to affect the mean statistics and mixing properties of a flow.

In summary, the LES approach to turbulent flow simulation takes advantage of two characteristics of turbulence. First, the small scales lose orientation with respect to the geometry of the flow, thus becoming easier to model in a universal way. Secondly, the smaller scales do not contain as much TKE as larger eddies, thus having less influence on the dynamics of the mean flow, which is of most interest to engineers. In this manner, LES represents an advantageous compromise between the difficulties of achieving accurate RANS simulations and the insurmountable computational costs of Direct Numerical Simulations (DNS) for engineering flows. Figure 7 shows a typical distribution of the turbulent energy spectrum, where wave number (κ) is the inverse of the eddy size. A comparison of the RANS, LES, and DNS approaches is overlaid on the plot.

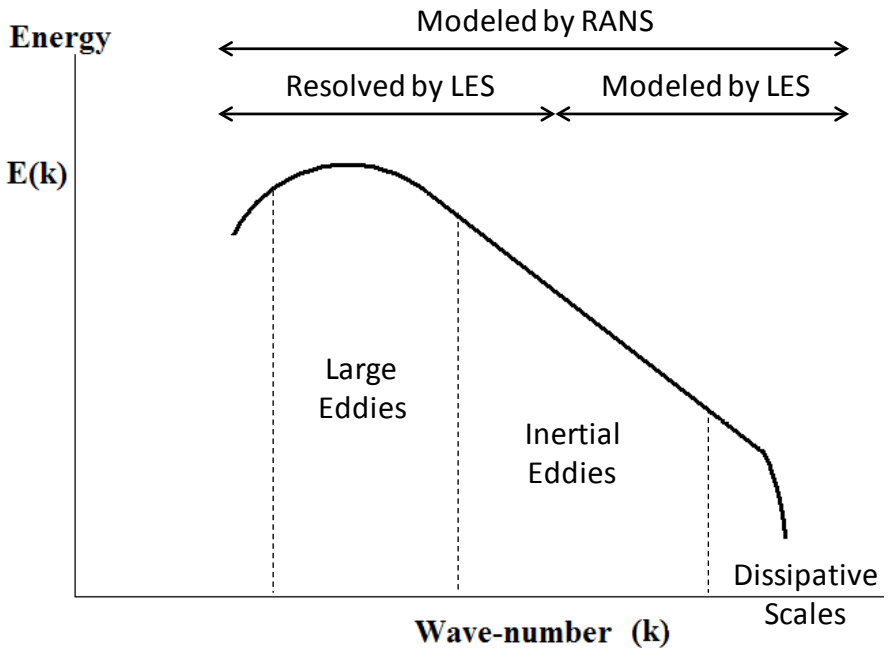

Figure 7 Typical turbulent energy spectrum: LES directly resolves the large scale eddies, which tend to carry more energy.

CHAPTER 2 BACKGROUND

The background for the present topic is set in two complementary fields. The first is computational fluid dynamics. In presenting background for this, the focus will be primarily on turbulence modeling and simulation, that being of primary interest in complex turbulent flows. Other details of the implementation of CFD are mentioned but not elaborated. The reader can refer to established textbooks on CFD such as Ferziger and Peric (1996), Anderson (1995), Tannehill et al. (1997), or Patankar (1980) for more details.

2.1 Computational Fluid Dynamics

Computational Fluid Dynamics (CFD) refers to the broad range of numerical strategies for solving a discretized set of governing equations to provide computational results for problems in fluid dynamics. CFD solutions are based on the Navier-Stokes equations, stemming from the continuum assumption. Discretization, though possible through finite element (FE) and finite difference (FD) methods, is more commonly realized using the finite volume method (FVM) (Patankar 1980). Once discretized, the governing equations take the form of a large sparse matrix representing the system of algebraic equations. Though a direct method for solving the matrix could indeed be applied, iterative methods have proven much faster in providing approximate solutions. Various methods for iteration and time advancement (for unsteady simulations) have been developed. The single most challenging and vexing component of CFD analysis is turbulence modeling. The wide range of length and time scales alluded to above make direct simulation impossible for engineering flows. Filtering and time averaging are two of the prominent methods for modeling turbulent flows. A brief presentation of the mathematical approach to CFD of turbulent flows is presented below.

2.1.1 Governing Equations

The governing equations for fluid dynamics are built on the continuum assumption (Pope 2000). This assumption states that a fluid flow can be treated as a continuous media and that the microscopic discrete structure of its individual molecules can be ignored. This assumption is justified by noticing that the smallest length and time scales relevant to the flow (the Kolmogorov scales) are generally orders of magnitude larger than the scales of the molecular motion (typically related to the speed of sound in the medium and the mean free path). In this way, the spectrum of molecular and continuum scales maintain healthy separation and do not interact. The molecular motions are thus easy to model with relatively simple models (Newton's law of viscosity and Fourier law of conduction, for example).

With the continuum assumption, the governing equations can be written down to provide for the conservation of mass, momentum, and energy. For compressible flows:

$$\frac{\partial(\rho)}{\partial t} + \frac{\partial\left(\rho u_j\right)}{\partial x_j} = 0 \qquad (9)$$

$$\frac{\partial(\rho u_i)}{\partial t} + \frac{\partial\left(\rho u_j u_i\right)}{\partial x_j} = -\frac{\partial p}{\partial x_i} + \frac{\partial}{\partial x_j}\left[\mu\left(\frac{\partial u_i}{\partial x_j} + \frac{\partial u_j}{\partial x_i} - \frac{2}{3}\frac{\partial u_k}{\partial x_k}\delta_{ij}\right)\right] \qquad (10)$$

$$\frac{\partial(\rho T)}{\partial t} + \frac{\partial\left(\rho u_j T\right)}{\partial x_j} = \frac{\partial}{\partial x_j}\left[\frac{k_{th}}{c_p}\left(\frac{\partial T}{\partial x_j}\right)\right] \qquad (11)$$

Here, the second viscosity has been assumed to its value for a monotonic gas (-2/3 μ) (Wilcox 2006). The specific heat (c_p) under constant pressure has been assumed constant such that $dh = c_p\, dT$ (Cengel and Boles 2008). The gravitational, as well as any other source term forces, have been left out of the momentum equations. A number of other terms have been neglected in the energy equation, such as the viscous dissipative heating and kinetic energy of

the flow. The above assumptions are justifiable for the problem at hand, which is modeling low Mach number film cooling experiments with relatively small temperature differences. The temperature differences, however, could be enough to influence density, thus the equations here have been left in compressible form. The handling of compressibility is tackled on a case-by-case basis.

The right-most term in both equations for momentum and energy represent Newton's constitutive relation for molecular (viscous) stresses and Fourier's law of conduction, respectively (Wilcox 2006). These two terms are analogous in their effect on the two relevant physical quantities, representing the diffusion of momentum and energy by molecular motion. In the presence of turbulence, however, these terms become negligibly small in comparison with the stress-like effect of larger, stronger turbulent motions (Tennekes and Lumley 1972).

2.1.2 Direct Numerical Simulation

The mass, momentum, and energy equations account for five transport equations, when solved simultaneously, can full characterize any flow-field, even turbulent fields. Should a variable-density flow arise, an appropriate equation of state (usually algebraic) can be used to close the system.

Such a simulation, however, must be diligent in resolving all scales of motion, all the way down to the Kolmogorov length and time scales. Of course, this must be accomplished while modeling the entirety of the relevant domain, which is on the order of the integral scales of turbulence. Order of magnitude analysis (Tennekes and Lumley 1972) reveals that the ratio of Kolmogorov scales to integral scales behaves as $Re^{-3/4}$. This is true of both length and time scales. The amount of numerical grid points (or cells in FVM) is then seen to behave as $Re^{-9/4}$

for three dimensional flows (all DNS must be carried out in three-dimensions, because the fundamental process of the turbulent energy cascade is vortex stretching, an inherently three dimensional phenomenon (see Tennekes and Lumley 1972). On top of this, a time step must be taken small enough to characterize the Kolmogorov eddies while the simulation must be run long enough to converge the statistics. This constraint factors in another $Re^{-3/4}$ dependency. The final result for DNS is a hefty Re^3 scaling of cost. Experience has shown that low-Re number flows, for example thin boundary layers, are in fact very feasible with current supercomputer capabilities. As Reynolds number increases, the above analysis shows that DNS quickly becomes infeasible with current computing technologies. In fact, most flows of engineering interest are well beyond the range of Reynolds numbers currently feasible for DNS. While the scientist may be satisfied that the continuum model for fluid dynamics is sound and makes turbulent flows incredibly predictable, the engineer is left to create substitutions with which to practically calculate the effects of turbulence on his/her flow on interest.

2.1.3 Reynolds Averaging and the Fundamental Problem of Turbulence

The engineer is mostly concerned with statistical mean quantities. The most practical approach to simulating a turbulent flow, then, is to derive equations for the mean flow and model the effects that turbulence introduces. The basic idea is to decompose the instantaneous continuum quantities into mean and fluctuating components. This leads to:

$$u_i(\boldsymbol{x}, t) = \langle u_i \rangle(\boldsymbol{x}) + u_i'(\boldsymbol{x}, t) \quad \textbf{(12)}$$

$$T(\boldsymbol{x}, t) = \langle T \rangle(\boldsymbol{x}) + T'(\boldsymbol{x}, t) \quad \textbf{(13)}$$

$$p(\boldsymbol{x}, t) = \langle p \rangle(\boldsymbol{x}) + p'(\boldsymbol{x}, t) \quad \textbf{(14)}$$

$$\rho(\boldsymbol{x},t) = \langle\rho\rangle(\boldsymbol{x}) + \rho'(\boldsymbol{x},t) \tag{15}$$

where the statistical mean is defined as:

$$\langle\varphi\rangle(\boldsymbol{x}) = \lim_{T\to\infty}\frac{1}{T}\int_{t_0}^{t_0+T}\varphi\,(\boldsymbol{x},t)dt \tag{16}$$

And its fluctuating counterpart takes on the definition:

$$\varphi'(\boldsymbol{x},t) = \varphi(\boldsymbol{x},t) - \langle\varphi\rangle(\boldsymbol{x}) \tag{17}$$

Applying this formulation to Eqs. (9) - (11) and averaging in time, assuming for now that density is constant (ρ' = 0), the incompressible Reynolds-Averaged Navier-Stokes (RANS) equations are deduced:

$$\frac{\partial\left(\langle u_j\rangle\right)}{\partial x_j} = 0 \tag{18}$$

$$\frac{\partial\left(\rho\langle u_j\rangle\langle u_i\rangle\right)}{\partial x_j} = -\frac{\partial\langle p\rangle}{\partial x_i} + \frac{\partial}{\partial x_j}\left[\mu\left(\frac{\partial\langle u_i\rangle}{\partial x_j} + \frac{\partial\langle u_j\rangle}{\partial x_i}\right)\right] - \frac{\partial}{\partial x_j}\left(\rho\langle {u_i}'{u_j}'\rangle\right) \tag{19}$$

$$\frac{\partial\left(\rho\langle u_j\rangle\langle T\rangle\right)}{\partial x_j} = \frac{\partial}{\partial x_j}\left[\frac{k}{c_p}\left(\frac{\partial\langle T\rangle}{\partial x_j}\right)\right] - \frac{\partial}{\partial x_j}\left(\rho\langle T'{u_j}'\rangle\right) \tag{20}$$

The unsteady (d/dt) terms of the momentum and energy RANS equations are not included here, but an engineer desiring an unsteady simulation which resolves low frequency, non-turbulent motions (such as the periodic passing of a wake region) could leave these terms in the governing equations. The equations as written above allow for the solution to a statistically stationary (non-periodic) fluid flow, such as the topic of this thesis.

The so-called fundamental problem of turbulence (Wilcox 2006) is now seen in the two right-most terms in the momentum and energy equations, respectively. Before this averaging endeavor, the flow was described in a time-accurate manner by five equations and five

unknowns. Now, after the averaging process, the equations are almost identical. The main caveat is the introduction of the second-order statistics $<u_i',u_j'>$ and $<T',u_j'>$ into the transport equations, without the introduction of additional equations to facilitate their calculation. RANS turbulence modeling, thus, rests on introducing a set of algebraic and/or transport equations in order to calculate these 'turbulent stresses'. Finding such a model that satisfactorily reproduces the turbulent stresses (six independent momentum stresses and three independent thermal stresses) for a wide range of given mean flow fields has proven an excessively difficult and frustrating task to researchers world-wide.

Before diving into the subject of RANS modeling, it is worthwhile to extend the above averaging technique to variable density flows. Indeed, Reynolds averaging, as performed above, would be very inconvenient, for example:

$$\langle \rho u_i \rangle = \langle \rho \rangle \langle u_i \rangle + \langle \rho' u_i' \rangle \quad \textbf{(21)}$$

and even worse

$$\langle \rho u_i u_j \rangle = \langle \rho \rangle \langle u_i \rangle \langle u_j \rangle + \langle \rho' u_i' \rangle \langle u_j \rangle + \langle \rho' u_j' \rangle \langle u_i \rangle + \langle \rho \rangle \langle u_i' u_j' \rangle + \langle \rho' u_i{}' u_j{}' \rangle \quad \textbf{(22)}$$

Instead, a density-weighted averaging is performed:

$$\{\varphi\}(\boldsymbol{x}) = \frac{1}{\langle \rho \rangle} \lim_{T \to \infty} \frac{1}{T} \int_{t_0}^{t_0+T} \rho(\boldsymbol{x}, t) \varphi(\boldsymbol{x}, t) dt \quad \textbf{(23)}$$

such that,

$$\langle \rho u_i \rangle = \langle \rho \rangle \{u_i\} \quad \textbf{(24)}$$

$$\langle \rho u_i u_j \rangle = \langle \rho \rangle \{u_i\}\{u_j\} + \langle \rho \rangle \{u_i" u_j"\} \quad \textbf{(25)}$$

where

$$\varphi"(\boldsymbol{x}, t) = \varphi(\boldsymbol{x}, t) - \{\varphi\}(\boldsymbol{x}) \quad \textbf{(26)}$$

This leads to equations similar in form to the RANS equations for incompressible flow, including of course, the usual unclosed turbulent stresses. This method is Favre-averaging and is used for compressible flows, where solutions are sought in terms of the density weighted average variables. For simplicity, and because the mathematics remain similar (with the exception of the density-weighting), the remaining discussion will assume incompressible flow. Extension to compressible flow is simple and trivial.

2.1.4 The Boussinesq Approximation: Isotropic Eddy Viscosity

Mathematically, the simplest method for treating the unclosed turbulent stresses is the isotropic eddy viscosity approach (Boussinesq 1877), sometimes referred to as the Boussinesq approximation (not to be confused with the Boussinesq approximation of neglecting small density changes in buoyancy driven flows). The basic premise of this approach is to treat the turbulent stresses in a mathematically similar manner as the molecular stresses, i.e. ascribe to the turbulent stresses a constitutive equation in the form of Newton's viscosity law. In this way, a 'turbulent viscosity' is introduced:

$$R_{ij} = \langle u_i' u_j' \rangle = -2(\mu_t/\rho)\left(\langle S_{ij}\rangle - \frac{1}{3}\langle S_{kk}\rangle \delta_{ij}\right) + \frac{2}{3}k\delta_{ij} \qquad \textbf{(27)}$$

where the strain-rate tensor is defined as,

$$\langle S_{ij}\rangle = \frac{1}{2}\left(\frac{\partial\langle u_i\rangle}{\partial x_j} + \frac{\partial\langle u_j\rangle}{\partial x_i}\right) \qquad \textbf{(28)}$$

for incompressible flows,

$$\langle S_{kk}\rangle = \frac{\partial\langle u_k\rangle}{\partial x_k} = 0 \qquad \textbf{(29)}$$

thus,

$$R_{ij} = \langle u_i' u_j' \rangle = -2\nu_t \langle S_{ij} \rangle + \frac{2}{3} k \delta_{ij} \qquad (30)$$

(the trace of the strain-rate remains for compressible flows and Favre-averaging is used).

It is clear that this approach simplifies the situation mathematically. The six independent Reynolds stresses are expressed in terms of the mean flow field and one other variable. The mean variables are in closed form, so only the turbulent viscosity (ν_t) is needed. The physical basis for this isotropic eddy viscosity model rests in the fact that the primary effect of turbulence on a mean flow field is to increase the mixing rate (spreading) of the mean variables. In this way, the turbulence appears to cause the mean flow to act like extra viscosity has been given to its fluid medium.

The key flaw of the isotropic eddy viscosity approach is one and the same with its key asset. Certainly much simplification has been achieved by relating the Reynolds stress terms with the local strain-rate. The key error here is that the so-called turbulent viscosity is a property of the flow, not a property of the fluid. Therefore, for a given flow (especially for complex flows), the turbulent viscosity is a function of not only the present state of the turbulent flow field (not just locally, but also with neighboring effects, e.g. near walls) but also a function of the history of turbulence. Hence, the turbulent viscosity is a complicated, non-local, viscoelastic-type function of the mean flow field (Lumley 1970, Pope 1975). The linear constitutive equation given by Eqs. (27) and (30) is a vast over-simplification, but this is also its strength, that the complex interactions of turbulence can be roughly modeled so simply.

2.1.5 Prandtl's Mixing Length Formulation

The isotropic eddy viscosity approach does not directly lend an applicable turbulence model; it only simplifies a symmetric tensor with six components needing to be modeled into one single component. It is the first building-block for turbulence models; a model for this turbulent viscosity is still needed. Prandtl (1925) added the next building block with his so-called mixing-length hypothesis:

$$\nu_t = \upsilon_{mix}\lambda_{mix} \quad \textbf{(31)}$$

At first, this appears to be disadvantageous, in that one unclosed variable has been swapped for two. This issue is easily resolved by taking the mixing velocity (υ_{mix}) to be related to the mixing length (λ_{mix}) and the mean strain-rate (S_{ij}) by:

$$\upsilon_{mix} = \lambda_{mix}|S_{ij}| \quad \textbf{(32)}$$

thus,

$$\nu_t = {\lambda_{mix}}^2|S_{ij}| \quad \textbf{(33)}$$

Now, the turbulent viscosity takes on a model with a physically intuitive meaning. The effect of turbulence, according to the Prandtl mixing-length hypothesis, can be described in terms of a characteristic length scale of the flow field. This length scale is best interpreted as a geometrically imposed length scale. For example, in the inertial sub-layer of a turbulent boundary layer, the length scale is the product of the von Karman constant (κ~0.4) and the distance to the wall (y). In a side note, recent evidence suggests that the 'universal' von Karman constant is not so universal and can vary based on the type of wall-bounded flow (Smits et al. 2011, Nagib and Chauhan 2008, Marusic et al. 2010).

The key flaw of the mixing-length model follows from the flaw in the isotropic eddy viscosity approximation. Analogy to the kinetic theory of gases is typically drawn upon to legitimize the physical intuition of the mixing length model. In other words, just as the random motion of molecules in a gas produce the large scale effect of isotropic viscosity based on a characteristic length and velocity scale, so turbulent eddies can be seen in the same way. The molecular viscosity, in analogy to Eq. (31) takes the form:

$$\nu = Ca\xi \tag{34}$$

where C is a constant of order unity. The error here can be seen in view of Knudsen number analysis. The length and time scales of molecular motion are much smaller than those of the mean flow field. Hence, the molecular motion adjust instantaneously (for all practical purposes) to the flow field. Not so with turbulent eddies. In fact, integral length and time scales of turbulence are on the same order as those of the mean flow. Hence, there is strong interaction between the mean flow field and the large eddies of turbulence. Analogy to kinetic theory is flawed and so is the mixing-length model. Nevertheless, its simplicity and decent accuracy in simple flows has proven it a valuable resource in turbulence modeling. See Pope (2000) or Tennekes and Lumley (1972) for a more in-depth discussion.

2.1.6 Zero-Equation Models

With the Boussinesq and Prandtl models in hand, the simplest of turbulence models are now within reach. For a given type of flow, physical intuition and dimensional analysis can yield sensible algebraic estimates for the mixing length distribution in a flow. This is usually most practical for statistically two-dimensional flows. Such models are referred to as ‘zero-equation models’ because they do not use additional transport equations in solving for the turbulent

viscosity or mixing length. Two good examples are the Cebeci-Smith model (Smith and Cebeci 1967) and the Baldwin-Lomax model (Baldwin and Lomax 1978), both developed specifically for turbulent boundary layers. A slightly more complicated version of this approach is the Johnson-King model (Johnson and King 1985), which uses a relaxation eddy viscosity model to account for non-equilibrium effects in the turbulent boundary layer. Its use of an ordinary differential equation has earned it the description '1/2-equation model'. The non-equilibrium modification helps significantly in cases with separated flow (Wilcox 2006).

2.1.7 One-Equation Models

The limitations of the zero-equation models are severe: a physical description of the mixing length must be known a-priori, before solving for the mean flow. The use of additional transport equations can help to ease the specificity of the turbulence model and provide more general applicability. An early attempt at this approach is Prandtl's one-equation model (Wilcox 2006), which uses the transport equation for the TKE:

$$\frac{\partial k}{\partial t} + \frac{\partial\left(\langle u_j \rangle k\right)}{\partial x_j} = P - \varepsilon + \frac{\partial}{\partial x_j}\left[(\nu + \nu_t/\sigma_k)\frac{\partial k}{\partial x_j}\right] \quad \textbf{(35)}$$

where the production of TKE (P) is given by:

$$P = -R_{ij}\frac{\partial \langle u_i \rangle}{\partial x_j} \quad \textbf{(36)}$$

and the dissipation rate (ε) is given by:

$$\varepsilon = C_\mu \frac{k^{3/2}}{\lambda} \quad \textbf{(37)}$$

with the Reynolds stresses given by the Eq (30) and the turbulent viscosity given by:

$$\nu_t = C_\mu \frac{k^2}{\varepsilon} = k^{1/2}\lambda \qquad \textbf{(38)}$$

The kinetic energy transport equation can be derived by subtracting the Reynolds-averaged equations from the Navier-Stokes equations and multiplying by a fluctuating velocity to obtain the Reynolds stress transport equations (shown later). The trace is then taken to obtain a transport equation for the TKE, Eq. (35). The left hand side of the k-equation is the sum of the unsteady and advective terms (which gives the substantial derivative). The right hand side includes a source (*P*), a sink (ε) and a gradient-diffusion approximation for the turbulent transport of kinetic energy. The turbulent Prandtl number of TKE (σ_k) is typically specified near unity, with the physical argument that turbulent eddies transport TKE with the same effectiveness as momentum.

While this approach has avoided the assumption that the mixing velocity is given by Eq (32), using instead the square root of the TKE, the need for specifying a length scale distribution a-priori has not been averted. The model is still incomplete. Completeness of a model entails that no flow dependent quantities (such as a mixing length) need be specified a-priori (Pope 2000, Wilcox 2006).

In more recent times, complete one-equation models have been proposed by Baldwin and Barth (1990) and Spalart and Allmaras (1992). These models solve a single transport equation for a term closely related to the turbulent viscosity. Specific application of these models requires only the specification of pertinent boundary conditions. The Spalart-Allmaras model has proven useful in wall-bounded flows (though quite inaccurate in free-shear flows), commonly combined with an LES approach further from the wall to produce a hybrid RANS-LES approach commonly referred to as Detached Eddy Simulation (DES).

2.1.8 Two-Equation Models

While the Baldwin-Barth and Spalart-Allmaras models are the simplest complete models, they represent a departure from Prandtl's mixing length hypothesis Eq. (31). For this reason, their physical intuitiveness is less established and their overall flexibility to model a wide range of flows is diminished. In order to derive a complete model based on the mixing-length hypothesis, one needs two transport equations, of course. Thus, with appropriate boundary conditions, the model can produce two quantities, which can be combined to form a length scale and a velocity scale. Equation (35) remains a preferable method for determining a velocity scale. The two most common ways to determine a length scale is to introduce a transport equation for the dissipation rate (ε), or the specific dissipation rate (ω = ε/k). This second transport equation replaces the need for Eq. (37). The basic form of the dissipation rate equation is (Launder and Sharma 1974):

$$\frac{\partial \varepsilon}{\partial t} + \frac{\partial\left(\langle u_j \rangle \varepsilon\right)}{\partial x_j} = -C_{\varepsilon 1}\frac{\varepsilon}{k}R_{ij}\frac{\partial \langle u_i \rangle}{\partial x_j} - C_{\varepsilon 2}\frac{\varepsilon^2}{k} + \frac{\partial}{\partial x_j}\left[(\nu + \nu_t/\sigma_\varepsilon)\frac{\partial \varepsilon}{\partial x_j}\right] \quad \textbf{(39)}$$

thus the length scale is given by rearranging Eq. (37)

$$\lambda = C_\mu \frac{k^{3/2}}{\varepsilon} \quad \textbf{(40)}$$

And application of Eq. (31) leads to:

$$\nu_t = k^{1/2}\lambda = C_\mu \frac{k^2}{\varepsilon} \quad \textbf{(41)}$$

The form of Eq. (39) is not very rigorous, in fact, holds no particular relation to the form of a dissipation equation derived from Reynolds decomposition. Such a derived equation would be incredibly inconvenient to model, since dissipation occurs on the smallest of scales, whereas the

rest of the two-equation models are focused on the large scales of turbulence. Instead, it is simple to view the transport equation for dissipation rate as simply the multiplication of the k-equation by the factor ε/k, with appropriate adjustment and addition of closure coefficients ($C_{\varepsilon 1}$, $C_{\varepsilon 2}$, σ_ε). The lack of physical rigor in the dissipation equation is often cited as a leading reason for its inaccuracy, along with its use of the flawed isotropic eddy viscosity and mixing-length approximations. The combination of Eq. (35) and Eq. (39) yields the popular k-ε model. The determination of the closure coefficients as well as damping functions or two-layer treatments near walls is varied and determined by the particular form of the k-ε model used. Popular forms of the k-ε model include the standard model (Launder and Sharma 1974), the renormalization-group theory (RNG) model (Yakhot and Orszag 1986, Yakhot et al. 1992, Orszag et al. 1993), and the realizable k-ε model (Shih et al. 1995).

An alternative to the k-ε model is the closely related k-ω model, with

$$\omega = \frac{\varepsilon}{\beta^* k}, \quad \varepsilon = \beta^* k\, \omega \tag{42}$$

$$\lambda = \frac{k^{1/2}}{\omega} \tag{43}$$

$$\nu_t = k^{1/2}\lambda = \frac{k}{\omega} \tag{44}$$

As in the k-ε model above, the ω-equation is derived simply by multiplying the k-equation by the factor ω/k:

$$\frac{\partial \omega}{\partial t} + \frac{\partial\left(\langle u_j \rangle \omega\right)}{\partial x_j} = -\alpha \frac{\omega}{k} R_{ij} \frac{\partial \langle u_i \rangle}{\partial x_j} - \beta \omega^2 + \frac{\partial}{\partial x_j}\left[\left(\nu + \sigma \frac{k}{\omega}\right)\frac{\partial \omega}{\partial x_j}\right] \tag{45}$$

A second path of derivation is to start with the ε-equation, Eq. (39) ,and divide through by k. This yields Eq. (P) except for the addition of a ‘cross-diffusion’ term on the right hand side:

$$\sigma_d \frac{\partial k}{\partial x_j} \frac{\partial \omega}{\partial x_j} \quad (46)$$

Again, various types of k-ω formulations are found in open literature, with different closure methods and forms of the ω-equation. Popular k-ω models include the shear stress transport (SST) model (Menter 1992) and the Wilcox model (Wilcox 2006).

The two-equation models are complete, based on the isotropic eddy viscosity and mixing length approximations. The boundary conditions are rather easy to specify and the models perform adequately for a wide variety of flows. The lack of physical basis for the starting approximations as well as the formulations of the ε or ω equations spell the downfall of these models in more complex statistically three-dimensional flows. In addition, the problem of wall treatment remains a nuisance. Nevertheless, this class of models remains the most popular for modern application in industry and research, due to its low computational cost, relative simplicity, and broad applicability.

2.1.9 Reynolds Stress Transport Models

In the previous modeling endeavors, the Boussinesq approximation has been the basis for developing the turbulence model. A more costly turbulence model can be developed by refusing this approximation. Instead, the full set of six independent Reynolds stresses can be modeled with six transport equations. With this, of course, our turbulence model is now more costly than the solution of actual mean flow variables themselves, except that the coupling of velocity and pressure is tricky. Nonetheless, this so-called Reynolds Stress Transport (RST) model is a useful step toward more accurate turbulence modeling. The evolution of the Reynolds stresses can be derived from Navier-Stokes using the Reynolds decomposition in the same way the k-equation is

derived, except without taking the trace at the end. In fact, the k-equation is simply the trace of the Reynolds stress tensor equation:

$$\frac{\partial\langle u_i'u_j'\rangle}{\partial t}+\frac{\partial\big(\langle u_j\rangle\langle u_i'u_j'\rangle\big)}{\partial x_j}=P_{ij}-\varepsilon_{ij}+\frac{\partial}{\partial x_j}\left[\nu\frac{\partial\langle u_i'u_j'\rangle}{\partial x_j}\right]-\frac{\partial}{\partial x_k}\langle u_i'u_j'u_k'\rangle+\Pi_{ij} \quad (47)$$

with production tensor:

$$P_{ij}=-\langle u_i'u_k'\rangle\frac{\partial\langle u_j\rangle}{\partial x_k}-\langle u_j'u_k'\rangle\frac{\partial\langle u_i\rangle}{\partial x_k} \quad (48)$$

dissipation tensor:

$$\varepsilon_{ij}=2\nu\,\langle\frac{\partial u_i'}{\partial x_k}\frac{\partial u_j'}{\partial x_k}\rangle \quad (49)$$

and velocity-pressure-gradient tensor:

$$\Pi_{ij}=-\frac{1}{\rho}\langle u_i'\frac{\partial p'}{\partial x_j}+u_j'\frac{\partial p'}{\partial x_i}\rangle \quad (50)$$

Three terms of Eq. (47) are not in closed form: the dissipation tensor, the velocity-pressure-gradient tensor, and the triple-correlation gradient tensor. The dissipation tensor is assumed to be isotropic, since the dissipation happens at the smallest scales of turbulence, where the energy has had ample time to return to isotropy:

$$\varepsilon_{ij}=\frac{2}{3}\varepsilon\delta_{ij} \quad (51)$$

The dissipation is then modeled with a transport equation as in the two-equation models, such as Eq. (39). The velocity-pressure-gradient tensor is commonly split into the pressure-rate-of-strain tensor and a pressure-transport term:

$$\Pi_{ij}=\langle\frac{p'}{\rho}s_{ij}'\rangle-\frac{1}{p}\frac{\partial}{\partial x_k}\big(\langle p'u_i'\rangle\delta_{jk}+\langle p'u_j'\rangle\delta_{ik}\big) \quad (52)$$

The first term on the right hand side of Eq. (53) the pressure-strain-rate correlation tensor, is the chief modeling difficulty in the RST model. The second term of (53) ,the pressure-transport term, is lumped in with the turbulent transport term (triple-correlation gradient) and treated with an anisotropic gradient diffusion hypothesis (Daly and Harlow 1970):

$$-\frac{\partial}{\partial x_k}\langle u_i' u_j' u_k' \rangle - \frac{1}{\rho}\frac{\partial}{\partial x_k}\left(\langle p' u_i' \rangle \delta_{jk} + \langle p' u_j' \rangle \delta_{ik}\right) = C\frac{k}{\varepsilon}\langle u_k' u_l' \rangle \frac{\partial \langle u_i' u_j' \rangle}{\partial x_l} \qquad (53)$$

The chief focus is on the pressure-strain-rate correlation, which serves to redistribute TKE between velocity components. The commonly used Launder-Reece-Rodi model with isotropization of production (LRR-IP) (Launder et. al. 1975) models this term with a combination of Rotta's linear return to isotropy model (Rotta 1951) and the isotropization to satisfy the rapid distortion theory (RDT) limit:

$$\langle \frac{p'}{\rho} s_{ij}' \rangle = -1.8\frac{\varepsilon}{k}\left(R_{ij} - \frac{1}{3}R_{kk}\delta_{ij}\right) - \frac{3}{5}\left(P_{ij} - \frac{1}{3}P_{kk}\delta_{ij}\right) \qquad (54)$$

While the RST models certainly offer a more detailed approach that is generally more accurate than a two-equation model, the increase in fidelity given by RST is hindered by difficulties in modeling the pressure-strain-rate redistribution term as well as the lingering need for a dissipation equation. For these reasons, more expensive RST has not drawn the popular use that the two-equation models have enjoyed.

2.1.10 Algebraic Stress and Non-linear Models

A compromise between RST and two-equation models is offered by algebraic stress models and non-linear two-equation models. The algebraic stress model is built from the above RST equations, except that the terms containing derivatives of the Reynolds stresses are simplified to algebraic expressions via:

$$\partial\langle u_i{'}u_j{'}\rangle = \frac{\langle u_i{'}u_j{'}\rangle}{k}\partial k + k\,\partial\left(\frac{\langle u_i{'}u_j{'}\rangle}{k}\right) \approx \frac{\langle u_i{'}u_j{'}\rangle}{k}\partial k \quad \textbf{(55)}$$

The Reynolds stress equations then reduce to (Pope 2000):

$$\frac{\langle u_i{'}u_j{'}\rangle}{k}(P-\varepsilon) = P_{ij} - \frac{2}{3}\varepsilon\delta_{ij} + \langle\frac{p'}{\rho}s_{ij}{'}\rangle \quad \textbf{(56)}$$

With an appropriate pressure-strain-rate model (e.g. LRR-IP), Eq. (Y) gives an implicit non-linear algebraic expression relating the Reynolds stresses to k and ε. By merging these expressions with a two-equation model, an algebraic stress model (ASM) is created. The advantage of the ASM approach is that only two transport equations are needed but the isotropic eddy viscosity assumption is not needed. However, in strongly inhomogeneous flows, the assumption regarding the transport terms becomes inaccurate. As far as computational cost, the solution to the algebraic system of equations is difficult and the benefits gained over the RST model are minimal in this regard (Pope 2000).

Working on the same idea, non-linear eddy viscosity models gives much more cost benefits than ASM while also managing to overcome some of the short-comings of the (linear) isotropic eddy viscosity approach. Lumley (1970) and Pope (1975) laid the groundwork for the non-linear approach, which assumes the Reynolds stresses are a local function of both the strain-rate and the rotation:

$$\langle u_i{'}u_j{'}\rangle - \frac{2}{3}k\delta_{ij} = fn(\langle S_{ij}\rangle, \langle\Omega_{ij}\rangle) \quad \textbf{(57)}$$

The Cayley-Hamilton theorem allows for a finite expansion of Eq. (57). Quite a few terms exist in the fully expanded constitutive equations, each term having its own tunable coefficient (Shih and Lumley 1993). In statistically two-dimensional flows, not nearly as many terms

remain (Pope 1975). However, a useful model is sought in three dimensions. Such a model can be generated by truncating the finite expansion after the first few terms (Shih et al. 1998). Algebraic stress models may be used to derive non-linear models as well (Pope 2000).

Non-linear and algebraic stress models provide means of escape from the ill-fated Boussinesq approximation while avoiding the high cost of RST models. Improvements in prediction are seen in flows with secondary motions caused by anisotropic stresses (flow in a non-circular duct), flows with streamline curvature, and strongly rotating flows.

2.1.11 Turbulent Heat Fluxes

The energy equation equivalent of the Reynolds stresses in the momentum equations, the turbulent heat flux $Q_{ij} = \langle u_i'T' \rangle$ also needs a model. Generally, this problem is solved quite easily once an appropriate turbulence model is used for the Reynolds stresses. A turbulent Prandtl number is used to directly relate the turbulent thermal diffusivity to the turbulent viscosity. Then a simple gradient diffusion assumption fills out the energy equation.

$$Q_i = \langle u_i'T' \rangle = -\alpha_{th,t} \frac{\partial \langle T \rangle}{\partial x_i} = \frac{-\nu_t}{Pr_t} \frac{\partial \langle T \rangle}{\partial x_i} \quad \textbf{(58)}$$

In the case of non-linear models, a finite expansion may also be formed for the thermal stresses, and a non-linear algebraic formulation can be made for the turbulent heat flux as well as the Reynolds stresses (Shih et al. 1998, Shih and Lumley 1993).

2.1.12 Large Eddy Simulation

For Large Eddy Simulations, the RANS equations are rejected in favor of spatially filtered equations. Instead seeking a time-averaged flow-field, a time-accurate spatially-filtered simulation is performed. This allows for the direct simulation of large, influential eddies while

leaving the small, less energetic eddies to a subgrid-scale (SGS) model. Of course, the SGS models are typically much simpler than the popular RANS models, since they are much less important and the cost of LES is already high due to its time-accurate nature.

The Navier-Stokes equations are spatially filtered by applying the filtering operation:

$$\bar{\varphi} = \int_{-\infty}^{\infty} G(\boldsymbol{x}, \boldsymbol{r}, t)\varphi(\boldsymbol{x} - \boldsymbol{r}, t)dr \quad \textbf{(59)}$$

where the filter is normalized by:

$$\int_{-\infty}^{\infty} G(\boldsymbol{x}, \boldsymbol{r}, t)dr = 1 \quad \textbf{(60)}$$

Applying an homogenous filter G(**r**) to the incompressible Navier-Stokes equations:

$$\frac{\partial \bar{u}_j}{\partial x_j} = 0 \quad \textbf{(61)}$$

$$\frac{\partial(\bar{u}_i)}{\partial t} + \frac{\partial\left(\bar{u}_j\bar{u}_i\right)}{\partial x_j} = -\frac{1}{\rho}\frac{\partial \bar{p}}{\partial x_i} + \frac{\partial}{\partial x_j}\left[\nu\left(\frac{\partial \bar{u}_i}{\partial x_j} + \frac{\partial \bar{u}_j}{\partial x_i}\right)\right] - \frac{\partial}{\partial x_j}B_{ij} \quad \textbf{(62)}$$

$$\frac{\partial(\bar{T})}{\partial t} + \frac{\partial\left(\bar{u}_j\bar{T}\right)}{\partial x_j} = \frac{\partial}{\partial x_j}\left[\alpha_{th}\left(\frac{\partial \bar{T}}{\partial x_j}\right)\right] - \frac{\partial}{\partial x_j}q_{ij} \quad \textbf{(63)}$$

where residual, or subgrid, stresses appear:

$$B_{ij} = \overline{u_i u_j} - \bar{u}_i\bar{u}_j = -2\nu_{SGS}\bar{S}_{ij} + \frac{2}{3}k_{SGS}\delta_{ij} \quad \textbf{(64)}$$

$$q_i = \overline{u_i T} - \bar{u}_i\bar{T} = -2\alpha_{th,SGS}\frac{\partial \bar{T}}{\partial x_i} \quad \textbf{(65)}$$

The fundamental problem of turbulence modeling remains because of these unclosed stresses, but now they are much less influential, since they only represent the effect of the unresolved eddies. Equations (64) and (65) of course, represent the isotropic subgrid-scale

viscosity assumption and gradient subgrid-scale diffusion assumption, respectively. These simplifications are almost always used for LES.

It is worth noting that in practical implementation of LES, the filter operation is actually implemented implicitly by the grid:

$$G(\boldsymbol{x},\boldsymbol{r}) = \begin{cases} \dfrac{1}{\Delta_f(\boldsymbol{x})} & if \quad |r| \le \Delta_f(\boldsymbol{x}) \\ 0 & otherwise \end{cases} \tag{66}$$

where Δ_f is the characteristic length of the cell volume (i.e. the cube root of the cell volume).

Thus, for engineering applications, where a non-uniform grid is necessary, the filtering operation on the Navier-Stokes equations does not quite simplify to Eqs. (61)-(63). Extra terms remain involving the gradient of the filter, grad(G). Thus, an error in the governing equations is incurred from the outset in LES, but this error can be kept small by designing a grid with low stretch ratios (van der Bos and Guerts 2005).

Using the filter width as the length scale for the mixing-length formulation (Eq. E), the Smagorinsky SGS model is formed (Smagorinsky 1963):

$$\nu_{SGS} = C_s {\Delta_f}^2 \left|S_{ij}\right| \tag{67}$$

where C_s is the Smagorinsky constant, theoretically between 0.15-0.2 for homogeneous flows, but often set to 0.1 (Pope 2000) for best results on a wide variety of flows. Used in conjunction with a subgrid-scale Prandtl number,

$$\alpha_{th,SGS} = \frac{\nu_{SGS}}{Pr_{SGS}} \tag{68}$$

Germano et al. (1991) devised a scheme for dynamically calculating the value of the Smagorinsky constant (C_s) using information from the resolved scales. The formulation applies

a test filter (with twice the filter width of the grid filter) to find the constant. Lilly (1992) applied a least-squares minimization to the mathematically over-defined system to find the C_s. Ghosal et al. (1995) perceived a mathematical flaw in the formulation, developed a more general approach as well as a method of localizing the formulation. This complicated method is not necessarily needed, as *ad hoc* measures can be taken to stabilize the dynamic formulation in a local manner. Moin et al. (1991) derived the compressible form of Germano's procedure, as well as providing a dynamic procedure for calculating the SGS Prandtl number. Even more accurate SGS models can be derived using the Leonard stresses and scale-similarity (Bardina et al. 1980, Vreman et al. 1997). Also, one-equation models can be used to solve for the SGS kinetic energy and bring transport terms into consideration in the turbulent model. For practical engineering calculations, however, the dynamic procedure first devised by Germano has proved the most practical, as numerical effects from the grid and discretization scheme counteract the accuracy of refined SGS models.

2.1.13 Other Approaches

Another approach which has received much attention in the past decade is the so-called Detached Eddy Simulation (DES). This approach recognizes that, near walls, the separation between large eddies and dissipative eddies is not a great, hence, a fully resolved LES in the near-wall region would approach DNS and the expense thereof (Spalart et al. 2006). DES attempts a hybrid RANS-LES model, where RANS methods are applied near the wall while LES is applied away from the wall. Blending and interface problems have made this approach highly research and increasingly complicated in recent years.

Another approach is to derive transport equations for the probability density functions of flow variables. This approach is used most heavily to model chemistry interactions in LES of reacting flows (Pope 2000). Finally, it is the author's opinion that fractional calculus could provide another powerful means of modeling turbulence due to its non-locality properties and its well-known application in viscoelastic modeling (Bagley and Torvik 1983).

2.1.14 Discretization

The present thesis is focused on the finite volume method (FVM) for computational fluid dynamics (CFD). In FVM, the computational domain is split into small control volumes on which the basic conservation equations can be written (conservation of mass, momentum, and energy) using the divergence theorem. These equations rely on values on the boundary faces between two volumes, which must be found as a function of the neighboring cell-center values. This interpolation process is the basis of the numerical approximation scheme for FVM-CFD. While second-order interpolation (linear interpolation between the two cell center values) is the simplest form, many CFD applications, especially at low resolutions introduce biased interpolation schemes toward the upwind direction. This introduces additional diffusion into the solution, which is highly undesirable in the context of LES.

Breuer (1998) varied spatial discretization schemes, sub-grid model and spatial resolution in studying the solid cylinder in crossflow problem using LES. Recall that this scenario is only vaguely similar to the JICF film cooling scenario, as shown by Fric and Roshko (1994). Breuer used a predictor-corrector Runge-Kutta scheme for temporal discretization because of its reduction in computing time. For spatial discretization, he used a total of five different techniques, both upwind and central differencing techniques. Based on comparison with

experimental results, he determined that the central differencing techniques outperformed the upwind techniques. He showed insignificant differences between second- and fourth-order central difference discretization. He reasoned that the central differencing techniques were more accurate because of the flows high dependence on downstream conditions. In this respect, his conclusions seem to apply to film cooling scenarios as well. In comparing LES with no sub-grid scale model, with simulations using constant and dynamic Smagorinsky models, Breuer concluded that only a small benefit was gained by the use of more complicated sub-grid models. This conclusion fits less with film cooling flows because of the more complicated, three-dimensional nature of the JICF interactions. Finally, he concluded that only the dynamic sub-grid scale model showed noticeable improvements with grid refinement, emphasizing spanwise refinement especially. While providing insight into the considerations of LES for the solid cylinder in crossflow, the conclusions of this paper should be taken lightly when the film cooling problem is considered.

Meinke et al. (2002) provided more insight in the computational approach when using LES. Two different discretization schemes were utilized in the study of a turbulent channel flow and planar jet: a second-order upwind scheme and a sixth order compact scheme. The effect of sub-grid scale was also studied: no model versus dynamic model. The sub-grid scale model is shown to have less important than the spatial resolution of the grid (filter width). The second-order scheme keeps pace with the sixth-order scheme in accuracy while requiring less computer resources. It should be emphasized that neither then channel nor jet fully compare with the film cooling scenario, in which shear and wall bounded flows are combined. For this reason, the

results again should not be taken too heavily for application to film cooling, though along with (Breuer 1998), provide excellent insight into the importance of discretization in LES.

2.1.15 Iterative Solution

Once the conservation equations are constructed and stacked into a sparse matrices, iterative methods are employed to solve these matrices in succession (for a segregated pressure-velocity coupling). Two popular segregated schemes are the SIMPLE and PISO algorithms. Each matrix is solved (in this thesis) using a multi-grid method in which successive coarsening and refinement is used on the base grid to solve smaller matrices to obtain initializations for the larger matrices. The Gauss-Seidel method is used for the solution of matrices.

In SIMPLE, the mass conservation equation is reposed as a Poisson equation for pressure by substituting the momentum equation into the mass equation. The first step is a momentum predictor, in which the three momentum equations are solved in succession given the conditions from the previous iteration. Next, the pressure Poisson equation enforces mass conservation. Finally, any additional equations such as energy of turbulence quantities are solved in succession before progressing to the next step. Relaxation is typically applied to each equation for iterative methods.

The PISO (Pressure-Implicit Splitting of Operators) algorithm is similar to SIMPLE, but often employed for unsteady simulations. For this method, the momentum predictor steps and pressure correction are used as in SIMPLE. In PISO, however, multiple pressure corrections are used (hence, Pressure Implicit). Then the remaining equations (energy, turbulent kinetic energy, etc…) are then solved before moving to the next time step. This method, is often used in conjunction with fine temporal resolution and explicit or semi-implicit temporal schemes.

If the unsteady simulation has stability issues, a combination of SIMPLE and PISO can be used (the PISO-SIMPLE or PIMPLE method). This is the method used in the LES in the thesis. Here, the momentum predictor is solved followed by multiple pressure corrections (as in PISO). Then, without advancing to the next time step, the solution is iterated with more rounds of momentum predictors and pressure corrections. This can be iterated until satisfactory convergence patterns are observed.

2.2 Film Cooling

In this section, a quick tour of the basic advances in film cooling technology is presented. This review is by no means thorough, with the availability of literally thousands of research papers in open literature on film cooling.

2.2.1 Experimental Film Cooling

Prior to the 1950s, film cooling was relatively unrepresented in the open literature. In a similar technique, (Wieghardt 1946) studied the de-icing of airplane wings using an injection of heated air from discrete circular jets. Film cooling studies sparsely populated the literature in the 1950s, and first exploded onto the research scene in the 1960s with focus mostly on continuous slot injection. Goldstein (1971) provides a robust review of the film cooling research available published in this time period. The two approaches taken in these early efforts were theoretically derived correlations and experimental measurements.

The early work in theoretical correlations for film cooling effectiveness was for the most part constrained to two-dimensional analysis (Goldstein et al. 1971). Two-dimensional film cooling refers to a coolant ejected from a continuous slot, such that the flow is statistically homogeneous

in the spanwise direction. Most correlations used heat sink model relying on boundary layer mass and energy balances. These analytical approximations predicted film cooling as a function of coolant hole Reynolds number, the dimensionless parameter x/Ms, as well as fluid properties such as viscosity, specific heat, and Prandtl number. Analytical correlations were impressively adept at film cooling predictions in the continuous slot cases. Early experimental work, as reviewed by (Goldstein 1971), also focused mostly on continuous slot film cooling. Continuous slot film cooling, however, became recognized as an unrealistic solution because of the structural compromises necessary for the implementation of these geometries in gas turbine components. The analytical approaches to film cooling were destined for obscurity in the case of three-dimensional film cooling, that is, film cooling from discrete holes.

Starting around the 1970s, the experimental focus shifted to discrete hole film cooling. Goldstein et al. (1968) reported film cooling effectiveness values for a single cylindrical hole, inclined at an angle with the crossflow. These results were compared to a row of cylindrical holes in (Goldstein et al. 1970). Eriksen and Goldstein (1974) contributed heat transfer coefficient enhancement data for cylindrical hole film cooling. Goldstein et al. (1974) studied holes with expanded exits. These studies mostly focused on the centerline effectiveness values, measured by thermocouples. The expanded exits were shown to decrease the effective blowing ratio, resulting in higher effectiveness values. In addition, increase lateral spreading, an important consideration in discrete hole film cooling, was also observed from the expanded-exit holes. Another conclusion of Goldstein et al. (1974) is that, while blowing ratio is the most important flow parameter for continuous slot configurations, the momentum flux ratio is more important in discrete hole configurations because of the tendency of the jet to lift off the wall.

Pedersen et al. (1977) presented the effects of the density ratio on film cooling effectiveness from cylindrical holes. The large density ratios of this study were achieved using foreign gases injected into a mainflow of air. Effectiveness values were measured using the heat-mass transfer analogy, which eliminates conduction errors. Other significant density ratio studies include Pietrzyk et al. (1990) and Sinha et al. (1991) at the University of Texas. In Pietrzyk's study, the film cooling flow is characterized for various density ratios. This was followed in Sinha's investigation with the characterization of film cooling effectiveness values for different density ratios, using a thermally resistive plate to damp out conduction errors and an arrangement of thermocouples to ascertain laterally-averaged effectiveness values as well as the traditional centerline values.

Perhaps the most studied effect on film cooling has been the geometry of the discrete holes. Many variations departing from the cylindrical holes have been studied. Initially, Goldstein et al. (1974) showed the benefits available by means of an expanded exit. One variation on expanded holes, the fan-shaped hole, has been extensively studied, as reviewed by Bunker (2005). Another notable version of an expanded hole is the conical shaped hole (Cho et al 1999, Taslim and Ugarte 2004, and Zuniga 2006), among others. The benefits of expanded hole exits are well known (Bunker 2005).

Another means of increasing film cooling efficiency has been the introduction of the compound angle holes (Ligrani et al. 1994a,b, Sen et al. 1996, Schmidt et al. 1996, Ekkad et al. 1997a,b, Goldstein and Jin 2001, to name a few). Ligrani et al. studied the flow structure from two different configurations of compound angle holes: two staggered rows with three diameter pitch and one row with six diameter pitch. Sen et al. and Schmidt et al. studied the heat transfer

coefficient enhancement and adiabatic effectiveness results from various geometries and various compound angles. Ekkad et al. applied a transient liquid crystal technique to measure the heat transfer and effectiveness results from compound angle injection. Goldstein and Jin applied a naphthalene sublimation technique to measure heat transfer coefficients for compound angled holes via the heat-mass transfer analogy. Each of these studies reported significant benefits of the compound angle on the film cooling coverage.

Embedding a coolant hole in a spanwise trench has been introduced by Bunker (2001, 2002). More complete studies of various geometrical parameters associated with trenched film cooling have been completed (Lu et al. 2005, Waye and Bogard 2006, and Zuniga 2009). The trenched configuration creates an impingement-like effect of the coolant jet on the inside wall of the trench, taking momentum out of the coolant jet and allowing it to more easily attach to the downstream surface while maintaining higher blowing ratios.

2.2.2 Jet-in-Crossflow

The studies above have focused on the steady, time-averaged features of film cooling scenarios: heat transfer coefficient, adiabatic effectiveness, and various flow features. Another class of studies has focused on the various steady and unsteady flow structures in the general jet-in-cross-flow (JICF) scenario. These studies, though not immediately applicable to turbine film cooling, give added insight into the fluid dynamics influencing film cooling flows.

Scorer (1958) is considered the first to recognize what is now known as the counter-rotating vortex pair (CVP) or kidney-vortices. He introduced the idea of the CVP development in the interaction between a jet and crossflow. A large number of papers studied the intricate and complicated interactions that accompany the dominant CVP in a JICF situation. A few key

studies include (Fric and Roshko 1994, Kelso et al. 1996, and Haven and Kurosaka 1997). Fric and Roshko focus primarily on the upright tornado-like vortices formed in the wake of the jet. The important insight from this study was the fundamental differences between the wake vortices in the JIFC scenario and the classic solid cylinder in crossflow. Kelso et al. provided a complete overview of all the vortex systems present in the JICF interaction while adding more insight through flow visualization techniques. Haven and Kurosaka explored the CVP (or kidney vortices) in depth using laser-induced fluorescence (LIF) and particle image velocimetry (PIV), proposing a two-layer schematic to explain the various forms of the CVP. While these studies focused on scenarios outside the immediate realm of turbine film cooling, their conclusions shed light on the unsteady interactions that would be expected in a discrete film cooling flow.

2.2.3 Numerical Film Cooling

Alongside the numerous experimental studies regarding film cooling for gas turbines and general JICF, the recent advances in computing resources has given rise to powerful numerical techniques in predicting film cooling flows without the need for expensive experimental setups. Historically, most film cooling simulations have been performed with a RANS time-averaged approach with empirical turbulence models. A good example of RANS film cooling study was published in a four part series by researchers at Clemson University (Walters and Leylek 2000, McGovern and Leylek 2000, Hyams and Leylek 2000, Brittingham and Leylek 2000). This series looked at both cylindrical and shaped holes, with and without a compound angle. The study focused on the steady flow features, but also compared cooling effectiveness distributions to experimental results, with somewhat disappointing agreement despite a carefully constructed systematic approach.

Complicated corrections to the k-ε model have been proposed to correct the poor predictive capability of RANS two-equation models. Anisotropy and turbulent Prandtl number corrections yielded better results for the spreading of the coolant film (Azzi and Lakehal 2002). The improvement of prediction was merely a surface effect, however, as the cross-sectional temperature profiles presented in this study proved strange and unphysical. The use of non-linear two-equation models (on par with algebraic stress models) did not yield significant improvements over the standard isotropic eddy diffusivity models (Shyam 2011).

Acharya et al. (2001) presented a robust study of numerical solutions to cylindrical film cooling flows. They employed seven two-equation turbulence models alongside the RANS equations, comparing the results with experimentally determined values. Following the RANS computations, Large Eddy Simulations (LES) and Direct Numerical Simulations (DNS) were performed for the same geometry. The subsequent comparisons with experimental data suggested the ability of LES to predict the lateral spreading of film cooling jets more accurately than even the best of the RANS models. Harrison and Bogard (2008) also showed convincingly that the RANS isotropic eddy viscosity models fail to predict the lateral spreading, though either the centerline or laterally-averaged effectiveness values can be matched depending on the specifics of the model. The open literature contains other documentation of the inaccuracies of RANS approaches (Leylek and Zerkle 1994, Walters and Leylek 1997, Hoda and Acharya 2000, Heidmann and Ekkad 2007, Li 2010, Natsui et al. 2011, to mention a few). Tyagi and Acharya (2003) further displayed the utility of LES in presenting detailed time-dependent flow fields in a cylindrical film cooling scenario. They resolved a dominant coherent ‘hairpin’ vortex which united the CVP, wake vortices, and roller vortices (or shear layer vortices). This study only

reported centerline effectiveness results, however, so the question of LES being able to better predict the spreading of the jet went unanswered.

In summary, film cooling research before the 1970's focused mainly on continuous slot cooling because of the two-dimensional nature that made it easy to predict. Starting with Goldstein's 1968 paper studying a single cylindrical film hole, discrete hole quickly became a popular research topic and has grown worldwide up to the present. The controlling parameters such as velocity ratio, density ratio, mass flux ratio (or blowing ratio), and momentum flux ratio have been studied for a large variety of geometries. The important geometrical advances in discrete film cooling can be classified as expansion (or diffusion-shaped) holes, compound angle holes, and trenched (or masked) holes. Numerous studies, such as have emphasized the influence of the CVP, as well as other steady and unsteady flow structures in determining the effectiveness of a particular film cooling design. Computational predictions of film cooling using RANS equations and empirical turbulence equations have shown a certain inability to correctly characterize the flow field, though they certainly are of some worth in gaining insight into film cooling performance. LES predictions, however, have promise for more accuracy and insight regarding the near field flow interactions in a JICF scenario.

CHAPTER 3 STATE OF THE ART REVIEW

The cylindrical film hole predictions of Tyagi and Acharya (2003) was, to the knowledge of the author, the first use of Large Eddy Simulations in the context of film cooling. Because of the rather small domain needed to simulate one film hole, the usual barriers of computing resources were smaller in this particular field. In constructing a numerical approach using LES, a number of considerations are important, including but not limited to: filter width/grid resolution (eddy size defining which eddies are fully resolved and which are modeled), extent of the numerical domain, inlet velocity profile boundary conditions, discretization scheme (temporal and spatial), sub-grid scale model, grid structure, time step size, and compressibility of flow.

Having reviewed LES studies comparing solution techniques in the discretization section above, the focus is now turned to film cooling simulations that have been documented in open literature. The first significant LES of film cooling is the previously mentioned cylindrical hole simulation of Tyagi and Acharya (2003). A dynamic mixed model (DMM) was used for the sub-grid scale eddies, with incompressible treatment of the fluids. The spatial discretization scheme in this study was for the most part fourth-order central difference, with some deviation for specific terms. Temporal discretization is accomplished with an explicit second-order Adams-Bashforth scheme. A $1/7^{th}$ power law is used to specify the mainflow inlet velocity profile in accordance with experimental measurements and enhanced with a Gaussian random number generator to simulation incoming turbulence. No coolant plenum is modeled, but a RANS determined boundary condition is placed at the inlet to the coolant delivery tube (cylindrical, with M=1.0). This inlet condition was mapped from a RANS solution which included the plenum. Despite the fact that this method may capture the mean velocity well, the unsteady

separation events at the inlet to the flow cannot be captured this way, so the plenum-fed film cooling is not well-modeled in this study. The mainflow is modeled to a height of 4 diameters above the cooled surface, and the grid seems to have contained between 1-2 million cells. Agreement with time-averaged experimental velocity and temperature measurements is questionable at times near the wall and the comparisons are only made for a limited number of line probes in the flow. The ability of the LES predictions to replicate experimental data is questionable at best. Iso-surfaces of the pressure laplacian are used to discover the unifying 'hairpin' coherent vortex pattern, which is transient in nature. Transient wall temperatures are correlated with the unsteady nature of the hairpin vortices. Despite the apparent insight of this paper, the attempt to connect the hairpin structure with structures observed by (Fric and Roshko 1994, Kelso et al. 1996, Haven and Kurosaka 1997) is unconvincing. The placement of the upright wake vortices above the CVP is in direct disagreement with the structure shown by these papers. In reality, the existence of neatly ordered hairpin vortices remaining intact several diameters downstream seems an unrealistic outcome of poor inlet boundary conditions and poor resolution for the coolant flow. Another limitation of this study is that no parameters are varied, with the exception of the length of the delivery tube and blowing ratio (but these are not varied independently).

Iourokina and Lele (2006a,b) and Peet and Lele (2008) developed a coupled LES code, combining both compressible and incompressible codes in the same film cooling problem. A large coolant plenum was modeled, but the mainstream was modeled to only two diameters above the cooled surface. The compressible flow is used for the mainstream crossflow but not for the coolant hole, which has a velocity of 0.737 times the mainstream (M=0.7). The

compressible code uses a fourth-order central difference scheme, while the incompressible code uses a second-order central differencing scheme. Temporal discretization is accomplished with a second-order Crank-Nicholson scheme. The sub-grid model was the dynamic Smagorinsky model. An auxiliary boundary layer flow LES domain is used to determine time-dependent inlet boundary conditions with appropriate turbulence levels, based on the method of (Lund et al. 1998). Because of the inclusion of the plenum, the flow in the coolant hole is much more unsteady and chaotic than shown by the simulations of Tyagi and Acharya (2003). This is one factor that leads to a more disorganized wake downstream of the coolant hole. The time-averaged centerline effectiveness results, however, are strangely uneven and compare less favorably than Tyagi and Acharya (2003) with experimental data from Sinha et al. (1991). The less favorable disagreement can be explained by different density ratios and coolant hole lengths, but the uneven effectiveness remains peculiar. These studies are limited by the fact that no geometrical or flow parameters are varied, such that no insight into design trends can be accomplished. The code is also very specialized and complicated, not lending itself to broader applications or studies.

Leedom and Acharya (2008) presented Large Eddy Simulations for three different geometries: cylindrical, laterally-diffused, and converging slot hole (or console). Using a numerical scheme similar to that of Tyagi and Acharya (2008), except that inlet turbulence is completely neglected and a steady mainflow velocity inlet is prescribed using the $1/7^{th}$ power law approximation. A "grid independence study" is performed over four grid sizes: one, two, four, and eight million cells. The four million cell domain is decided to give a converged solution (less than 3% discrepancy with the eight million cell domain) with respect to grid size,

though little evidence is shown to support this conclusion. A sufficient plenum is included in the domain and the results are compared mostly on a time-averaged basis. The superiority of the console geometry is upheld. It is also shown that the CVP is severely weakened by the console's production of the (unsteady) anti-kidney upper deck vortex pair described by Haven and Kurosaka (1997). While representing an intriguing comparison of various hole geometries with LES solutions, the paper complicates the results by adding crossflow to the plenum. No reasons are provided for the seemingly arbitrary choice of geometries.

Guo (2006) and Renze et al (2008a-b) also perform LES of cylindrical film cooling. Guo et al. simulated film cooling for perpendicular and angled injection. Renze et al. used the heat-mass transfer analogy to study density ratio effects of film cooling using Large Eddy Simulation. Like (Meinke et al. 2002), the upwind second-order AUSM discretization scheme is implemented (that which performed well for the planar jet simulation). A 5-step explicit Runge-Kutta method is employed for temporal discretization. Like Iourokina/Peet and Lele (2006a-b, 2008), an auxiliary simulation is simultaneously solved to provide time-dependent velocity profiles to the mainstream inlet (Lund et al. 1998). A sufficient plenum is included to properly simulate the coolant flow, with a hole length of 12.5 diameters. The grid consists of 5.65 million cells and the mainstream extends to seven diameters above the cooled surface. The incompressible Navier-Stokes equations are applied throughout the domain (Ma=0.2). The coolant flow is varied between low velocity ratios of 0.1, 0.28, and 0.48. CO_2 is used to generate a density ratio of 1.53, whereas air gives a simple density ratio of unity. Agreement with time-averaged velocity and temperature experimental results (using PIV and data from Sinha et al. 1991) is impressive. Velocity ratio is determined to be the highest influencing factor over

density ratio or other parameters. Results are also shown in terms of realizability and the Lumley triangle, showing the state of the incoming boundary layer and the much more chaotic turbulence states in the recirculation region downstream of the hole.

In a subsequent study, Renze et al (2008c) used LES for the trenched hole geometry. The same numerical approach was used as in his previous works, with the exception of the heat-mass transfer analogy, which is foregone here in favor of a temperature difference and straight-forward heat transfer and temperature calculations. LES proves to provide excellent insight into the instantaneous profiles as well as accurate time-averaged solutions for the trenched hole case, though the discussion and post-processing is limited in this study.

A final, less related study was performed by Renze et al (2009), in which they studied a compact array of fan-shaped coolant holes, presumably for the application to a combustor liner. The interactions and growth of the boundary layer is discussed in detail. A staggered array led to a cancelling of the CVP and improved effectiveness.

The current state of the art in Large Eddy Simulations of film cooling desires a more comprehensive study of hole geometries, including the three main variations in geometry from the simple cylindrical hole: expanded exit, compound angle, and transverse trench. While much focus in the available studies focuses on time-averaged results, more focus can be placed on comparing instantaneous (unsteady) flow field interactions and their effects on the overall effectiveness. Also, mostly low blowing ratios have been simulated, none venturing into higher blowing ratios where cylindrical holes tend to lift away from the surface dramatically and the benefits of other hole shapes are most notable.

CHAPTER 4 PROBLEM DEFINITION

4.1 Problem Statement

4.1.1 General Problem

The needs of modern society for electrical power and air travel are quite evident. More specifically, there is a constant push to develop more efficient means of energy usage. The gas turbine engine continues to be a key machine in the electrical power production and aircraft propulsion fields. Like other similar technologies, scientific and engineering research has led to constant advancements in the efficiency of the gas turbine engines. One of the primary means of improving gas turbine efficiency is increased combustion firing temperature. Today's engines have firing temperatures well in excess of the melting point of the engine components. In addition to the advances in materials, such as high temperature super-alloys and ceramic thermal barrier coatings, convective cooling has also brought about important advances in this arena. One such method is film cooling, which protects the inner surfaces of the turbine which would otherwise be exposed to the extreme temperatures of the hot gas path.

The designer for film cooling must be mindful of a careful balance. As more coolant is taken out of the compressor stage of the engine and used for film cooling, the efficiency of the turbine is lowered. That is, some of the input work in compressing the intake air is being used simply to cool the turbine components without contributing anything to the output work. In fact, film cooling causes minor aerodynamic losses in the turbine expansion flow. In addition, the overuse of coolant flow may cause coolant lift-off in some injection geometries, leading to vastly reduced effectiveness values. On the other hand, as less coolant is supplied for film cooling, the

effectiveness of the coolant in protecting the metal components can limit the life of the components or the turbine inlet temperature, which limits the ideal Brayton cycle efficiency of the engine. Therefore, there is a need for careful consideration in the optimization of the effects of film cooling on overall engine efficiency. As a result, the flow characteristics, film cooling effectiveness, and aerodynamic performance of film cooling flows must be understood in as great detail in order to equip designers with as much knowledge as possible in designing gas turbine engines for higher efficiencies.

4.1.2 Specific Problem

While early film cooling designs incorporated a continuous slot injection, these ideas were found to be too harmful to the structure of the metal component. From this, the idea of discrete hole film cooling arose, first with cylindrical holes, then with a number of geometrical variations. Popular geometries such as expanded exit holes, compound angle holes, and trenched holes have each been studied experimentally, with time-averaged effectiveness and heat transfer results reported.

Experimental studies of the unsteady interaction of a JICF scenario have shown extensive complexity in the vortical structures. These complex vortical dynamics have been initially linked to the mixing characteristics of the JICF as well as the effectiveness of a film cooling injection. The further investigation of the vortical interactions of film cooling flows and their influence on the effectiveness of the film in cooling the surface could not only provide designers with more insight into the dynamics of film cooling, but also could lead to a better understanding for designing new or optimized hole geometries for film cooling.

With rapid advancements in computing technology, computational fluid dynamics has risen as a powerful tool in the design and optimization process. Fluid flows, however, have proven extremely difficult to model accurately. A major reason for this difficulty is the intricacy of turbulence in complex flows. While RANS models have been shown to be of questionable accuracy in film cooling predictions, Large Eddy Simulations have shown early promise in quality prediction as well as insight into the unsteady phenomena occurring in a JICF scenario. Because of the numerical complexity and intensity of LES, great care must be taken in the method of solution. Grids must be generated with caution in order to properly model the flow regions. Boundary conditions, discretization schemes, sub-grid models, and filter widths must be implemented with accuracy and computational efficiency in mind.

Specifically, this thesis attempts to use LES to predict the mid-to-high blowing ratio cases for cylindrical film cooling and show the relationship between lift-off and reattachment behavior and the turbulent stresses governing the spreading of the coolant in all directions. The accuracy of an LES approach near the wall is also investigated, as resolving the influential eddies in the near wall region is particularly difficult.

4.2 Hypothesis

The comparative effectiveness of film cooling geometries can be directly linked to the nature and intensity of their respective instantaneous coherent structures and turbulent statistics of large scale turbulence using Large Eddy Simulations.

4.3 Contributions

- A qualitative visualization of unsteady coherent vortex patterns in film cooling flows and the effect of each structure on film cooling trajectory, effectiveness and uniformity.
- The quantitative validation with experimental results from a laboratory wind tunnel experiment.
- The quantitative prediction of statistical properties, in some cases not measured in the laboratory wind tunnel experiment, such as those quantities relevant to RANS turbulence models and the spreading rates of the jet.
- The utilization and extension of the open source CFD tools available in OpenFOAM for completing the above simulation and analysis.
- The exploration of the effect of numerical domain size on the accuracy of RANS predictions for film cooling flows.
- The investigation of the impact of finite volume flux interpolation schemes on Large Eddy Simulations of film cooling flows.

4.4 Attributes

With the recent emergence of Large Eddy Simulations in film cooling prediction development, the novelty of this thesis will reside in the use of LES techniques developed in open literature to provide insight into the unsteady interactions governing the flow structure and surface effectiveness. Such a correlation, along with the use of supplemental validation experiments, will deepen the state of the art understanding of cooling flows and the turbulent transport phenomena responsible for the effectiveness of film cooling in extending the

performance and life of gas turbine components. The insight from this study should allow researchers further understanding into means of increasing film cooling effectiveness. Film cooling effectiveness plays a vital role in the continual push for more efficient gas turbine engines, not only for power generation, but also for aircraft propulsion.

CHAPTER 5 APPROACH

The vortical structures of a general JICF interaction have been experimentally documented for high velocity ratios and simple geometries in (Fric and Roshko 1994, Kelso et al. 1996, Haven and Kurosaka 1997). Specifically, the four main vortex groups are: (1) the counter-rotating vortex pair (or kidney vortices), which has both steady and unsteady components and dominates the mixing properties of the flow, (2) the wake vortices (or upright vortices), which are shed in alternating patterns behind in the wake of the coolant jet, on the surface of interest in film cooling, (3) the horseshoe vortex system, which wraps around the jet injection site along the surface of interest and gives rise to the wake vortices in alternating separation events, and (4) the shear layer vortices (or roller vortices), which result from Kelvin-Helmholtz instabilities in the intersection of the two flows. In the case of lower velocity ratio (compared to the normal injection experimental studies) injection at inclination angles, such as the target of this thesis, the horseshoe system will likely be less pronounced and the wake region drastically reduced.

Tyagi and Acharya (2003) resolved these flow structures in the case of a cylindrical hole with a blowing ratio of 1.0, with the exception of the horseshoe vortices. Their proposed 'hairpin' coherent vortex structure needs further investigation with more realistic coolant flow inlet conditions. For this reason, the geometry of interest is the cylindrical hole. The higher blowing ratio cases, in which the cylindrical hole fails to remain attached and provide sufficient coverage in the near hole region, should be investigated alongside the lower blowing ratio cases already studied in literature. This can later serve to provide contrast with similar studies of high blowing ratios through shaped holes.

Experimental results from a wind tunnel test at NASA Glenn Research Center provides full field velocity and temperature measurements for a more rigorous validation of the statistical predictions made by LES approaches. Before such LES can be run, a number of preliminaries issues are dealt with.

The preliminary investigations utilize the comfort of the commercial solver Ansys Fluent (Ansys 2009). First, in Chapter 6, the motivation for using LES to predict film cooling flows will be thoroughly investigated with a range of RANS predictions and their comparison with experimental results in open literature. Then, in Chapter 7, the question of appropriate numerical domain is investigated using a response surface methodology (RSM) approach and the RANS equations with realizable k-ε turbulence model. Later in Chapter 7, the effect of various discretization schemes for the crucial advective terms of the Navier-Stokes equations is investigated. Finally, a preliminary LES simulation is completed in Chapter 8 with statistical calculations to test comparison measures for post-processing the vast amount of data produced by LES runs. Chapter 9 then presents the climax of the thesis with thorough validation, post-processing, and exploration of the LES predictions for mid-to-high blowing ratio film cooling flows from angled cylindrical holes.

CHAPTER 6 INVESTIGATION I: MOTIVATION

6.1 Introduction

Walters and Leylek (1997, 2000) provided a robust methodology for RANS simulations of film cooling flows. Using the standard k-ε turbulence model with a gradient adapted unstructured grid and two-layer wall treatment, they compared against the surface data of Sinha et al. (1991). Azzi and Lakehal (2002) and Lakehal (2002) made anisotropic and turbulent Reynolds number corrections to the k-ε equations, showing improvement in the centerline effectiveness predictions of the experiments of Sinha et al. (1991). Computational domain, boundary conditions, and grid resolution are important balances of computational efficiency and solution accuracy.

This chapter motivates the use of LES by exploring the deficiencies of the RANS approach to film cooling. This chapter investigates the domain, boundary, and resolution considerations using a RANS approach in the context of the L/D and I comparisons available in the experimental work of Sinha et al. (1991) and Thole et al. (1992). The shortfalls of RANS are shown by working to minimize the other sources of modeling error: discretization and iterative error.

6.2 Approach

Grid resolution, as in any numerical simulation, is key to the proper computational solution of film cooling. Overly coarse grids will lead to gross inaccuracies in the solution while overly fine grids will waste time and computational resources. In regions with high gradients in flow properties, finer grids are needed to properly resolve the flow, whereas, more uniform regions

can be accurately represented by a coarser grid. The design of a grid should incorporate the minimum number of cells while still accurately capturing the physics of the flow field. This current study investigated a number of different grid structures in evaluating the ability of RANS approaches to predict film cooling flows.

Because film cooling from cylindrical holes tends to exhibit a large range of jet trajectories, the current study was designed to look at how this may affect the ability of the current RANS approach to predict film cooling effectiveness. The highest momentum ratios, with complete detachment, are generally avoided in film cooling design. Therefore, the current study simulated two momentum flux ratios at an engine-like density ratio of 2.0. The low momentum ratio, with expected full attachment, was 0.125, mirroring the experiments of Sinha et al. (1991) and Thole et al. (1992). The moderate momentum ratio, I = 0.5, also matched experiments from the same investigations. These two studies were performed at different length-to-diameter ratios, thus, the current study also needed to reflect this. Sinha et al. used very short holes with L/D = 1.75, while Thole et al. studied longer holes with L/D =3.5. With these two variables (momentum-flux and length-to-diameter ratios), a total of four cases were defined for the current study. Table 1 summarizes the test matrix. Table 2 gives the common parameters for all studies.

Table 1 Test matrix for motivating investigation

Scope of Investigation	$I = 0.125$	$I = 0.5$
$L/D = 1.75$ (Sinha et al.)	Case 1	Case 2
$L/D = 3.5$ (Thole et al.)	Case 3	Case 4

Table 2 Geometry and flow conditions for motivating investigation

D	12.7 mm	T_∞	300 K
α	35º	T_c	150 K
p/D	3.0	DR	2.0
U_∞	20 m/s	M	0.5, 1.0
$Tu\%_\infty$	0.2%	δ_{99}/D	0.52

Within each of these four cases, a variety of different grids were tested. First, a basic grid with a thin layer of wall refinement was used as a baseline to test boundary condition effects. Type 'a-c' grids fell into this category, of which the grid structure near the hole is shown in Figure 8a. Type 'c' grids used the full computational domain of Walters and Leylek (2000). Type 'b' grids shortened the modeled crossflow by a factor of two while type 'a' grids went a step further and shortened the modeled crossflow inlet length, replacing its effects with a 1/7th law boundary layer profile, Eq. (69), with experimentally specified boundary layer thickness. In all, this led to a 40% reduction in grid cells.

$$U(y) = U_\infty \left(\frac{y}{\delta}\right)^{1/7} \quad \textbf{(69)}$$

Next, the grid was highly refined in the region near the hole, with regions away from the hole generally unaffected. This new refinement gave rise to grids 'd' and 'f', Figure 8b. The 'f' grids encompassed the entire domain of Walters and Leylek (2000) while the 'd' grids represented the full domain reduction similar to 'a' grids. Following the near-hole refinement in 'd' and 'f' grids, a coarsening was applied to the entire flow field to generate grid 'i', Figure 8c. This coarsening was an attempt to generate similarly accurate solutions as grid 'd', but with greatly reduced computation time. Finally, the jet region, as defined by the upper 0.5 diameters of the plenum,

the coolant hole, and the lower two diameters above the crossflow surface, was refined using hanging node adaption. The result of this final grid refinement was labeled 'j', Figure 8d.

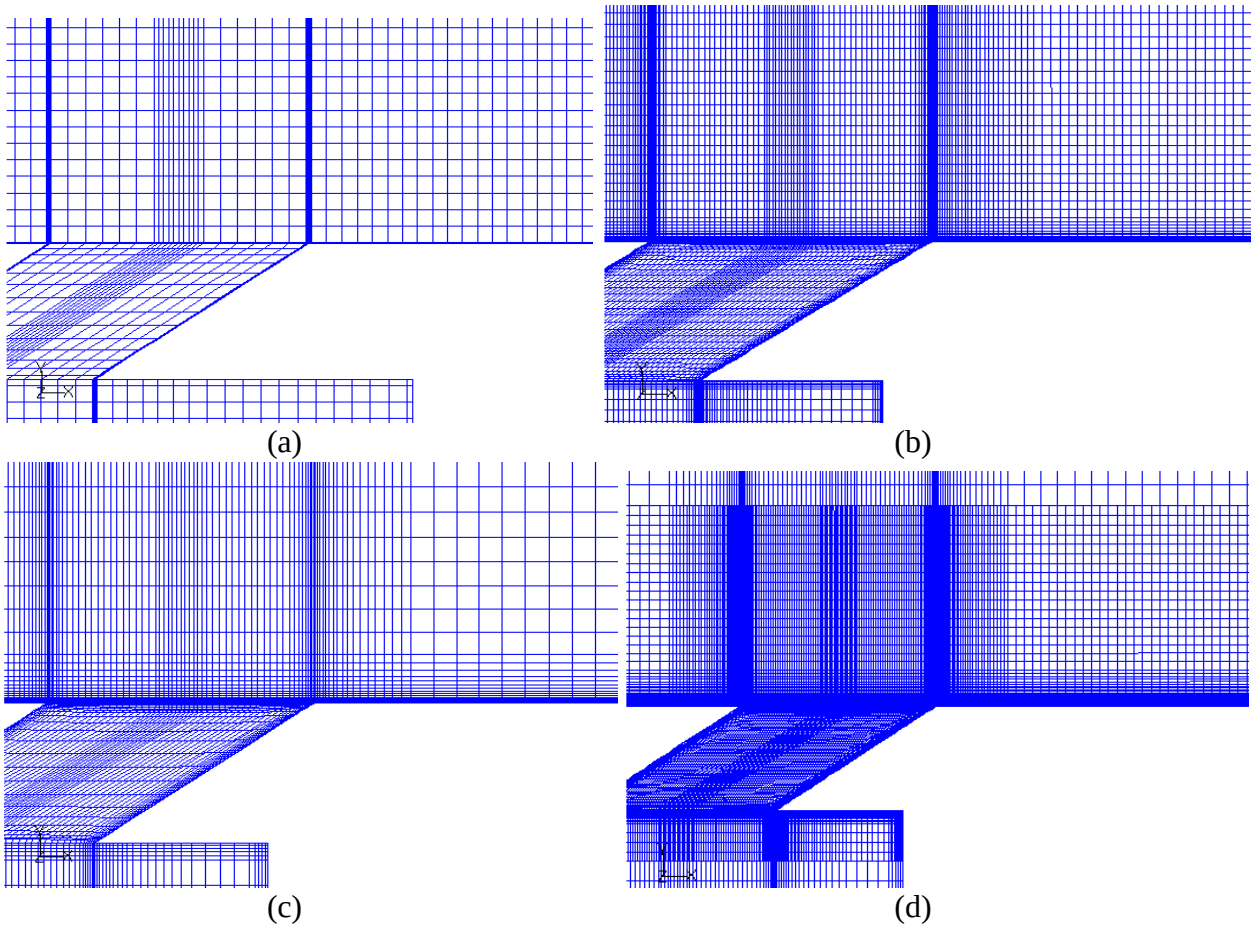

Figure 8 Grid topologies used: (a) initial spacing ('a','b', and 'c'), (b) with near-hole refinement ('d' and 'f'), (c) with subsequent total coarsening ('i') and (d) with hanging node adaption in the jet region ('j').

In hanging node adaption, parent hexahedral cells are split into four children hexahedral cells. If the adaption is performed only for a portion of the grid, the boundary of the adapted and non-adapted regions gives rise to hanging nodes, which results from a parent face's connection with four children faces. Extra memory overhead is needed to maintain connectivity, but effective use can significantly reduce cell count and computation time. A two-dimensional schematic of a hanging node is shown in Figure 9.

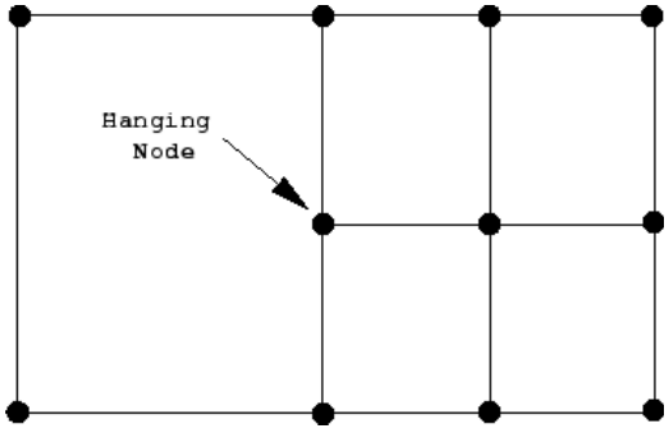

Figure 9 Illustration of a hanging node resulting from hexahedral adaption (Ansys 2009).

To appreciate the domain reductions involved in changing from the Walters and Leylek grids 'c' and 'f' to grids 'a' and 'd', the domains are shown side by side in Figure 10 with identical plenum and hole sizes. In all, this reduction led to about a grid with about 40% of the cells of the full domain.

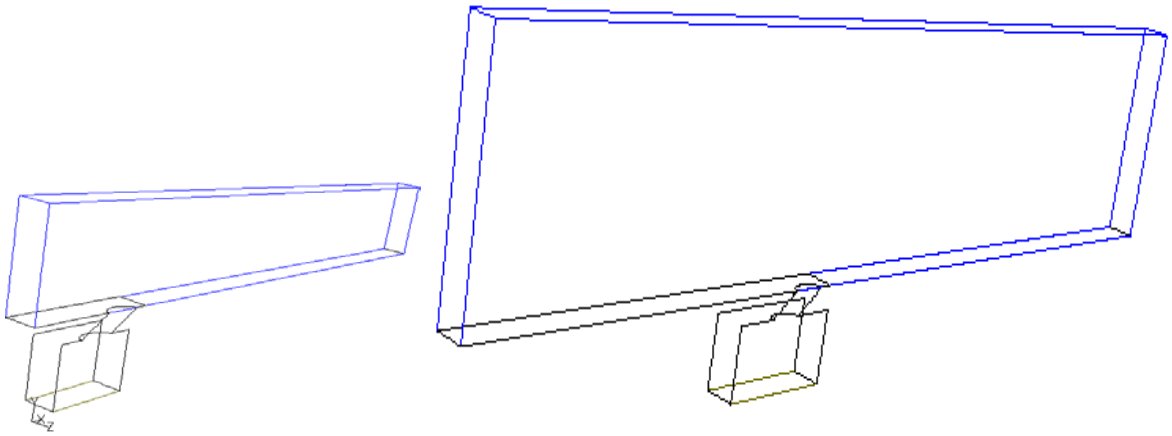

(a) (b)

Figure 10 Computational domains: (a) reduced grids 'a','d','i','j' and (b) full grids 'c','f'.

Not all cases were run for each grid. Table 3 summarizes the entire spectrum of numerical simulations performed in the current study. With four cases and seven grid structures, a total of

19 simulations were completed. These solutions enabled comparisons with respect to momentum-flux ratio, length-to-diameter ratio, and grid refinement/coarsening.

Table 3 List of grids used for each case.

Grid letter	Description	Cell count in millions	Cases used
a	Fully reduced domain	0.21	1,2,3,4
b	Partially reduced domain	0.29	1,2
c	Full domain of [13]	0.50	1,2,3,4
d	Grid ‘a’ with near hole refinement	0.77	1,2,3,4
f	Grid ‘c’ with near hole refinement	1.31	1,2
i	Grid ‘d’ with universal coarsening	0.19	1,2
j	Grid ‘i’ with hanging node adaption in jet region	1.03	2

6.3 Numerical Methodology

The numerical domain was established to mirror the experiments of Sinha et al. (1991) and Thole et al. (1992), the important difference between the two experiments being the length of the hole. Some of the grids represented the domain used by Walters and Leylek (2000), which stretched ten diameters above the no-slip surface and 20 diameters upstream of the hole. The fully-reduced domain modeled only five diameters above the surface and five diameters upstream of the holes. Because a row of holes was being modeled, only one-half of the hole needed to be modeled for the steady solution.

The plenum and crossflow walls were specified with adiabatic no-slip conditions, while symmetry planes in the span-wise direction were specified with zero shear stress and zero heat-flux. The freestream condition was approximated using a symmetry boundary as well. The plenum and crossflow inlets were specified by a velocity profile. The near-stagnation plenum was always supplied with a uniform inlet velocity profile while the crossflow was given a uniform profile for the long upstream length cases ('b','c','f') and a 1/7th law velocity profile of

Eq. (69) for the reduced upstream length cases ('a','d','i','j'). A pressure-outlet condition controlled the pressure (101.325kPa) at the crossflow outlet, though the absolute pressure was unimportant for the incompressible solution.

Gambit (2008) grid generation software was used for all grids. The structured hexahedral grids, though varying for each case, maintained overall the same structure, with certain refinement or coarsening in certain areas. All cases, to varying degrees, maintained refinement near no-slip walls, placing the first node with a y+ on the order of unity.

Fluent's pressure-based incompressible solver (Ansys 2009) with energy equation was used to solve the governing equations with the specified boundary conditions. The governing equations were solved in the Reynolds-Averaged Navier-Stokes form with the realizable k-ε turbulence model to achieve closure. Though modeled as incompressible with respect to pressure, the ideal-gas relation was used with nominal pressure to relate density to temperature, Eq. (70). This relationship allowed for the creating of a density ratio of 2.0 as previously discussed.

$$\rho = \frac{P_o}{RT} \qquad \textbf{(70)}$$

Near the walls, Fluent's enhanced wall treatment (two-layer model) was used for improved accuracy over standard wall-functions. Discretization was accomplished with a second-order upwind scheme for the convective terms and central differencing scheme for the diffusive terms. The SIMPLE segregated algorithm was used to deal with pressure/velocity coupling. For a given iteration, the three momentum (velocity) equations were solved sequentially, followed by a pressure-correction continuity equation. After the fluxes were updated based on these new solutions, scalar values such as temperature and turbulence quantities were updated.

Convergence was dictated by three criteria: scaled residuals below 10-6, iterative convergence of local surface temperature monitors, and global conservation errors for mass and energy more than three orders of magnitude below the overall mass and energy flows. The aggression of the solution convergence process was dictated by relaxation factors for each of the equations. These relaxation parameters were started low to avoid divergence, then increased as the solution began successfully converging toward lower scaled residuals. For detail on the above techniques, the reader is referred to the Fluent User's Guide (Ansys 2009).

6.4 Results and Discussion

6.4.1 Validation with Previous Studies: Grid Effects

Each of the four cases is first compared against their respective experimental results from Sinha et al. (1991) or Thole et al. (1992). Case 1 was the low momentum ratio for the short holes from Sinha (1991). Figure 11 compares the experimental results of centerline effectiveness with the various numerical solutions from the current investigation. The results from the unstructured, adaptive grid of Walters and Leylek (2000) as well as the structured grid of Azzi and Lakehal (2002) are shown alongside the present results. In general the present results over-predict the centerline effectiveness, as would be expected based on previous knowledge of the turbulent anisotropy of the film cooling flow. Cases 'a', 'b', and 'c' produced effectiveness values identical to one another, indicating that the domain reductions had no effect on the surface conditions predicted by the solver. Grids 'd' and 'f', however, slightly deviate from the first three with slightly lower effectiveness near the hole but slightly higher effectiveness 5-15 diameters

downstream. Other grid coarsening and refinement still failed to closely predict the experimental results, as one might expect given the assumptions of the turbulence models.

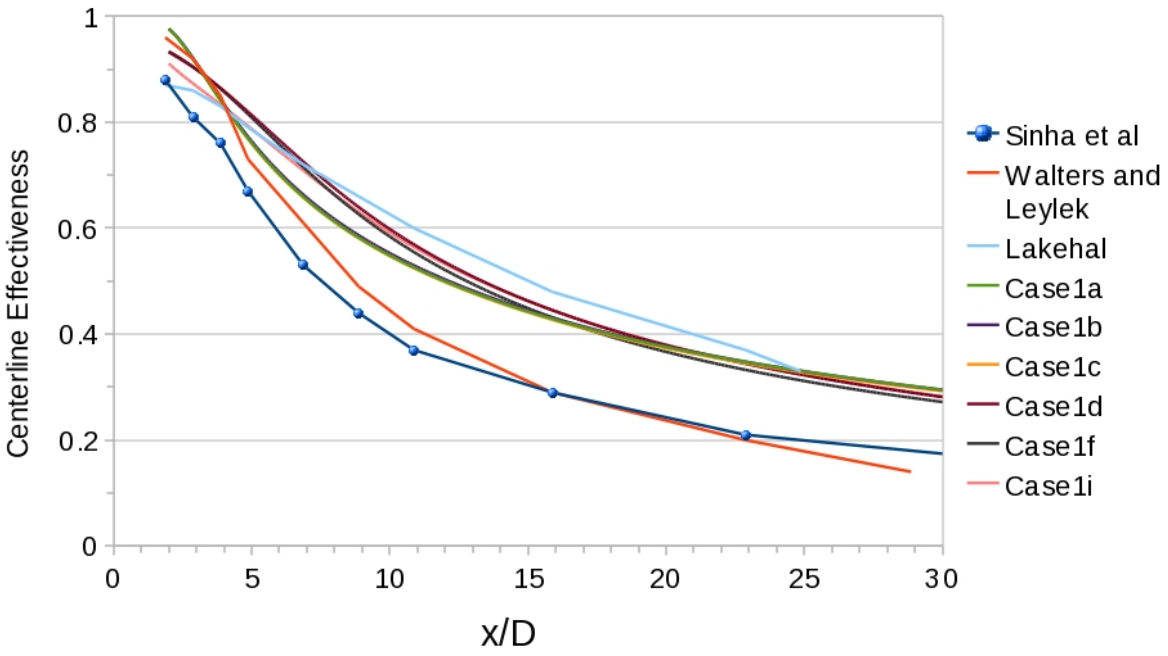

Figure 11 Centerline effectiveness for Case 1: L/D = 1.75, I = 0.125.

Figure 12 presents the span-wise averaged effectiveness trends with downstream distance for the same case. Numerical solutions here show under-prediction of the effectiveness, further reinforcing the under-prediction of the lateral spreading as the cause for over prediction of centerline effectiveness.

The under-prediction of lateral spreading is clearly shown in Figure 13, where effectiveness is shown in the spanwise direction. Over-prediction of effectiveness at the centerline is balanced by under-prediction of effectiveness at the mid-span. The overall effect, referring back to fig. 5, is a slight under-prediction of laterally-averaged effectiveness.

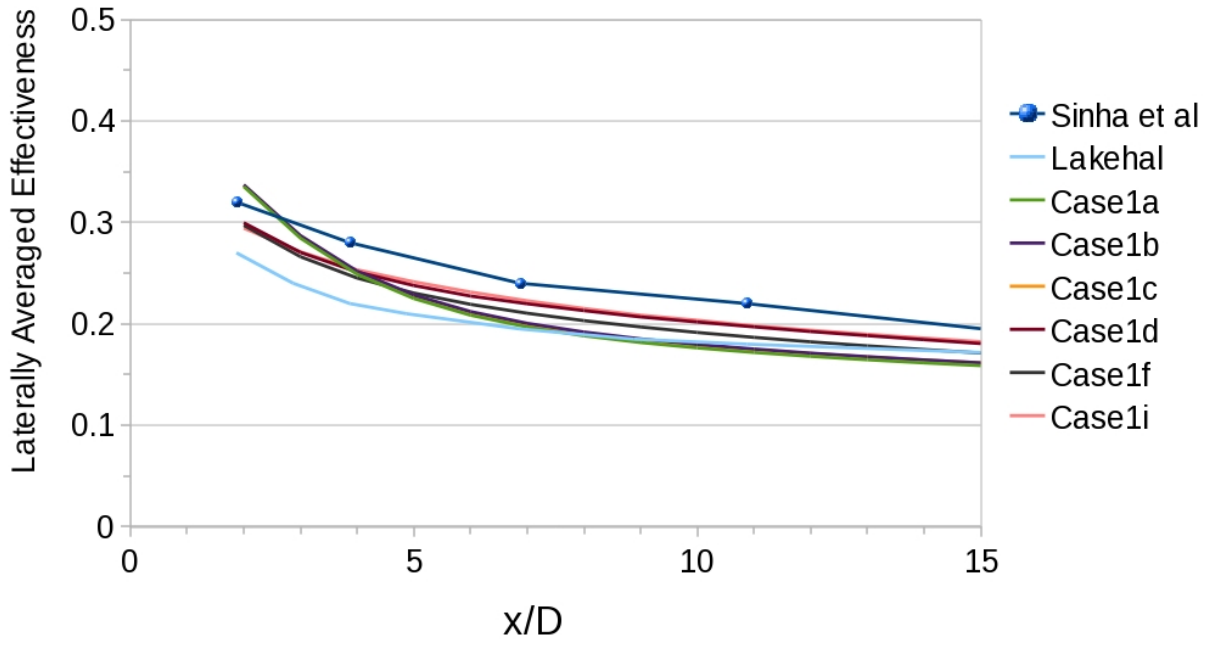

Figure 12 Laterally-averaged effectiveness for Case 1: L/D = 1.75, I = 0.125.

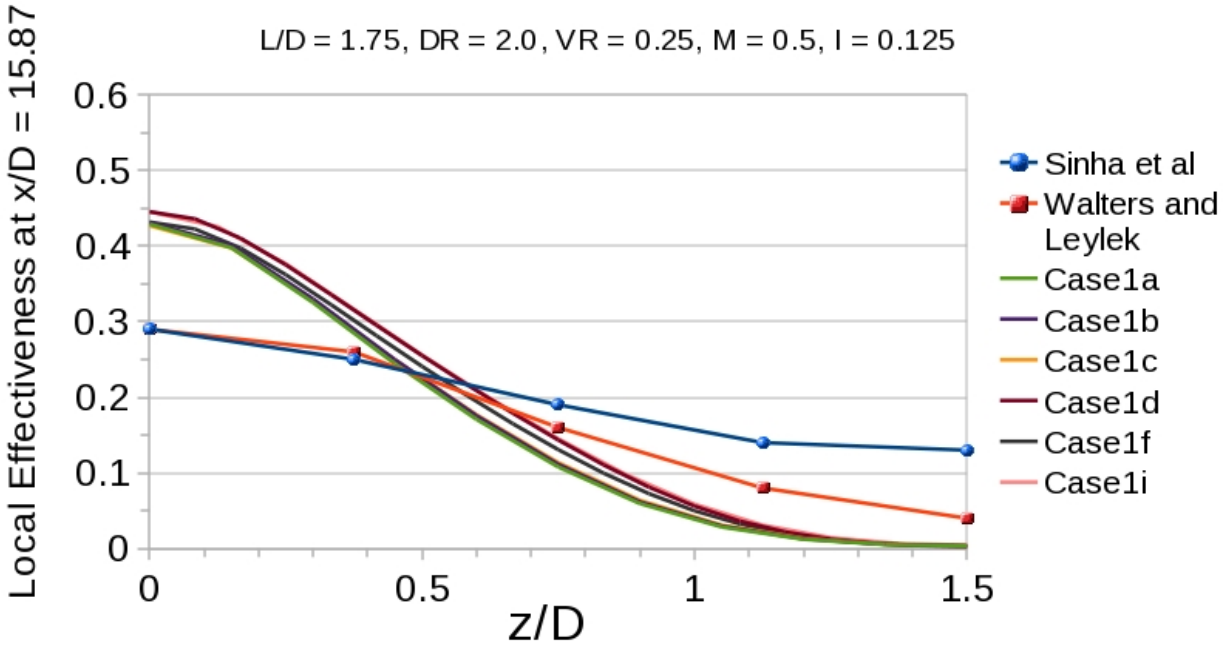

Figure 13 Local effectiveness in the span-wise direction for Case 1: L/D = 1.75, I = 0.125.

Case 2 results are compared in Figure 14 - Figure 16 against the higher momentum ratio (I = 0.5) from [1]. The experimental centerline results in Figure 14 suggest a lift-off and reattachment regime, yielding far lower effectiveness values near the hole. The 'a', 'b', and 'c' grids (again, agreeing with one another) fail to predict any sort of jet lift-off. The grid refinement in the near-hole region (grids 'd' and 'f') do capture the jet lift-off region. The lift-off is still captured, even with the coarsening of grid 'i' down below 200,000 cells. The failure to predict the near hole lift-off (grids 'a', 'b', 'c') is detrimental to the rest of the prediction downstream. The correct prediction, however, does not need great resolution in the main body of flow, just in the region near the exit lip of the hole. There is still an overall over-prediction of centerline effectiveness for the refined numerical solutions, indicating the under-prediction of lateral spreading still applies at the higher momentum ratio. The original grids ('a','b', and 'c') show an under-prediction of centerline effectiveness at most x/D. The trends suggest that the separation of the jet is delayed by a coarse grid in the region of the jet exit. This exaggerates the effect of the lift-off and fails to capture a noticeable reattachment. Therefore, the coarseness in the region of the hole exit throws off the rest of the solution downstream.

Case 2 laterally averaged results in Figure 15 again show an under-prediction compared to the experiments, reiterating the lack of lateral spreading. The trend of the effectiveness with x/D is matched much closer by the refined grids. The near hole resolution greatly effects the solution at all x/D. Again, the general coarsening in grid 'i' confirms that the extra refinement needed in near the hole can be balanced by a coarser mainstream, yielding similar solutions with significant reduction in computational cells.

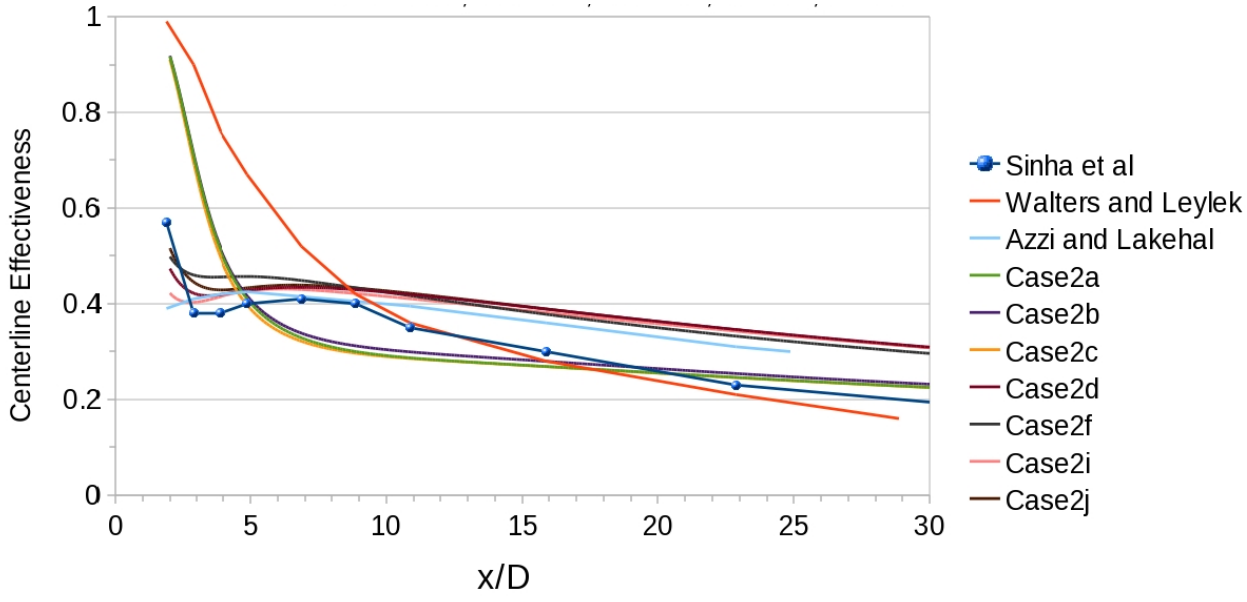

Figure 14 Centerline effectiveness for Case 2: L/D = 1.75, I = 0.5.

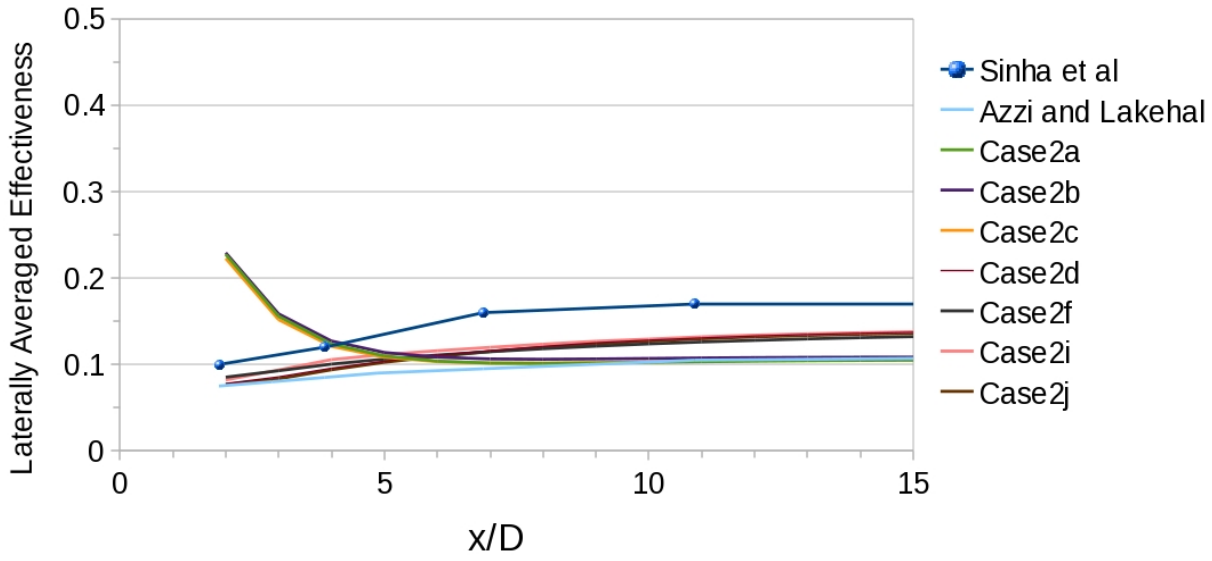

Figure 15 Laterally averaged effectiveness for Case 2: L/D = 1.75, I = 0.5.

Figure 16 compares lateral spreading predictions from the current simulations with the experimental data from Sinha et al. Again, there is obvious lack of lateral spreading. The higher effectiveness at the centerline is balanced by lower effectiveness near the mid-span. As in the

case with the lower momentum ratio, the net result is slight under-prediction of laterally-averaged results. In general, the current simulations are able to capture the trends of effectiveness values fairly accurately, though the quantitative values may not be correct.

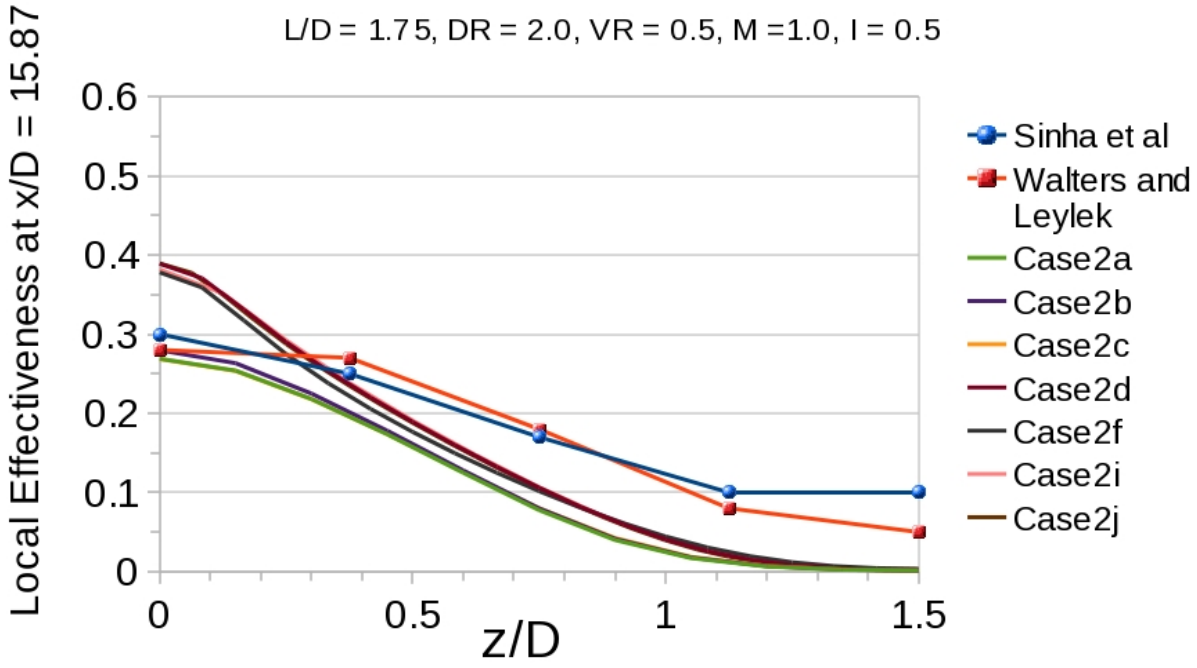

Figure 16 Local effectiveness in the span-wise direction for Case 2: L/D = 1.75, I = 0.5.

Cases 3 and 4 correspond to the temperature field measurements of Thole et al. (1992). For Case 3 validation, temperature profiles in the wall normal direction are compared at three different downstream distances in Figure 17. Near the hole, a slight over-prediction of jet trajectory seems to be apparent in the profiles. The refined grid at the hole exit captures the shape of the profiles much more closely than the original grids.

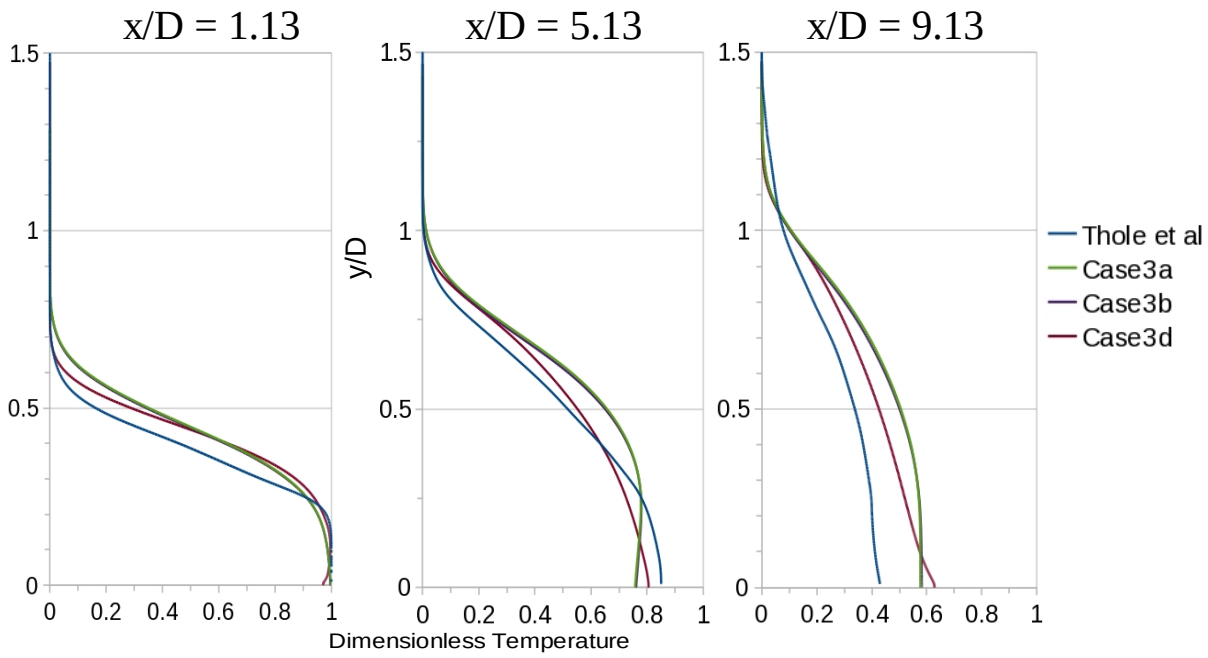

Figure 17 Wall normal non-dimensional temperature profiles for Case 3: L/D = 3.5, I = 0.125.

Case 4, with higher momentum ratio, provides a better chance for comparison. Figure 18 shows the temperature profiles in the wall normal direction for the same x/D locations as above. It is clear from these profiles that the under-prediction seen in Case 2 effectiveness plots is due to a significant over-prediction of the jet trajectory. This is not a feature of the turbulence model, however, as the refinement in the near hole region corrects the disagreement and leads to much closer agreement in effectiveness and jet trajectory. Figure 19 presents the contours of temperature throughout the flow. Here, the trajectory differences are quite clear. Even the refined grid projects a slightly higher trajectory than the experimental results, but this could be attributable to the turbulence model. Still, as in all previous results, it is worth reiterating that, trajectory aside, the jet core temperature is over-predicted, perhaps as a consequence of the turbulent model assumption of isotropic eddy diffusivity or constant turbulent Prandtl number (see Lakehal 2002).

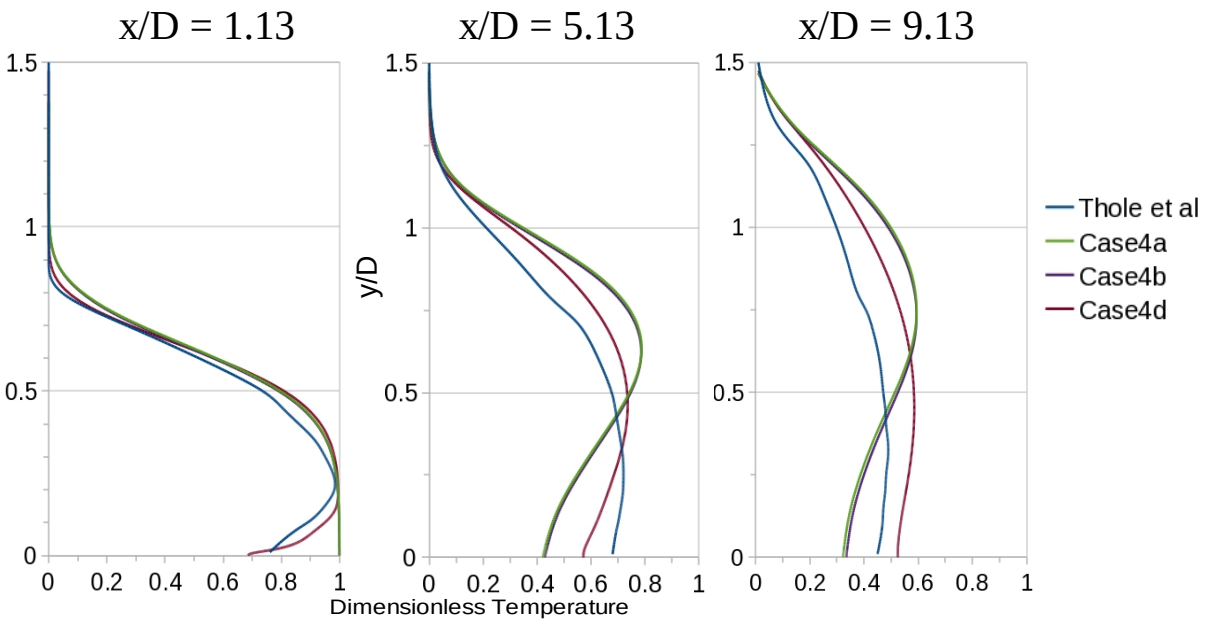

Figure 18 Wall normal non-dimensional temperature profiles for Case 4: L/D = 3.5, I = 0.5.

6.4.2 Momentum Ratio Effects

For the remainder of the paper, grid 'd' results will be used to compare between cases, as this grid yielded the best results and most accurately reflects the behavior of the turbulence model. Figure 20 compares centerline effectiveness results for Cases 1 and 2, corresponding to the shorter length holes with two different momentum ratios. It is obvious that the lift-off occurring in the higher momentum ratio yields a much lower effectiveness in the near hole region. Upon reattachment, however, the higher momentum jet approaches and overtakes the low momentum jet in effectiveness around x/D = 15 in the experiment and x/D = 23 in the numerical solution. In the far field, the higher momentum ratio yields slightly better effectiveness, despite near hole lift-off, as shown by both experimental and numerical evidence. The common theme is over-prediction of centerline results.

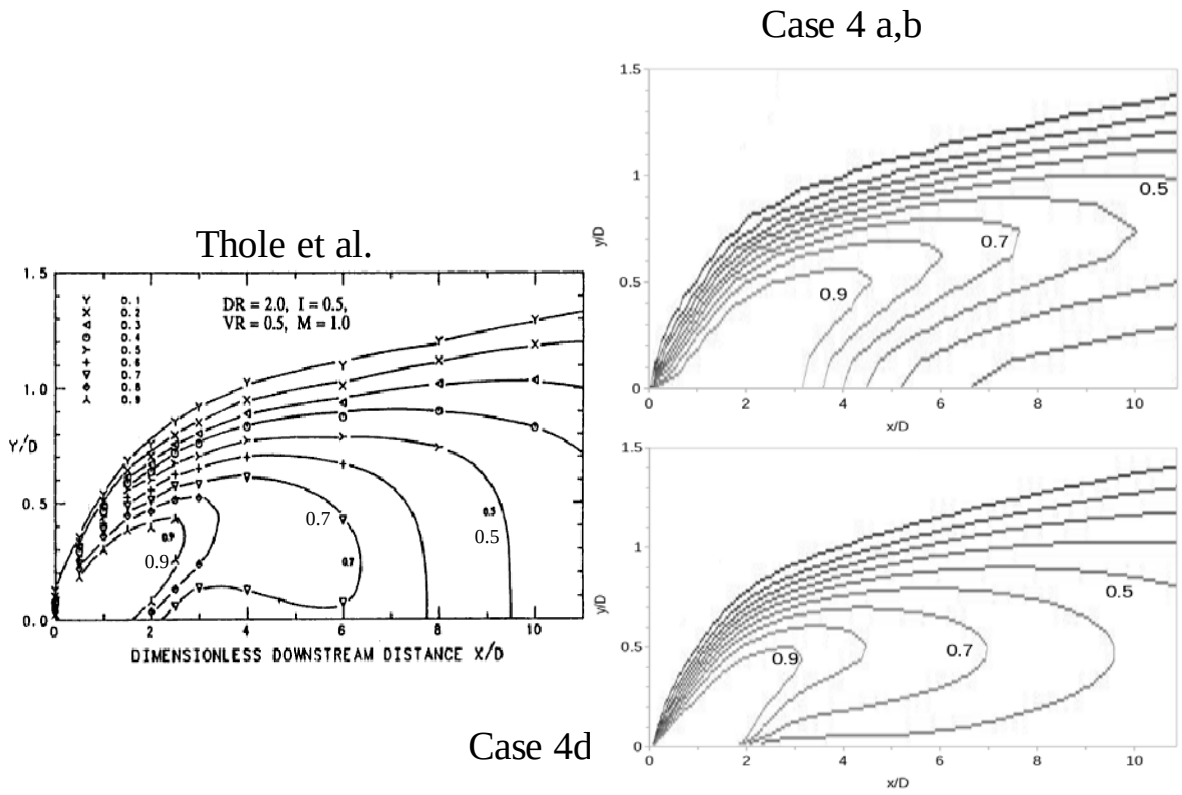

Figure 19 Center-plane non-dimensional temperature contours for Case 4: L/D = 3.5, I = 0.5.

The corresponding laterally averaged results for Cases 1 and 2 are compared in Figure 21. Here, the low momentum jet gives rise to a monotonically decreasing effectiveness, as in the centerline. The higher momentum jet, however, appears to monotonically increase in effectiveness within the first 15 diameters. It is clearly flattening out, however, and if the results were extended further, would be shown to decrease. Again, it appears as though, despite beginning much lower near the hole, the effectiveness of the high momentum jet is overtaking the low momentum jet somewhere downstream of 15 diameters.

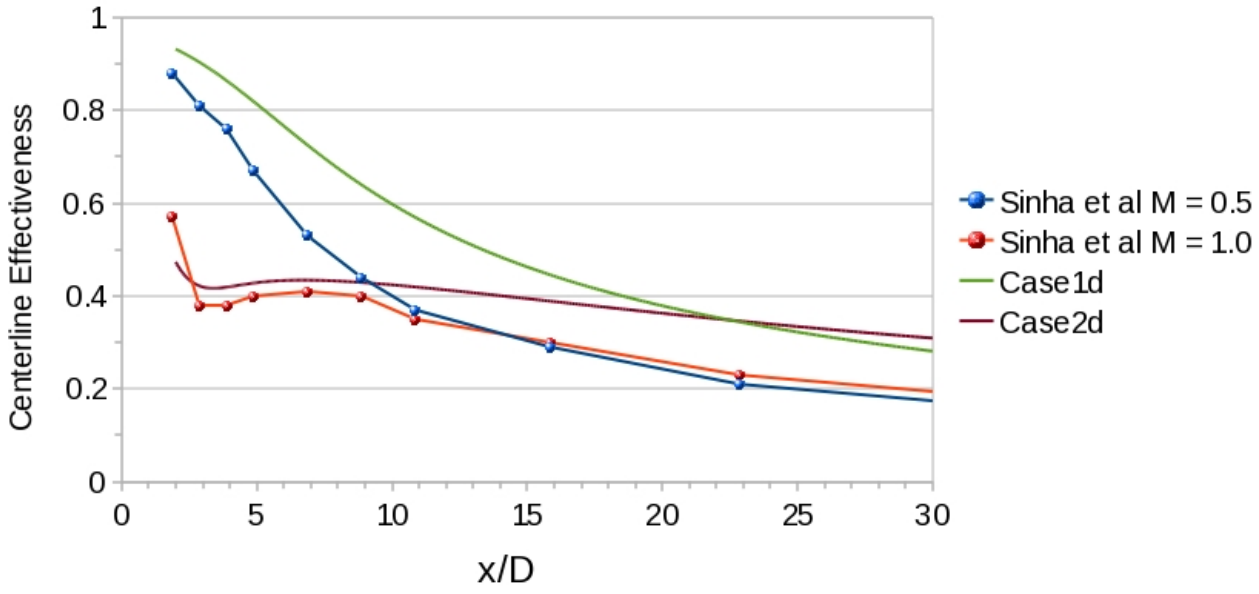

Figure 20 Centerline effectiveness comparison for L/D = 1.75 at I = 0.125 vs. 0.5.

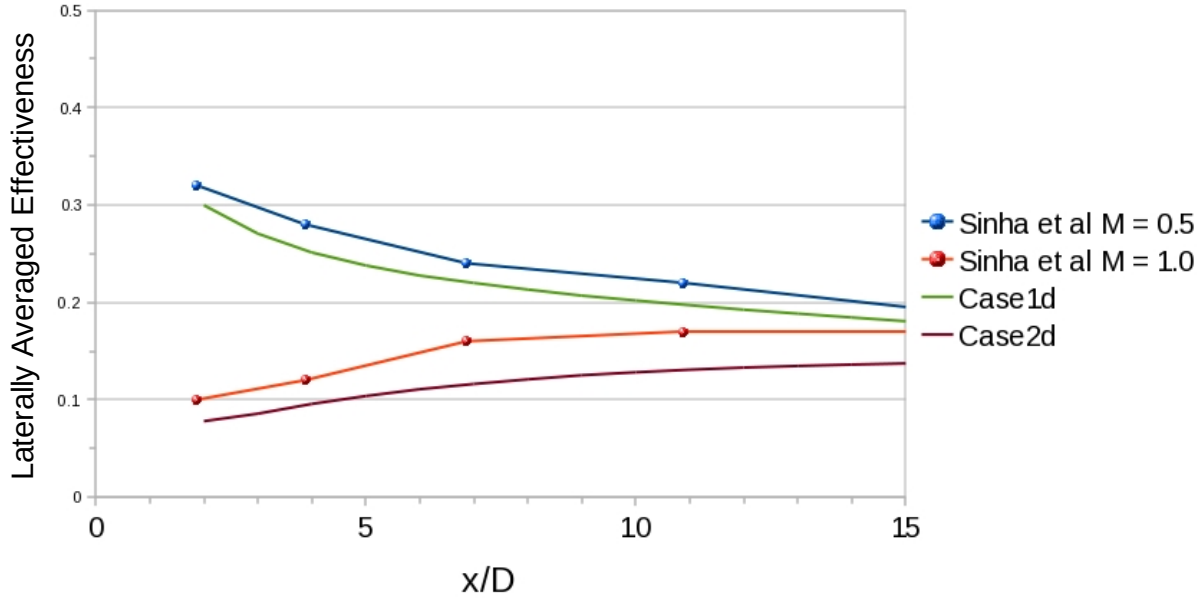

Figure 21 Laterally averaged effectiveness comparison for L/D = 1.75 at I = 0.125 vs. 0.5.

Cases 3 and 4, with longer holes corresponding to the experiments of Thole et al (1992), present another chance to investigate the effects of momentum ratio. Wall normal temperature profiles are presented in Figure 22. At both momentum ratios, the numerical solution tends to slightly over-predict the jet trajectory. Despite the higher mass flux rate, the higher momentum jet does not show higher jet core dimensionless temperatures than the lower momentum jet, with the slight exception of the experimental results at the further downstream point. This is perhaps due to increased entrainment of hot crossflow fluid into the jet of higher momentum balancing out the higher mass flow rate of coolant. The higher momentum jet does eventually overcome this and overtake the low momentum jet further downstream, as shown in previous results.

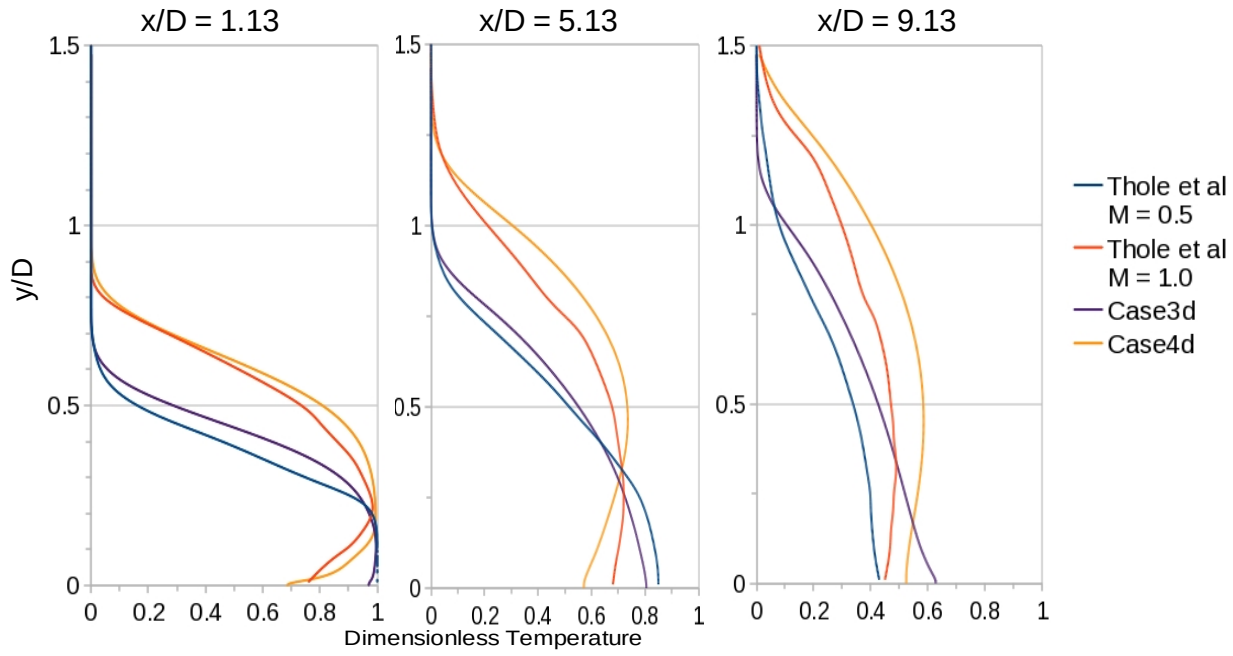

Figure 22 Wall normal non-dimensional temperature profiles for L/D = 3.5 at I = 0.125 vs. 0.5.

6.4.3 Length-to-Diameter Ratio Effects

Besides varying the momentum ratio, the scope of the current study also allows for a brief discussion of length-to-diameter ratio. Cases 1 and 2 correspond to the shorter hole lengths of Sinha et al. (L/D=1.75), whereas Cases 3 and 4 have longer hole lengths, those of Thole et al. (L/D = 3.5). Hole length effects can be compared at low momentum ratios between Cases 1 and 3 and high momentum ratios between Cases 2 and 4.

Shorter holes give the coolant flow less time to develop inside the tube before injection into the crossflow. Due to the inclination angle of the jet, the coolant flowing into the hole from the plenum separates from the trailing edge of the hole inlet, unable to complete the 145 degree turning angle. Figure 23 shows this separation region for the higher momentum ratio case. This separation is not mirrored on the leading edge side of the coolant hole. This jetting effect produces higher velocities toward the leading edge and lower velocities in the trailing edge region, as shown in Figure 24.

If the hole is long enough, the jetting effect attenuates and has little effect on the injection velocity profile. A shorter hole length will not provide the means for the jet to develop as such inside the hole. The hole exit profile, then, yields higher velocities at the leading edge. This can be seen as a higher effective inclination angle at the injection; the flow enters the hole from the plenum traveling roughly normal to the crossflow and the hole is not long enough to completely turn the coolant hole before injection. The higher effective inclination leads to lower effectiveness values, as discussed by Burd et al. (1996) and Lutum and Johnson (1999).

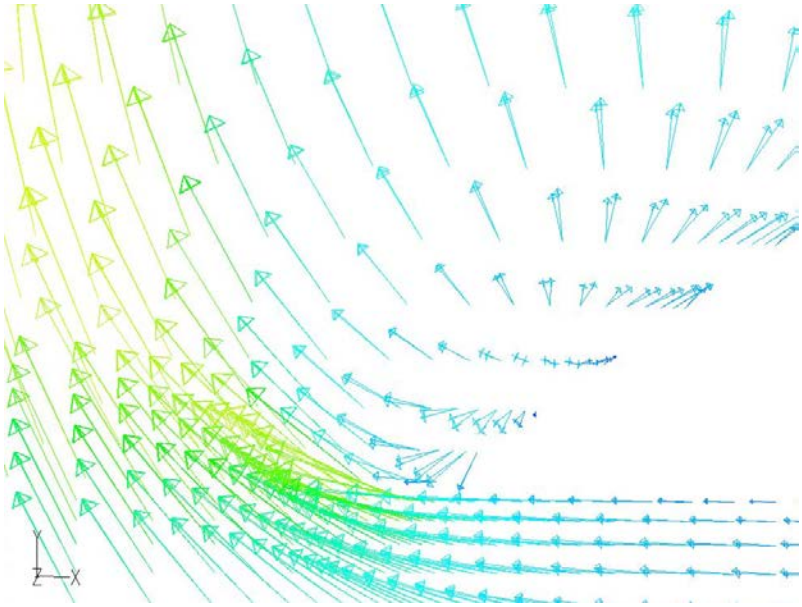

Figure 23 Velocity vectors, colored by velocity magnitude, showing flow separation at the trailing edge of the coolant hole inlet at I = 0.5.

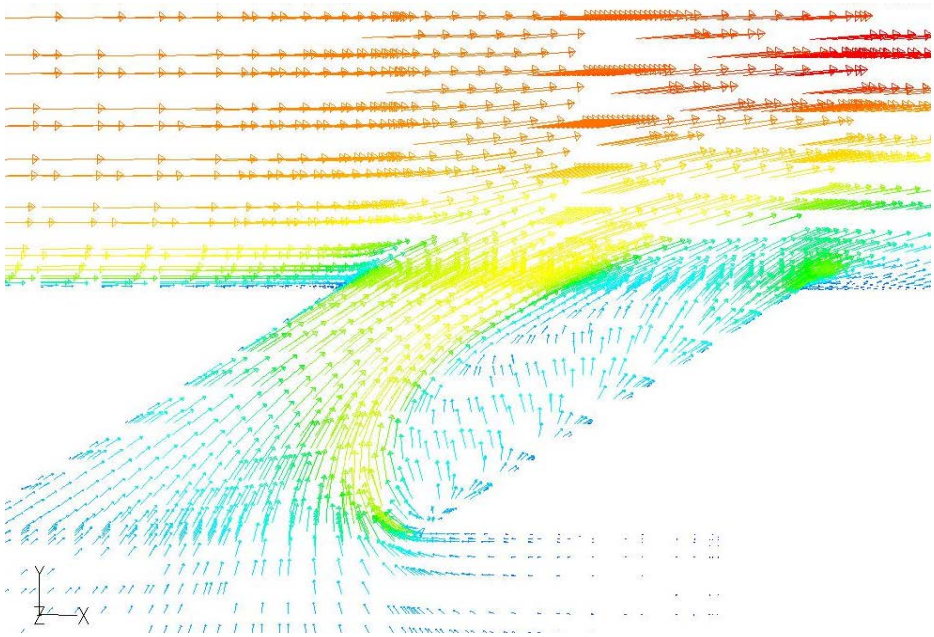

Figure 24 Velocity vectors, colored by velocity magnitude, showing the jetting effect of the coolant inside the short hole (L/D = 1.75) at I = 0.5.

Figure 25and Figure 26 compare centerline and laterally-averaged effectiveness values downstream of the low momentum jets. The two hole lengths provide the same effectiveness curve. The effects of hole length is thus negligible at low momentum ratios from the viewpoint of these simulations. The coolant flow moves slowly enough that the hole quickly turns the coolant flow and there is not a significant difference between a hole of length 1.75 diameters and one twice as long. The flow at the exit of the 1.75 diameter hole may not be fully developed in the strict sense, but it is developed enough such that adding additional length to the hole does not significantly change the downstream effectiveness of the jet.

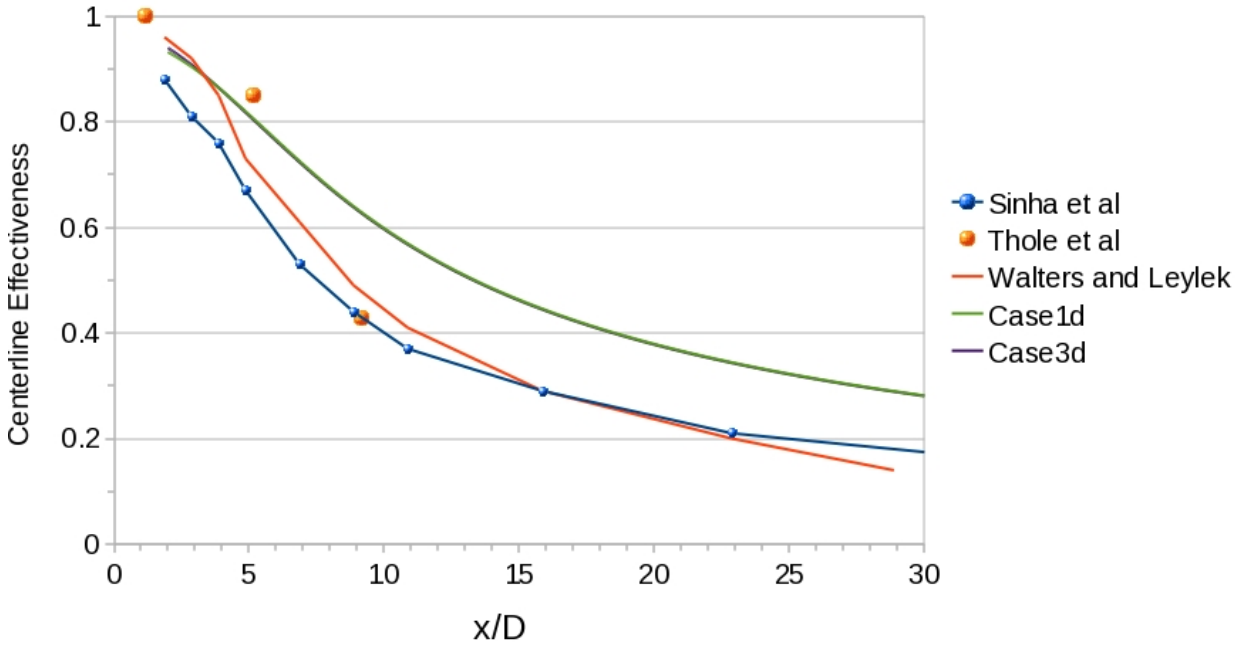

Figure 25 Centerline effectiveness for I = 0.125 at L/D = 1.75 vs. 3.5.

For the same two cases, Figure 27 shows wall normal temperature profiles at the selected downstream locations. Again, the change in the length of the hole results in no distinguishable difference in the temperature profiles.

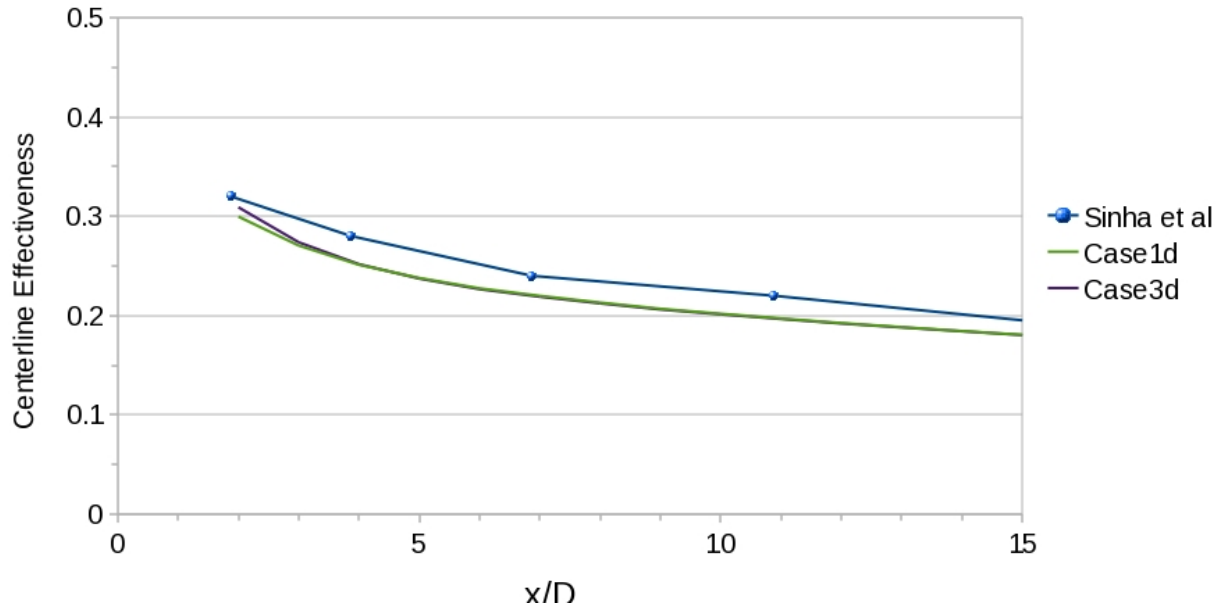

Figure 26 Laterally Averaged effectiveness for I = 0.125 at L/D = 1.75 vs. 3.5.

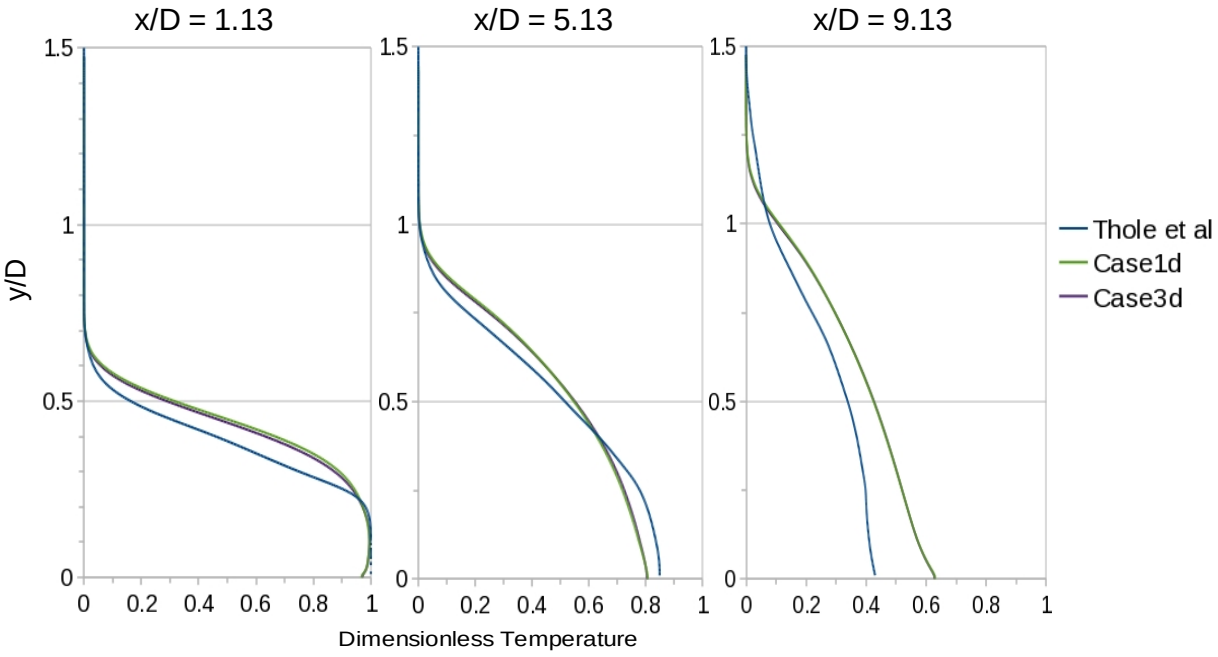

Figure 27 Wall normal dimensionless temperature profiles for I = 0.125 at L/D = 1.75 vs. 3.5.

When the momentum of the jet is increased, however, length to diameter ratio plays a larger role. Figure 28 and Figure 29 show the effectiveness curves for the higher momentum jet (I = 0.5). There is now a clear difference in the effectiveness of the jet. As suspected by the above analysis, the longer hole leads to higher effectiveness values. The matching of laterally-averaged effectiveness between Case 4 and the Sinha et al. results is mere coincidence. The two results are from two different holes lengths. The proper comparison with Sinha et al. is Case 2. The inclusion of Thole et al. results in these curves is achieved by taking the asymptotic values from the wall normal profiles and plotting the three points to get a rough feel for the effectiveness predicted by those experiments.

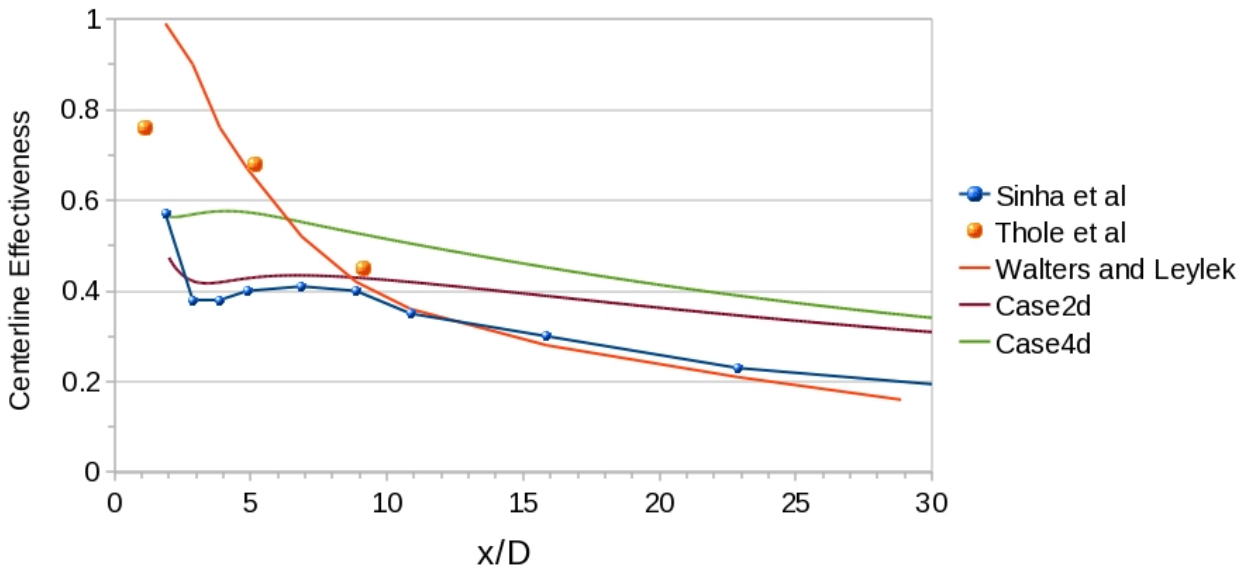

Figure 28 Centerline effectiveness trends for I = 0.5 at L/D = 1.75 vs. 3.5.

This situation is further confirmed in Figure 30, where the wall normal temperature profiles are compared. The proper comparison with experimental data is Case 4. The shorter hole results show a minimum temperature (maximum non-dimensional temperature) at higher wall normal distances than the longer hole results. This indicates a higher trajectory of the

coolant jet, as expected.

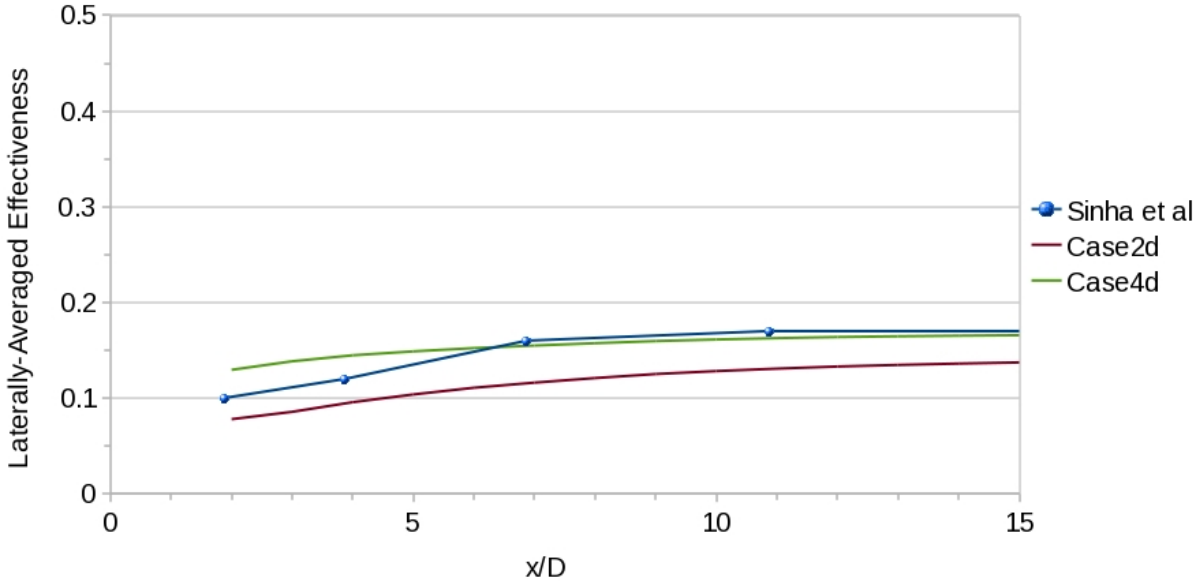

Figure 29 Laterally averaged effectiveness trends for I = 0.5 at L/D = 1.75 vs. 3.5.

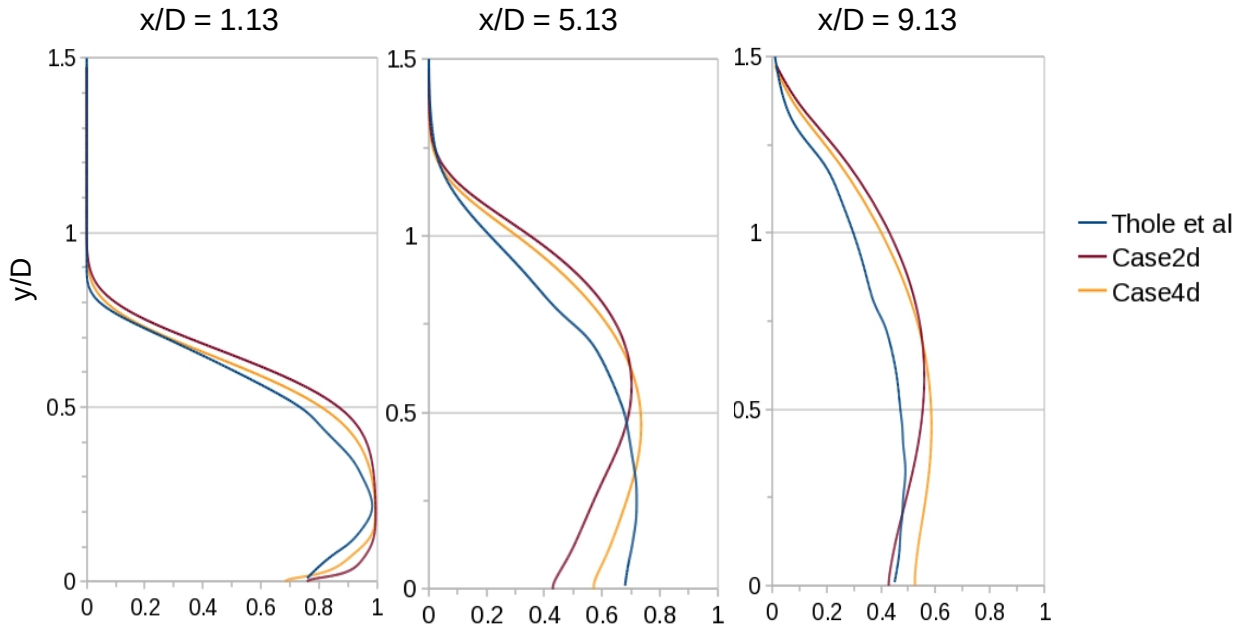

Figure 30 Wall normal dimensionless temperature profiles for I = 0.5 at L/D = 1.75 vs. 3.5.

6.5 Conclusions

1) The domain of Walters and Leylek (2000), which is typical of RANS film cooling simulations, can be dramatically reduced in both the wall normal and upstream directions without affecting much change to the resulting solution. The reduction of the domain is more rigorously studied in the next chapter, but the results here strongly suggest already that this is the case. The reduction in upstream crossflow length can be safely compensated for by the application of a 1/7th law boundary layer profile with appropriate thickness. The current case showed a 60% reduction in cell count with these considerations.

2) The grid refinement in the area near the trailing edge of the hole exit is crucial to the prediction of high momentum coolant jets. The RANS equations (with k-ε turbulence model) have trouble predicting the nature of recirculation in the under-side of the detached jet without ample grid points clustered near the lip. This restriction does not lead to a dramatic increase in cell count if balanced by the view that a coarser grid can be used in the crossflow. In all, a grid count under 200,000 produced results indistinguishable from the finest grid used in this study.

3) The errant nature of the k-ε model's isotropic assumption cannot be corrected by grid refinement. The universal under-prediction of lateral spreading, manifested in over-prediction of centerline effectiveness and wall normal contours in conjunction with under-prediction of laterally-averaged effectiveness, is an artifact of the turbulence model and not of discretization error.

4) Experimental trends with respect to momentum ratio and length-to-diameter ratio can be matched well with the RANS results. Higher momentum jets and shorter holes diminish the film cooling effectiveness by increasing the trajectory of the jet above the cooled surface.

5) The results of this study serve as motivation for the use of LES in attempting to more accurately resolve the behavior of the film cooling jet. The observations of this study serve as a guide to the development of an LES film cooling approach for obtaining time-accurate solutions while resolving the larger scales of turbulence.

CHAPTER 7 PREPARATION

With the motivation for higher fidelity simulations of film cooling scenarios established in the previous chapter, the implementation of Large-Eddy Simulation (LES) is the next logical topic. The governing equations for LES have been thoroughly studied since the advent of the technique (Smagorinsky 1963), including the constitutive equation for turbulence modeling of small eddies (a.k.a. the 'subgrid-scale model'). While the standard Smagorinsky model has been the most popular, the dynamic Smagorinsky (Germano et al. 1991) represents a significant improvement without noticeably increasing computational cost. While one-equation models have also gained recent attention, their benefits typically do not justify the added cost of an extra transport equation (typically for the subgrid-scale kinetic energy) (Pope 2000). With the governing equations and modeling aside, the remaining errors in computational modeling are the discretization and boundaries. (There is also iterative error, but at a small enough time step for LES resolution, namely, one that satisfies the Courant condition, this error is not a driving factor in time resolved simulations.) This chapter undertakes two investigations: (1) a more rigorous test of the domain boundary placement for film cooling, particularly with respect to plenum size and freestream boundary placement, and (2) a comparison of LES results using a variety of discretization schemes available in the Fluent code. Both studies use Gambit for meshing and Fluent for solving and post-processing.

7.1 Boundary Placement Study: Formulation and Methodology

The majority of computational fluid dynamics studies for turbine film cooling have employed the Reynolds-Averaged Navier-Stokes equations with various turbulence modeling techniques to achieve closure, most notably the various two equation (k-ω or k-ε) models. For computational

simulation of film cooling, modeling the entire testing domain with a row of multiple holes while sustaining a sufficiently fine mesh would demand a large number of grid cells and a hefty computational expense. A significant reduction in the computational domain can be and has been achieved without much harm to the overall accuracy of the film cooling prediction. The current study aimed to investigate the necessary domain parameters for reducing the grid cell count without significantly affecting the accuracy of the solution. The Box-Behnken design for response surface methodology was employed to determine the relative influence of each parameter on the cooling effectiveness prediction. The experimental design matrix was executed for multiple blowing ratios (0.5, 1.0, 2.0) to include the effects of the blowing ratio on the computational domain. The work was carried out using a three-dimensional computational fluid dynamics finite volume method with the RANS equations and k-ε turbulence model. A cylindrical film cooling hole with a pitch-to diameter ratio of 3.0, a length-to-diameter ratio of 7.5, and an inclination angle of 35° was studied. The results are compared against existing data in the literature as well as in-house experimental data. The data from each case is compared in terms of spatially-averaged effectiveness. The modeled entrance length was found to be the most important parameter, with the mainflow height a distant second. The size of the modeled plenum was not found to exert any significant influence on the effectiveness results. Explanations are offered for notable trends in the data and conclusions are drawn concerning the grid optimization process.

7.1.1 Geometry and Domain

For the present case, a coolant hole diameter of 2mm was chosen, and all other geometry and domain considerations non-dimensionalized with reference to this parameter. The length of the

coolant hole was set at 3 diameters, with an inclination angle of 35° from the mainflow. The length of the coolant hole was set at 7.5 diameters, which is typical for land-based power generation turbines. The downstream distance (x) was measured from the intersection of the coolant hole axis with the plane coinciding with the film cooled surface. This point was established as the origin of the domain, with all values being measured with respect to this point. The geometric considerations for a cylindrical film cooling hole are illustrated in Figure 31. The Reynolds number of the simulation was 7,530 based on the jet diameter and freestream velocity.

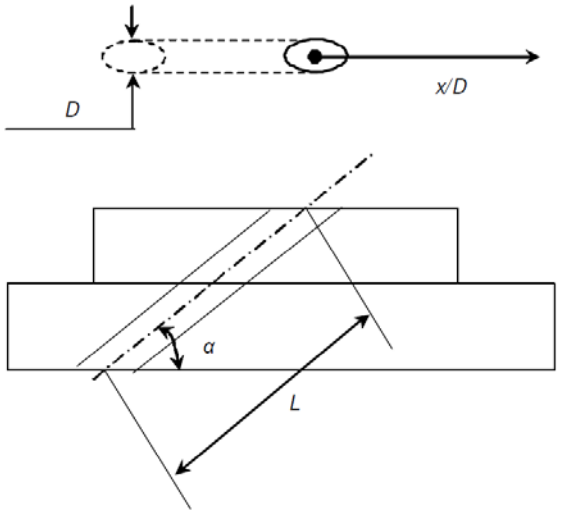

Figure 31 Schematic of geometric parameters for cylindrical film cooling holes.

The objective of this study was to limit the domain so as to minimize the computational cost of obtaining a converged solution, while maintaining the relative accuracy of the solution. With this in mind, only half of one pitch was modeled, with symmetric boundary conditions applied on each side. To obtain a sufficient amount of downstream wall data, a length of 30 diameters was modeled downstream of the coolant hole. The remaining domain parameters were left as variables for the focus of this study. The length of the entrance region (L_e) from the mainflow inlet to the center of the coolant hole exit is the first important parameter, which effects the

mainflow velocity profile at the coolant exit. The mainflow height (M_h) of the computational domain is the next variable for the present study. At the top of the domain, a zero-shear slip wall is used to model the mainstream conditions. This boundary should be placed far enough away from the cooled bottom surface so as to minimally affect the region of interest. Figure 32 illustrates the computational domain for present study. Aside from these two mainflow considerations, two parameters of plenum size were also varied. The width of the plenum (P_w) affects the velocity needed in the plenum to produce the desired blowing ratio. Increasing the width of the plenum allows the velocity in the plenum to approach the ideal stagnant (zero-velocity) conditions. Finally, the modeled height of the plenum (P_h) was held as a variable. Like the mainflow entrance length, an increase in plenum height allows the flow to develop further before entering the coolant hole. Table 4 summarizes the values for each of the geometric and domain parameters. The '0' values for each parameter were approximately the typical values in the numerical procedures of (e.g. Leylek and Zerkle 1994, Walters and Leylek 1997, 2000).

Table 4 Hole geometry and domain parameters

D	2mm
L/D	7.5
P/D	3
α	35 deg
L_e/D	10,20,30
M_h/D	5,10,15
P_h/D	4,8,12
P_w/D	4,8,12

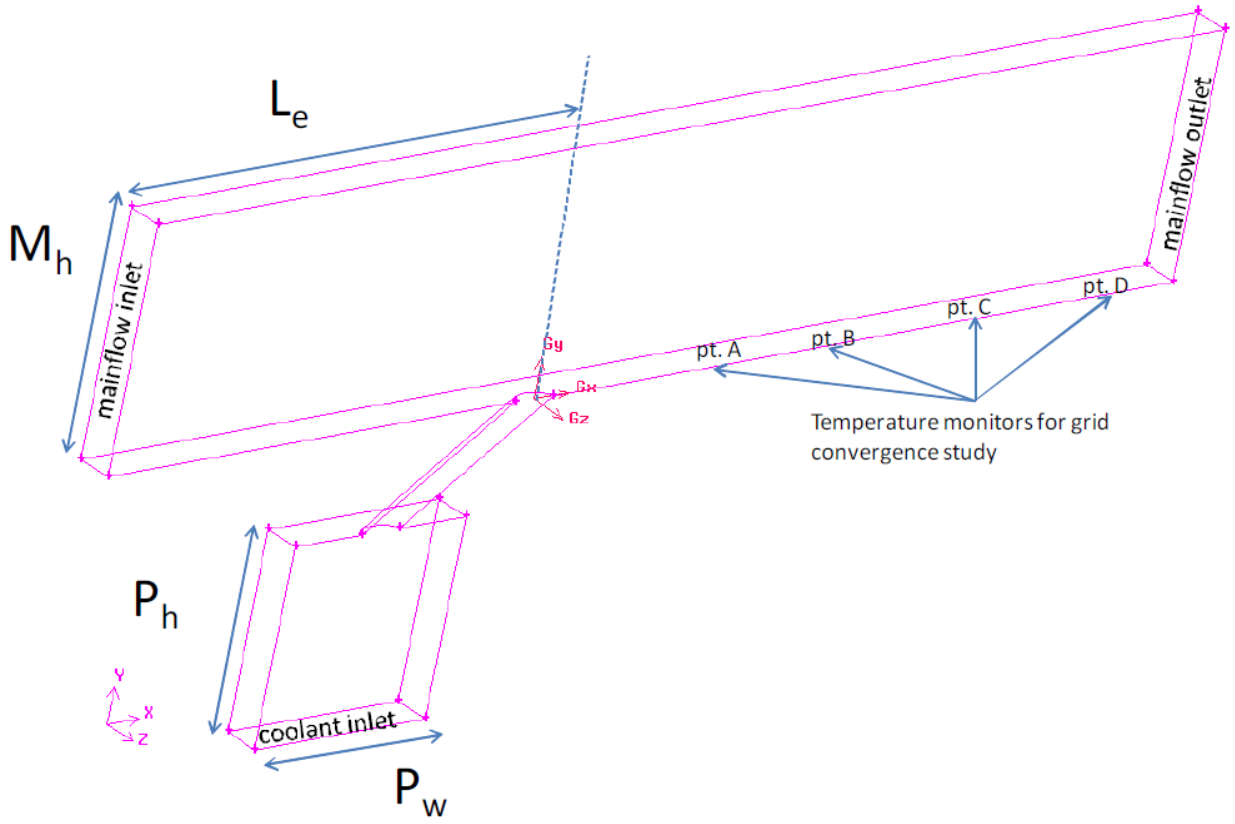

Figure 32 Computational domain schematic for boundary placement study.

7.1.2 Grid Structure

A full 3D grid was carefully constructed for the each case using the Gambit (2008) mesh generation software. The cell topology was solely hexahedral and y+ was close to 5 (with enhanced wall treatment). Refined element layers were assigned near the solid surfaces to capture the increased rates of momentum and heat transfer. Figure 33 shows the typical grid structure for this study. In each case of the DOE (design of experiment) sequence, separate grids had to be created. For this reason, an automated grid generation technique was specially created for the current study using Gambit's text command journal files. In this way, each grid, though consisting of a various number of cells, was exactly similar in cell structure and spacing. Only in

the grid convergence study was the grid spacing changed. In these cases, the same domain was considered, but with an increasing number of cells.

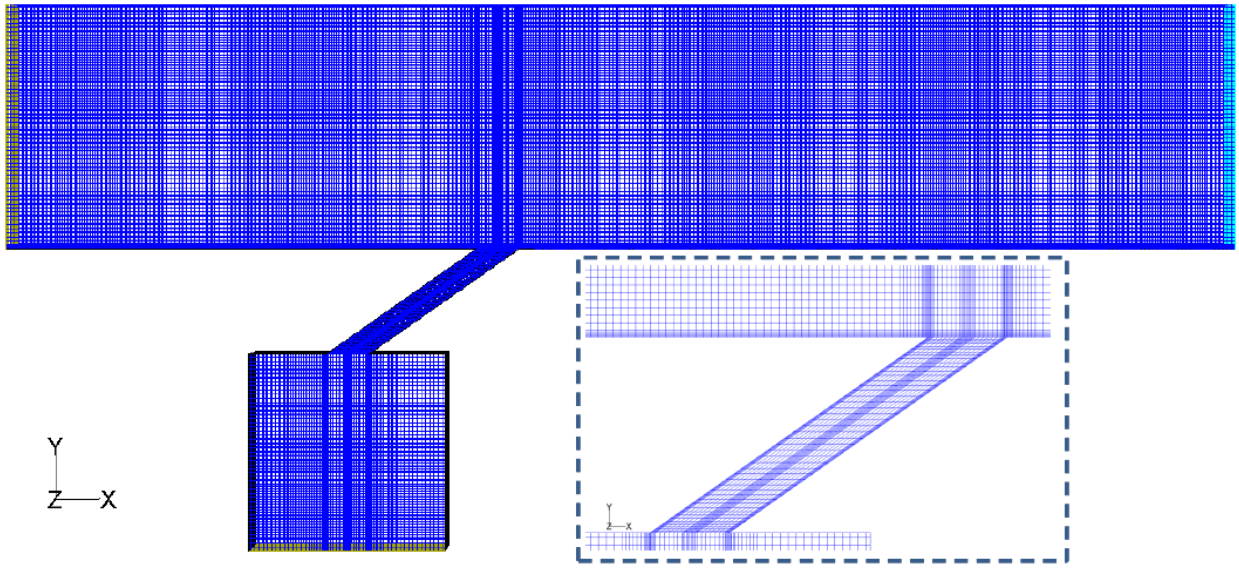

Figure 33 Typical grid for boundary placement study.

7.1.3 Solution Methodology

The Fluent software (Ansys 2009) was utilized to solve the above grid with specified boundary conditions to obtain a converged solution for this film cooling model. A symmetric boundary condition was applied on both sides of the pitch, as well as the top (freestream) boundary. An adiabatic no-slip wall was specified for the bottom mainflow surface, coolant hole wall, and non-symmetric plenum walls. Uniform inlet velocity profiles were prescribed for both the coolant plenum entrance and the mainflow entrance. The magnitude of the inlet velocities was set in such a way to provide the desired blowing ratio.

The solution process for the grids utilized Fluent's realizable k-ε turbulent model with enhanced wall treatment for closure with the RANS equations. Rodriguez (2008) compared Fluent's realizable k-ε and standard k-ω turbulence models, concluding that the k-ε model

yielded better predictions of film cooling effectiveness. For this reason, the authors employed the realizable k-ε model, rather than the standard k-ω model, for conducting this study.

Once initialized, the iterative process was begun with monitors set on both residual and iterative convergence. The iterative convergence monitors included local temperature and velocity at a point downstream of the hole. The following criteria were set for a solution to be considered 'converged': (1) the normalized residual less than 1e-6 for the velocity and energy equations and 1e-5 for the continuity and turbulence parameter (k and ε) equations; and (2) the temperature and velocity monitors varying less than 0.01% of their value over 100 iterations. Relaxation factors were tailored to enhance the convergence of the iterative process. Specifically, the following relaxation factors were used; pressure: 0.15; density: 0.5; body forces: 0.5; momentum: 0.35; turbulent kinetic energy: 0.4; turbulent dissipation rate: 0.4; turbulent viscosity: 0.5; energy: 0.5.

Once a converged solution was achieved, the iterative process was terminated and the effectiveness results were processed in Fluent. The area over which the spatially-averaged effectiveness and spatial uniformity was calculated included the entire half-pitch from x/D=1.5 to the extent of the downstream domain at x/D=30. Once all cases were completed, the Minitab (2007) software product was used for the statistical analysis of the data.

7.1.4 Grid Convergence

In order to ensure that the mesh was fine enough to obtain a grid independent solution, a grid convergence study was performed with grid sizes from 100,000 to 500,000 grid cells. Each grid size was solved with the above solution process, with surface temperature monitored at a few points on the cooled surface of the mainflow. These monitored values were compared between

the coarser and finer meshes. Figure 34 displays the convergence tendencies of these temperature values. After a grid size of 300,000, the change in local temperatures is seen to be less than 0.15K, which is considered negligible for the current study. The solution for this grid size is thus considered grid independent. The grid convergence study was performed with the domain parameters as follows: L_e=20D, M_h=10D, P_h=8D, P_w=8D. When these parameters were varied for the DOE study, the grid spacing was held constant, which caused an increase or decrease in the number of cells employ by each grid. This method, however, enabled fair comparisons between the grids and their solutions, because none of the grids were finer, coarser or structurally different in any way other than the variation of the size of the domain.

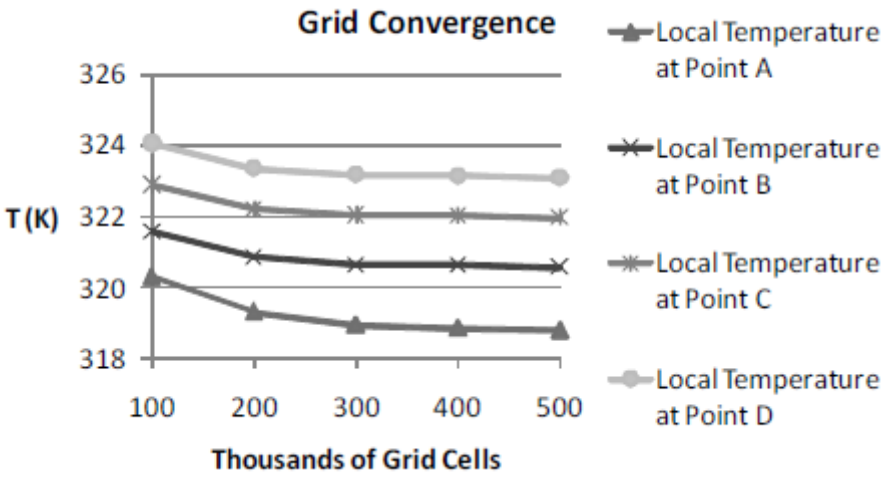

Figure 34 Local temperatures at selected monitored points (A-D) along the downstream wall for different grid sizes showing grid convergence.

7.1.5 Response Surface Methodology

Each of the four domain variables introduced earlier were varied between three levels, which can be labeled ‘-1’, ‘0’, and ‘1’ respectively from smallest to largest. Table 5 provides the values that each domain variable, labeled ‘A’ through ‘D’, takes for each of the three levels.

Table 5 Definition of boundary placement parameter levels for Box-Behnken analysis.

Parameters		-1	0	1
A	L_e/D	10	20	30
B	M_h/D	5	10	15
C	P_h/D	4	8	12
D	P_w/D	4	8	12

Nonlinear behavior and interaction of those four factors that may affect the prediction of film cooling performance will be studied. Subsequently, at least 3 levels of each factor need to be considered. By using a classical full factorial 3k=4 design, an excessive number of design points would need to be run, which is impracticable. That would also cost a great amount of time and represents a very inefficient way of studying the parameters. Central Composite Design (CCD) would be an ideal selection since it does not require knowledge of safety operation zone (known safety range of each factor). With the CCD, one can reduce the number of runs from 81 down to 16, but one needs to have two or more replicates for the axial point (central point). Unfortunately, with a numerical simulation tool, we cannot generate more than one result for any specific problem.

In 1960, Box and Behnken generated a very creative and special design for the three-level designs. This design is used for studying second-order response surfaces that is based on the balanced incomplete block designs. Since, each input factor is studied at three levels which will produce a second order polynomial of surface regression for the output (a fitted model). Just like the Central Composite Design, Box-Behnken design is efficient tool that fits for sequential experimentation. It allows a reasonable amount of information for testing lack of fit while not involving a tremendous amount of design points as in the full factorial design (Myers et al.

2009). As a result, for the 34-factorial design, only 25 cases need to be run. For a more complete inspection, the same methodology is repeated for three blowing ratios: M=0.5, M=1.0, M=2.0.

7.2 Boundary Placement Study: Validation of Results

To validate the numerical solution, our own in-house experimental cases were executed on our closed-loop film cooling rig at the Center for Advanced Turbines and Energy Research (CATER). Temperature differences were achieved by heating the mainflow with the blower work as well as cooling boil-off nitrogen with liquid nitrogen for coolant flow. For more complete details on the experimental setup and methodology, see Zuniga et al. (2007). Figure 35 contains a comparison of the results from the present case with our own in-house experimental results. Also included are experimental results from Goldstein et al. (1974), Pedersen et al. (1977), Sinha et al. (1991), as well as the computational results of Walters and Leylek (2000). There is, as would be expected from a RANS simulation, a slight over-prediction of the centerline effectiveness as compared to our in-house data, especially further downstream, indicating the lack of lateral spreading (as observed in the previous chapter). Goldstein et al. (1974) as well as Sinha et al. (1991) have lower effectiveness results, which could be explained by their lower L/D values and noticeably larger hole diameters. Meanwhile Pederson (1977) had a much longer L/D. Table 6 compares the experimental parameters for each of the data sets used in the validation plot. Overall, the comparison is satisfactory, except for the noticeable lack of lateral spreading in the numerical solution manifested in higher centerline effectiveness values further downstream.

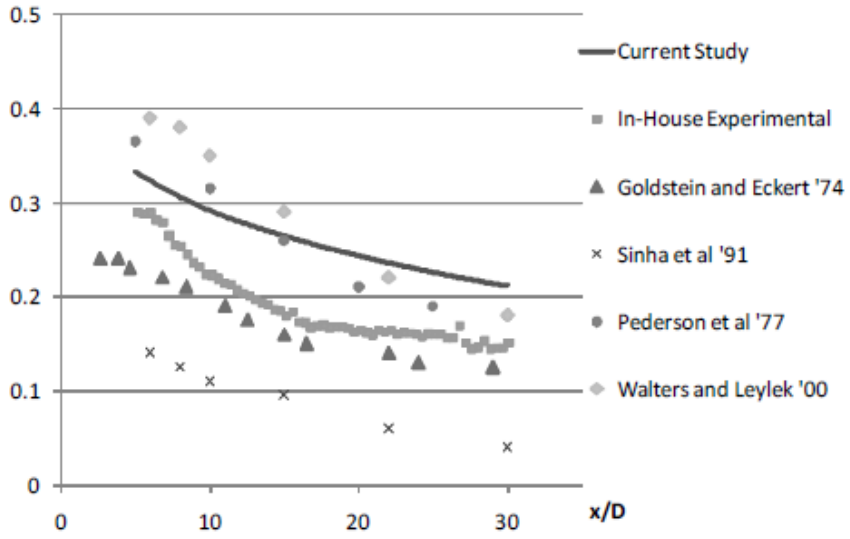

Figure 35 Validation of centerline effectiveness vs. x/D for M=1.0.

Table 6 Flow Parameters of Validation Curves for Figure 35.

	Num.	Exp.	Goldstein '74	Pedersen '77	Sinha '91	W & L '00
D(mm)	2	2	6.35	N/A	12.7	12.7
L/D	7.5	9.5	5.2	~40	1.75	3.5
P/D	3.0	3.5	3	N/A	3	3
DR	1.0	1.26	N/A	1.18	1.20	1.2
M	1.0	1.0	1.0	1.05	1.0	1.0
α (deg)	35	30	35	N/A	35	35

7.3 Boundary Placement Results and Discussion

The results for the 25 cases solved for all 3 blowing ratios are summarized in Table 7. The left side of the table shows the design matrix of cases. To the right, the spatially-averaged effectiveness for each case is recorded for three blowing ratios alongside the number of cells.

Table 7 The Box-Behnken matrix design and output.

Standard Order	Coded Factors				$\bar{\eta}$			N
	A	B	C	D	M=0.5	M=1.0	M=2.0	Thousands of grid cells
1	-1	-1	0	0	0.1592	0.1261	0.0538	171
2	1	-1	0	0	0.1560	0.1155	0.0465	212
3	-1	1	0	0	0.1603	0.1281	0.0565	350
4	1	1	0	0	0.1566	0.1152	0.0485	463
5	0	0	-1	-1	0.1584	0.1200	0.0506	268
6	0	0	1	-1	0.1584	0.1196	0.0499	307
7	0	0	-1	1	0.1584	0.1199	0.0498	279
8	0	0	1	1	0.1584	0.1196	0.0502	342
9	-1	0	0	-1	0.1600	0.1272	0.0553	249
10	1	0	0	-1	0.1565	0.1150	0.0476	326
11	-1	0	0	1	0.1600	0.1272	0.0553	272
12	1	0	0	1	0.1564	0.1148	0.0474	349
13	0	-1	-1	0	0.1577	0.1196	0.0489	167
14	0	1	-1	0	0.1587	0.1201	0.0509	381
15	0	-1	1	0	0.1576	0.1193	0.0484	217
16	0	1	1	0	0.1586	0.1198	0.0507	432
17	-1	0	-1	0	0.1601	0.1274	0.0556	236
18	1	0	-1	0	0.1565	0.1152	0.0481	312
19	-1	0	1	0	0.1595	0.1249	0.0535	286
20	1	0	1	0	0.1565	0.1149	0.0477	363
21	0	-1	0	-1	0.1577	0.1197	0.0489	180
22	0	1	0	-1	0.1587	0.1203	0.0512	395
23	0	-1	0	1	0.1577	0.1195	0.0481	203
24	0	1	0	1	0.1586	0.1201	0.0510	418
25	0	0	0	0	0.1584	0.1199	0.0505	300

The results of the statistical analysis from the Box-Behnken design are presented in Table 8. A coefficient is found for the variables and their second order combinations. The coefficients are computed from the second order curve fit obtained from the spatially-averaged effectiveness values obtained from each case. From this, the relative effect of each variable (and combination of variables) can be easily found.

For the all blowing ratios, factor A, which is the entrance length (Le), has by far the most influence on the effectiveness. Other consistently (over the range of blowing ratios) strong factors include the mainflow height (M_h) and second order influence of the entrance length. The next tier of factors includes a variety of second order combinations, which are small compared to the stronger influences. Especially noticeable is the contrast between the mainflow domain parameters (L_e and M_h) with the plenum parameters (P_h and P_m). The plenum width is the

weakest variable, and the plenum height is not much stronger. Comparing between blowing ratios, it is interesting to note the noticeably smaller influence of B (M_h) for the middle blowing ratio compared to the two extreme blowing ratios. This is accompanied by an opposite trend in the total influence of M_h. Meanwhile, the two plenum variables seem to increase in influence as blowing ratio increases.

Table 8 Percentage contribution of factors to the spatially-averaged effectiveness.

Term	M=0.5		M=1.0		M=2.0	
	Coefficient	Percent Contribution	Coefficient	Percent Contribution	Coefficient	Percentage of Contribution
A	-1.71E-03	56.4	-5.86E-03	63.8	-3.69E-03	43.1
B	4.60E-04	15.2	3.19E-04	3.5	1.18E-03	13.8
C	-6.31E-05	2.1	-3.39E-04	3.7	-3.03E-04	3.5
D	-2.22E-05	0.7	-4.18E-05	0.5	-1.42E-04	1.7
*A*A*	-1.94E-04	6.4	1.09E-03	11.8	1.10E-03	12.9
*B*B*	-2.13E-04	7.0	7.05E-05	0.8	-4.55E-04	5.3
*C*C*	-5.68E-05	1.9	-2.90E-04	3.2	-3.26E-04	3.8
*D*D*	1.21E-05	0.4	2.86E-05	0.3	-2.06E-04	2.4
*A*B*	-1.19E-04	3.9	-5.63E-04	6.1	-1.86E-04	2.2
*A*C*	1.33E-04	4.4	5.20E-04	5.7	4.10E-04	4.8
*A*D*	-3.02E-05	1.0	-3.82E-05	0.4	-6.64E-05	0.8
*B*C*	4.59E-06	0.2	1.51E-05	0.2	5.54E-05	0.6
*B*D*	-2.20E-06	0.1	-5.79E-08	0.0	1.37E-04	1.6
*C*D*	-1.07E-05	0.4	7.91E-06	0.1	2.98E-04	3.5

Figure 36 provides a visual representation of the relative weights of each variable and the second order combinations for the three blowing ratios. Out of the 14 total contributing factors, a few of the factors dominate the influence on the effectiveness. The three strongest factors (A, B, and A*A) combine to form about 70% at M=2.0, of the influence on the effectiveness. When the next two strongest factors (B*B and A*C) are added in, this rises to about 80%. The other two blowing ratios show similar trends, though the order of influence may vary slightly.

A closer look provides more insight. Nine of the 14 factors involve plenum variables, but these factors consist of less than 25% of the total contribution for M=2.0. This number decreases with decreasing blowing ratio, near just 10% for M=0.5. That is, almost 90% of the variation in

effectiveness prediction at M=0.5 comes from the mainflow variables only. In the range studied, the size of the plenum has little effect on the outcome of the prediction. Now that the relative strengths of the domain parameters have been initially explored, the next consideration is the nature of these effects. Figure 37 presents a closer look at the four first order effects, as the four variables vary from -1 to 1, holding the other three variables constant. Immediately apparent is the same observation from above, that the two mainflow parameters influence the effectiveness solution much more than the two plenum variables. The mainflow height (B), again, seems to have a weakened influence for the M=1.0 case.

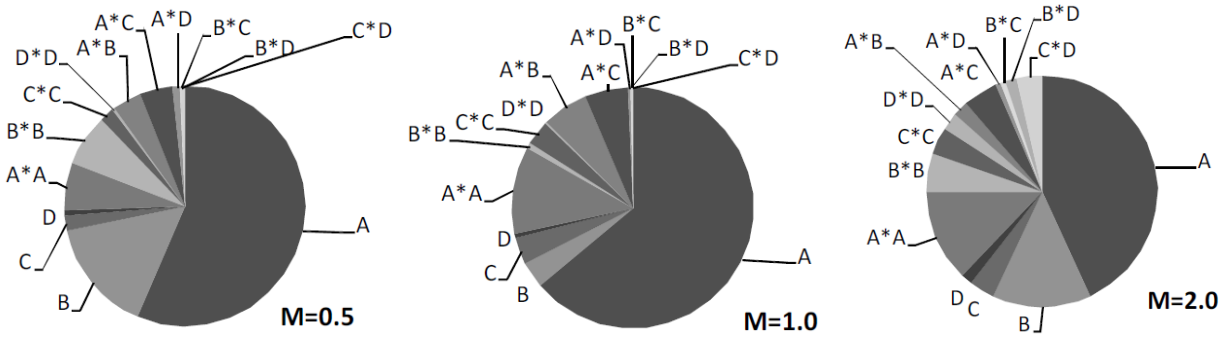

(a) (b) (c)

Figure 36 Relative influence of each first and second order effects on spatially-averaged effectiveness for blowing ratios of (a) M=0.5, (b) M=1.0, and (c) M=2.0

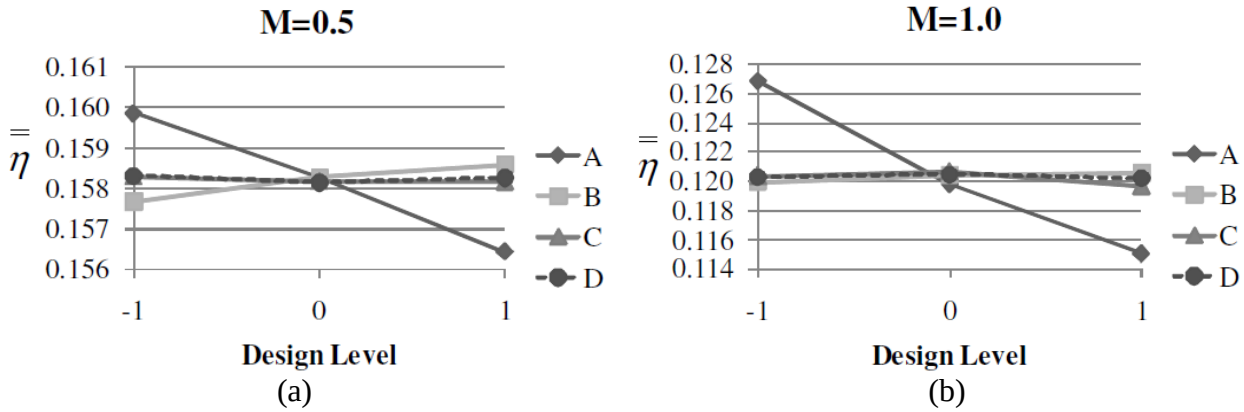

(a) (b)

Figure 37 First order effects of (a) M=0.5 and (b) M=1.0.

The L_e curves in Figure 38a show the strongest of the four effects: the entrance length of the mainflow. Here we observe that a short entrance length (10 diameters) yields a comparatively much higher effectiveness that the other two entrance lengths. The relationship between entrance length and the effectiveness of the coolant appears to be non-linear (specifically, upwardly concave). The maximum variation due to entrance length is about 12% at M=1.0 and just 2% at M=0.5, relative to the middle entrance length. It does not appear as if the solution becomes relatively independent of entrance length at the largest entrance length of 30 diameters.

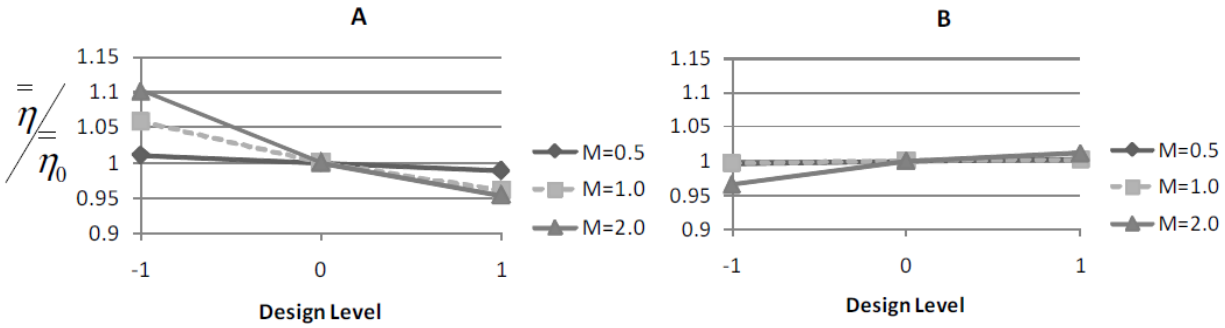

(a) (b)

Figure 38 First order effects of (a) Le and (b) Mh at all three blowing ratios.

The other important relationship to observe is the effect of the mainflow height, shown in Figure 38b. Here, the relative variation of the smallest mainflow height is small compared to the entrance length. As previously noted, in the M=1.0 case, it seems to have no more effect on the prediction than the two plenum variables. For M=0.5, though not as exaggerated as the entrance length, there is still a noticeable non-linear pattern to the relationship. The smallest mainflow height leads to the lowest effectiveness. As the mainflow height is increased, it appears to approach a steady effectiveness value, independent of the height of the mainflow. The previously noted fluctuation of the M_h influence can be explained using Figure 38, where the effectiveness predictions are normalized by the value of the prediction at the median value. For the L_e factor,

there is a relatively even difference in percent variance between blowing ratios. This is not the case for the M_h factor. Although the M=2.0 yields a much higher variance, the two lower blowing ratios give about the same curve. At M=0.5, Le fairly dominates M_h. When the blowing ratio is increased to M =1.0, the influence of Le begins to increase relatively steadily (linearly), but the influence of M_h remains constant. This leads to a decrease in the relative influence of M_h, as seen in the pie charts of Figure 37. As the blowing ratio is increased further, however, M_h begins to have much stronger influence (a highly non-linear increase with blowing ratio), while the Le continues to increase influence at about the same rate. This leads to an increase of the influence of the M_h relative to the other variables and a reversal in its relative influence trend.

Returning to Figure 38, the two plenum variables do not exhibit significant changes over the range of the study. The middle point in each of the four graphs represents the predictions of effectiveness from the same domain consideration, but each are based on the statistical predictions focusing on one of the four parameters. Ideally these would be the exactly the same, but statistical uncertainty yields a certain variation in these values. Thus, such variation can be used to estimate the statistical uncertainty coming out of the response surface method. With this in view, the plenum variables do not change by much more than the statistical variation, leading to the confirmation that the effectiveness prediction is relatively independent of the plenum size in the studied range. As a quick note, the effectiveness does drop slightly as the height and width of the plenum is increased to 12 diameters, perhaps indicating that there the possibility is still open for a non-constant behavior outside the studied range.

Having explored the first order effects of the domain parameters, the second order effects are now investigated. As mentioned before, none of the second order effects involving two different

parameters exhibited strong influence on the prediction of effectiveness. Figure 39, which illustrates the M=2.0 case but is typical for all three blowing ratios, serves to confirm this: none of the plots exhibit strong variation.

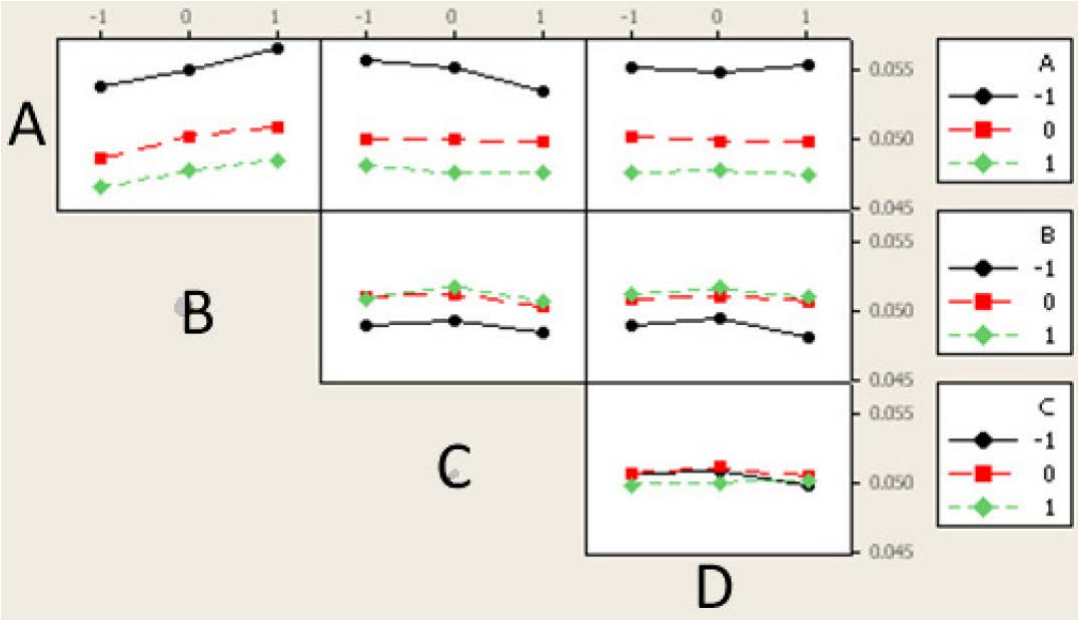

Figure 39 Summary of second order effects (M=2.0), typical for all blowing ratios.

The strongest interaction factors here are the A*C and A*B factors. For the former (top center graph), at the -1 level of A, there is a decrease of effectiveness associated with an increase in plenum height. For the longer entrance lengths, the effectiveness prediction appears independent of the plenum height. A similar trend is observed for the A*B factors (top left graph). The mainflow height and plenum height seem to have large influence on the effectiveness prediction if the entrance length is short. Otherwise, their effect is diminished.

Now that the statistical data has been interpreted, explanations of the various effects will be presented. The dominance of the mainflow entrance length commands attention first. After applying a uniform velocity profile at the mainflow inlet, the boundary layer develops as the flow progresses towards the hole. A hole that is further away from the uniform velocity inlet will

experience a thicker boundary layer (δ_{95}). Figure 40 confirms that there is a significant difference in the boundary layer thickness meeting the exiting coolant jet.

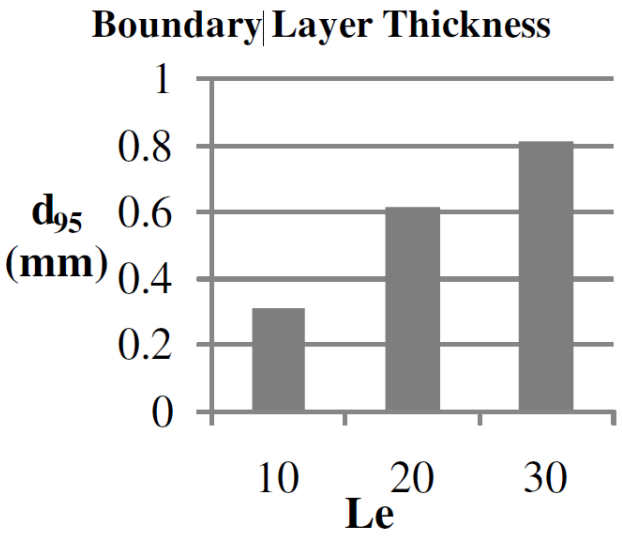

Figure 40 Boundary layer thicknesses for varying mainstream entrance lengths

As the coolant jet exits the hole, the mainflow forces the jet back against the downstream wall and increases the effectiveness. For the case of a mainflow with a smaller boundary layer, the jet is more quickly met with the full impulse of the mainflow and forced back toward the surface. A thicker mainflow boundary layer will be slower to force the jet back toward the surface, resulting in a higher jet trajectory and lower effectiveness values. This explanation not only agrees well with the observations from the sensitivity analysis, but also agrees with experimental data and conclusions of Goldstein et al. (1974) regarding boundary layer thickness.

Next, the question of the M_h influence is interesting. As hinted above, the coolant jet trajectory after exiting the hole has a large effect on the effectiveness of the coolant. At M=2.0, the jet has such large momentum compared to the mainstream that it is not forced back to the surface, but lifts off into the mainstream, giving the lowest effectiveness. Because of its high

trajectory, it is also the most susceptible to be effected by the proximity of the applied mainstream boundary condition. Figure 41 shows a comparison of trajectories between the three blowing ratios. Both the M=0.5 and M=1.0 jets remain far enough away from the artificial freestream boundary condition that they are minimally effected, but the M=2.0 jet shoots up close enough that there is a strong effect if the M_h is set too low. As the M_h increases, the effectiveness value non-linearly approaches a steady value.

The relatively constant effectiveness values across the range of plenum sizes, both height and width, suggests that the velocity profiles at the inlet and exit of the holes are similar. Figure 42 compares inlet and exit hole velocity contours at M=2.0 for each of the plenum widths, which was the blowing ratio in which the plenum variables had the highest influence. Here, the velocities can be seen to be quite similar. Similarly, Figure 43 compares inlet and exit velocity contours with varying the plenum height. Again, these are very similar. At the inlet of the hole, the dense contours represent the contraction of the flow exiting the plenum and being contracted around the sharper angle of the upstream side of the coolant hole inlet. After the length of the hole, the contraction of the flow spreads, giving a more uniform velocity profile at the hole exit, which is seen in the uncrowded contours.

In addition to the effects of domain size on the effectiveness values downstream of the hole, the number of grid cells added by each of the domain parameters should also be considered in designing efficient computing methodologies. It should not be assumed that each of the four parameters studied effect the total grid cell count equally. Figure 44 plots the grid cell counts related to variations in each of the four parameters. The center point of convergence represents the baseline case. It is clear that the mainflow height (B) is the most costly dimension to expand.

The other three factors have similar impacts on cell count, with the entrance length (A) slightly higher than the plenum dimensions (C, D).

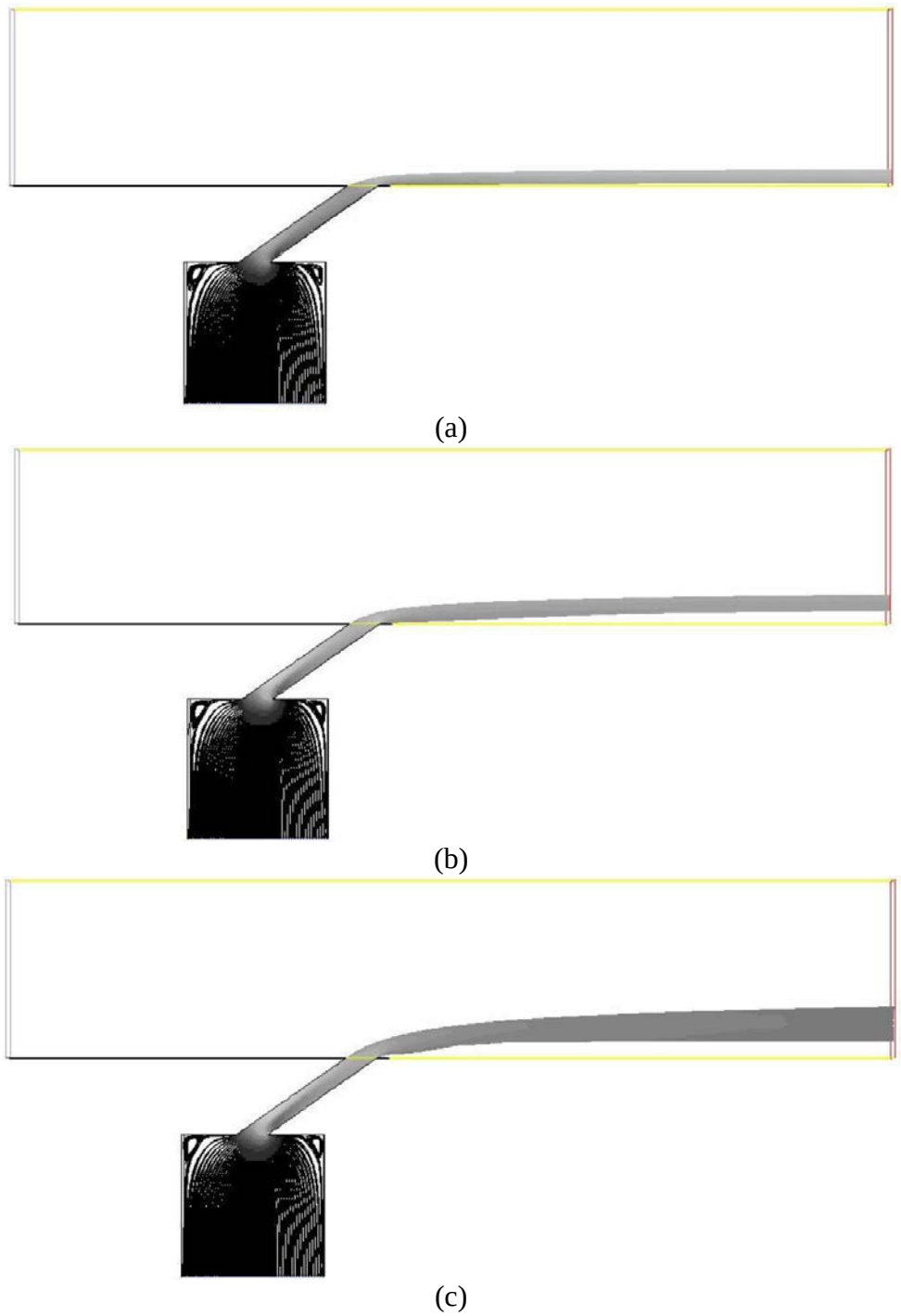

(a)

(b)

(c)

Figure 41 Streamlines showing jet trajectories for (a) M=0.5, (b) M=1.0, and (c) M=2.0

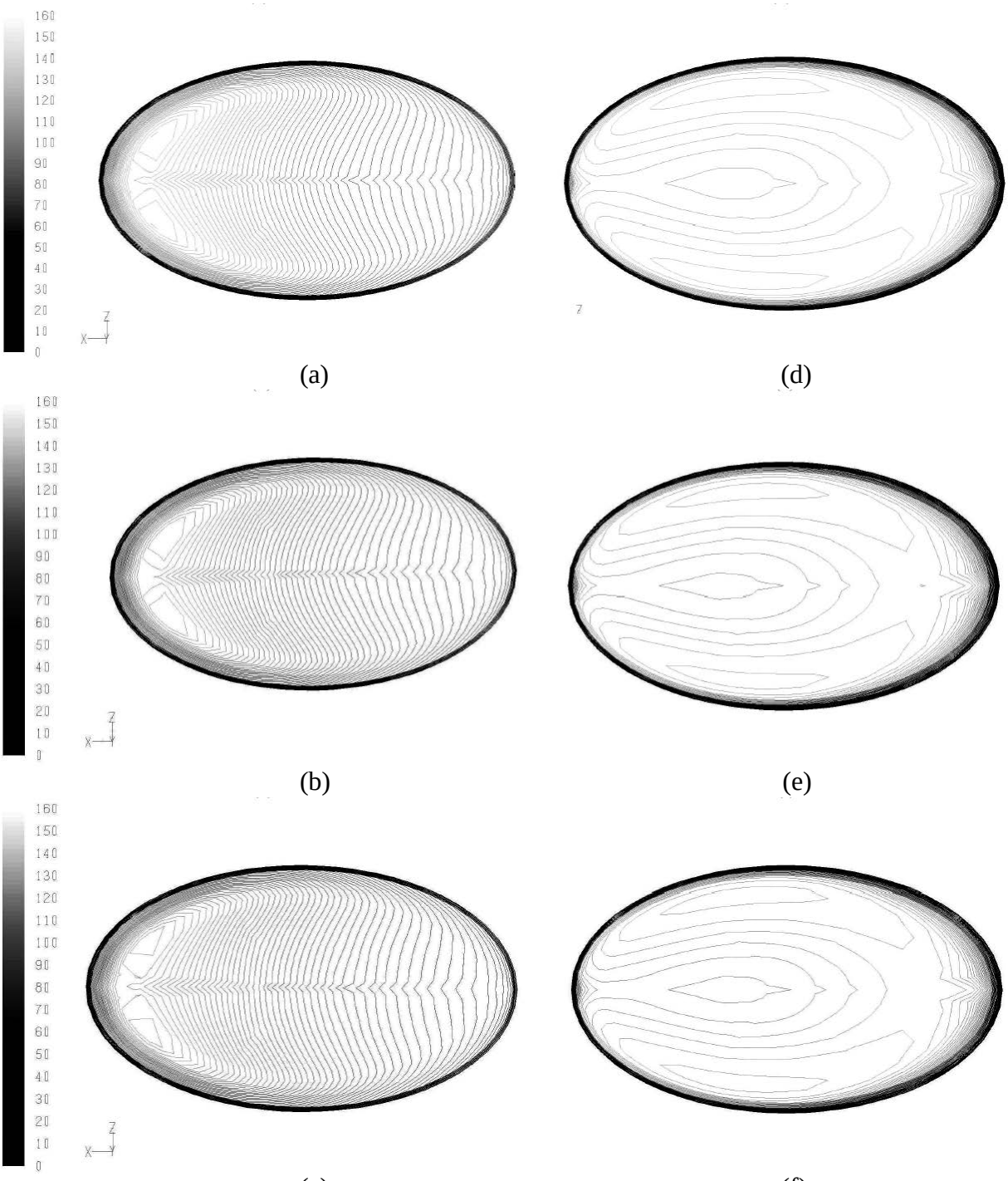

Figure 42 Velocity contours for M=2.0, (a) P_w=4D hole inlet, (b) P_w=8D hole inlet, (c) P_w=12D hole inlet (d) P_w=4D hole outlet, (b) P_w=8D hole outlet, (c) P_w=12D hole outlet

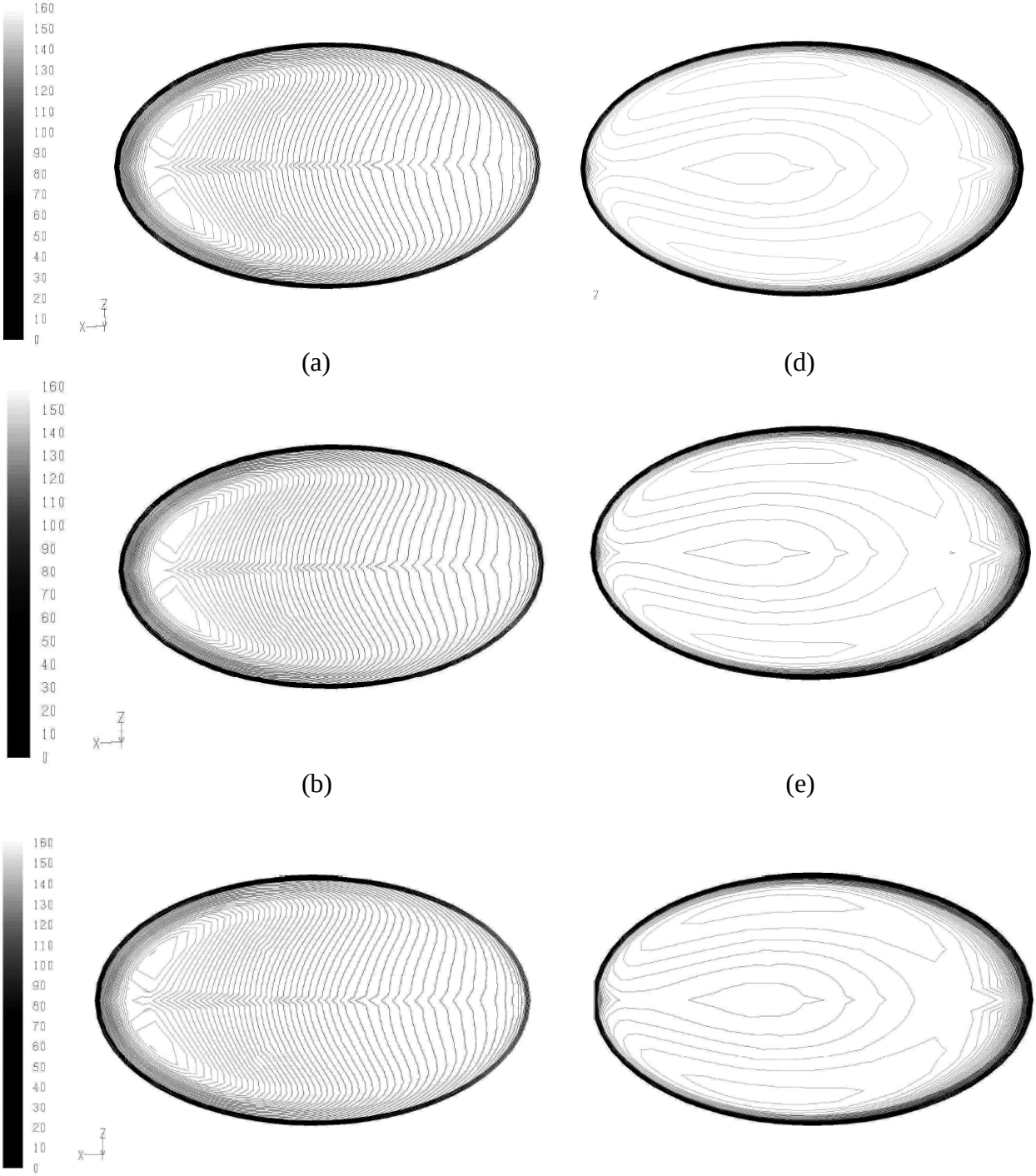

Figure 43 Velocity contours for M=2.0, (a) P_h=4D hole inlet, (b) P_h=8D hole inlet, (c) P_h=12D hole inlet (d) P_h=4D hole outlet, (e)P_h=8D hole outlet, (f) P_h=12D hole outlet.

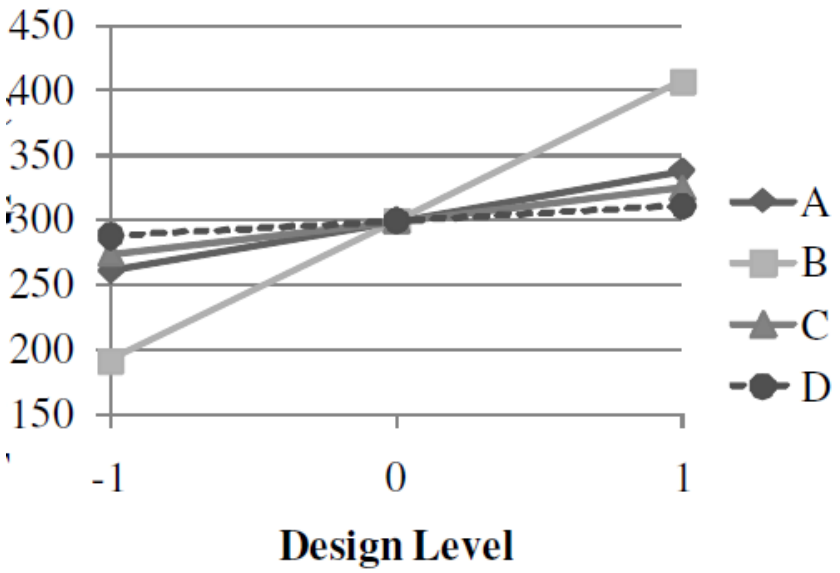

Figure 44 Thousands of grid cells vs. design level for each of the four parameters.

Table 9 presents the influence coefficients confirming the above discussion points. The influence coefficients from the spatially-averaged effectiveness results can then be divided by the grid cell count coefficients to obtain results on an accuracy benefit per computational cost basis. This statistic roughly represents the ratio of the relative added benefit in accuracy to the relative increase in computational cost for increasing a certain dimension. The ratios are presented for the first order effects in Table 10. In Table 10, the entrance length (A) dominates with the highest benefit to cost ratio by an order of magnitude. This is to be expected given its position as the most influential parameter on the effectiveness prediction. The other three parameters remain close to each other, with some blowing ratio effects as previously discussed. The mainflow height has a low ratio due to the steep computational price of adding more cells. The two plenum variables hold even with the mainflow height because of their relatively low effect on the prediction.

Table 9 Contribution coefficients for grid size.

Term	N	
	Coefficient	Percent Contribution
A	38.4	18.74
B	107.4	52.40
C	25.3	12.36
D	11.5	5.61
*A*A*	-0.5	-0.26
*B*B*	-0.5	-0.26
*C*C*	-0.2	-0.08
*D*D*	-0.4	-0.20
*A*B*	18.0	8.78
*A*C*	0.3	0.12
*A*D*	0.0	0.00
*B*C*	0.3	0.12
*B*D*	0.0	0.00
*C*D*	5.5	2.68

Table 10 'Benefit to cost' ratio for the first-order parameters.

Term	M=0.5	M=1.0	M=2.0
A	3.01	3.40	2.30
B	0.29	0.07	0.26
C	0.17	0.30	0.28
D	0.12	0.09	0.30

7.4 Boundary Placement Conclusions

The current study aimed at exploring the various domain considerations in the reduction of computational grid size for the optimization of computer resource usage. Under the considerations of the studied range of domain sizes, the following conclusions are recommended by the authors:

1) The most influential consideration on the effectiveness prediction is the entrance length of the mainstream (L_e). This consideration could be avoided all together by employing boundary conditions with a robust empirically, mathematically, or numerically determined velocity profile

at the mainflow entrance. Employing a uniform velocity profile demands a long (30+ diameters) entrance length unless a certain upstream length is desired for study.

2) For jets with high penetration into the mainstream, the mainflow height must be selected carefully to avoid its artificial influence on the effectiveness results. Otherwise, the mainflow height can be shortened even to around 5 diameters without too much harm to the solution. This can drastically help in the reduction of grid size. The mainflow height has the highest influence on grid cell count, making it the most important consideration in terms of computational cost. One method for reducing this effect is to coarsen the grid as it progresses away from the cooled surface, such that the wake region remains finely meshed but the region relatively unaffected by the coolant flow costs less in computational effort.

3) A small plenum should suffice for accurate effectiveness predictions with geometric parameters similar to those in the current study. It should be noted that shorter coolant holes ($L/D < 7.5$) may lead to a greater effect of plenum size on the solution. Second order interactions between parameters were found to be small as well.

The conclusions drawn in this boundary placement study are vital for minimizing the computational cost of Large-Eddy Simulations without harming accuracy. The study was performed with a RANS model due to the extreme cost of performing 25 LES runs, but the results can be safely extrapolated to LES because the flow physics are the same regardless of the simulation technique.

7.5 LES Discretization Formulation and Methodology

A common topic of interest relating to LES techniques is the influence of discretization scheme on the accuracy of the solution. While central differencing schemes are usually applied to the

diffusive terms of the governing equations, a number of different schemes have been advocated for the convective terms. The previous LES work in film cooling has displayed the variety discretization schemes. Rozati and Tafti (2007a, b, 2008) utilized a second-order central difference scheme in their incompressible solver, while Tyagi and Acharya (2003) and Leedom and Acharya (2008) used a third-order upwind scheme. Iourokina/Peet and Lele (2006a, b, 2008) applied the third-order QUICK scheme to their incompressible domain and fourth order central differencing to the compressible equations. Renze et al. (2008a, b, c, 2009) used the advective upstream splitting method (AUSM) for their compressible code, the validation of which can be found in Meinke et al. (2002) against a sixth-order compact central differencing scheme. Breuer (1998) compared five different schemes in an LES of a solid cylinder in crossflow, recommending a second- or fourth-order central scheme.

The focus of the present paper is to better understand the film cooling predictions of numerical solutions using LES. As stated by Breuer (1998) concerning LES techniques, "the most important component is the discretization of the non-linear convective fluxes." For this reason, the impact of discretization schemes on the LES predictions of film cooling is investigated.

7.5.1 Geometric and Hydrodynamic Parameters

The cylindrical geometry for the present study was chosen to allow for comparison with multiple previous experimental studies which reported different aspects of the film cooling scenarios. One cylindrical hole is modeled with an inclination angle of 35°, pitch-to-diameter ratio of 3.0, and length-to-diameter ratio of 3.5. The density ratio (DR =1.25) allows for close comparison with the center-plane temperature measurements from Case 8 of Thole et al. (1992). This selection also allowed for the consideration of another experimental study: the flow field

velocity and temperature measurements of Rydholm (1998), specifically Series 1 from that study. Key differences with Rydholm include its longer hole (L/D = 8.0) and lower inclination angle (α). As shown by Sinha et al. (1991), Burd et al. (1996), and Lutum and Johnson (1999) the effect of the lower injection angle used in Rydholm (1998) is augmented by the longer delivery tube.

In addition to flow field temperature and velocity, experimental results for film cooling effectiveness were chosen for validation purposes. The results of Sinha et al. (1991), which uses shorter cooling holes (L/D=1.75), are commonly used in numerical film cooling validation. Pedersen et al. (1977) contrasts this with cooling from much longer holes (L/D=40). Since the L/D differs significantly, the data from Lutum and Johnson (1999) are also considered so clarify the effects of L/D on effectiveness. Table 11 presents the important geometrical and fluid mechanical parameters for the present baseline case, as compared with the various experimental results chosen for validation.

Table 11 Geometric and Hydrodynamic Parameters for Current Study and Experimental Studies.

	Current Study	Sinha et al (Case 5)	Thole et al (Case 8)	Rydholm (Series 1)	Pedersen et al (two cases)	Lutum & Johnson (two cases)
D	2mm	12.7mm	12.7mm	5mm	11.7mm	4mm
L/D	3.5	1.75	3.5	8.0	~40	3.5
p/D	3.0	3.0	3.0	3.0	3.0	2.86
α	35°	35°	35°	30°	35°	35°
DR	1.25	1.2	1.2	1.17	1.18, 1.57	1.15
M	1.0	1.0	1.0	1.01	1.05	0.81. 1.15
I	0.8	0.83	0.83	0.88	0.936, 0.716	0.58, 1.16
δ_{99}/D	1.0 (x/D=-3)	0.52 (x/D=-2)	0.52 (x/D=-2)	0.7 (x/D=-3)	N/A**	~1.0
U_∞	56.4 m/s	20 m/s	20 m/s	47.4 m/s	15.4 m/s	115m/s
Tu_∞	1%	<0.2%	<0.2%	~1%	0.3-0.4%	3.5%

** displacement thickness close to double that of Refs. 10 and 11

While choosing a single experimental case to model with full fidelity for geometry and flow conditions might have been a preferred validation method, the authors wished to compare several

aspects of the data with experiment and therefore needed to combine these data sets together to provide a more complete picture of the simulation's relation to experimental data.

7.5.2 Computational Domain and Boundary Conditions

A row of film cooling holes is simulated using a reduced domain which includes just one film cooling hole. Periodic or symmetric boundary conditions can be enforced in the spanwise directions, allowing for the single hole to mirror the results of the entire row of holes. The mainstream is modeled to a height of five diameters above the cooled surface, at which a symmetry boundary condition models free stream conditions without causing significant inaccuracies in the modeling of the film cooling flow (see previous sections of this chapter). The crossflow inlet is placed three diameters upstream of the origin where a velocity profile obtained from a RANS simulation is applied. Inlet turbulence is modeled using a spectral synthesizer method to imitate velocity fluctuations in the crossflow.

The length of the coolant tube is 3.5 diameters with its entrance fed from a coolant plenum. The height and width of the plenum are both modeled at four diameters. A constant velocity profile with no inlet turbulence is applied at the inlet to the plenum (bottom surface). The numerical domain of the current study is illustrated in Figure 45.

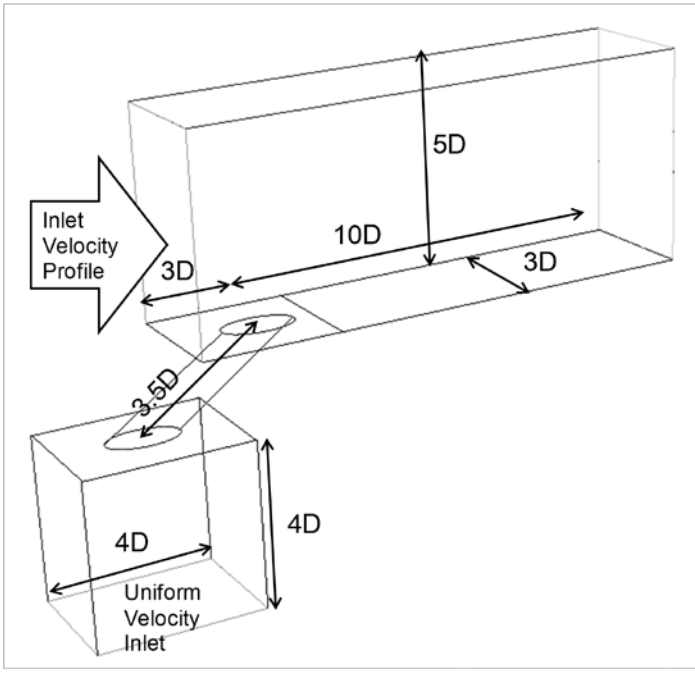

Figure 45 Computational domain considered for LES discretization study.

For the grid structure, the crossflow and plenum were each split into two regions: one region of finely spaced grid cells and a neighboring region of more coarsely spaced cells. The fine grid region extends two diameters into the mainflow above the cooled surface and the fine region of the plenum extends one half of a diameter below the coolant tube inlet. Figure 46 shows the grid structure of the simple cylindrical case. The grids were constructed using the Gambit (2008) meshing software. A grid consisting of around three million cells was used for each case.

7.5.3 Numerical Method

Once completed in Gambit, the grids were exported into the Fluent (Ansys 2009) CFD solver. The boundary conditions, as prescribed above, were applied in the Fluent software, preparing the grid for solution. Before solving in the temporal domain, a RANS solution was

found for each grid using the realizable k-ε turbulence model. This RANS solution served as the initialization for the LES solution process.

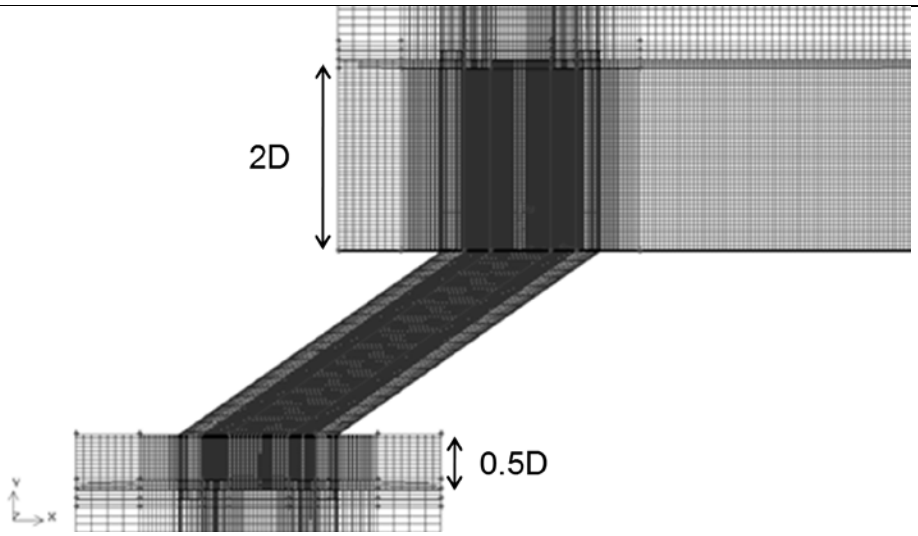

Figure 46 Block-structured grid for LES discretization study.

The SIMPLE algorithm was used for pressure-velocity coupling in Fluent's segregated pressure-based solution algorithm. At each iteration, the three momentum predictor equations are solved sequentially, followed by a pressure-correction through the continuity equation. Once the mass fluxes, pressures, and velocities have been updated, the scalar equations, such as the energy equation, are solved.

The specified density ratio was applied using an incompressible ideal gas formulation for the density. That is, the ideal gas law, Eq. (70), was used to calculate density at each iteration, with the pressure set to a constant operating pressure of P_o = 101.325 kPa. In this way, the temperature ratio was used to control the density ratio. Compressibility effects were negligible due to the low Mach numbers in the flow, even in the jetting region of the film cooling hole (Ma < 0.3).

The temporal discretization was accomplished using a second order implicit time-stepping approach. Iterations were performed at each time step to ensure convergence. The relaxation factors were started very low, (e.g. 0.1-0.3), to avoid divergence as the LES process was introduced. As the LES flow developed, the relaxation factors were gradually increased and scaled residuals on the order of 1e-4 for continuity and 1e-6 for momentum and energy equations were reached for each time step. Once the simulations reached statistical stability, mean quantities of time-averaged data and turbulence statistics were calculated. The time step size was set equal to $0.0275*D/U_{\infty}$, which was estimated to be on the order of the Kolmogorov microscale for the present simulation. After the statistical sampling was enabled, the flow was allowed to run for five crossflow flow-through times.

Four complete and independent large eddy simulations were performed with identical methodologies as described above. The only variation in the solution technique between the four cases was the discretization scheme for the non-linear convective terms of the governing equations. The diffusive terms were discretized with a second-order central differencing scheme. The first scheme applied to the simulation was bounded central differencing (BCD), which switches between a second-order central/upwind scheme and a first-order upwind scheme based on the NVD approach. The first-order upwind scheme is only used when the convection boundedness criterion is violated. This scheme is designed to provide a reliably stable solution with low numerical diffusion. Two purely second-order schemes were also implemented: upwind (PUW) and central differencing (PCD). Finally, the third order QUICK scheme (upwind biased) was the fourth and final case.

7.6 Discretization Study Results and Discussion

7.6.1 Mean Surface Effectiveness

Figure 47 displays time-averaged effectiveness on the downstream surface for each of the four LES schemes. Each scheme resolves a region of low effectiveness just downstream of the hole, suggesting film lift-off. The four simulations each show different reattachment behavior. The BCD solution shows the weakest reattachment with maximum effectiveness falling short of 0.3, whereas the PCD solution shows the strongest reattachment, reaching effectiveness values in excess of 0.4. It could also be said, because of the lower effectiveness values further downstream compared with the other three simulations, the BCD solution shows faster entrainment of the coolant jet. This statement will be evaluated in a later discussion. All but the PCD solution demonstrate a severe initial necking of the contours as the crossflow wraps around the protruding jet. These simulations suggest a stronger influence of the CVP in lifting the jet from the surface than the PCD. Overall, the PCD simulation provides the best coverage of film (highest effectiveness, most lateral spreading, and quickest to re-attach) and the BCD shows the worst coverage.

Figure 48 shows the centerline and laterally-averaged results. Alongside the four LES variations in each figure are shown the effectiveness results to which the current scenario is comparable, as previously discussed (Table 11). The large spread of experimental data possibly indicates the importance of other parameters not held constant.

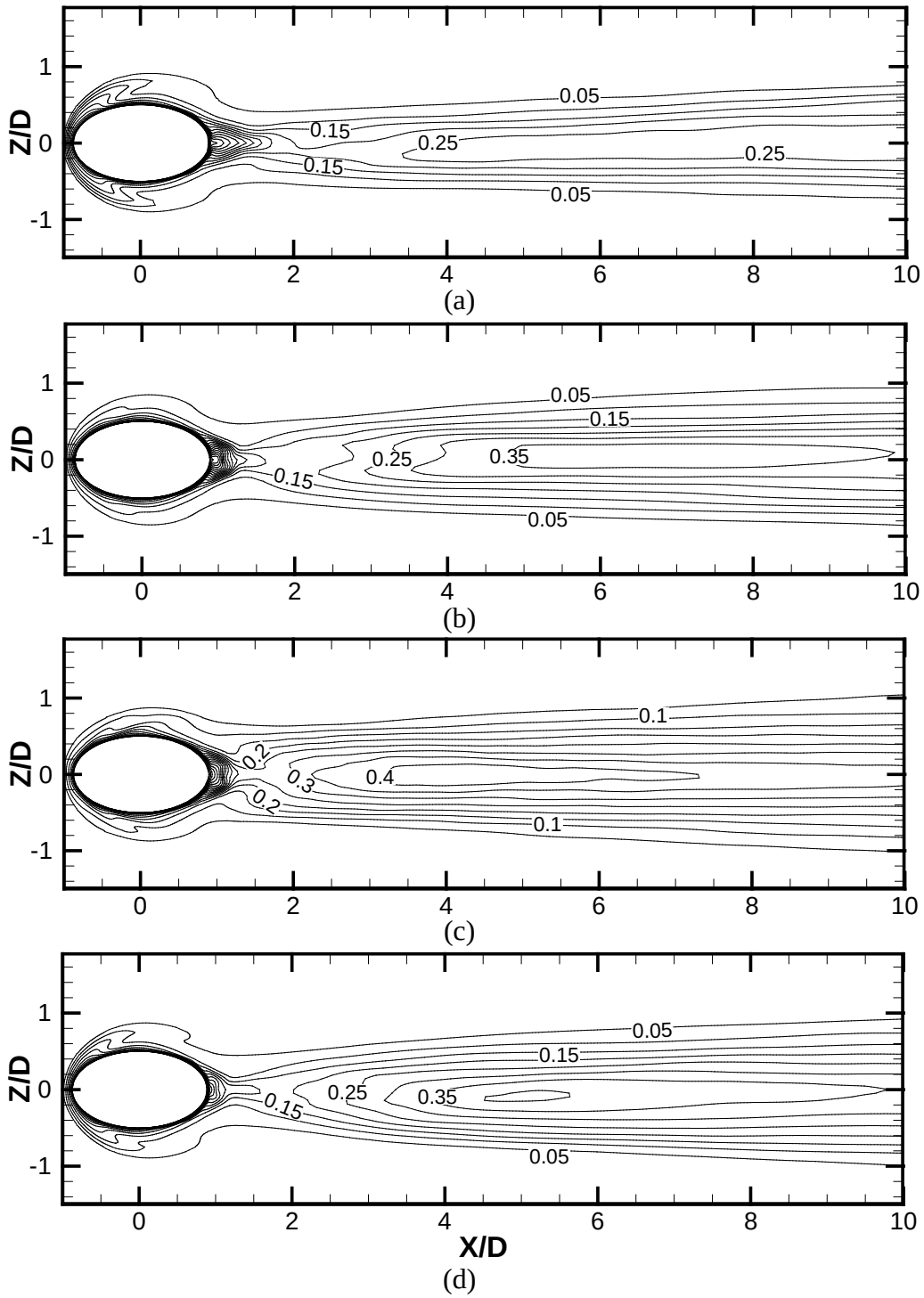

Figure 47 Adiabatic effectiveness contours on the downstream surface following the discrete film injection as predicted by (a) BCD, (b) PUW, (c) PCD, and (d) QUICK.

Three of the four schemes give similar centerline results farther from the hole (X/D > 5). The BCD results are much lower than its three counterparts; lower than would be expected from the data. The extreme effect of the shorter holes from Sinha et al. (1991) is seen. The steeper slopes of the Burd et al. (1996) data are most likely attributable to the higher freestream turbulence in those experiments. The three similar results from the present simulations fall between the bounding momentum ratios from Pedersen el al. (1977). Near the injection site, the schemes differ from each other significantly. Each scheme shows different lift-off behavior of the jet.

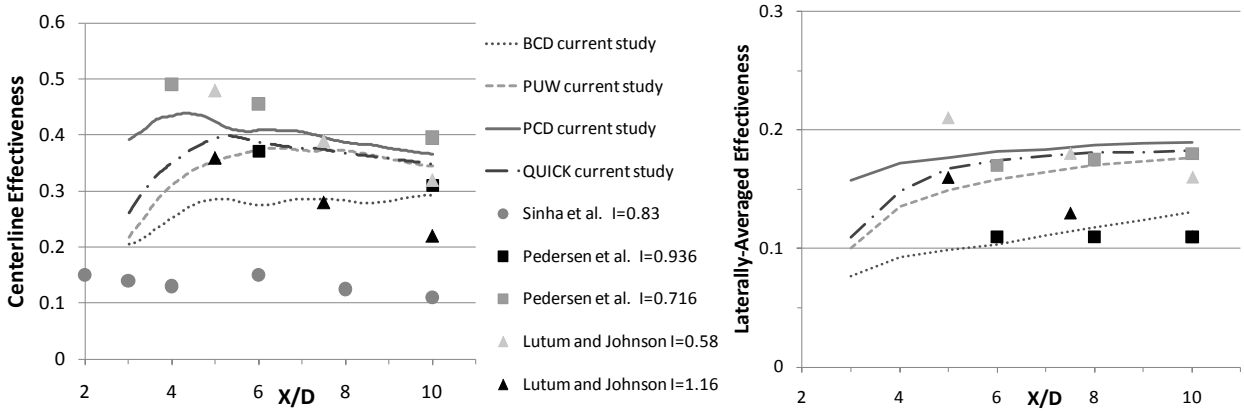

(a) (b)

Figure 48 (a) Centerline and (b) laterally-averaged effectiveness downstream for each simulation compared with experimental data.

The laterally-averaged data communicates similar trends as the centerline results. The PUW, PCD, and QUICK solutions again converge away from the hole but the PUW and QUICK show much lower effectiveness near the hole. The slope of the effectiveness curve (slightly positive) matches well with the Pedersen data. The increased turbulent intensity of the Lutum tests likely causes enhanced mixing and quicker diminishes the film jet, leading to the negative slope observed.

The final method of evaluating the downstream surface is the spatially-averaged effectiveness. Table 12 gives the simple comparison. As seen in the previous results, the BCD gives the lowest effectiveness, while PCD yields the highest effectiveness.

Table 12 Spatially-averaged effectiveness for the four cases.

Bounded Central (BCD)	2nd-Order Upwind (PUW)	2nd-Order Central (PCD)	QUICK
0.076	0.107	0.131	0.115

7.6.2 Mean Temperature Field

Figure 49 contains the four center-plane contours of mean non-dimensionalized temperatures compared with the experimental data from Thole et al. (1992). The non-dimensional temperature is calculated using Eq. (71). The limit of the non-dimensional temperature as it approaches the surface is the adiabatic effectiveness. As noted in Thole et al. (1992), the temperature contours best mark the trajectory of the jet.

$$\theta = \frac{T - T_c}{T_\infty - T_c} \qquad (71)$$

The upper side of the jet is similar in all of the four cases, but significant differences are seen in the underside of the jet, in the jet's wake. The BCD shows a higher trajectory throughout the domain as the jet lifts from the surface and shows little tendency to reattach. The BCD scheme does not show elevated entrainment of hot gas into the cold jet as mentioned in the previous discussion. Reattachment behavior is evident in the other three cases. These contours clarify the previous surface data. The PUW and QUICK schemes predict an exaggerated lift-off near the hole and later reattachment when compared with the PCD scheme and experimental results.

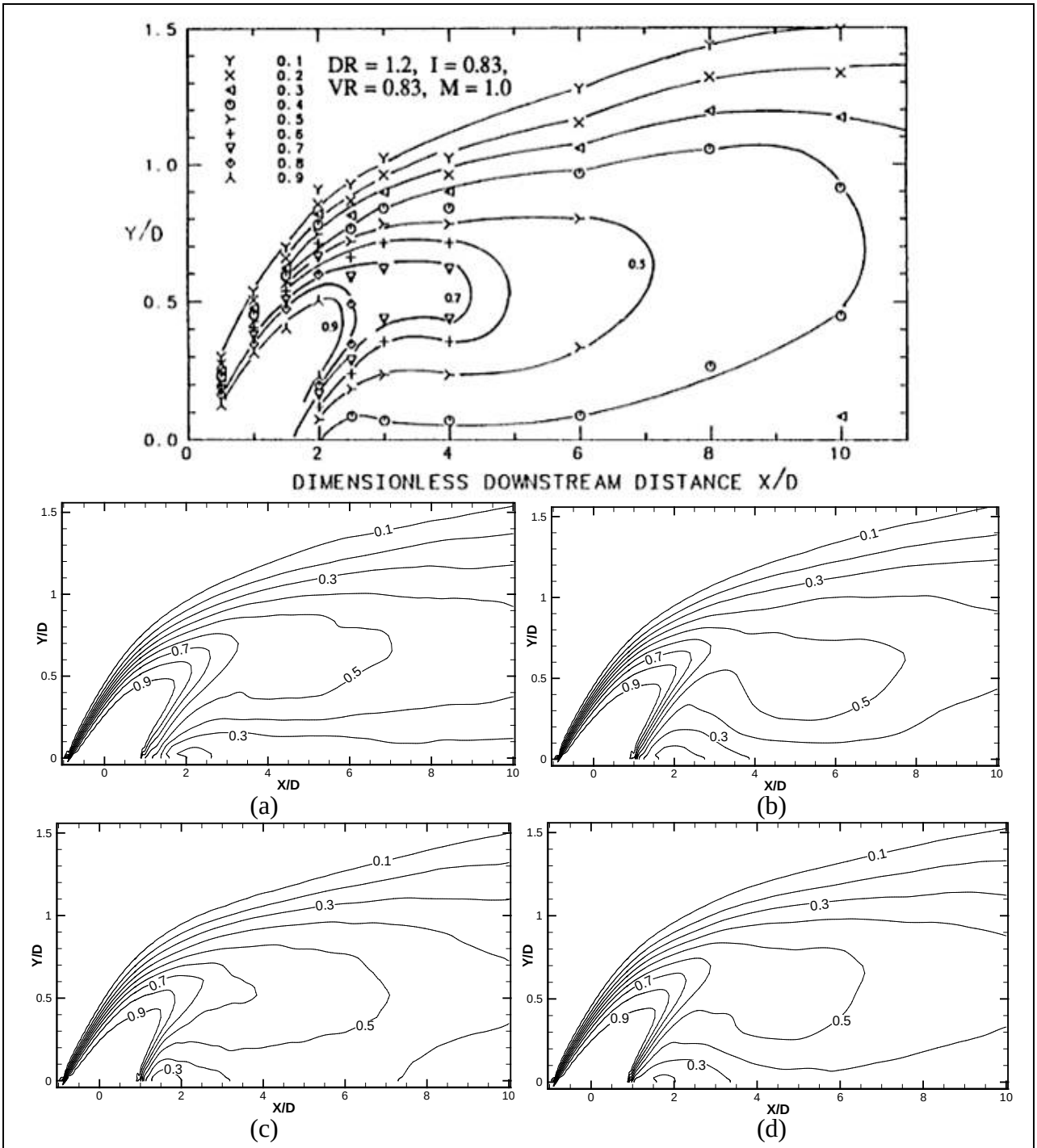

Figure 49 Comparison of non-dimensional temperature (θ) contours on the center-plane (z/D=0) with (a) experimental results of Thole et al. (1992): non-dimensional temperature profiles: (b) BCD results, (c) PUW results, and (d) PCD results, and (e) QUICK results.

Figure 50 presents non-dimensional temperature contours in the X/D = 4 plane alongside experimental data. Recall that Rydholm (1998) used a lower inclination angle and longer coolant hole, which combines to give a lower effective injection angle of the coolant. The simulation results indeed show a higher jet trajectory of the jet compared with the Rydholm data.

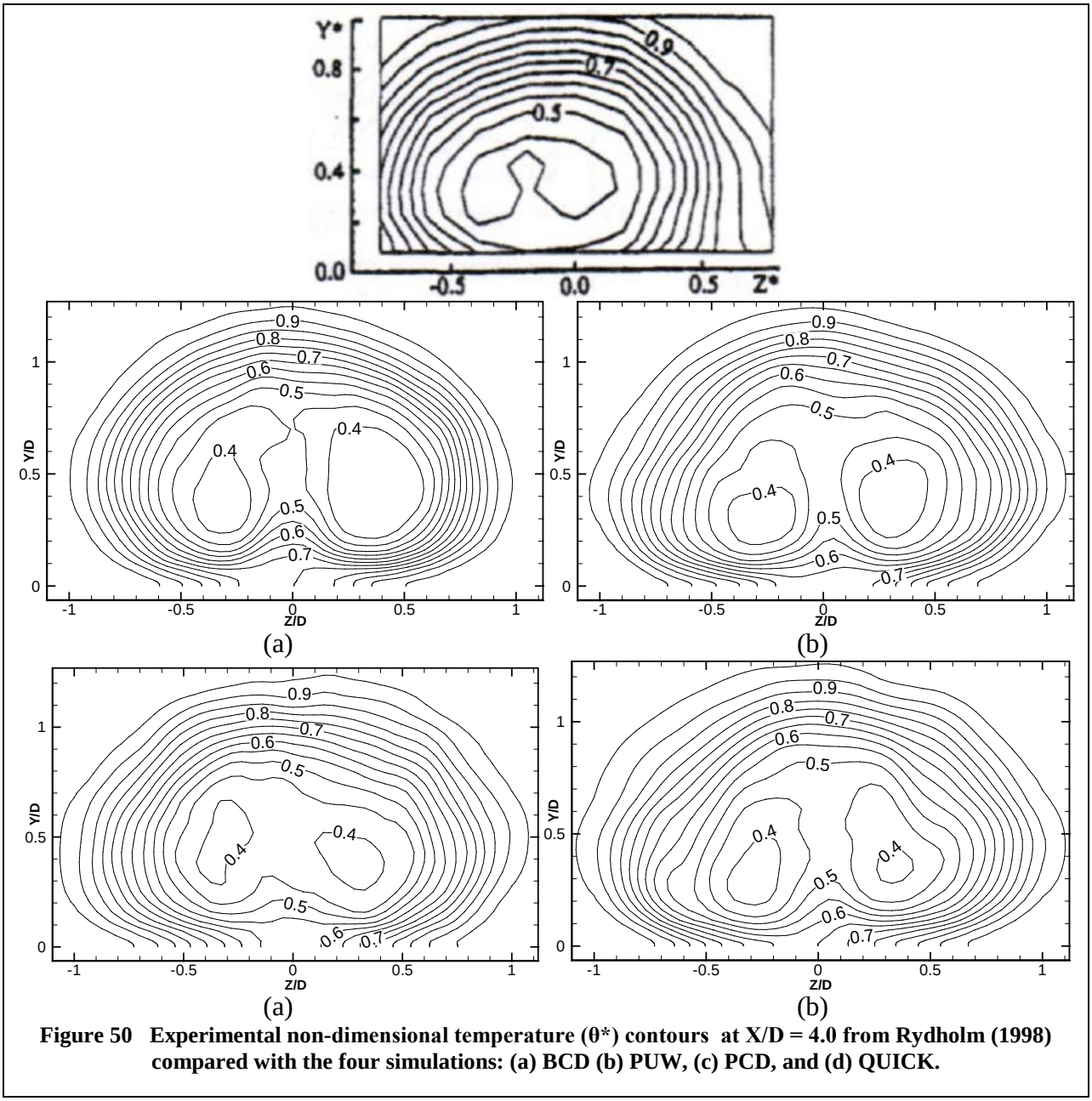

Figure 50 Experimental non-dimensional temperature (θ*) contours at X/D = 4.0 from Rydholm (1998) compared with the four simulations: (a) BCD (b) PUW, (c) PCD, and (d) QUICK.

The comparisons made in Figure 50 lend further insight into the differences of the LES solutions. The lateral spreading of the jet seen from the surface in Figure 47 is here shown to be more closely tied to the trajectory of the jet than to its spanwise diffusion. The BCD jet remains furthest away from the wall, resulting in its lower effectiveness and lateral spreading (as seen from the wall). The PCD simulation, with more lateral spreading at the wall, gains its advantage by primarily by its lower trajectory.

The BCD, PUW, and QUICK contours here show that their center-plane trajectories were caused perhaps more by the splitting of the coolant core by the CVP rather than the gross over-prediction of the overall trajectory of the jet. The apparent contraction of the PUW and QUICK jets along the center plane can also be explained in this manner. The BCD case yields a higher trajectory and more the near-wall pinching by the CVP, leading to the under-prediction seen in the effectiveness values. The PCD results show the lowest splitting of the coolant core, which corroborates best with the experimental evidence from Rydholm et al. (1998). This is a loose corroboration, keeping in mind the differences in injection angle, coolant hole length, and density ratio (see Table 11). A lower jet trajectory gives the CVP less room for turning over, likely diminishing its influence on the thermal field in the wake of the jet.

7.6.3 Mean Velocity Field

The velocity field can also provide insight into the physics of the film cooling flow and its numerical simulation. Figure 51 presents the streamwise velocity contours as normalized by the crossflow freestream velocity. It is seen from Figure 51 that the present simulations over-predict the velocity in the wake of the jet, that is, they under-predict the effect of the wake on the streamwise velocity. This can be seen as the cause of the over-prediction of the jet's ability to

maintain a colder core temperature further downstream (Figure 49). On the other hand, this suggests much more rapid mixing of crossflow momentum into the jet, which is not mirrored in the temperature profiles. There is no dramatic difference in the streamwise velocity contours, other than slight differences apparent with regard to the lateral spreading of the wake, which follows the previous discussions in favoring the PCD solution, which stays closer to the wall and spreads laterally.

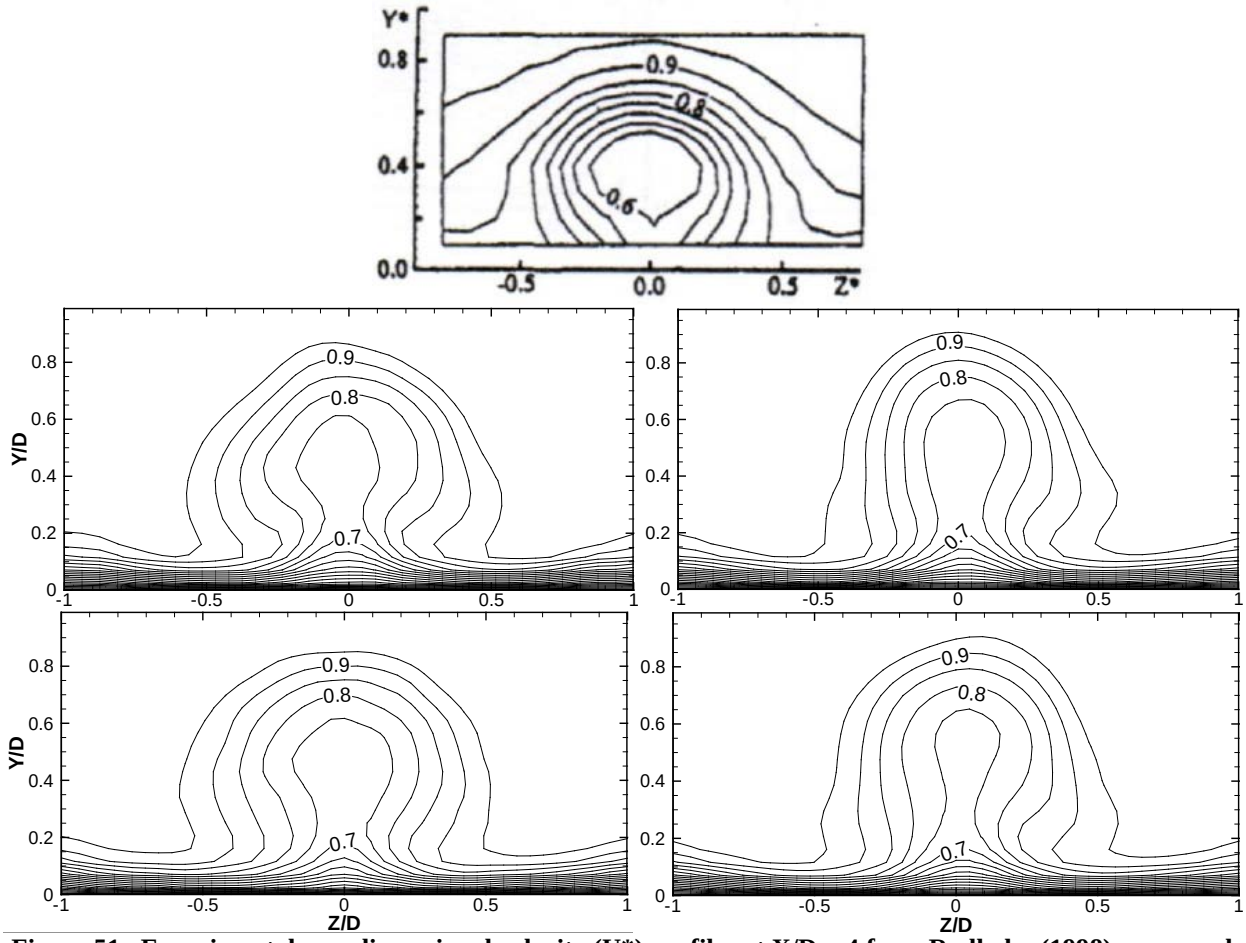

Figure 51 Experimental non-dimensional velocity (U*) profiles at X/D = 4 from Rydholm (1998) compared with contours from current simulations: (a) BCD, (b) PUW, (c) PCD, and (d) QUICK.

Now that the mean flow has been assessed, instantaneous snapshots of the flow field can give insight into the mechanism causing the differences in the discretization schemes. Because of the

unsteady nature of the flow, only qualitative comparisons can be made from instantaneous results.

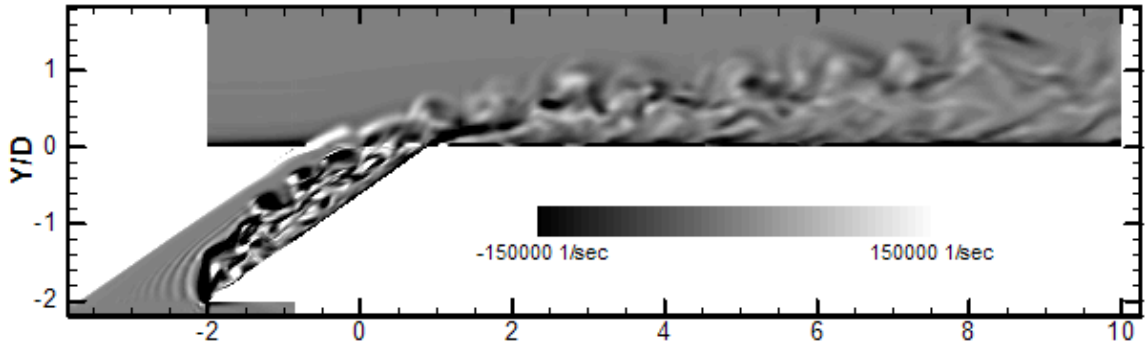

(a)

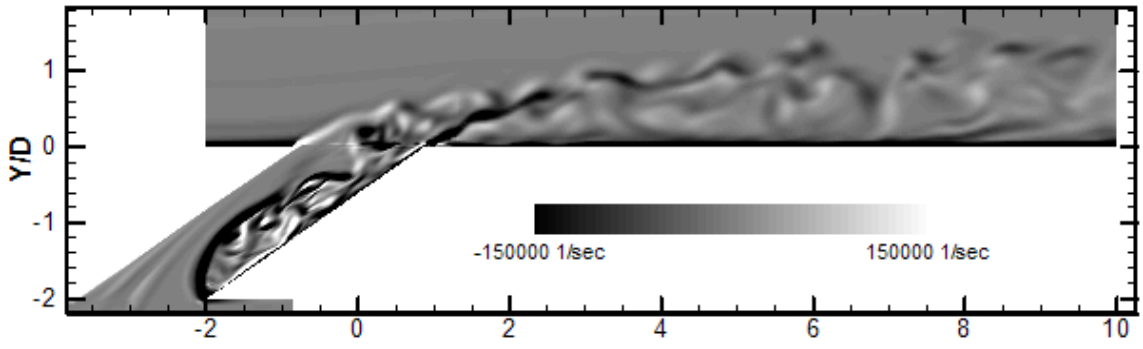

(b)

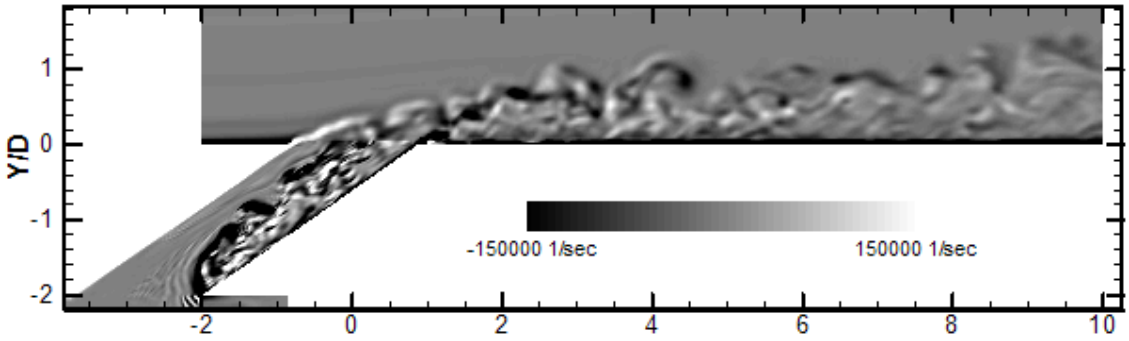

(c)

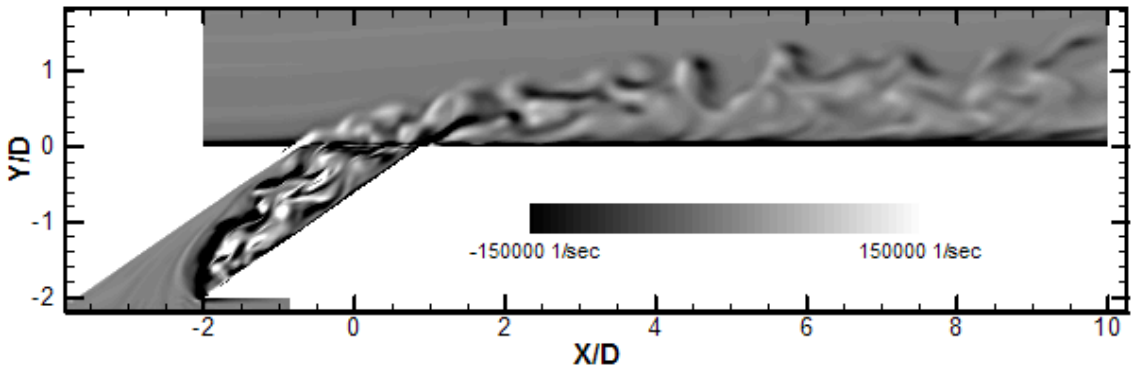

(d)

Figure 52 presents the instantaneous z-vorticity contours along the center-plane for the three cases. The folding of the ring vortices into the roller vortices on the upper half of the jet as it progresses downstream (Fig. 10 of Ref. 16) can be identified in all four cases. The chaotic flow within the coolant tube is highlighted, which is caused by the separation around the lip at the upstream side of the hole entrance. Without the inclusion of the plenum within the LES domain, this behavior is lost.

The primary insight from

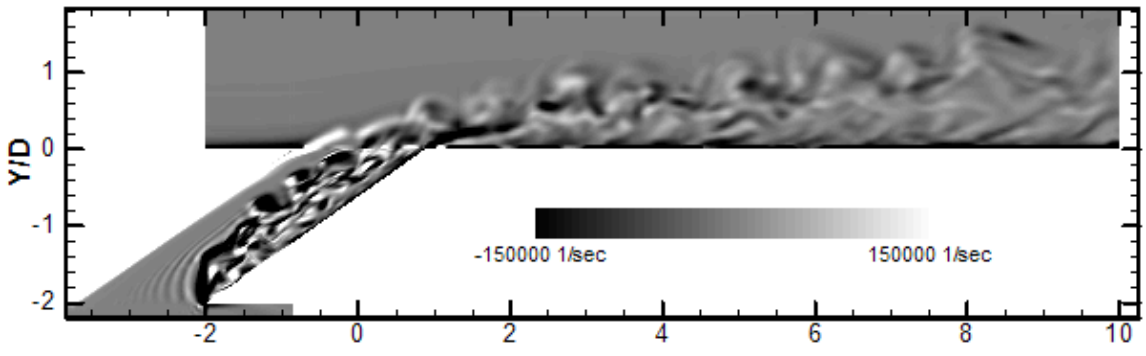

(a)

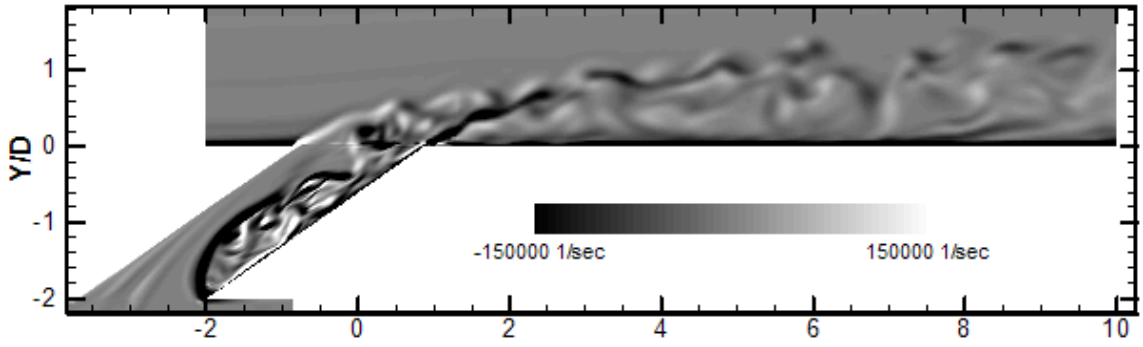

(b)

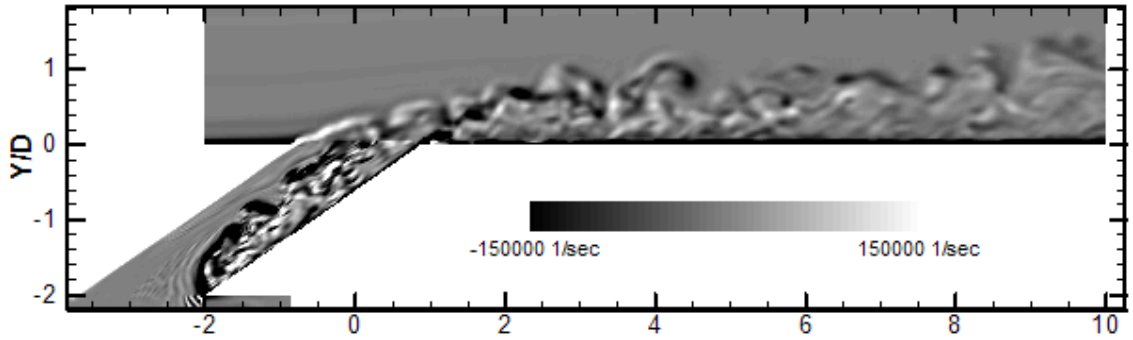

(c)

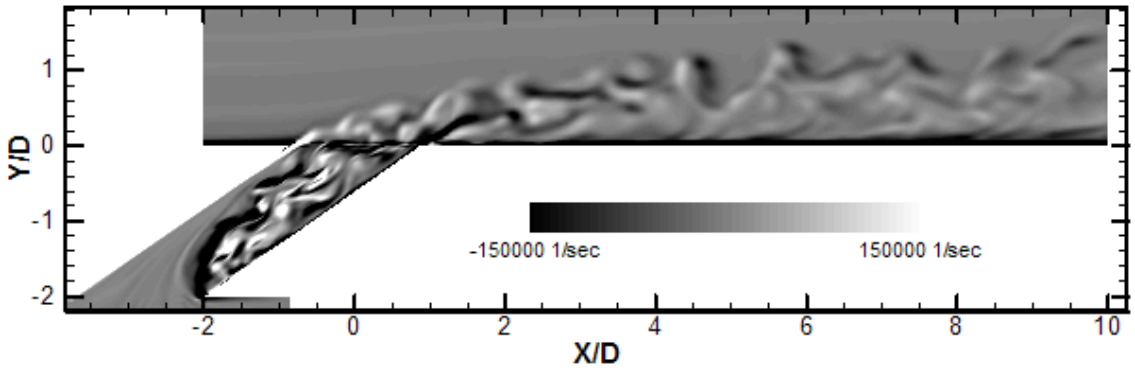

(d)

Figure 52 is the nature of the chaotic vortices resolved by each scheme. Comparison of PCD with PUW and QUICK shows clear contrast. The vortical elements of the PUW and QUICK scheme are blurred and elongated in comparison to the fine resolution apparent in the PCD results. Apparently, the PCD is able to capture finer vortical fluctuations within the flow field than the other two schemes.

An instantaneous temperature field for each of the three cases is captured in with which the turbulence fluctuations are resolved. Of the three solutions yielding mean results that compared well with experimental data, the PCD again is seen to resolve the temperature field to a finer extent than the PUW or QUICK. The relative trajectories of the jets, though not available for direct comparison, behave as previously discussed the mean temperature field.

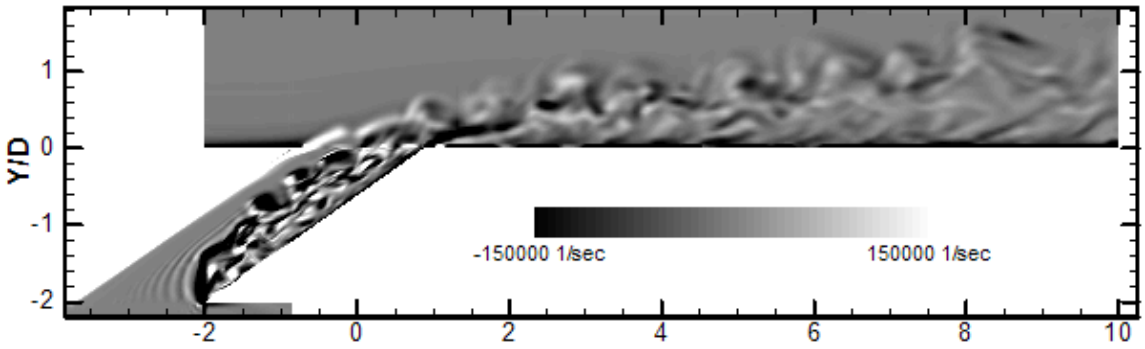

(a)

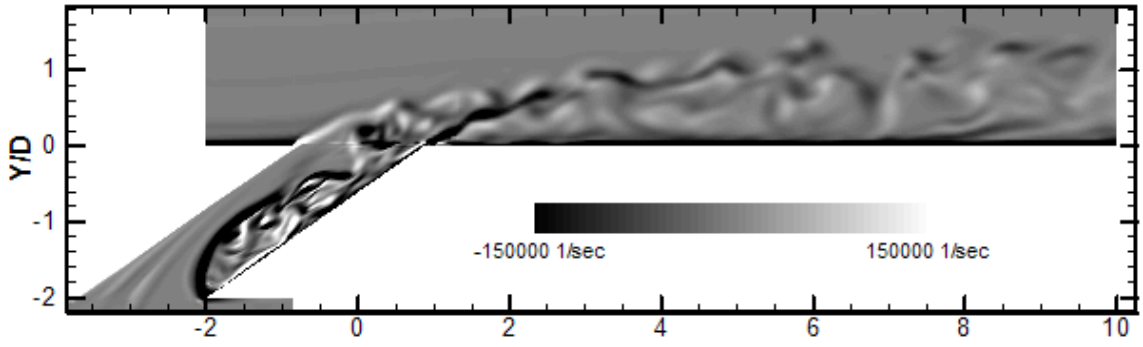

(b)

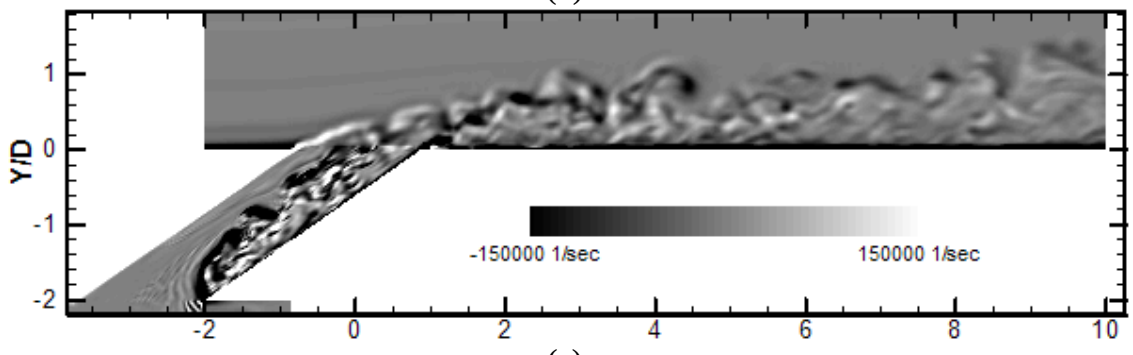

(c)

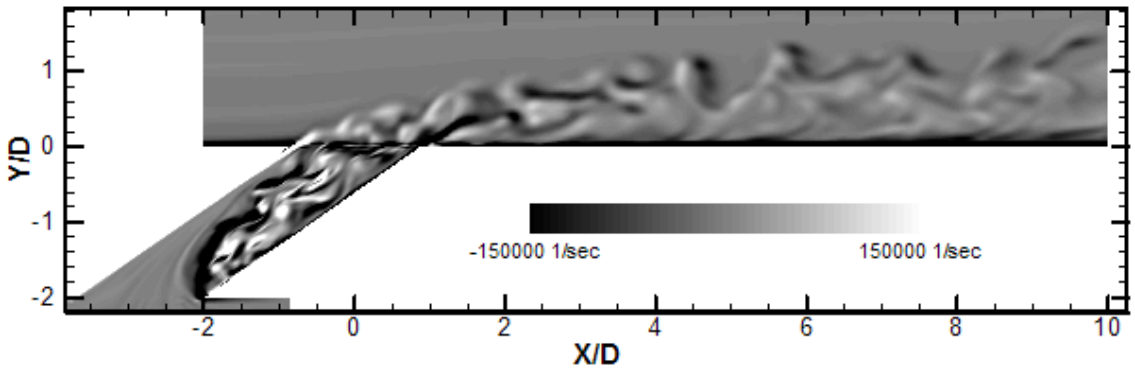

(d)

Figure 52 Instantaneous z-vorticity contours along the z = 0 plane for (a) BCD, (b) PUW, (c) PCD, and (d) QUICK.

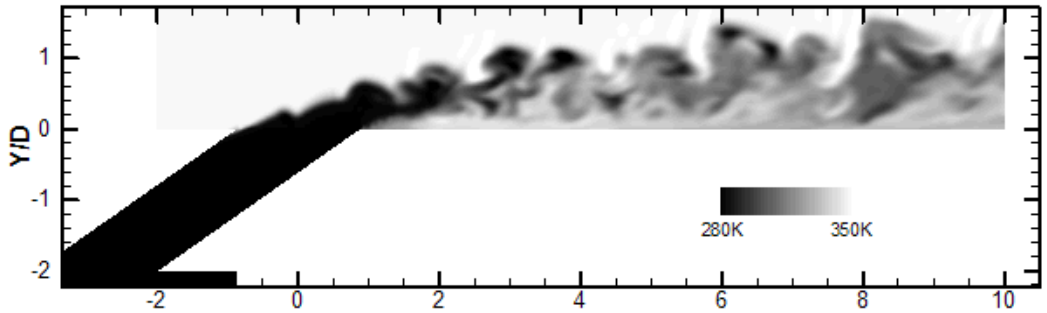

(a)

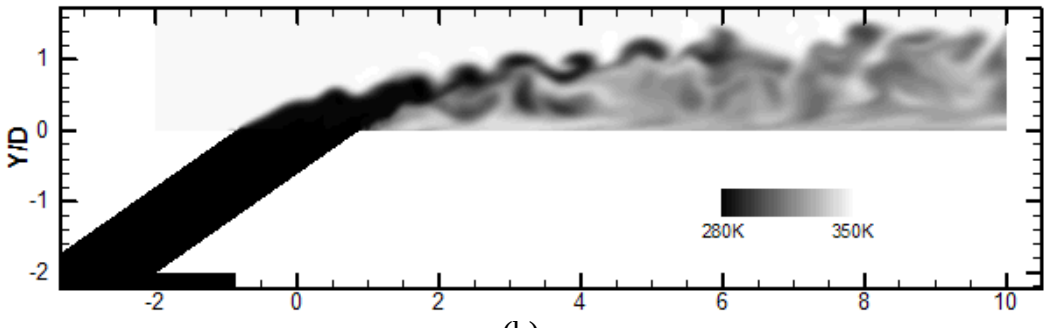

(b)

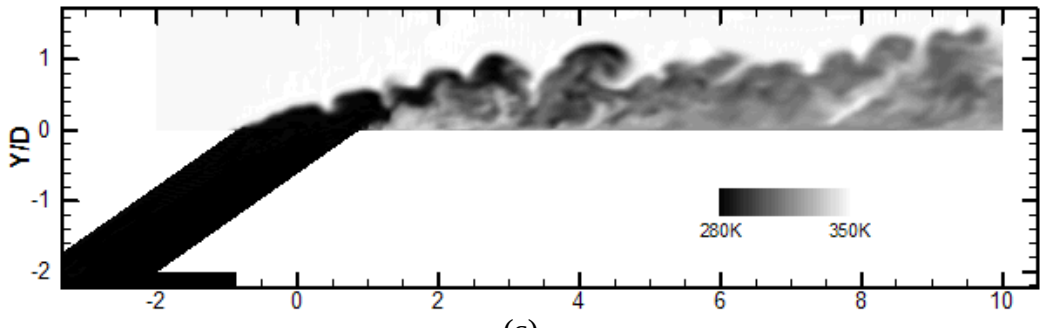

(c)

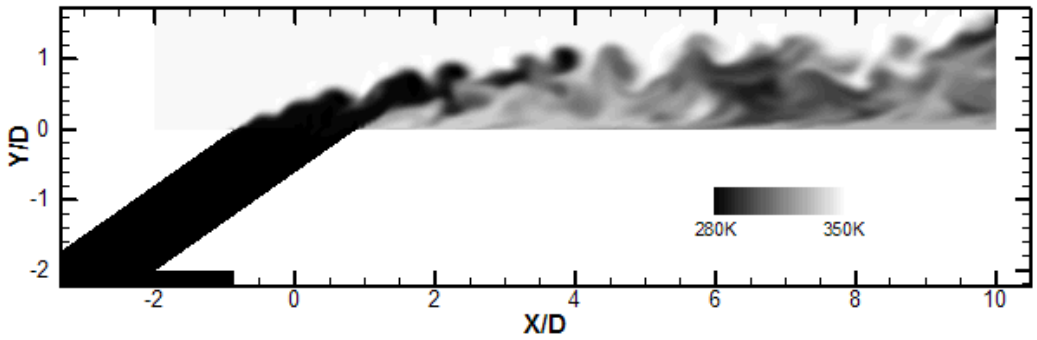

(d)

Figure 53 Instantaneous temperature field along the center-plane (z/D=0) for (a) BCD, (b) PUW, (c) PCD, and (d) QUICK.

These instantaneous results lead to the conclusion that the PCD scheme is able to resolve turbulent eddies on smaller scale than the PUW and QUICK schemes. The upwind bias of the two ladder schemes lend them to the influence of numerical diffusion in comparison with a purely central scheme. This effect likely allows the PCD to resolve the eddies to a finer extent than the other two schemes. The ability of the PCD to more closely mirror the experimental data regarding the behavior of the coolant jet is likely traceable to this superiority in the PCD solution. In a similar flow scenario, that of a solid cylinder in crossflow, Breuer (1998) also concluded that the purely central schemes performed better in matching experimental data. His conclusion suggested that the numerical diffusion of a particular discretization scheme was the attribute of highest importance in and LES solution rather than simply its formal order of accuracy. Because of the similarities of these two flow regimes, the tendency of the PCD to yield better prediction is consistent with the results of Breuer (1998).

7.7 Discretization Study Conclusions

Various discretization schemes have been used in large eddy simulations of film cooling. Four different schemes were directly compared using Fluent's LES code. The hybrid scheme (BCD) provided the poorest solution, while pure central and upwind schemes were able to match

experimental data more closely. The current results suggest that the upwind-based schemes (PUW and QUICK) over-predict the detachment of the jet, while the pure central differencing scheme yields the most accurate simulation of the film cooling flow. These results mirror the observations previously made for a solid cylinder in crossflow (Breuer 1998). The apparent advantage of the PCD scheme is its lower numerical diffusion, which allows the scheme to resolve and more accurate picture of the instantaneous flow field.

CHAPTER 8 SIMULATION USING COMMERCIAL CFD CODE

With the motivation and preliminary studies established in the preceding chapters, this chapter focuses on the film cooling simulation using the commercial code Fluent (Ansys 2009). This chapter begins the main thrust of this thesis, to numerically investigate the turbulent transport a film cooling jet in crossflow scenario and gain insight into its effect on film cooling effectiveness and heat transfer reduction into a turbine blade. Experimentally, the turbulent transport of heat and momentum in film cooling flows have been studied a number of ways. The hydrodynamic transport processes were studied by Burd and Simon (1999) using spectral analysis on data obtained from a single hot-wire placed in the exit plane of the coolant injection. This study found dominant frequencies in the $0.5 < St < 0.9$ range. Wang et al. (1996) used a triple-wire to measure mean velocity gradients and Reynolds stresses in the mid-span between two film holes, concluding that the calculated eddy diffusivity based on the Boussinesq hypothesis, Eqs. (72) and (73) following from Eq. (30), was noticeably different in the wall-normal and spanwise directions. Kaszeta and Simon (2000) expanded this investigation using a two-dimensional traverse at constant streamwise-coordinate planes. The anisotropy of eddy diffusivities was shown to be as high as a factor of four in some regions, while small pockets of negative diffusivity were also reported.

$$\nu_{t,y} = \frac{-\langle u'v' \rangle}{\partial \langle U \rangle / \partial y} \quad (72)$$

$$\nu_{t,z} = \frac{-\langle u'w' \rangle}{\partial \langle U \rangle / \partial z} \quad (73)$$

The turbulent transport of heat is an equally important topic in film cooling. The fluctuating thermal field of film cooling scenarios was studied by Kohli and Bogard (2005), mostly in the

form of RMS-temperature contours and probability density functions (PDF). Strong thermal intermittence was found in the shear layer, as well as high RMS-temperatures, leading to quick dilution of the coolant jet. A subsequent paper by Kohli and Bogard (2005) aimed at clarifying turbulent dilution of the coolant jet by reporting correlation coefficients and eddy diffusivities for heat and momentum. In the case of thermal eddy diffusivity, Eqs. (74) and (75) following from Eq. (58), are used to express the effects of turbulent transport. The variations of turbulent Prandtl number along the center-plane of the coolant jet are shown to be much stronger with low freestream turbulence (0.6%) when compared with a higher turbulence case (20%).

$$\alpha_{t,y} = \frac{-\langle v'T' \rangle}{\partial \langle T \rangle / \partial y} \quad (74)$$

$$\alpha_{t,z} = \frac{-\langle w'T' \rangle}{\partial \langle T \rangle / \partial z} \quad (75)$$

Recently, the technological advancements in the availability of computational resources have caused LES to become a more widely used technique in numerical film cooling predictions. It is the objective of this chapter to study discrete film cooling holes using an LES model in the commercial Fluent code. Instantaneous snapshots, turbulence statistics, and time-averaged values in the simulated flow will be used to investigate streamwise-inclined cylindrical holes.

8.1 Computational Formulation and Methodology

8.1.1 Geometric and Hydrodynamic Parameters

The current numerical configuration was constructed to mimic the parameters from Schmidt et al. (1996), which studied the benefits of introducing the compound angle. Their study included streamwise-oriented holes as well as compound angle holes. The original intent of this

study included the expansion to compound angle holes, therefore the experimental comparisons from the previous chapters were not considered. The present model is compared against the experimental conditions in Table 13. The scope of the current study is two simulations: a streamwise-oriented hole and a hole with compound angle of 60°. The density ratio from the experiment was matched and a momentum flux ratio of unity was chosen. This gave a blowing ratio of 1.25 and a velocity ratio of 0.78, matching one of the cases reported in Ref. 8. At the inlet boundary, the momentum thickness of the boundary layer was matched using a 1/7th power law profile.

Table 13 Summary of important geometric and hydrodynamic parameters.

	D [mm]	L/D	P/D	β_i	U_∞ [m/s]	DR	M	δ_θ/D
Schmidt et al.[8]	11.1	4.0	3.0	35°	7.5–30	1.6	0.5-2.5	.081-.103
Current model	11.1	4.0	3.0	35°	12.8	1.6	1.25	.104

8.1.2 Computational Grid and Boundary Conditions

A row of film cooling holes is simulated using a reduced domain which includes just one film cooling hole. Periodic boundary conditions are enforced in the spanwise directions, allowing for the single hole to mirror the results of the entire row of holes. For the baseline case, it is expected that the difference between using periodic and symmetry conditions in the spanwise direction should be minimal. When compound angles are introduced, however, the periodic boundary conditions become extremely important.

The mainstream is modeled to a height of five diameters above the cooled surface, at which a symmetry boundary condition models free stream conditions without causing significant inaccuracies in the modeling of the film cooling flow (see previous chapter). The origin of the

domain is placed at the center of the exit plane of the jet, where the centerline axis of the coolant delivery tube intersects with the cooled surface plane. The flow inlet is placed three diameters upstream of the origin. Here, a 1/7th law velocity profile is applied inside the boundary layer, Eq. (69), which is set at a boundary layer thickness to meet the prescribed conditions above. Outside of the boundary layer, the velocity profile is constant at the freestream velocity. Inlet turbulence can be modeled using a spectral synthesizer method to imitate velocity fluctuations in the mainflow. For this current study, in an attempt to meet the low freestream turbulence, no velocity fluctuations were introduced. One of the primary motivations for the use of open source code in the final chapter is the ability to program more complex, time-accurate inflow methods for the incoming boundary layer.

The computational domain extends downstream of the origin by eleven diameters, allowing for the consideration of the evolution of the jet as it is swept downstream and the comparison with effectiveness results within this region. The length of the coolant tube is 4.0 diameters with its entrance fed from a coolant plenum. The plenum, like the mainstream, is given periodic boundary conditions in the spanwise directions. The height and width of the plenum are both modeled at four diameters. A constant velocity profile with no inlet turbulence is applied at the inlet to the plenum (bottom surface). No turbulence is added to the inlet flow in the plenum due to expected calm/near-stagnant flow.

The numerical domain typical of the current study is illustrated in Figure 54a, which shows the domain for the simple cylindrical case. For the grid structure, the mainflow and plenum were each split into two regions: one region of finely spaced grid cells and a neighboring region of more coarsely spaced cells. The fine grid region extends two diameters into the mainflow above

the cooled surface and the fine region of the plenum extends one half diameter below the coolant tube inlet. Figure 54b shows the grid structure of the simple cylindrical case. The grid was constructed using the Gambit (2008) meshing software. Grids consisting of around three million cells were used for each case.

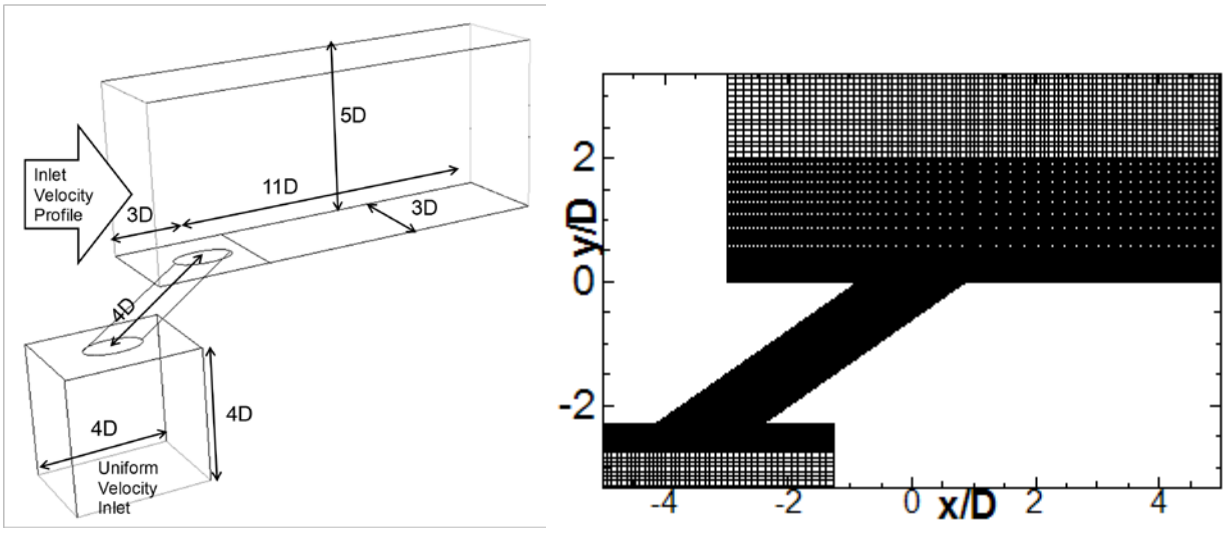

(a) (b)

Figure 54 (a) Computational domain and (b) structured grid for LES.

8.1.3 Numerical Method

Once completed in Gambit, the grid was exported into the Fluent CFD solver. The boundary conditions, as prescribed above, were applied in the Fluent software, preparing the grid for solution. Before solving in the temporal domain, a RANS solution was found using the realizable k-ε turbulence model. This RANS solution served as the initialization for the LES solution process.

The SIMPLE algorithm was used for pressure-velocity coupling in Fluent's segregated pressure-based solution algorithm. At each iteration, the three momentum (or velocity) equations are solved sequentially, followed by a pressure-correction continuity equation. Once

the mass fluxes, pressures, and velocities have been updated, the scalar equations, such as the energy equation, are solved.

The specified density ratio was applied using an incompressible ideal gas formulation for the density. That is, the incompressible ideal gas law, Eq. (70),was used to calculate density at each iteration, with the pressure set to a constant operating pressure of P_o = 101.325 kPa. In this way, the temperature ratio was used to control the density ratio. Compressibility effects were negligible due to the low Mach numbers in the flow, even in the jetting region of the film cooling hole (M < 0.1).

The temporal discretization was accomplished using a second order implicit time-stepping approach. Iterations were performed at each time step to ensure convergence. The relaxation factors were tuned to avoid divergence throughout the simulation yet to allow optimized convergence patterns. At each time step, sub-iterations were executed until scaled residuals on the order of 1e-4 for continuity, 1e-6 for momentum, and 1e-7 for energy equations were reached. Once the simulations reached statistical stability, mean quantities of time-averaged data and turbulence statistics were calculated. The time step size was set equal to 0.023*D/U∞, which was estimated to be on the order of the Kolmogorov time microscale for the present simulation. This corresponded to a physical time step of 2e-5 seconds. After the statistical sampling was enabled, the flow was allowed to run for five mean residence times.

Spatial discretization for the diffusive terms is accomplished using a second-order central scheme. In following with the results of Breuer (1998) and the previous chapter, a second-order pure central differencing scheme is also used for the convective terms, as this has a lower amount of numerical diffusion, which becomes highly important in large eddy simulations.

8.2 Results and Discussion

8.2.1 Center-plane

Figure 55 shows the mean velocity (x-component) and temperature contours along the center-plane (z/D = 0) of the jet in the near-hole region. The velocity contours through the coolant hole show the effect of jetting cause by the turning of the flow exiting the plenum. The velocity toward the windward side of the jet is close to the freestream velocity. As the jet is turned by the crossflow, the upper side of the jet (formerly the windward side) is quickly accelerated to the crossflow velocity and only the lower half of the jet appears in the velocity deficit contours. As the jet progresses downstream, the CVP sweeps higher momentum freestream air underneath the jet, as evidenced by the extended 0.6 contours in Figure 55a. A recirculation region just downstream of the hole's leeward lip (x/D=0.87) is also visible, extending to an x/D of about 1.5.

Figure 55b shows that this recirculation region is filled mostly with hot crossflow fluid being pulled underneath the lifting jet by the low pressure region created there. This creates the jet lift-off phenomena to be expected at the present momentum ratio of unity. After the recirculation region, the jet, as seen from the thermal point of view, begins spreading back toward the wall, though the core of the jet does not tend in this direction but assumes a trajectory parallel to the surface. This results in mild re-attachment from the adiabatic effectiveness point of view.

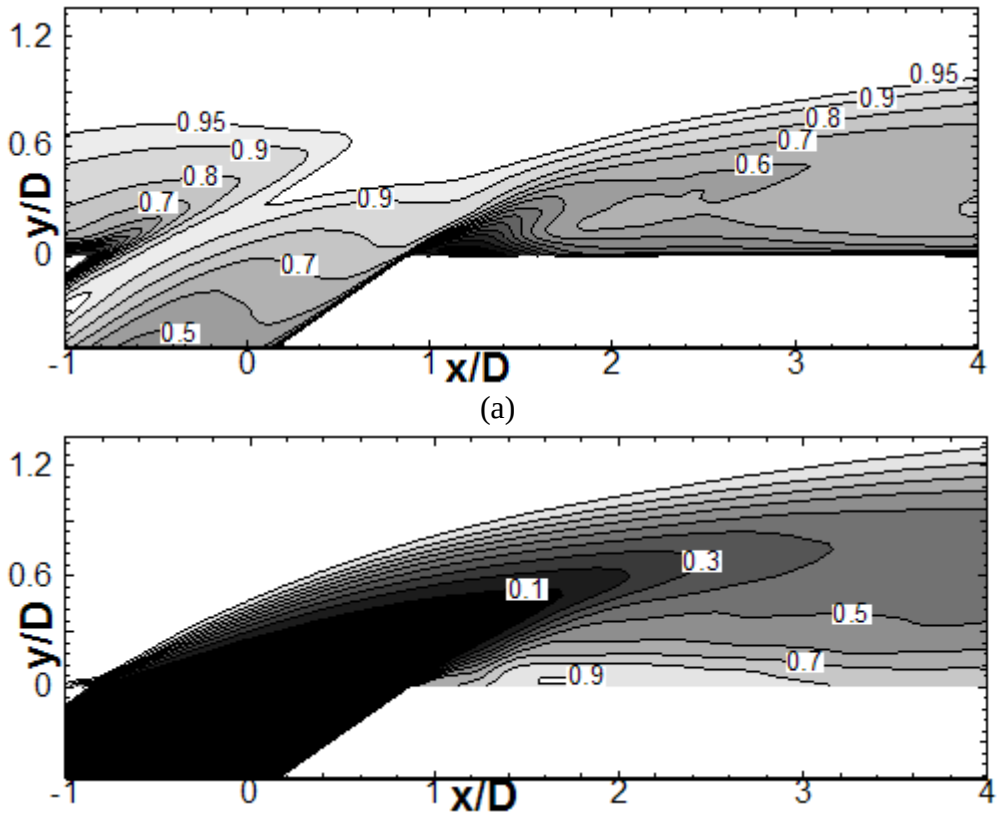

(a)

(b)

Figure 55 Normalized contours at z/D = 0 of (a) mean streamwise velocity (U/U_∞) (b) mean temperature (θ).

Figure 56 shows the gradients of x-velocity and temperature along this center-plane cut (Figure 56a,d). The corresponding turbulent stress terms are presented in the following row (Figure 56b,e). Representing the eddy diffusivity, the quotient of these two is shown in (Figure 56c,f). The diffusivity contours, here and throughout this study, are marked by (usually thin) regions in which the gradient term approaches zero. The diffusivity becomes uncharacteristically large as any uncertainty (especially due to finite sampling time) overwhelms any conclusions that could be drawn concerning these regions.

The windward side momentum interaction (Figure 56a-c), while strong initially, fades quickly as that side of the jet is quickly accelerated to the freestream velocity, both by the re-orientation of existing jet momentum and the rapid exchange of streamwise momentum at the

injection site. This windward/upper side, however, is the site of prolonged dominant thermal interaction (Figure 56d-f) as it is the shear layer with steep thermal gradient between the jet and crossflow. In general, the shapes/patterns of the gradients and turbulent stresses are similar, showing that the eddy viscosity approach works as a first approximation.

In contrast, the leeward side of the jet is the source for prolonged dominant velocity interaction, while the thermal interaction here is short-lived. The turbulent mixing of momentum already occurring within the hole is visible, with noticeably higher eddy diffusivity than the rest of the flow. This mixing region is bent toward the leeward side of the exit plane by the crossflow and attenuates as the bending jet is accelerated. The remnant of this region then merges, at the leeward side of the jet exit, with the mixing region cause by the strong velocity gradients between the lifting jet and the recirculation region. The resulting region of primary velocity interaction continues far downstream with eddy diffusivities similar to those seen at the windward side of the jet (though by no means uniform). It is seen that this region maintains a slight upward trajectory, even as the thermal contours reveal that the jet begins travelling parallel to the wall. As a result, the velocity gradient/mixing region crosses over toward the upper side of the jet as the wake region spreads.

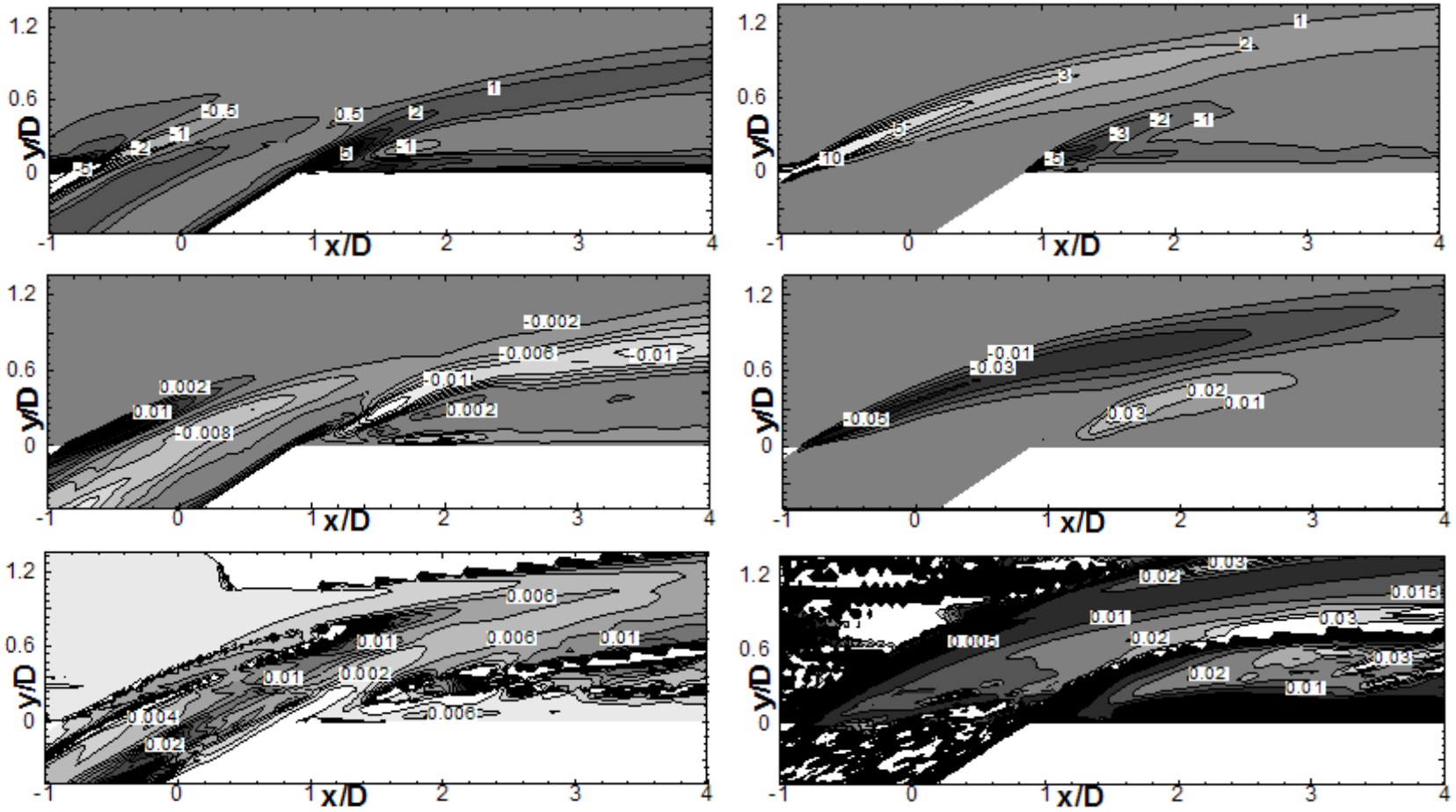

Figure 56 Normalized contours at z/D = 0 of velocity (a) gradient $(\partial U/\partial y)/(U_\infty/D)$, (b) turbulent stress $-\langle u'v'\rangle/{U_\infty}^2$, and (c) eddy diffusivity $\nu_{t,y}/(U_\infty D)$; as well as temperature (d) gradient $(\partial T/\partial y)/((T_\infty - T_c)/D)$, (e) turbulent stress $-\langle v'T'\rangle/U_\infty(T_\infty - T_c)$, and (f) eddy diffusivity $\alpha_{t,y}/(U_\infty D)$.

The thermal mixing seen at the leeward side of the jet is cause by the hot crossflow wrapping underneath the jet in the recirculation region, creating a local region of high thermal gradient and turbulent mixing that dissipates shortly after the end of the recirculation region. An interesting result of this particular blowing ratio is that the regions (along the center-plane) of high velocity gradient and turbulent transport are generally regions of low thermal gradient and turbulent transport, and vice-versa.

8.2.2 Streamwise planes

More insight into the development of the jet can be obtained from contours along streamwise-normal planes downstream of injection. Figure 57 shows the mean streamwise velocity and temperature contours at x/D = 1, just downstream of the leeward lip. The recirculation zone is seen in Figure 57a extending about 0.2 diameters on either side of the centerline. The velocity deficit is constrained to within 0.5 diameters of the wall as the majority of the coolant jet is about equal to the crossflow velocity. The CVP is beginning to pull the high momentum crossflow underneath the jet, drawing it in close proximity with the recirculation region and creating a sharp velocity gradient in the spanwise direction. Figure 57b shows that the CVP effectively lifts the jet off the surface. The core of the jet remains at about the coolant plenum temperature, but the surface sees a much higher temperature due to this separation.

The motion of the CVP also squeezes the boundary layer at about 0.5 diameters on either side of the jet, creating sharp velocity gradients at the wall (high skin friction). Only in this region does the grid resolution exceed $y+ = 1$, but the viscous sub-layer is still resolved ($y+ < 2$). Large temperature gradients exist on all sides of the jet, but the highest gradients are on the underside of the jet, between the jet core and the CVP-under-swept crossflow.

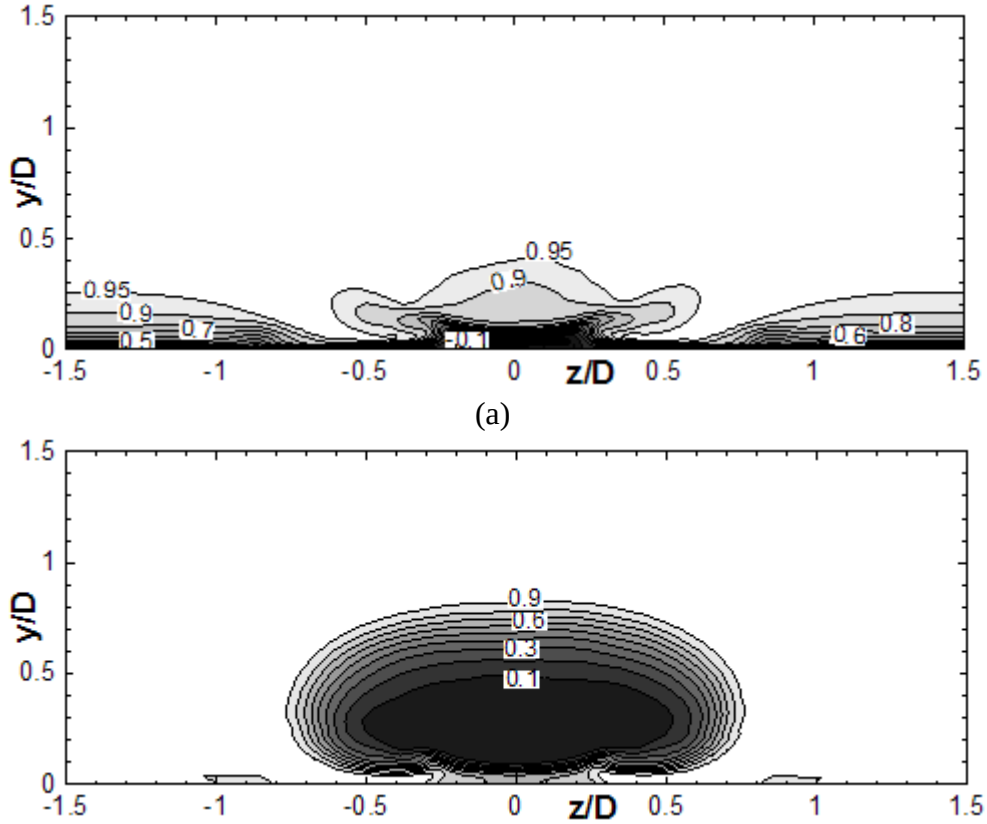

Figure 57 Normalized contours at x/D = 1 of (a) mean streamwise velocity (U/U_∞), (b) mean temperature (θ).

Figure 58 shows the spanwise and wall-normal velocity gradients, along with their corresponding turbulent stresses and eddy diffusivities. Figure 58a reveals velocity gradients not apparent in Figure 57, located above the wake region where the flow appears to be at the freestream velocity. A layered form is created in the wall-normal direction (Figure 58a-c) with a region of high velocity gradient but low eddy diffusivity from $0 < y/D < 0.2$ underneath a region of lesser velocity gradient but much higher eddy diffusivity from $0.2 < y/D < 0.6$. Above this, there is a region of negative velocity gradient ($0.6 < y/D < 0.8$) and a final region of positive gradient ($0.8 < y/D < 1.0$). The thin negative gradient region is seen to have appreciable eddy viscosity (still less than its neighbor underneath), while the upper most gradient provokes less turbulent interaction, having much lower eddy viscosity.

The spanwise interaction is shown with Figure 58d-f. The warping of the crossflow boundary layer as well as the jet wake region by the CVP entrainment of crossflow fluid creates a complex gradient field (Figure 58d), which is relatively well-predictive of the turbulent stresses (Fig. 5e) via the eddy viscosity model (Figure 58f). This is not to say that uniform eddy diffusivity is seen throughout the flow field, but it remains on the same order of magnitude. A rough comparison of Figure 58c and f reveals that, in general, the jet experiences much higher eddy diffusivity in the spanwise direction than in the wall-normal direction. This follows the results of Kaszeta and Simon (2000) and many preceding studies in highlighting the inaccuracies of two-equation isotropic RANS turbulence models. Typically, such models under-predict lateral spreading (Acharya et al. 2001).

Figure 59 shows the corresponding temperature gradient and turbulent transport contours. The temperature field is much simpler than its corresponding velocity field. The largest gradient occurs below the jet, but there is little to no turbulent stresses corresponding to it. The wall-normal gradient above the jet core is accompanied (as expected by the eddy viscosity model) by a region of strong turbulent stresses. The spanwise gradients are likewise accompanied by expected turbulent stress regions, but the thermal eddy diffusivity is seen to be much lower in the spanwise interaction region than in the wall-normal region. This anisotropy stands in contrast to the observations from the momentum diffusivity fields.

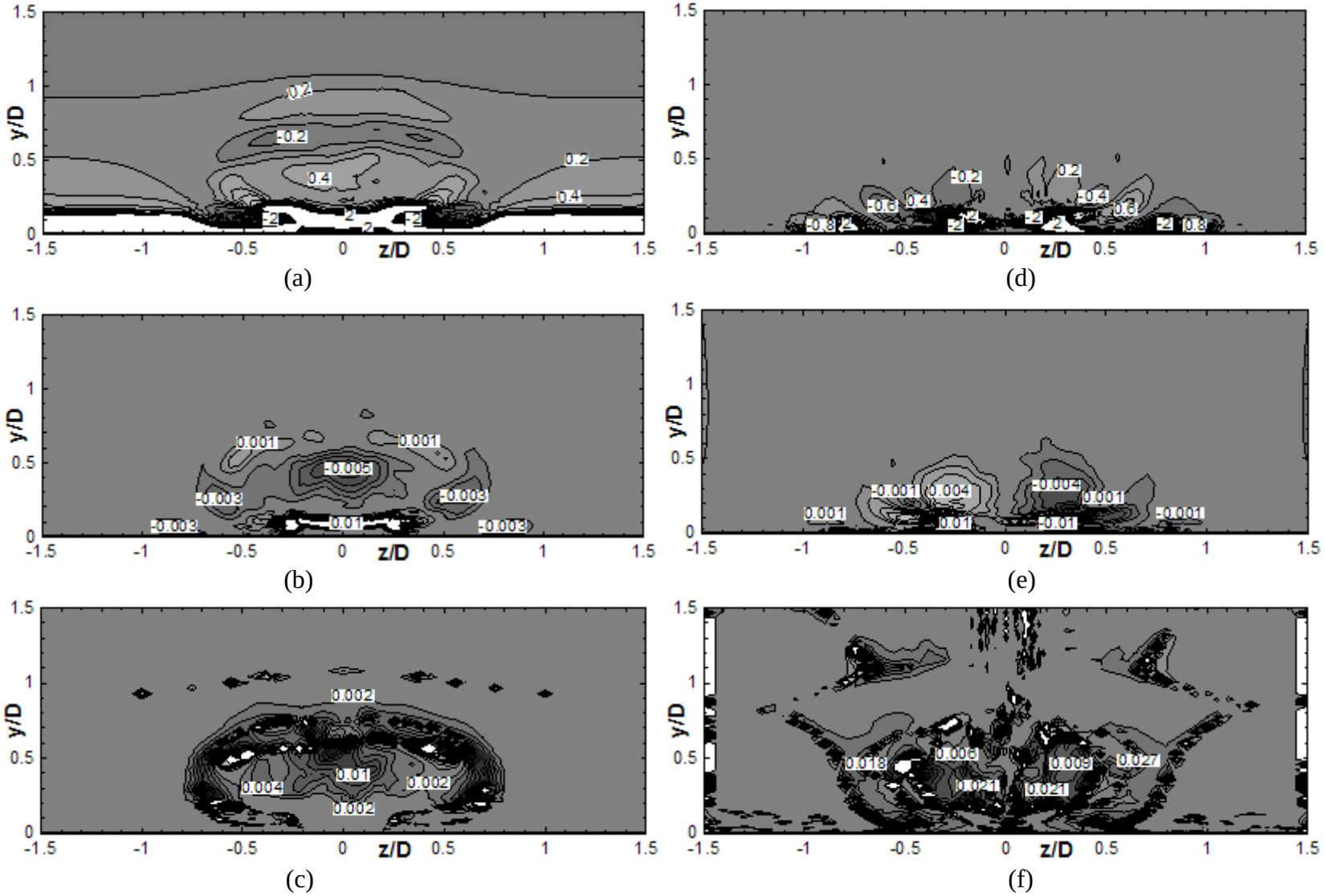

Figure 58 Normalized velocity contours at x/D = 1 of wall-normal (a) gradient $(\partial U/\partial y)/(U_\infty/D)$, (b) turbulent stress $-\langle u'v'\rangle/{U_\infty}^2$, and (c) eddy diffusivity $\nu_{t,y}/(U_\infty D)$; as well as spanwise (d) gradient $(\partial U/\partial z)/(U_\infty/D)$, (e) turbulent stress $-\langle u'w'\rangle/{U_\infty}^2$, and (f) eddy diffusivity $\nu_{t,z}/(U_\infty D)$.

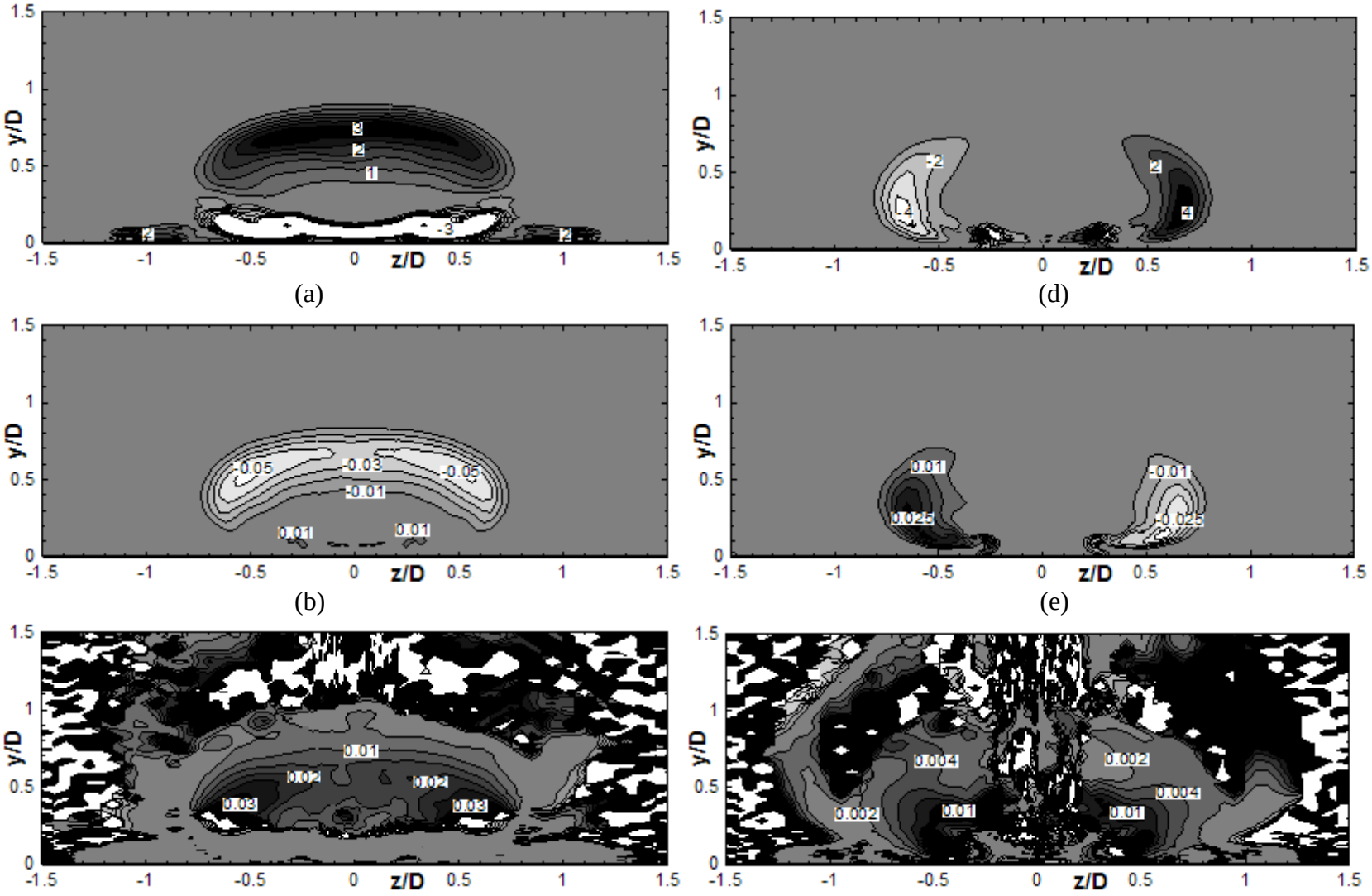

Figure 59 Normalized temperature contours at x/D = 1 of wall-normal (a) gradient $(\partial T/\partial y)/((T_\infty - T_c)/D)$, (b) turbulent stress $-\langle v'T'\rangle/U_\infty(T_\infty - T_c)$, and (c) eddy diffusivity $\alpha_{t,y}/(U_\infty D)$; as well as spanwise (d) gradient $(\partial T/\partial z)/((T_\infty - T_c)/D)$, (e) turbulent stress $-\langle w'T'\rangle/U_\infty(T_\infty - T_c)$, and (f) eddy diffusivity $\alpha_{t,z}/(U_\infty D)$.

As the film jet progresses downstream, the jet is spread out and the CVP begins to dominate the flow field. Figure 60 shows mean streamwise velocity and temperature contours at x/D = 2.5. The velocity deficit region (Figure 60a) has spread quickly away from the wall by the two lower strong Reynolds stress regions in Fig. 5c. The lateral spreading of the jet seems to have been hindered, despite its high eddy diffusivities, by adjacent regions of opposing gradients (and accompanying turbulent stresses). The effect of the CVP, though not as sharp, is still seen in sweeping higher momentum fluid underneath the jet and promoting jet-liftoff. The core of the velocity deficit is beginning to detach from the boundary layer because of the CVP's motion. The extent of the velocity deficit extends about 0.8 D above the surface and 0.7 D on either side.

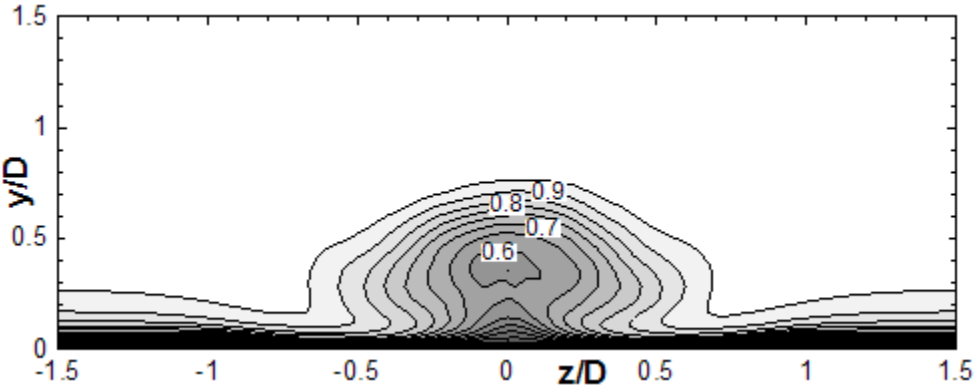

(a)

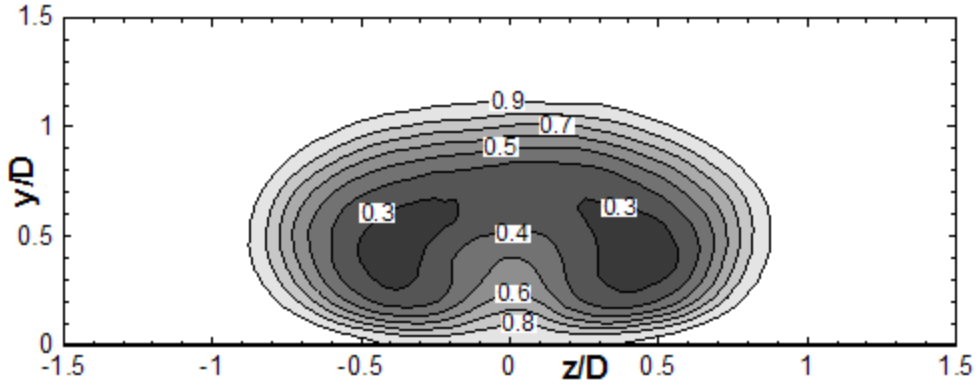

(b)

Figure 60 Normalized contours at x/D = 2.5 of (a) mean streamwise velocity (U/U_∞), (b) mean temperature (θ).

The temperature field of the jet likewise as undergone rapid spreading by x/D = 2.5 (Figure 60b). Similar to the velocity field, the thermal field has spread rapidly in the presence of strong gradients and turbulent stresses near the hole exit. Spreading has occurred more rapidly in the vertical direction (away from the wall) than in the spanwise direction, likely attributable to higher eddy diffusivities seen in Figure 59f. The CVP has split the thermal core of the jet into two pockets on either side of the jet, with higher temperatures along the center-plane. The core temperature has been significantly weakened over such a short distance by the rapid turbulent mixing and CVP motion. The extent of the thermal field of the jet extends more than 1 D above the surface and past 0.8 D on either side, though the surface only sees the coolant to about 0.45 D on either side of the centerline. In general, as noted in the center-plane analysis, regions of high velocity gradient contain low temperature gradients and vice-versa. The thermal core of the jet tends to wrap around the velocity deficit core, such that the dominant velocity gradients lie within the temperature core and the dominating temperature gradients lie outside of the extent of the velocity deficit.

By x/D = 2.5, the turbulent mixing and evolution of the jet has simplified the velocity gradients in the wall-normal direction (Figure 61a). Here, the CVP has caused two negative gradient regions on either side of the centerline, sandwiched vertically between two positive gradient regions: the near-wall boundary layer satisfying the no-slip condition and the upper half of the core velocity deficit region. This upper-most region dominates with regard to turbulent stresses (Figure 61b) while the negative gradient pockets are accompanied only by slight companion stresses. The eddy diffusivities (Figure 61c) show that misalignment of the gradient and turbulent stresses results in a negative diffusivity region. This shows that, though a gradient

exists to drive the velocity deficit back toward the wall, the turbulent stresses do not align with the gradient well. The spanwise spreading is dominated by two pairs of gradients and their accompanying turbulent stresses (Figure 61d,e). The lower pocket pair is seen to have stronger gradients and eddy diffusivity as compared to the upper pair. This interaction will tend to aid the CVP in mixing higher momentum fluid from the crossflow underneath the core velocity deficit region of the jet.

Figure 62 shows the wall-normal and spanwise thermal gradients with their respective turbulent stresses. The upper half positive gradients in the wall-normal direction (Figure 62a) are accompanied by expected turbulent stresses (Figure 62b). Similar to the velocity field, however, the underside of the jet, though populated by strong negative gradients, the turbulent stresses do not overlap, creating a large region of negative and low eddy diffusivity in the lower region of the jet away from the centerline (Figure 62c). The consequence of this is that, at the periphery of the jet, the coolant fails to spread back to the surface and the pinching nature (as caused by the CVP) of the temperature contours will remain further downstream.

The spanwise temperature gradient field is dominated by two pairs of opposing regions (Figure 62d). Closer to the center-plane, a smaller pair of gradient pockets (with accompanying turbulent stresses, Figure 62e) are aligned to spread the split core back to the center-plane. Outside of these pockets, a larger, stronger gradient marks the edges of the jet's thermal field. The thermal eddy diffusivity in this outer region decreases as the spanwise extent of the jet is approached. This suggests that the temperature gradients in these regions will be relaxed as the jet progresses downstream, but the overall spanwise extent of the jet may increase very little.

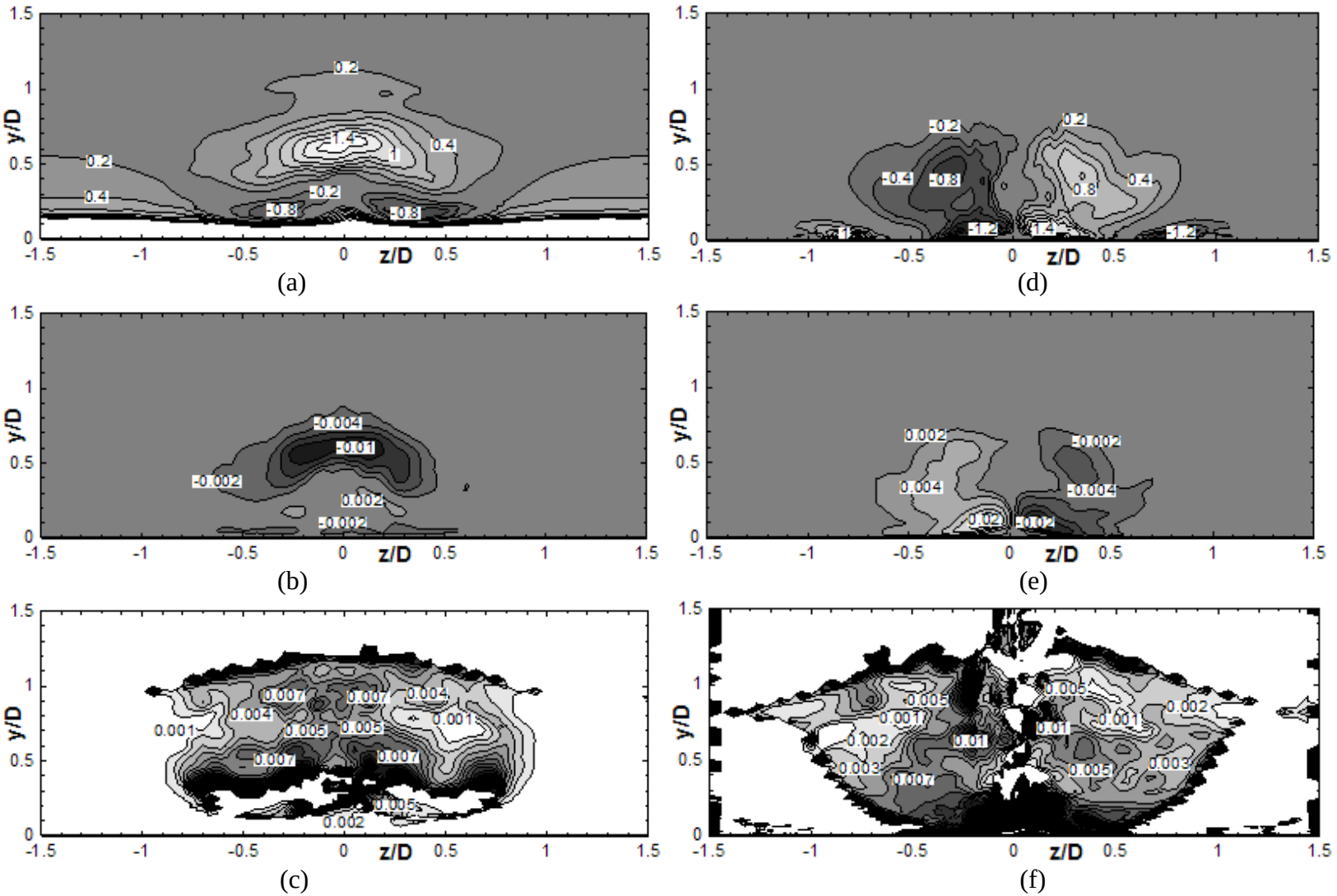

Figure 61 Normalized velocity contours at x/D = 2.5 of wall-normal (a) gradient $(\partial U/\partial y)/(U_\infty/D)$, (b) turbulent stress $-\langle u'v'\rangle/{U_\infty}^2$, and (c) eddy diffusivity $\nu_{t,y}/(U_\infty D)$; as well as spanwise (d) gradient $(\partial U/\partial z)/(U_\infty/D)$, (e) turbulent stress $-\langle u'w'\rangle/{U_\infty}^2$, and (f) eddy diffusivity $\nu_{t,z}/(U_\infty D)$.

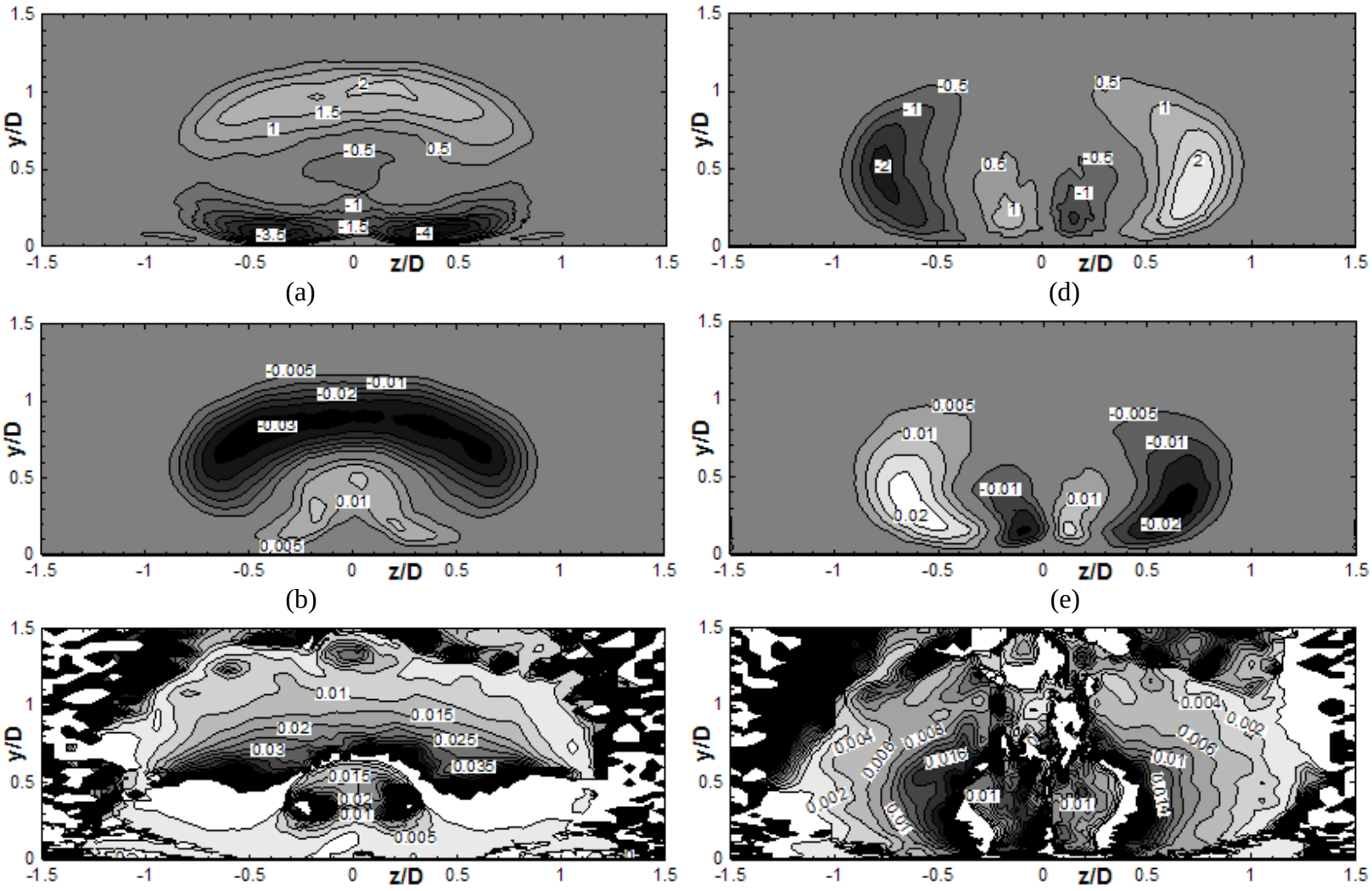

Figure 62 Normalized temperature contours at x/D = 2.5 of wall-normal (a) gradient $(\partial T/\partial y)/((T_\infty - T_c)/D)$, (b) turbulent stress $-\langle v'T'\rangle/U_\infty(T_\infty - T_c)$, and (c) eddy diffusivity $\alpha_{t,y}/(U_\infty D)$; as well as spanwise (d) gradient $(\partial T/\partial z)/((T_\infty - T_c)/D)$, (e) turbulent stress $-\langle w'T'\rangle/U_\infty(T_\infty - T_c)$, and (f) eddy diffusivity $\alpha_{t,z}/(U_\infty D)$.

Figure 63 shows the mean contours of the jet at four diameters downstream of the injection site. As predicted at x/D = 2.5, the CVP and turbulent mixing below the velocity deficit core (Figure 61f) has further exaggerated its separation with the entrainment of higher momentum fluid below the jet (Figure 63a). Spreading back toward the surface by negative gradients has failed to combat this effect due to low (and negative) eddy diffusivity (Figure 61c). The velocity deficit region now extends up toward 1 D above the surface but its spanwise extent is relatively unchanged due to relatively weak eddy diffusivities at the spanwise periphery of the jet (Figure 61f).

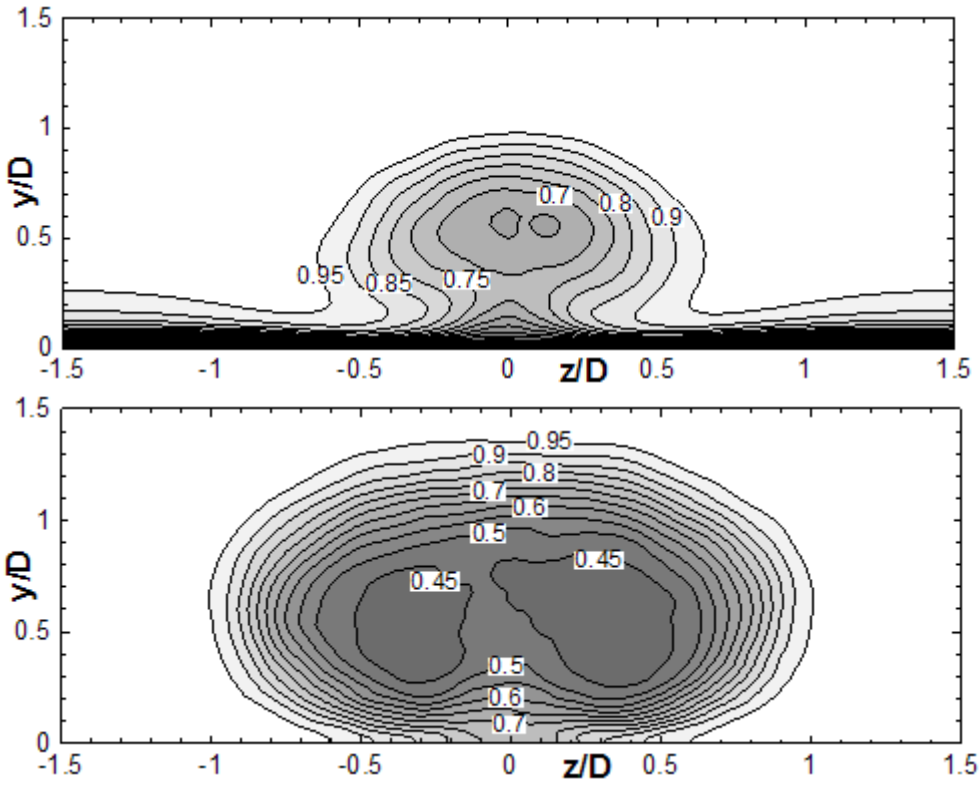

Figure 63 Normalized contours at x/D = 4 of (a) mean streamwise velocity (U/U_∞), (b) mean temperature (θ).

Figure 63b reveals the inner pair of temperature gradients in Figure 62d have successfully made the thermal core of the jet more uniform and spread back toward the center-plane. The upper side of the jet's thermal core has continue to expand in the wall-normal direction, but the

spanwise expansion has been much slower due to the lower eddy diffusivities seen in Figure 62f as compared with Figure 62c. As predicted from the low and negative diffusivities in Figure 62b,c, the negative temperature gradients in the lower half of the periphery of the jet have failed to spread back toward the wall and the surface sees much less thermal protection than available in the core of the jet.

The velocity gradients of the jet are still mainly enclosed within the low gradient thermal core of the jet. On the upper side of the jet the velocity and temperature fluctuations still occur, for the most part in separate regions of the flow, with the upward spreading velocity gradients and turbulent stresses occurring from $0.6 < y/D < 1.0$ (Figure 64a,b) and the upward spreading temperature gradients occurring from $0.9 < y/D < 1.4$ (Figure 65a,b). Likewise, the thermal gradients in the spanwise direction ($0.5 < z/D < 1$) lie outside of the spanwise velocity gradients ($0.2 < z/D < 0.6$), see Figure 64 d,e and Figure 65 d,e.

The sandwiched negative velocity gradient region remains in Figure 64a. The corresponding region of low and negative diffusivity below the velocity core of the jet still exists to hinder the spreading of the jet back toward the wall (Figure 64c). The pair of spanwise gradients (Figure 64d) remains relatively unchanged with higher eddy diffusivities closer to the center of the jet and lower diffusivities progressing outward toward the spanwise extent of the jet. In general, the gradients and turbulent stress become slightly weaker and the eddy diffusivities become higher and slightly more uniform (Figure 64 c/f vs. Figure 61 c/f). The wall-normal thermal transport remains relatively unchanged from $x/D = 2.5$. The region of misaligned overlap still creates a relatively large region of negative thermal diffusivity on either side of the jet.

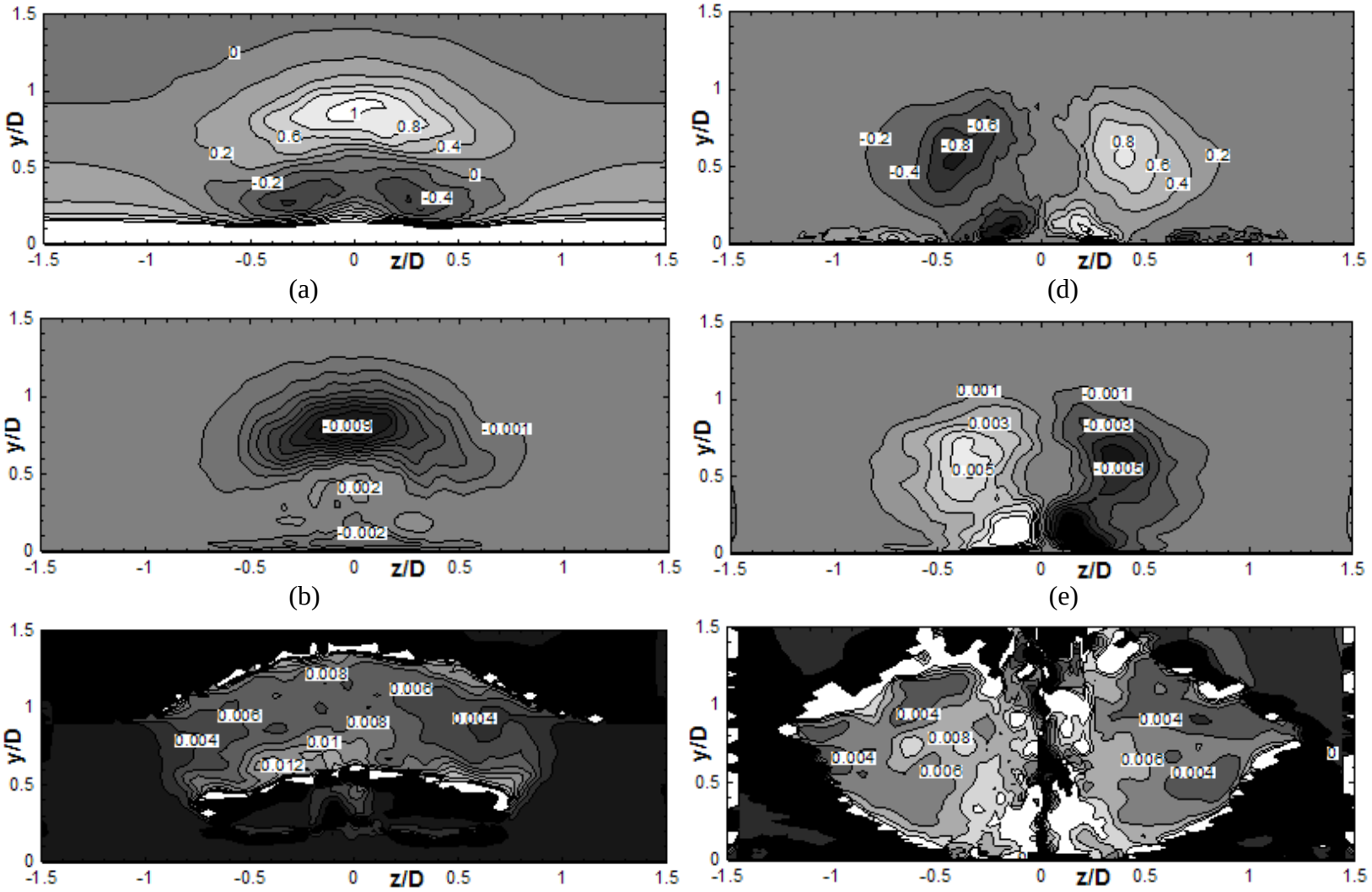

Figure 64 Normalized velocity contours at x/D = 4 of wall-normal (a) gradient $(\partial U/\partial y)/(U_\infty/D)$, (b) turbulent stress $-\langle u'v'\rangle/{U_\infty}^2$, and (c) eddy diffusivity $\nu_{t,y}/(U_\infty D)$; as well as spanwise (d) gradient $(\partial U/\partial z)/(U_\infty/D)$, (e) turbulent stress $-\langle u'w'\rangle/{U_\infty}^2$, and (f) eddy diffusivity $\nu_{t,z}/(U_\infty D)$.

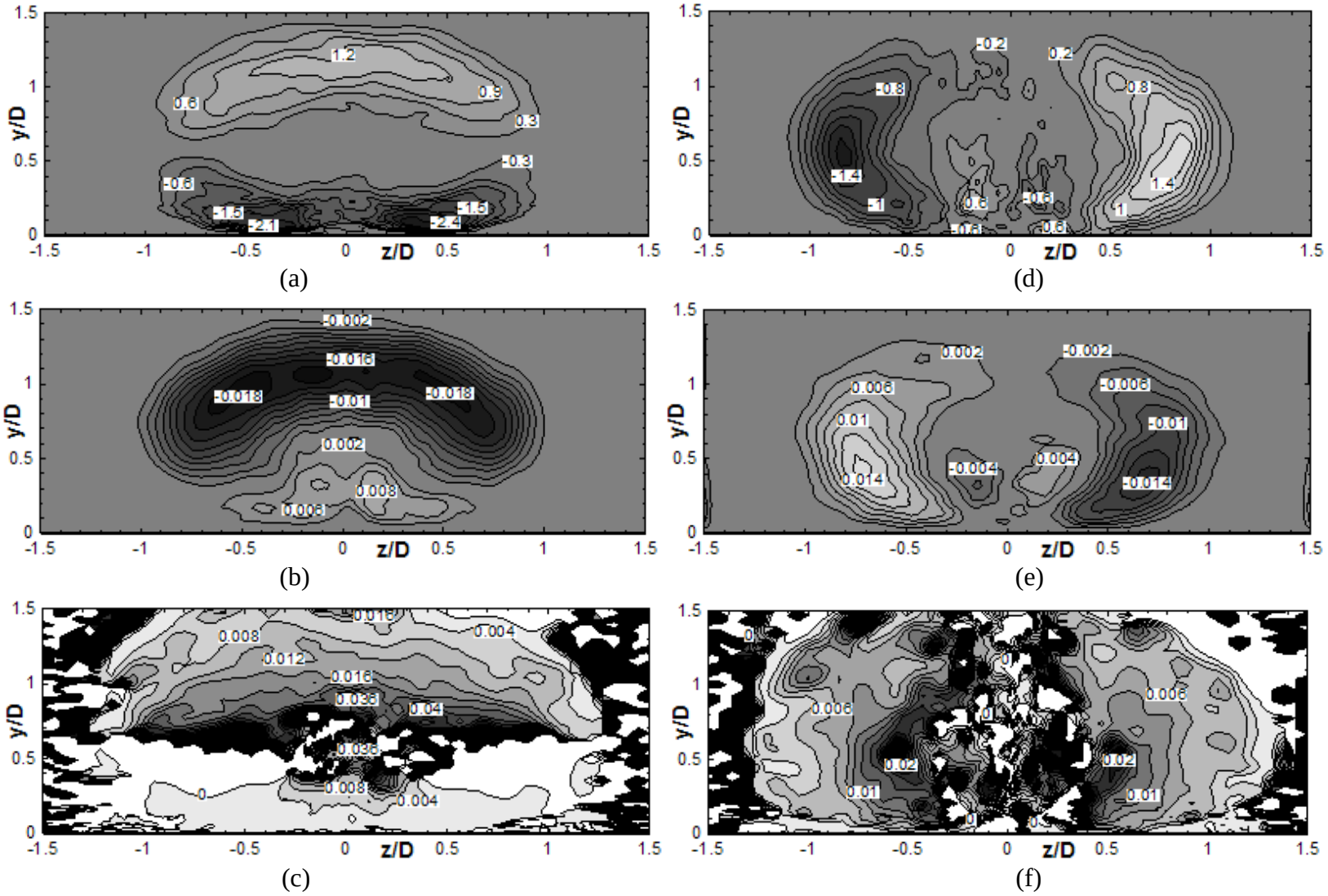

Figure 65 Normalized temperature contours at x/D = 4 of wall-normal (a) gradient $(\partial T/\partial y)/((T_\infty - T_c)/D)$, (b) turbulent stress $-\langle v'T'\rangle/U_\infty(T_\infty - T_c)$, and (c) eddy diffusivity $\alpha_{t,y}/(U_\infty D)$; as well as spanwise (d) gradient $(\partial T/\partial z)/((T_\infty - T_c)/D)$, (e) turbulent stress $-\langle w'T'\rangle/U_\infty(T_\infty - T_c)$, and (f) eddy diffusivity $\alpha_{t,z}/(U_\infty D)$.

Figure 66 shows the mean contours of the jet at seven diameters downstream of the injection site. The velocity deficit core of the jet has begun to reunite with the boundary layer, showing that the turbulent momentum transport on the underside of the jet near the centerline is successfully spreading the jet back toward the surface. Overall, the velocity in the wake of the jet is being accelerated effectively on all sides by mixing with the crossflow. The dilution of the wake from x/D = 4 to x/D = 7 shows similar progress as from x/D = 2.5 to x/D = 4, indicating that the dilution continues to slow as the gradients are lowered.

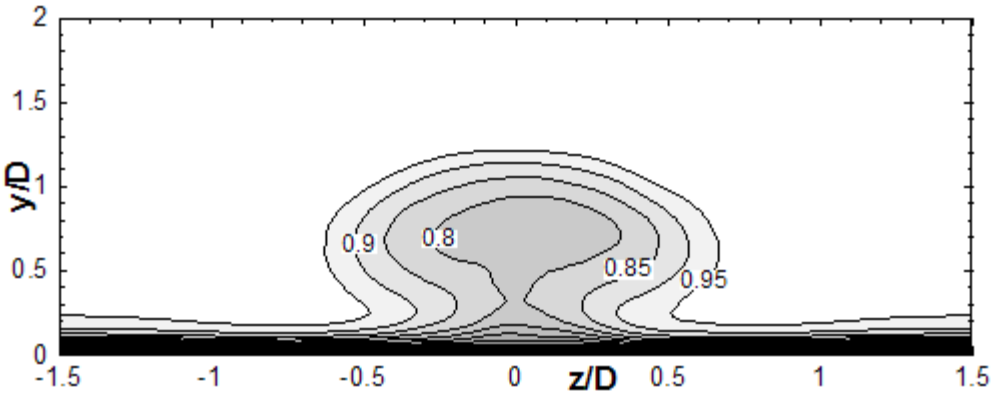

(a)

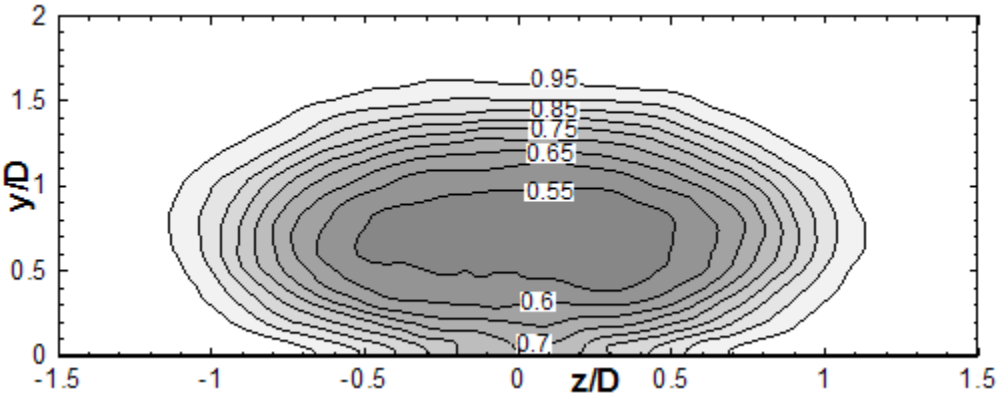

(b)

Figure 66 Normalized contours at x/D = 7 of (a) mean streamwise velocity (U/U_∞), (b) mean temperature (θ).

The mean temperature contours (Figure 66b) at x/D = 7 show that the coolant core that was once two distinct regions on either side of the jet (having been split by the CVP) is now reunited.

The temperature field of the jet continues to spread in the wall-normal and spanwise directions as it is further diluted (though the dilution process is slowing as the gradient become smaller).

Figure 67 shows the velocity gradient and mixing at x/D = 7. The gradients and turbulent stresses have weakened but the eddy diffusivities, though not uniform, do no exhibit much difference over this period. The velocity mixing region still lie mostly within low temperature gradient regions and the thermal outline of the jet still extends much farther than the velocity deficit. The negative diffusivity region shows signs of shrinking and the flow is overall becoming more nicely behaving.

The turbulent thermal transport processes (Figure 68) also shows little change with respect to the previous streamwise position. The contours, as the solution progresses downstream, become less orderly, indicating that finite sampling time is having more of an influence in scattering the data. This is especially noticeable in the turbulent stress terms (second-moments) which take longer sampling times to achieve convergence. The convergence of mean and second-moment values was decided based on point monitors near the hole exit. It is evident from these contours further downstream that longer simulation time may be needed for more orderly data in far from the injection. The negative diffusivity region appears to be shrinking in the thermal sense as well, but otherwise the diffusivity contours remain similar to those of x/D = 4.

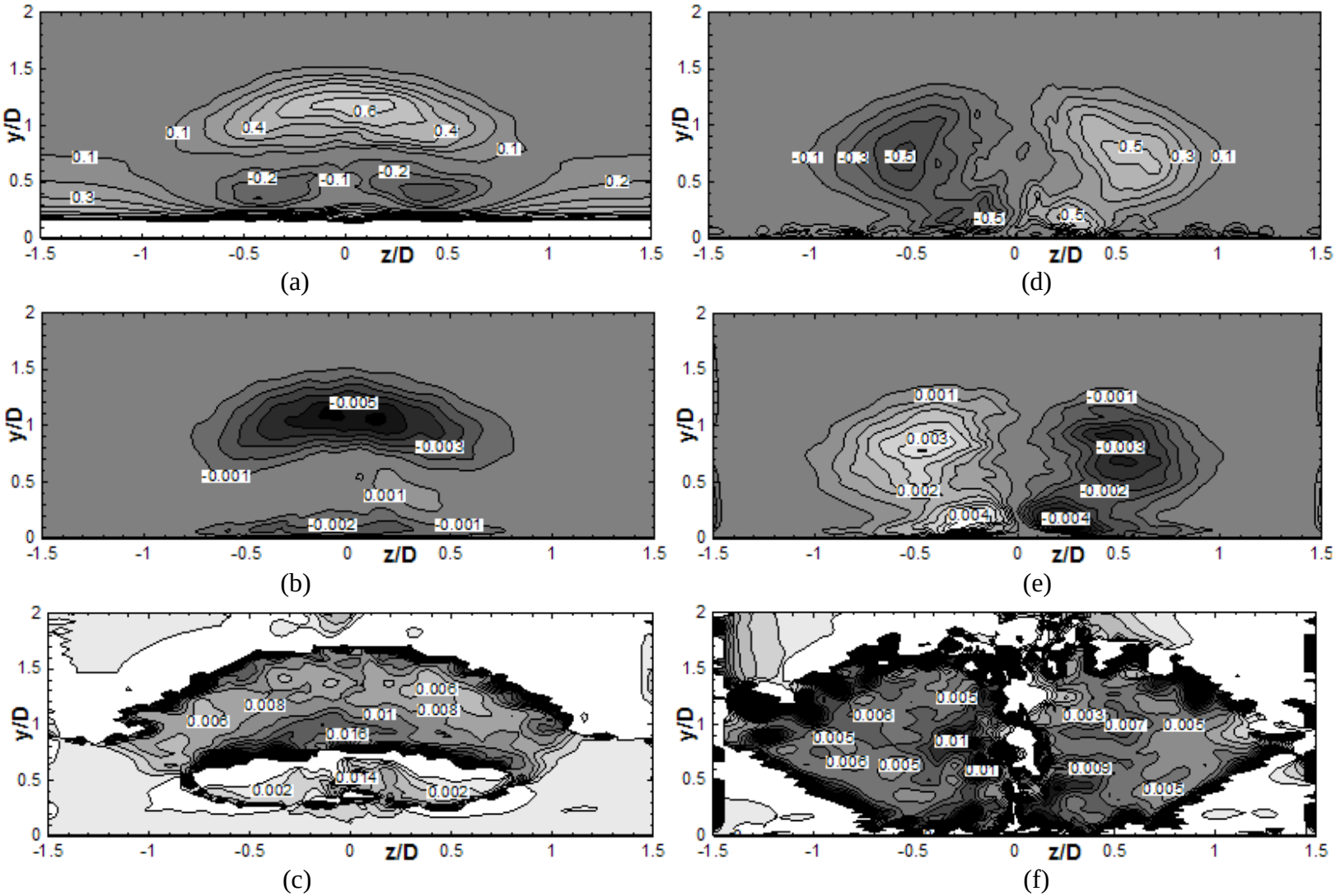

Figure 67 Normalized velocity contours at x/D = 7 of wall-normal (a) gradient $(\partial U/\partial y)/(U_\infty/D)$, (b) turbulent stress $-\langle u'v'\rangle/{U_\infty}^2$, and (c) eddy diffusivity $\nu_{t,y}/(U_\infty D)$; as well as spanwise (d) gradient $(\partial U/\partial z)/(U_\infty/D)$, (e) turbulent stress $-\langle u'w'\rangle/{U_\infty}^2$, and (f) eddy diffusivity $\nu_{t,z}/(U_\infty D)$.

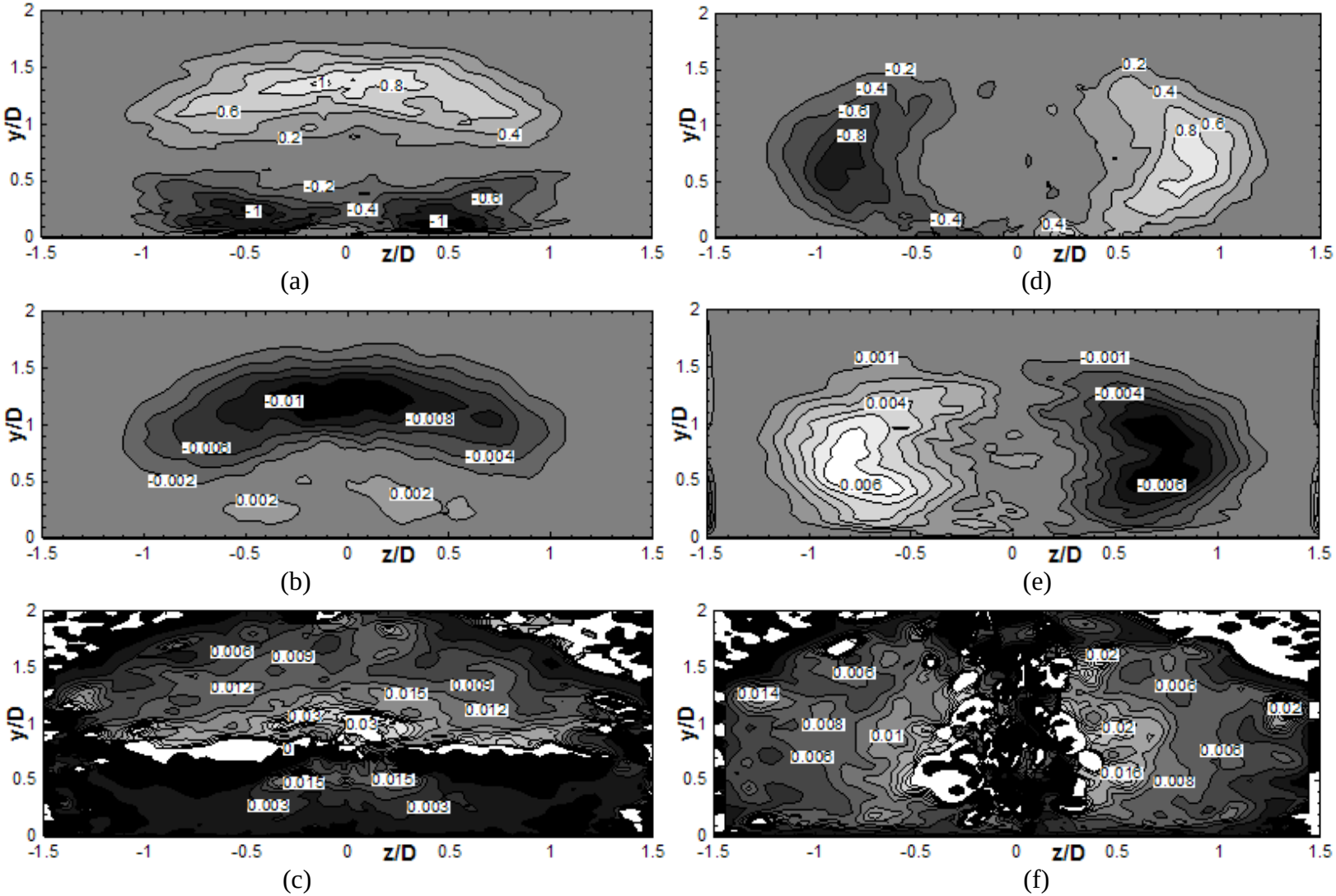

Figure 68 Normalized temperature contours at x/D = 7 of wall-normal (a) gradient $(\partial T/\partial y)/((T_\infty - T_c)/D)$, (b) turbulent stress $-\langle v'T'\rangle/U_\infty(T_\infty - T_c)$, and (c) eddy diffusivity $\alpha_{t,y}/(U_\infty D)$; as well as spanwise (d) gradient $(\partial T/\partial z)/((T_\infty - T_c)/D)$, (e) turbulent stress $-\langle w'T'\rangle/U_\infty(T_\infty - T_c)$, and (f) eddy diffusivity $\alpha_{t,z}/(U_\infty D)$.

Figure 69 shows the mean contours of the jet at four diameters downstream of the injection site. The wake region core, though once fully separated from the boundary layer, has now reunited with it. The dilution of the velocity and temperature profiles of the jet continues, but now at an even slower rate. The wake region has been slowly shrinking in the spanwise direction but continues to grow away from the wall. The thermal contours of the jet continue to expand, but at slower rates than before. The under-side of the thermal profiles still are not spreading toward the surface to provide better film coverage in the mid-span region.

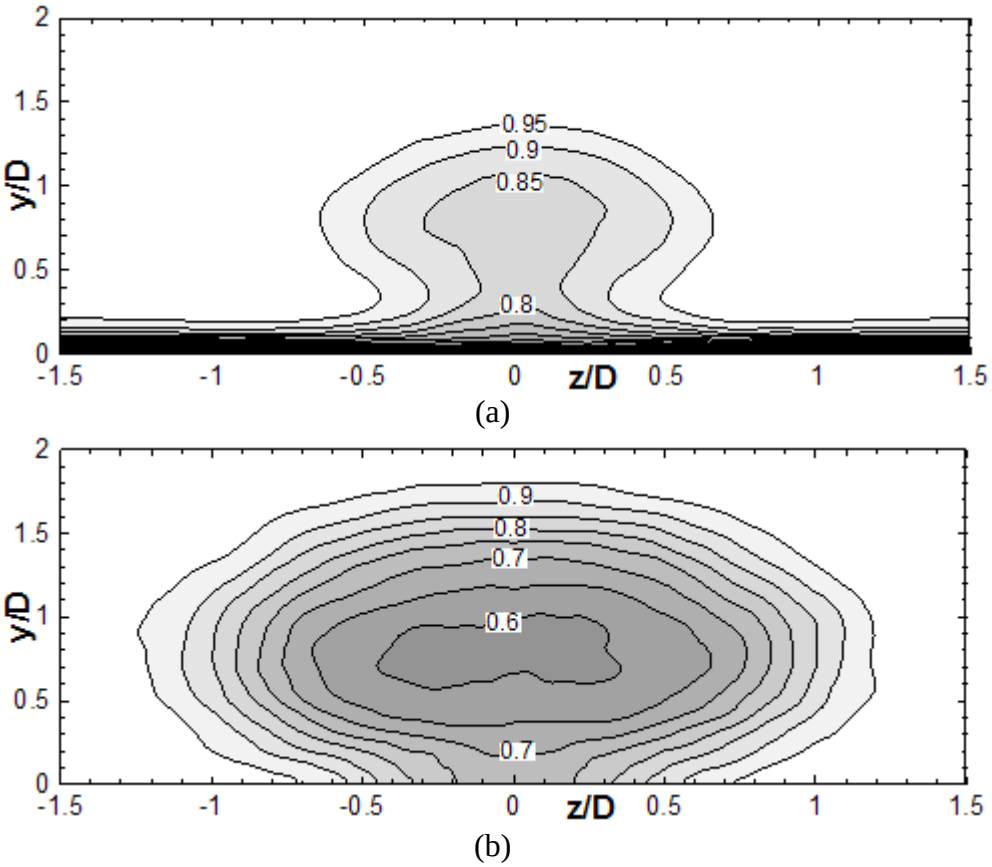

Figure 69 Normalized contours at x/D = 10 of (a) mean streamwise velocity (U/U_∞), (b) mean temperature (θ).

Figure 70 and Figure 71 show the gradient and turbulent stress fields for momentum and temperature at x/D = 7. The slowly developing jet at this point still shows similar diffusivity

contours as the last few locations. The authors hesitate to state anything certain regarding the distribution of the turbulent stress terms given that the present simulation only resolves the larger scales of turbulence and the sampling time is perhaps unsatisfactory. The present results indicate that both the velocity and temperature diffusivities, like their mean-value counter-parts, appear to have reached a somewhat steady distribution and the jet continues into the gradual development regime.

It is important, given the preceding analysis to validate engineering characteristics related to the mixing processes analyzed so that the accuracy of the current numerical model can be assessed. The next section reveals some of the inadequacies in the preceding numerical description of the film cooling flow.

8.2.3 Surface Mean Effectiveness Validation

The contours of adiabatic effectiveness are shown in Figure 72. The jet lift-off near the injection site is seen in relatively low effectiveness, but the slow reattachment begins at about x/D = 2, at the conclusion of the recirculation region. The failure of the jet to fully spread back toward the surface results in a relatively narrow footprint of the jet as compared to its true spanwise extent. Recall that this failure to spread back to the surface was related to the apparent negative/low eddy viscosity regions seen in the lower half of both the velocity and temperature diffusivity contours. This is seen to drastically reduce the ability of the jet to effectively cover the surface in a more uniform manner.

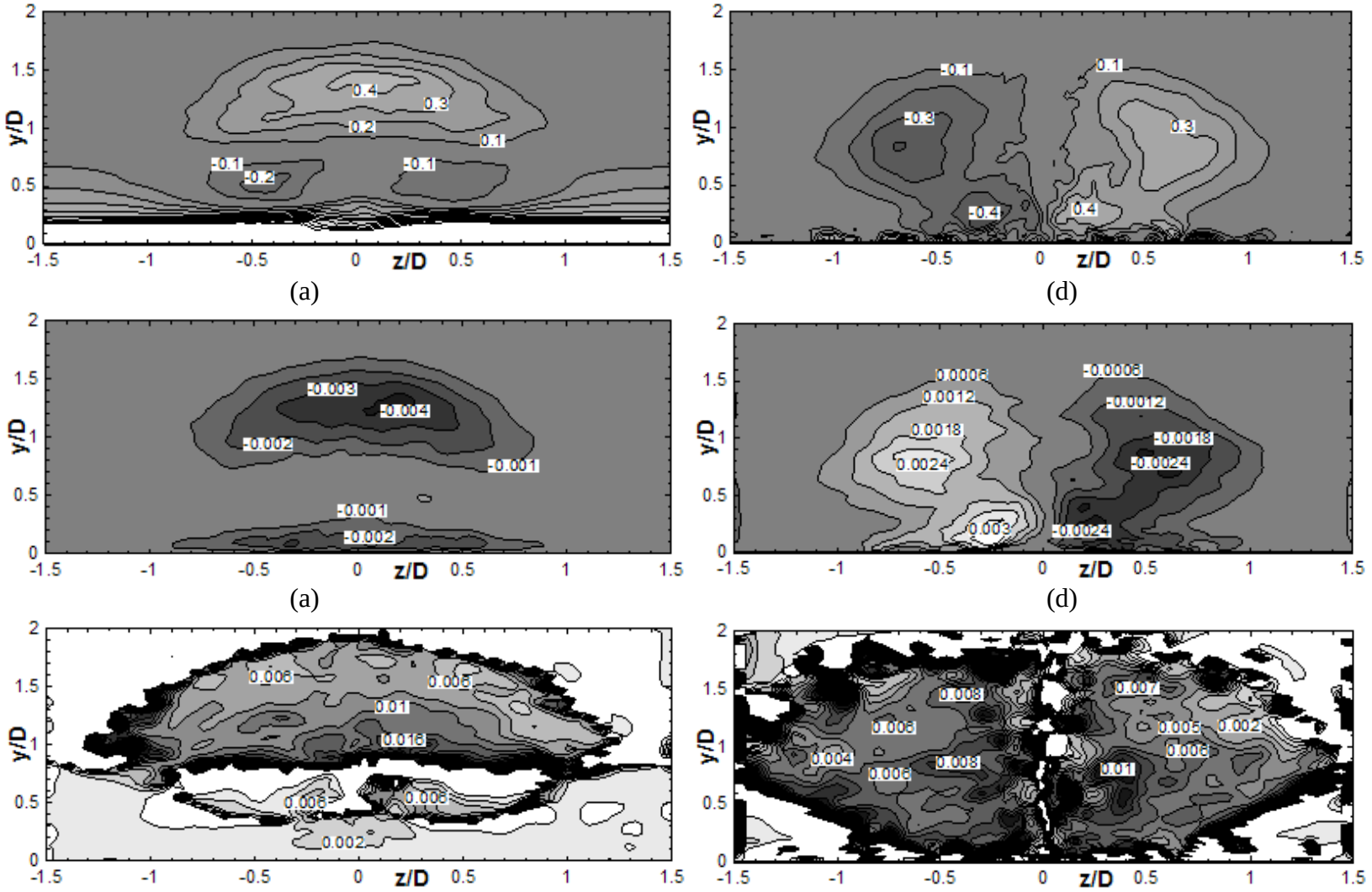

Figure 70 Normalized velocity contours at x/D = 10 of wall-normal (a) gradient $(\partial U/\partial y)/(U_\infty/D)$, (b) turbulent stress $-\langle u'v'\rangle/{U_\infty}^2$, and (c) eddy diffusivity $\nu_{t,y}/(U_\infty D)$; as well as spanwise (d) gradient $(\partial U/\partial z)/(U_\infty/D)$, (e) turbulent stress $-\langle u'w'\rangle/{U_\infty}^2$, and (f) eddy diffusivity $\nu_{t,z}/(U_\infty D)$.

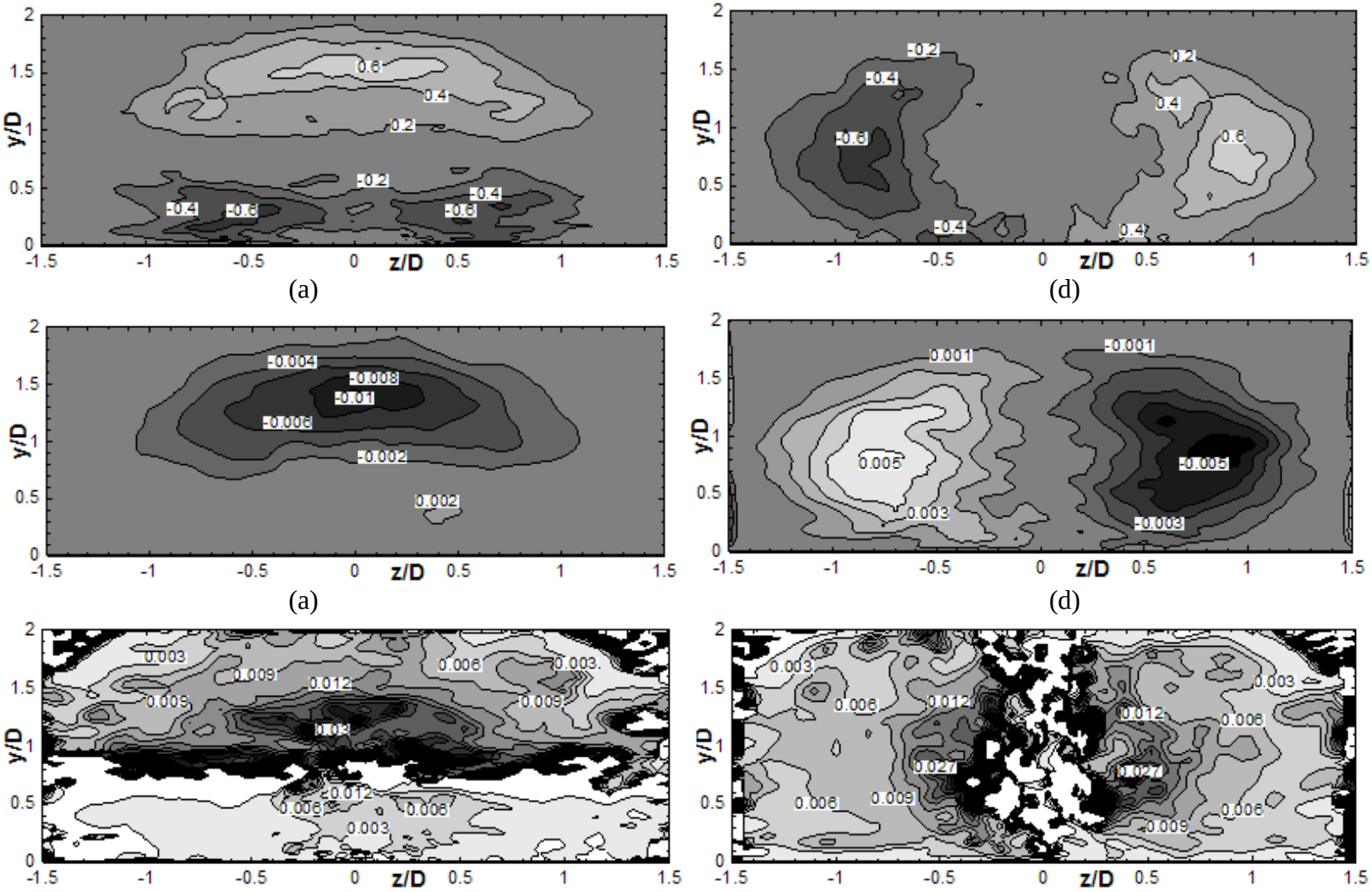

Figure 71 Normalized temperature contours at x/D = 10 of wall-normal (a) gradient $(\partial T/\partial y)/((T_\infty - T_c)/D)$, (b) turbulent stress $-\langle v'T'\rangle/U_\infty(T_\infty - T_c)$, and (c) eddy diffusivity $\alpha_{t,y}/(U_\infty D)$; as well as spanwise (d) gradient $(\partial T/\partial z)/((T_\infty - T_c)/D)$, (e) turbulent stress $-\langle w'T'\rangle/U_\infty(T_\infty - T_c)$, and (f) eddy diffusivity $\alpha_{t,z}/(U_\infty D)$.

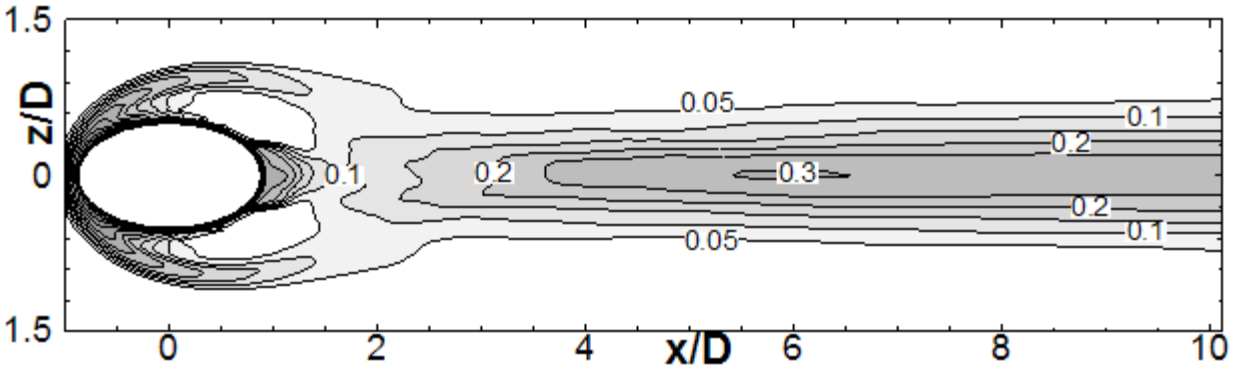

Figure 72 Mean effectiveness contours on the adiabatic surface.

Figure 73 compares the present simulation's effectiveness results with the thermocouple data from Schmidt et al. (1996). The spanwise distribution of the experimental data exhibits skewness toward the right hand side of the plot. Such skewness and its effect on effectiveness validations of CFD results are discussed by Walters and Leylek (1997). The spanwise-distribution of effectiveness in Figure 73a, even if corrected for skewness, matches only in the $-0.5 < z/D < 0.5$ region. Outside of this region, there is considerable under-prediction of effectiveness. This can be linked to the LES prediction of low/negative diffusivity in the lower part of the outer region of the jet which greatly hindered the coolant spread back to the surface. It seems that the LES under-predicts this spreading and therefore under-predicts the effectiveness away from the centerline. The under-prediction of effectiveness could also be due to an under-prediction of spanwise diffusivity, though there is less evidence from the present results to support this explanation. In reality, it is probably a combination of these two effects that results in the effectiveness under-prediction of away from the centerline. The spanwise averaged results of Figure 73b show noticeable under-prediction of spanwise averaged results, as would be expected given Figure 73a.

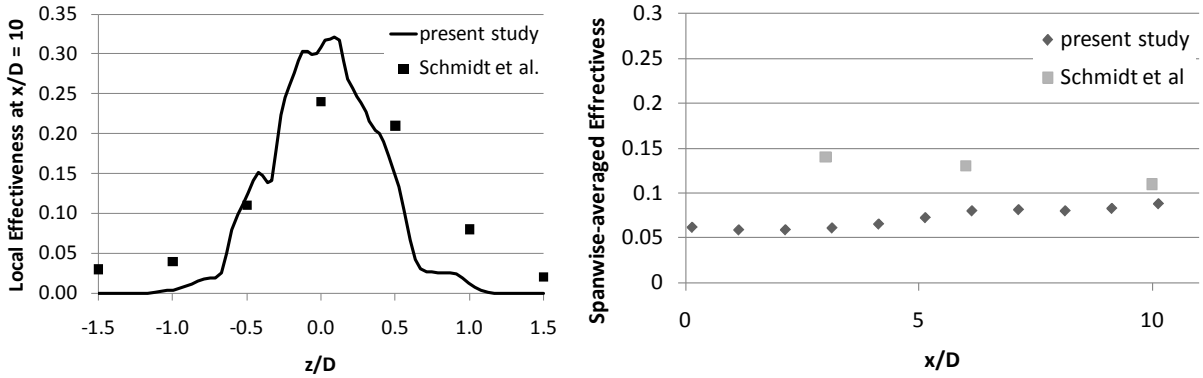

(a) (b)

Figure 73 Validation of effectiveness against experimental data.

In order to put the comparison with experiment in a broader context, the current LES results are compared with RANS results using (1) realizable k-ε and (2) Launder-Reece-Rodi (LRR) Reynolds Stress Model (RSM) in Figure 74. The improvement of prediction with the increase of the physical fidelity of the model is observed.

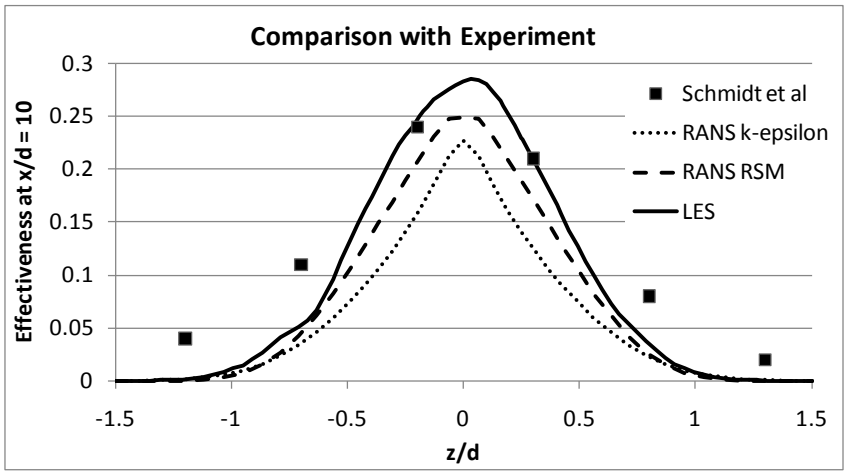

Figure 74 Comparison of effectiveness predictions by RANS and LES models.

8.2.4 Spectral Analysis

Now that the spatial phenomena have been discussed, the time and frequency domain results of the simulations are now presented. First, the spectral results are presented for a point in the

center of the exit plane of the hole in Figure 75. The dominant Strouhal number at this point is around unity (that is, the point just before the power spectral density begins to roll off).

Next, the spectral distribution at a point inside the coolant hole is shown in Figure 76. This point is located on the axis of the cylindrical hole, one diameter from the hole exit plane along the direction of the axis. This point lies in between the jetting region and the separation region within the hole. The dominant Strouhal number here is less than one, at about 0.8.

Finally, the spectrum from a point in the shear layer above the downstream lip of the hole is shown in Figure 77. This point is located one diameter downstream of the origin and 0.8 diameters above the surface. From Figure 57 - Figure 59, it is seen that this point lies in the dominant thermal gradient region and the upper-most weaker positive velocity gradient region. The dominant Strouhal number here is actually slightly greater than unity.

These three spectra indicate dominant Strouhal numbers near unity, similar to those found by Burd and Simon (1999) who measured along the exit plane of the coolant jet. The indicated integral length scales from the wave number plots are also similar to those found in Burd and Simon (1999), namely, 0.1 to 0.5 diameters. It is also seen that the wave number spectra match the equilibrium -5/3 slope before dropping off much faster after the filter size.

8.3 Conclusions

A large eddy simulation of discrete injection film cooling was completed using commercial software from ANSYS Fluent. The geometric and flow parameters were set to mimic the experimental study of Schmidt et al.8 with momentum ratio of unity. The evolution of the jet as it progresses downstream is discussed in terms of mean velocity, temperature contours, along with their respective gradients and turbulent stresses.

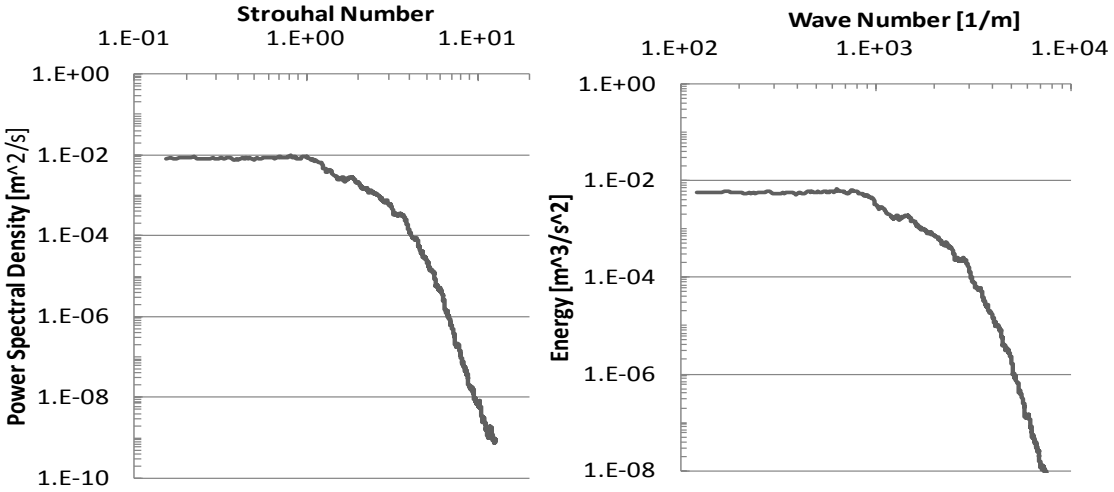

Figure 75 Spectral distributions at a point located on the exit plane of the hole.

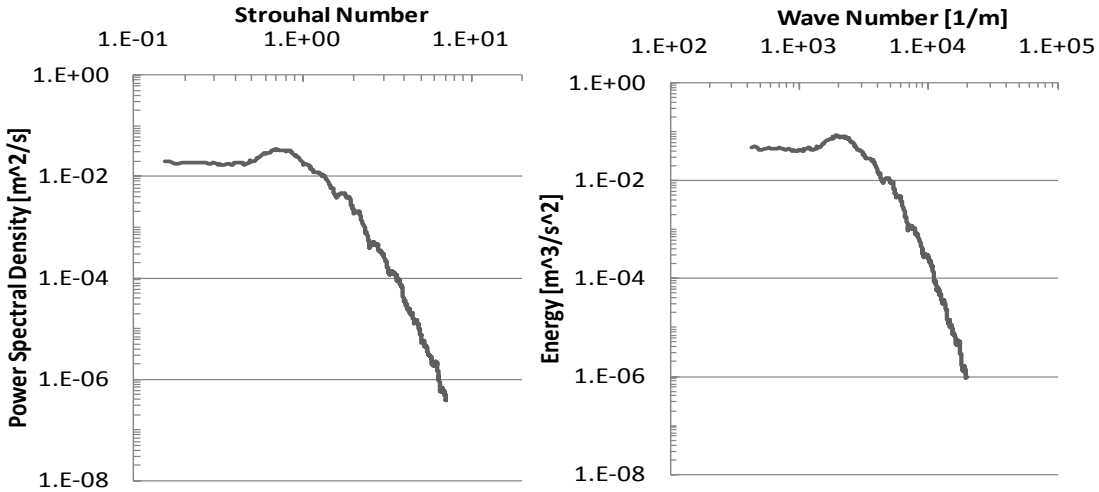

Figure 76 Spectral distributions at a point located inside the hole.

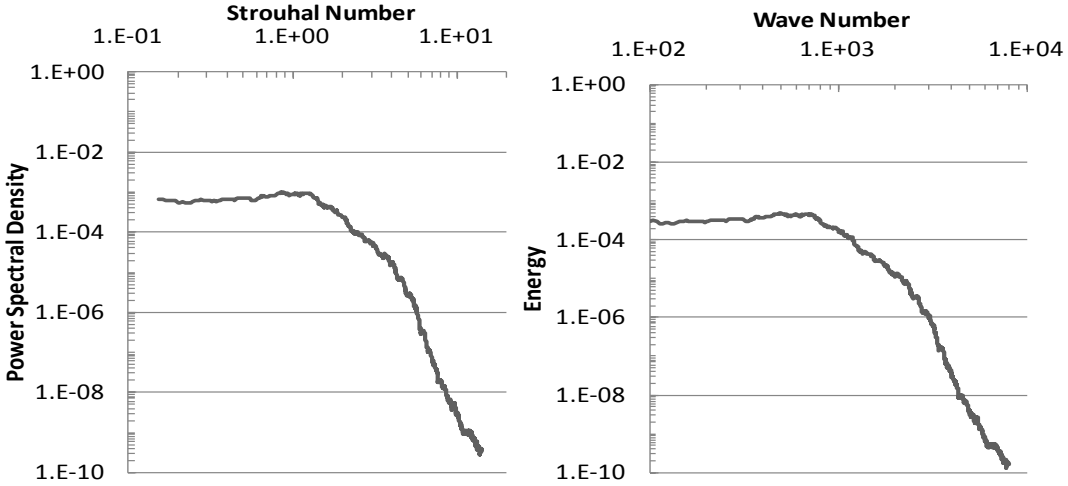

Figure 77 Spectral distributions at a point located in the shear layer above the hole.

Previous LES studies of film cooling have shown good agreement with experimental data for low blowing ratios (attached jet), but the current study finds comparatively poor agreement with the experimental data for this detaching jet. Though the experimental jets appear skewed (Walters and Leylek 1997), the disagreement in laterally averaged effectiveness and spanwise spreading suggests that the LES under-predicts the reattachment of the jet, especially away from the centerline. This under-prediction could be caused by the poor performance of the LES technique close to walls in the presence of higher aspect ratio cells. With attached jets, the near wall region is generally populated by the core of the jet, with its associated low temperature gradients.

The following bulleted list highlights areas of focus for the next chapter:

1) More complete validation using NASA experimental data with full field measurements of mean and fluctuating velocity and temperature values

2) More realistic treatment of inlet boundary conditions using a recycling method similar to that of Lund et al. (1996); open source code will allow more access to develop such an inlet condition

3) Finer grid to capture more of the turbulent spectrum; open source code will free the investigation from financial restraints typically encountered in the use of commercial software when running on a large number of processors.

CHAPTER 9 SIMULATION USING OPEN SOURCE CODE

This chapter presents the main body of LES results for this thesis. Having the preliminary investigations of the previous chapters as motivation, this chapter presents LES results with finer resolution in space and time, more physically sound boundary conditions, and more complete validation with experiments. The above advantages are mainly enabled through the use of open source CFD code and the use of recent NASA wind tunnel data (El-Gabry et al. 2011, Thurman et al. 2011).

Use of the OpenFOAM software allowed for numerical processing without the hindrance of licensing for commercial products. This increase in computational ability, coupled with the hardware provisions of the STOKES cluster, opened the door for finer spatial and temporal resolution. In addition, access to the source code provided the opportunity to implement a recycling-rescaling technique (Lund et al. 1996, Jewkes et al. 2011) for the turbulent boundary layer inflow condition.

The experiments with which the LES results are validated were performed at NASA Glenn Research Center by injecting slightly cooled air from an ice bath heat exchanger through a row of three cooling holes, using the middle hole for gathering data. Velocity measurements are taken using a cross-wire anemometer and temperature measurements using a thermocouple. Full traverses of these probes yielded detailed velocity and temperature maps along several planes in the flow, allowing for much more complete validation than previously presented in this thesis. Collaboration with the experimentalists at NASA during two summer internships led to greater confidence in the matching of flow and boundary conditions. Initial LES studies in OpenFOAM were performed during the second of these internships.

9.1 Computational Formulation and Methodology

9.1.1 Geometry and Flow Conditions

The geometry and flow conditions of the current numerical simulation were designed for specific validation with the experimental results of El-Gabry et al.(2011) and Thurman et al. (2011). This two-part study provided detailed two-dimensional maps of mean and fluctuating velocity components, as well as mean temperatures on many planes throughout the flow-field. The main features of the geometry and flow are given in Table 14. The large diameter of the hole (compared with actual engine components) allowed for higher resolution measurements and is exactly matched by the current simulation model. This scaling, of course, necessitated a much slower freestream velocity for Reynolds number matching and disallowed any high-Mach number effects (compressibility effects).

Table 14 Geometry and flow parameters for current LES model and experimental validation data.

	D [mm]	L/D	P/D	α_i	U_∞ [m/s]	DR	M	δ/D
Experiment	19.05	15.0	3.0	30°	9.8	1.05	~1.0,~2.0	0.75
Current model	19.05	10.0	3.0	30°	9.8	1.0	1.0,1.9	0.75

The experiment contained no coolant plenum for conditioning of the coolant flow, but rather provided for a long development section of about 15 diameters within the angled coolant tube. The current model abbreviated the length of the coolant tube and specified fully developed turbulent pipe flow at the inlet. The coolant temperature was ~283 K compared to a crossflow temperature of ~297 K, yielding a density ratio of 1.05. For the present simulation, the simplification offered by an incompressible scalar transport solution technique outweighs the

benefits of using a compressible fluid model. Two blowing ratios were simulated, a moderate M = 1.0 and a high M = 1.9, as done in the matching experiment. This thickness of the boundary layer was set to match that of the experimental profile. The experimental velocity profile was not specified directly, only the thickness. The recycling-rescaling technique (Lund et al. 1996, Jewkes et al. 2011) determined the velocity profile at the inlet for the specified thickness.

9.1.2 Grid and Boundary Conditions

Two block-structured hexahedral grids, one for each blowing ratio, were created in GridPro with minimized non-orthogonality and skewness measures. Each grid was created with two unconnected pieces: the first for the main simulation and the second for the simulation of the developing boundary layer. The instantaneous boundary layer inflow velocities were mapped from the secondary domain at each time step to the inlet of the primary domain. In this way, the developing boundary layer was enforced at the main inflow, without information from the primary domain affecting the boundary layer simulation. The extent of each domain is shown in Figure 78. The M = 1.9 grid extends further from the surface due to the higher trajectory of the coolant jet and interaction region.

The M = 1.0 grid consisted of about 8.8 million hexahedral cells while the grid for M = 1.9 grid consisted of slightly more than 10 million hexahedral cells. The upstream boundary layer and secondary domain portions were designed for an y^+ less than unity to the first cell center with stretching ratios less than 1.2 in the wall normal direction. The x^+, y^+ and z^+ values for the approaching boundary layer, downstream interaction, and coolant pipe flow are shown in

Table 15. The grids themselves are shown in Figure 79.

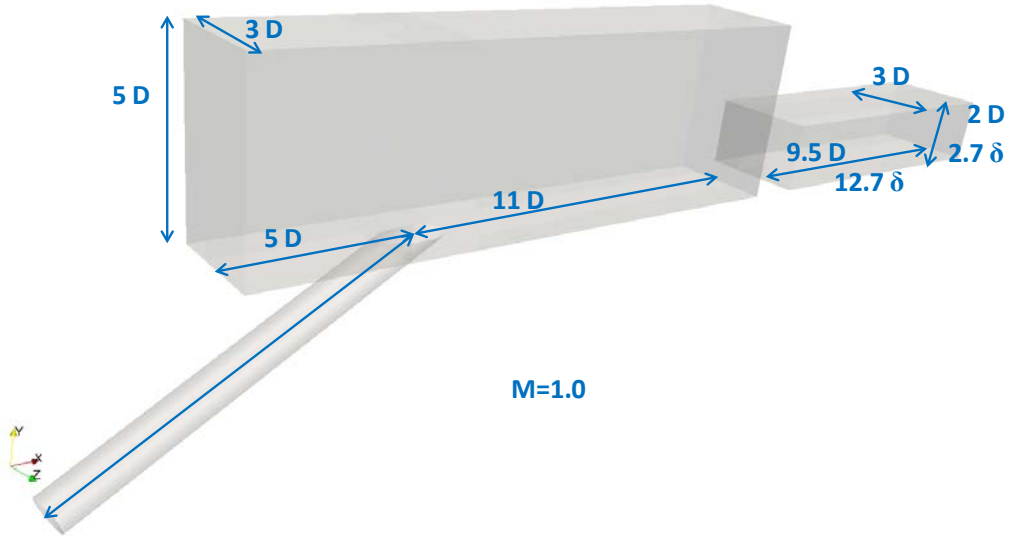

(a)

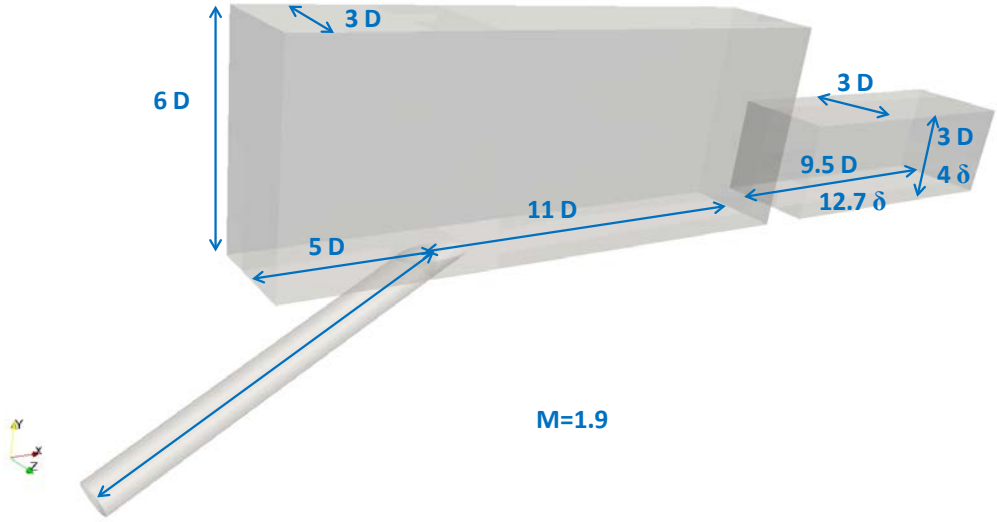

(b)

Figure 78 Domains for (a) M = 1 and (b) M = 1.9 simulations.

Table 15 Grid spacing relative to inner scaling, predicted and realized

	x+	y+	z+
B. Layer	37	0.30	14
Interaction	38	0.55	28
Pipe Flow	36/53	0.35/0.65	14/25

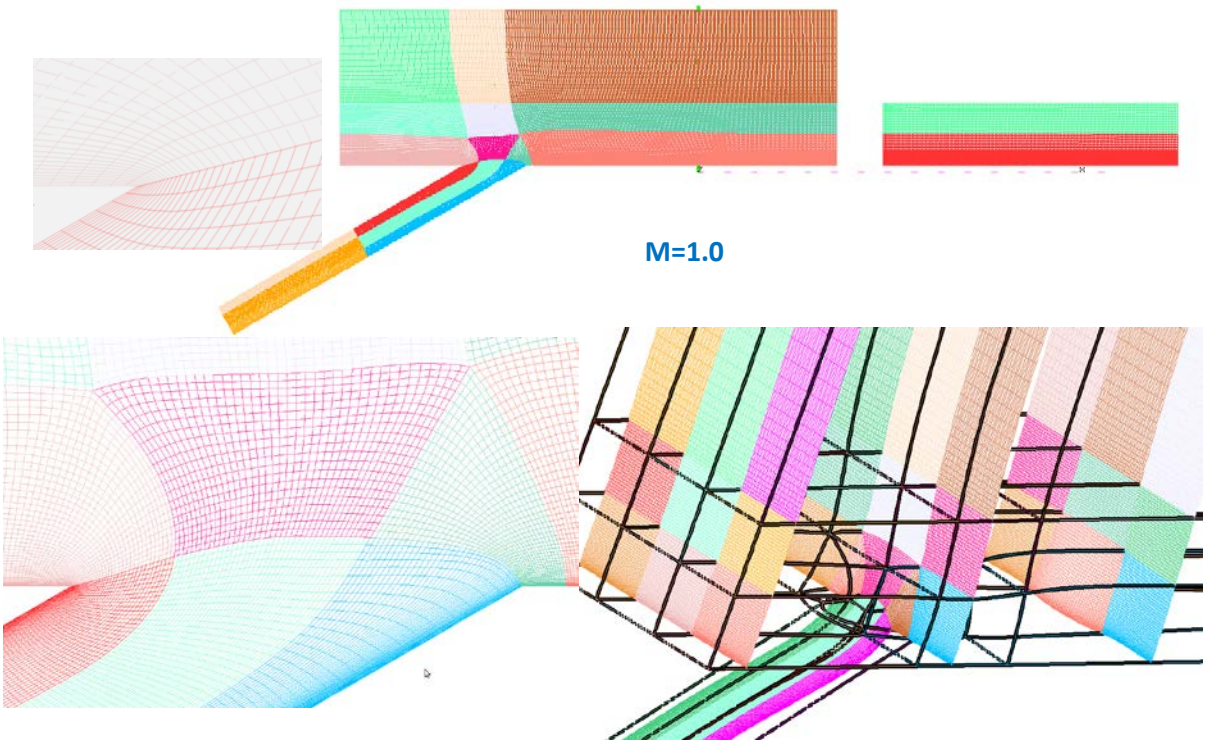

(a)

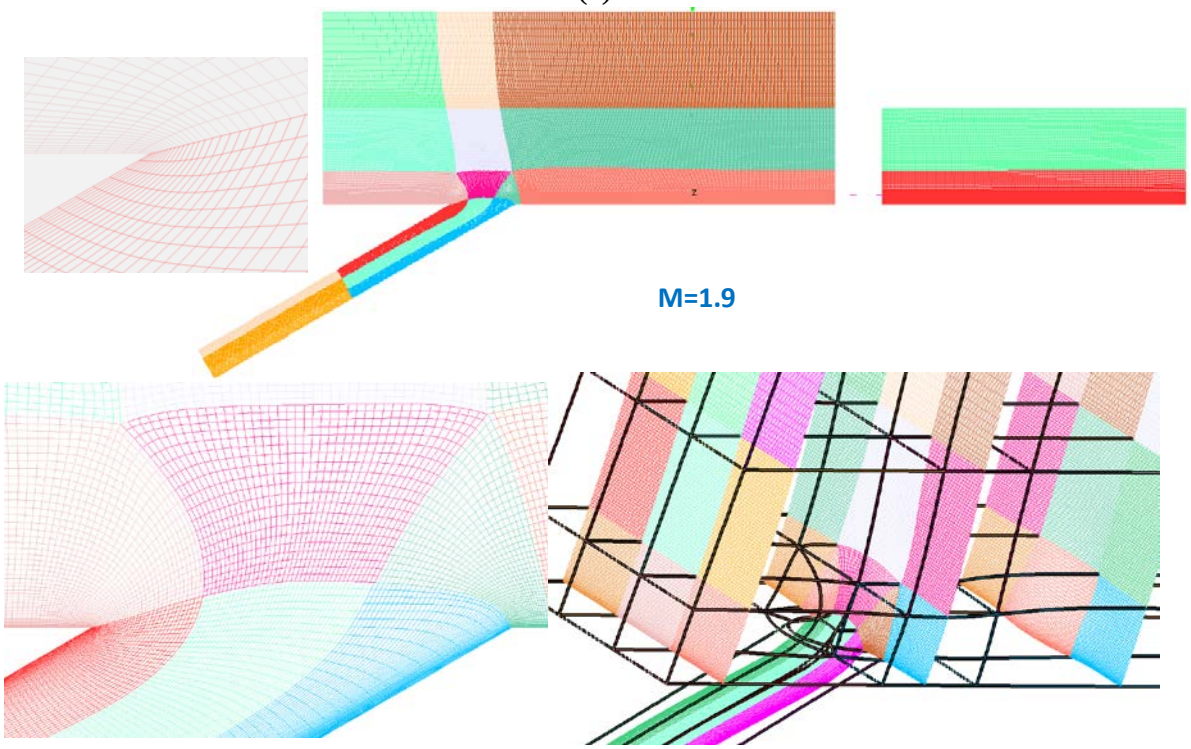

(b)

Figure 79 Block-structured hexahedral grids for (a) M = 1.0 and (b) M = 1.9.

The boundary conditions for the simulation are summarized in Figure 80. The walls are specified with no-slip first kind boundary conditions in velocity and adiabatic second-kind boundary conditions in temperature. The outflows are based on the advective boundary condition with local advection velocity. The freestream boundaries are given the specified freestream velocity first-kind boundary conditions in the streamwise direction (Table 14) and zero-gradient second-kind boundary conditions in the other two velocity components as well as the temperature field. The baseline pressure is specified uniform across the freestream boundary and zero-gradient at all other boundaries.

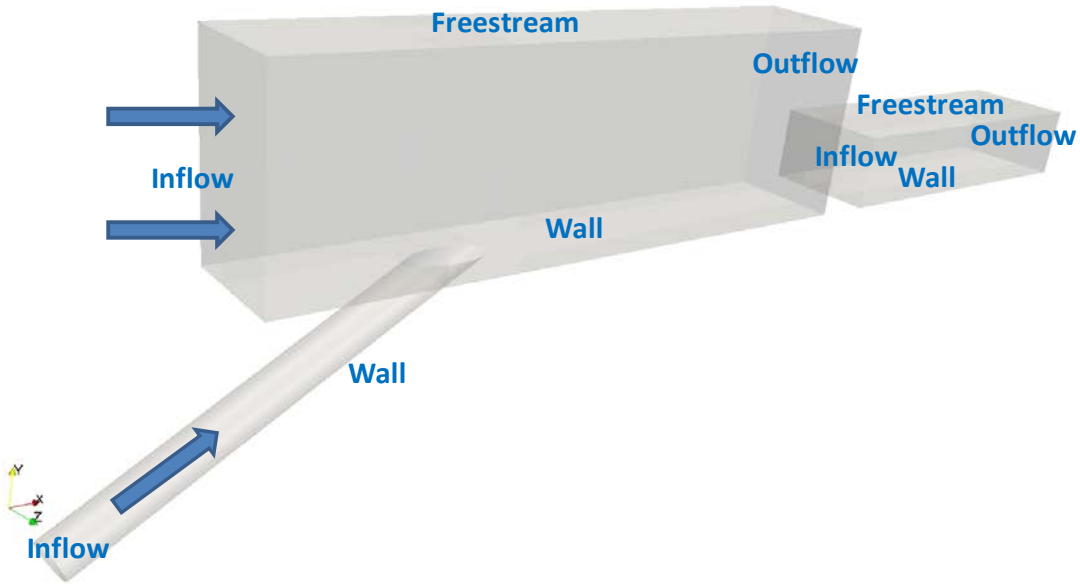

Figure 80 Summary of boundary conditions for both OpenFOAM simulations.

The inflow boundaries constitute a more complicated scheme, Figure 81. The objective of the secondary domain is the supply of a realistic turbulent boundary layer (in the instantaneous sense) for the main simulation. For fully-developed pipe flow, the coolant inflow velocity is directly mapped from the interior of the domain, with the only operation performed to ensure the flow rate remains at the desired blowing ratio. This functions similarly to a periodic domain in

developing fully turbulent pipe flow. The secondary domain inlet likewise receives its mapped velocity vectors via a rescaling method first introduced by Lund et al. (1996). The rescaling method, as described in the next section, functions to scale down the boundary layer from its state in the internal of the domain to a thinner boundary layer at the inlet, thus establishing a spatially developing turbulent boundary layer in the secondary domain. Finally, a plane of the secondary domain is directly mapped to the main inflow at each time step.

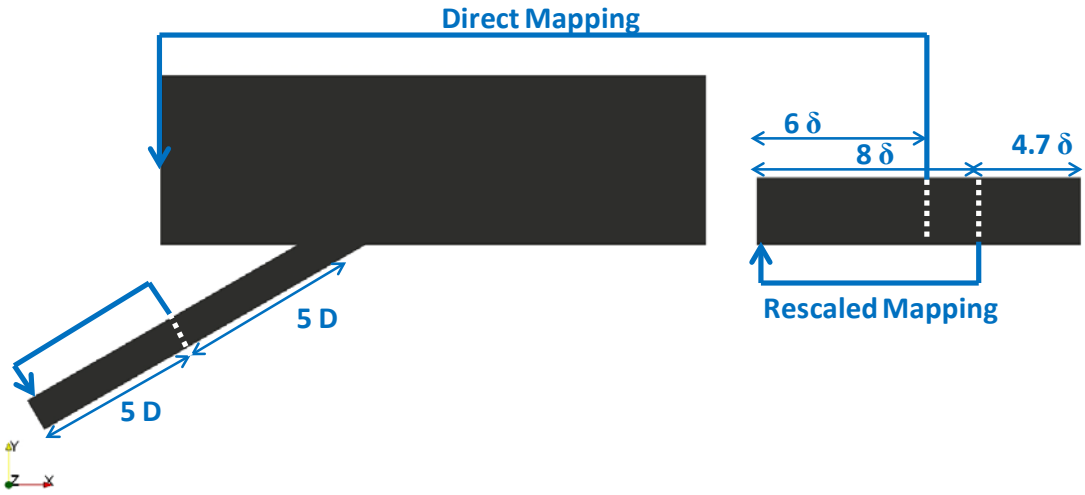

Figure 81 Schematic of feedback mapping for inflow boundary conditions.

9.1.3 Rescaling Procedure for Spatially-Developing Boundary Layer

Spalart (1988) first introduced the idea of using inner and outer boundary layer scaling arguments to facilitate a numerical simulation of a turbulent boundary layer. Lund et al. (1996) modified Spalart's technique to a recycling-rescaling procedure. Recently, Jewkes et al. (2011) suggested minor tweaks to the method of Lund et al. (1996) to enable easier application of the idea. The present work involved coding a rescaling procedure in the OpenFOAM framework similar to these two papers. The reader is referred to Lund et al. (1996) for the details of the physical arguments and mathematical operations of this method. The suggestions of Jewkes et

al. (2011) with respect to the use of displacement thickness and initial conditions were taken into account in this code. Jewkes' suggestion of the displacement thickness as $1/8^{th}$ the disturbance thickness was replaced with $1/6^{th}$ due to the author's analysis using the equations developed in the appendix of Lund et al. (1996). For the procedure, a desired displacement thickness is given by the user. The simulation itself produces the rest of the inflow condition.

9.1.4 Numerical Method

OpenFOAM is a C++ library with application and utilities designed for unstructured finite volume solvers. The LES solution procedure took place in three steps. First, simulations using reduced domains or simplified equations provided initial conditions for main simulation. Then, The main simulation was started and allowed to progress until initial conditions were immaterial. Finally, statistical sampling was enabled and the simulation was continued until these statistics converged.

The initialization took place via three separate simulations. Motivated by the initial transient time for establishing realistic turbulent wall-bounded flow for the boundary layer and pipe flow, two simulations on smaller domains were used to work through these initial transients with a much lower cell count than the full simulation. Figure 82 shows the two smaller grids used for these startup simulations, which were simply extracted from the main simulation grid. These two smaller domains were advanced in time with a PISO algorithm for velocity-pressure coupling. The temperature (energy) equation was not solved for these two initial simulations. The physical time step was set for the Courant number to remain safely below unity for the every cell and both were simulated for about 10 flow-through times. Wall shear stress was monitored

and used to indicate when the simulation had developed realistic turbulence by matching existing correlations.

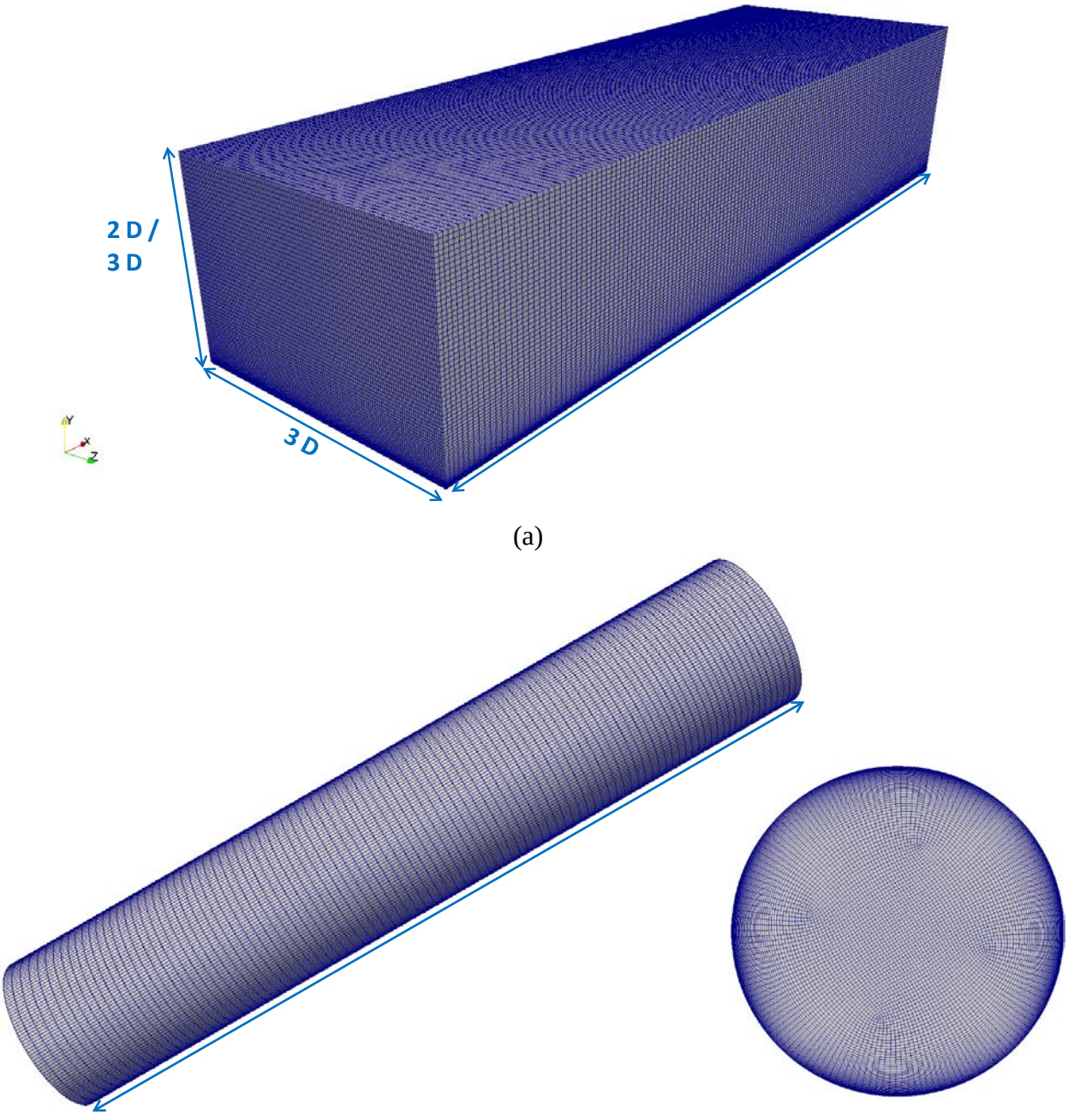

(a)

(b)

Figure 82 Sub-domains used for initialization simulations of (b) crossflow spatially-developing turbulent boundary layer and (b) coolant pipe flow fully developed turbulence.

The dynamic Smagorinsky subgrid model is used, as implemented in the Fluent code (Ansys 2009). Implementation in the OpenFOAM code, as with Fluent, uses a local averaging of the dynamic coefficient. This prevents the solution from diverging (Lilly 1992). The scalar transport of heat via turbulence is modeled with a constant $Pr_t = 0.85$. The equations were integrated to the wall with no special wall treatment, thus, the simulation is regarded as WR-LES, with the given inner scaled grid spacing given in Table 15.

The initial conditions for both simulations were based on an empirical turbulent wall layer fit (law-of-the-wall + law-of-the-wake) based on the equations of Liakopoulos (1984). These mean profiles were added to random fluctuations generated according to the suggestions of Jewkes et al. (2011). Figure 83 shows the initial random fields for the two sub-simulations of the M=1.9 case. After an initial drop in wall shear stress due to partial re-laminarization, the conditions within each sub-domain experience re-transition to realistic turbulence. The velocity fields at the completion of the sub-simulations are shown in Figure 84.

The third part of the initialization step was the Reynolds-averaged (RANS) solution to the full domain using the k-ω SST model. This was accomplished with a SIMPLE pressure-velocity coupling algorithm supplemented with a scalar transport equation for temperature. The turbulent velocity fields of the two other startup simulations were mapped onto the RANS solution to the full domain to complete the initialization process. Note: the mapping was conformal because the sub-domain grids were directly extracted from the main simulation grid. The final mapped initial conditions are shown in Figure 85.

The main simulation was started and continued for two flow-through times until the effect of the initial conditions were seen to vanish. Then, the simulation was continued for close to 10

flow-through times before statistical convergence was observed for all monitors. The main simulation used an iterative PISO-SIMPLE algorithm in which 3 SIMPLE iterations of the PISO algorithm with two pressure corrections. A second-order fully implicit discretization was used in time along with a physical time step ensured to keep the Courant number below unity. In space, a second order pure central scheme was used for advective interpolation, which was kept stable via the conservative time-advancement scheme described above.

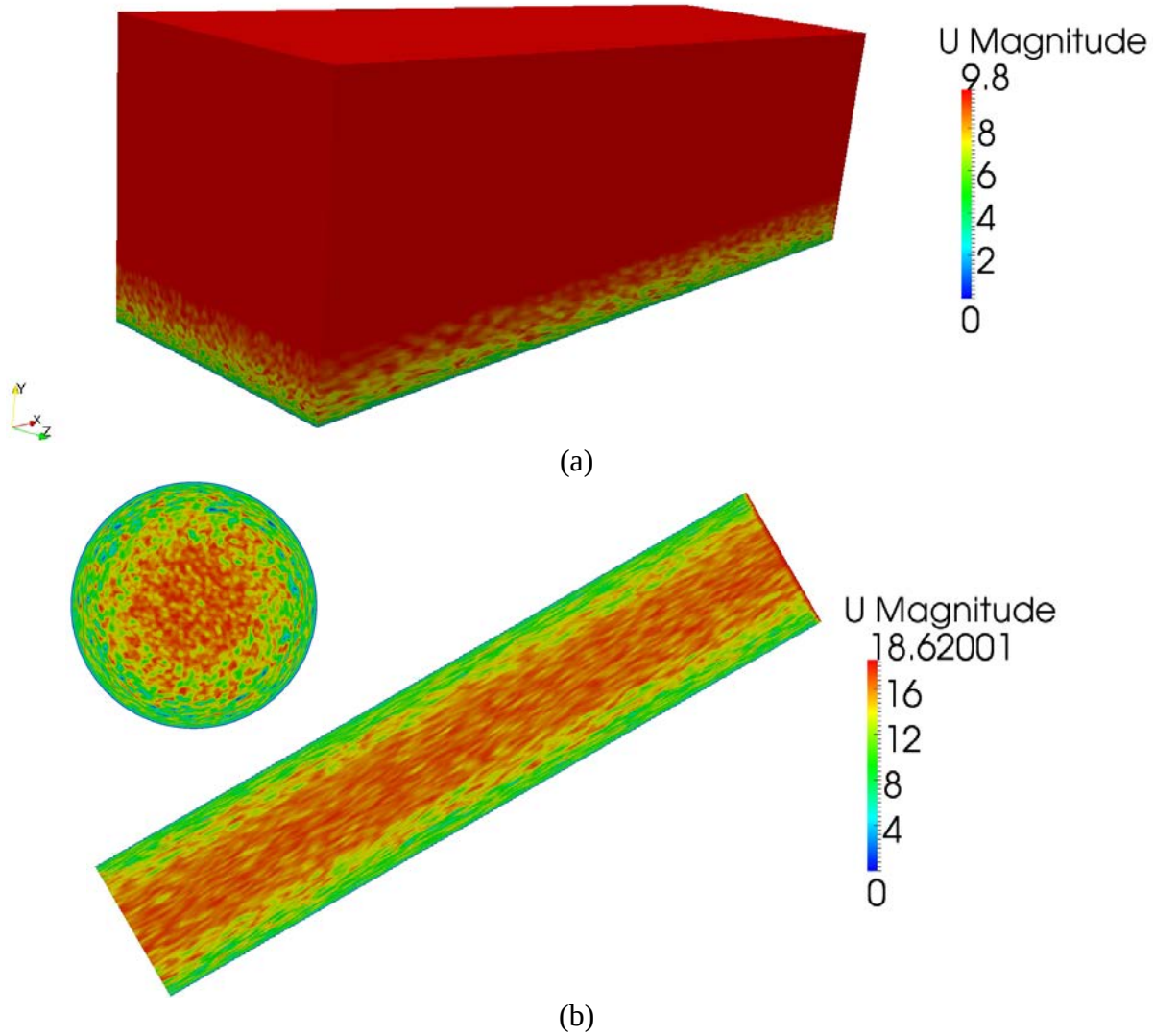

Figure 83 Initialized sub-domains with empirical mean profile and random perturbations for (a) turbulent boundary layer and (b) cylindrical pipe flow.

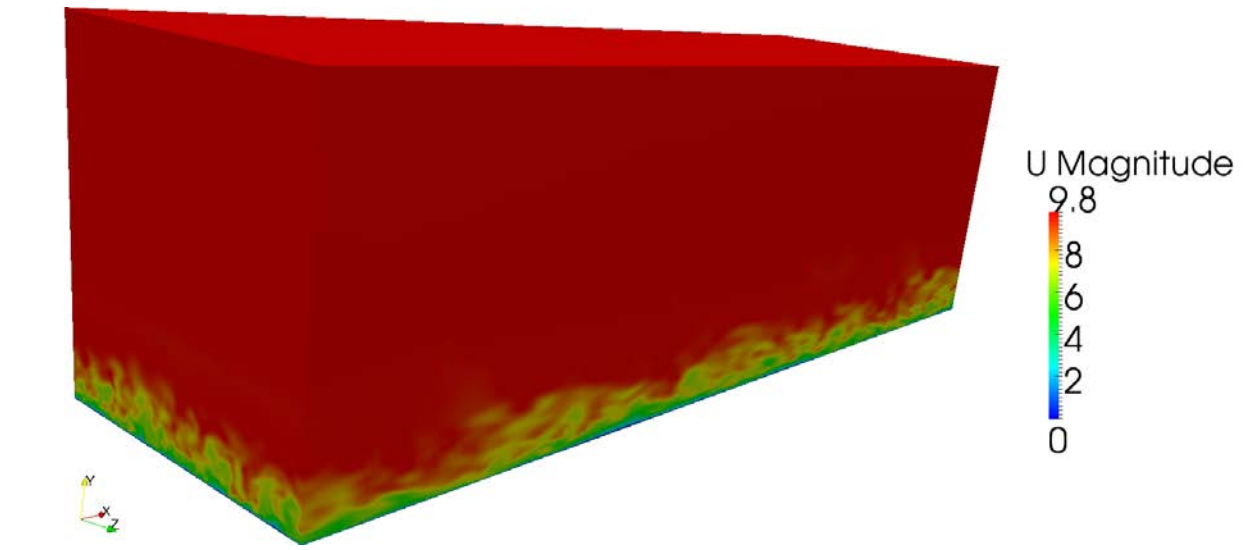

(a)

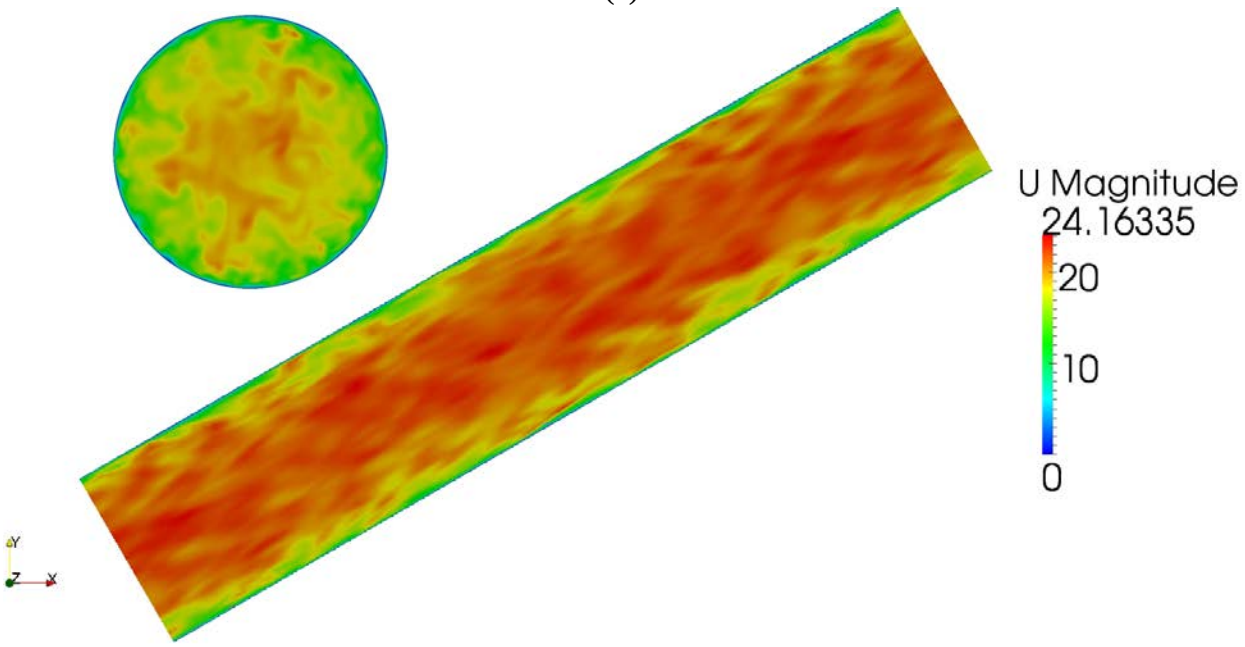

(b)

Figure 84 Velocities at the completion of the transient startup sub-simulations for (a) spatially-developing boundary layer and (b) pipe flow.

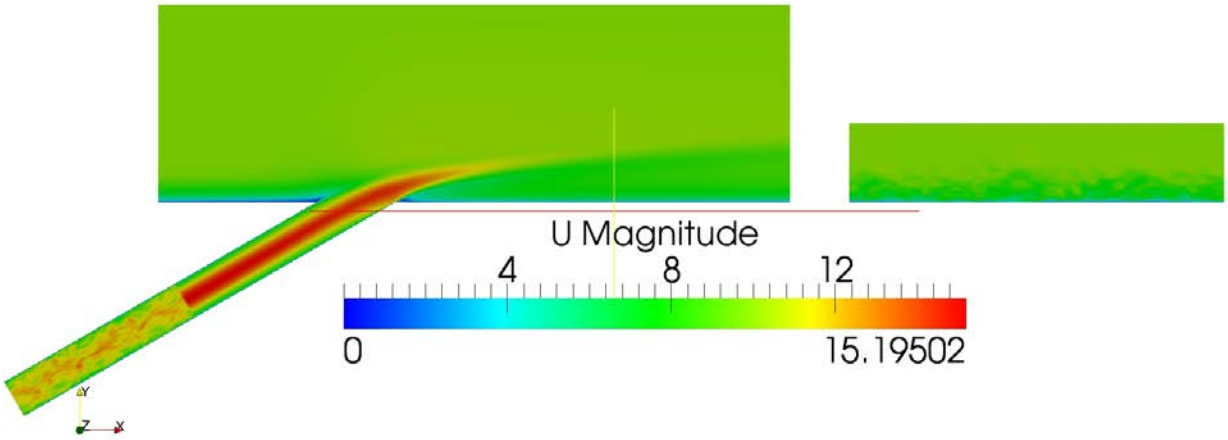

Figure 85 Initial velocity along the center-plane for the main simulation with M=1.0.

9.2 Moderate Blowing Ratio (M=1) Validation

9.2.1 Mean Velocity Field

The first concern for validating mean velocity fields is the approaching boundary layer. Great lengths were taken via the recycling-rescaling procedure to give a realistic turbulent boundary layer at the inlet to the film cooling domain. Figure 86 shows the first and second order statistics for the validation of the boundary condition code. In this run, the grid was generated using OpenFOAM's blockMesh utility and spanwise averaging was performed in addition to time averaging. The data shows very good agreement with DNS and LES data from Spalart (1988) and Lund et al. (1996), respectively. The Re based on momentum thickness from the validation run was 1600, slightly higher than that of Spalart (Re = 1410) and Lund et al. (Re =1530).

The velocity and Reynolds stress profiles for the approaching boundary layer in the current simulation is shown in Figure 87. Again, the data is compared with Spalart (1988) and Lund et al. (1996), though in this case, the Re based on momentum thickness is around 1240, compared to 1410 of Spalart DNS and 1530 of Lund et al. LES. Nevertheless, the data is largely in good

agreement. It is noted that, because the grid for this simulation was created in GridPro, spanwise averaging in the unstructured sense was not feasible, thus the curves appear less smooth. The most notable disagreement is in the wall-normal fluctuations, which do not asymptote to zero at the edge of the boundary layer. This is likely due to spurious feedback which is a well-known problem for recycling-rescaling methods (Jewkes et al. 2011).

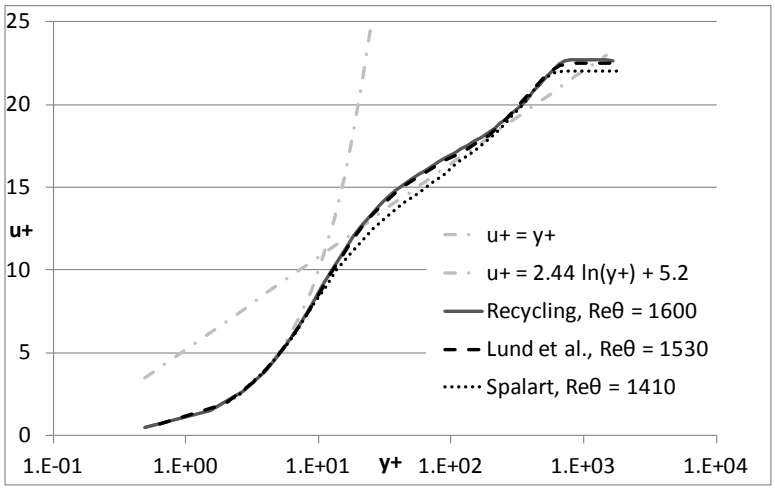

(a)

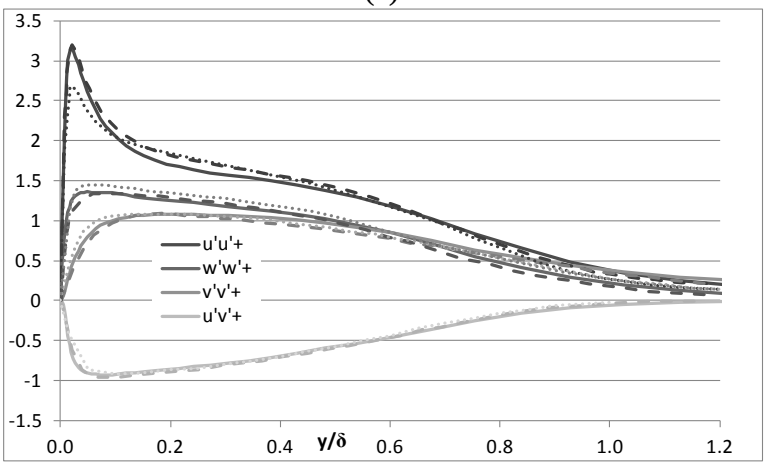

(b)

Figure 86 Validation of recycling-rescaling method: (a) mean velocity profile, (b) Reynolds stress tensor profiles.

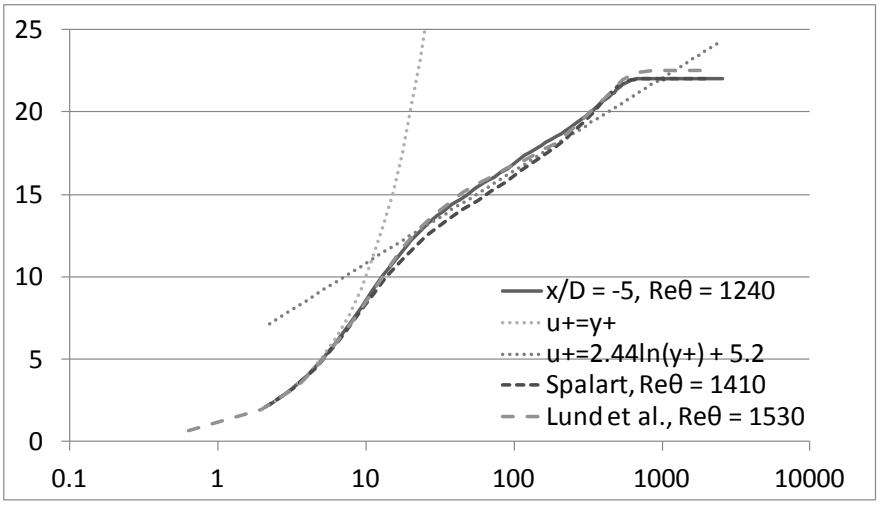

(a)

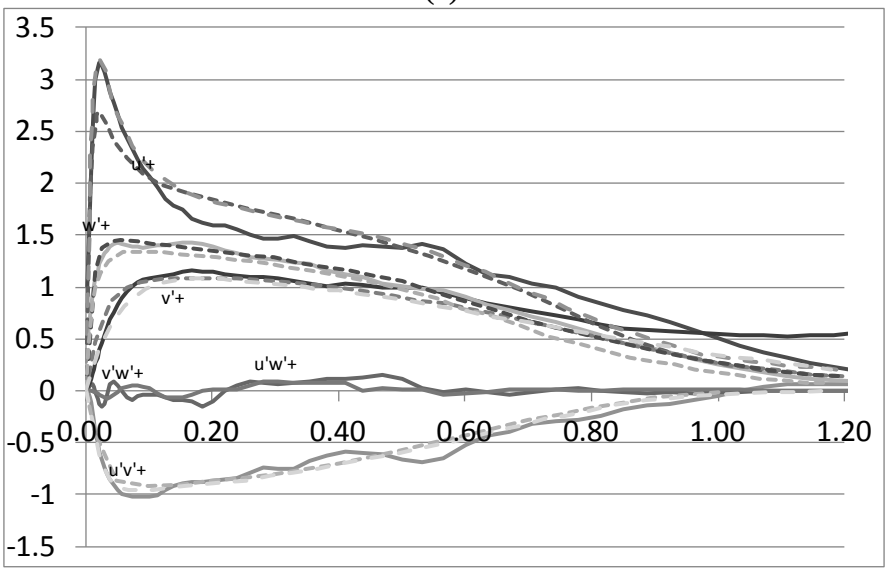

Figure 87 Validation of approaching boundary layer profiles for the M = 1 simulation (a) mean x-velocity and (b) Reynolds stresses

The mean velocity field along the center-plane is shown in Figure 88, compared with experimental data. The trajectory of the jet is predicted well by the LES in general. Both RANS and LES results over-predict the extent of the separation region (blue) as well as the extent of the jet portion of the coolant. The "jet portion" of the coolant is used to describe regions where the velocity magnitude is greater than the freestream velocity, where regions of velocity less than freestream velocity is denoted as the "wake portion". With M=1, the coolant is contracted

(accelerated) by the crossflow and achieves velocities in excess of the freestream velocity. Below this jet region, the separation of the jet produces a wake region.

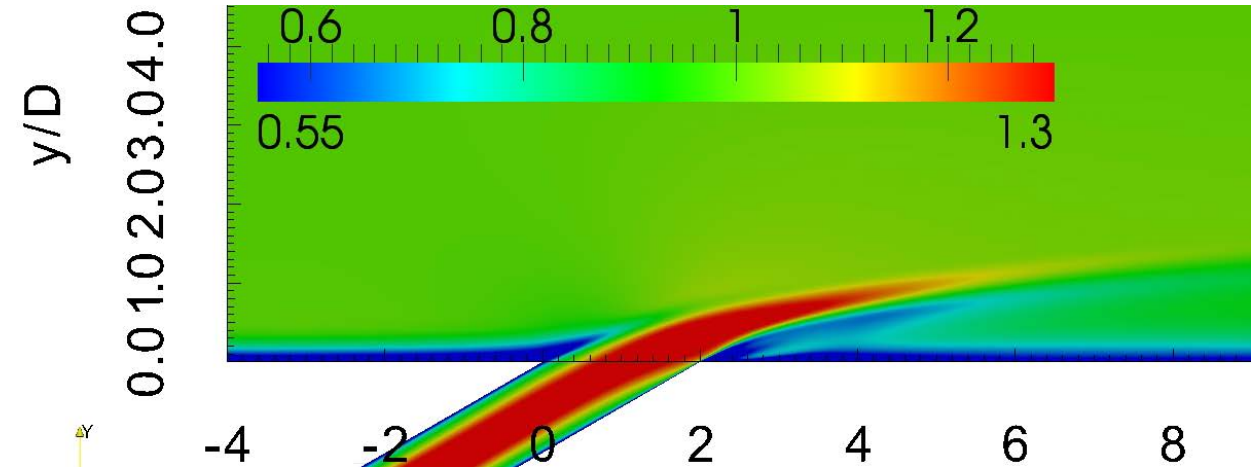

(a)

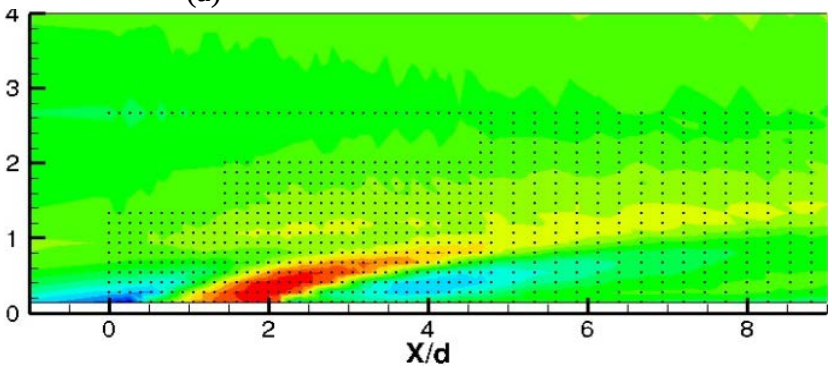

(b)

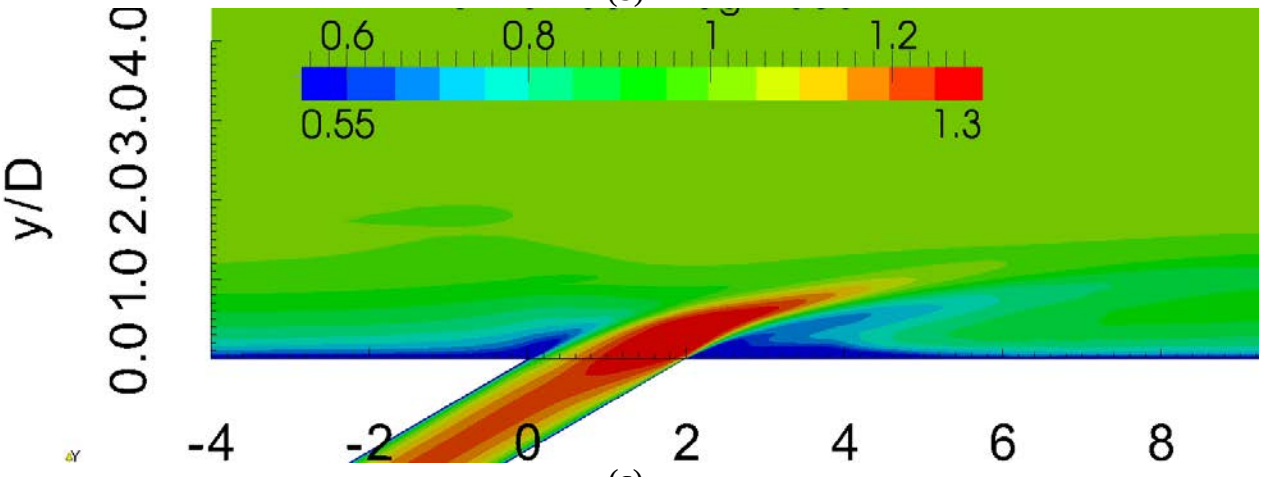

(c)

Figure 88 Mean velocity contours along the center-plane of the jet for (a) RANS , (b) experiment, and (c) LES.

Next, to compliment the center-plane validation, mean velocity magnitude contours from a number of stream-wise normal planes are presented to compliment the center-plane data and show a more comprehensive illustration of the comparison between experiment and numerics. Figure 89 shows the velocity at the trailing edge lip of the hole. The RANS and LES profiles are similar and not noticeably different from the experimental data.

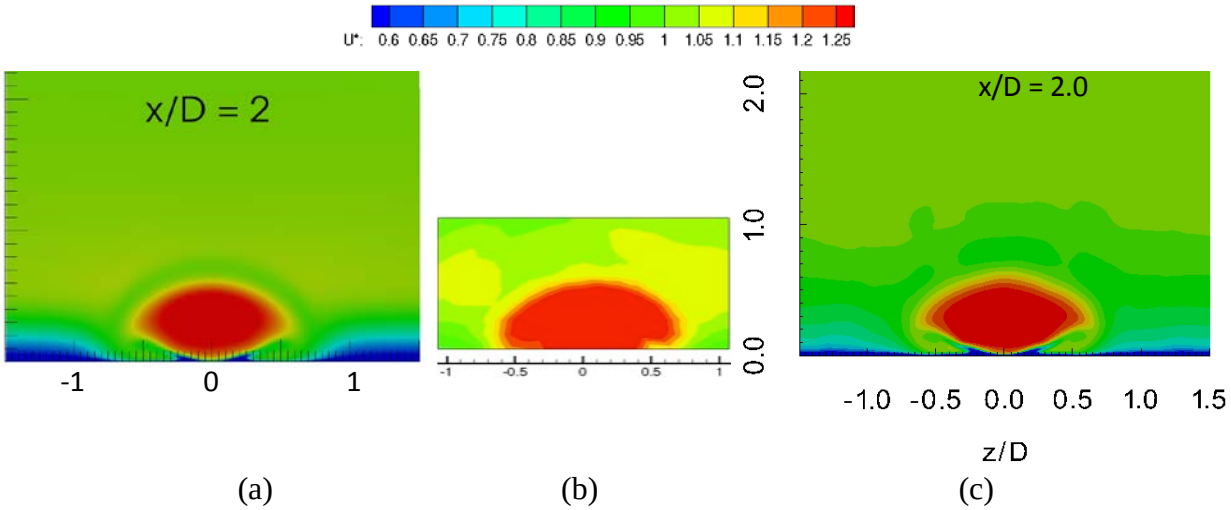

(a) (b) (c)

Figure 89 Mean normalized velocity magnitude at x/D of 2 from (a) RANS, (b) experiment, and (c) LES.

Figure 90 shows the velocity contours two diameters later (x/D = 4). All three show that the jet region of the injection is bent to form an upside-down 'U'-shape. The CVP is the cause of this shaping of the jet. The RANS, however, severely over-predicts the magnitude of the jet and wake region. This can be seen as an under-prediction of mixing. The LES likewise over-predicts the magnitude of the jet and wake regions, but to a lesser extent. It is expected that RANS should under-predict the spreading in the near-hole region because the production of TKE due to rapid shearing ($Sk/\varepsilon >> 1$). The dissipation is over-predicted, leading to an under-prediction of turbulent viscosity ($\sim k^2/\varepsilon$).

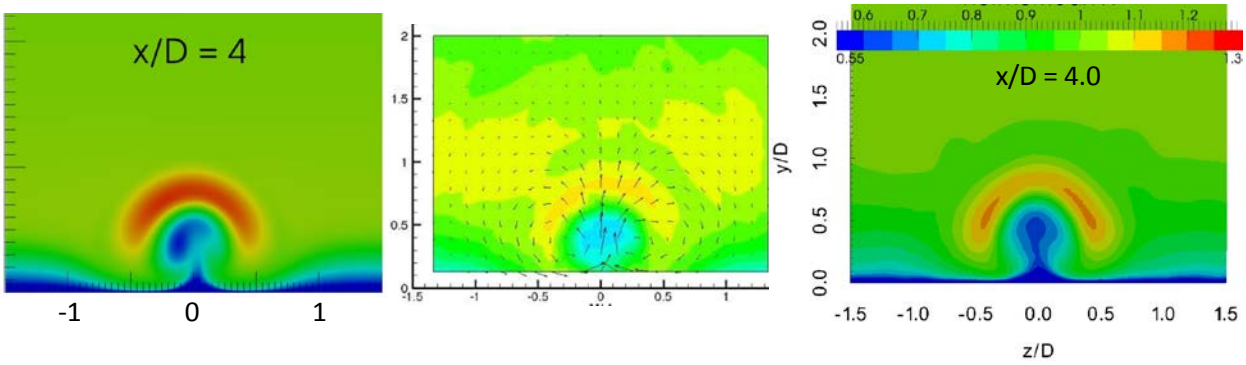

(a) (b) (c)

Figure 90 Mean normalized velocity at x/D of 4 from (a) RANS, (b) experiment, and (c) LES.

Lastly, Figure 91 shows the velocity contours at x/D = 6. The LES now under-predicts the magnitude of the jet while continuing to over-predict the wake magnitude. The LES results show good trajectory prediction, while the tendency of the RANS model to over-predict penetration is becoming evident. There appears to be some discrepancy in the measurements at x/D of 4 and 6, as the jet region appears to grow spatially without weakening. It is duly noted at this point that the velocities were experimentally measured with a cross-wire (2 probes), and the third direction assumed negligible, despite the fact that the flow is three-dimensional.

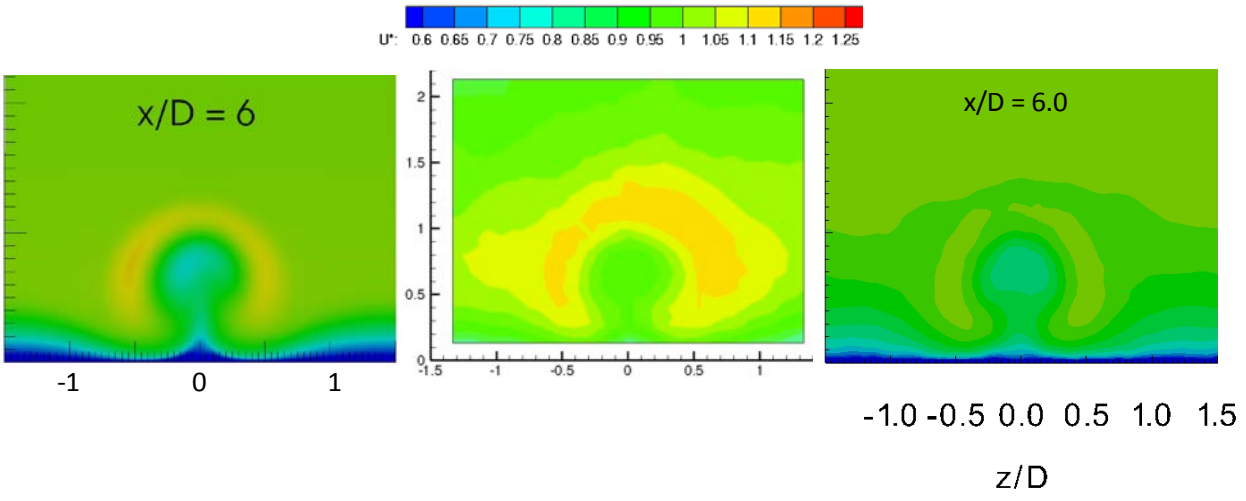

(a) (b) (c)

Figure 91 Mean normalized velocity at x/D of 6 from (a) RANS, (b) experiment, and (c) LES.

9.2.2 Mean Temperature Field

The mean effectiveness along the centerline is shown in Figure 92. The RANS appears to deliver an excellent prediction, noticeably superior to LES. This is a deceptive result. Subsequent images will show that the centerline prediction from RANS is extremely fortunate, not the product of correct physics, but rather of many incorrect predictions compounding to give a correct solution *at this particular line, namely the centerline*.

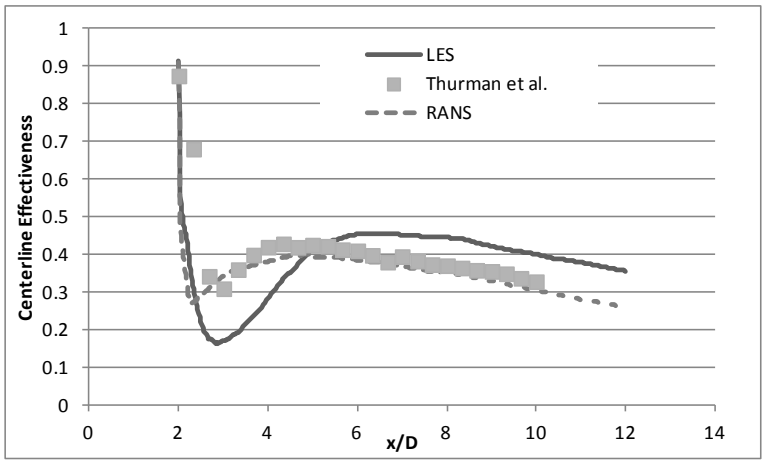

Figure 92 Centerline effectiveness validation for RANS and LES against experimental data.

The mean temperature field along the center-plane of the jet is shown in Figure 93. Confirming results from the velocity profiles, the separation region seems to be more pronounced in the LES results than in the experiment. The tendency of LES to exaggerate the separation region extent was also noticed in the previous chapter. The RANS trajectory appears noticeably higher than the experiment, and LES as well appears higher to a lesser extent. The RANS simulation over-predicts the ability of the coolant core (on the center-plane) to persevere further downstream. This is also evident in the LES results to a lesser extent.

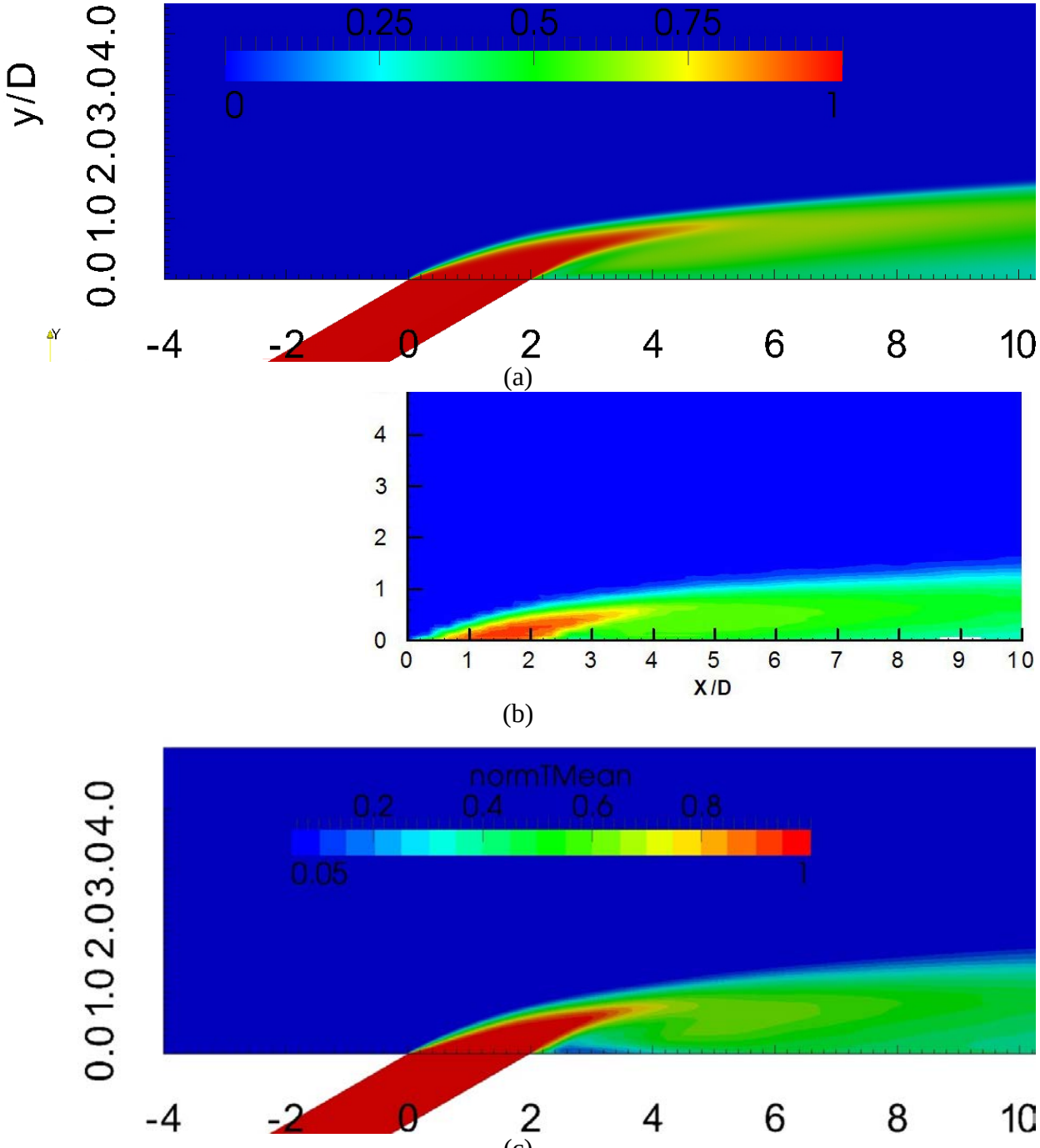

Figure 93 Mean temperature (normalized, with same color scale) along the center-plane (axes normalized by diameter) (a) RANS results, (b) experiment (Thurman et al. 2011), and (c) LES.

Viewing the jet just from the center-plane data can be deceitful regarding the development of the jet as it progresses downstream, especially in view of the strong streamwise-normal effects of

the CVP. In the next few figures, the development of the jet will be illustrated using a sequence of stream-wise normal planes.

Figure 94 shows the jet two diameters downstream of the leading edge of the hole, compared with experimental data. This is the streamwise location of the holes trailing edge, showing the thermal contours of the jet just as it exits the hole. At this point, the upper half of the jet has already experienced strong mixing with the crossflow, but the lower half of the jet has just exited the hole and has yet to mix with the crossflow. A large core of the coolant jet remains near the coolant temperature. The prediction of the RANS and LES models are similar and only differ from experiment mainly in the lower region of the jet near the wall.

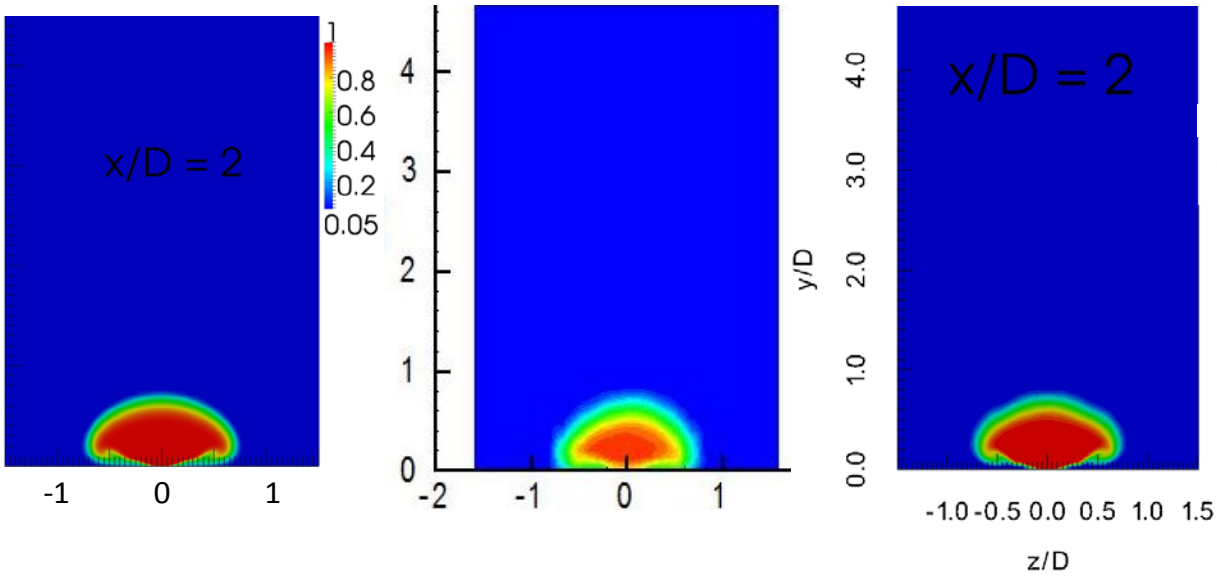

(a) (b) (c)

Figure 94 Mean normalized temperature contours at x/D = 2 from (a) RANS, (b) experiment, and (c) LES.

Just one diameter later, at x/D = 3, the temperature contours reveal significant thermal mixing. Figure 95 shows that the core of the jet has been rapidly heated and spread. The upward momentum of the jet continues to carry much of the coolant away from the surface.

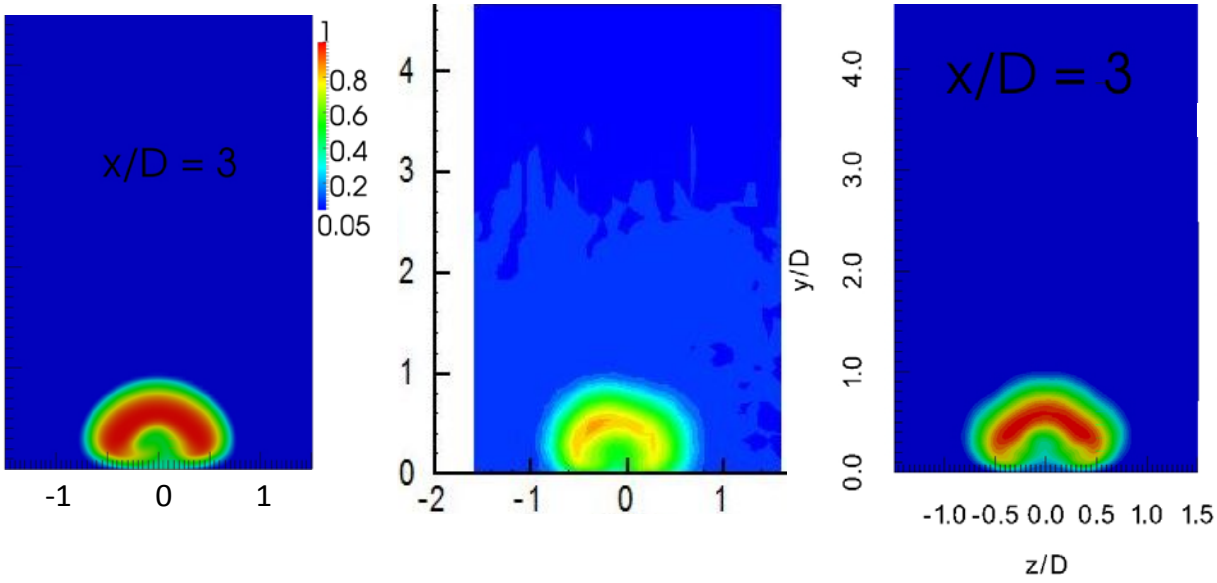

Figure 95 Mean normalized temperature contours at x/D = 3 from (a) RANS, (b) experiment, and (c) LES.

Figure 96 shows the temperature contours at x/D of 4. The coolant core continues to be rapidly mixed with the hot crossflow and its core it further weakened. The numerical tendency, as shown also in the velocity results, is to under-predict the mixing (momentum and energy). The LES is closer to the experimental profiles.

Advancing to x/D of 6, the coolant core has lost its upside-down "U" shape as the thermal mixing has overtaken the effects of the CVP, Figure 97. This stands in contrast to the behavior of the velocity contours, which maintains its upside-down "U" shape further downstream. The RANS does not show that the U-shape has collapsed, however. There is now stark contrast between the prediction of the LES and that of the RANS. The LES still struggles near the wall, where the spreading of the jet is still lack-luster. The RANS, however, is in much worse shape, over-predicting the trajectory and showing that the jet only touches the wall very near the centerline. This shows not only the luck of the centerline effectiveness prediction, but also the uselessness of its matching the experimental results.

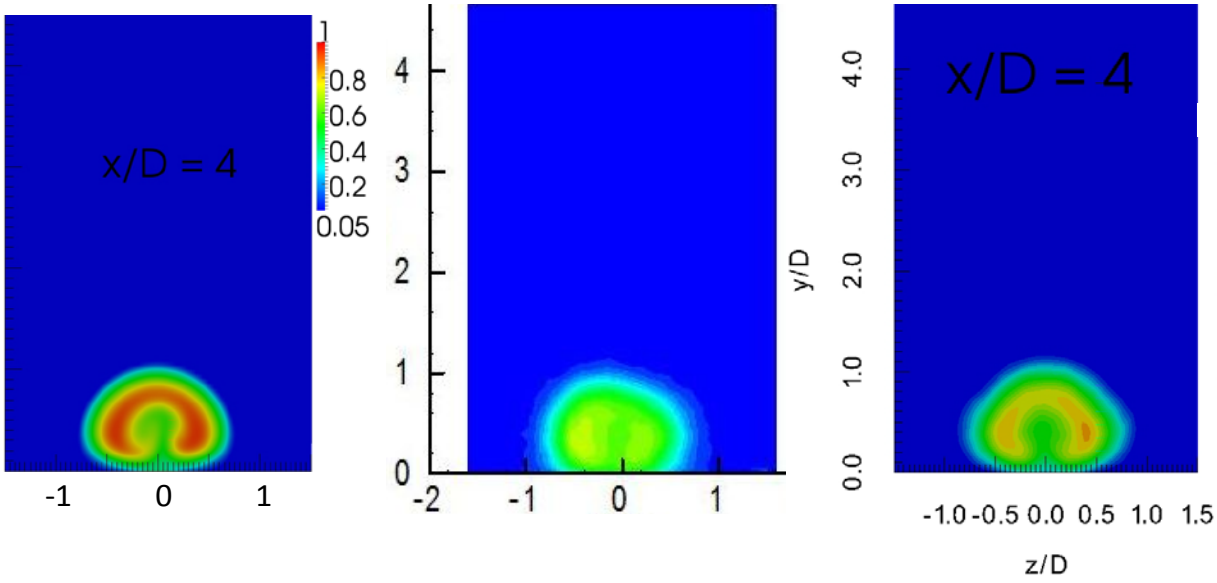

Figure 96 Mean normalized temperature contours at x/D = 4 from (a) RANS, (b) experiment, and (c) LES.

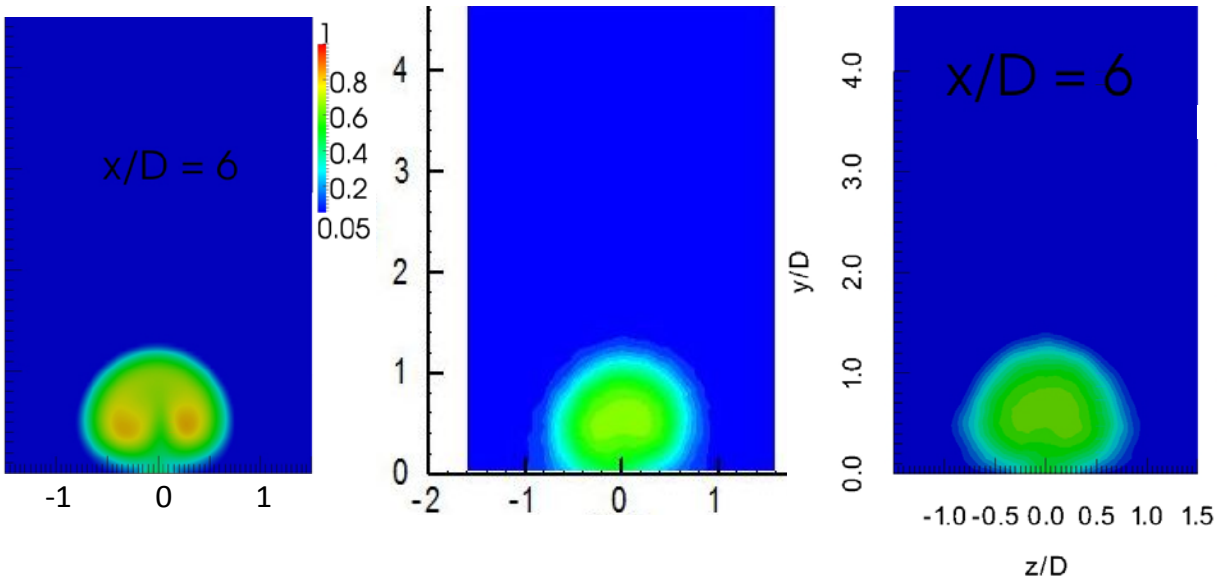

Figure 97 Mean normalized temperature contours at x/D = 6 from (a) RANS, (b) experiment, and (c) LES.

Finally, the temperature contours at x/D = 8 are shown in Figure 98. At this point, visualization of instantaneous contours revealed that the coolant jet begins slight interaction with its neighboring jets and the periodic boundary conditions become questionable. Nevertheless, the LES shows remarkable agreement with the experimental data except near the wall. Once

again, the jet seems unnaturally pinched near the wall by the numerical model. The RANS model prediction not only maintains the 'U' shape, but also shows the jet almost completely lifted from the surface. The correct prediction of centerline effectiveness from the RANS prediction is even more ironic in this light.

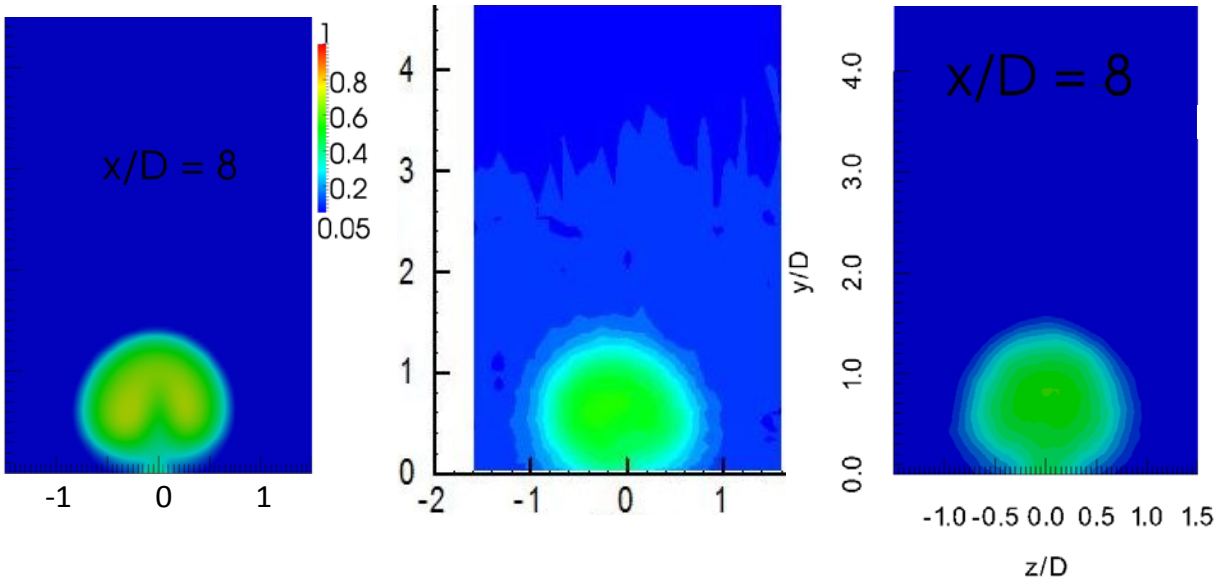

Figure 98 Mean normalized temperature contours at x/D = 8 from (a) RANS, (b) experiment, and (c) LES.

In one sense, the LES has given a much more accurate prediction of the thermal field of the coolant injection development progressing downstream. However, the remaining deficiencies of LES in the near-wall region prevent its accurate picture of the physics in this region. This is the crucial region for adiabatic effectiveness, so the successes of LES shown above are severely dampened by its near-wall struggles. One improvement that could yield a better prediction (more thermal diffusion near the wall) is to apply a dynamic procedure for Pr_t such as one suggested by Moin et al. (1991). This could free the thermal diffusivity from being severely dampened by the lack of spanwise velocity gradient in this region.

9.2.3 Reynolds Stress Tensor Field

To further investigate the forces behind the mean profiles shown above, the simulation data is compared with experiment in terms of Reynolds stress predictions. These stresses, along with the CVP are the main causes of momentum and thermal transport in the film cooling interaction. For LES, the resolved and subgrid stresses are added together to form the Reynolds stress tensor field. To match the presentation of the experimental data (El-Gabry et al. 2011), the diagonal elements are shown in terms of RMS values normalized by U_∞ and the off-diagonals are simple normalized by U_∞^2.

The root-mean square streamwise fluctuations are shown in Figure 99. The LES data shows a long streak of very high u' coming from the trailing edge of the hole, not seen in the experimental data, though perhaps missed in the experiment due to low resolution. The trends in u' fluctuations are matched well by the LES prediction, but the LES does noticeably over-predict the fluctuations in the wake of the jet. The over-prediction is noticeable, but not dramatic. One of the factors potentially contributing to this over-prediction is the un-boundedness of the centered interpolation scheme. The scheme was used because of its meritoriously low numerical diffusion, but this is known to produce unphysical oscillations. Such oscillations in velocity and temperature were noticed in the instantaneous results.

It is worthwhile to briefly mention the spot of high u' fluctuation located x/D = 0, y/D = 1in Figure 99. This is seen in all the subsequent Reynolds stress and vorticity data. The grid skewness due to an intersection of five blocks near this point is the culprit. The grid introduces unphysical velocity gradients, which are quickly dissipated and do not affect the solution as a whole.

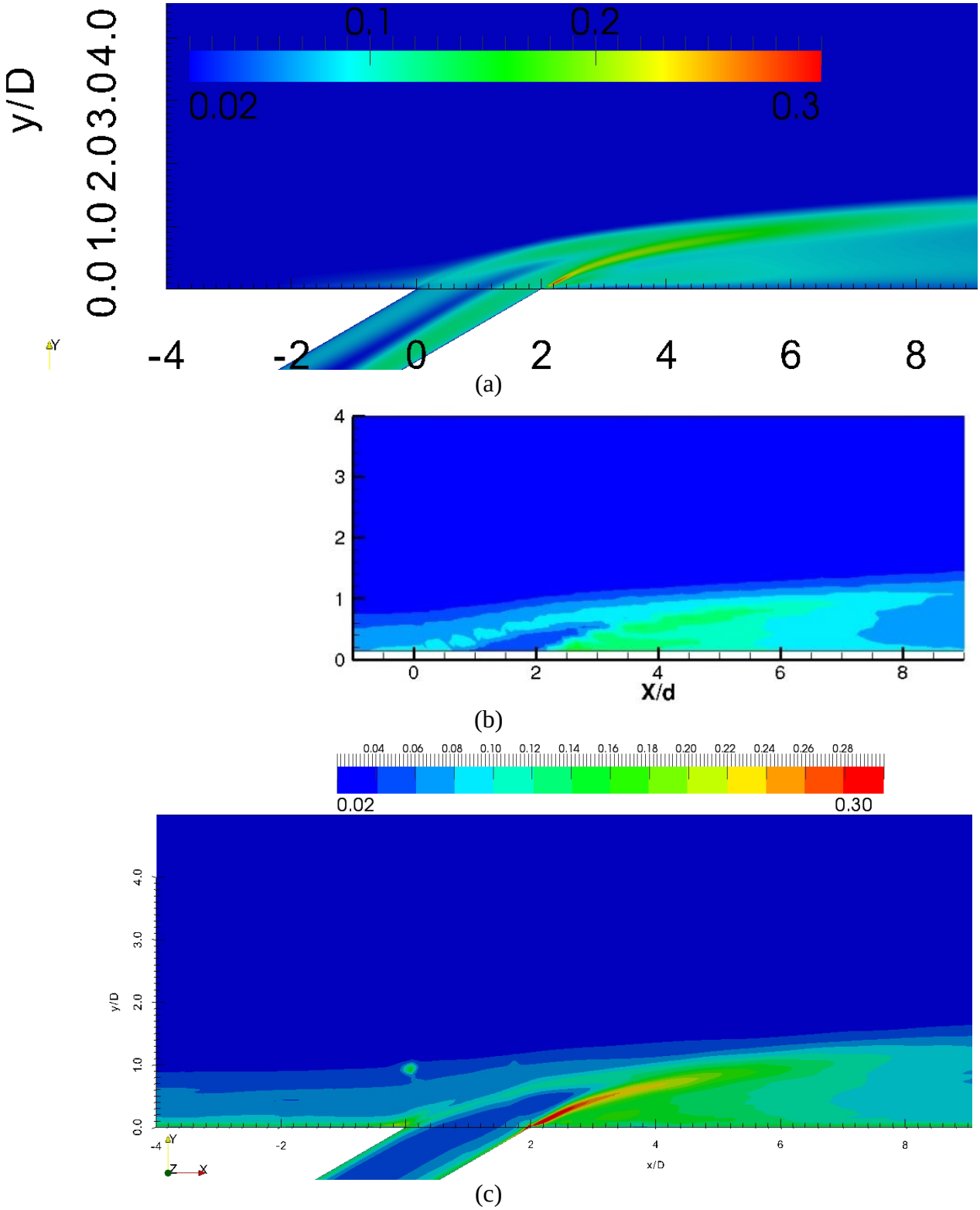

Figure 99 Streamwise RMS velocity fluctuations (u'/U_∞) along the center-plane from (a) RANS, (b) experiment and (b) LES/

The root mean square of wall normal velocity fluctuations is shown in Figure 100. Both RANS and LES show higher wall-normal fluctuation levels throughout most of the jet, despite under-predicting turbulent mixing. This shows that the correlation coefficients of the numerical simulations may be under-predicted.

The experiment displays a three-layered system of wall-normal Reynolds shear stress concentrations, Figure 101. At the top of the jet, the positive turbulent stresses work to transport the excess momentum in the jet upward into the freestream. In the wake region, there (experimentally) appears to be another positive stress, seeming to transport momentum away from the wall, though there does not seem to be any such region in the numerical simulations. This indicates that it is under-predicted by the RANS model and the LES relies too heavily on the simplistic Smagorinsky model near the wall.

It is no surprise, in light of the previous two figures, that Figure 101 shows an LES over-prediction of the shear stress term $\langle u'v' \rangle / U_\infty^2$ in the other two regions (jet-wake boundary and jet-freestream boundary). It seems that perhaps the correlation of fluctuations in not necessarily the culprit, but rather the measurement of $\langle u'v' \rangle$. While it is generally unwise to blame measurement for non-matching simulation data, the previous mean quantity analysis shown under-spreading, especially in the case of the RANS results. This figure, however, seems to suggest that the Reynolds stresses responsible for this spreading are under-predicted. There appears, at this point, tension between these two sections, which awaits further evidence for resolution.

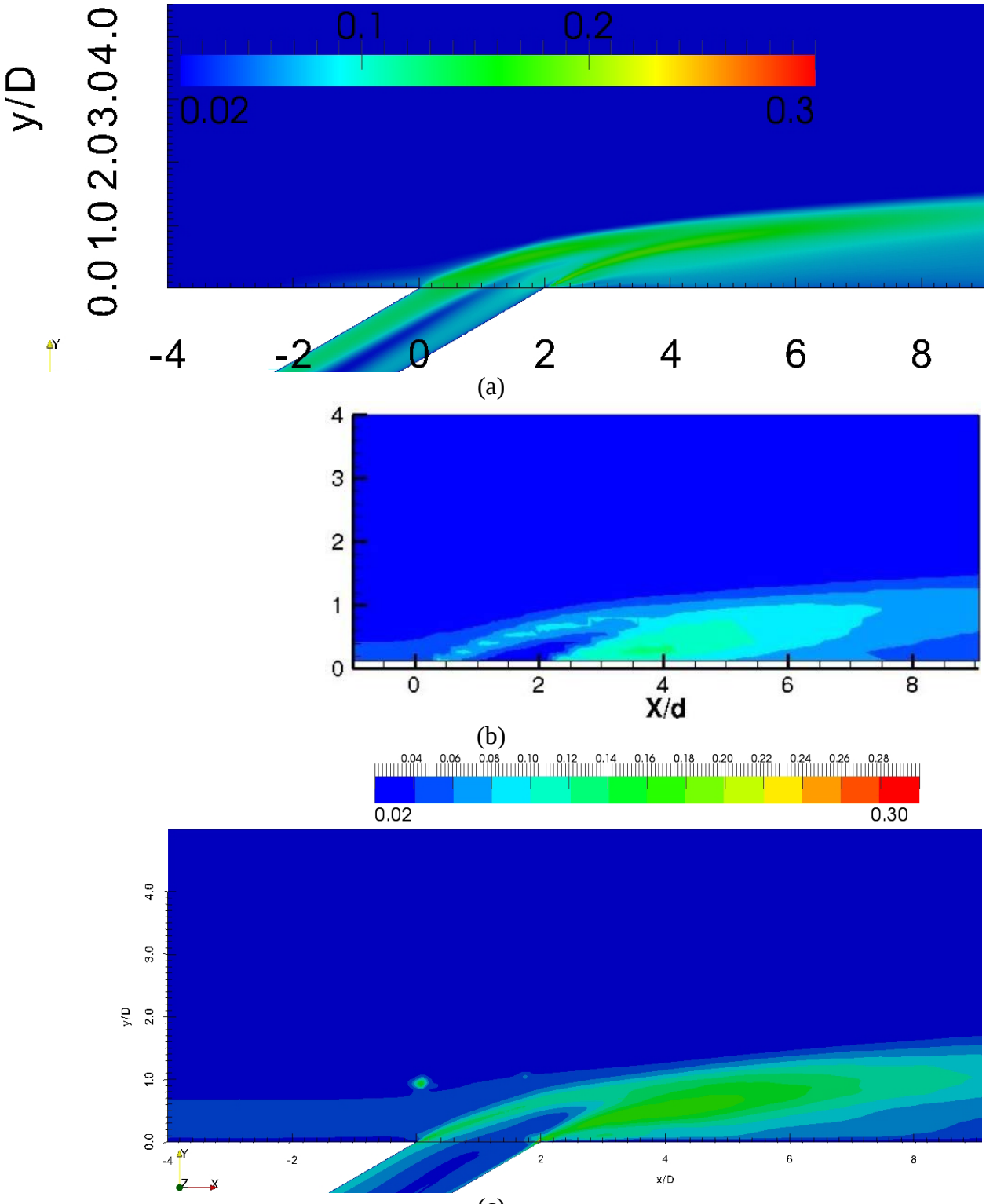

Figure 100 Wall-normal RMS velocity fluctuations (v'/U_∞) along the center-plane from (a) RANS, (b) experiment and (c) LES.

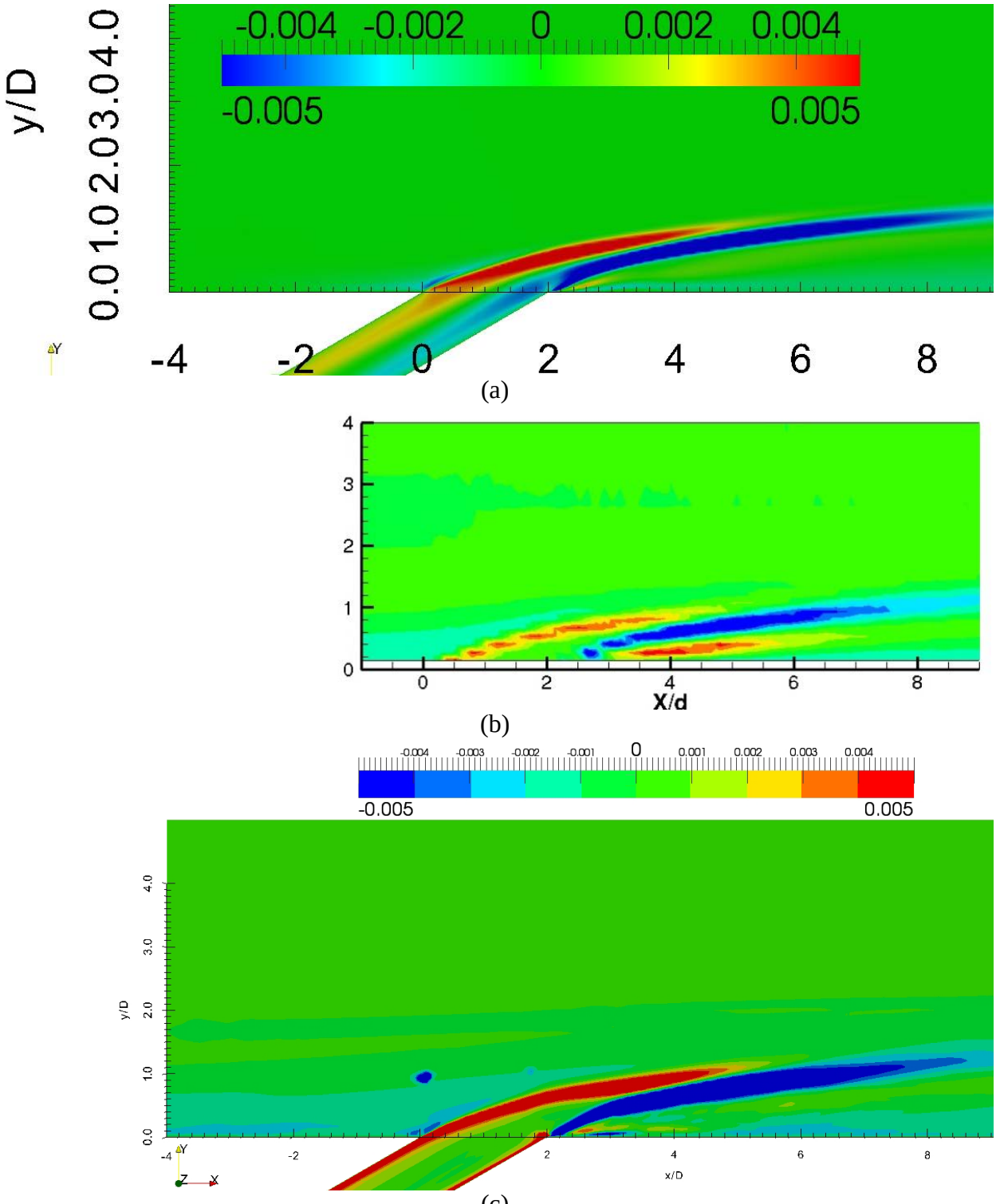

Figure 101 Reynolds shear stress $\langle u'v' \rangle / U_\infty^2$ on the center-plane for (a) RANS, (b) experiment, and (c) LES.

Again, the above analysis has just told part of the story. It is worthwhile to look beyond just center-plane analysis, to streamwise-normal planes to gain better perspective to comparing results. Figure 102 shows the streamwise velocity fluctuation levels at x/D = 4. This shows that the over-prediction of u' is ubiquitous over the entire coolant injection flow.

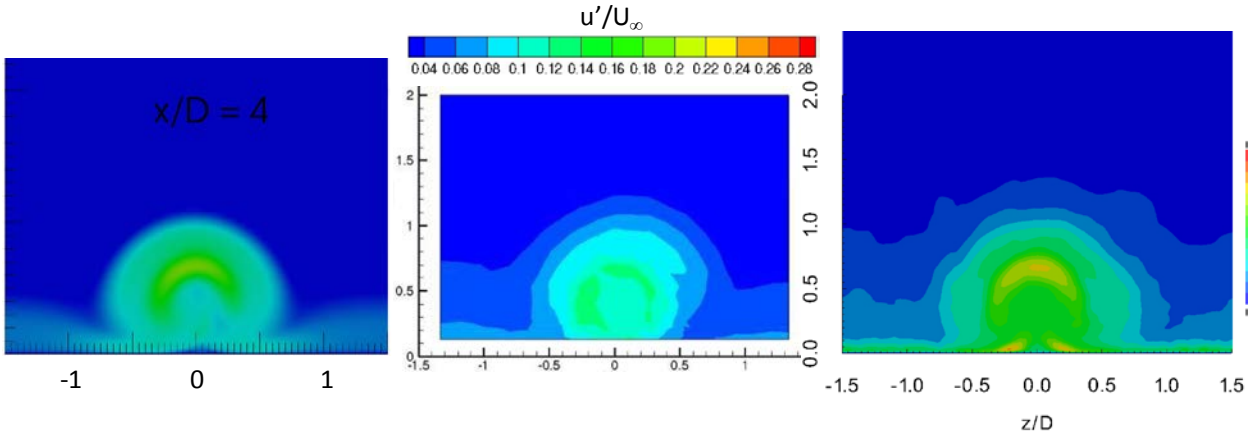

(a) (b) (c)

Figure 102 Normalized streamwise RMS-fluctuation levels at x/D = 4 from (a) RANS, (b) experiment, and (c) LES.

Furthermore, the wall-normal fluctuations are also over-predicted, Figure 103.

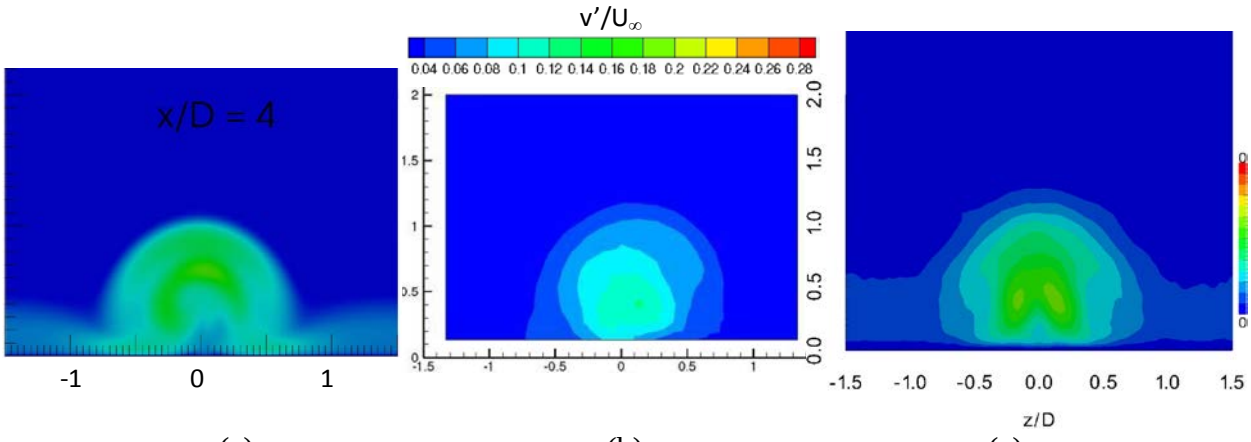

(a) (b) (c)

Figure 103 Normalized wall-normal RMS-fluctuation levels at x/D = 4 from (a) RANS, (b) experiment, and (c) LES.

Lastly, Figure 104 shows that the spanwise fluctuations are also over-predicted.

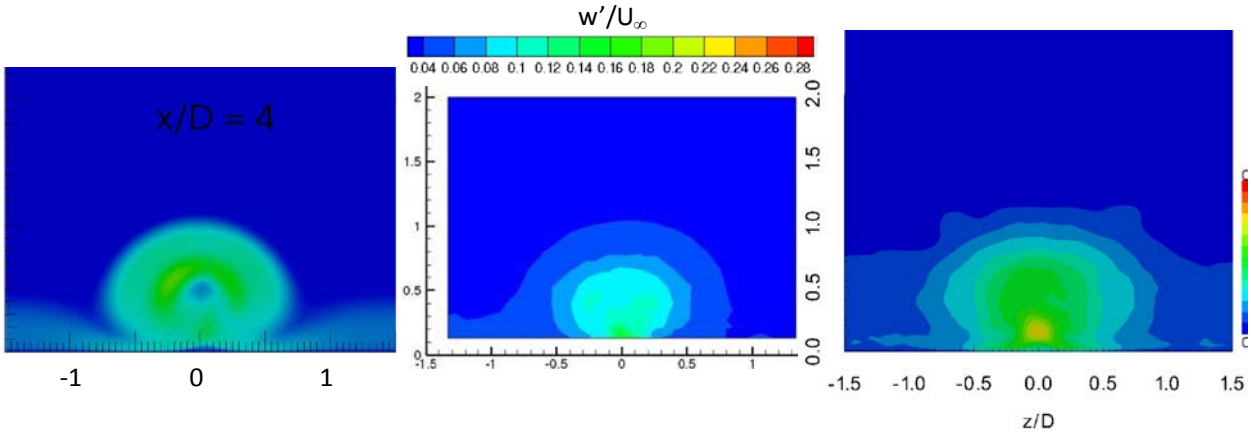

(a) (b) (c)

Figure 104 Normalized spanwise RMS-fluctuation levels at x/D = 4 from (a) RANS, (b) experiment, and (c) LES.

So the question remains whether the correlation coefficients, measurement error, or some other effect is the culprit for the seeming tension. The trace of the Reynolds stress tensor is clearly over-predicted by the simulations. Figure 105 yields interesting evidence. First, the experiment does not capture any negative stress, which is clearly evident and dominant over positive stresses in Figure 101. This casts doubt on the quality of the measurements. Meanwhile, RANS no longer seems to over-predict the positive stresses. Secondly, returning to the mean velocity profiles, the lack of spreading, especially in the LES case, was limited to very near the hole. Instead, LES seems to catch up with the experiment downstream, suggesting higher mixing rates.

A final piece of evidence, though not particularly useful, is the spanwise Reynolds stresses shown in Figure 106. The experiment lacks any negative fluxes. Somehow, a great deal of error has crept into the results, either from the measurements themselves, or from the processing of the data. In the end, the comparison of Reynolds stress components is not enlightening, due to apparent contradictions in the experimental data.

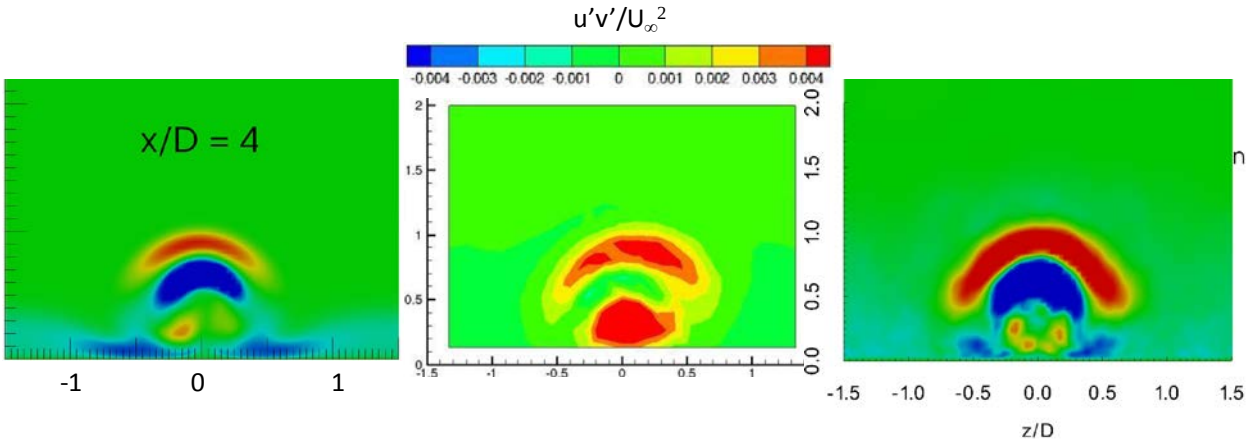

(a) (b) (c)

Figure 105 Normalized Reynolds stress <u'v'> at x/D = 4 from (a) RANS, (b) experiment, and (c) LES.

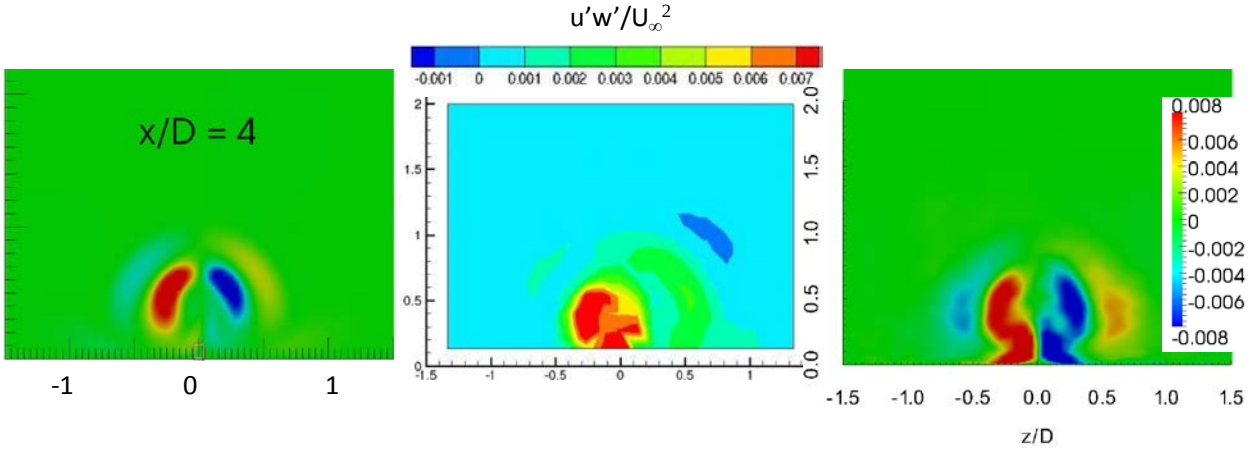

(a) (b) (c)

Figure 106 Normalized Reynolds stress <u'w'> at x/D = 4 from (a) RANS, (b) experiment, and (c) LES.

9.3 High Blowing Ratio M = 1.9 Validation

Before further analyzing the M = 1.0 case, the validation for the high blowing ratio case is shown. For the high blowing ratio, a much fuller set of experimental contours are available for validation. For this reason, it was the hope of the author to have better insight into the predictions from RANS and LES.

9.3.1 Mean Velocity Field

The inflow boundary layer mean and Reynolds stress data is shown in Figure 107 against LES and DNS data. Note that the boundary layer for this case is thinner than the M=1 case (closer to experimental boundary layer). As a consequence, the friction velocity is higher and the freestream u+ is lower. Otherwise, the profiles match well.

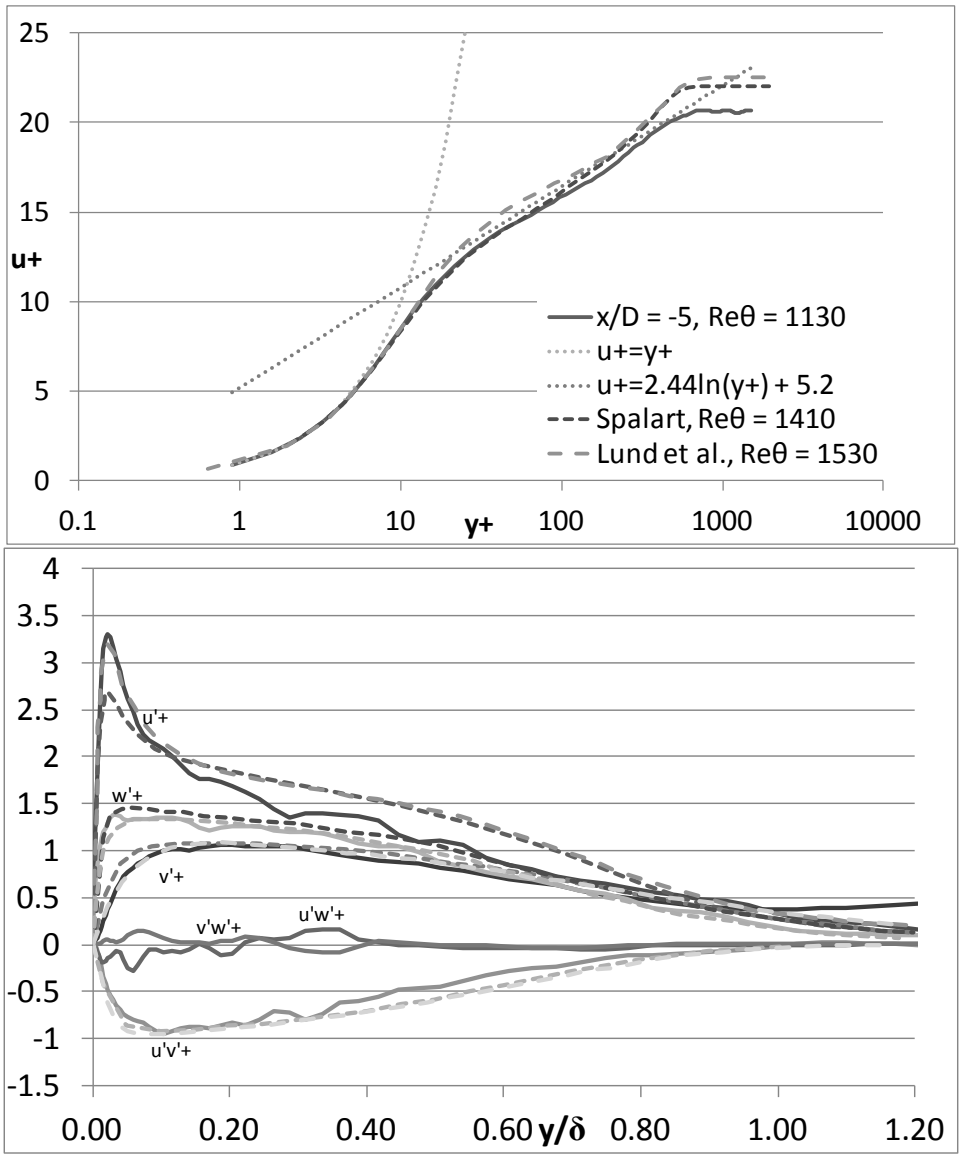

Figure 107 Validation profiles of inflow boundary layer against previous LES and DNS data; (a) mean velocity profile, (b) Reynolds stress profiles.

The mean velocity magnitude profiles along the center-plane are shown in Figure 108 for the high blowing ratio case. The trajectory is noticeably higher, as expected. A multi-layered regime is visible, with a high momentum jet region on top, a subsequent wake region below, and further downstream, another higher momentum region entering in the middle of the wake region. This second jet region is presumably (later confirmed) due to the actions of the CVP to wrap the upper region jet around and underneath the wake. As with the earlier simulation, the wake region extent is over-predicted in the simulations. The LES shows no inherent advantage from the center-plane data.

The development of the velocity magnitude over four streamwise-normal planes is investigated in Figure 109. The over-prediction of the spatial extent of the wake region is evident at all x/D locations. The LES appears the approach the experimental profiles better towards the end of the domain. It is key to notice, however, that the non-dimensional velocity in the experimental jet ranges up over 2.5 in the streamwise x/D = 2 cut, but does not range that high in the center-plane cut. This is a mild, yet interesting disagreement in the experimental data. The effect of the CVP in wrapping the jet around the wake region from an upside-down 'U'-shape to an 'O' shape is more dramatic in the RANS results than the LES and experiment. This is likely due, in conjunction with the RANS simulations' well-preserved jet region, to lower mixing rates (turbulent stresses). In the LES and experiment, the turbulent stresses mix out and over-power the effects of the CVP more effectively than in the RANS solution. From the velocity results, both RANS and LES appear to predict the trajectory of the coolant jet and wake regions well, though further judgment is reserved for the temperature profiles.

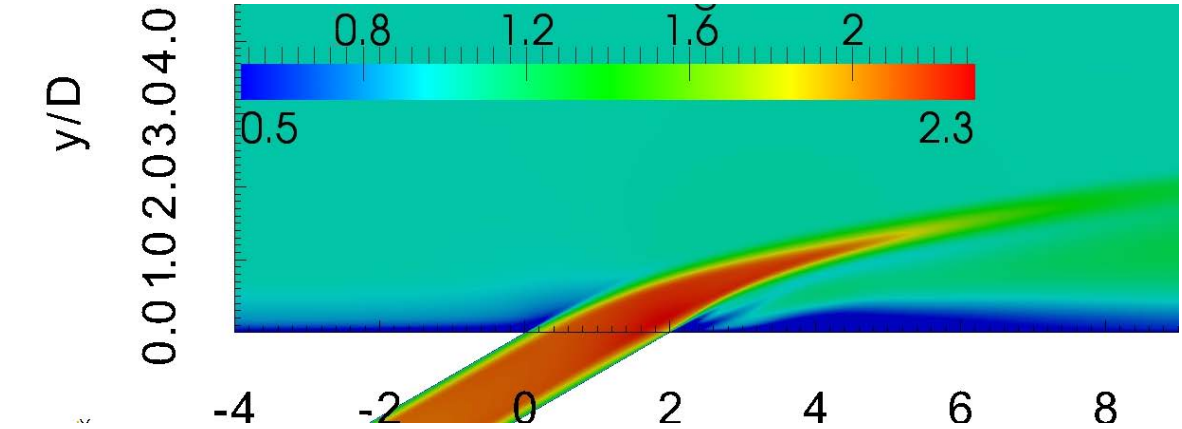

(a)

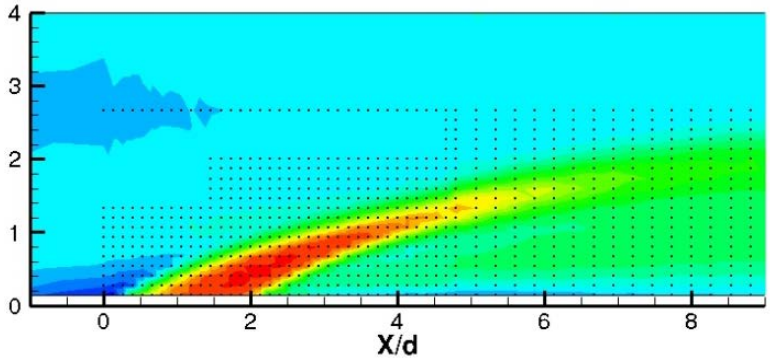

(b)

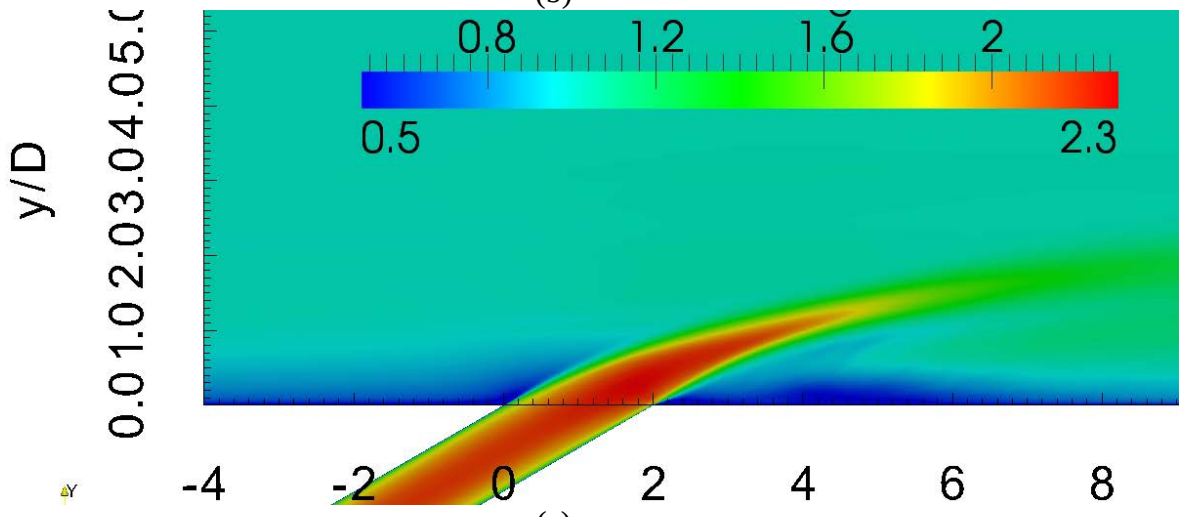

(c)

Figure 108 Mean velocity contours U/U_∞ at center-plane from (a) RANS, (b) experiment, and (c) LES.

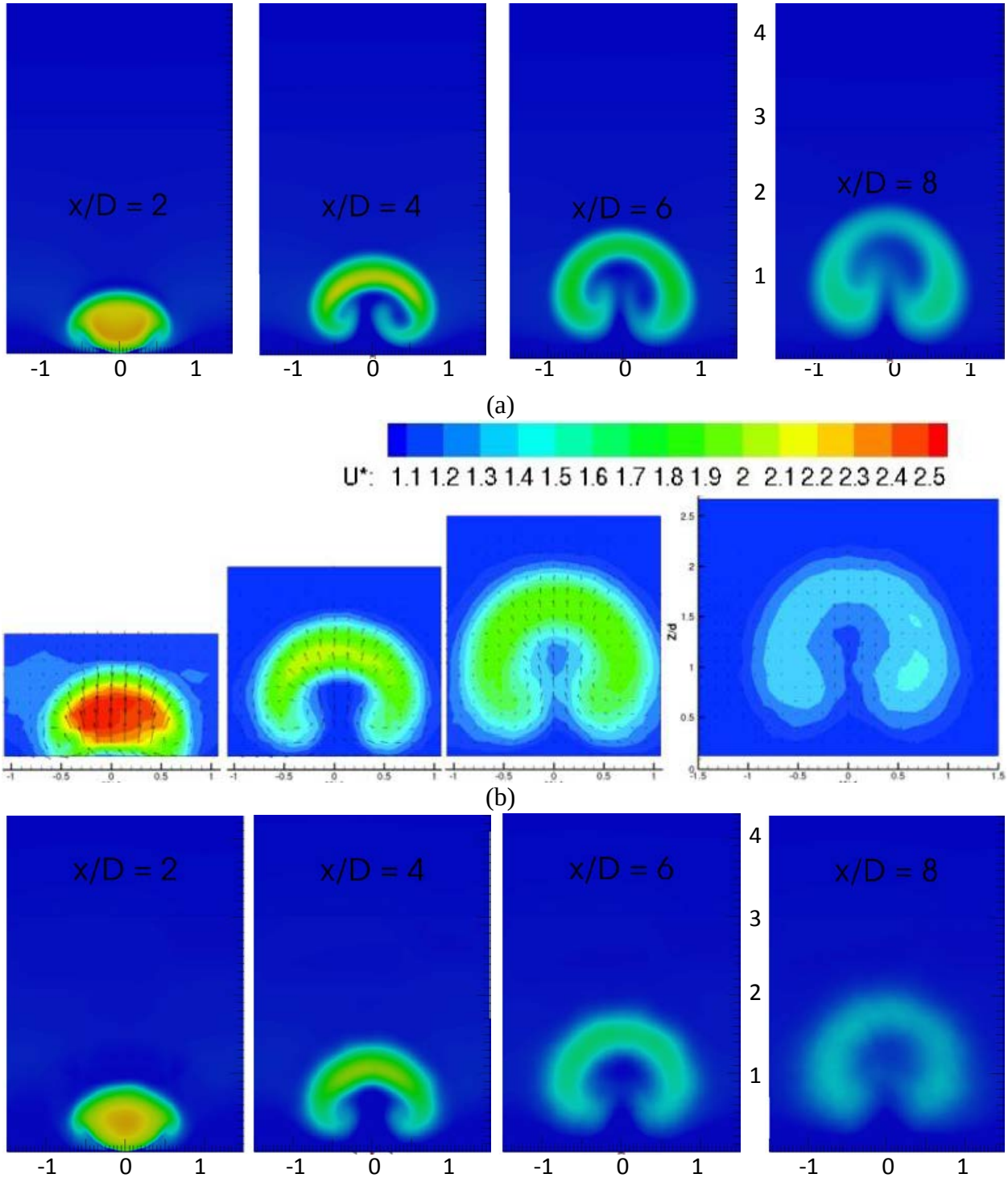

Figure 109 Streamwise development of U/ U_∞ at stream-wise normal planes (x/D = 2,4,6,8 from the leading edge of the hole) for (a) RANS, (b) experiment, and (c) LES.

9.3.2 Mean Temperature Field

Of more engineering interest is the temperature field. As with the moderate blowing rate, the effectiveness predictions of RANS and LES are validated with the experiment along the centerline, Figure 110. This time, the RANS is not so lucky. In fact, the RANS provides almost no coverage at all, while the LES predicts the centerline results well (slight under-prediction). Over-prediction of the separation region is suggested by the low dip in the LES for $3 < x/D < 6$.

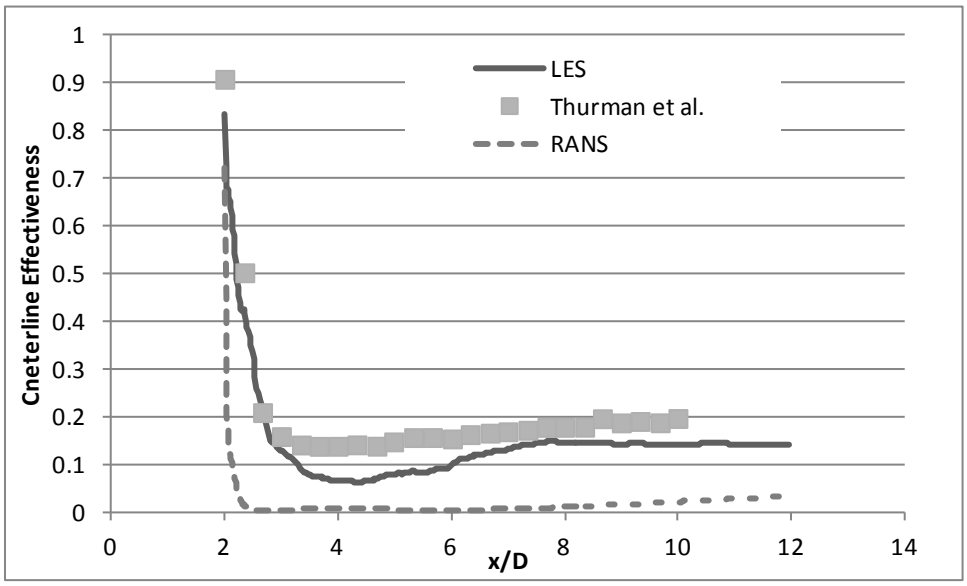

Figure 110 Centerline effectiveness for RANS and LES against experimental data (Thurman et al. 2011).

The temperature field along the center-plane is shown in Figure 111. Similar to the moderate blowing rate, the coolant core is preserved longer in the RANS case than the experiment. This is also true of the LES case, but not as dramatically. The over-prediction of the jet trajectory in the RANS data is also quite evident. There is a similar, but less dramatic over-prediction of trajectory evident in the LES data as well. Whereas the center-plane velocity results did not distinguish much between LES and RANS, the temperature contours certainly do, and quite in the favor of the LES predictions.

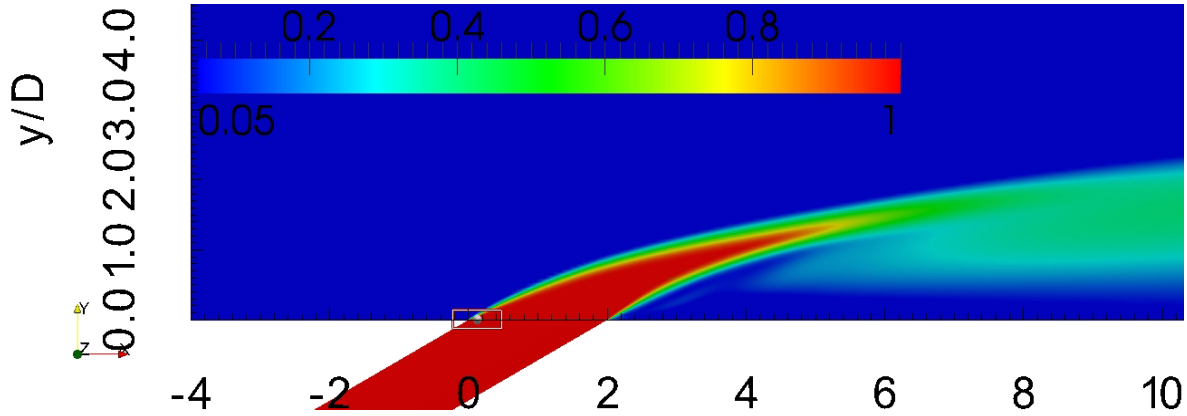

(a)

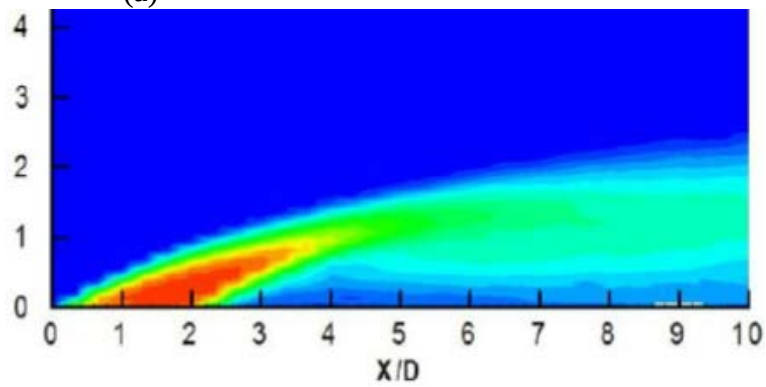

(b)

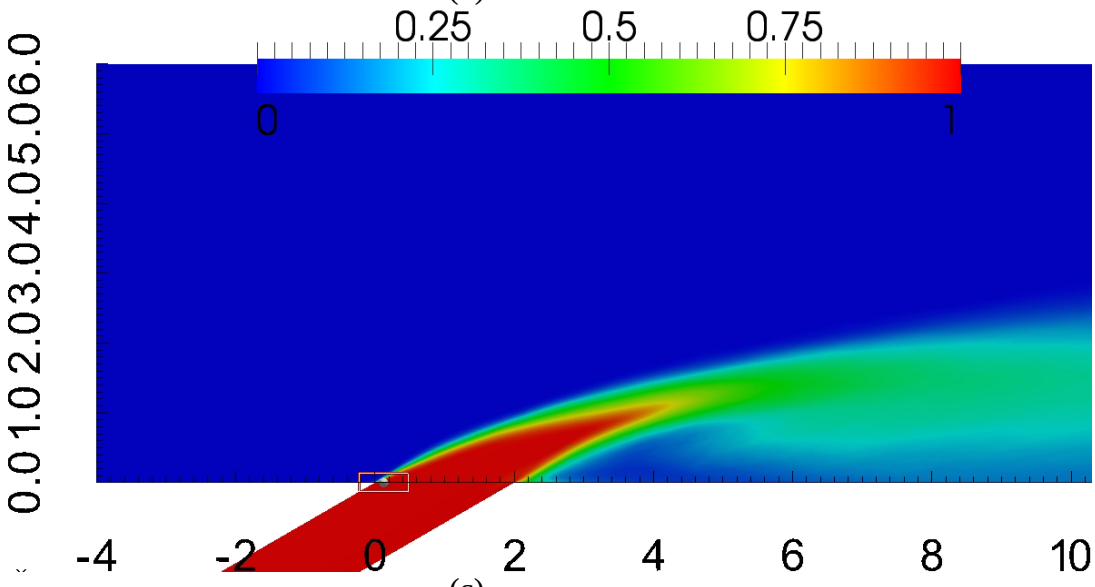

(c)

Figure 111 Mean normalized temperature contours along the center-plane from (a) RANS, (b) experiment, and (c) LES.

As with the previous discussions, the development of the jet across multiple streamwise-normal locations is shown to provide a clearer picture of the quality of predictions. Starting with Figure 112, the temperature profiles at the trailing edge of the hole show that the experimental coolant is already somewhat mixed even at this early stage. This suggests significant heat transfer into the coolant from the walls of the coolant tube, which were modeled as adiabatic in the simulations. It is of note to mention that the z-axis on the experimental results indicates that the data was scaled incorrectly by the Thurman et al. (2011).

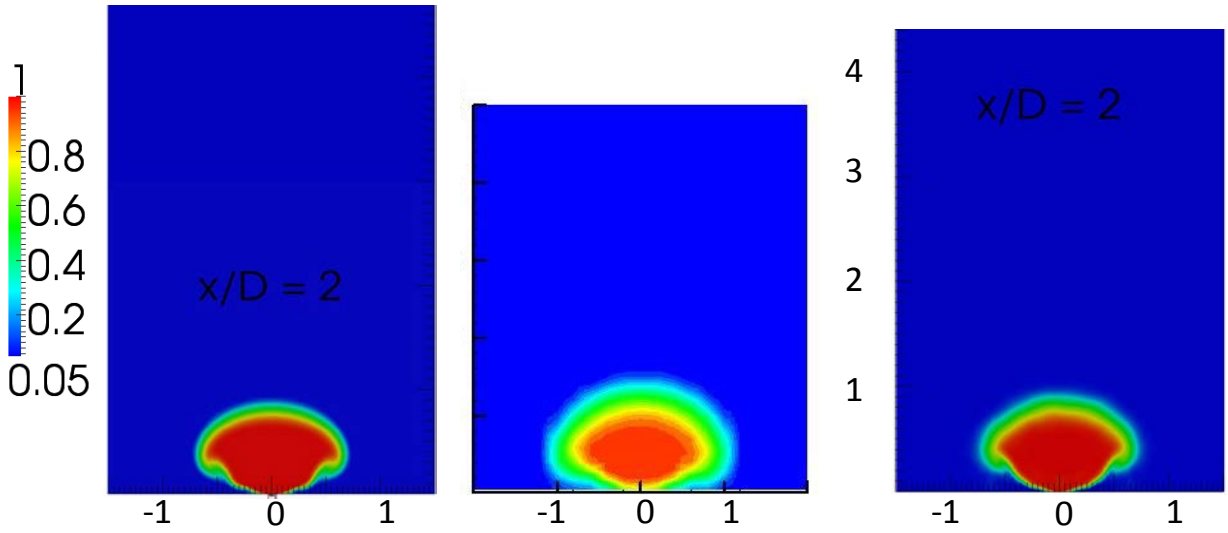

(a) (b) (c)

Figure 112 Mean normalized temperature contours at x/D = 2 from (a) RANS, (b) experiment, and (c) LES.

Moving to x/D = 3, Figure 113 reveals that, as in the moderate blowing ratio, the experimental jet is mixed more rapidly than either simulation in the near-hole region. The over-prediction of the separation region is evident in both simulations, whereas the experimental coolant remains in better proximity to the wall. The mixing on the LES coolant appears more rapid than the RANS, but clearly not well enough to match experiment.

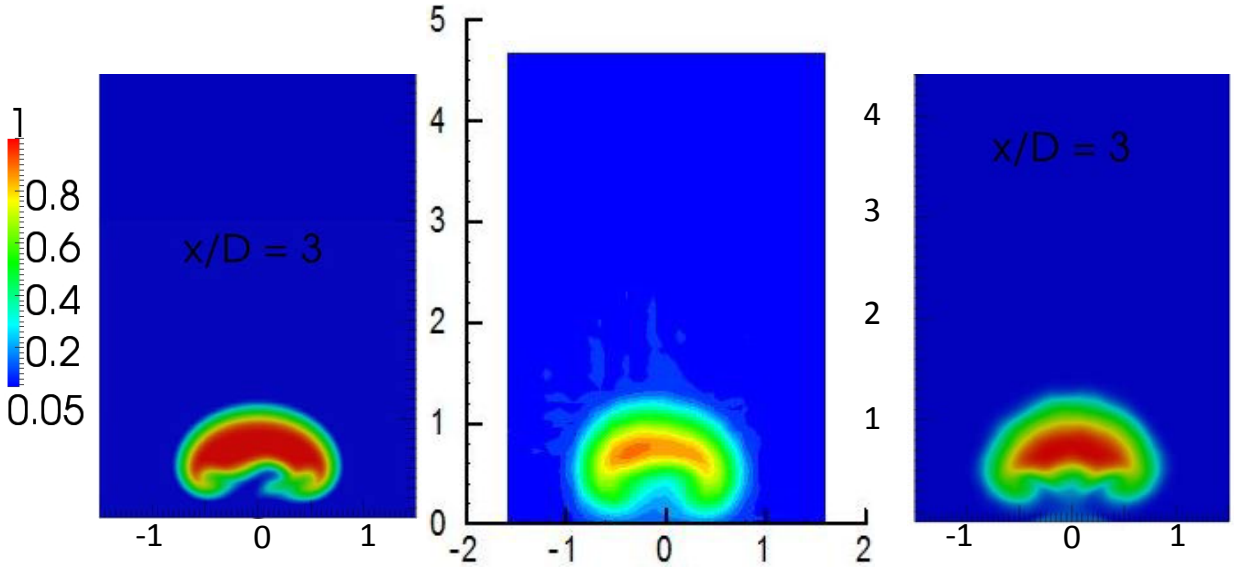

(a) (b) (c)

Figure 113 Mean normalized temperature contours at x/D = 3 from (a) RANS, (b) experiment, and (c) LES.

Progressing just one more diameter downstream, Figure 114 reveals that the LES is now in much better agreement with experiment than its RANS counterpart. The uncooled wake region is still over-predicted as well as the proximity to the wall, but the mixing of the jet appears to be catching up to the experimental mixing. The RANS coolant is completely separated off the wall.

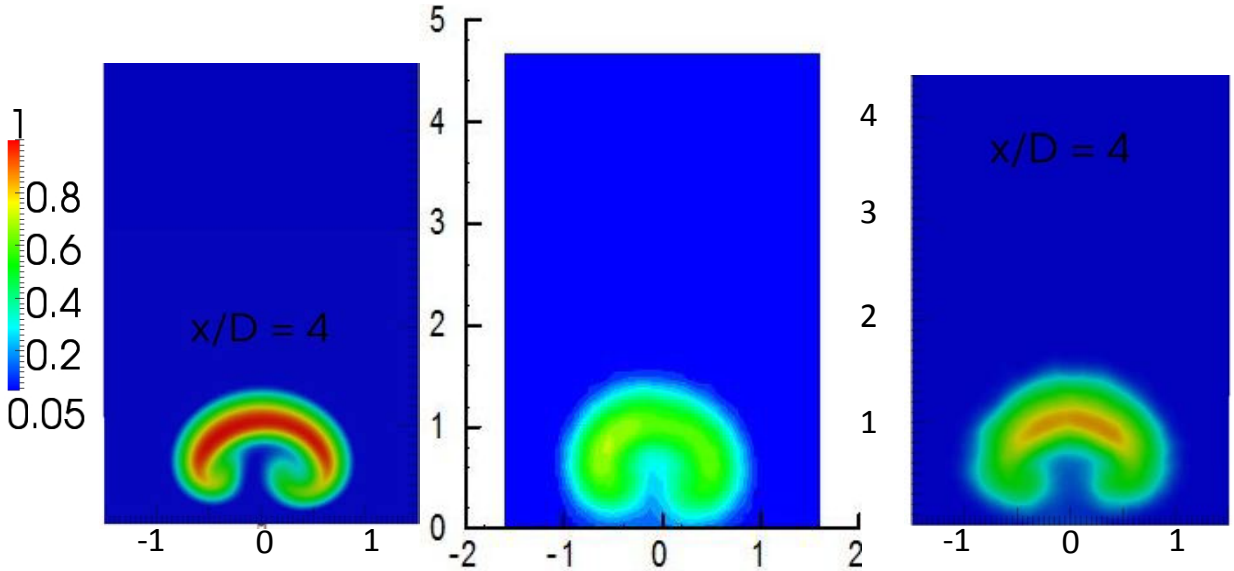

(a) (b) (c)

Figure 114 Mean normalized temperature contours at x/D = 4 from (a) RANS, (b) experiment, and (c) LES.

At x/D = 6, the LES prediction is rather impressive, Figure 115. It has improved in both mixing and proximity to the wall. Meanwhile, the RANS prediction remains unhelpful in any respect.

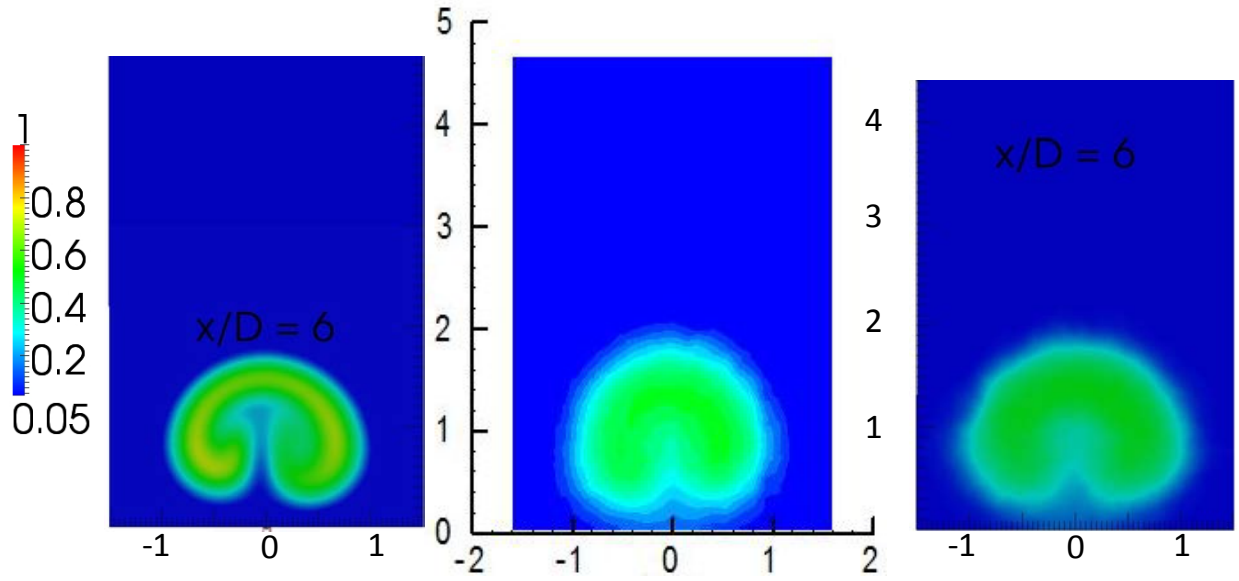

(a) (b) (c)

Figure 115 Mean normalized temperature contours at x/D = 6 from (a) RANS, (b) experiment, and (c) LES.

The final streamwise station is at x/D = 8, Figure 116. The key differentiation between the LES and RANS predictions is the lower half of the jet. While the LES has shown much better proclivity to match the experiment in spreading to the wall, the RANS has been too reluctant. The LES still fails to predict well near the wall, and this seems mostly due to a lack of vertical spreading back toward the wall than lateral spreading along the wall. Again, as with the moderate blowing ratio case, it is worth speculating that a dynamic Pr_t calculation procedure could improve this tendency in the LES. The final verdict on the current LES is mixed. While the LES shows dramatic improvement over the RANS in some features, the near wall behavior is not well-predicted, causing under-prediction of centerline effectiveness and probably worse prediction of span-averaged effectiveness.

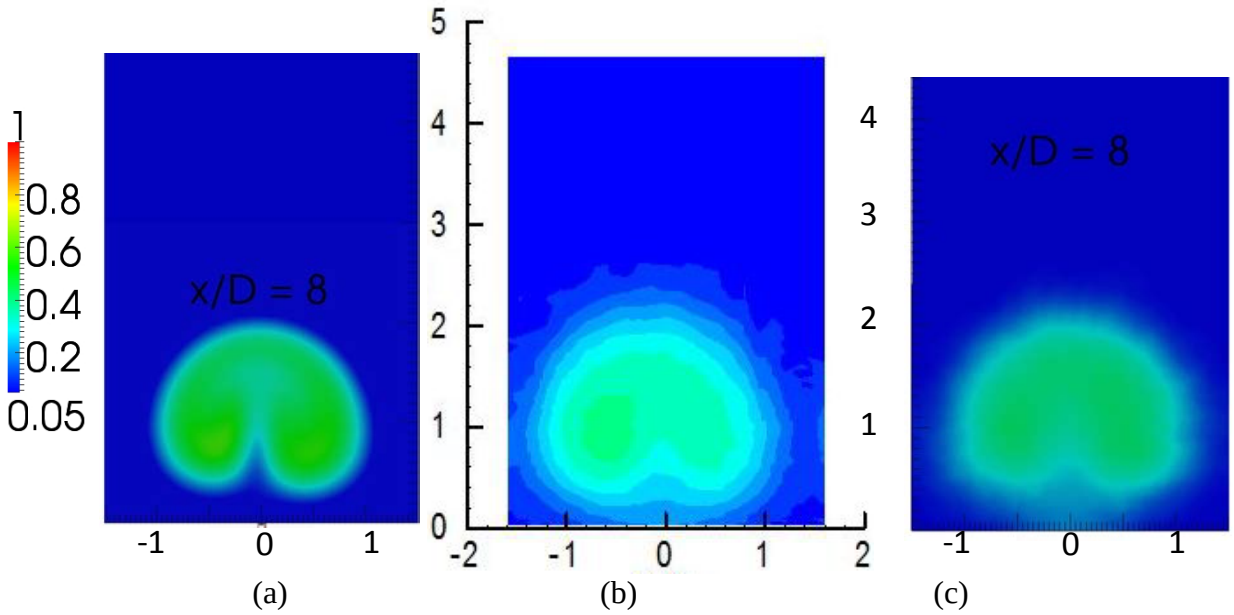

(a) (b) (c)

Figure 116 Mean normalized temperature contours at x/D = 8 from (a) RANS, (b) experiment, and (c) LES.

9.3.3 Reynolds Stress Tensor Field

As with the moderate blowing ratio (M = 1.0), the experimental data allows for further validation of the numerical simulations via the second order statistics, namely, the Reynolds stress tensor. Figure 117 shows streamwise fluctuations along the center-plane. The experiment reveals two regions of high fluctuation, one on either side (top and bottom) of the jet. This is caused by rapid shearing on both sides, as the high momentum jet lifts from the surface and encounters slow flow on either side, markedly different from the moderate blowing ratio case, where the jet velocity was much closer to the freestream velocity. The RANS simulation does not predict as high of a fluctuation layer in the upper half of the jet region. The LES matches the experiment admirable, however. This affirms the ability of the LES to better match the velocity development of the experiment.

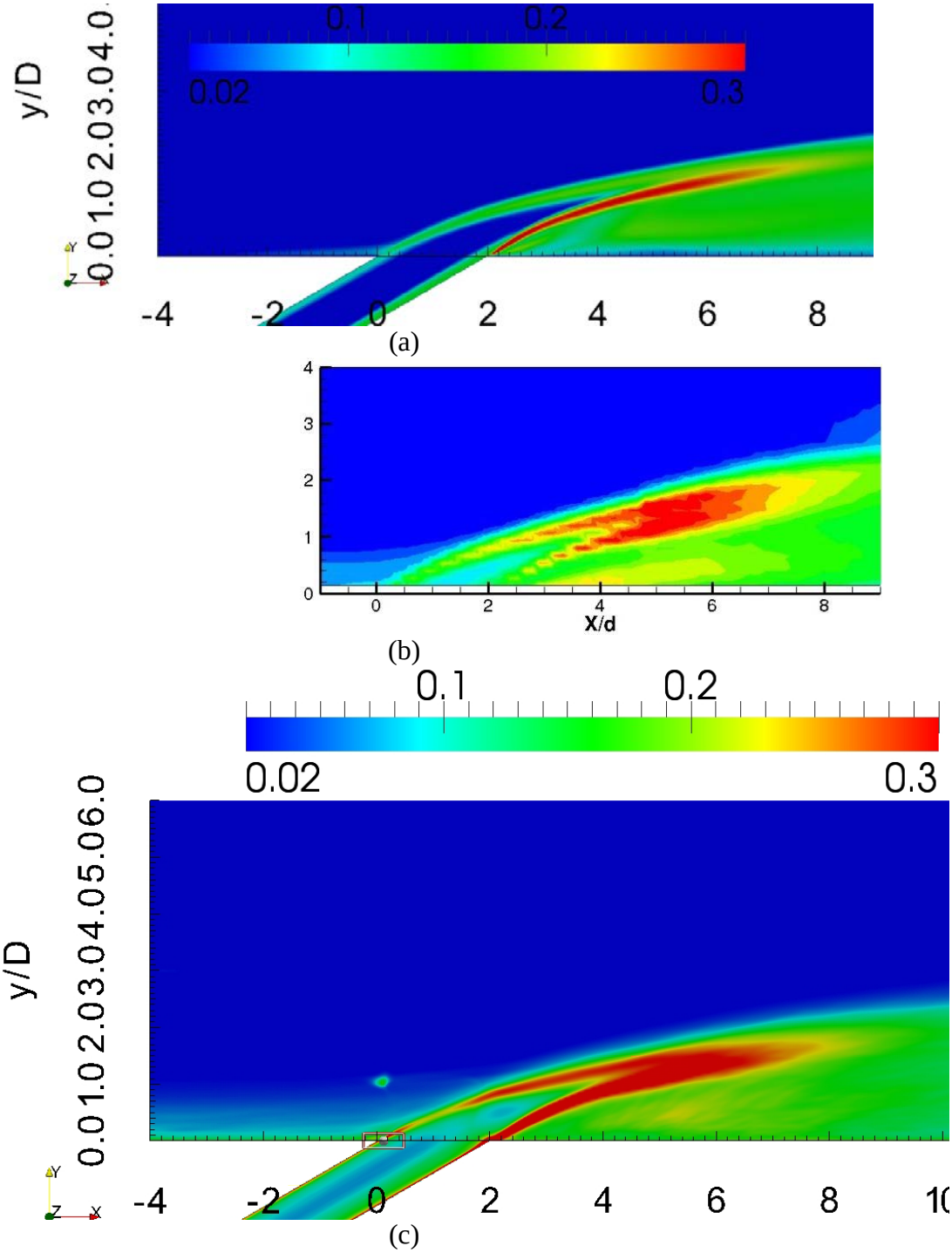

Figure 117 Normalized streamwise fluctuations (u'/U_∞) along the center-plane from (a) RANS, (b) experiment, and (c) LES.

The streamwise development of u' is further explored in Figure 118. The prediction of the LES data is quite impressive, especially in comparison with the RANS prediction.

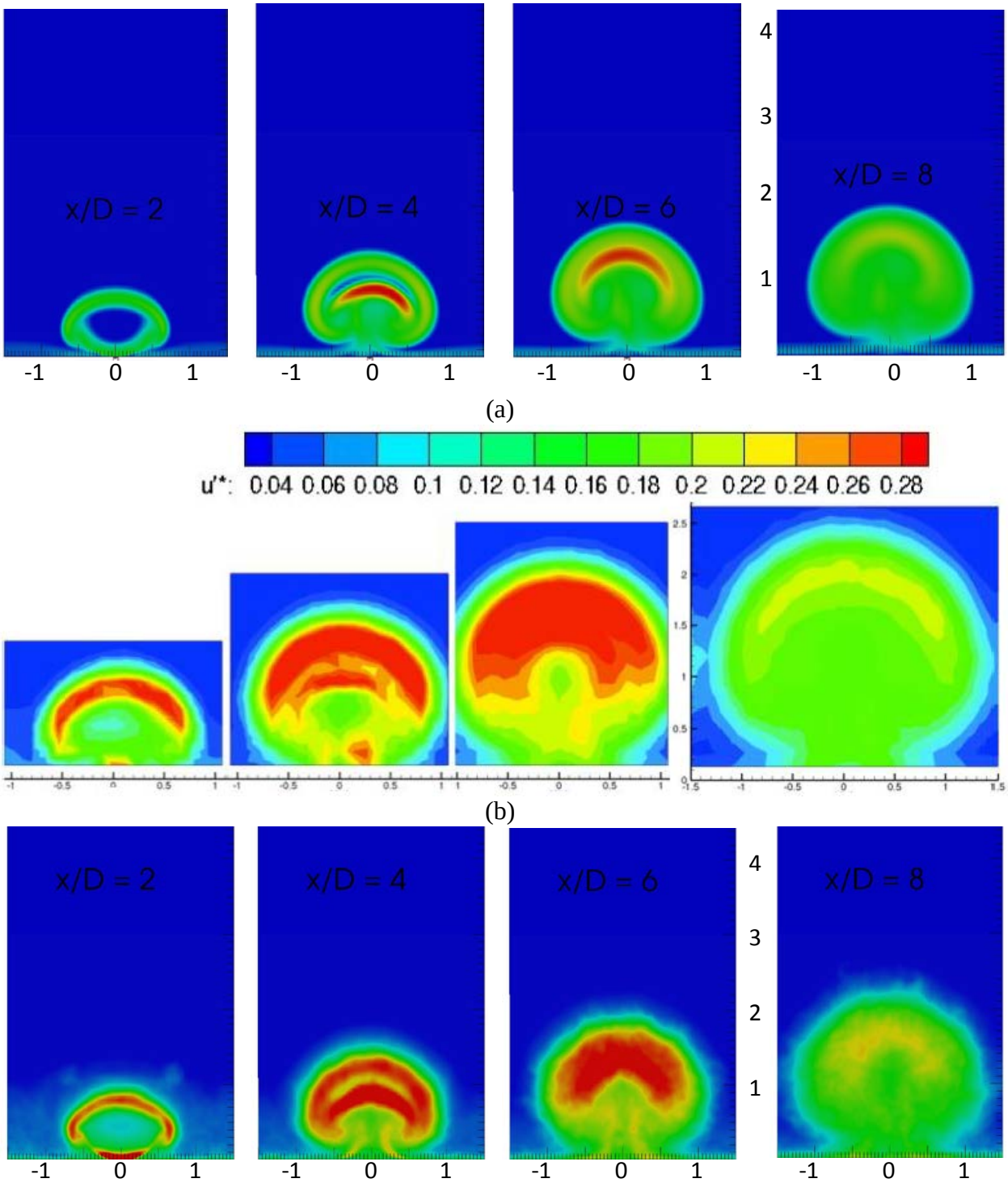

Figure 118 Streamwise development of streamwise fluctuations u'/U_∞ at x/D = 2,4,6,8 from (a) RANS, (b) experiment, and (c) LES.

The v' fluctuations in Figure 119 show an over-prediction on the part of the LES solution, but the RANS prediction does not match qualitatively the experimental results, which show a primary spot of higher fluctuation at about x/D = 5. The two layers of high fluctuation shown in the RANS results do not merge as they do in the LES prediction to form a larger region of high fluctuation.

Further investigation using the streamwise-normal planes, Figure 120, reveals that the LES prediction may not be as much of an over-prediction after all. There is some conflict between the center-plane results of Figure 119 and the streamwise planes of Figure 120, the latter showing better agreement with the LES data. The ability of the LES to predict patterns in v' development is far superior to the RANS. This is expected because the RANS model is relying on turbulent viscosity isotropy for its Reynolds stress determination.

The final piece of trace of the Reynolds stress tensor is shown in Figure 121. A similar picture emerges for the prediction of w' as seen for v' in the previous discussion. The RANS data does not develop the patterns seen in the experiment, but the LES is qualitatively correct. Three spots of high w' intensity form, one on either side of the jet (to spread the jet outward) and one in the middle to spread the jet into the wake region. The over-prediction of w' magnitude is clear, however. This likely plays a role, along with the over-prediction of v' in helping the mixing of the velocity to catch up with the experimental profiles.

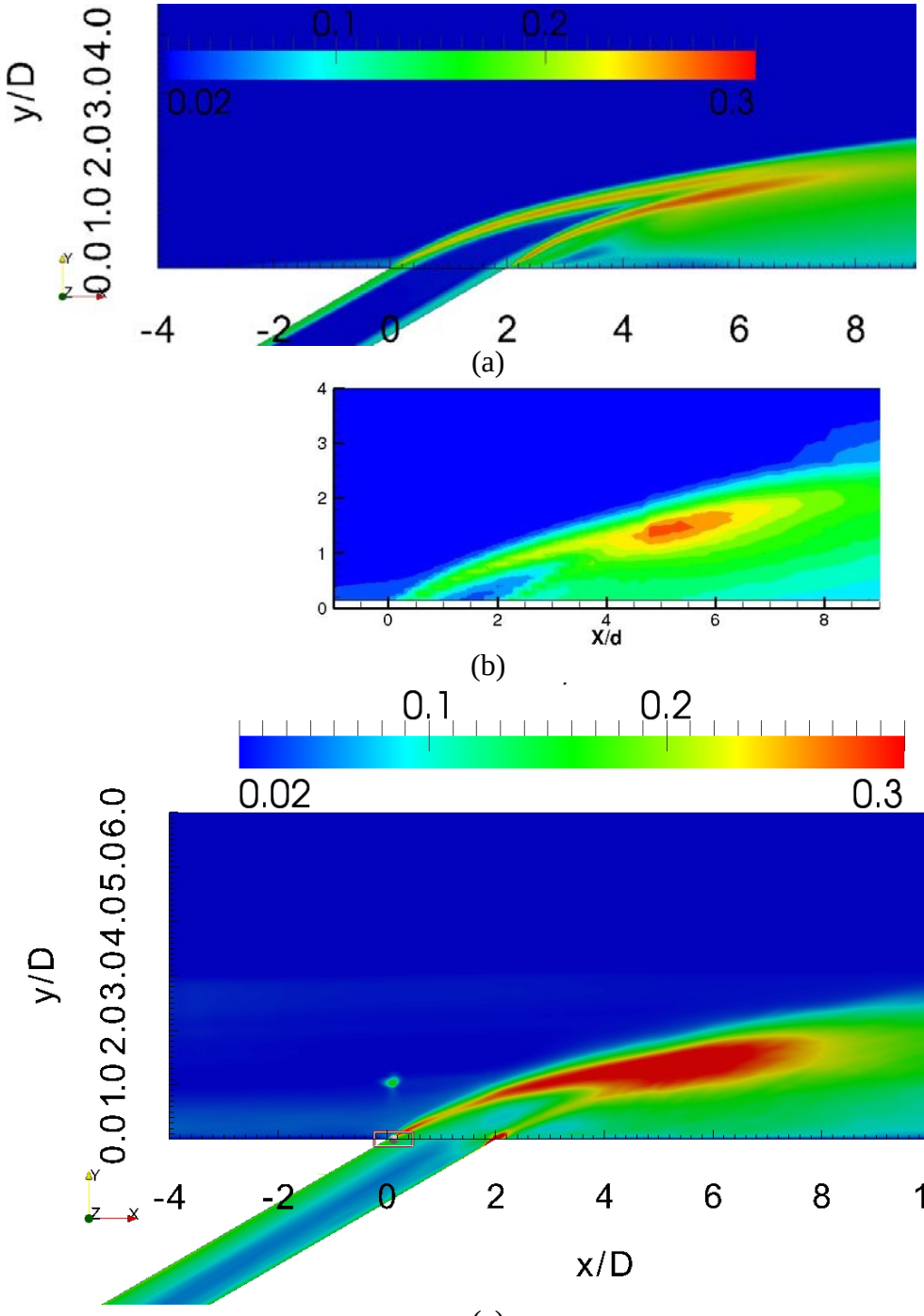

Figure 119 Normalized wall-normal fluctuations (v'/U_∞) along the center-plane from (a) RANS, (b) experiment, and (c) LES.

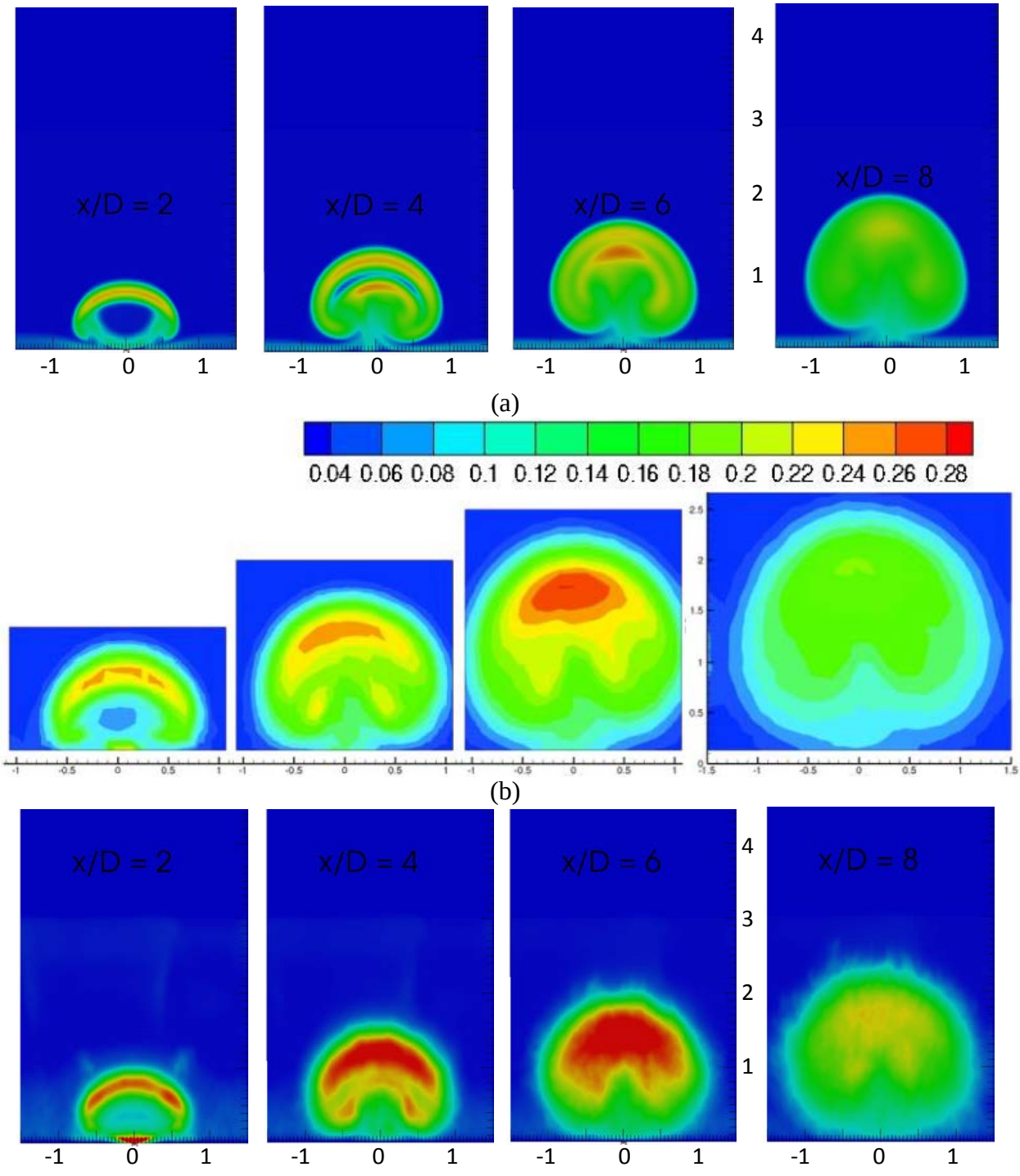

Figure 120 Streamwise development of wall-normal fluctuations v'/U_∞ at x/D = 2,4,6,8 from (a) RANS, (b) experiment, and (c) LES.

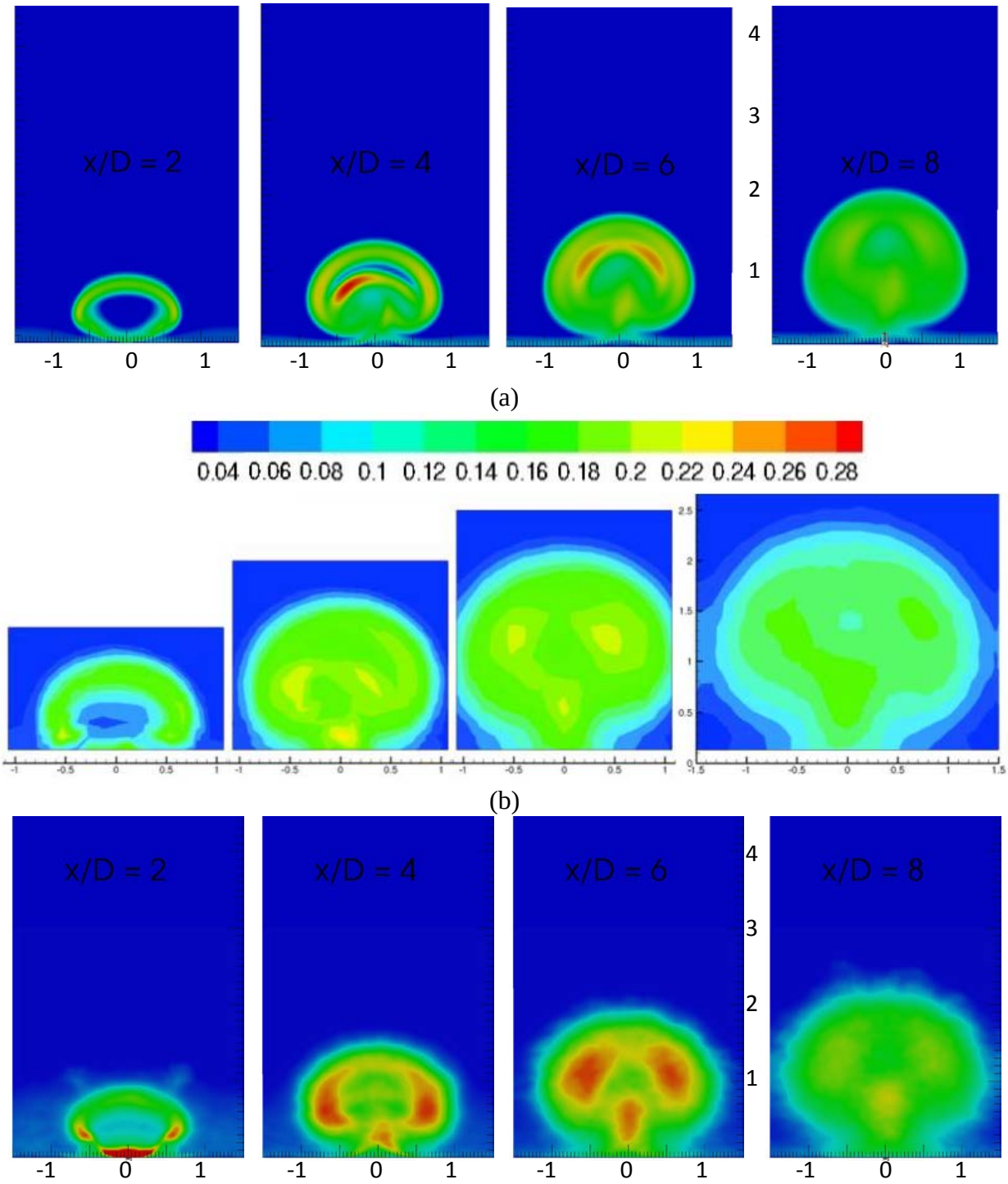

Figure 121 Streamwise development of spanwise fluctuations w'/U_∞ at x/D = 2,4,6,8 from (a) RANS, (b) experiment, and (c) LES.

The analysis of center-plane and streamwise-normal planes will be taken together for the <u'v'> Reynolds stress. Figure 122 shows the center-plane <u'v'> contours while Figure 123 shows various streamwise-normal planes. The center-plane data suggests that LES over-predicts the Reynolds stress while RANS does relatively better. The subsequent streamwise planes tell a different story, because once again there is conflict between the experimental profiles along the center-plane and at streamwise locations. The streamwise planes suggest that the LES actually under-predicts the <u'v'> stress, in direct conflict with the center-plane profiles. Accordingly, the streamwise planes suggest a dramatic under-prediction by the RANS simulation. These two figures further highlight a growing suspicion of the second-order statistical measurements.

A final comparison is afforded by the experimental measurements of <u'w'>, Figure 124. This time, in order to account for the seemingly clipped experimental results (lack of negative stresses), the numerical data is likewise clipped. Both simulations show that the general pattern is captured but under-predict the magnitude of the lateral stress. The LES data, in general, has a slightly better prediction of the profiles.

To summarize the Reynolds stress data, the RANS predictions are hindered severely by the isotropic eddy viscosity assumptions, sometimes qualitatively wrong. The LES manages to be qualitatively correct in all cases, but sometimes appears to over-predict. Some conflict between experimental profiles (and a single suggestion of LES under-prediction) shows that the conclusion that LES over-predicts Reynolds stresses must be held lightly. The mean profiles do tend to suggest, however, that the mixing rate is higher in the LES than the experiment, allowing the LES to 'catch up' to the spreading of the experimental jet.

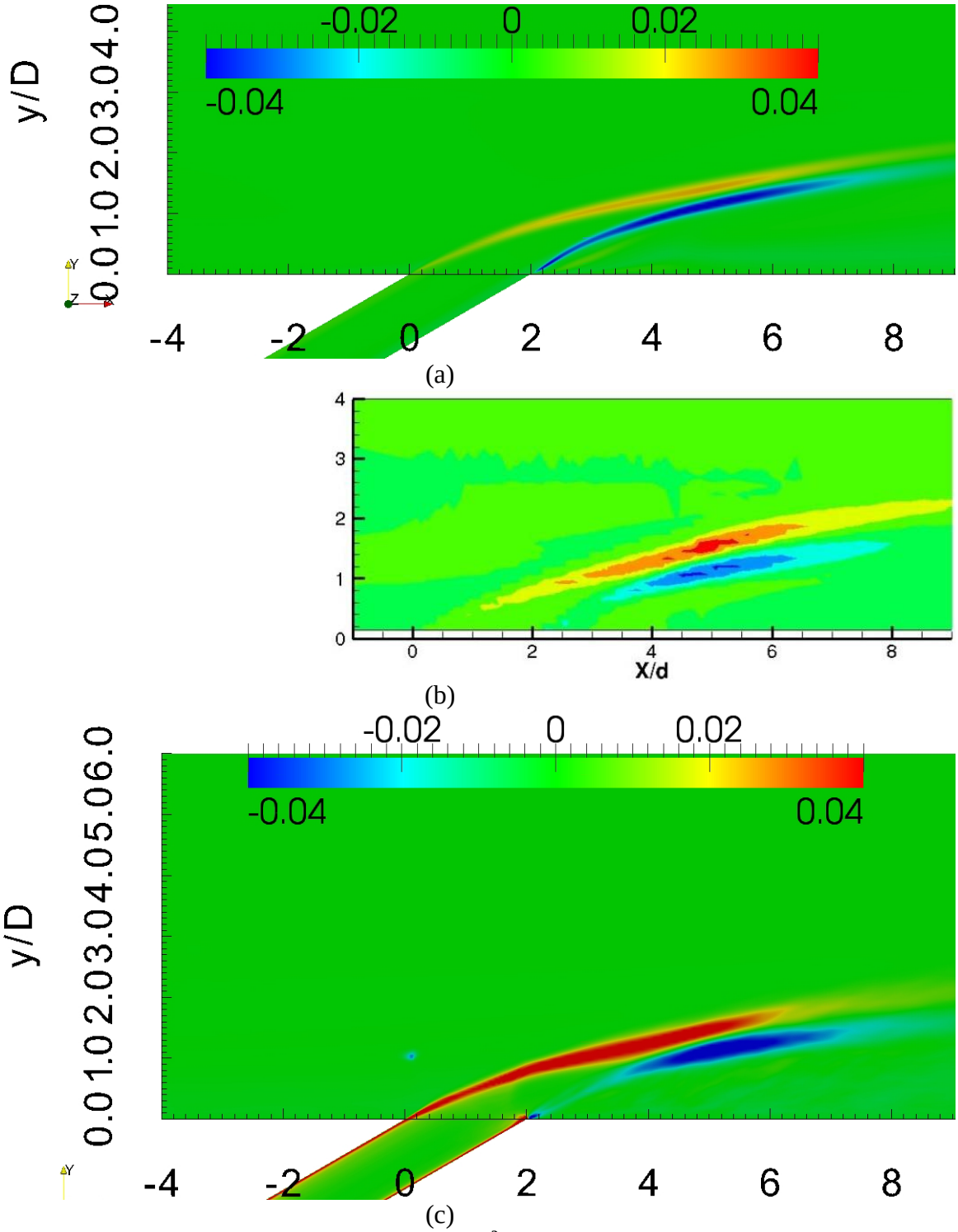

Figure 122 Normalized Reynolds shear stress ($u'v'/U_\infty^2$) along the center-plane from (a) RANS, (b) experiment, and (c) LES.

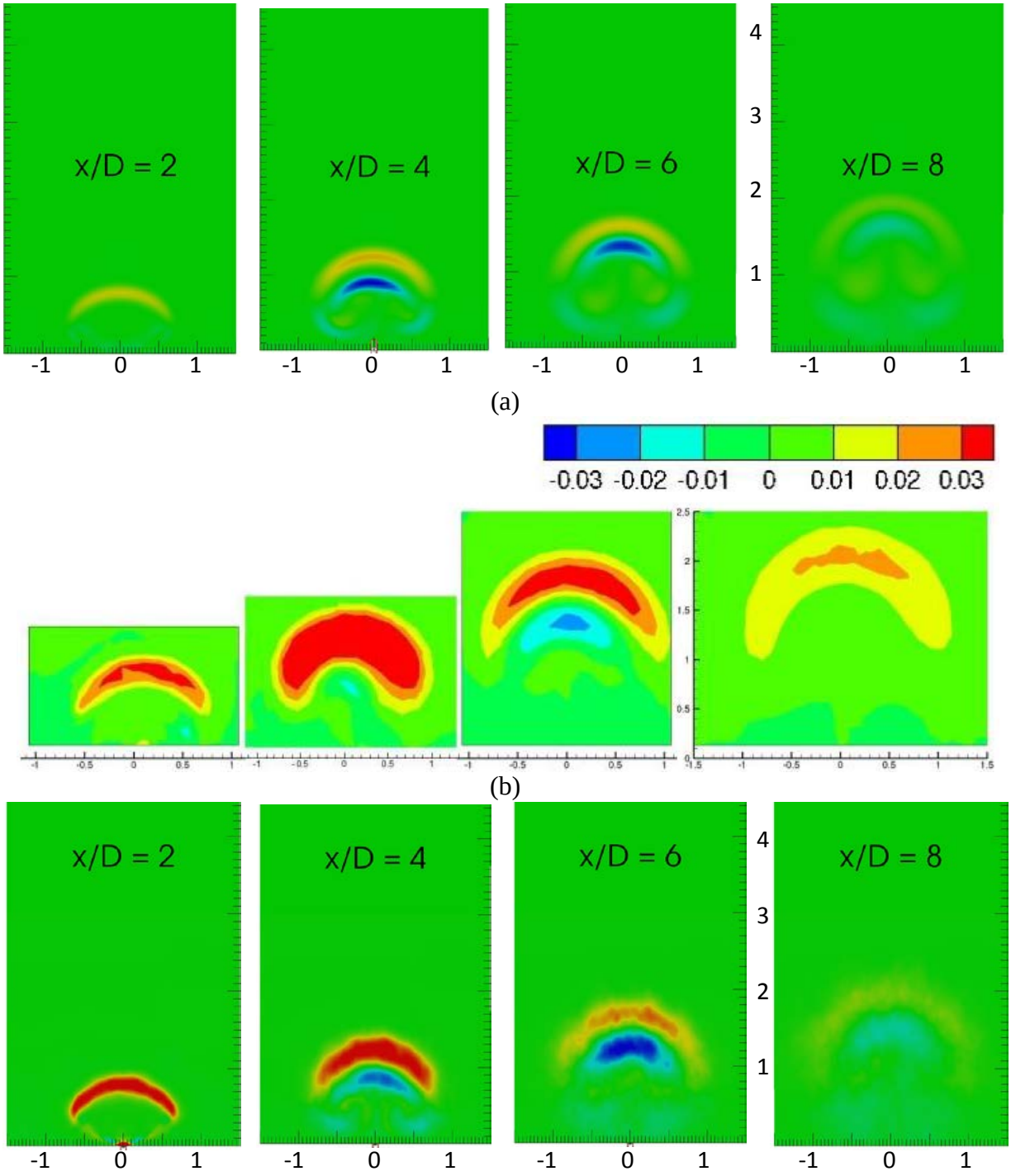

Figure 123 Streamwise development of Reynolds shear stress u'v'/U_∞^2 at x/D = 2,4,6,8 from (a) RANS, (b) experiment, and (c) LES.

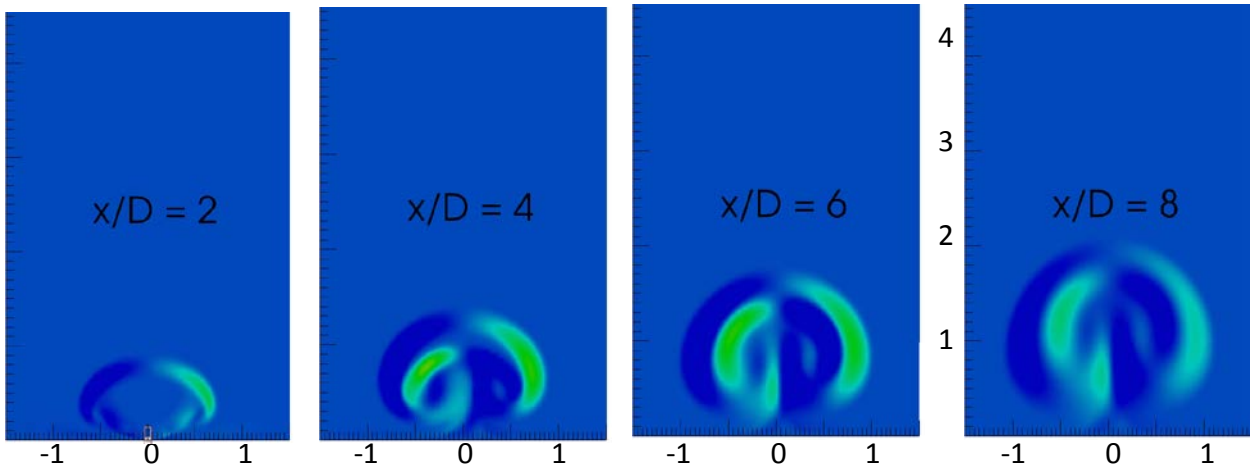

(a)

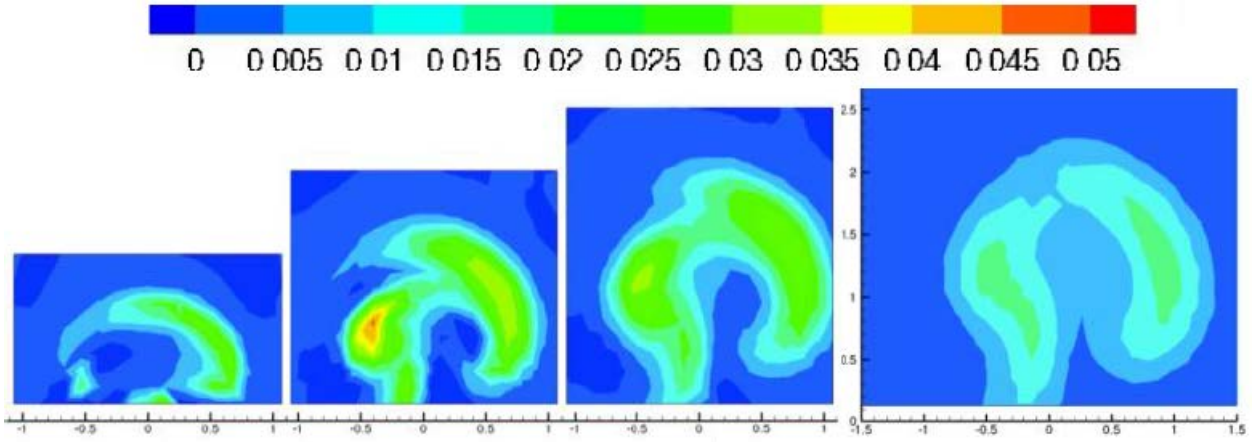

(b)

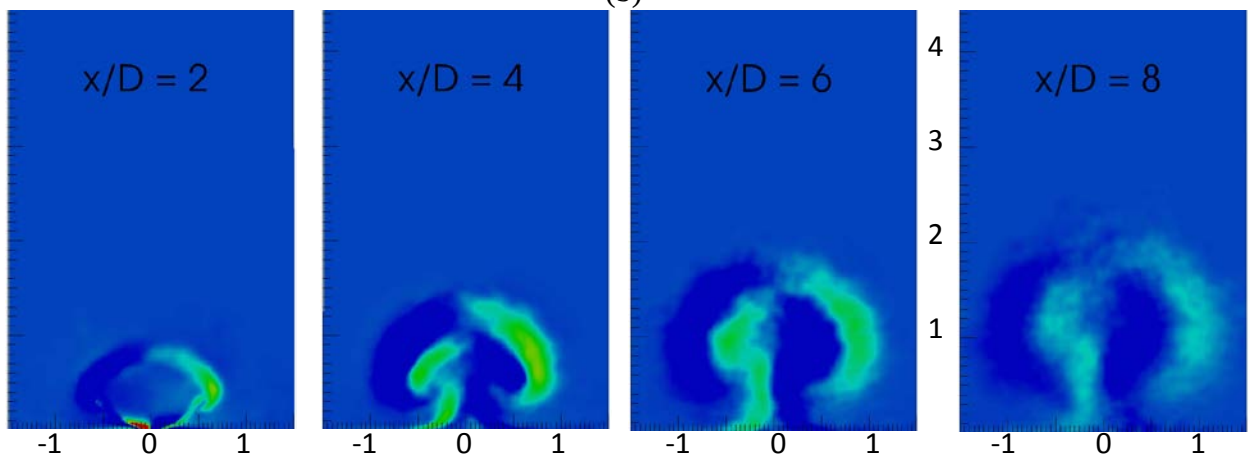

(c)

Figure 124 Streamwise development of Reynolds shear stress u'w'/U_∞^2 at x/D = 2,4,6,8 from (a) RANS, (b) experiment, and (c) LES.

9.4 Instantaneous Fields

Having shown extensive comparison between simulation and experiment, the exploration of the simulation data is the benefit to be reaped. The data will be presented in two steps. First, instantaneous snapshots of the flow field will give insight into the transient interactions and turbulent structures in the simulation. Later, the statistical quantities validated in the previous section will be explored from a more holistic perspective.

9.4.1 Moderate Blowing Ratio M = 1.0

A common technique for educing vortex structures in a chaotic turbulent flow was introduced by Jeong and Hussein (1995) in which the second largest eigenvalue of the velocity gradient tensor is computed. The iso-surfaces of this quantity is a common technique in processing LES data. Figure 125 shows such iso-surfaces for the current simulation.

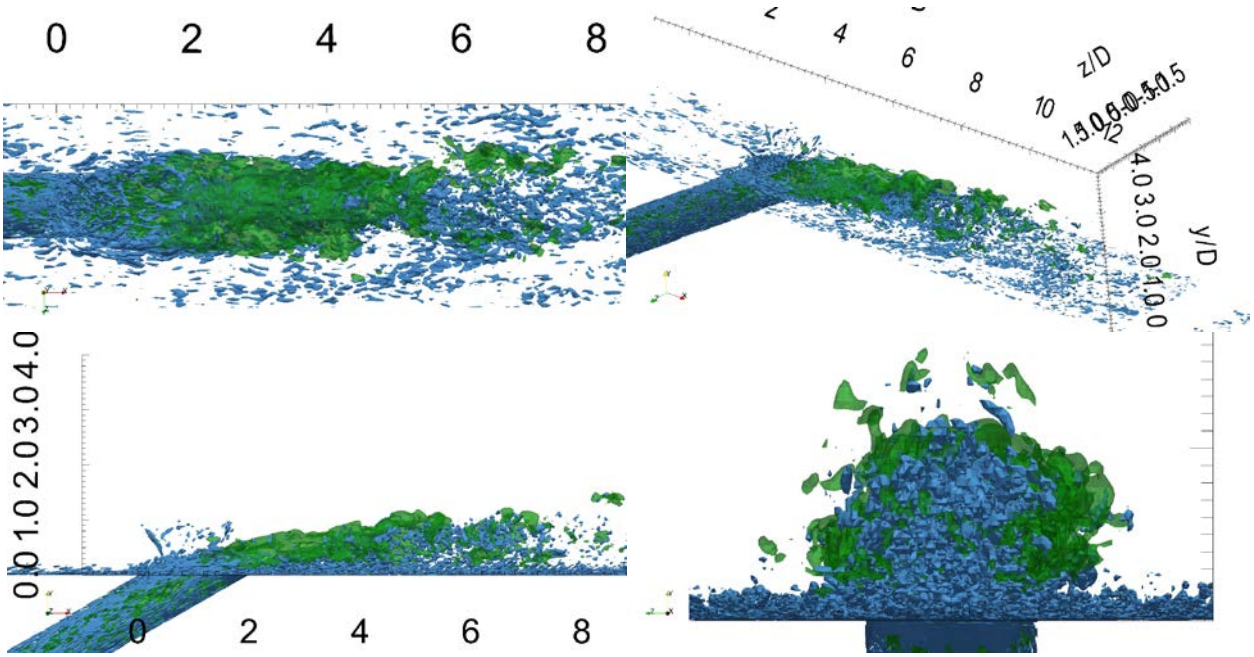

Figure 125 Iso-surfaces of lambda-2 (blue) and velocity magnitude (green) showing the educed vortex structures and jet region respectively.

The structures educed are primarily within the wake region of the coolant and not on the perimeter of the spreading jet. This can be seen as a disadvantage for the engineer wishing his coolant to spread in the spanwise direction, but also as an advantage for preventing the dilution of the jet with the freestream (from above).

Figure 126 shows three translucent iso-surfaces of temperature, which is the best indicator of the coolant characteristics. Within the domain, the coolant does not seem to have spread enough to interact with neighboring jets. This lack of spreading is likely due to the low strain-rates and hence low turbulent production on the perimeter of the jet. The spreading of the coolant (hence dilution) would be much higher if the velocity ratio were further away from unity.

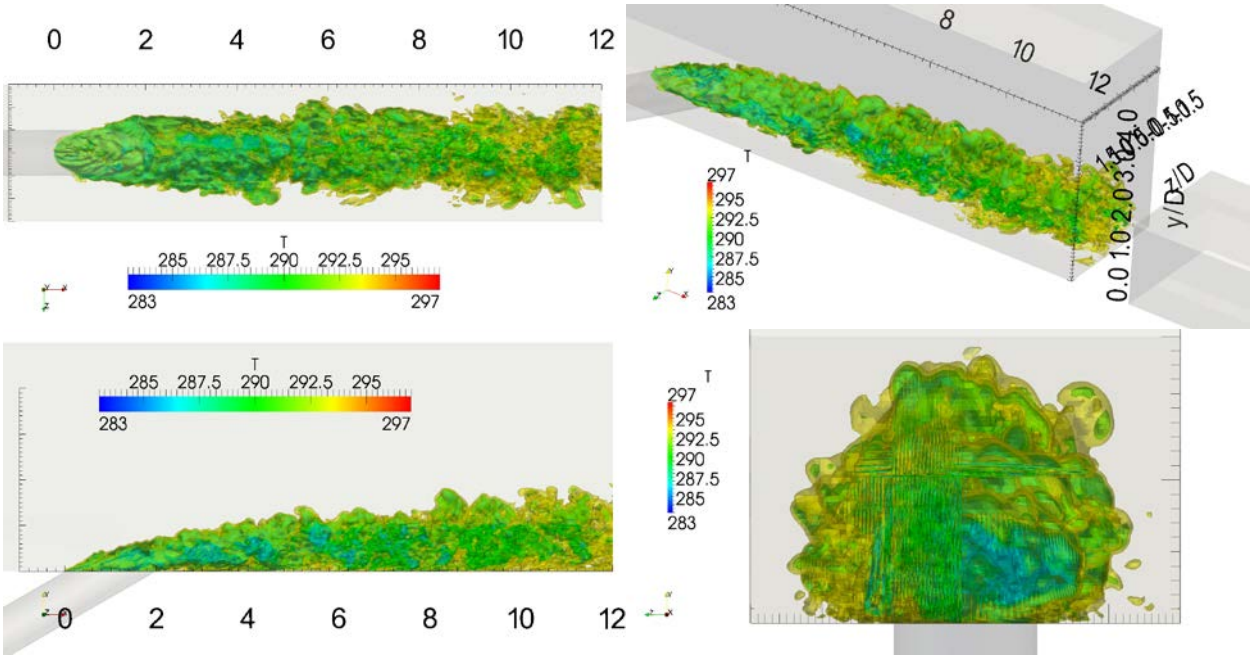

Figure 126 Iso-surfaces of instantaneous temperature (286.5, 290, 293.5 K).

Although the weak shear layer at the jet-crossflow perimeter boundary leads to a lack of strong roller vortices, the wake region is still very active due to the separation-reattachment behavior of the coolant. Thus, one may expect to find the presence of wake vortices, which arise when the crossflow boundary layer wraps around the side of the jet and then is lifted and turned

into tornado like vortices in the wake (Fric and Roshko 1994). Such vortices are indeed seen in the iso-surfaces of y-vorticity shown in Figure 127, though not in any organized pattern with a characteristic Strouhal number. The velocity ratio is too low and the added effect of inclined injection also narrows the wake region. Fric and Roshko (1994) showed that strong Strouhal number frequencies were detected at higher velocity ratios not practical for film cooling designs (e.g. VR = 4.0).

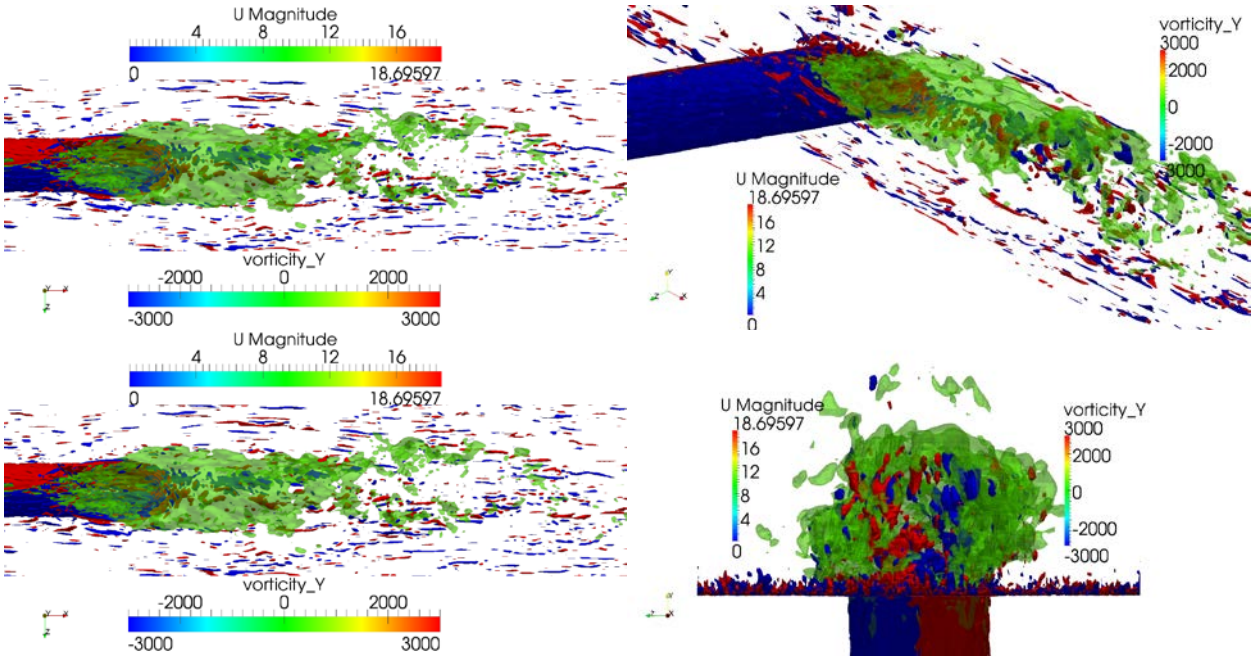

Figure 127 Iso-surfaces of instantaneous velocity magnitude (11 m/s) and instantaneous wall-normal vorticity (-3000, 3000 s^{-1}).

An instantaneous snapshot of the adiabatic surface temperature is shown in Figure 128. The separation region is clearly visible just downstream of injection with steady reattachment around x/D = 4. Reattachment is complete around x/D of 6. Unsteady reattachment events occur on either side of the jet in an unorganized manner at the CVP pull coolant down from the side of the jet and sweep it toward the surface. Further downstream, the coolant will venture far from the

centerline in one direction or the other at times. However, this usually occurs with coolant that has been diluted to near the freestream temperature.

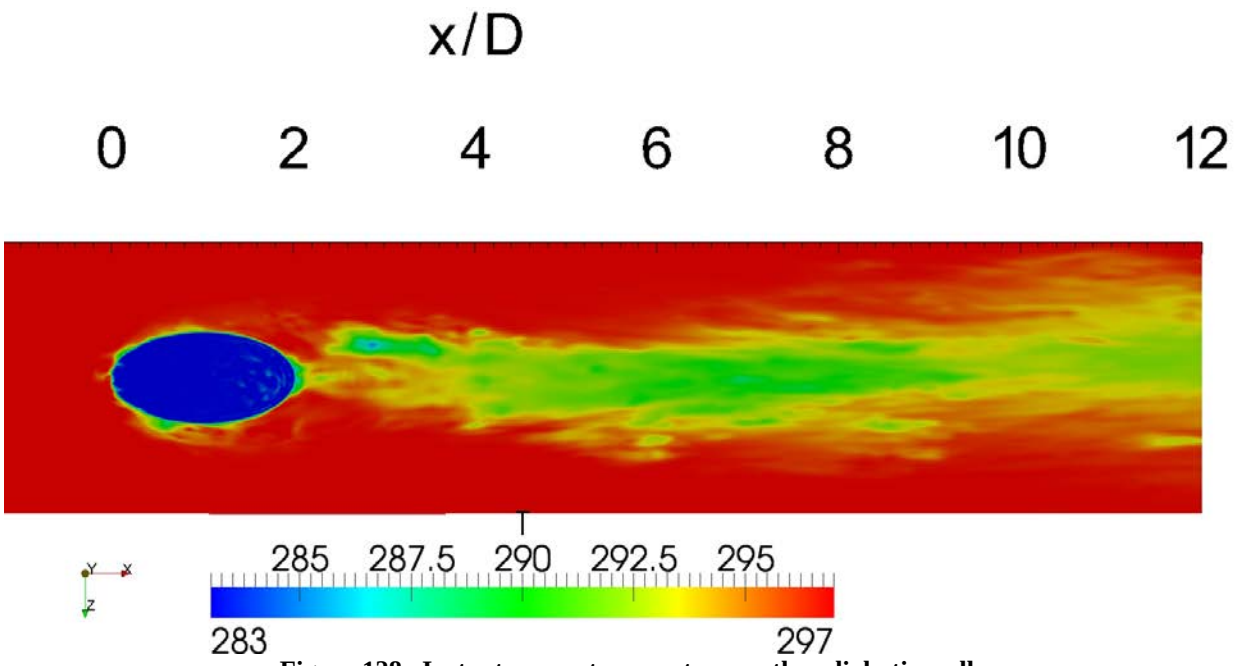

Figure 128 Instantaneous temperature on the adiabatic wall

The unsteady re-attachment events are also evidenced in the wall shear stress contours of Figure 129. In general, the wall shear stress in enhanced by the injection of the film, but unusually high enhancement is temporarily seen when the reattachment event occurs. In the wake region, however, the shear stress remains very low, much lower than that of the approaching boundary layer. The high wall shear stress was not problematic, however, from a resolution point of view. The mesh was constructed such that, by inner scaling, the wall distance of the first cell centroid would remain below a y^+ of unity. Figure 130 confirms that this is true. Finally, an instantaneous snapshot of the 286.5 K temperature iso-surface is shown in Figure 131 offering a view of the temperature structure hitting the surface under the influence of the CVP.

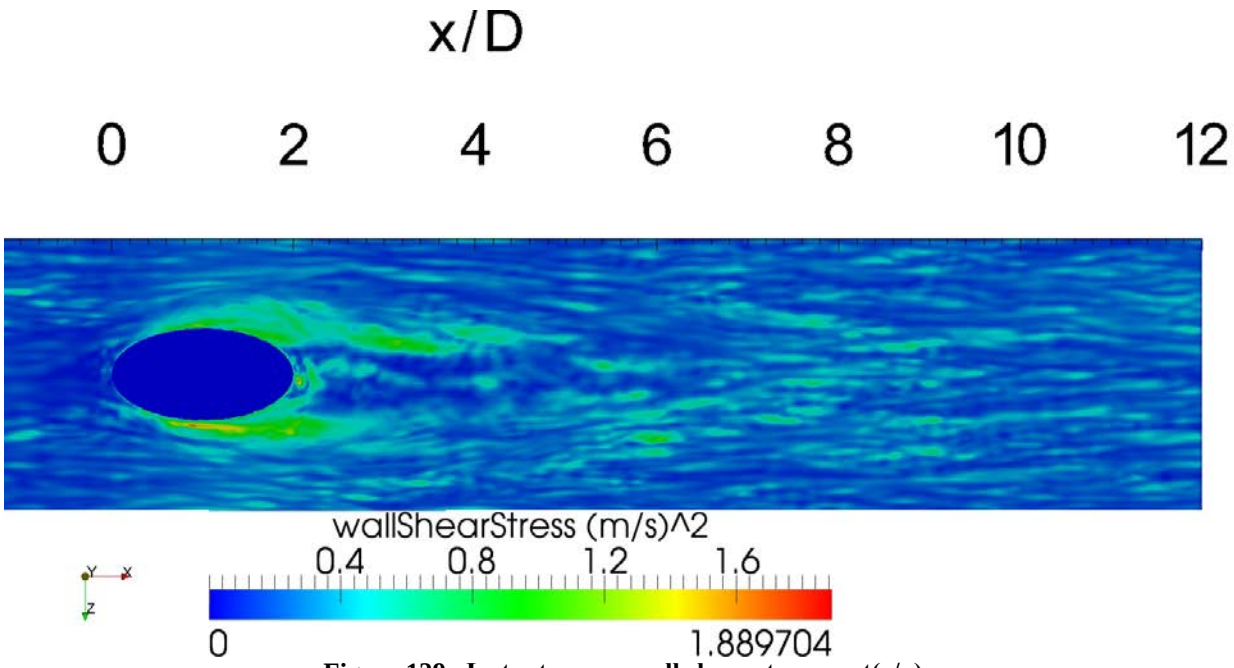

Figure 129 Instantaneous wall shear stress sqrt(τ/ρ).

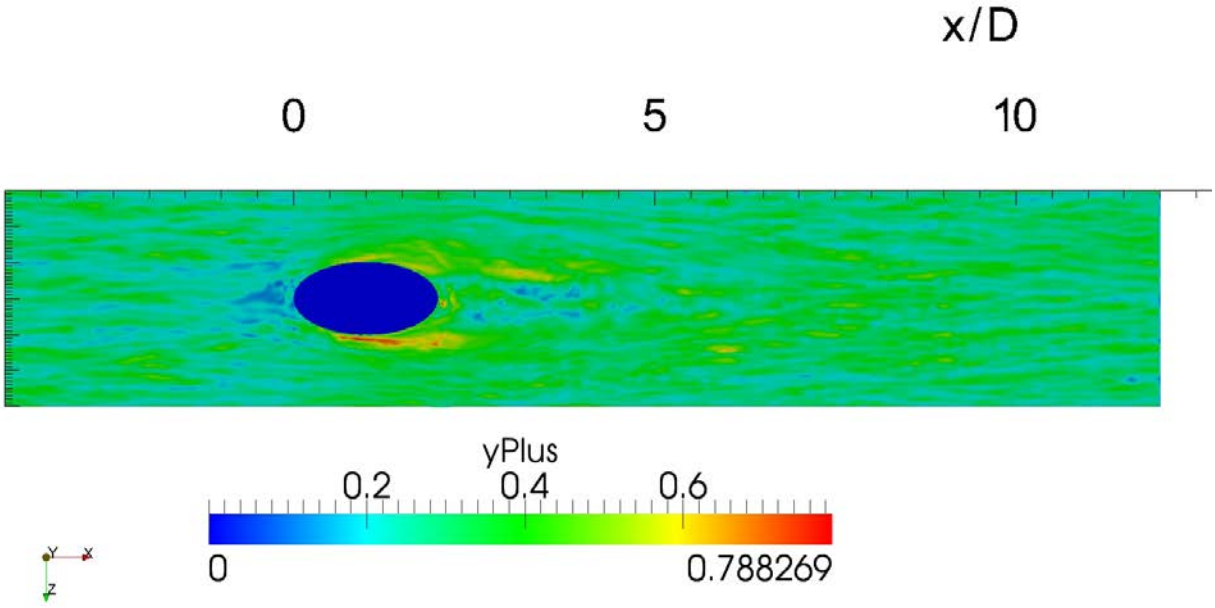

Figure 130 Instantaneous y-plus values for the cell centroid of the cells neighboring the surface.

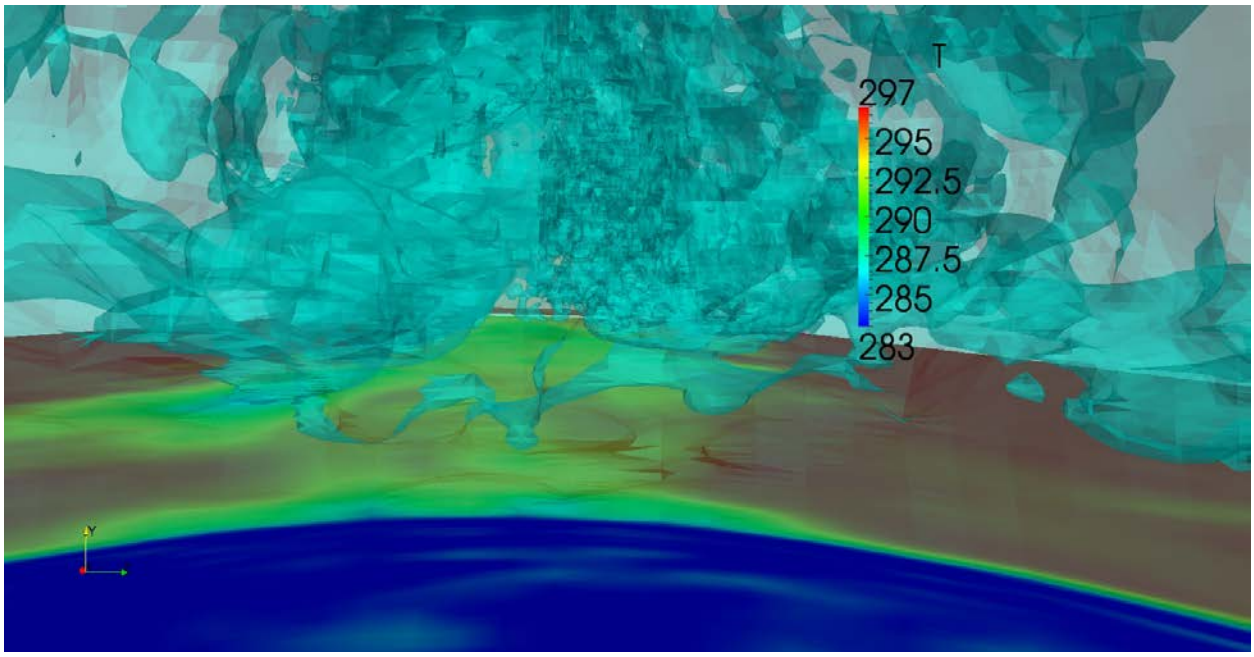

Figure 131 Translucent iso-surface of instantaneous T = 286.5 K showing reattachment event.

9.4.2 High Blowing Ratio M = 1.9

Iso-surfaces of the lambda-2 criterion are shown in Figure 132. Although the jet/wake system is mostly chaotic in appearance, a few features are more pronounced in the higher blowing ratio jet due to a higher velocity gradient between the jet and crossflow. Around the outside of the jet region, a U-shaped shear layer is present. Here, the shear layer roller vortices are seen. While these do not form coherent structures spanning the entire U-shape, there are large coherent structures in this layer than anywhere else in the flow. The influence of these structures is seen in the instantaneous temperature profiles of Figure 133, where large packets of coolant bulge from the jet in this shear layer. These large coherent structures are dominant in the mixing of the jet with the freestream, both in velocity and temperature. Figure 133 shows the separation of the jet and slow spreading of the jet back to the surface as well as the dramatic spanwise spreading, caused by the greater difference in velocity than the moderate blowing rate.

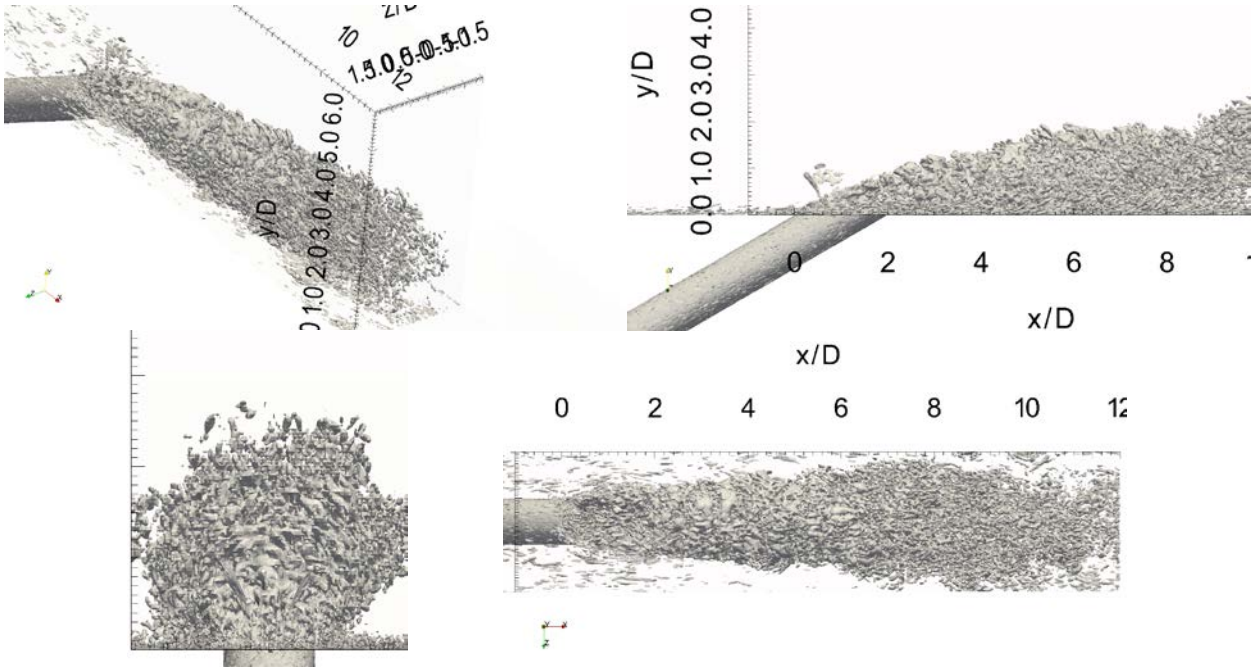

Figure 132 Lambda-2 iso-surfaces showing large shear layer structures in upside-down U-shape region.

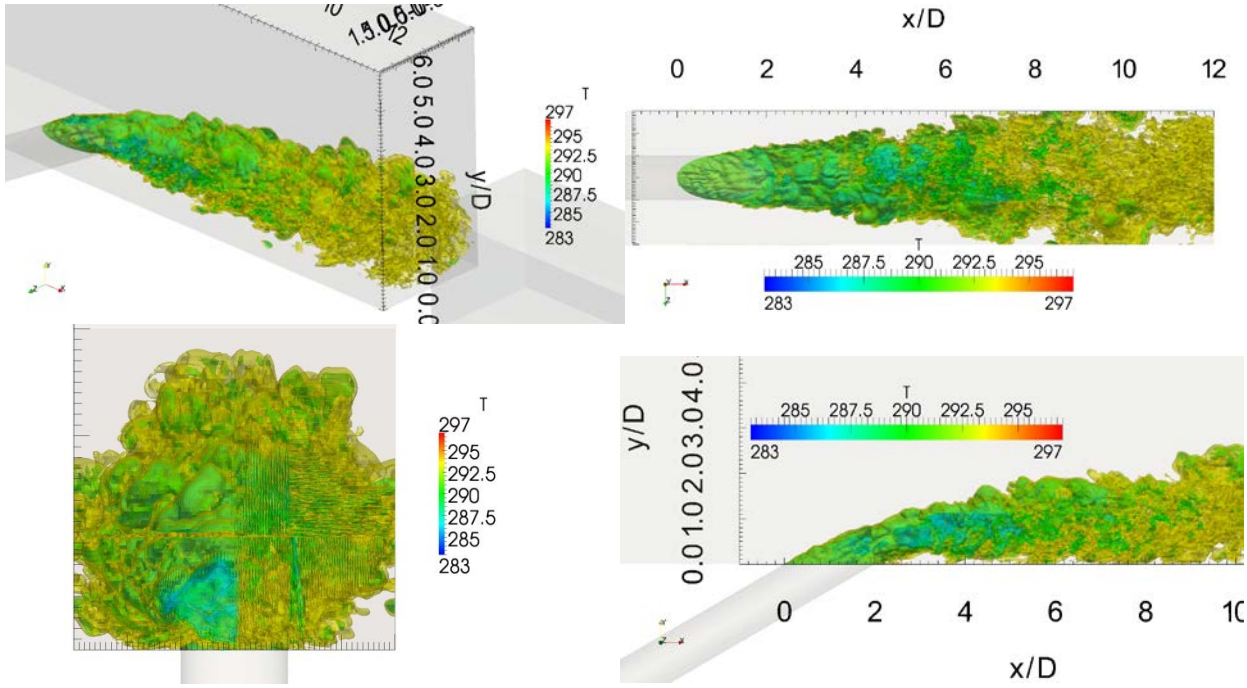

Figure 133 Iso-surfaces of temperature (blue- 286.5, green - 290, yellow -293.5 K).

Figure 134 shows iso-surfaces of y-vorticity. These are shown to highlight the two regimes of coherent vortices primarily aligned in the wall-normal direction. The first is the wake vortex system in the inner part of the coolant flow. These are akin to those observed in the M = 1.0 case. Unlike the moderate blowing rate, however, the high blowing rate introduces much higher magnitude structures in the shear layer between the jet and the crossflow. This gives rise to the structures seen along the outside of the coolant jet in Figure 134. Thus, a two layer system of vortices is uncovered, unlike the simplistic picture of Tyagi and Acharya (2003). The jet is simply more chaotic than they suggest. Their simulation was likely plagued by too coarse of a mesh as well as poor inflow boundary conditions.

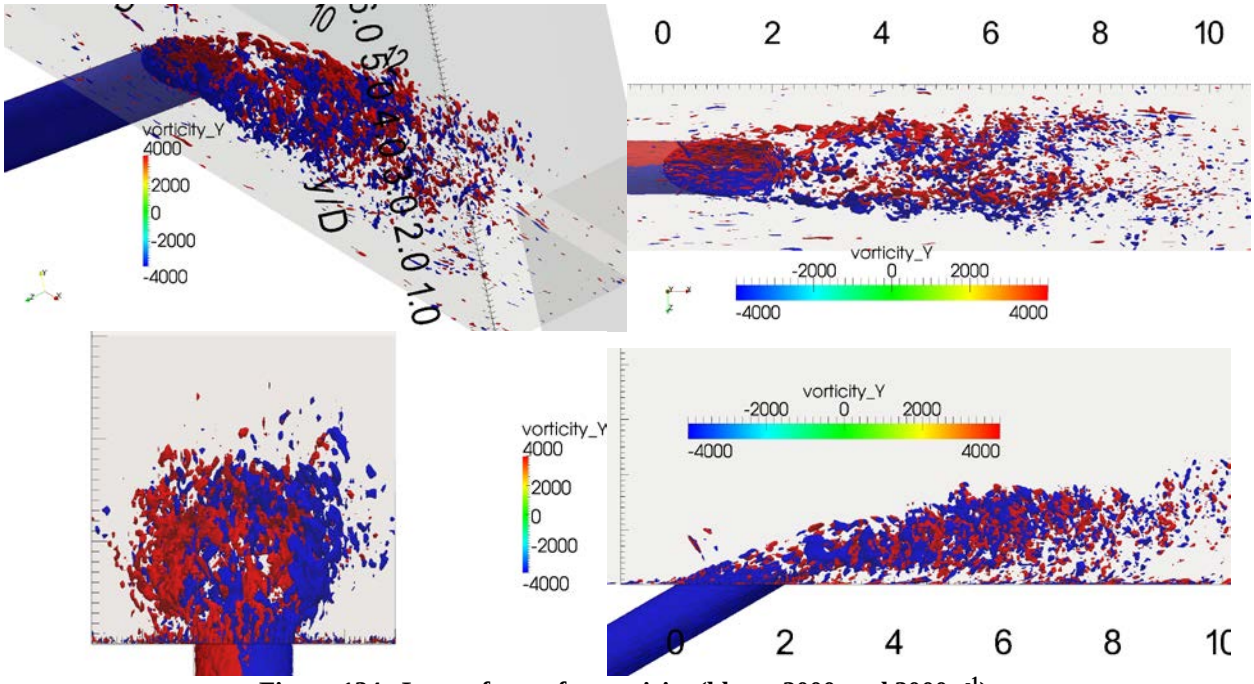

Figure 134 Iso-surfaces of y-vorticity (blue – 3000, red 3000 s^{-1}).

An instantaneous snapshot of the adiabatic wall temperature is shown in Figure 135. This shows that, like in the M = 1.0 case, there are unsteady reattachment events on the periphery of the coolant region. These occur much further downstream, however, now that the jet is fully

lifted and only reaching the wall via a spreading mechanism (rather than being force back to the surface by the momentum of the crossflow). The over-predicted separation region is also evident.

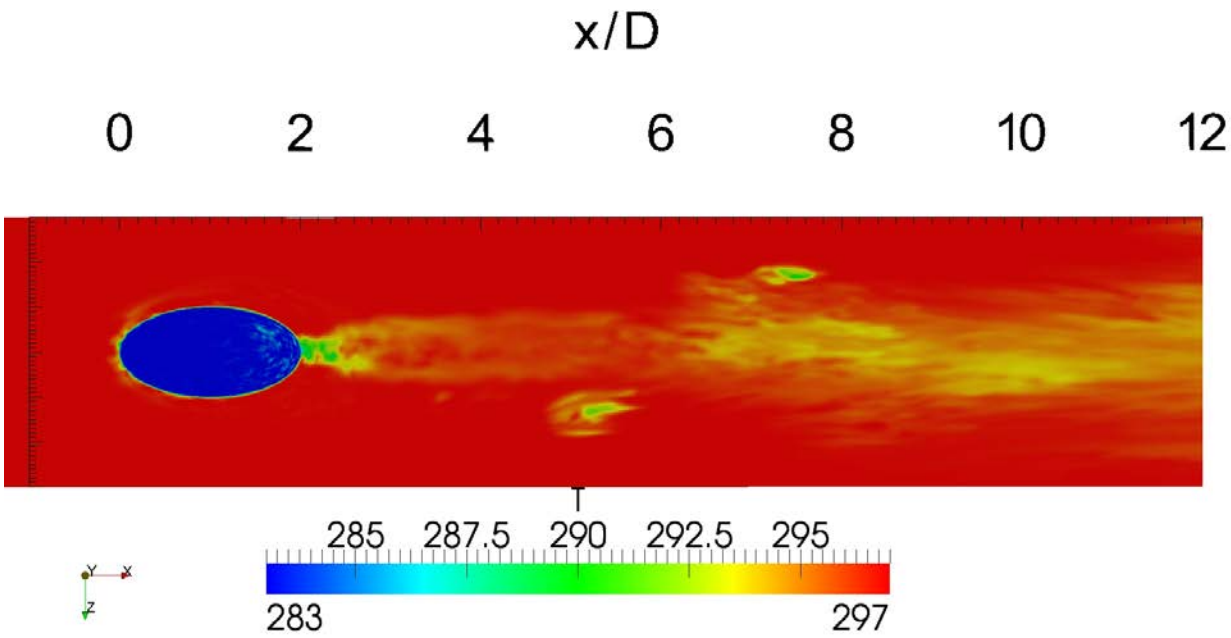

Figure 135 Instantaneous temperature on the adiabatic wall.

Figure 136, meanwhile, shows the shear stress along the surface of the adiabatic wall. Higher wall stress is noticeable around the region that the spreading jet comes back in contact with the surface around $7 < x/D < 9$. The low temperature reattachment events on the periphery of the jet are also seen has high shear stress events. Figure 137 shows that these, as in the case of the M = 1, result from the packets of temperature created in the sides of the U-shaped shear layer are swept toward the surface by the CVP.

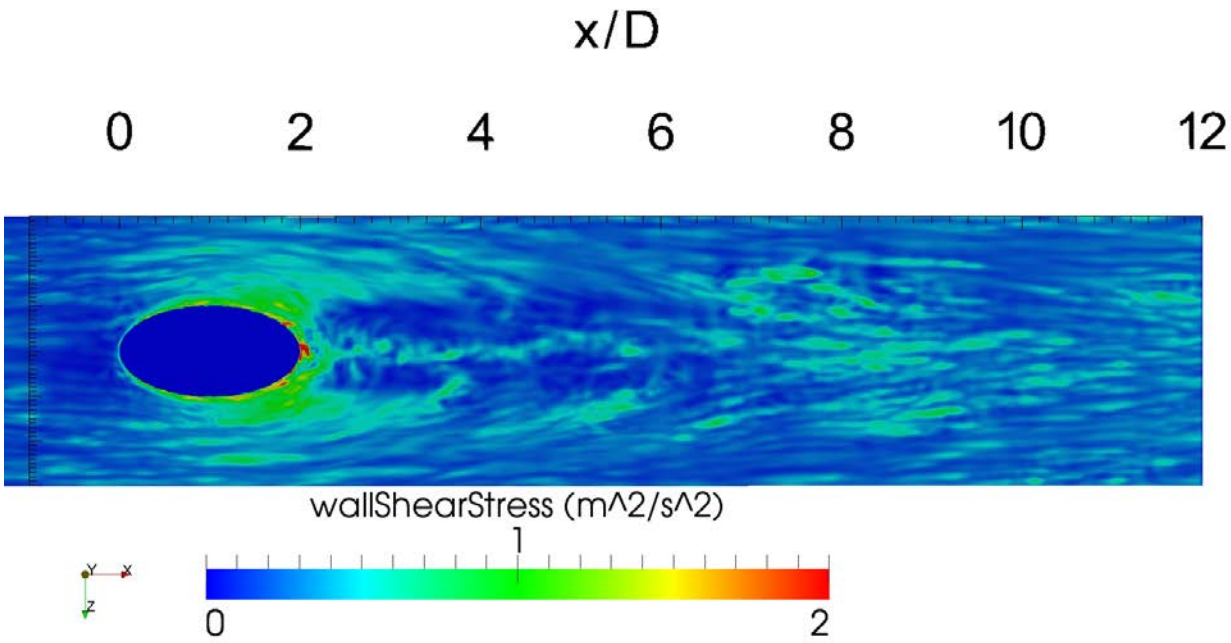

Figure 136 Instantaneous wall shear stress at the adiabatic wall.

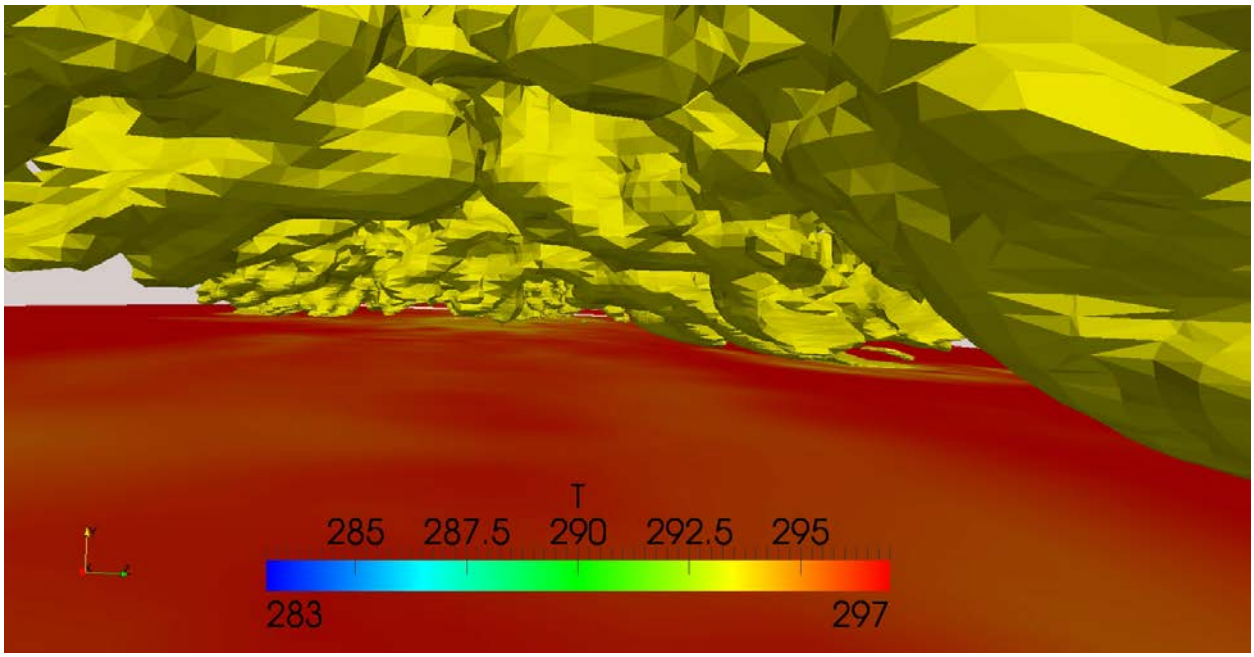

Figure 137 Iso-surfaces of instantaneous temperature; view from underneath the coolant jet.

9.5 Further Analysis and Discussion

Having evaluated the prediction of the current model with experiment and explored the unsteady physics predicted, the next task is further exploration of statistical quantities to further elucidate the behavior of the modeled film jet. This task will focus on the same statistical quantities from the validation section, but with a more holistic perspective in mind.

9.5.1 Moderate Blowing Ratio M = 1.0

An important criterion to consider regarding the temporal and spatial resolution of the simulation is the percent of the turbulent kinetic energy that is resolved. From dimensional analysis, the energy contained (per wave number) at a certain wave number tends to follow a -5/3 power-law spectrum. This means that the low wave-numbers (representing large eddies) contain the majority of the turbulent kinetic energy (TKE). Large eddy simulations typically target a resolution of at least 80-90% of the TKE. Figure 138 shows two iso-surfaces bounding regions of < 90% and < 95% TKE resolution, respectively. Only a small portion of the wake region immediately behind the jet is not 90% resolved. Other iso-surfaces (not shown) confirm that this region is mostly at least 80% resolved. Only a small portion of the flow directly around the trailing edge lip of the hole is less than 80% resolved. Most of the jet, however, is between 90% and 95% resolved.

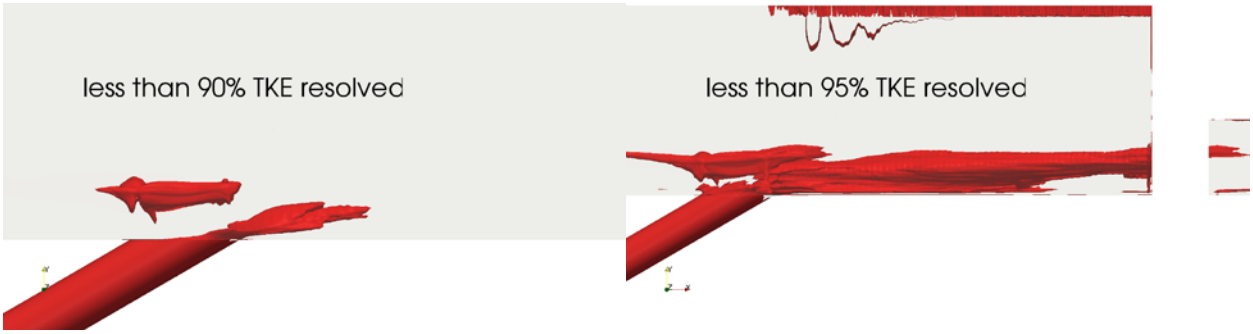

Figure 138 Iso-surfaces of percent turbulent kinetic energy resolved based on resolved Reynolds stress tensor and subgrid kinetic energy predicted by dynamic Smagorinsky model; the majority of the jet is between 90-95% resolved.

The mean streamwise velocity is, with the exception of the mean temperature, the simplest characteristic showing the cooling jet. Figure 139 shows two iso-surfaces of mean x-velocity from four viewpoints. The main characteristics of the jet are clearly seen. First, the boundary layer thickens dramatically as it approaches the leading edge of the jet. As the jet exits the hole, it is folded over by the momentum of the freestream and the CVP is formed. The core of the jet is squeezed and accelerated at the exit of the hole. Even though the blowing ratio and density ratio is unity (hence unity velocity ratio), the fact that the velocity of the coolant is a spatially averaged quantity means that there is considerably higher velocity in the core of the jet as it first exits the jet (up to 1.3 times the freestream velocity).

The CVP forces the higher velocity jet into a distinct upside-down 'U' shape, with the separated and low-velocity wake region within the underside of the 'U'-shape, Figure 139. This initial formation of the jet gives rise to sharp velocity gradients in the middle of the cooled region, which can be characterized with a two-layer model: a jet region with velocity higher than the freestream on top of a wake region, with lower velocity than the freestream. Later temperature contours will confirm that both the jet and wake regions contain the lower temperatures from the injection. The shear layers gives rise to rapid turbulent production and the

jet and wake quickly mix toward the freestream velocity with an equilibrium boundary layer profile. This is a slow process after the first few diameters, however. First, adjacent jets must merge completely, which does not occur within the current domain.

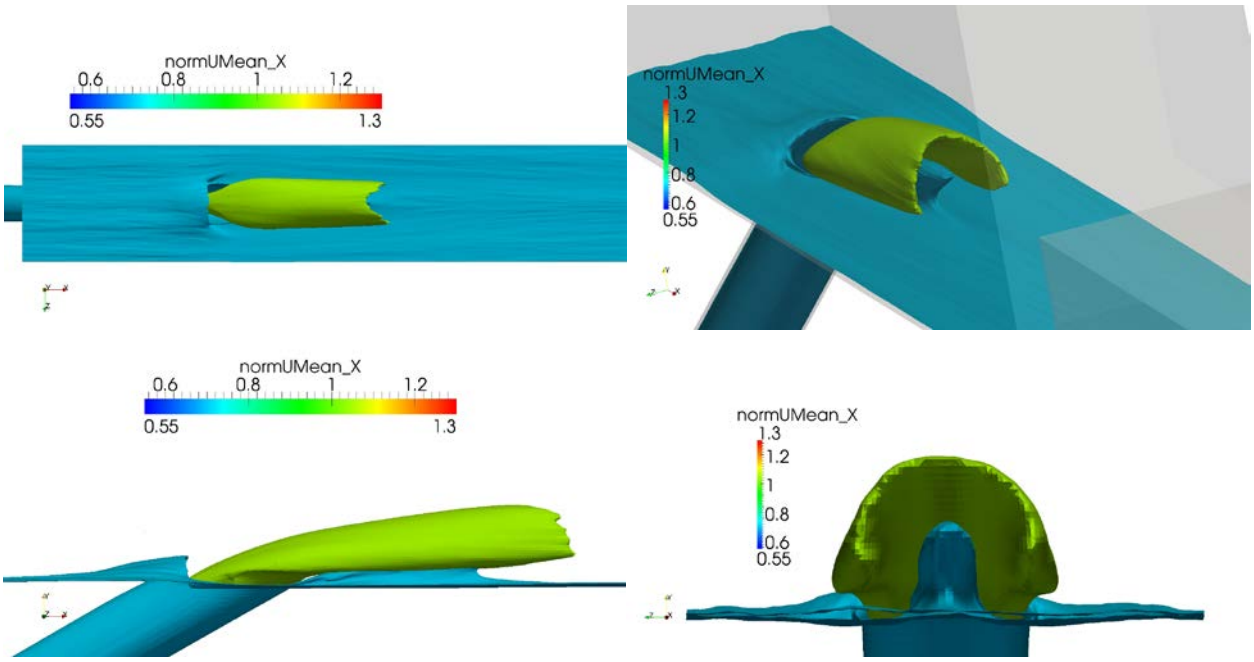

Figure 139 Iso-surfaces (1.05, 0.7) of normalized mean streamwise velocity.

Because the jet is injected at an angle rather than tangential to the flow, there is a significant wall-normal velocity at the hole exit. The jet is quickly turned at the exit of the jet, however, and the y-velocity is quickly converted to the streamwise direction, leaving only secondary flows to comprise the y-velocity component. Figure 140 shows two y-velocity iso-surfaces for the jet, one positive and one negative. The y-component of velocity from the main core of the jet diminishes to a point and vanishes before and x/D of 4 in the positive iso-surface. After this, there are still strong secondary flow components present (up to 0.6 times the freestream velocity). On either side of the jet, the downdraft of the CVP is visible in the negative iso-surface. Meanwhile, the wake region displays a strong updraft, which is also part of the CVP. As the jet is mixed out, the CVP is weakened and expanded in size so that the velocity

component normal to the surface is attenuated to zero (actually, it does not asymptotically approach zero, since there is always a slight positive wall-normal velocity component in a growing boundary layer (due to the application of a shearing force by the no-slip wall).

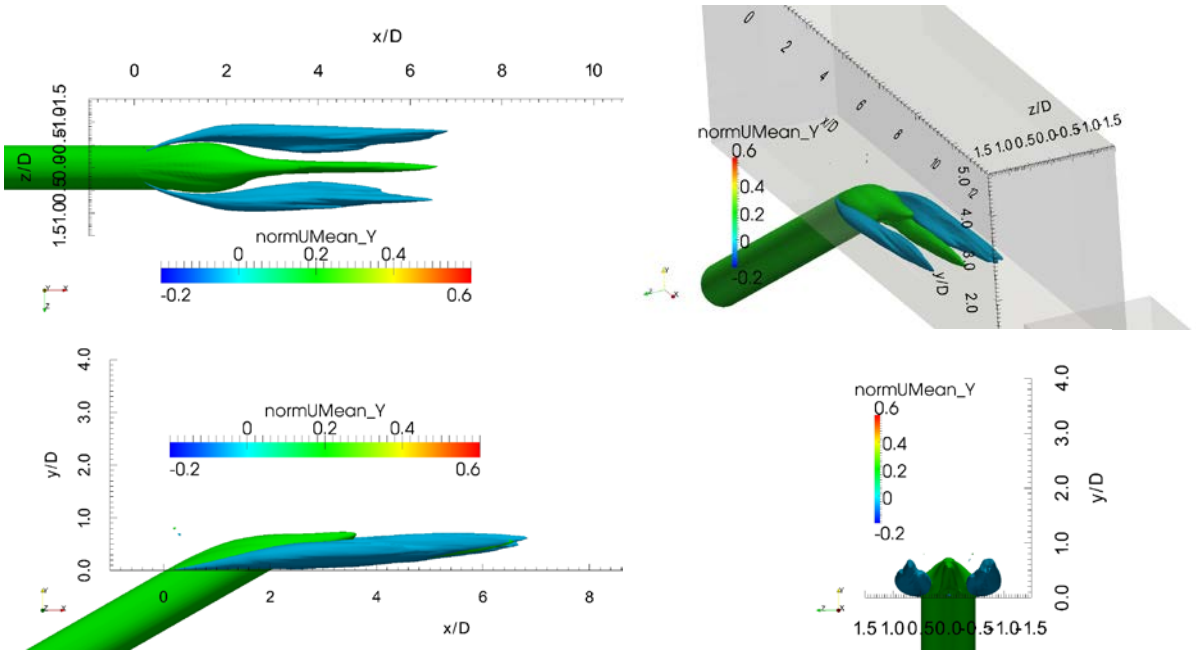

Figure 140 Iso-surfaces (-0.05, 0.2) of normalized mean wall-normal velocity.

The z-component of mean velocity is similarly shown in Figure 141. Here, the dynamics of the CVP is further apparent. Four structures are seen in the iso-surfaces of z-velocity. In the upper (jet) region, there is a z-velocity tending away from the center-plane. In the lower (wake) region, there is an opposite tendency towards the center-plane. This is a clear indication of a strong CVP.

The two components of the mean-velocity normal to the streamwise direction of the freestream are shown in Figure 142 colored by temperature. This shows the effect of the CVP in entraining hot gas from the crossflow underneath the jet. The outer downdraft and lower region inward velocity of the secondary flows pulls the crossflow down and in, underneath the jet.

Meanwhile, the center-plane updraft of y-velocity pulls coolant away from the surface and forms the upside-down ‘U’-shaped pattern seen in Figure 139.

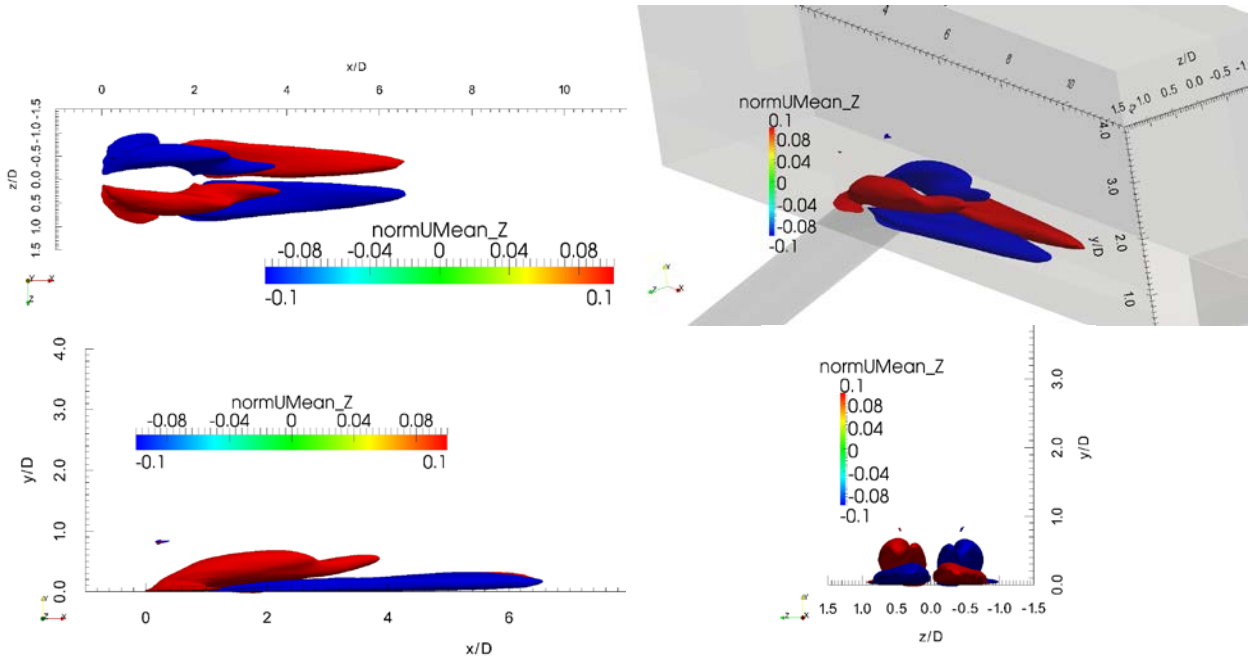

Figure 141 Iso-surfaces (-0.1, 0.1) of normalized mean spanwise velocity.

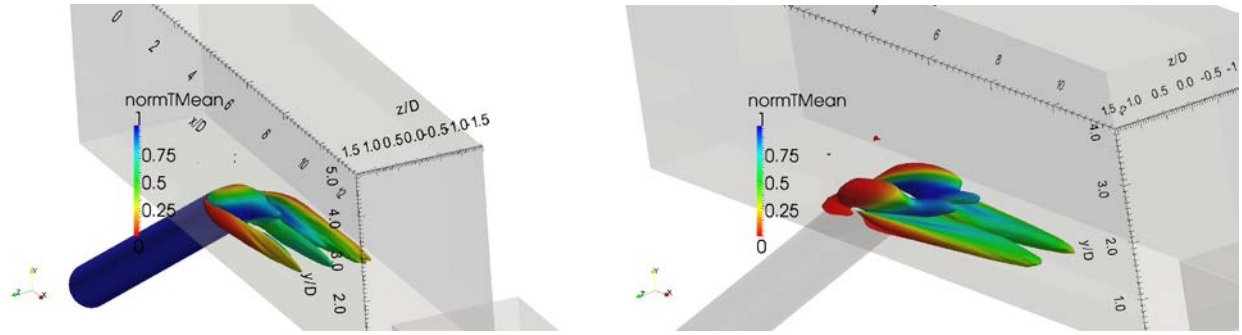

Figure 142 Iso-surfaces of (a) mean wall-normal velocity and (b) mean spanwise velocity, colored by normalized mean temperature.

The presence of the coolant film is best characterized by the temperature, since a high adiabatic effectiveness (low adiabatic wall temperature) is the goal of the injection in the first place. Figure 143 shows three translucent iso-surfaces of mean temperature. The cold core is seen to behave similarly to the velocity field, being forced by the CVP into an upside-down ‘U’-

shape. As the CVP weakens and turbulent mixing begins to have its way, the core of the coolant collapses into more of a circular shape.

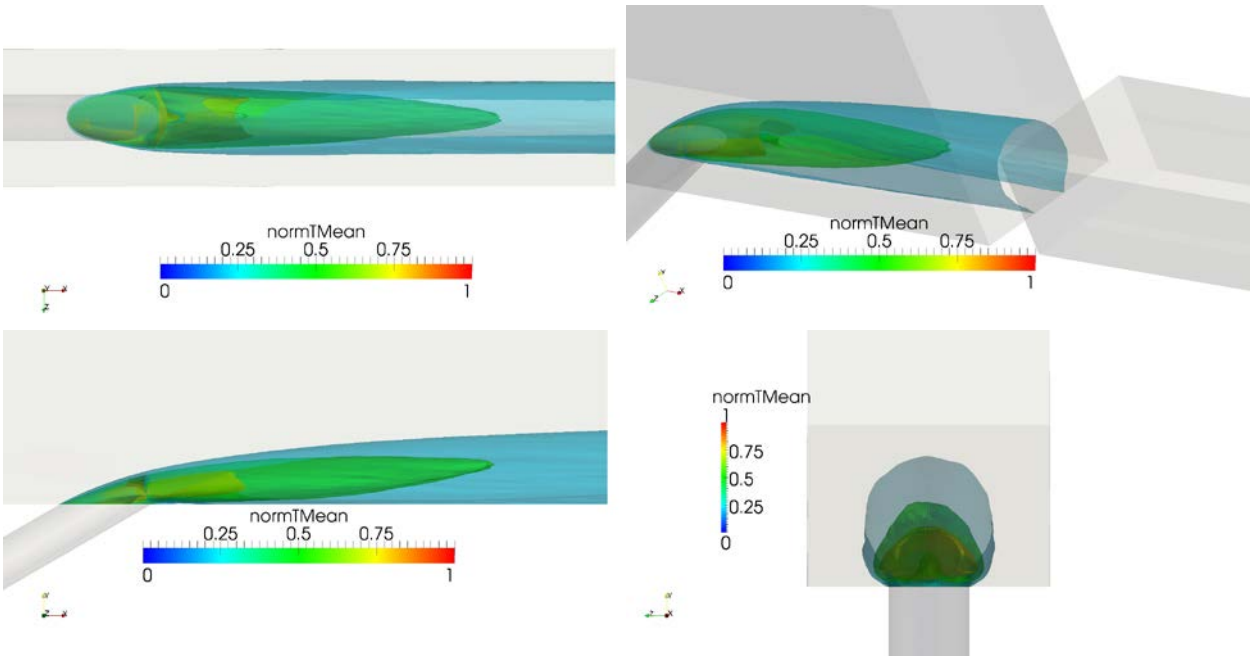

Figure 143 Iso-surfaces (0.2, 0.5, 0.8) of normalized mean temperature.

With the mean components explored, mostly in terms of the CVP, the next topic is the turbulent mixing which is promoted by mean gradients and executed by correlated fluctuating quantities (the Reynolds stress tensor and turbulent heat flux vector). Figure 144 shows the s-y component of the mean strain rate tensor, revealing the layered structure of the jet-wake velocity field. At the top of the jet, the blue iso-surface (negative strain rate) is caused mostly by the increase in x-velocity approaching the wall due to the 'U'-shaped portion of higher momentum fluid shown in Figure 139. This upper-most iso-surface shows the boundary between the freestream and the upper jet region. The next layer before that (red iso-surface) is a positive strain-rate, mostly indicating a subsequent drop in x-velocity approaching the wall. This shows the transition from the upper jet region to the lower wake region. Since the lower wake region prevails further downstream with more strength than the jet region, so this red-iso-surface

outlasts its northern neighbor. A third shear layer (in the S_{xy} sense) is detected for a short distance underneath the previously discussed iso-surfaces. This second blue iso-surface shows that the 'U'-shaped jet region continues to be stretched by the CVP, which acts to pull the jet region toward an 'O'-shape with the wake region fully enclosed. Before this can fully occur, however, the jet region is mixed-out (being in such close proximity to the no-slip wall). The lower blue iso-surface is short-lived indeed. The final iso-surface is the boundary layer straining, which blankets the wall in positive (red) strain and is slightly indented by the interruption of the film injection.

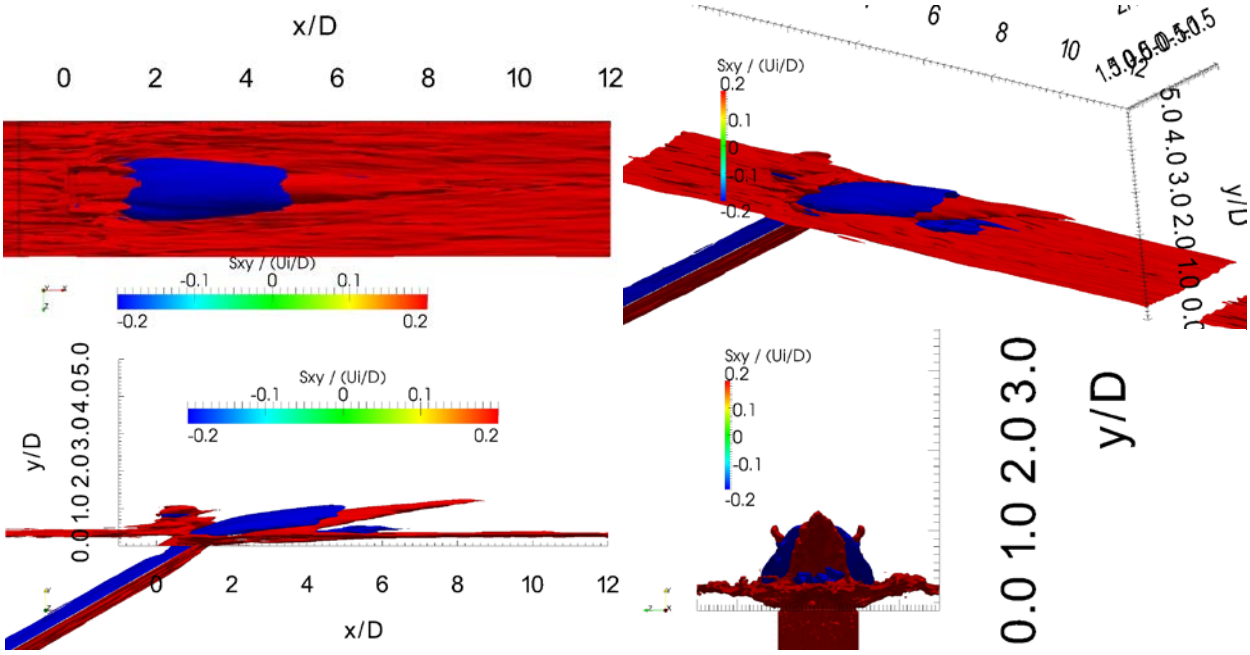

Figure 144 Iso-surfaces (-0.2, 0.2) of x-y component of mean strain rate tensor; normalized by U_∞/D.

According to the Boussinesq hypothesis, the turbulent fluctuations <u'v'> (or R_{xy}) are locally a function of the strain rate (S_{xy}). It is seen that the iso-surfaces of R_{xy} in Figure 145 do follow the same pattern as the strain rate layers in Figure 144. The positive R_{xy} shows the upward spreading of the jet momentum into the freestream while its lower neighboring blue iso-surface shows the downward flux of momentum from the jet into the wake. Near the wall, no layers

exist to match the strain rates, however. This is a result of two primary explanations. First, the Reynolds stresses near the wall are diminished as molecular stresses play a more vital role. Secondly, the Boussinesq hypothesis is qualitatively incorrect in rapidly developing shear layers because the turbulence shows a viscoelastic type memory. The shaping of the 'U'-shaped jet toward and 'O'-shape can be seen as an effect of this sort. In other words, the turbulent stresses cannot react fast enough to develop a substantial momentum flux to match the strain rate in the lower part of the wake region. Because the blowing ratio is unity, the jet's velocity is not much higher than the freestream. In addition, as it is brought close to the surface (toward the formation of an O-shaped jet), the closer proximity with the surface intensifies the strain rate to mix out the weak jet before the turbulent stresses can react strong enough to be seen in Figure 145

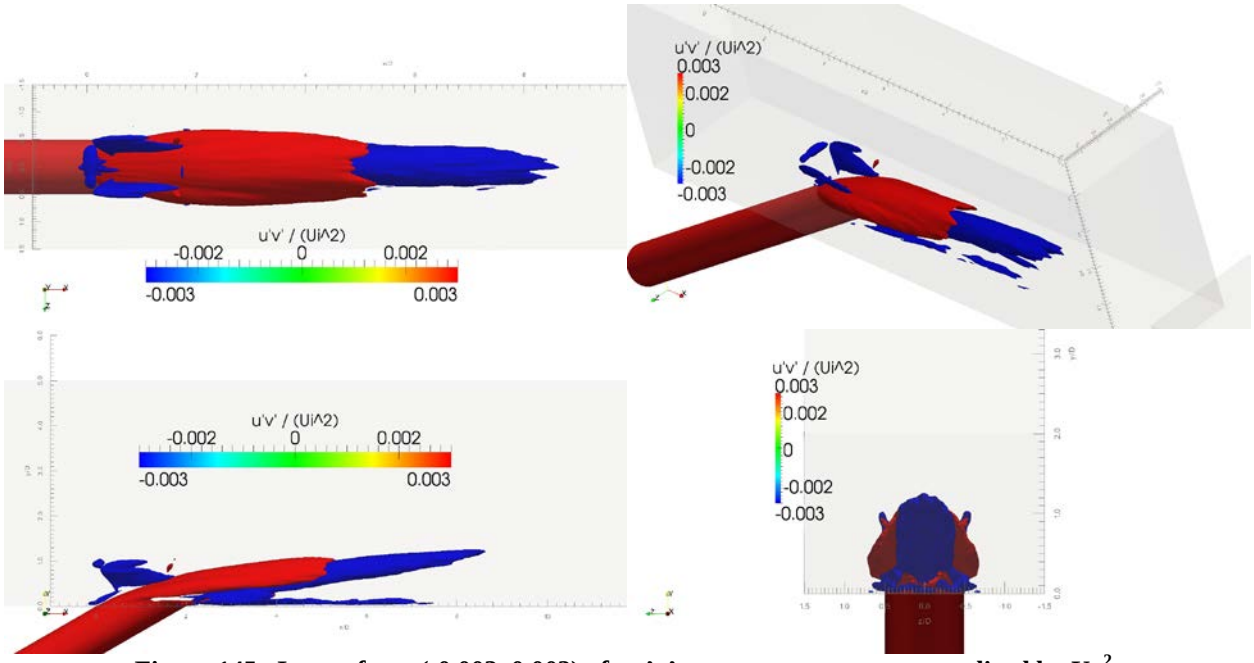

Figure 145 Iso-surfaces (-0.003, 0.003) of <u'v'> stress component normalized by U_∞^2.

At this point, the discussion has focused on wall-normal gradients and turbulent stresses. Next, Figure 146 shows the x-z strain-rate component. This component largely induces the spanwise spreading of the jet, which is important in the quest for more uniform film coverage

and accurate capturing of the spanwise spreading. It is interesting to first note the symmetry obtained in the LES data, which should further assure the reader of the simulation's statistical convergence. With this in mind, two straining layers are seen for either side of the jet. First, an outer layer on the sides of the jet shows the boundary between the freestream and the sides of the 'U'-shaped jet. As previously discussed, the blowing ratio of unity causes this shear layer to be weak comparative to the second shear layer, which marks the boundary between the jet and the inner wake region.

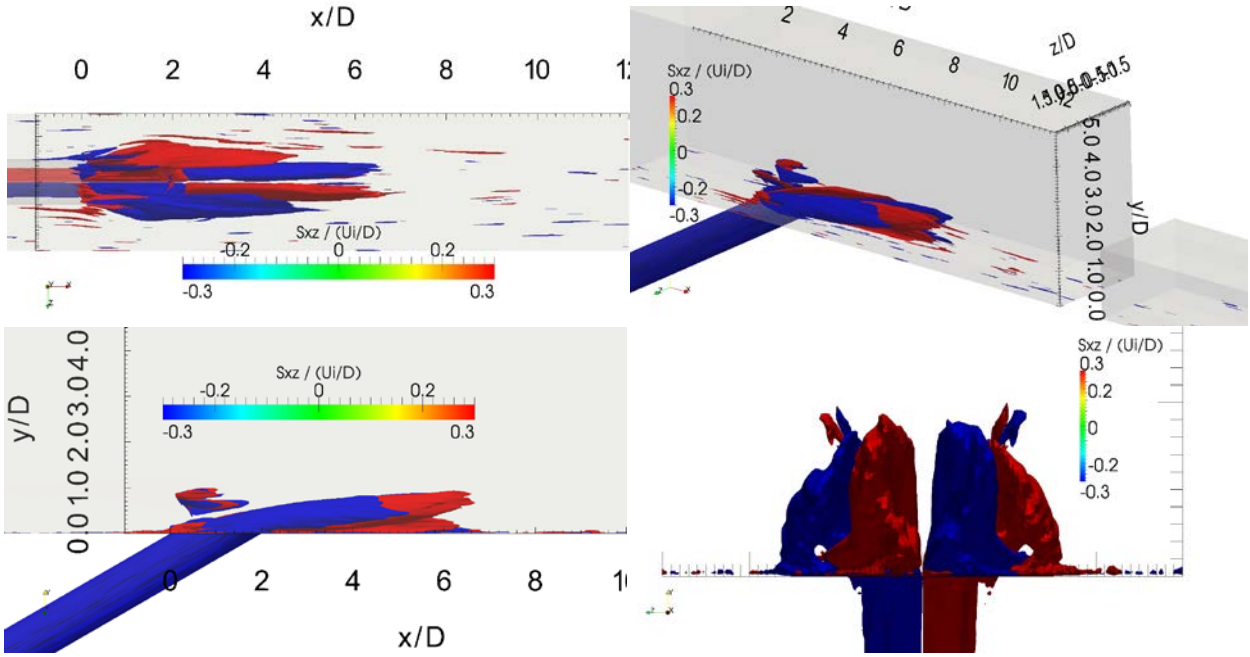

Figure 146 Iso-surfaces (-0.3, 0.3) of x-z component of mean strain rate tensor; normalized by U_∞/D.

The related spanwise turbulent stresses <u'w'> or R_{xz} are shown in Figure 147. The two shear layers are matched with two turbulent stress layers, as one might expect qualitatively from the Boussinesq hypothesis. The outer layer (between the jet and the hot crossflow) appears to be weaker than might be expected from Figure 146 (the discrepancy between the strength and endurance of the two layers is more dramatic in Figure 147). Again, the turbulent stresses are

struggling to adjust to the stretching of the shear layer by the CVP, but not nearly as much as in the previous S_{xy} vs. R_{xy} discussion.

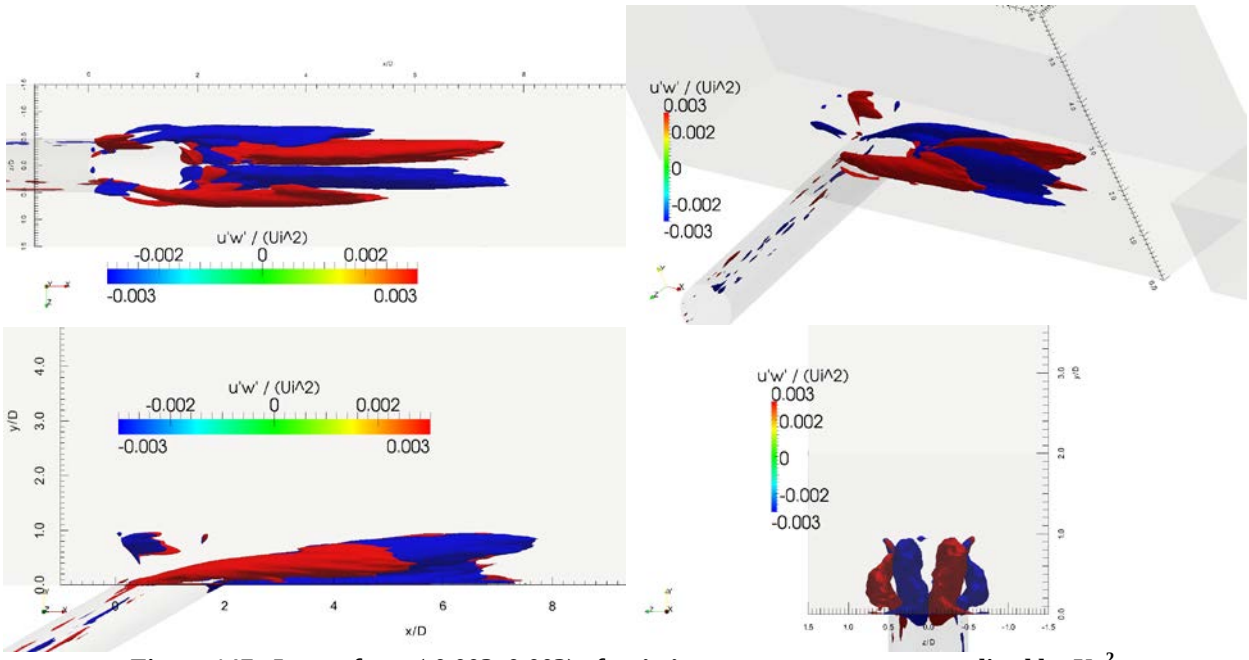

Figure 147 Iso-surfaces (-0.003, 0.003) of <u'w'> stress component normalized by U_∞^2.

Turning attention from turbulent stresses (momentum fluxes) to turbulent heat fluxes, the comparison between thermal gradients, which drive heat fluxes, and the turbulent heat fluxes themselves will now be explored. The wall-normal temperature gradient is shown in Figure 148 with a positive and negative gradient iso-surface. The structure of the temperature gradient field is simpler than the momentum, mostly because of the zero flux boundary conditions at the surface. The upper positive gradient (red surface) marks the boundary between the coolant jet-wake and the hot crossflow. The lower negative gradient (blue surface) shows that some of the hot crossflow has been brought underneath the jet by the CVP. These negative gradients would be expected (in the Boussinesq sense) to drive cooler air back to the surface (hence they should be beneficial).

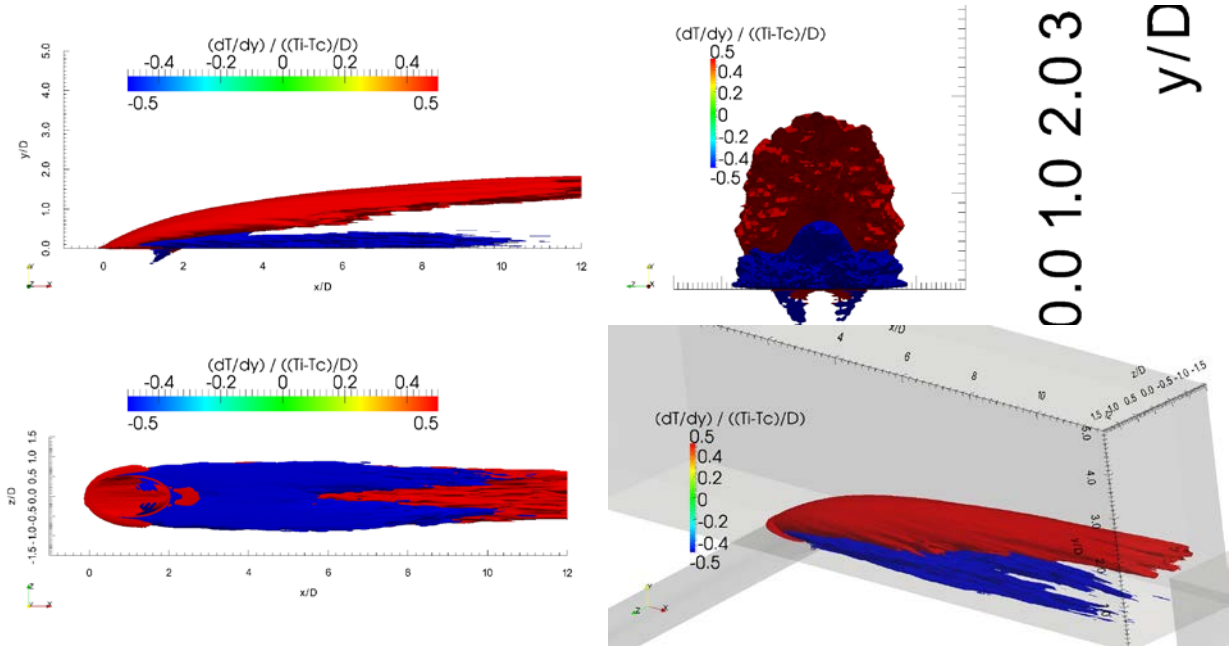

Figure 148 Iso-surfaces (-0.5, 0.5) of y component of mean temperature gradient vector; normalized by (T_∞-T_c)/D.

Figure 149 shows the corresponding <v'T'> turbulent heat flux in the wall normal direction. The negative heat flux on the boundary between the hot crossflow and coolant jet-wake shows that, as may be expected from Boussinesq, the hot crossflow is diluting the coolant. The lower region is more interesting and more vital to the purpose of film cooling. The thermal gradients suggest that the turbulent heat flux would be beneficial for the engineering task at hand, but the <v'T'> iso-surfaces show that this effect is not as strong as Boussinesq would suggest. It is vital to recall that this is the region of poor agreement with the temperature data from the experiment. So the observations here reflect the failure of the current simulation more than actual physics.

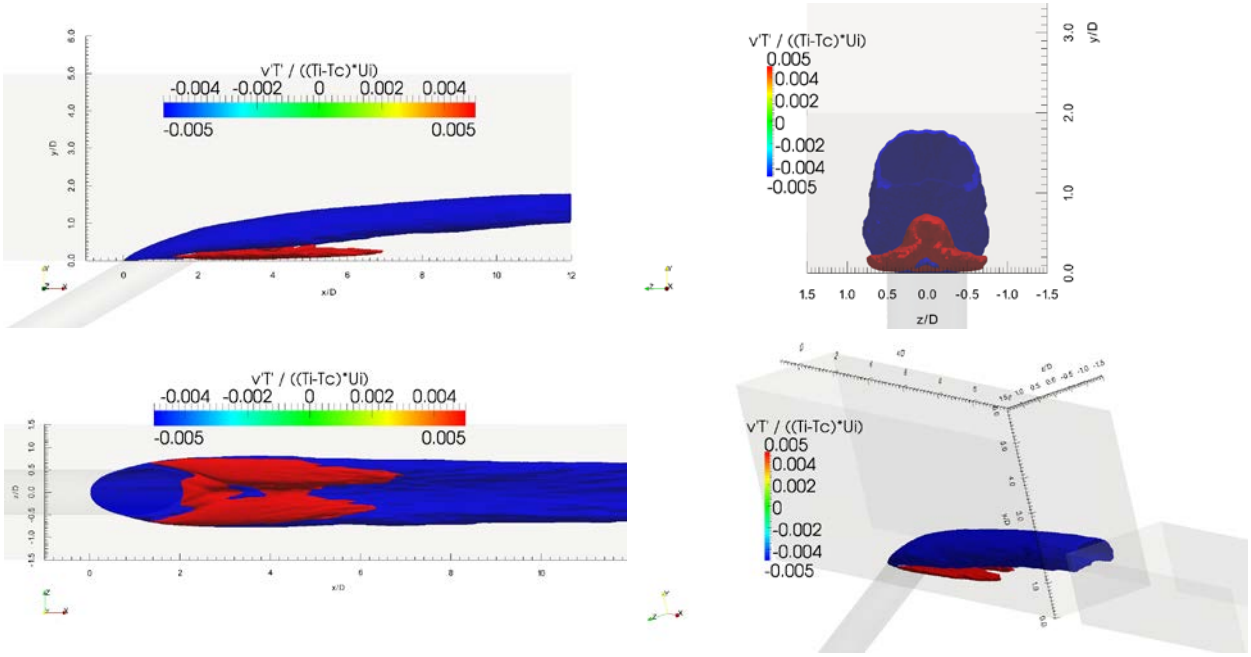

Figure 149 Iso-surfaces (-0.005, 0.005) of <v'T'> stress component normalized by $U_\infty*(T_\infty-T_c)$.

Finally, the spanwise temperature gradients and heat fluxes <w'T'> are shown in Figure 150 and Figure 151 respectively. There is more similarity with the x-z strain rate field than in the wall-normal case. As the case with the strain rate, there are two distinct regions of thermal gradients, symmetrically mirrored across the center-plane. The outer, dominant gradient region shows the spanwise boundary of the coolant whereas the inner gradient shows a small area of hot air that has made its way into the wake region via the CVP. This is mixed out rather effectively; much more so than the wake region itself (in terms of velocity). The heat fluxes qualitatively follow the Boussinesq expectation, except near the wall, where we have noted the main difference between simulation and experiment. This difference is the key to the main disagreement between numerical and experimental data. It is worthwhile to note that the current simulation used a constant turbulent Prandtl number for the subgrid-scale heat fluxes. A dynamic method similar to the compressible approach of Moin et al. (1991) could drastically improve the subgrid-stress model in the near-wall region.

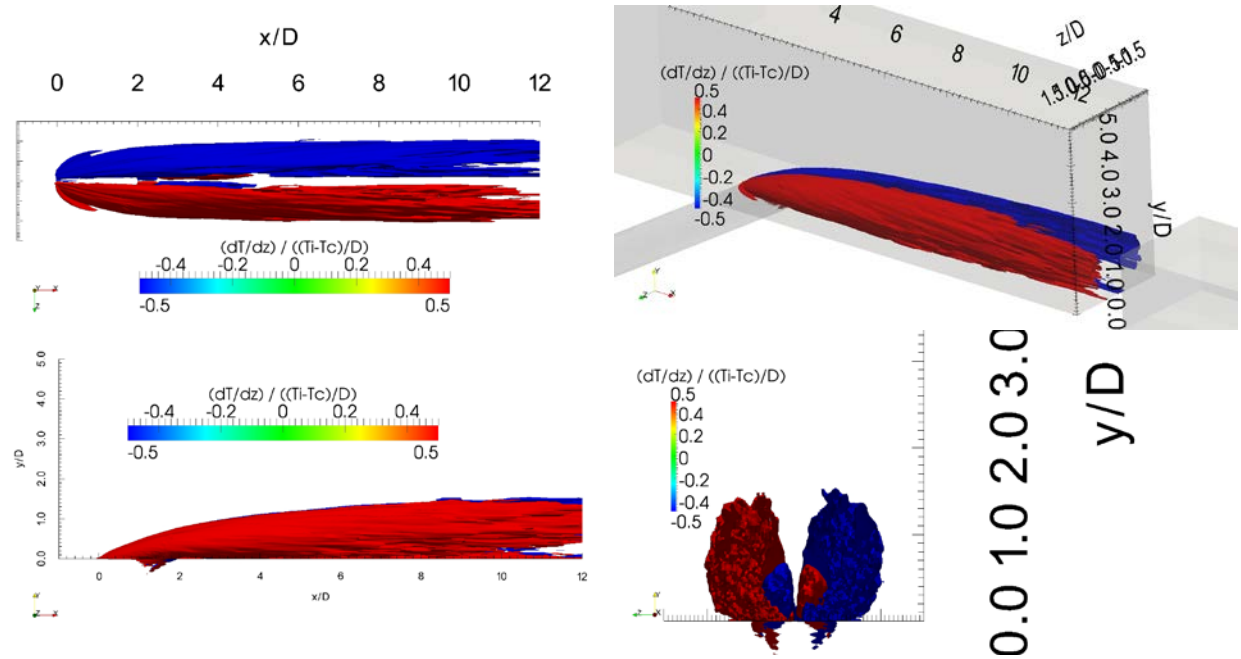

Figure 150 Iso-surfaces (-0.5, 0.5) of z component of mean temperature gradient vector; normalized by (T_∞-T_c)/D.

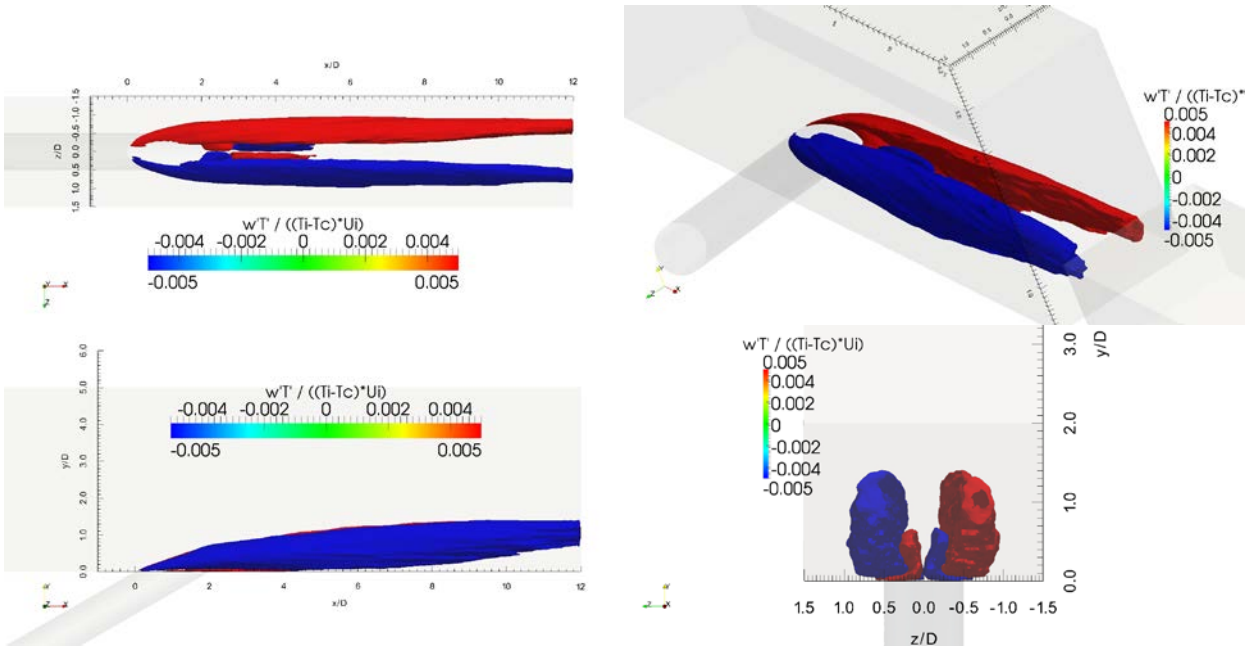

Figure 151 Iso-surfaces (-0.005, 0.005) of <w'T'> stress component normalized by U_∞*(T_∞-T_c).

9.5.2 High Blowing Ratio M = 1.9

The percent resolution of TKE is shown in Figure 152 with two iso-surfaces. The majority of the shear layers in the jet and wake regions are between 90% and 95% resolved, which is acceptable resolution for LES (Pope 2000). The portion not 90% resolved is the portion just downstream of the trailing edge of the hole in the wake region. This helps explain the lack of spreading here, as well as the over-prediction of the extent of the wake region. Further resolution here could dramatically improve the LES prediction by 'starting on the right foot' in the first few diameters downstream of the hole. This is also the case for the M = 1 simulation (see Figure 138).

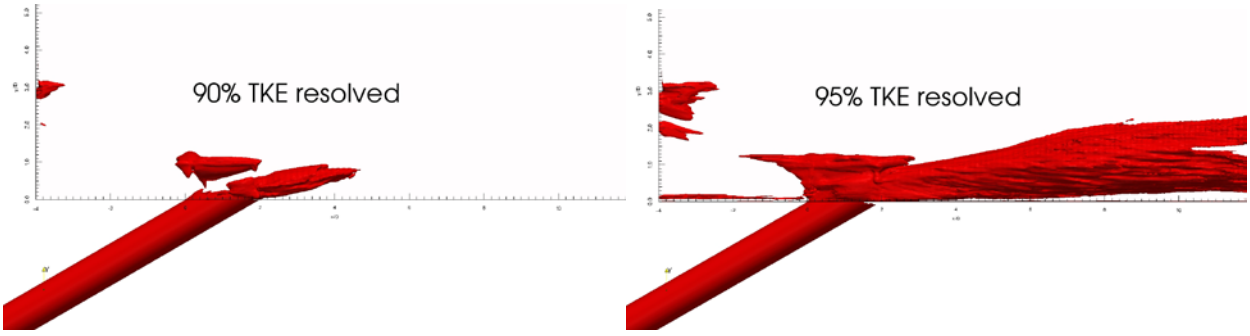

(a) (b)

Figure 152 Iso-surfaces of percent turbulent kinetic energy in the resolved scales; (a) 90% resolved, (b) 95% resolved.

The x-velocity mean contours are shown in Figure 153, clearly showing the upside-down 'U'-shaped topography with wake region in the middle. The boundary layer thickens as it approaches the injection and thins in the acceleration around the hole. The 'core' of the jet, as marked by streamwise velocity, is split into two spots on either side of the jet.

The mean wall-normal velocity iso-surfaces, Figure 154, show two phenomena: the vertical component of the initial injection and the secondary flow caused by the CVP. The initial vertical velocity region is the upper layer of positive (red) surface, shown coming to a tip around x/D = 5.

Afterward, the momentum of the freestream has redirected the jet such that it is primarily in the streamwise direction. Then the positive updraft in the middle (wake) of the coolant and the downdraft in the jet region of the coolant clearly marks the CVP pattern.

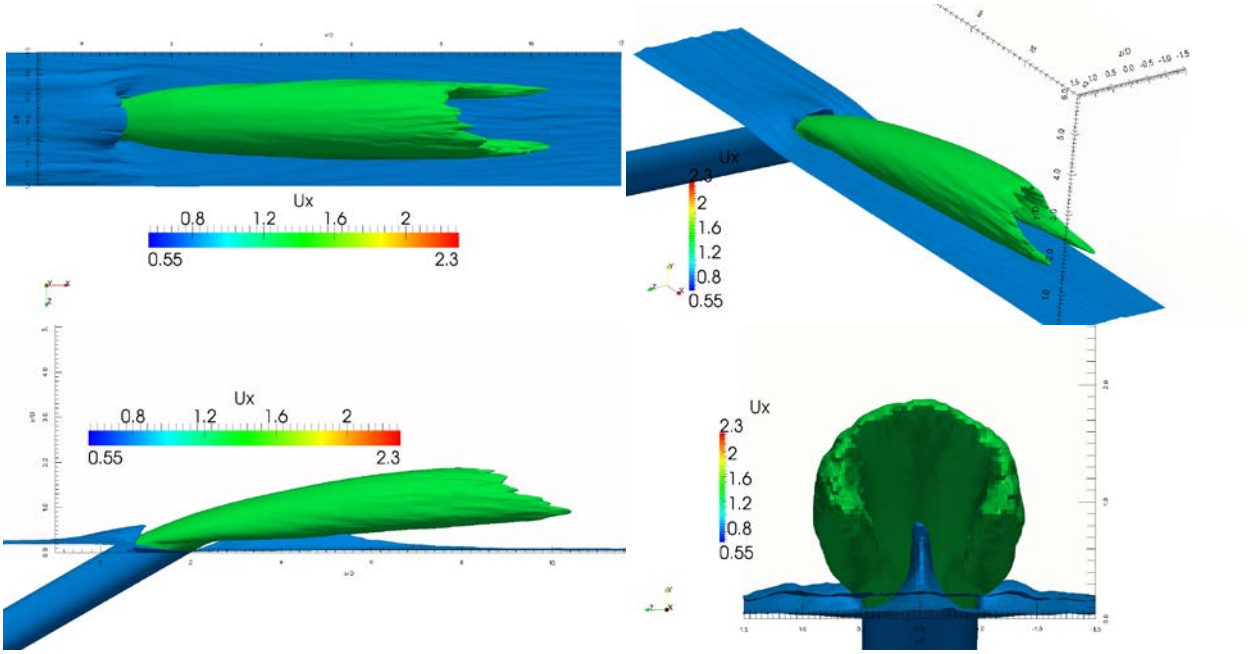

Figure 153 Iso-surfaces (0.8, 1.3) of mean streamwise velocity, normalized by U_∞.

The spanwise velocity mean contours of Figure 155 complete the picture of the CVP. Near the surface the secondary flow is toward the center-plane, while the jet region is pulled away from the center-plane (and down the sides of the coolant region), which gives rise to the upside-down 'U'-shaped streamwise velocity contours. This CVP action tends to sweep high temperature gas underneath the coolant, Figure 156. This is well-known to be detrimental to the film cooling effectiveness.

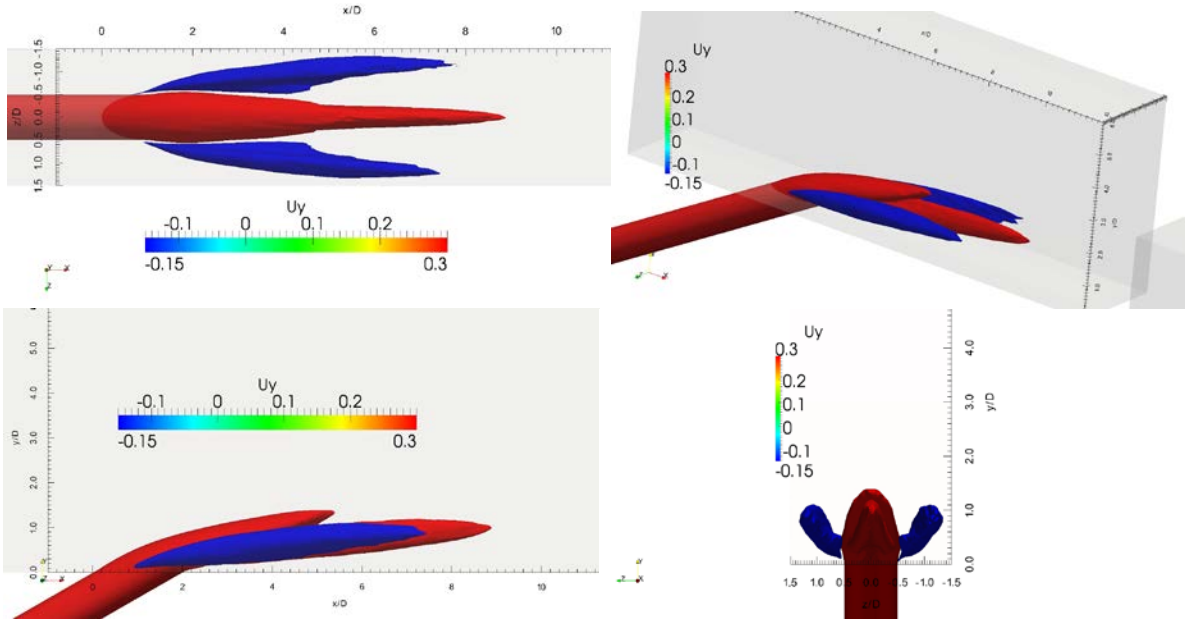

Figure 154 Iso-surfaces (-0.15, 0.3) of mean wall-normal velocity, normalized by U_∞.

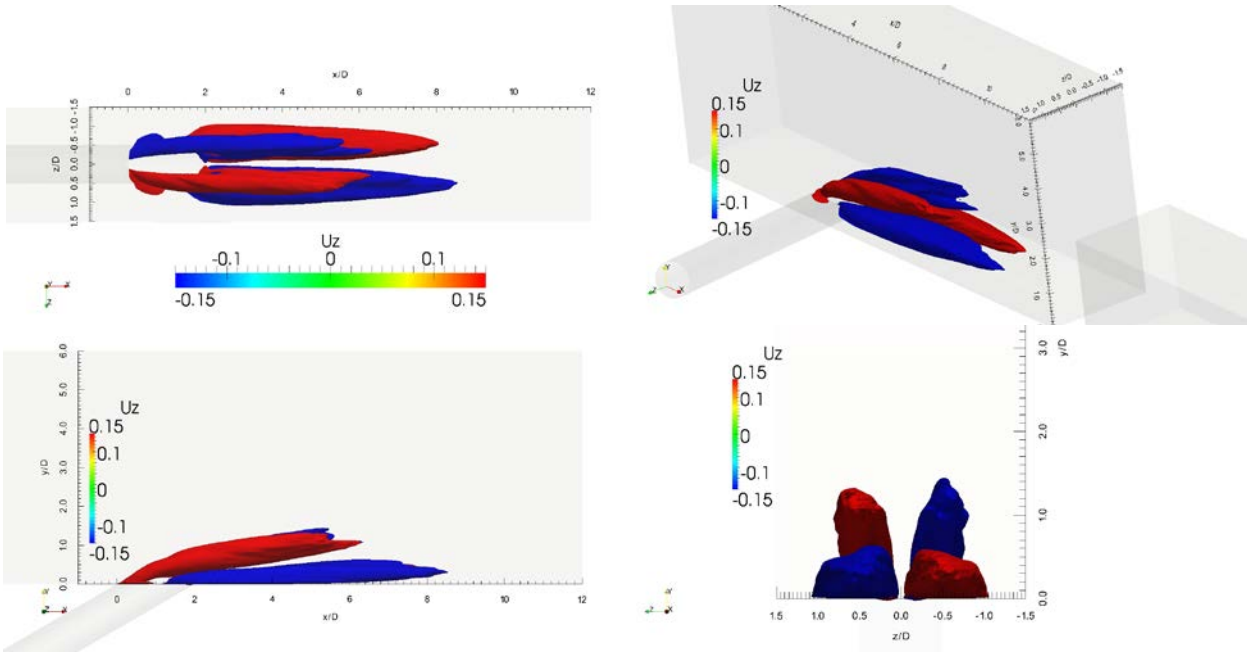

Figure 155 Iso-surfaces (-0.15, 0.15) of mean spanwise velocity, normalized by U_∞.

With the velocity fields in mind, the gradient and turbulent stress fields for velocity and temperature are discussed next. For velocity, since the Reynolds stress tensor is symmetric, the

symmetric part of the velocity gradient temperature is commonly used for the Boussinesq approximation of the turbulent stress field. If the constitutive relation between turbulent stresses and the velocity gradients were that simple, then the RANS models would likely perform much better.

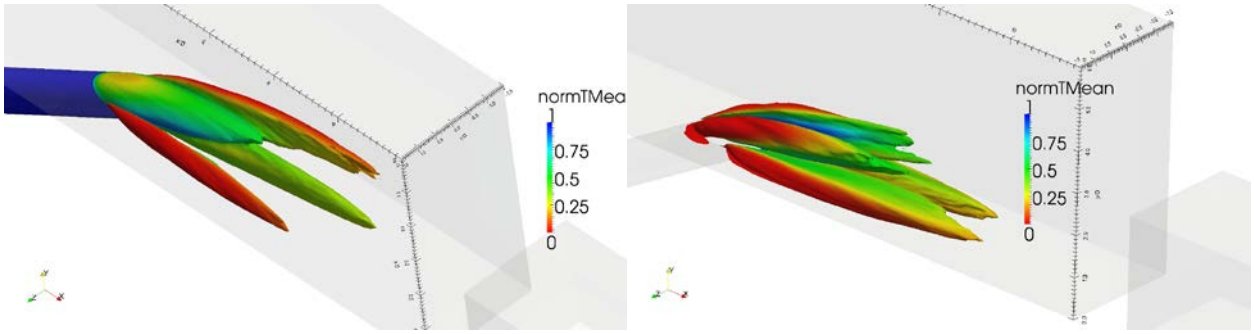

(a) (b)

Figure 156 Iso-surfaces of (a) mean wall-normal velocity and (b) mean spanwise velocity, colored by normalized temperature.

Figure 157 primarily shows the wall-normal gradient of streamwise velocity (du/dy >> dv/dx). The jet region is bounded by negative gradient on top with the freestream and positive gradient underneath with the wake region. The wake region has small negative gradients below and on either side (as it approaches an 'O'-shape) followed by a large region of positive gradient approaching the wall.

The related Reynolds stress <u'v'> is shown by iso-contour in Figure 158. The boundaries of the jet are clearly marked by the expected Reynolds stresses working to spread the jet. The wake region has much weaker stresses for its gradients. While the LES predicts the spreading of the jet region well, this region is less vital than the prediction of the near wall behavior. The lack of spreading in the LES was already demonstrated, but further shown here.

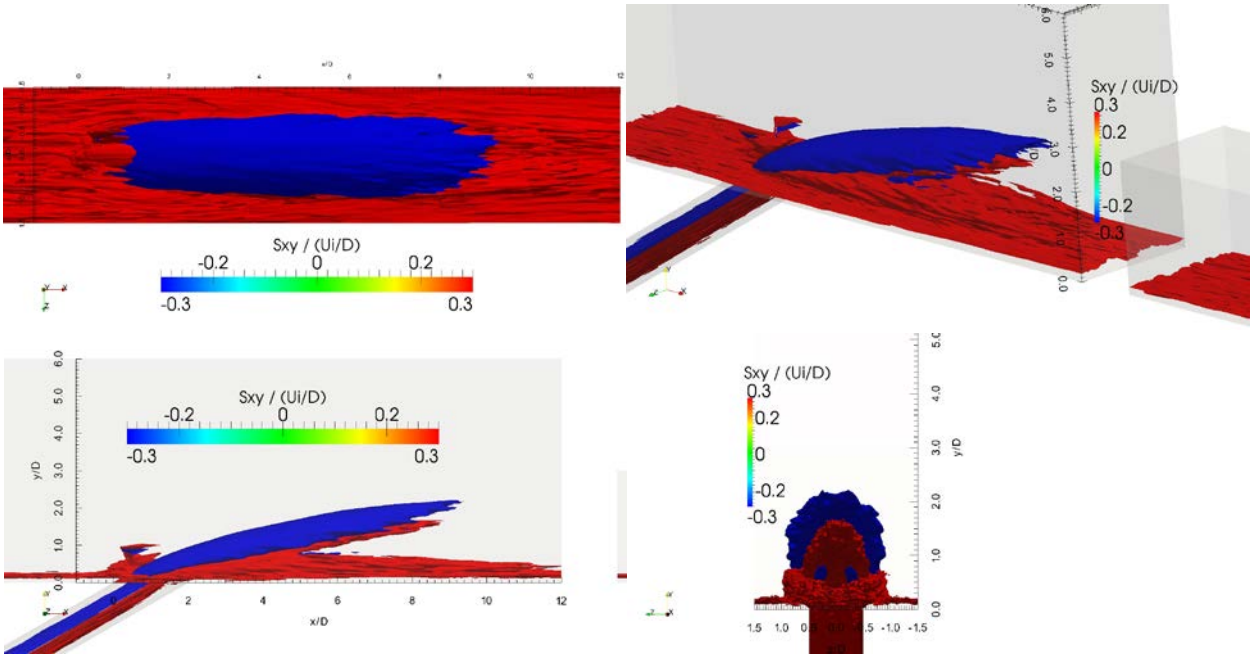

Figure 157 Iso-surfaces (-0.3, 0.3) of mean x-y strain-rate component, normalized by U_∞/D.

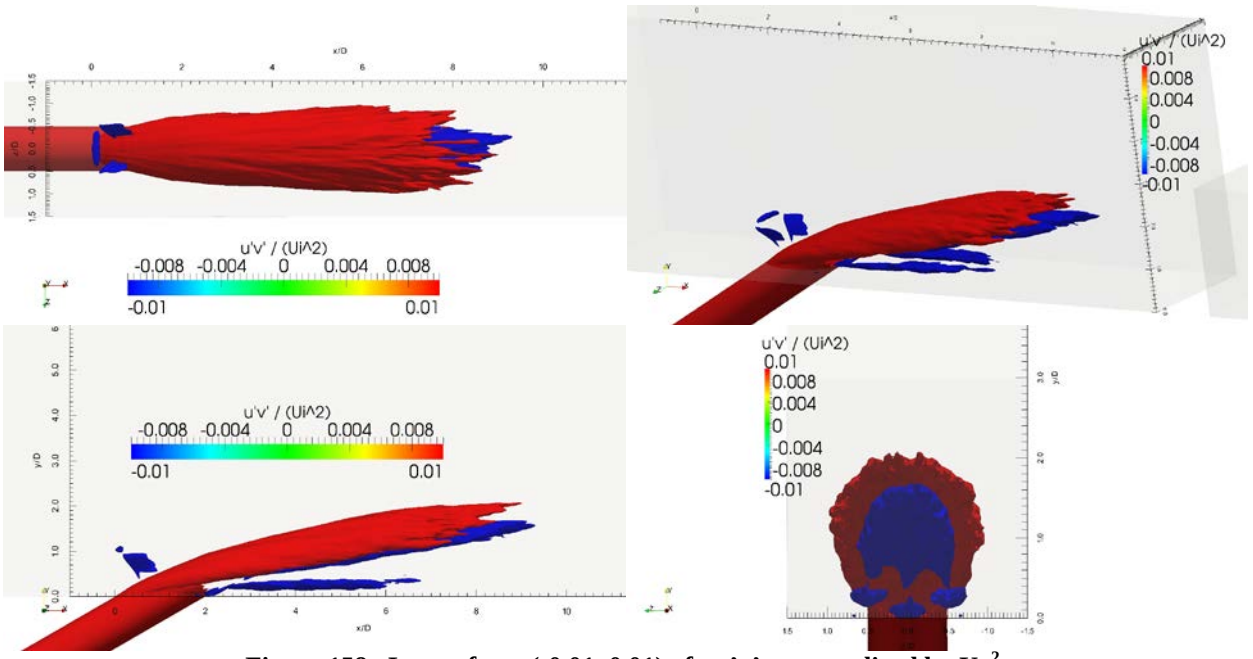

Figure 158 Iso-surfaces (-0.01, 0.01) of <u'v'>, normalized by U_∞^2.

The spanwise gradient iso-surfaces are shown in Figure 159 (assuming du/dz >> dw/dx).

The same layered system as the M = 1 case is apparent, highlighting the presence of the jet

region on either side of the central wake region. The spreading of the jet is also apparent in the divergence of these shear layers. The resulting spanwise stresses <u'w'> are shown in Figure 160. The Boussinesq approximation appears qualitatively correct, except around the hole, where the viscoelastic effects of the turbulent field are evident in its non-instantaneous adjustment to the rapid shear layers.

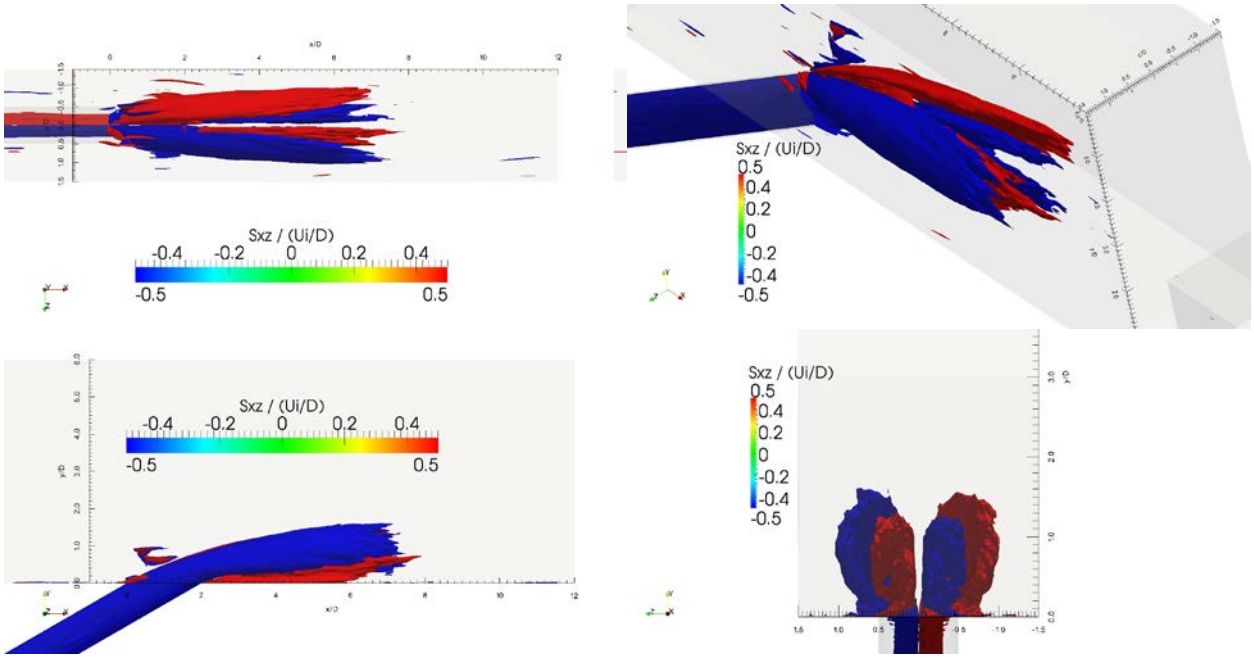

Figure 159 Iso-surfaces (-0.5, 0.5) of mean x-z strain-rate component, normalized by U_∞/D.

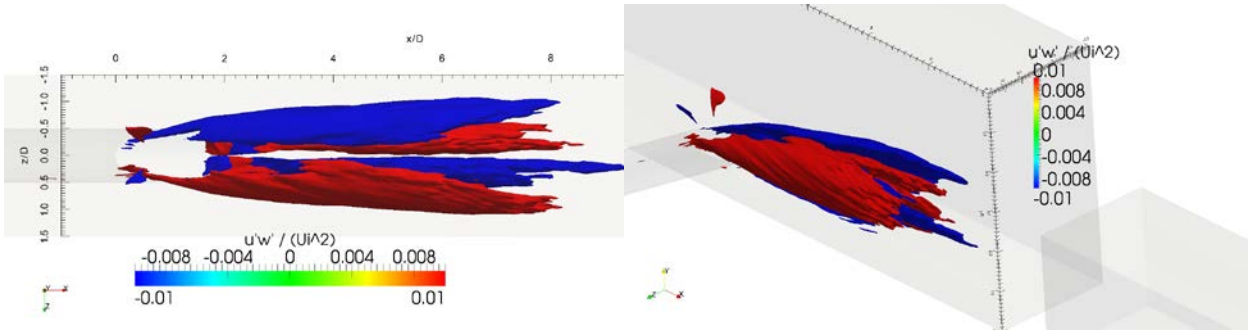

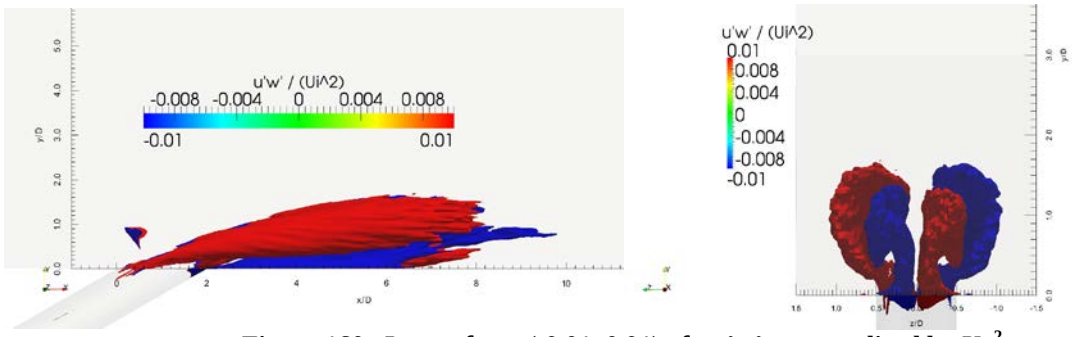

Figure 160 Iso-surfaces (-0.01, 0.01) of <u'w'>, normalized by U_∞^2.

Moving to the thermal gradient and stress fields, Figure 161 shows the wall-normal temperature gradient dT/dy. There are three primary features. First the strong positive gradient on the top of the jet marks the boundary with the freestream. Below this, there is a smaller, less persistent region of negative gradient marking a boundary between the jet and the wake region, where hot crossflow has penetrated into the separation region via the CVP action. Finally, near the wall, there is a larger, more persistent negative gradient region marking the transition from the jet's 'U'-shape arms to the hot gas swept near the surface. This gradient is crucial in driving cooler fluid back to the wall.

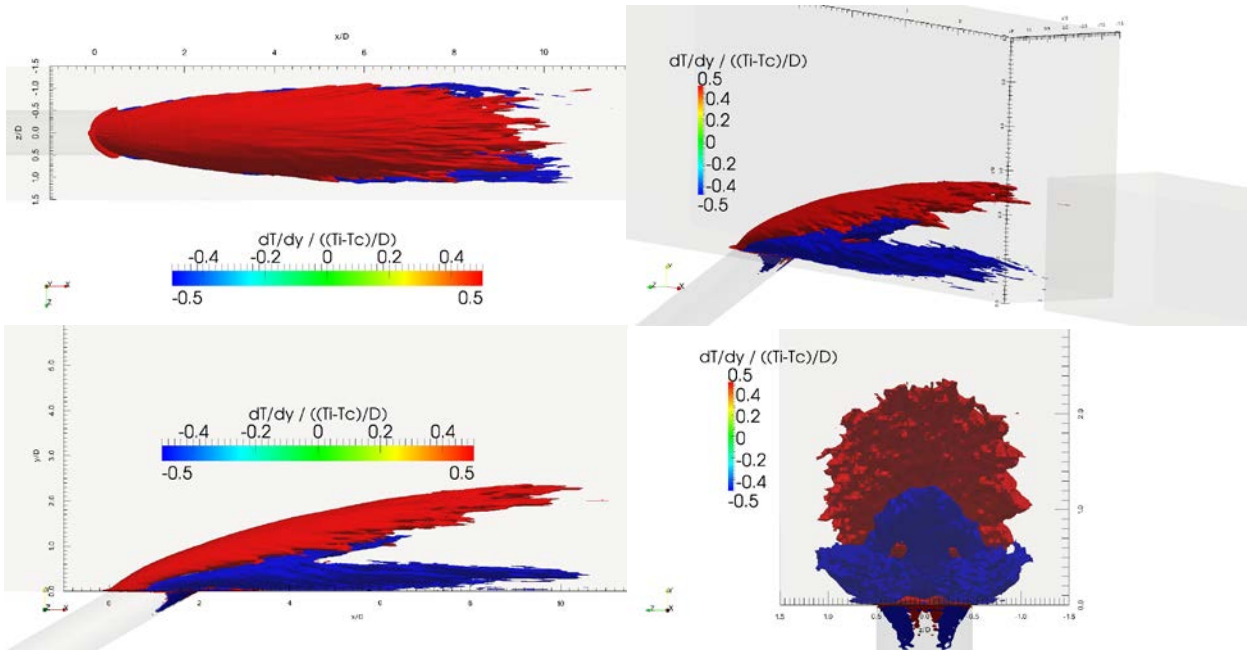

Figure 161 Iso-surfaces (-0.5, 0.5) of mean temperature y-gradient, normalized by $(T_\infty-T_c)/D$.

Figure 162 shows the related wall-normal turbulent heat flux <v'T'>. While the two upper regions of wall-normal gradient can be matched with their Boussinesq counterparts, the lower region (previously identified as crucial) does not produce the spreading back to the wall. This is primarily due to the blocking effect of the wall on the v' fluctuations. This wall-effect slows the progress of the jet in spreading to the wall and providing higher adiabatic effectiveness.

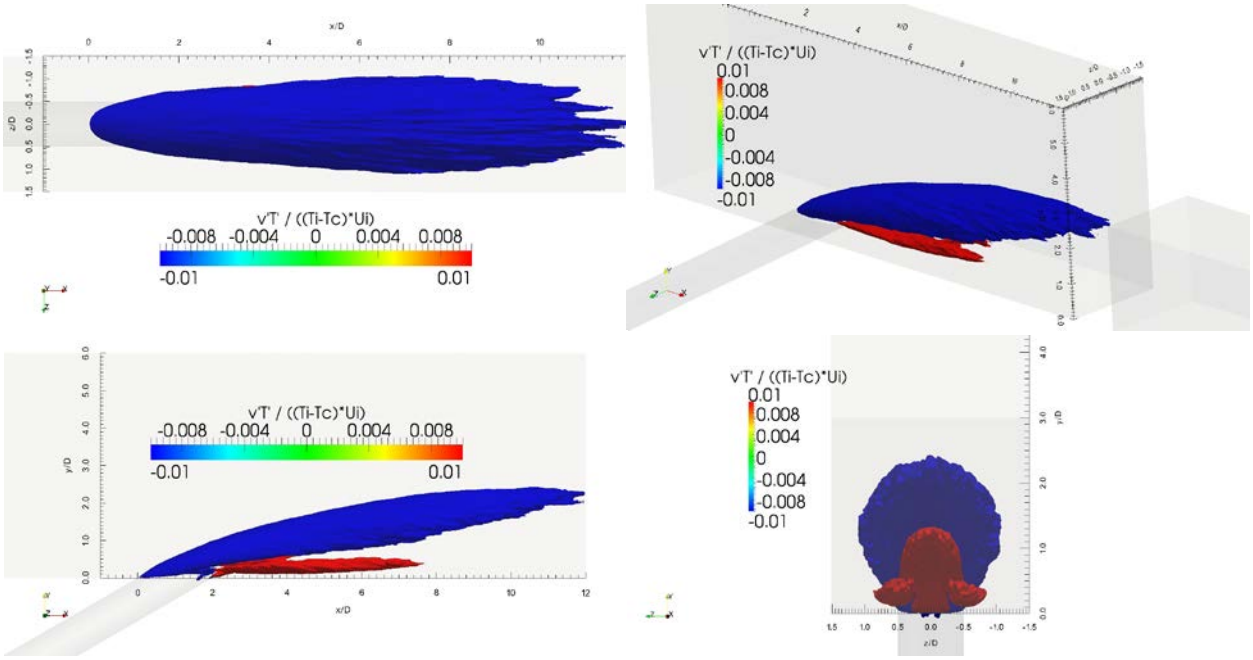

Figure 162 Iso-surfaces (-0.01, 0.01) of wall-normal turbulent heat flux <v'T'>, normalized by $(T_\infty-T_c)*U_\infty$.

The final gradient to be analyzed is the dT/dz spanwise temperature gradient, Figure 163. This has a similar structure to the x-z strain-rate of Figure 159 with outer and inner layers. The outer layer bounds the outside of the jet and the inner layer is the boundary of the jet and wake regions. Unlike the strain-rate, however, the thermal gradients in the wake region are more quickly dissipated by the mixing. This means that the 'U' shape of the thermal contours is more quickly washed out into a circular jet shape. The turbulent heat flux in the spanwise direction echoes the gradients in the Boussinesq sense, Figure 164, except near the wall at larger x/D.

This is the crucial region, however for spreading the near-wall coolant along the span an providing more uniform adiabatic effectiveness. This the main failure (as in the M = 1 case) of the current LES model, and the dynamic Pr_t calculation could provide better predictions of these stresses and hence a better match with experiment in the near wall region.

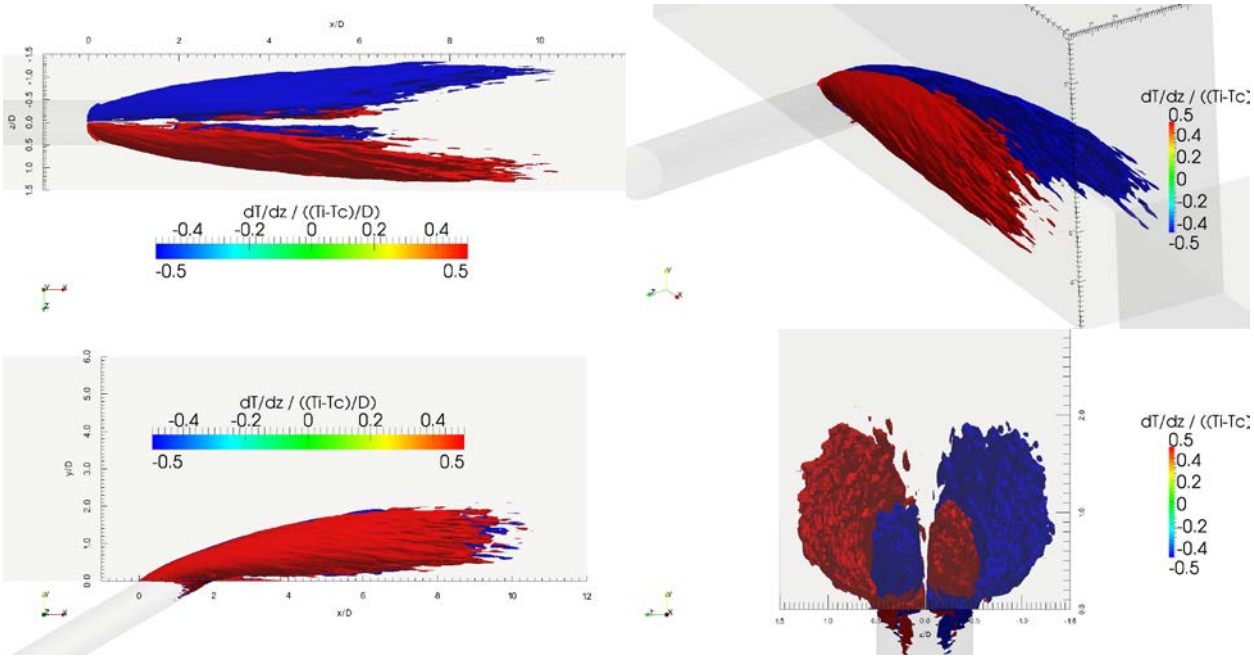

Figure 163 Iso-surfaces (-0.5, 0.5) of mean spanwise temperature gradient, normalized by $(T_\infty-T_c)/D$.

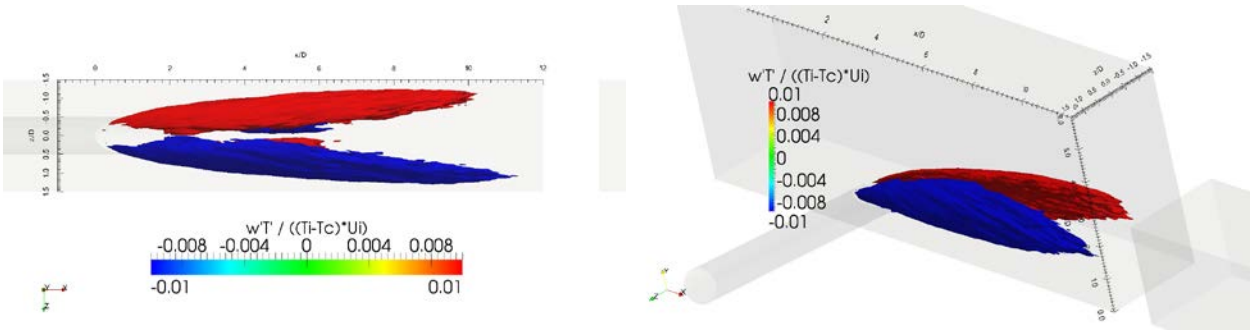

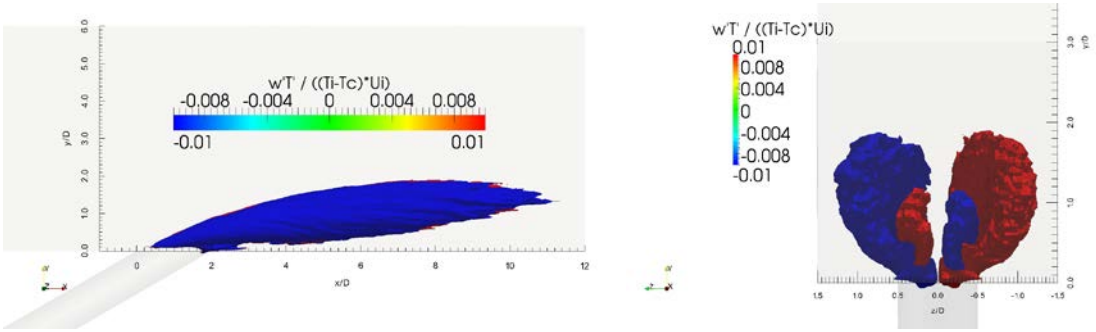

Figure 164 Iso-surfaces (-0.01, 0.01) of spanwise turbulent heat flux <w'T'>, normalized by $(T_\infty-T_c)*U_\infty$.

As it stands, the results of the M = 1.9 case upholds conclusions drawn from the M = 1.0 case. The LES does well to predict the coolant flown is vital for film cooling effectiveness.

9.6 Conclusions

In this final chapter, two large-eddy simulations were performed for a cylindrical film cooling hole: one moderate blowing ratio and one high blowing ratio. The moderate blowing ratio exhibited a small detached region of poor thermal protection followed by reattachment and dramatically improved protection of the surface. The higher blowing ratio lifted from the surface and provided only very meager protection due to the jet spreading back to the surface.

In both simulations, the LES model (control volume, dynamic Smagorinsky) predicted the dynamics of the jet with much more physical fidelity than the RANS data. Near the wall, however, the lateral spreading of the jet away from the centerline and vertical spreading of back to the surface were under-predicted by the LES results. This is one of the main findings of this thesis. While LES does well for the majority of the coolant jet, the near-wall region still suffers from inaccurate turbulence models. For film cooling applications, LES struggles in the most important region to the heat transfer engineer. Indeed, the difficulty of near-wall high-Re number turbulence predictions, even in LES, rears its ugly head for film cooling applications.

Meanwhile, the instantaneous snapshots of various quantities elucidated the wake vortices, roller vortices, and other features of the unsteady dynamics of a coolant jet. One interesting result was the unsteady reattachment events occurring to the sides of the centerline, where packets of coolant were swept downward by the CVP to the surface. These events were characterized by not only a higher film effectiveness, but also higher wall shear stress. This indicates that this region is likely to experience higher heat transfer coefficients, damping the effect of receiving packets of lower temperature.

CONCLUSIONS AND FURTHER WORK

The numerical prediction of film cooling was studied using both steady RANS and unsteady LES. Due to the inexpensive nature of RANS computations, two parametric studies were performed to show various aspects key to numerical analysis of film cooling. This laid the foundations for LES of film cooling, first through commercial software, then through open source software.

For RANS simulations, the effects of grid structure and resolution, as well as boundary placement and specification were studied. The placement of the inflow and thickness of the boundary layer was the most influential on the effectiveness results. To address this, the application of a $1/7^{th}$ power law velocity profile did well to replace a more naturally developed boundary layer. Such a profile was not satisfactory for an inflowing boundary layer in LES, however, even when random perturbations were added. Instead, a switch to open source CFD software enabled the coding and successful implementation of a recycling-rescaling method to provide a more realistic boundary condition. The other influential factor in the RANS studies was the placement of the freestream boundary. Since these studies were performed with commercial software, the study was limited to symmetry conditions at the freestream. This cause a noticeable difference for the high blowing ratio case M = 2. Upon switching to open source software, mixed boundary conditions were applied to allow for a more natural freestream boundary and better treatment of the high trajectory film jet (e.g. low freestream acceleration caused by mass injection effect). Another important conclusion of the RANS studies was the resolution near the exit of the hole. With higher resolution, the lift-off and reattachment behavior of the jet was captured well, despite the other shortcomings of RANS.

The LES study was begun with a comparison of discretization schemes. Using a flux-limited second-order scheme proved very detrimental to the results of the simulation. Upwind-biased schemes (PUW, QUICK) did well, but the pure central scheme (PCD) showed the best results, as would be expected due to its lack of numerical diffusion. The caveat with PCD is the unphysical oscillations and over-shoot at sharp gradients such as the thermal gradient between the jet and crossflow.

The main thrust of this thesis was the prediction of LES for film cooling, as well as insight into unsteady phenomena. Important vortex structures were noticed, but the structure of the wake region was much more chaotic than portrayed in previous works, which tend to attempt a simplistic picture of jet in crossflow structure. Unsteady reattachment events were noticed on the sides of the jet due to the force of the CVP working to pull intermittent low temperature regions from the side of the coolant jet underneath into the wake. This provides better adiabatic wall effectiveness, but also increases the wall shear stress (hence, likely increasing heat transfer coefficient).

The characterization of the coolant flow using the typical eddy diffusivity model is successful in the sense that the Reynolds stresses follow the gradients in general. The specifics of its predictions however, yield a highly chaotic and unclear picture. This indicates, as well known in literature, that the eddy diffusivity model, while useful, is flawed. The most important conclusion, in the opinion of the author, is the need for development in near-wall modeling for partial resolution simulations. DNS remains out of reach for high-Re or large scale engineering simulations. LES still struggles in the near wall region because the “large” eddies near the wall are actually quite small, yet still influential.

APPENDIX: STATISTICAL STEADINESS AND CONVERGENCE

APPENDIX: STATISTICAL STEADINESS AND CONVERGENCE

The following plots are included to illustrate the engineering judgment used to determine when the LES was statistically steady (ready to begin monitoring statistics) and when such statistics had converged. Statistical steadiness refers to the simulation becoming (for all practical purposes) independent of its initial conditions. This is judged by plotting the actual signal over the first flow through times of the unsteady simulation. Statistical convergence is declared when the mean and second order statistics are not changing much, relative to the mean calculated at the previous time steps. This is judged by plotting the evolution of the statistic as calculated at each time step using all information previous to that time step. This indicates that the simulation can be safely truncated in time at this point.

M = 1.0 Statistical Steadiness

These plots show the starting transients for M = 1.0 and the simulation reaching statistical steadiness. It is useful to note that these plots do not contain the very earliest time steps in the unsteady simulations, therefore the existence of starting transients is not fully shown.

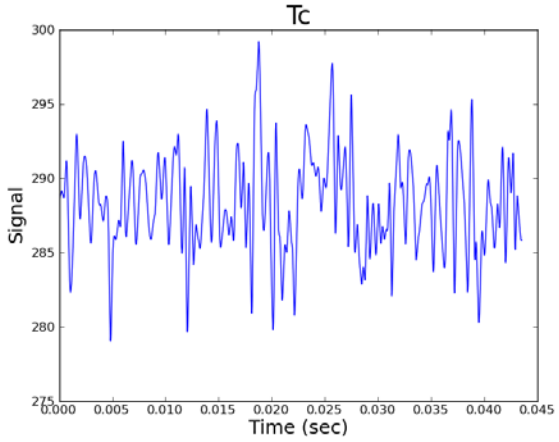

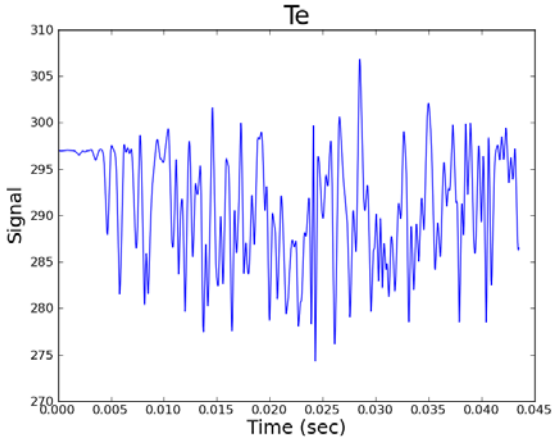

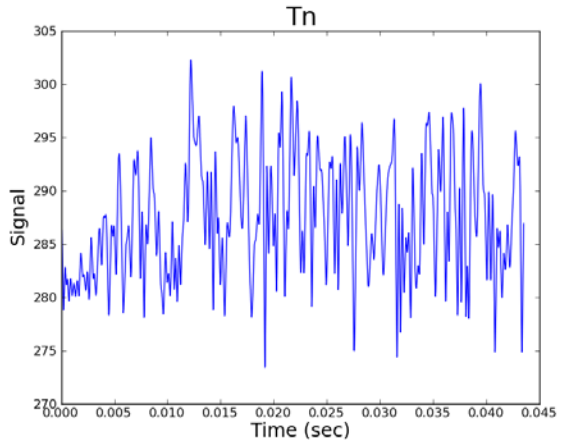
Tn
Signal
Time (sec)

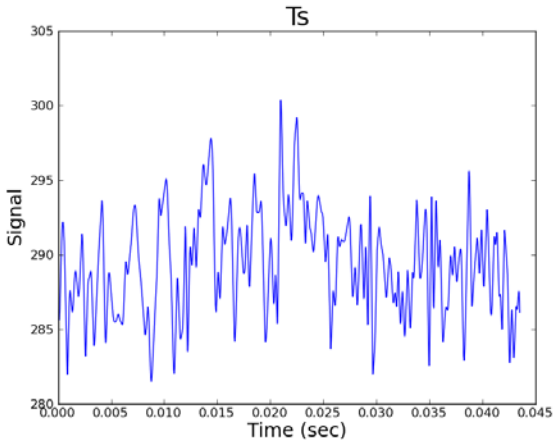
Ts
Signal
Time (sec)

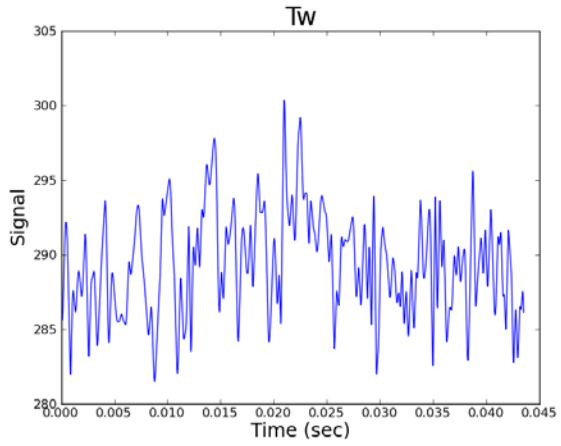
Tw
Signal
Time (sec)

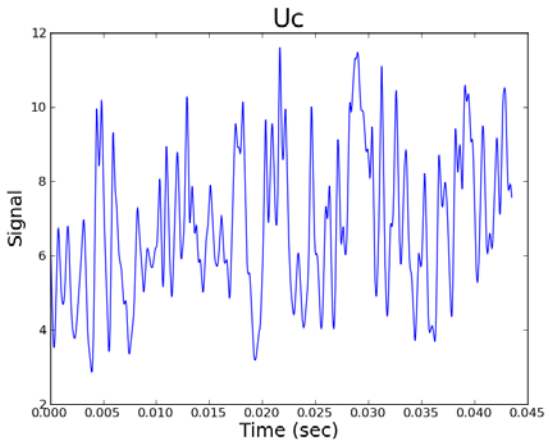
Uc
Signal
Time (sec)

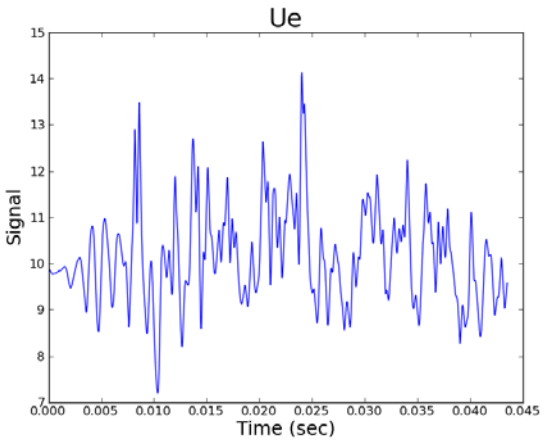
Ue
Signal
Time (sec)

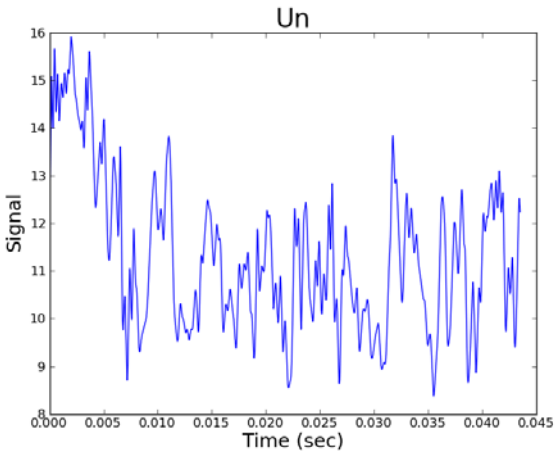
Un
Signal
Time (sec)

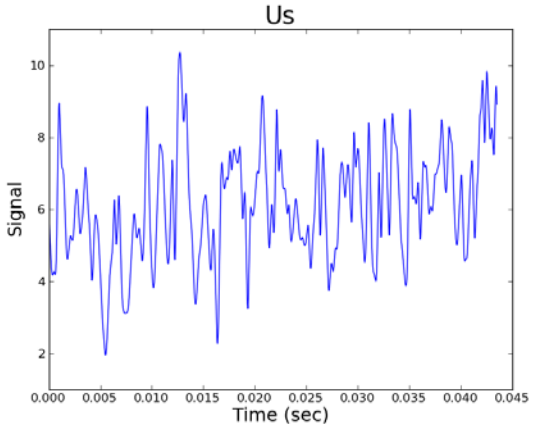
Us
Signal
Time (sec)

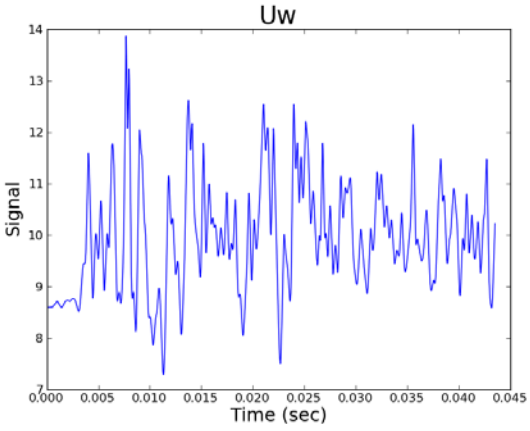
Uw
Signal
Time (sec)

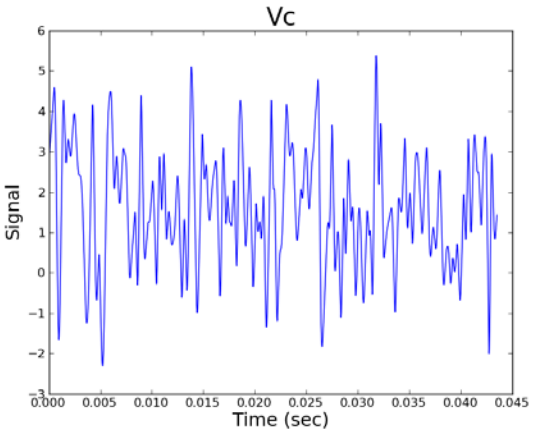
Vc
Signal
Time (sec)

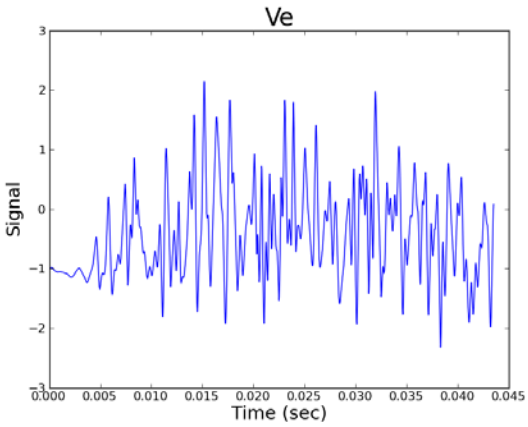
Ve
Signal
Time (sec)

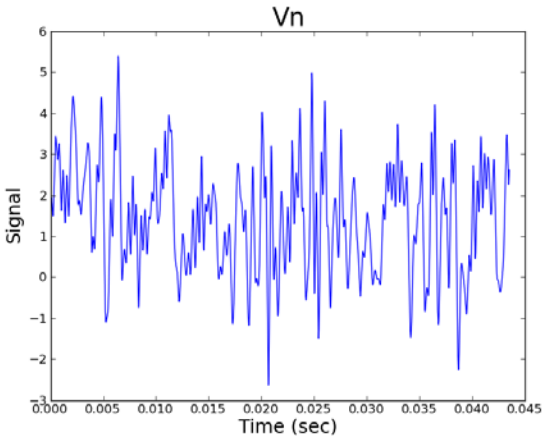
Vn
Signal
Time (sec)

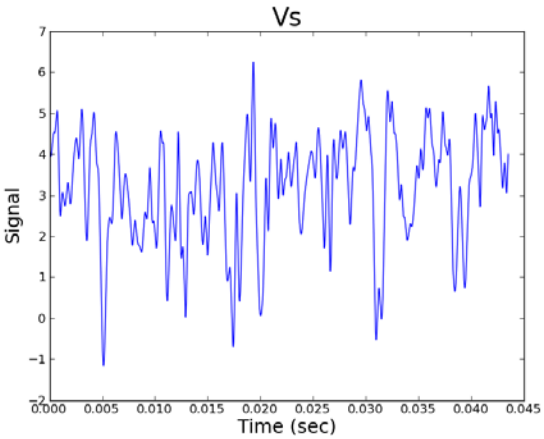
Vs
Signal
Time (sec)

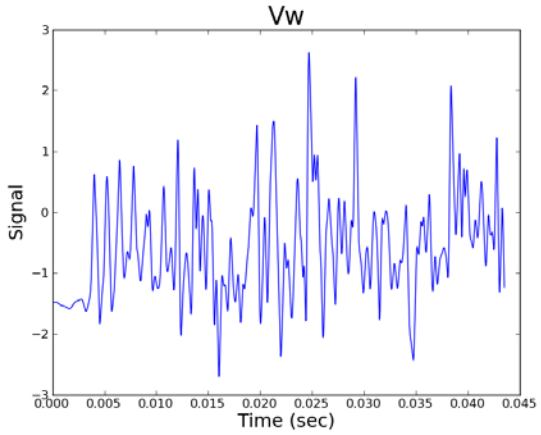
Vw
Signal
Time (sec)

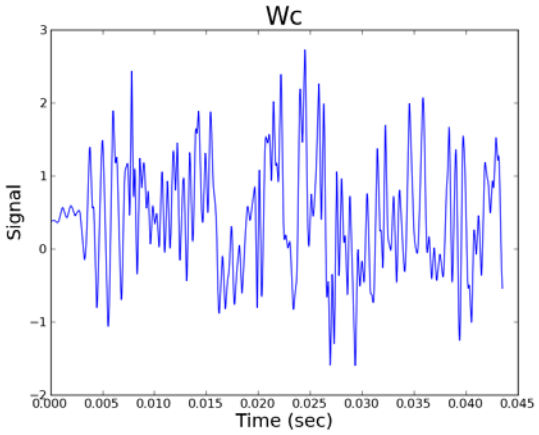
Wc
Signal
Time (sec)

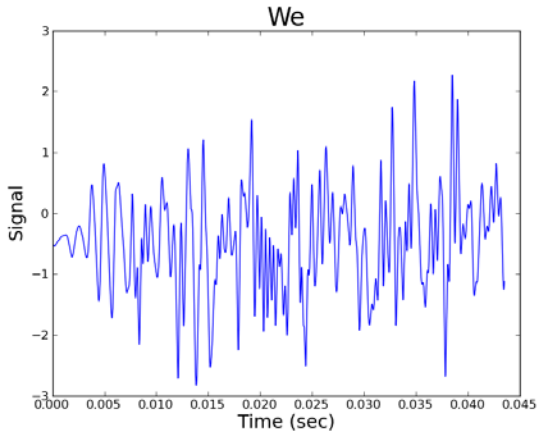
We
Signal
Time (sec)

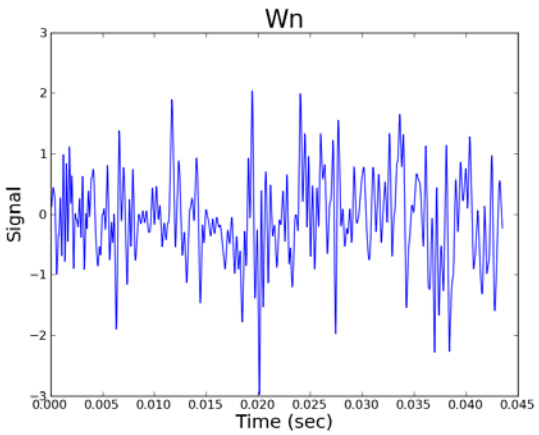
Wn
Signal
Time (sec)

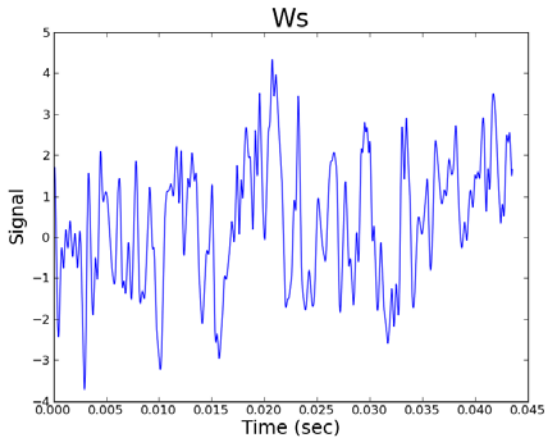
Ws
Signal
Time (sec)

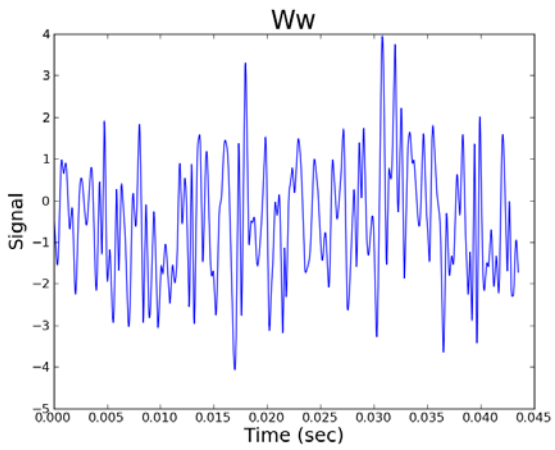
Ww
Signal
Time (sec)

M = 1.0 Statistical Convergence

The following plots show the evolution of the mean and second order statistics (entitled "correlation"). Theses plots show the statistics converging to the value at infinite time. The plots of course do not show perfect convergence, but good enough within the engineering judgment of the author for the task at hand.

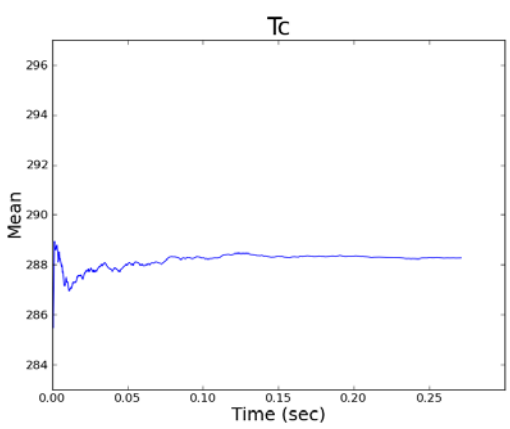

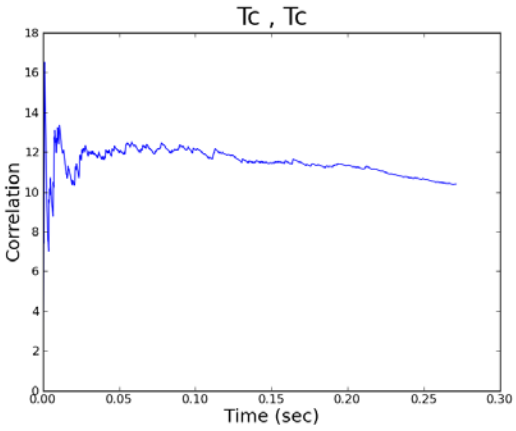

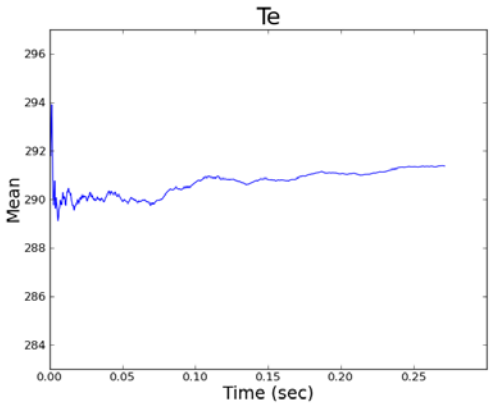

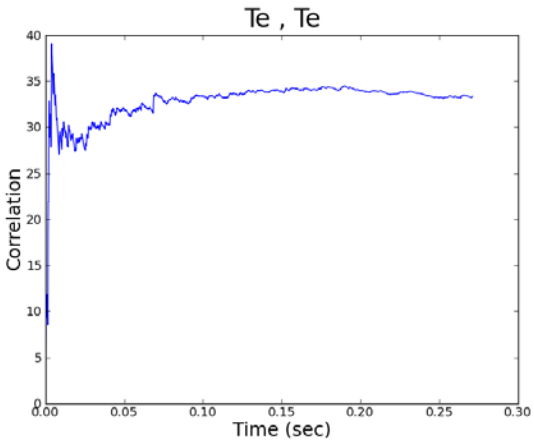

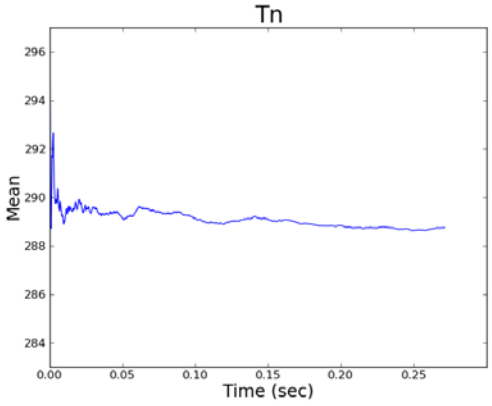
Tn
Mean
Time (sec)

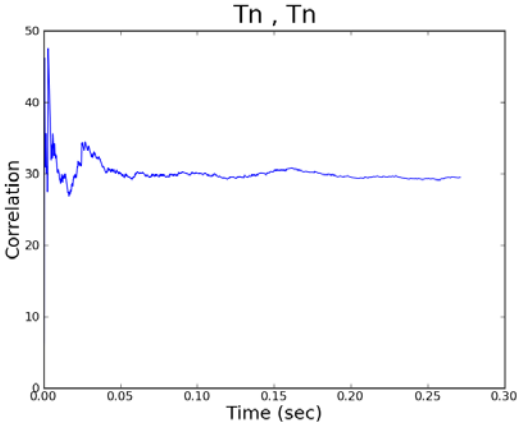
Tn , Tn
Correlation
Time (sec)

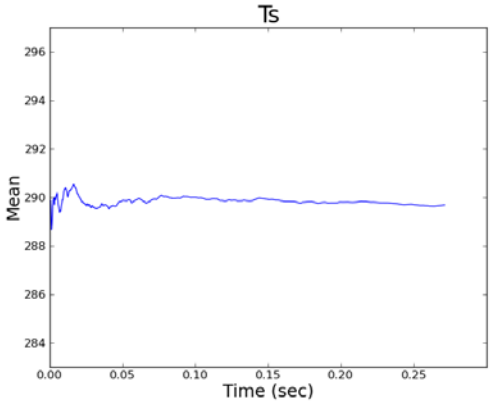
Ts
Mean
Time (sec)

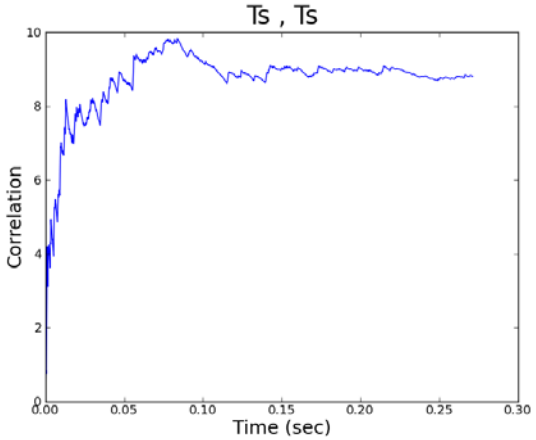
Ts , Ts
Correlation
Time (sec)

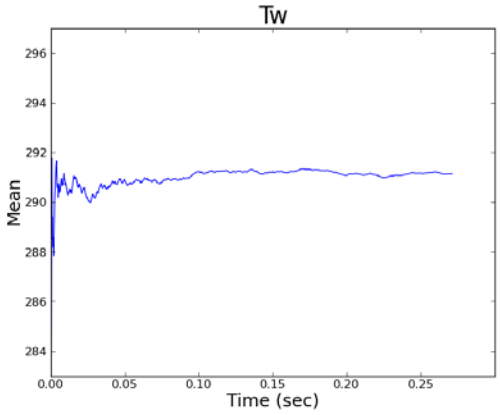
Tw
Mean
Time (sec)

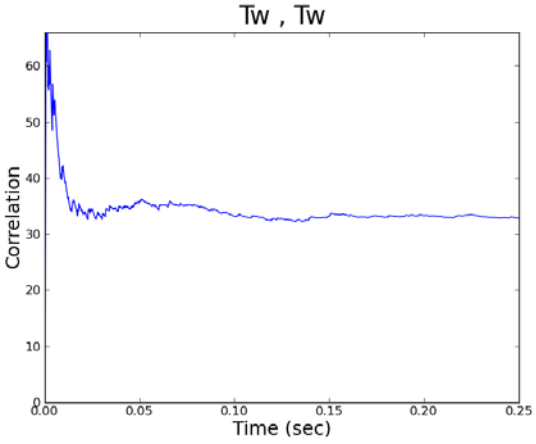
Tw , Tw
Correlation
Time (sec)

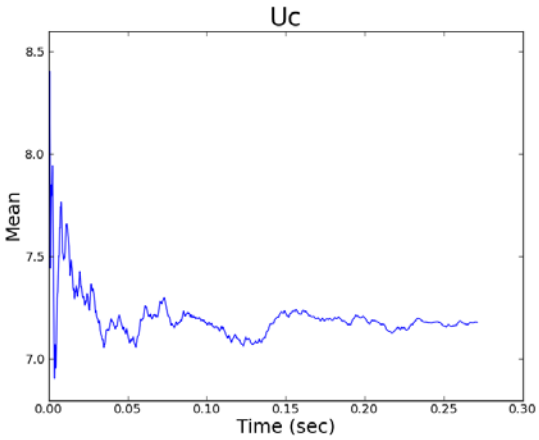
Uc
Mean
Time (sec)

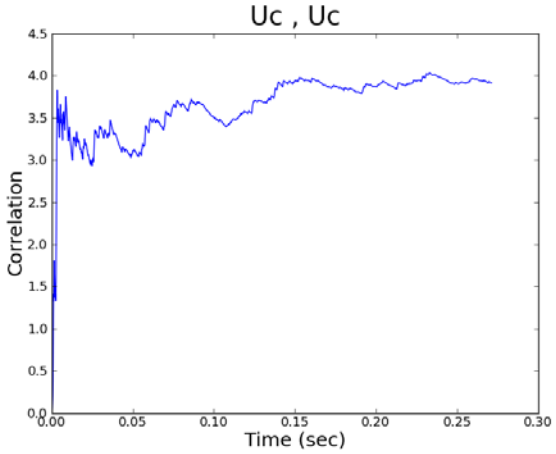
Uc , Uc
Correlation
Time (sec)

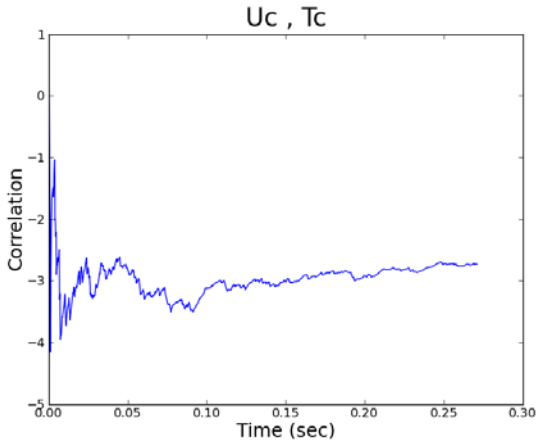
Uc , Tc
Correlation
Time (sec)

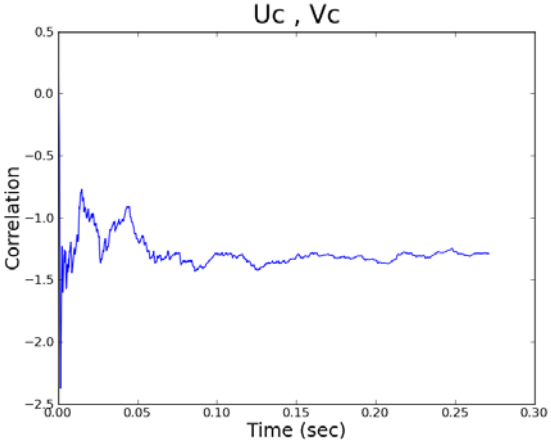
Uc , Vc
Correlation
Time (sec)

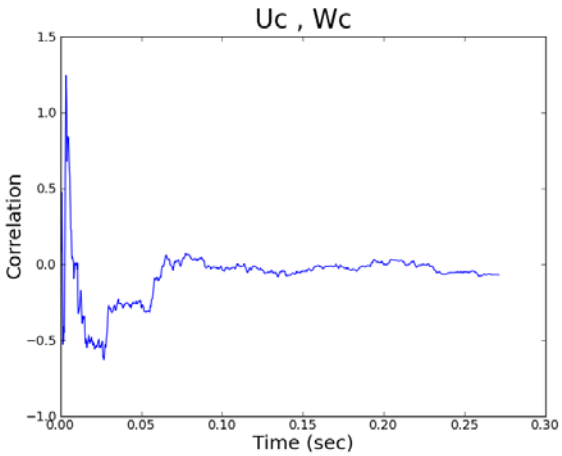
Uc , Wc
Correlation
Time (sec)

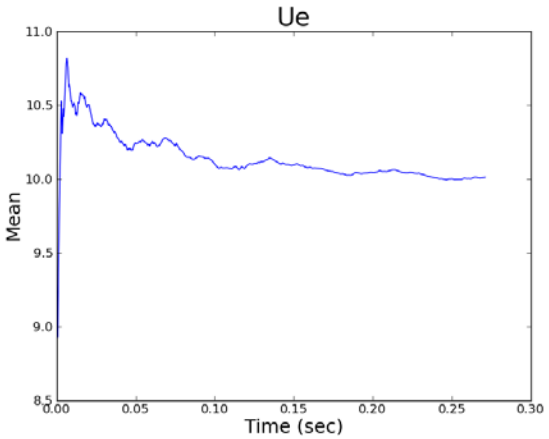
Ue
Mean
Time (sec)

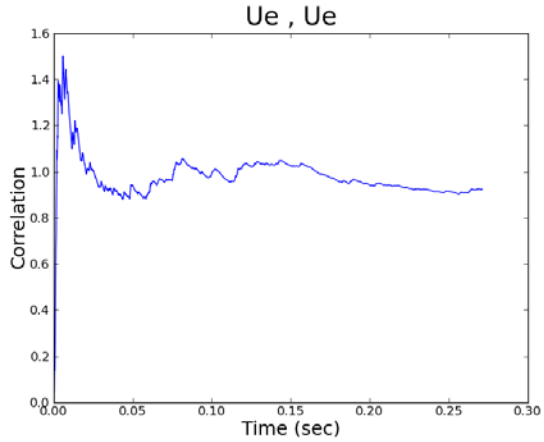
Ue , Ue
Correlation
Time (sec)

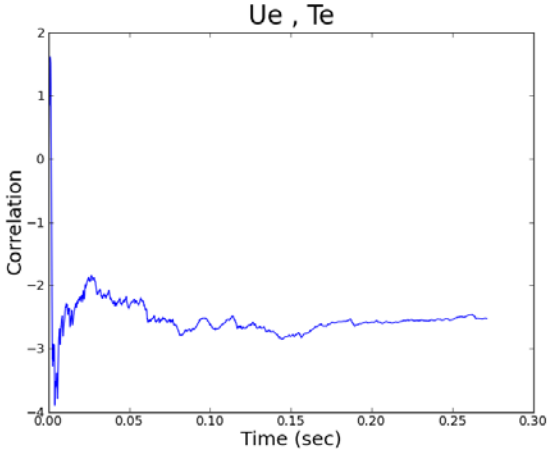
Ue , Te
Correlation
Time (sec)

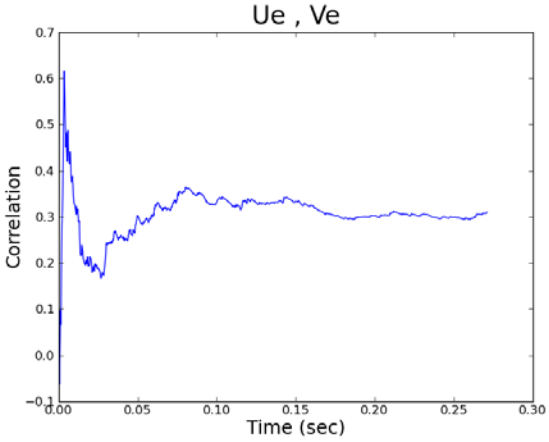
Ue , Ve
Correlation
Time (sec)

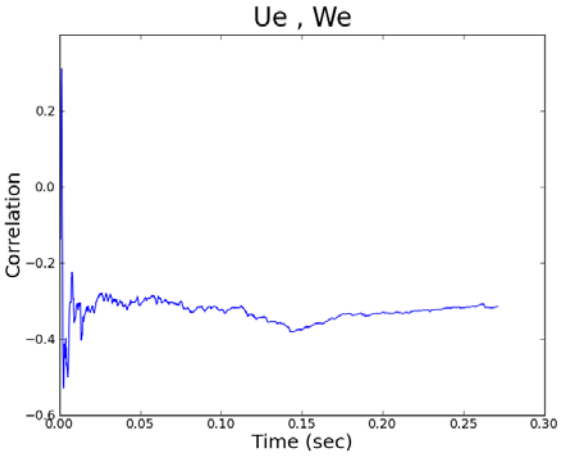
Ue , We
Correlation
Time (sec)

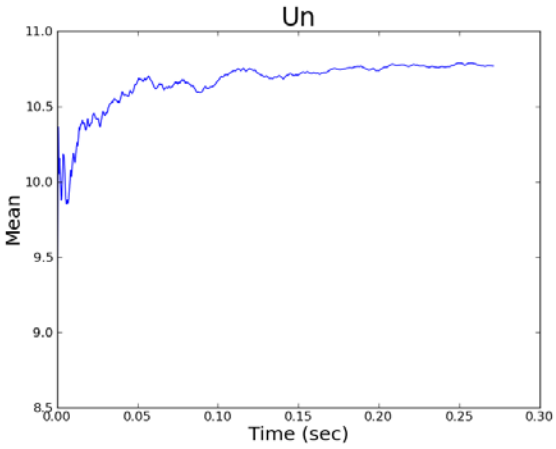
Un
Mean
Time (sec)

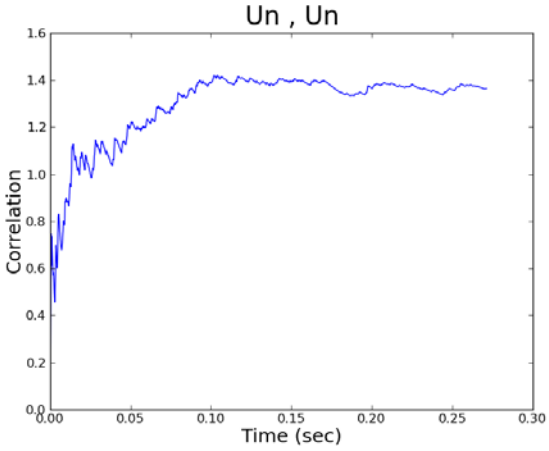
Un , Un
Correlation
Time (sec)

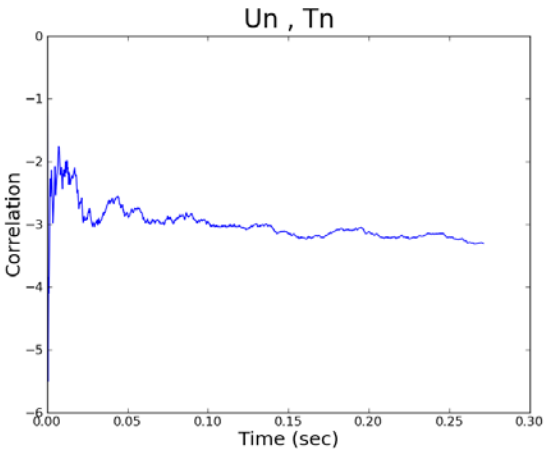
Un , Tn
Correlation
Time (sec)

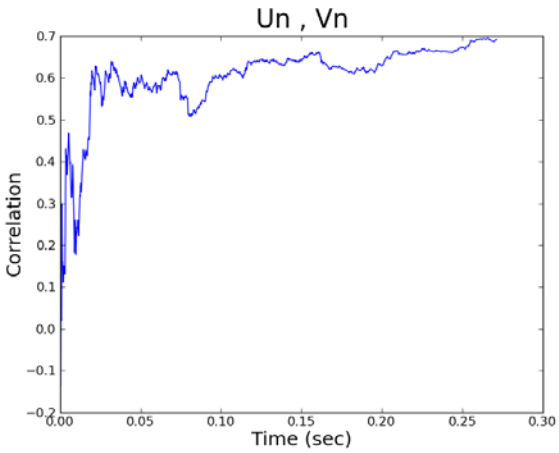
Un , Vn
Correlation
Time (sec)

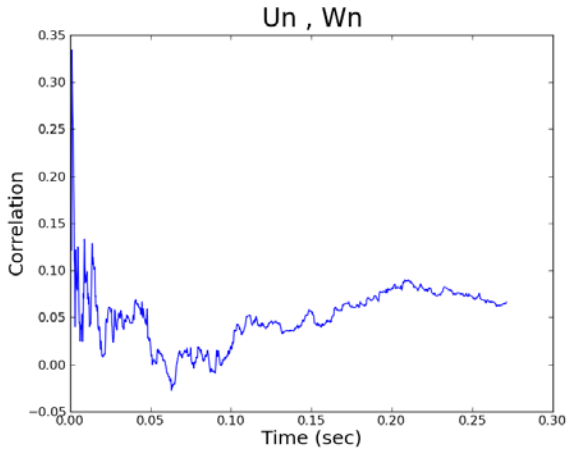
Un , Wn
Correlation
Time (sec)

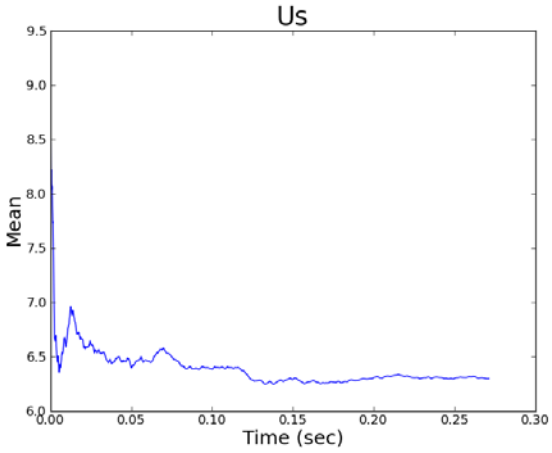
Us
Mean
Time (sec)

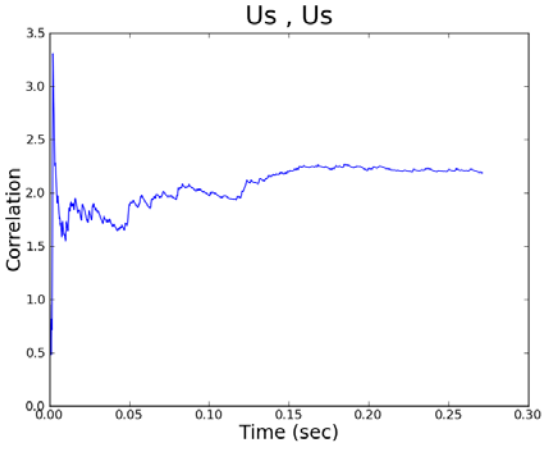
Us , Us
Correlation
Time (sec)

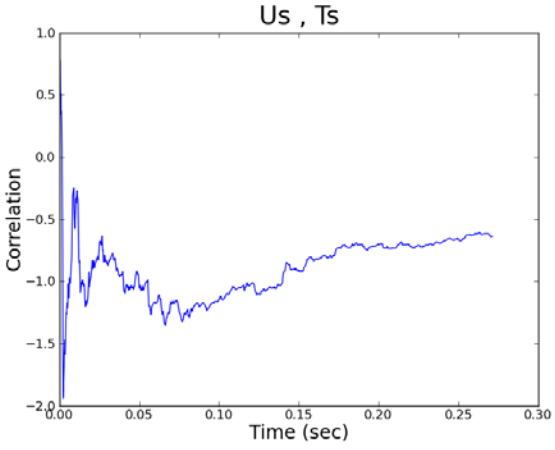
Us , Ts
Correlation
Time (sec)

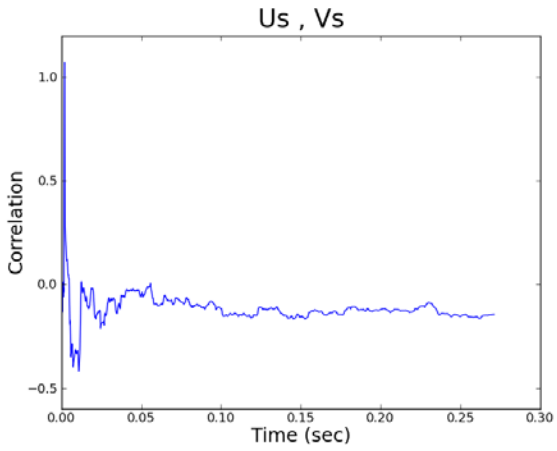
Us , Vs
Correlation
Time (sec)

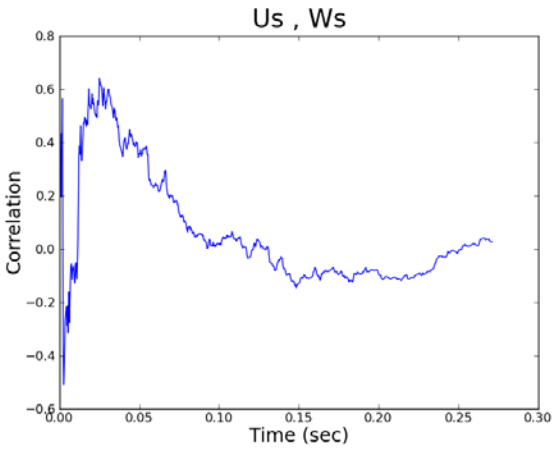
Us , Ws
Correlation
Time (sec)

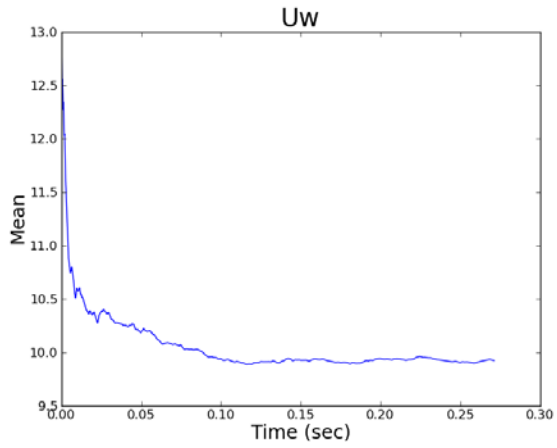
Uw
Mean
Time (sec)

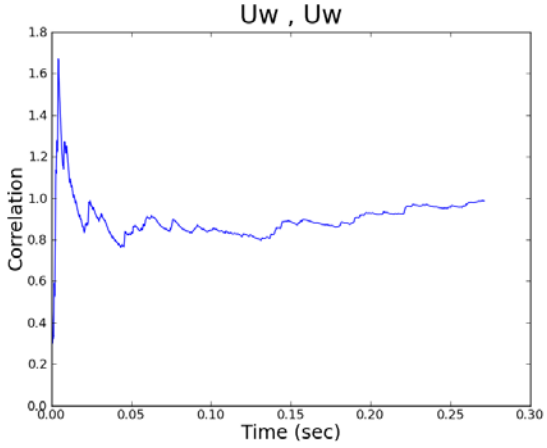
Uw , Uw
Correlation
Time (sec)

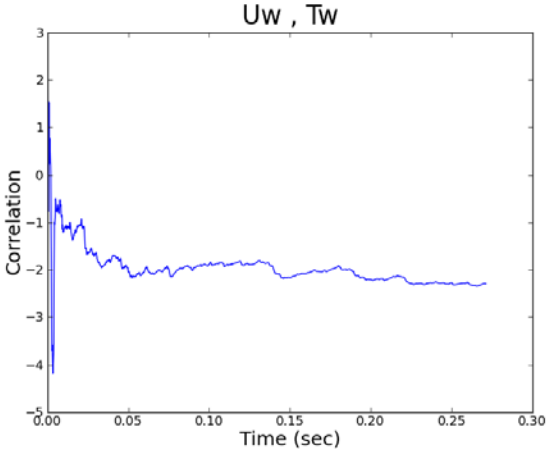
Uw , Tw
Correlation
Time (sec)

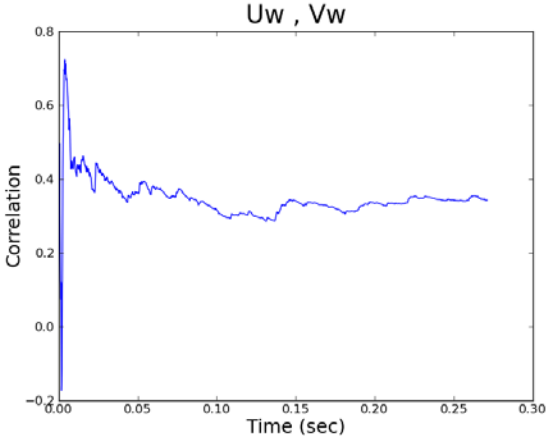
Uw , Vw
Correlation
Time (sec)

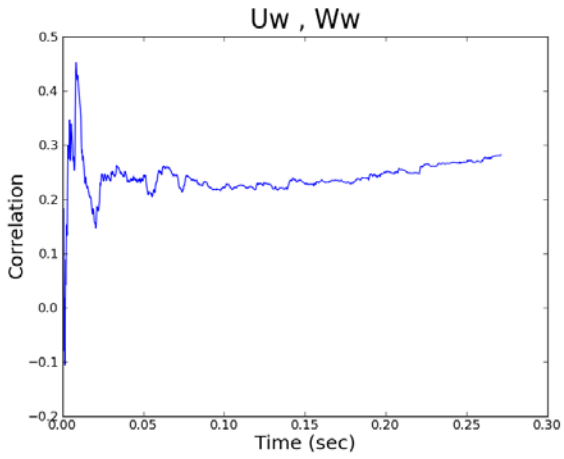
Uw , Ww
Correlation
Time (sec)

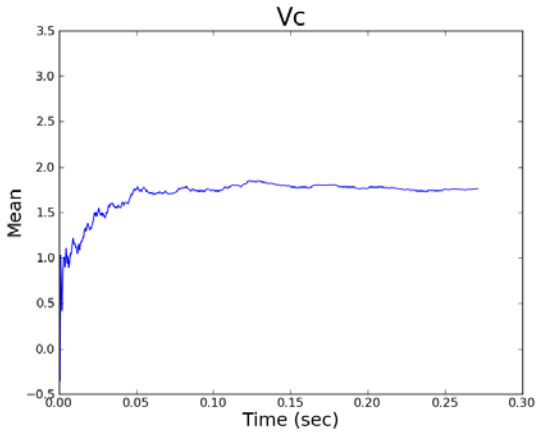
Vc
Mean
Time (sec)

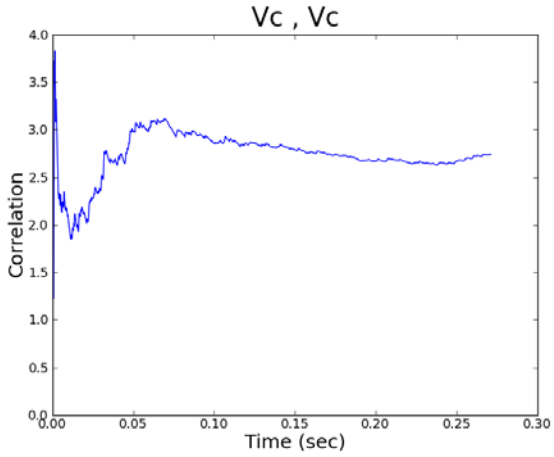
Vc , Vc
Correlation
Time (sec)

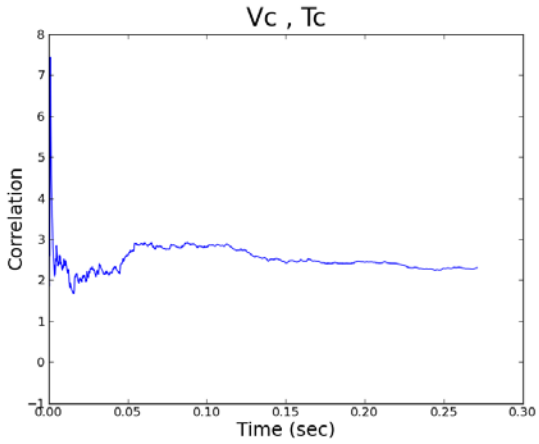
Vc , Tc
Correlation
Time (sec)

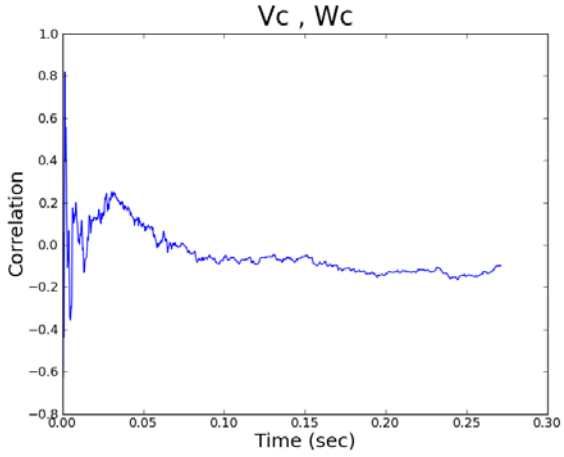
Vc , Wc
Correlation
Time (sec)

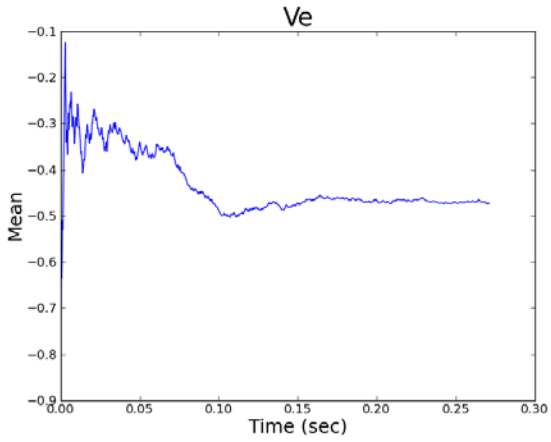
Ve
Mean
Time (sec)

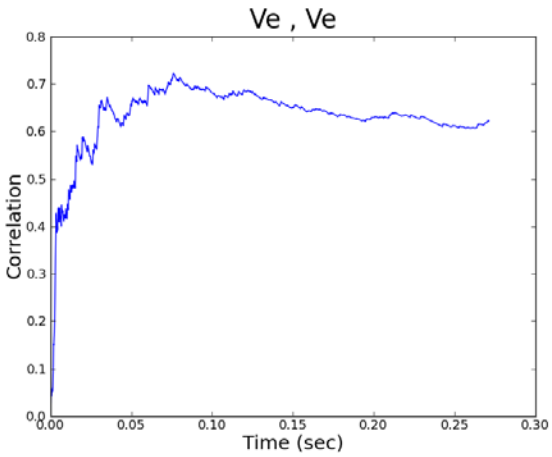
Ve , Ve
Correlation
Time (sec)

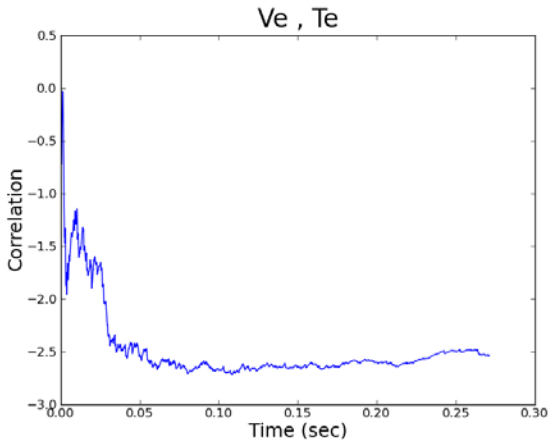
Ve , Te
Correlation
Time (sec)

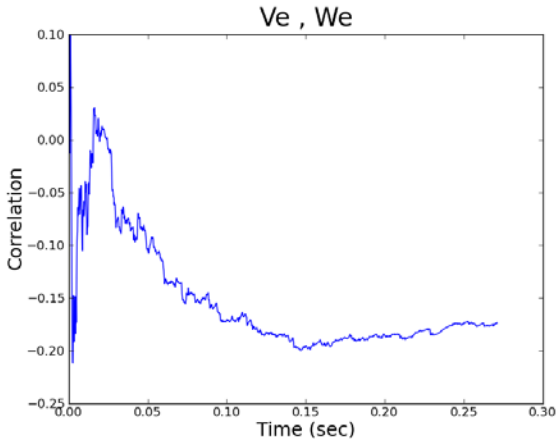
Ve , We
Correlation
Time (sec)

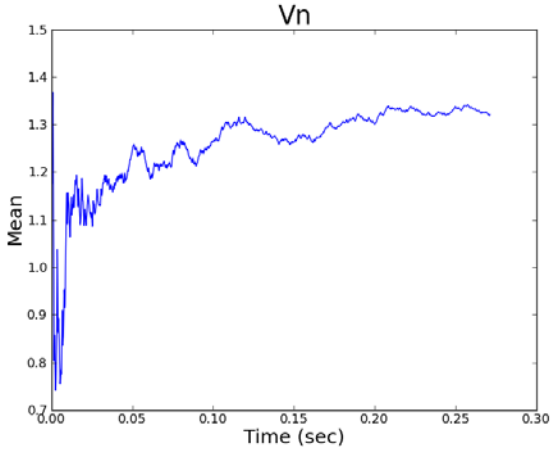
Vn
Mean
Time (sec)

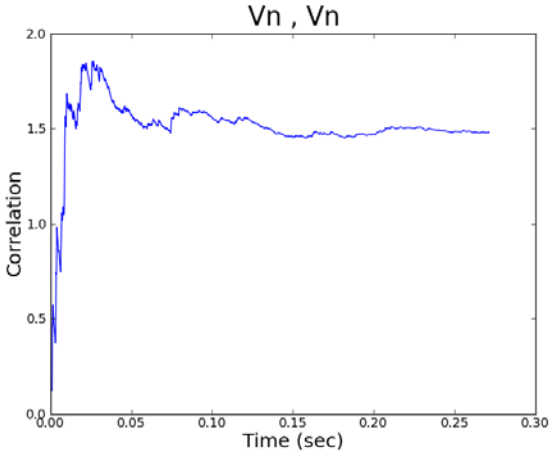
Vn , Vn
Correlation
Time (sec)

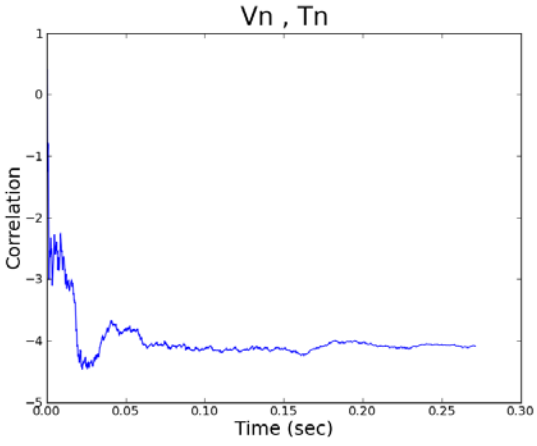
Vn , Tn
Correlation
Time (sec)

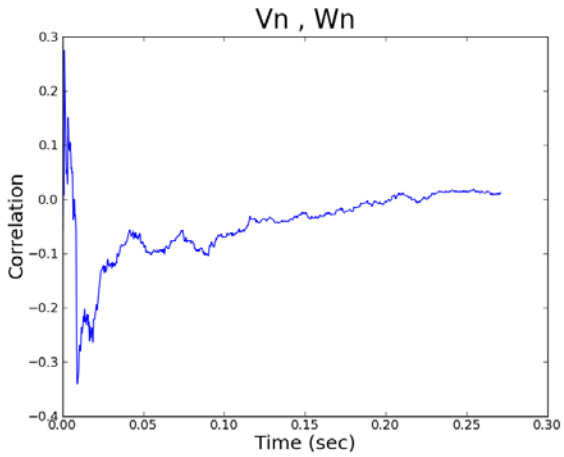
Vn , Wn
Correlation
Time (sec)

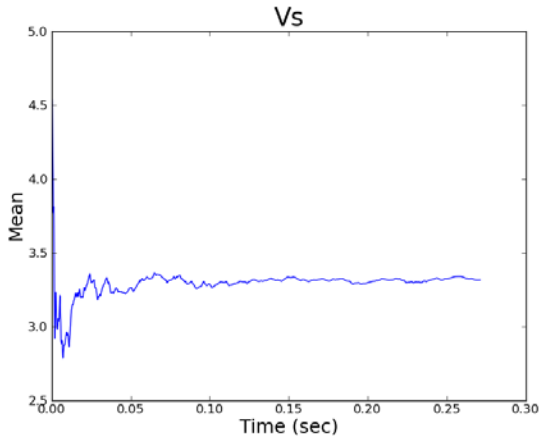
Vs
Mean
Time (sec)

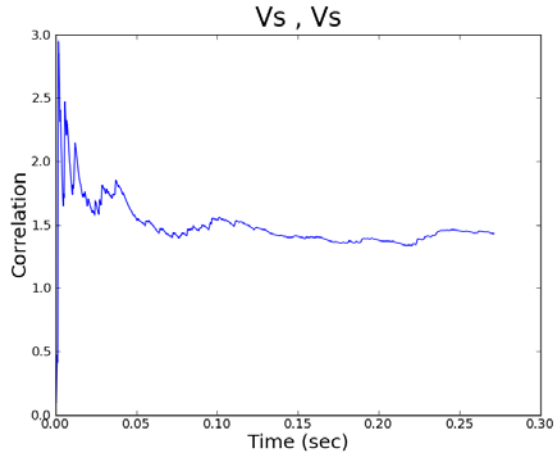
Vs , Vs
Correlation
Time (sec)

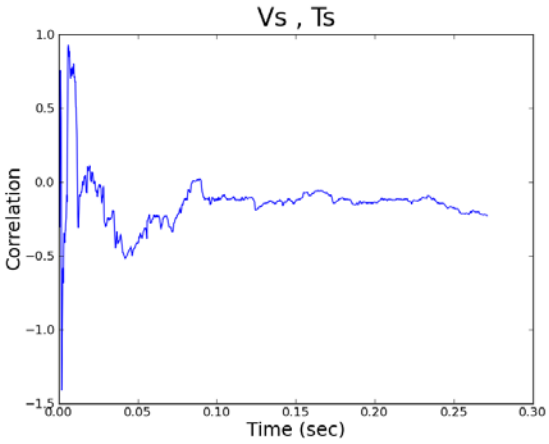
Vs , Ts
Correlation
Time (sec)

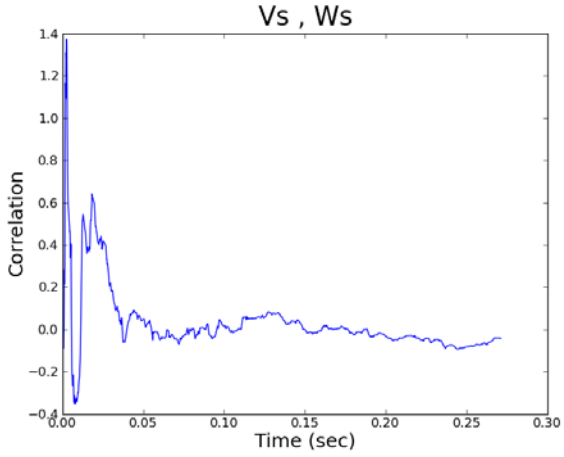
Vs , Ws
Correlation
Time (sec)

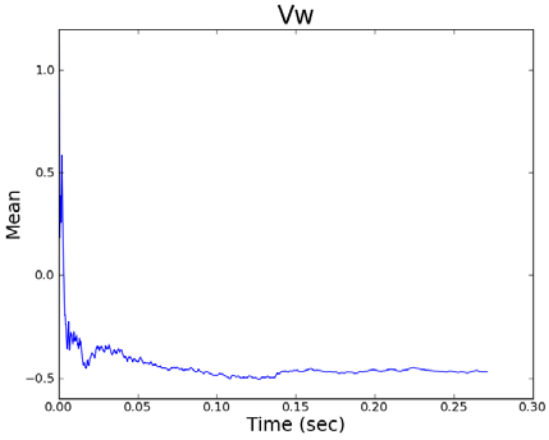
Vw
Mean
Time (sec)

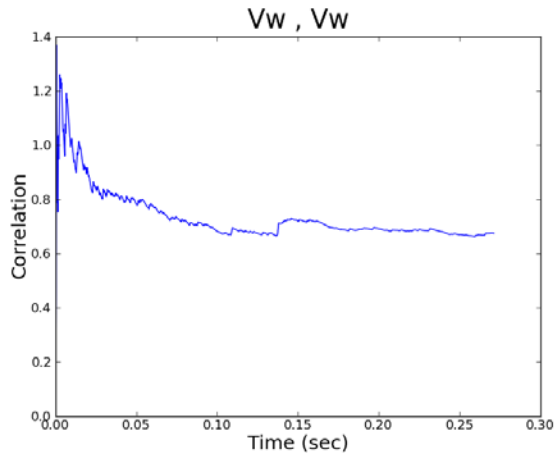
Vw , Vw
Correlation
Time (sec)

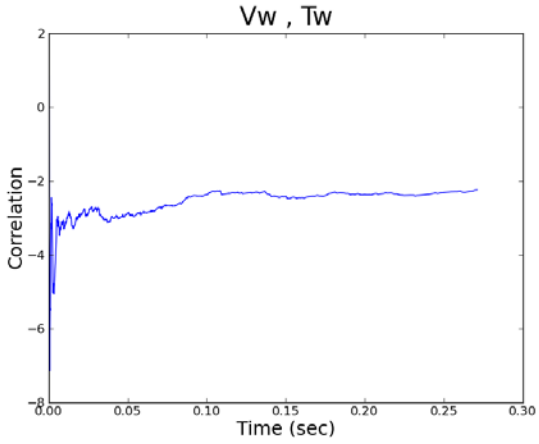
Vw , Tw
Correlation
Time (sec)

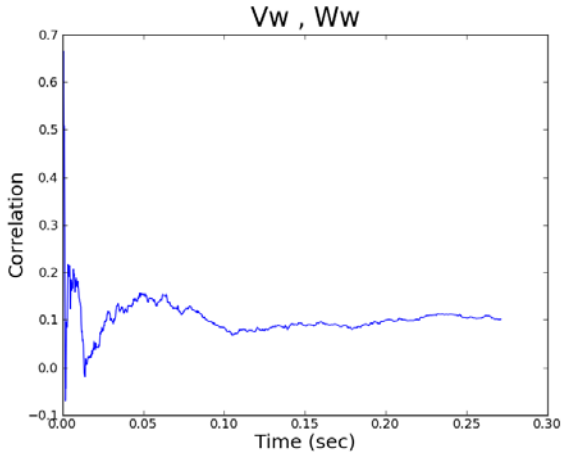
Vw , Ww
Correlation
Time (sec)

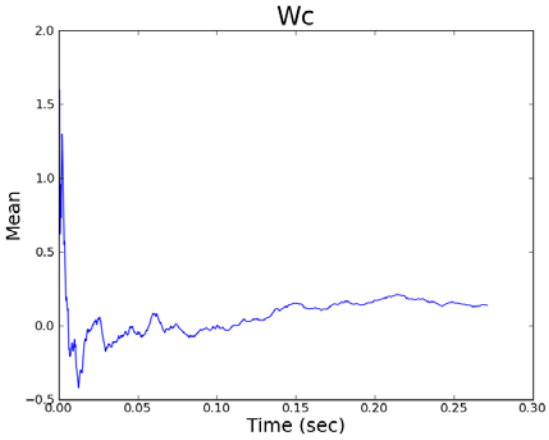
Wc
Mean
Time (sec)

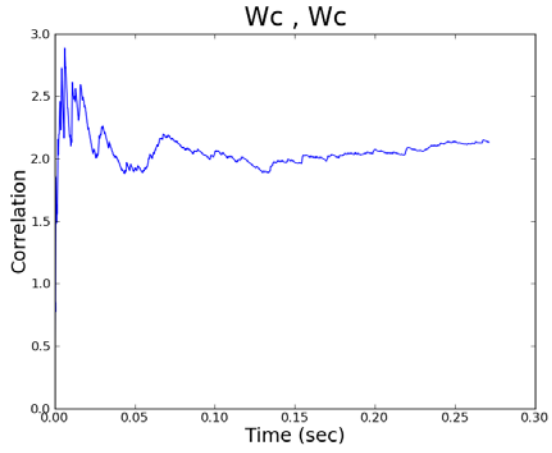
Wc , Wc
Correlation
Time (sec)

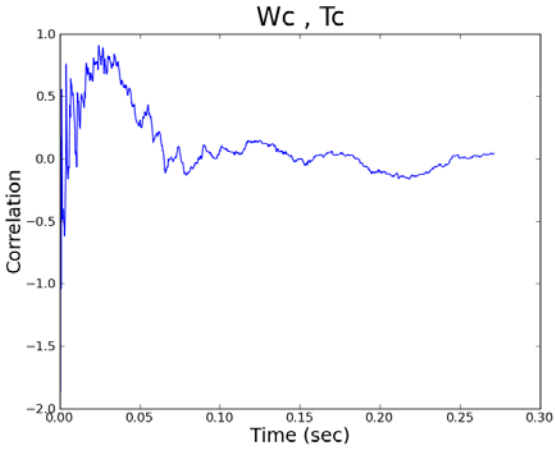
Wc , Tc
Correlation
Time (sec)

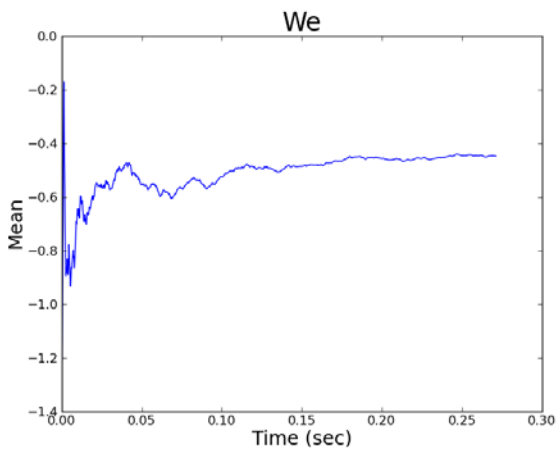
We
Mean
Time (sec)

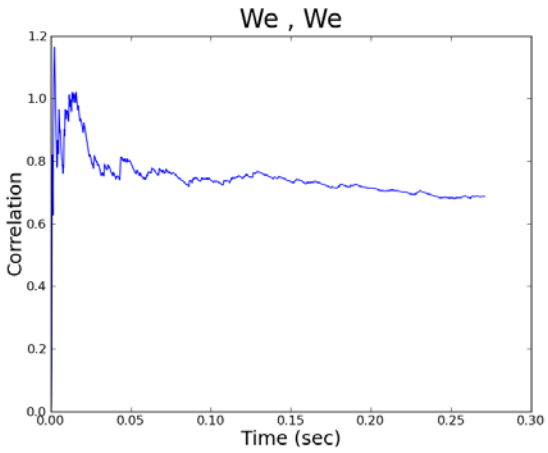
We , We
Correlation
Time (sec)

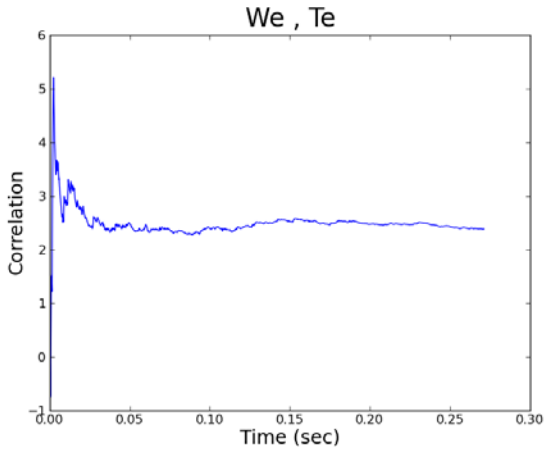
We , Te
Correlation
Time (sec)

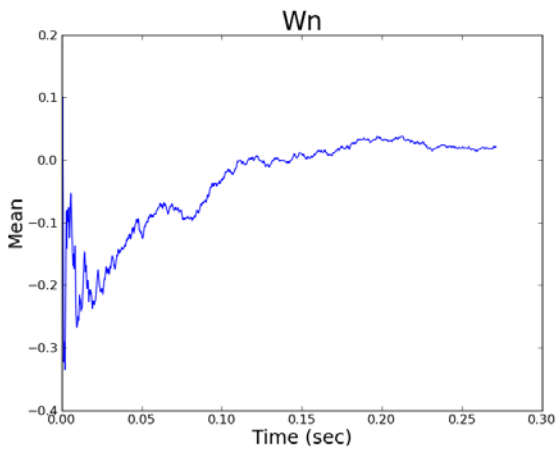
Wn
Mean
Time (sec)

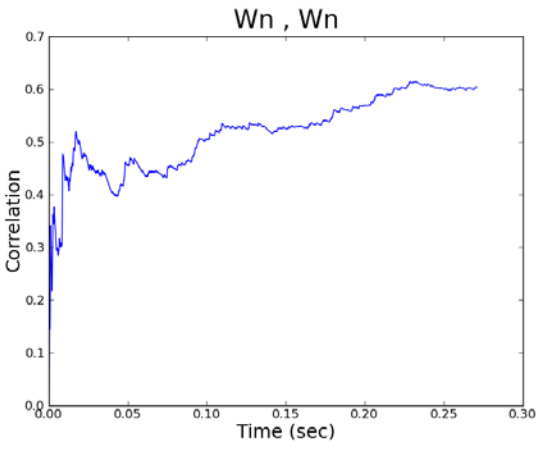
Wn , Wn
Correlation
Time (sec)

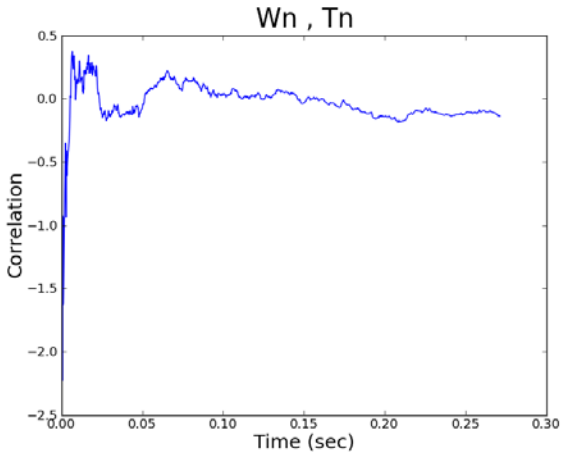
Wn , Tn
Correlation
Time (sec)

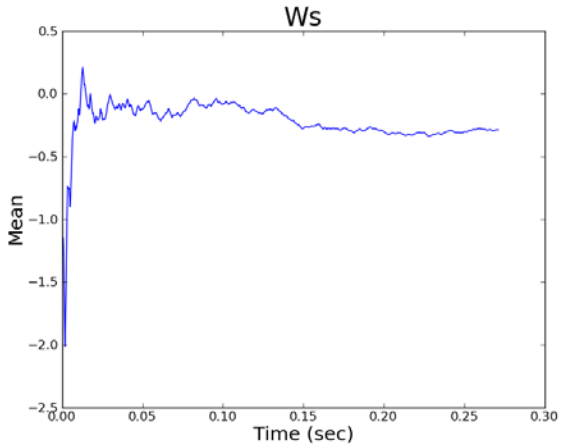
Ws
Mean
Time (sec)

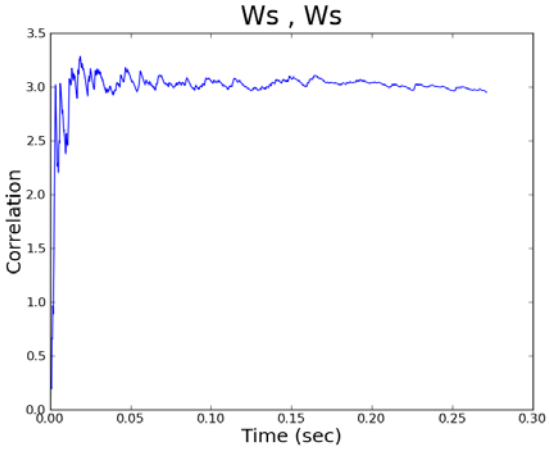
Ws , Ws
Correlation
Time (sec)

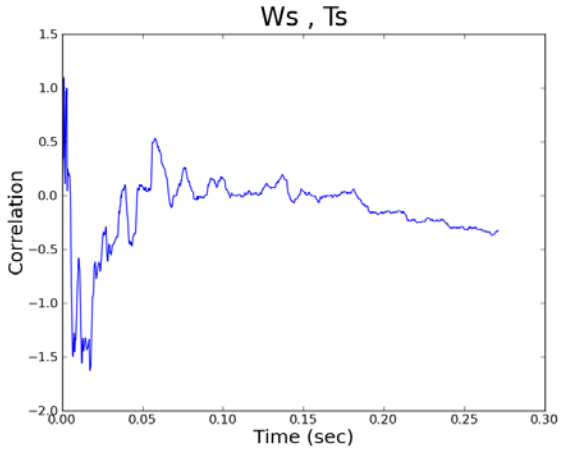
Ws , Ts
Correlation
Time (sec)

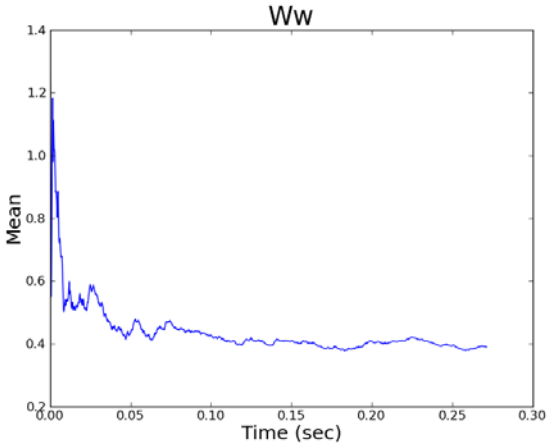
Ww
Mean
Time (sec)

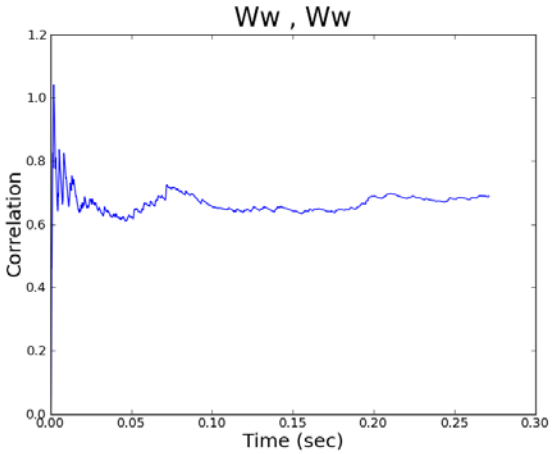
Ww , Ww
Correlation
Time (sec)

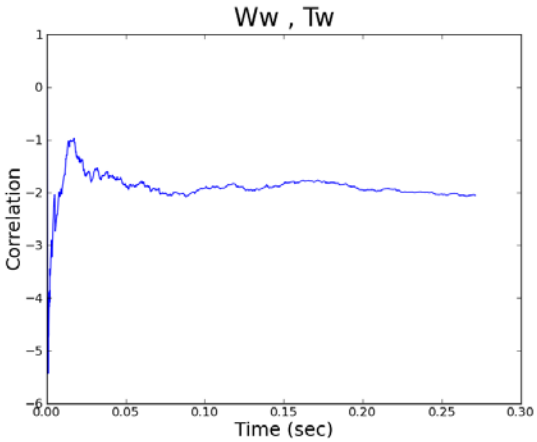
Ww , Tw
Correlation
Time (sec)

M = 1.9 Statistical Steadiness

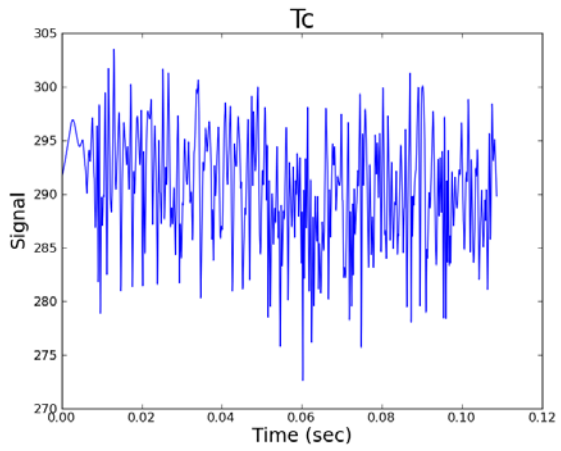

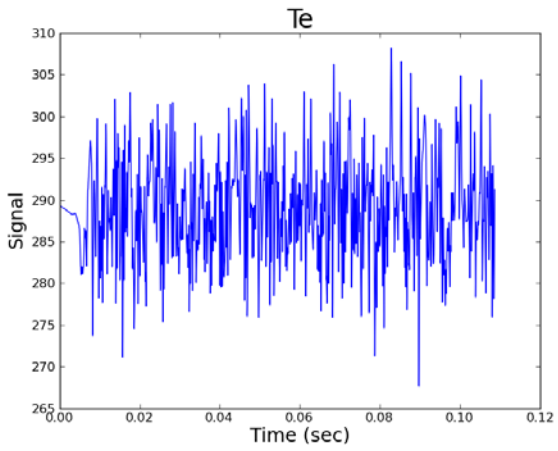

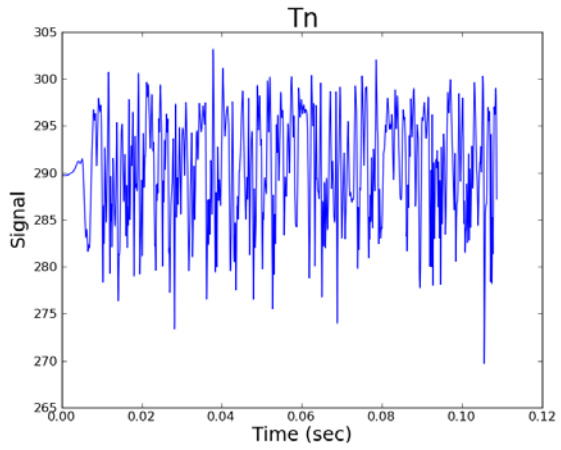

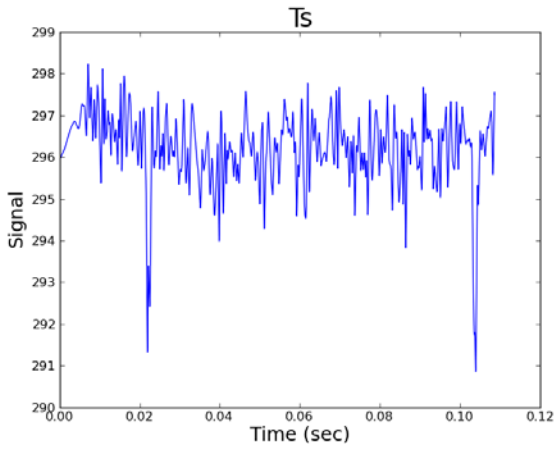

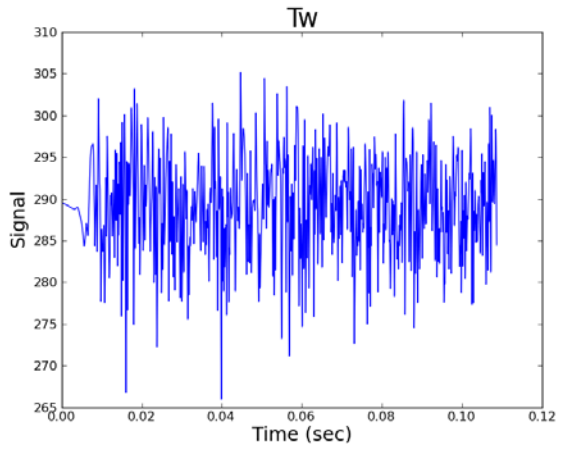

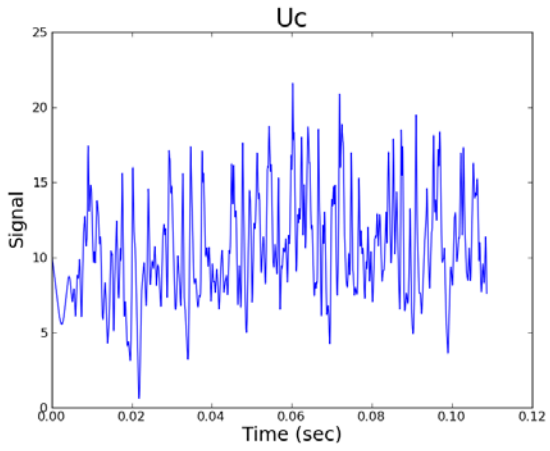

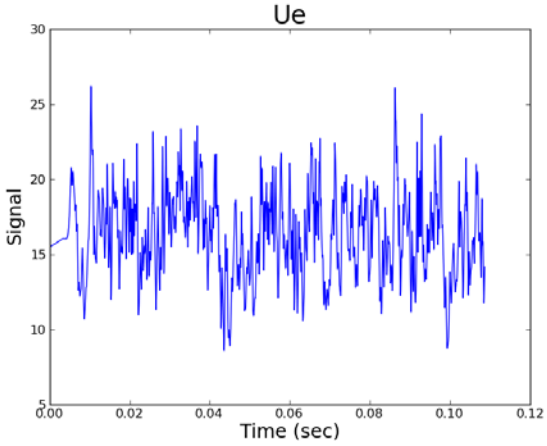
Ue
Signal
Time (sec)

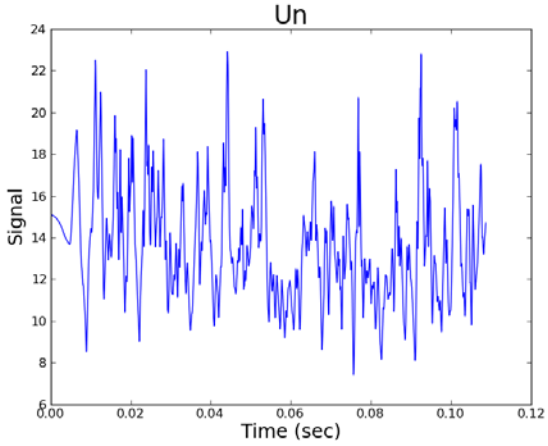
Un
Signal
Time (sec)

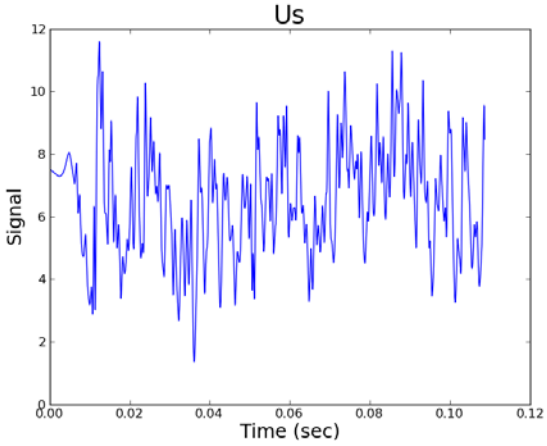
Us
Signal
Time (sec)

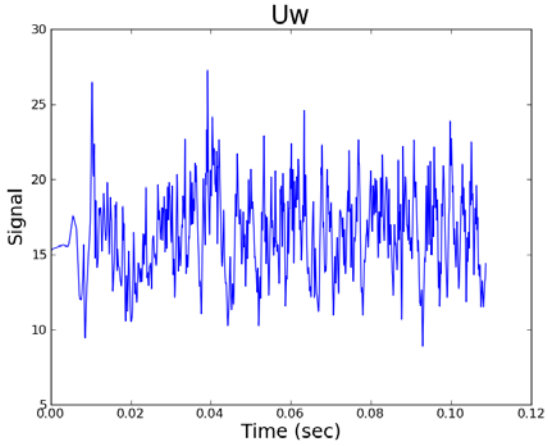
Uw
Signal
Time (sec)

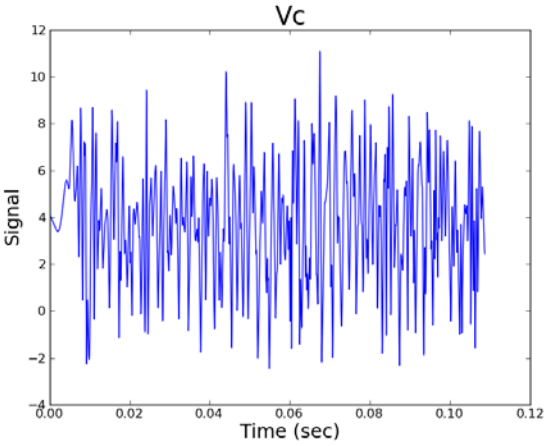
Vc
Signal
Time (sec)

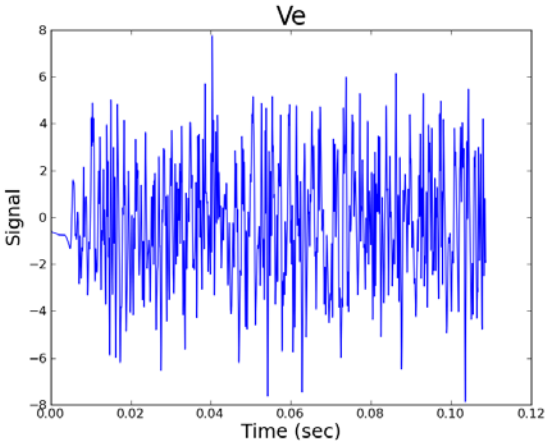
Ve
Signal
Time (sec)

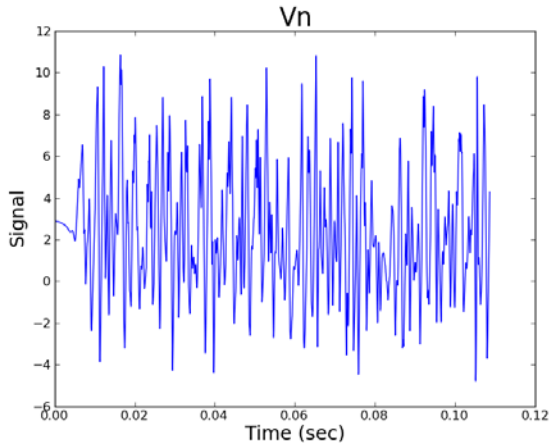
Vn
Signal
Time (sec)

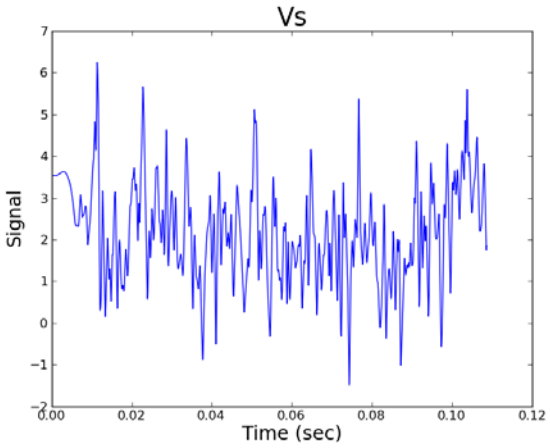
Vs
Signal
Time (sec)

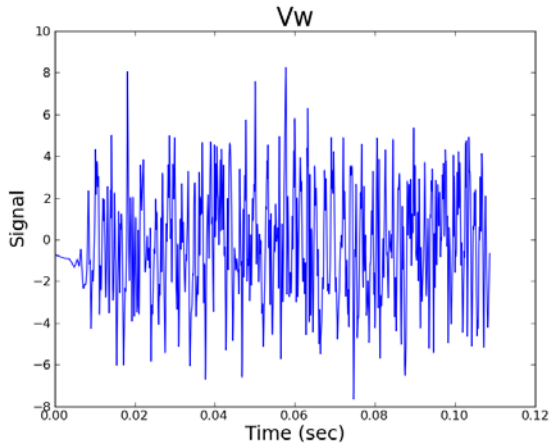
Vw
Signal
Time (sec)

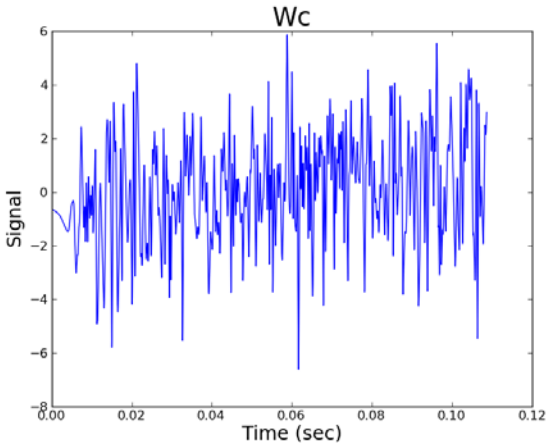
Wc
Signal
Time (sec)

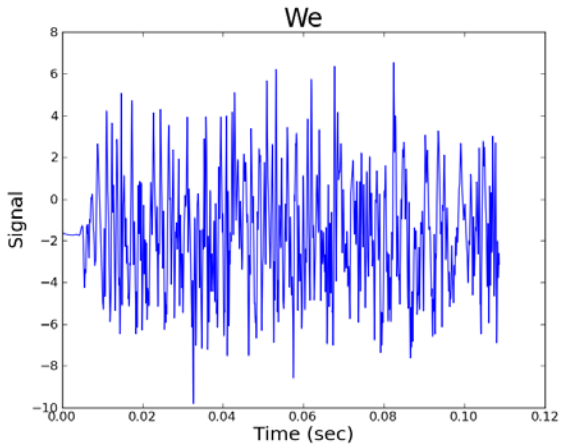
We
Signal
Time (sec)

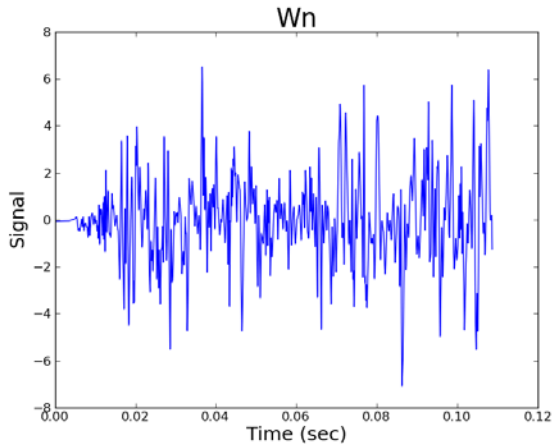
Wn
Signal
Time (sec)

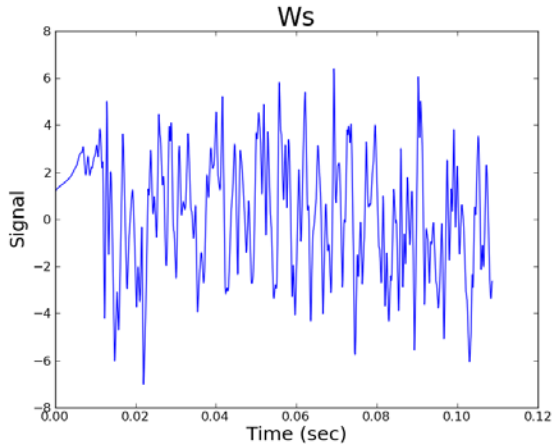

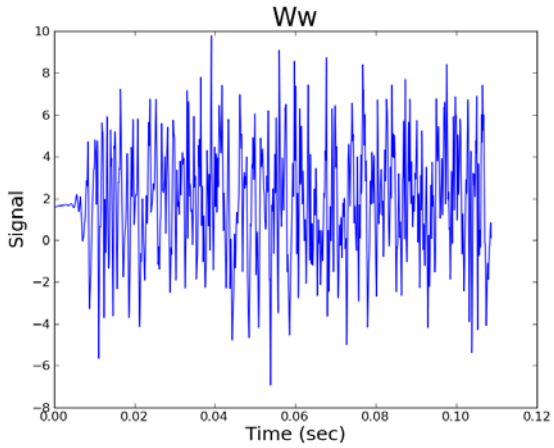

M = 1.9 Statistical Convergence

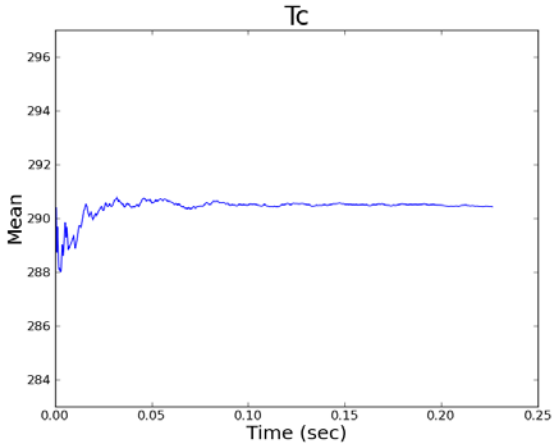

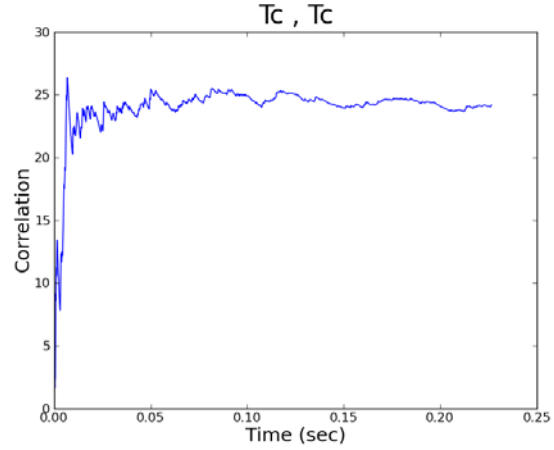

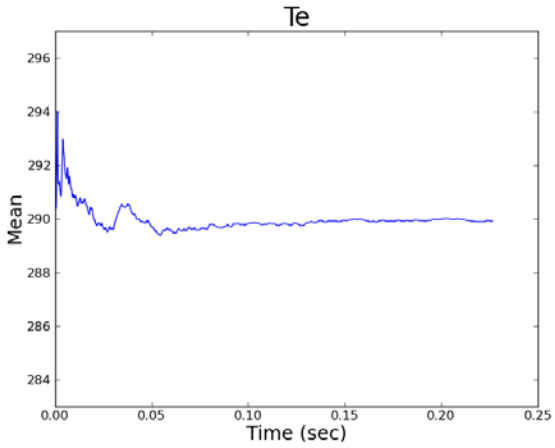

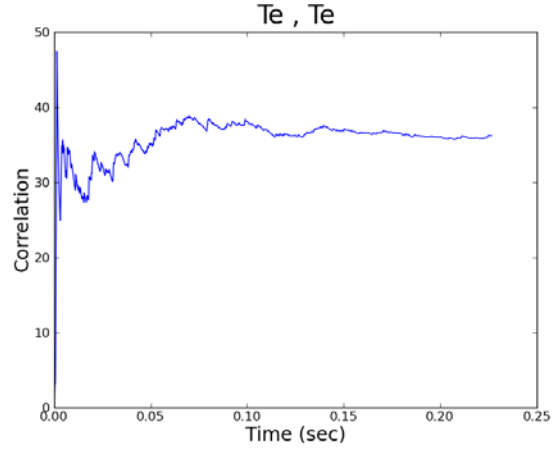

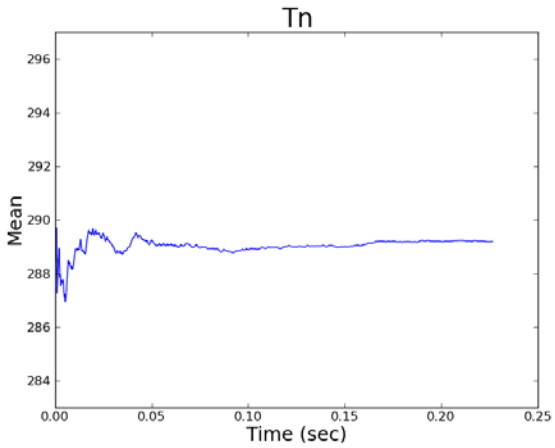
Tn
Mean
Time (sec)

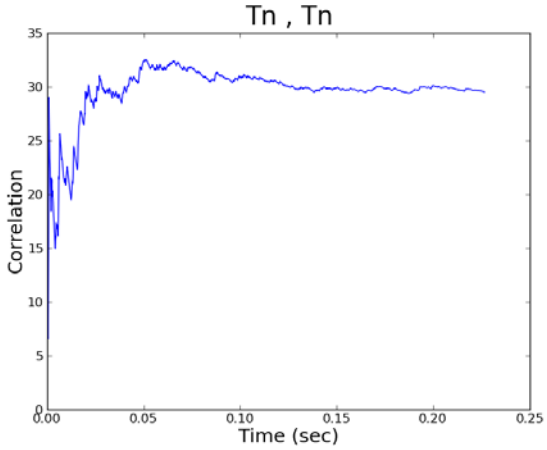
Tn , Tn
Correlation
Time (sec)

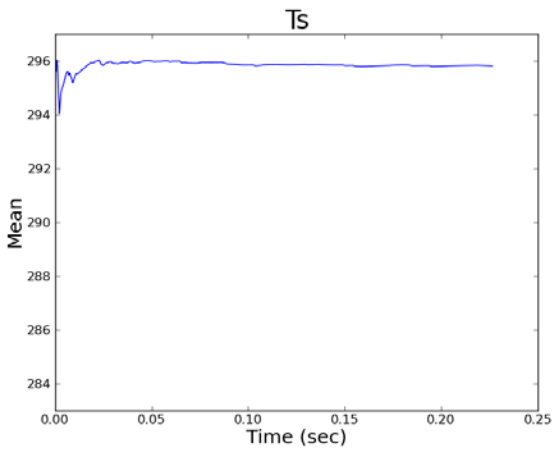
Ts
Mean
Time (sec)

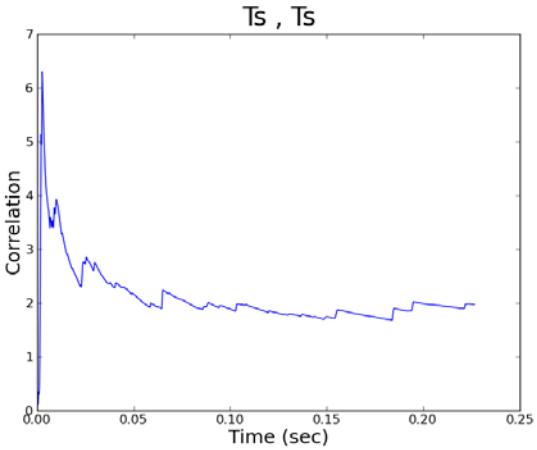
Ts , Ts
Correlation
Time (sec)

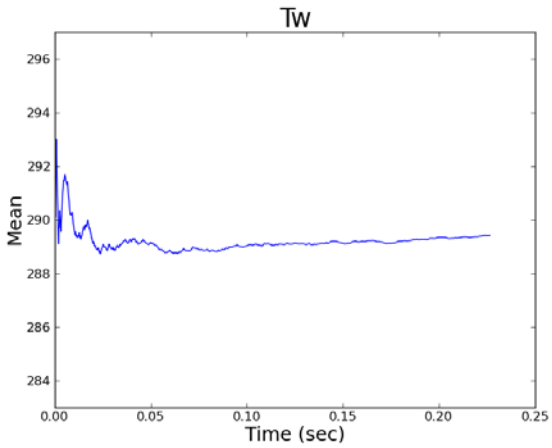
Tw
Mean
Time (sec)

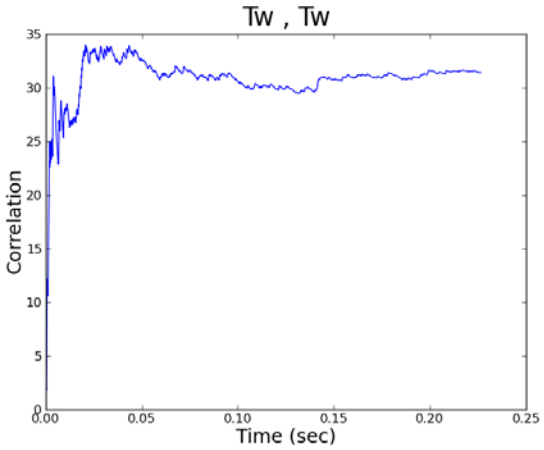
Tw , Tw
Correlation
Time (sec)

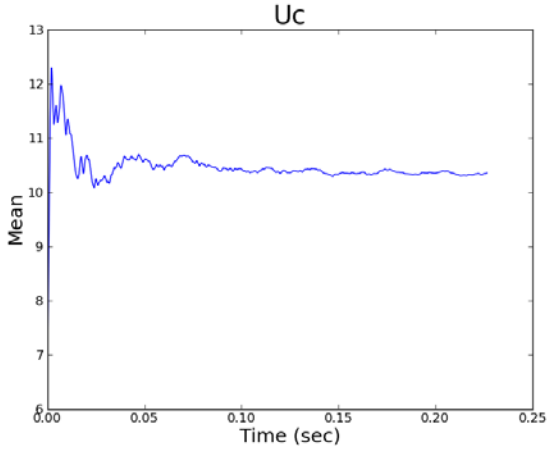
Uc
Mean
Time (sec)

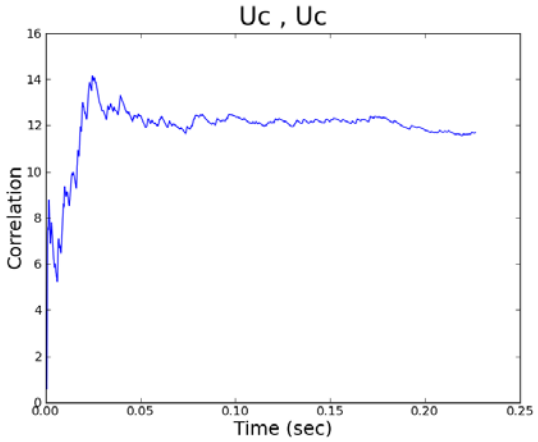
Uc , Uc
Correlation
Time (sec)

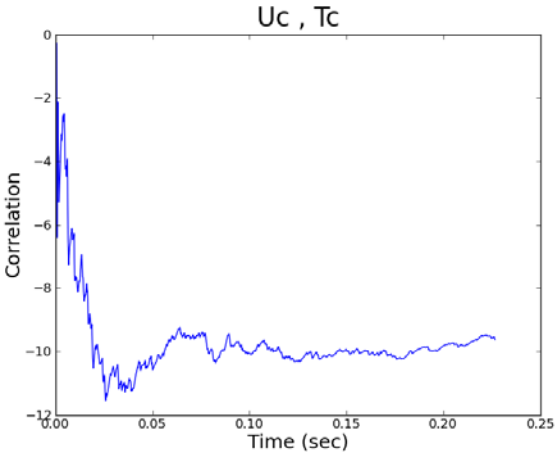
Uc , Tc
Correlation
Time (sec)

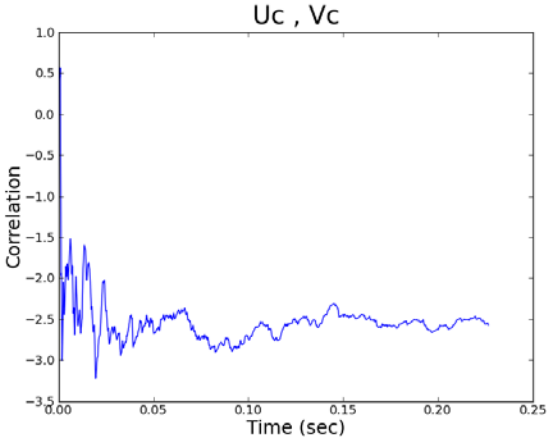
Uc , Vc
Correlation
Time (sec)

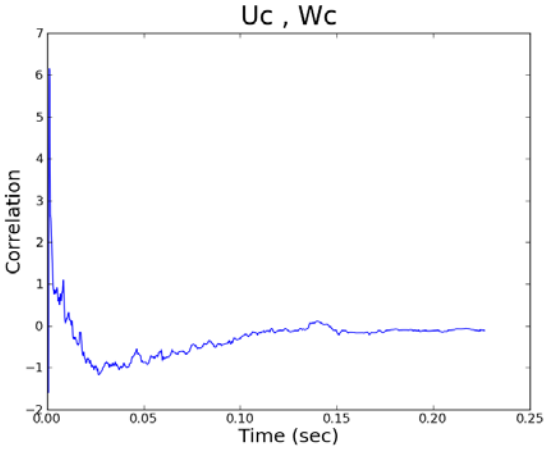
Uc , Wc
Correlation
Time (sec)

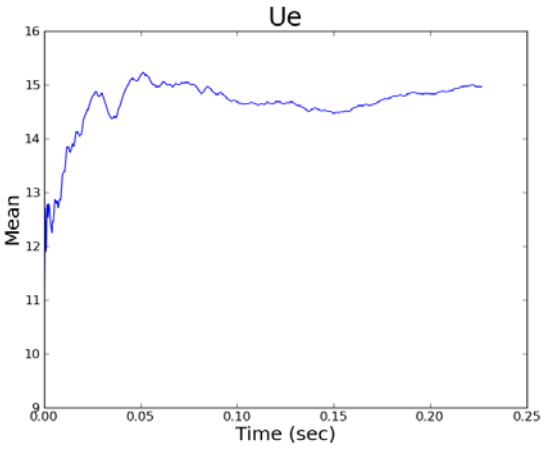
Ue
Mean
Time (sec)

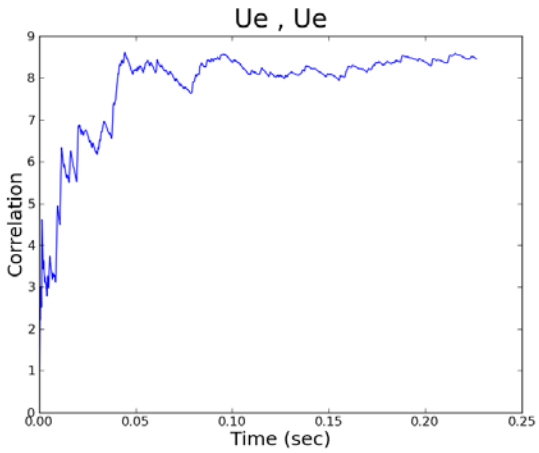
Ue , Ue
Correlation
Time (sec)

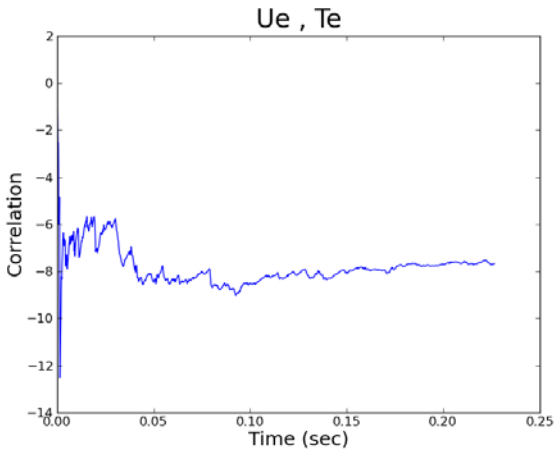
Ue , Te
Correlation
Time (sec)

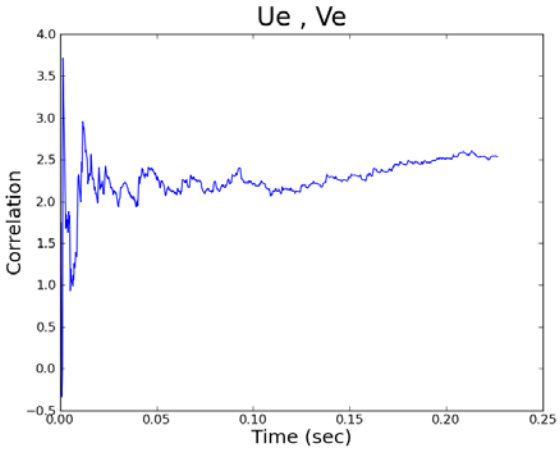
Ue , Ve
Correlation
Time (sec)

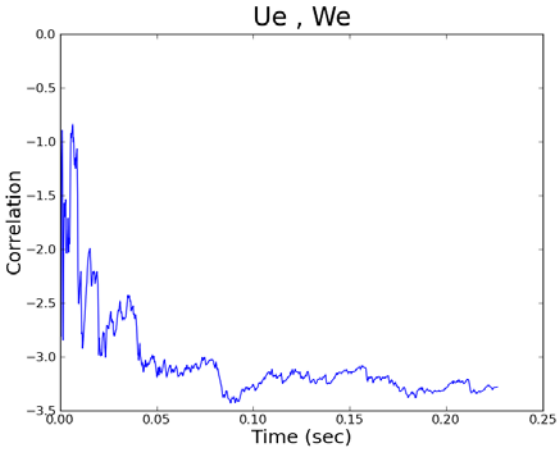
Ue , We
Correlation
Time (sec)

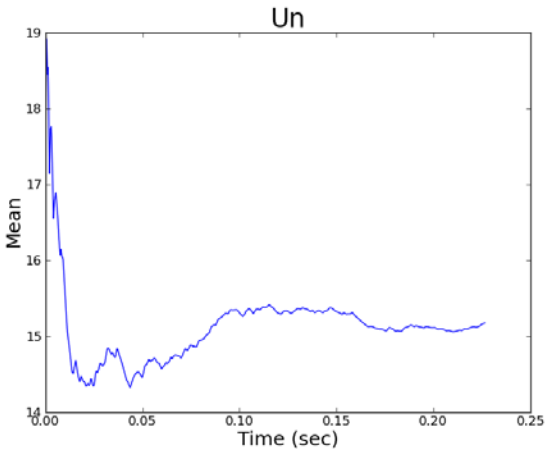
Un
Mean
Time (sec)

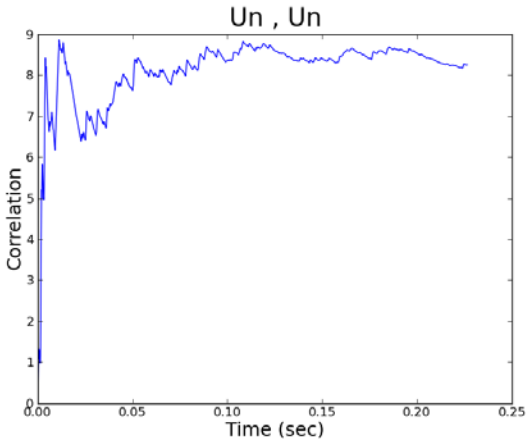
Un , Un
Correlation
Time (sec)

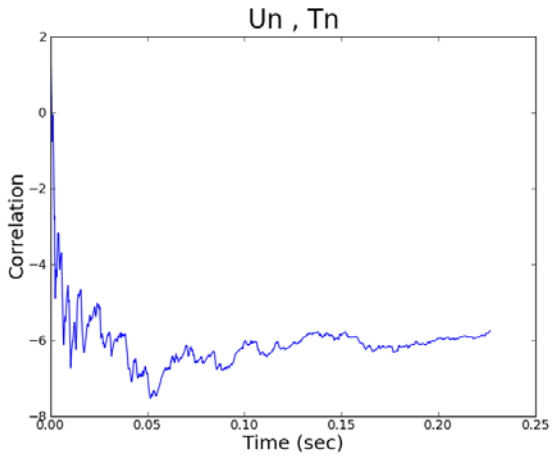
Un , Tn
Correlation
Time (sec)

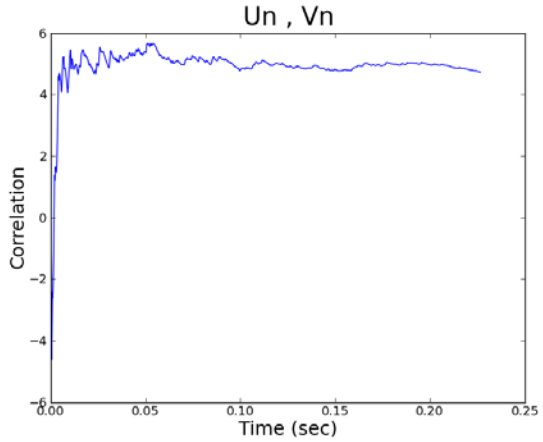
Un , Vn
Correlation
Time (sec)

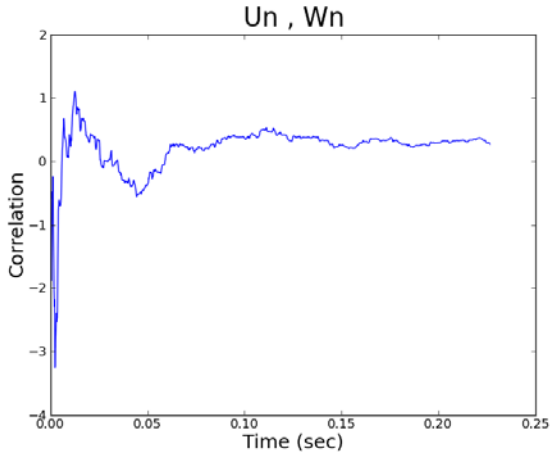
Un , Wn
Correlation
Time (sec)

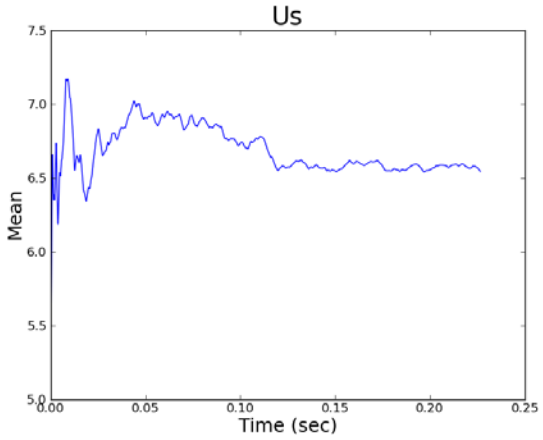
Us
Mean
Time (sec)

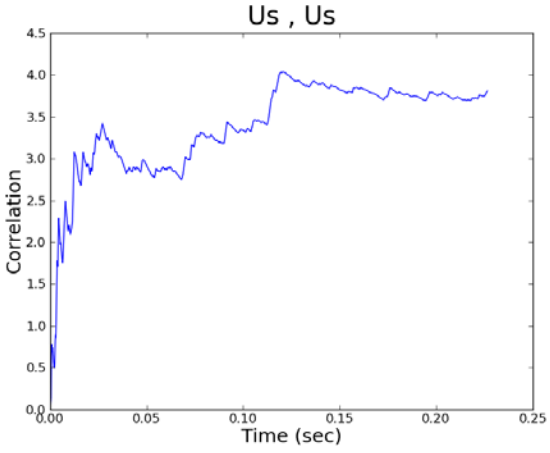
Us , Us
Correlation
Time (sec)

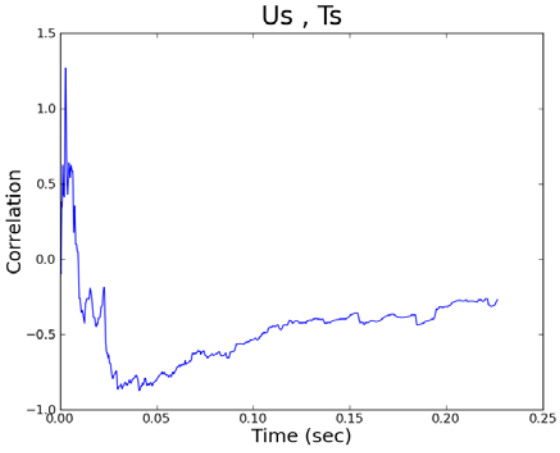
Us , Ts
Correlation
Time (sec)

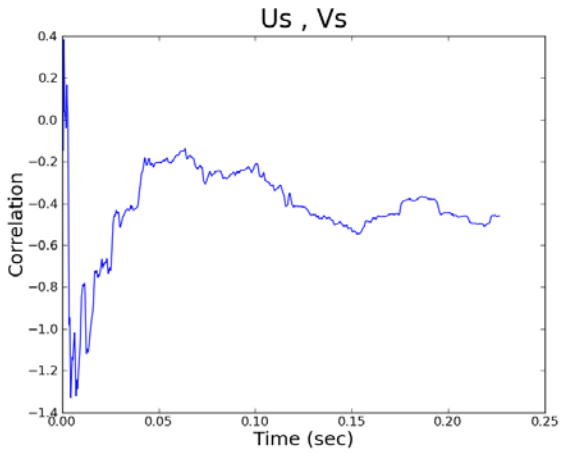
Us , Vs
Correlation
Time (sec)

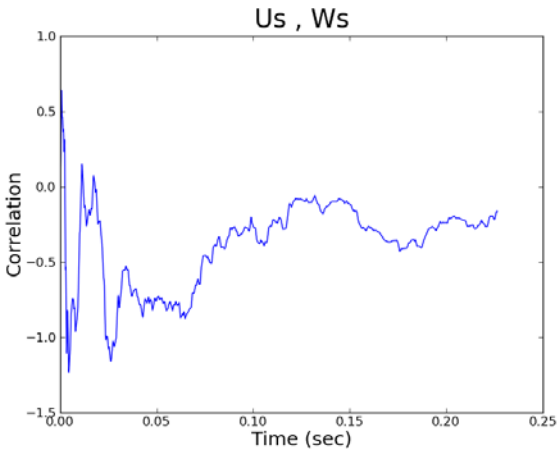
Us , Ws
Correlation
Time (sec)

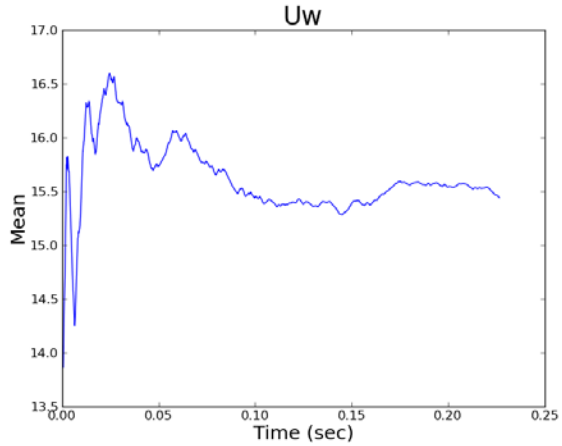
Uw
Mean
Time (sec)

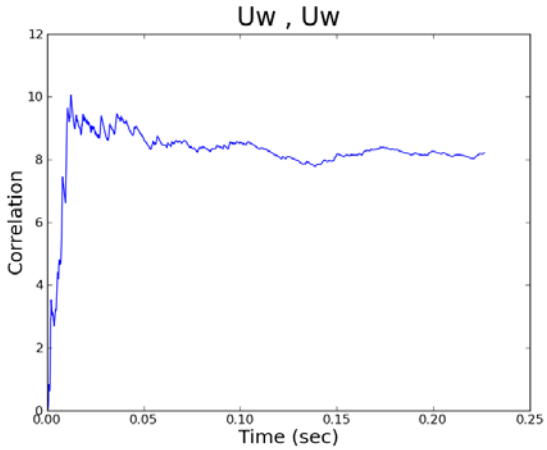
Uw , Uw
Correlation
Time (sec)

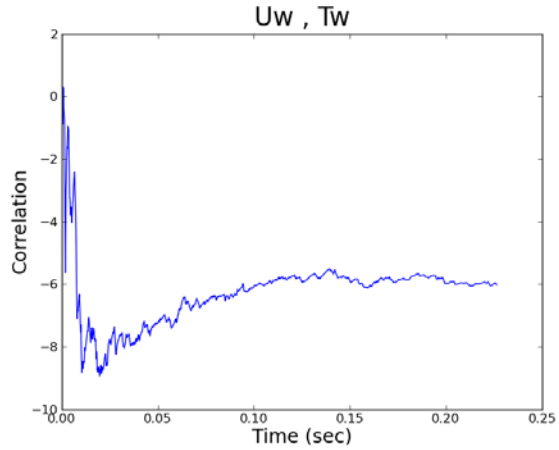
Uw , Tw
Correlation
Time (sec)

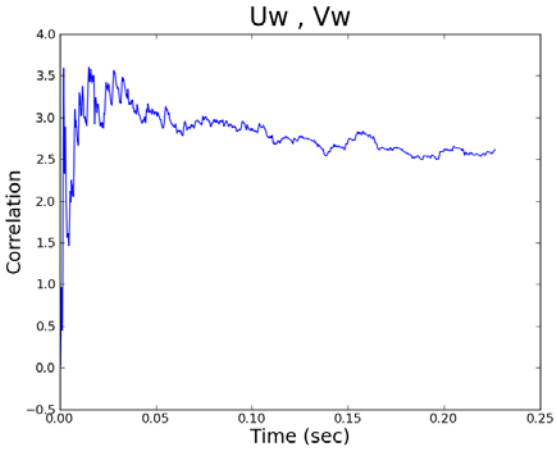
Uw , Vw
Correlation
Time (sec)

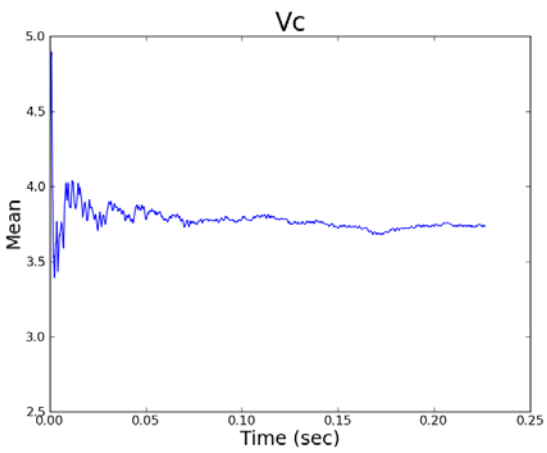
Vc
Mean
Time (sec)

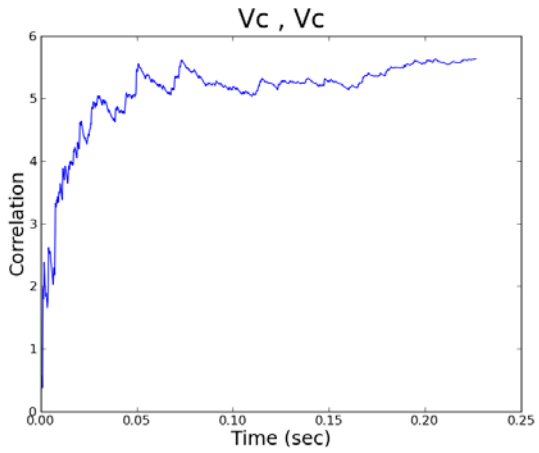
Vc , Vc
Correlation
Time (sec)

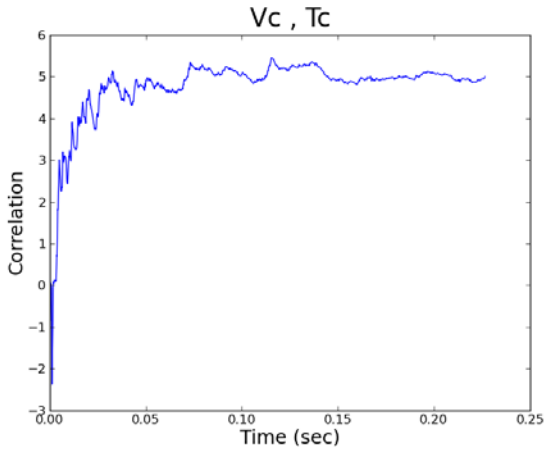
Vc , Tc
Correlation
Time (sec)

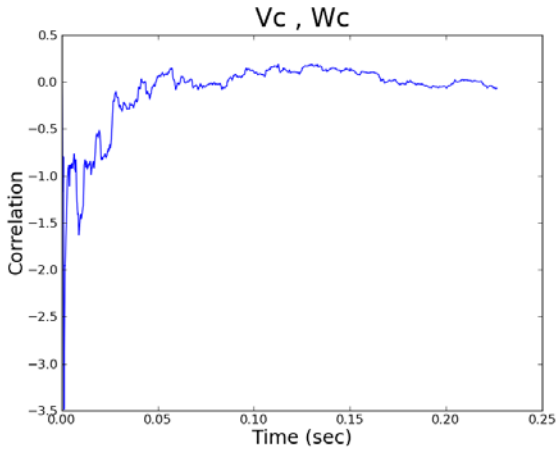
Vc , Wc
Correlation
Time (sec)

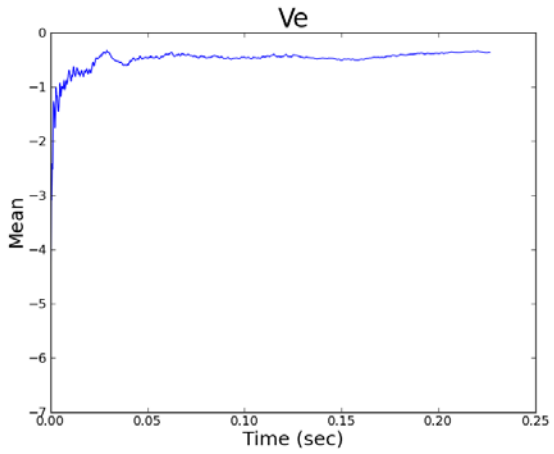
Ve
Mean
Time (sec)

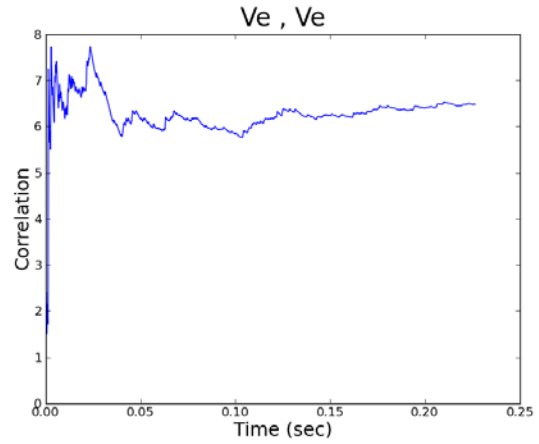
Ve , Ve
Correlation
Time (sec)

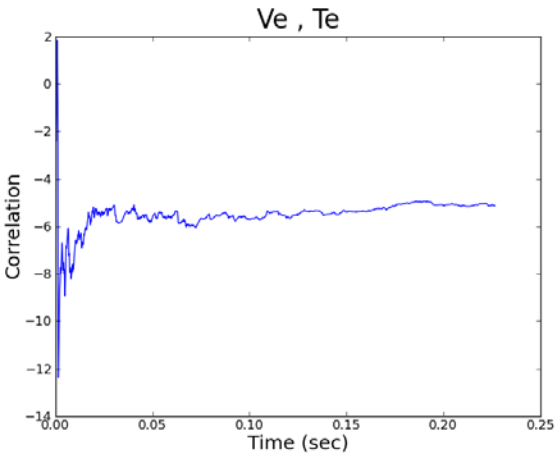
Ve , Te
Correlation
Time (sec)

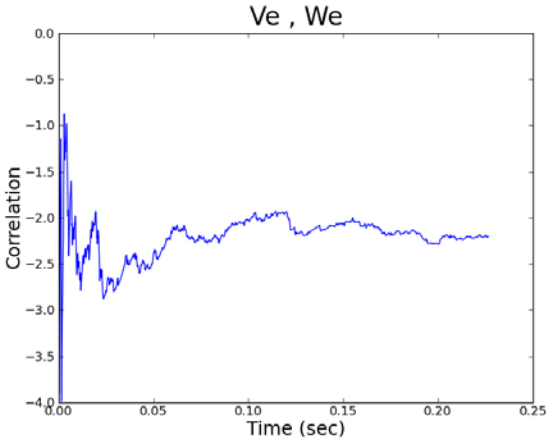
Ve , We
Correlation
Time (sec)

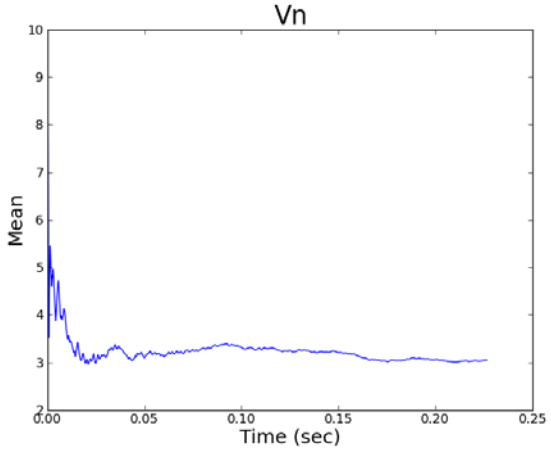
Vn
Mean
Time (sec)

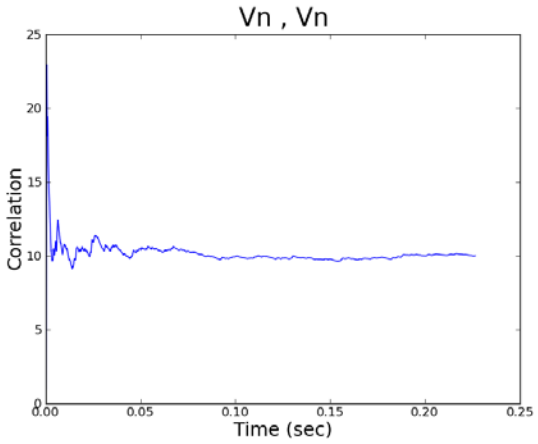
Vn , Vn
Correlation
Time (sec)

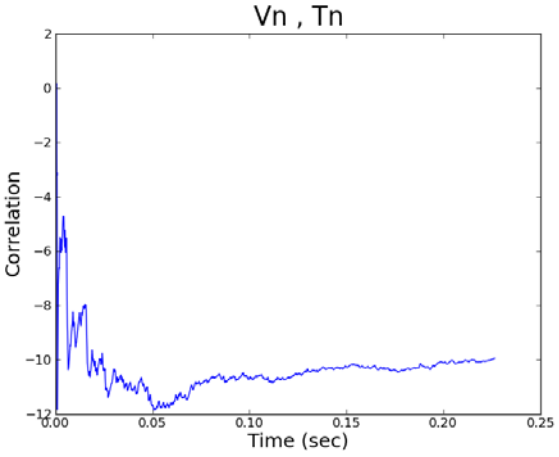
Vn , Tn
Correlation
Time (sec)

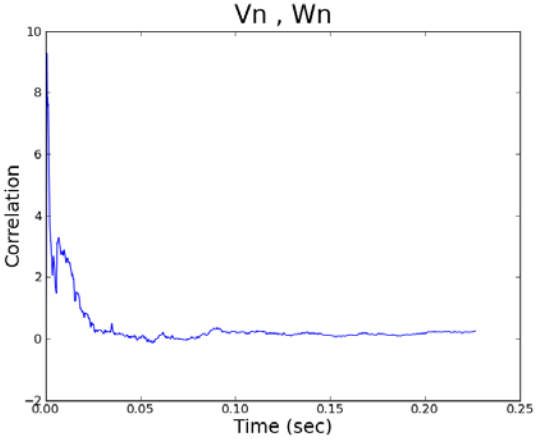
Vn , Wn
Correlation
Time (sec)

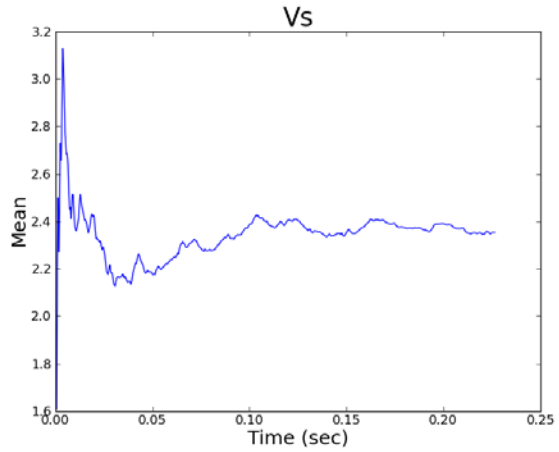
Vs
Mean
Time (sec)

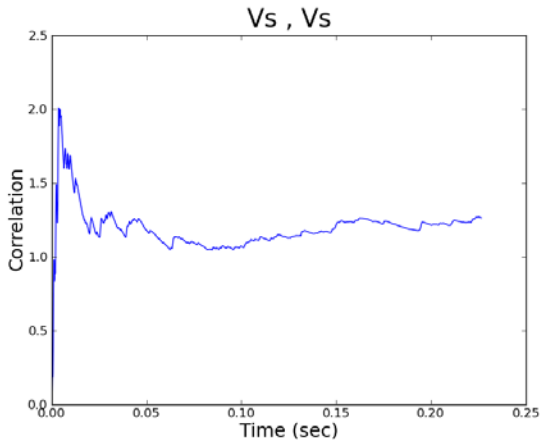
Vs , Vs
Correlation
Time (sec)

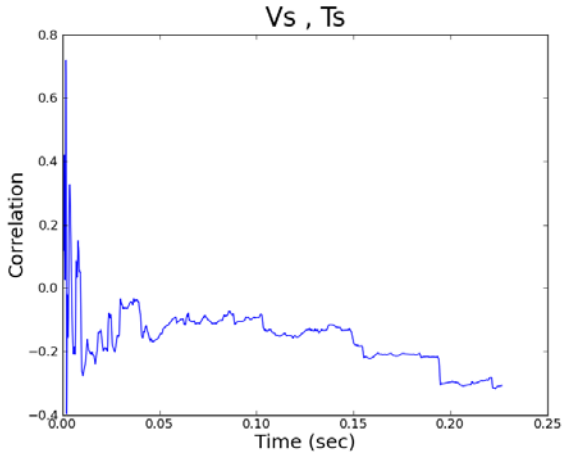
Vs , Ts
Correlation
Time (sec)

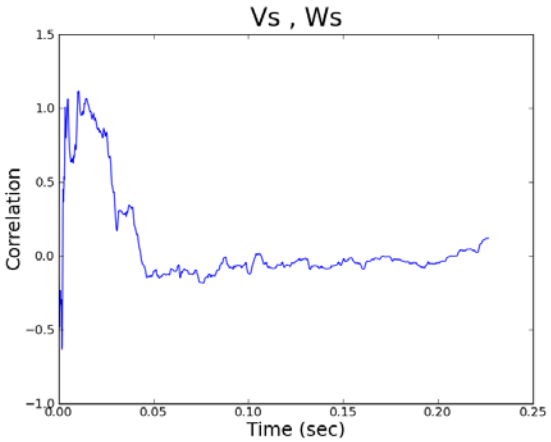
Vs , Ws
Correlation
Time (sec)

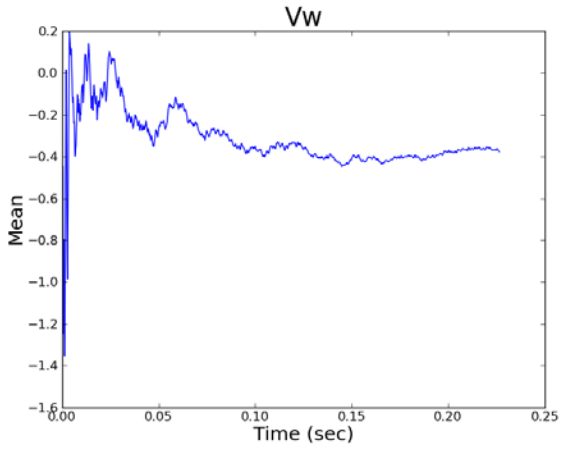
Vw
Mean
Time (sec)

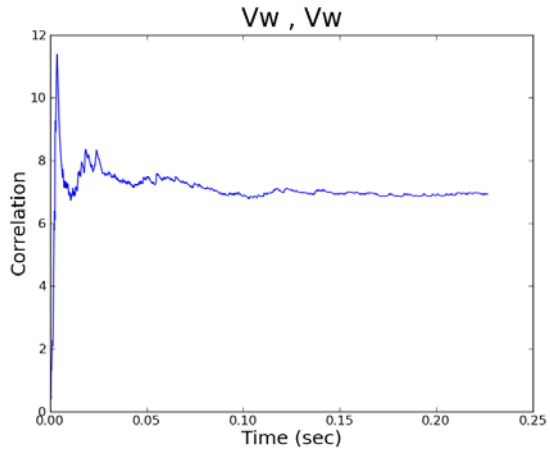
Vw , Vw
Correlation
Time (sec)

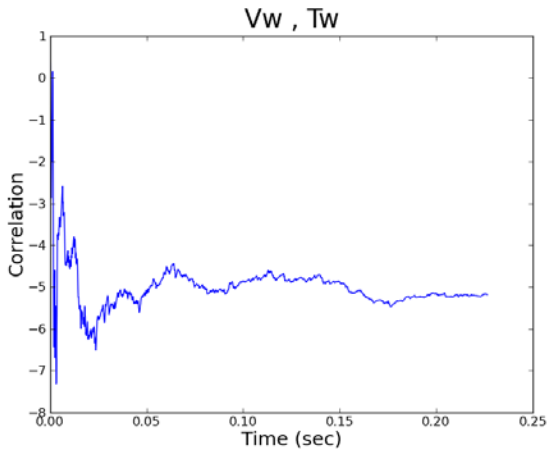
Vw , Tw
Correlation
Time (sec)

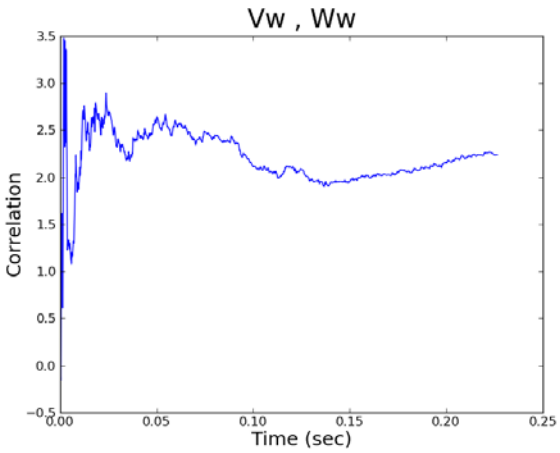
Vw , Ww
Correlation
Time (sec)

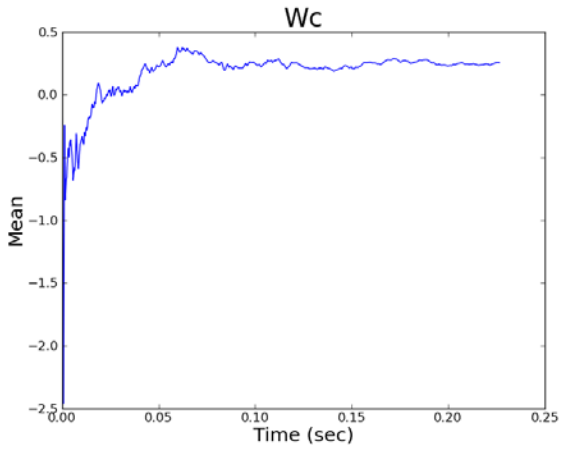
Wc
Mean
Time (sec)

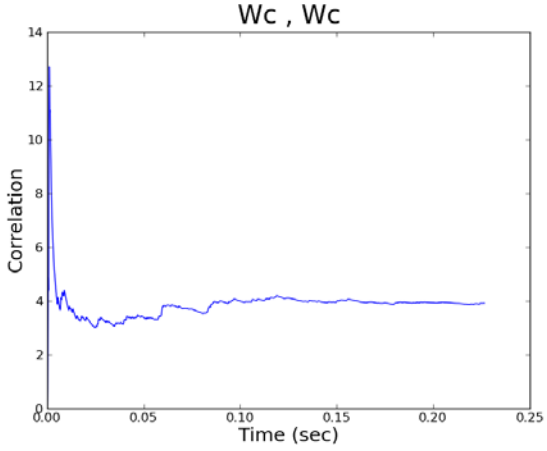
Wc , Wc
Correlation
Time (sec)

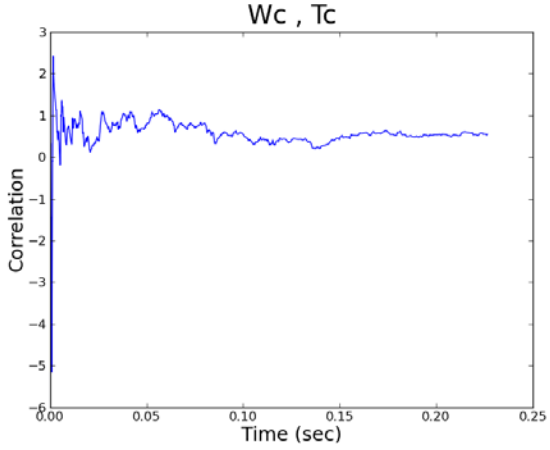
Wc , Tc
Correlation
Time (sec)

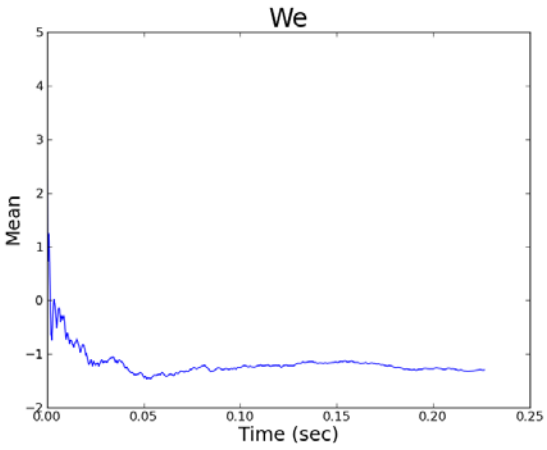
We
Mean
Time (sec)

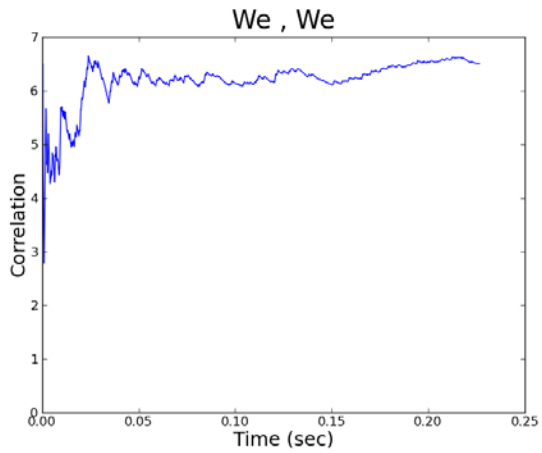
We , We
Correlation
Time (sec)

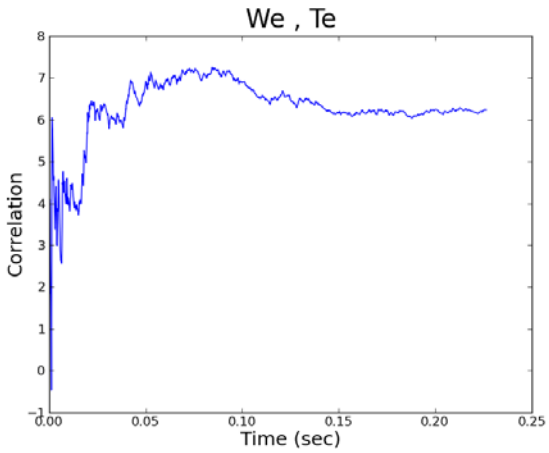
We , Te
Correlation
Time (sec)

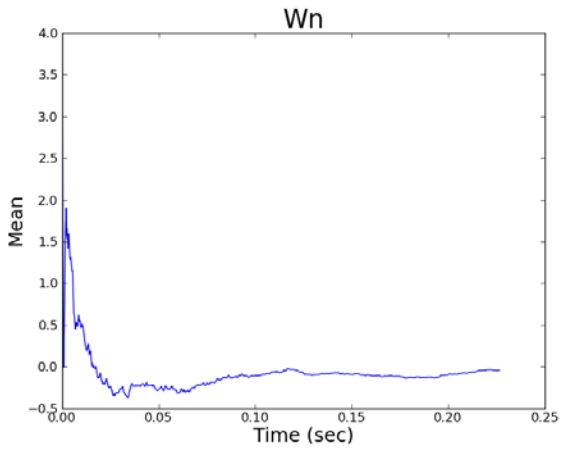
Wn
Mean
Time (sec)

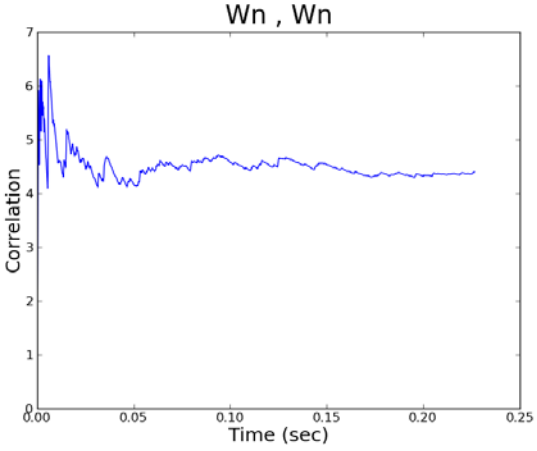
Wn , Wn
Correlation
Time (sec)

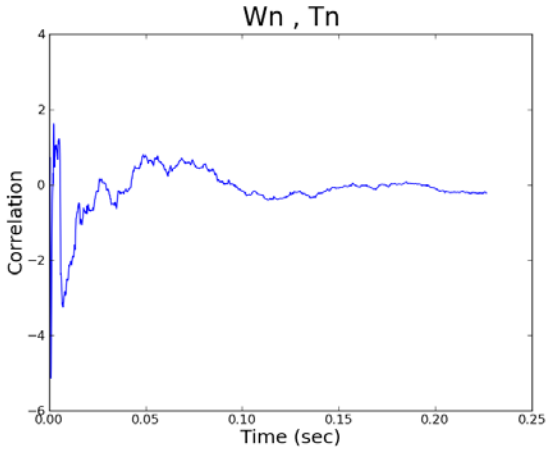
Wn , Tn
Correlation
Time (sec)

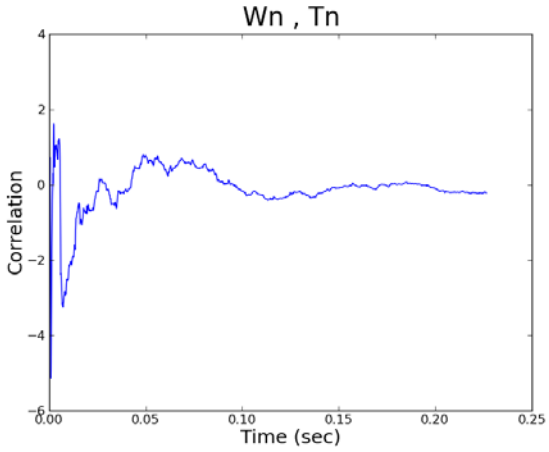
Wn , Tn
Correlation
Time (sec)

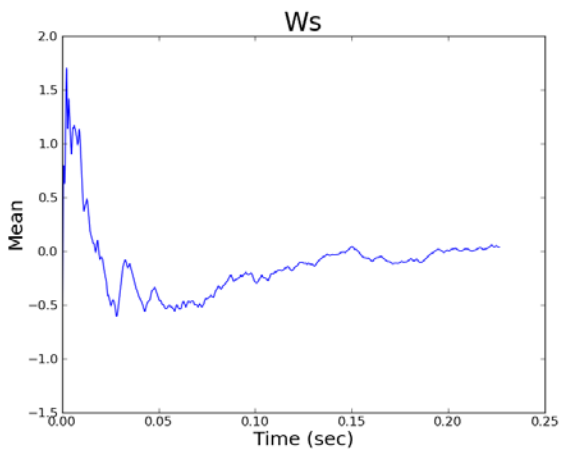
Ws
Mean
Time (sec)

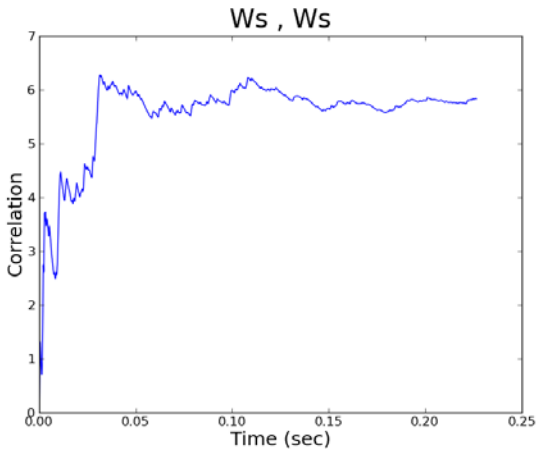
Ws , Ws
Correlation
Time (sec)

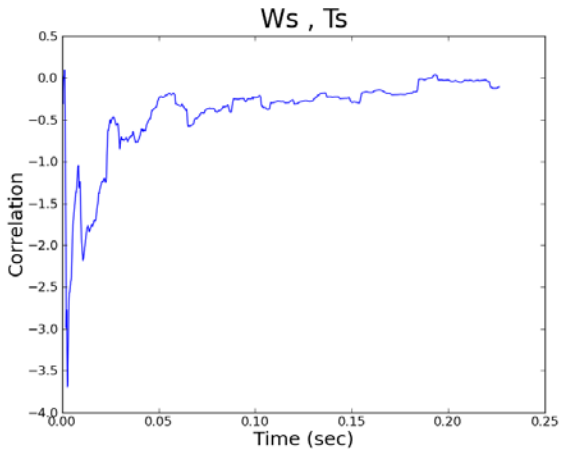
Ws , Ts
Correlation
Time (sec)

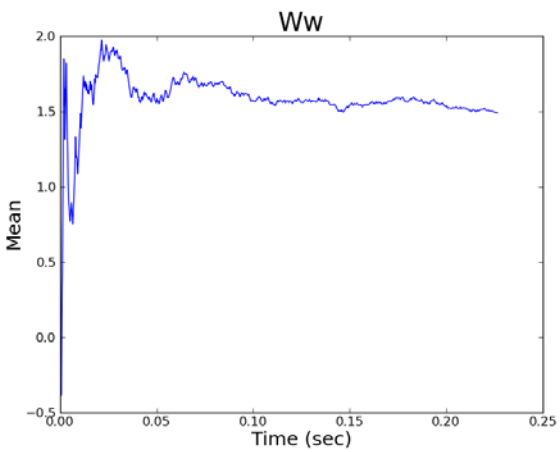
Ww
Mean
Time (sec)

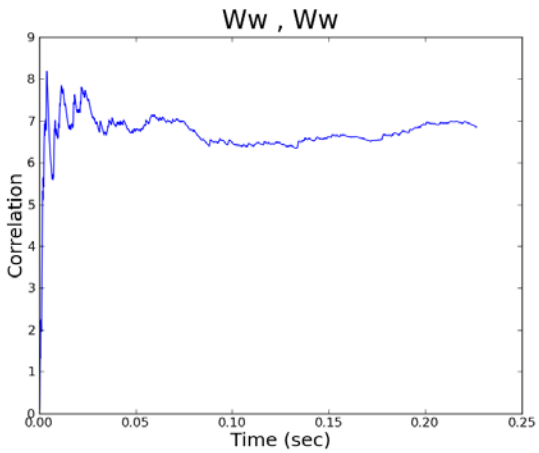
Ww , Ww
Correlation
Time (sec)

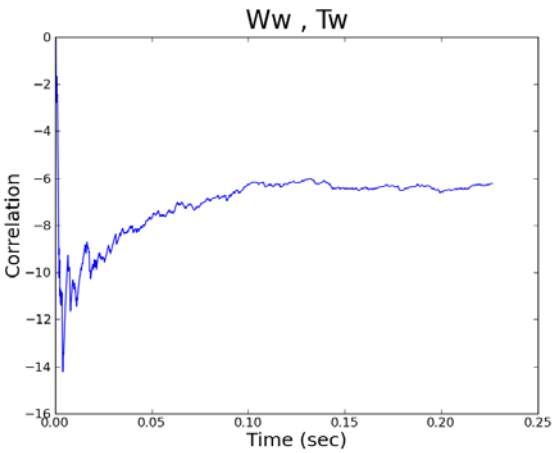
Ww , Tw
Correlation
Time (sec)

REFERENCES

Acharya, S., Tyagi, M., and Hoda, A., 2001, “Flow and Heat Transfer Predictions for Film Cooling,” Annals of the NY Academy of Sciences, Vol. 934, pp. 110-125.

Anderson, J. D., Computational Fluid Dynamics: the Basics with Applications, McGraw-Hill, 1995.

Ansys Fluent 12 Theory Guide, 2009, ANSYS Inc.

Azzi, A., Lakehal, D., 2002, "Perspectives in Modeling Film Cooling of Turbine Blades by Transcending Conventional Two-Equation Turbulence Models," ASME Journal of Turbomachinery, Vol. 124, pp. 472-484.

Bagley, R. L., and Torvik, P. J., 1983, “A Theoretical Basis for the Application of Fractional Calculus to Viscoelasticity,” J. Rheology, Vol. 27, pp. 201-210.

Baldwin, B. S., and Lomax, H., 1978, “Thin-Layer Approximation and Algebraic Model for Separated Turbulent Flows,” AIAA Paper 78-257.

Bardina, J., Ferziger, J., and Reynolds, W. C., 1980, “Improved Subgrid Models for Large Eddy Simulation,” AIAA Paper 80-1357.

Bell, C.M., Hamakawa, H., and Ligrani, P.M., 2000, “Film Cooling From Shaped Holes,” ASME Journal of Heat Transfer, Vol. 122, pp. 224-232.

Boussinesq, J., 1877, “Theorie de l’Ecoulement Tourbillant,” Mem. Presentes par Divers Savants Acad. Sci. Inst. Fr., Vol. 23, pp. 46-50.

Bradshaw, P., 1994, “Turbulence: the Chief Outstanding Difficulty of Our Subject,” Exp. Fluids, Vol 16, pp. 203-216.

Breuer, M., 1998, “Large Eddy Simulation of the Subcritical Flow Past a Circular Cylinder: Numerical and Modeling Aspects,” International Journal for Numerical Methods in Fluids, Vol. 28, pp. 1281-1302.

Brittingham, R.A., and Leylek, J.H., 2000, “A Detailed Analysis of Film-Cooling Physics: Part IV – Compound-Angle Injection with Shaped Holes,” ASME Journal of Turbomachinery, Vol. 122, pp. 102-112.

Bunker, R.S., 2001, “A Method for Improving the Cooling Effectiveness of a Gaseous Coolant Stream,” US Patent 6,234,755.

Bunker, R.S., 2002, “Film Cooling Effectiveness due to Discrete Holes within a Transverse Trench,” Proceedings of the ASME Turbo Expo 2002, Amsterdam, The Netherlands, GT-2002-30178.

Bunker, R.S., 2005, “A Review of Shaped Hole Turbine Film-Cooling Technology,” Journal of Heat Transfer, Vol. 127, pp. 441-453.

Burd, S.W., Kaszeta, R.W., and Simon, T.W., 1996, “Measurements in Film Cooling Flows: Hole L/D and Turbulence Intensity Effects,” ASME Journal of Turbomachinery, Vol. 120, pp. 791-798.

Burd, S., and Simon, T., 1999, “Turbulence Spectra and Length Scales Measured in Film Coolant Flows Emerging From Discrete Holes,” Journal of Turbomachinery, 121, pp. 551-557.

Cengel, Y. A., and Boles, M. A., *Thermodynamics: An Engineering Approach*, 6th ed., McGraw Hill: New York, 2008.

Cho, H.H., Rhee, D.H., and Kim, B.G., 1999, “Film Cooling Effectiveness and Heat/Mass Transfer Coefficient Measurement Around a Conical-Shaped Hole with a Compound Angle Injection,” ASME Paper No. 95-GT-38.

Daly, B. J., and Harlow, F. H., 1970, “Transport Equations in Turbulence,” Phys. Fluids, Vol. 13, pp. 2634-2649.

Ekkad, S.V., Zapata, D., and Han, J.C., 1997, “Heat Transfer Coefficient Over a Flat Surface with Air and CO_2 Injection Through Compound Angle Holes Using a Transient Liquid Crystal Image Method,” ASME Journal of Turbomachinery, Vol. 119, pp. 580-586.

Ekkad, S.V., Zapata, D., and Han, J.C., 1997, “Film Effectiveness Over a Flat Surface with Air and CO_2 Injection Through Compound Angle Holes Using a Transient Liquid Crystal Image Method,” ASME Journal of Turbomachinery, Vol. 119, pp. 580-586.

El-Gabry, L. A., Thurman, D. R., Poinsatte, P. E., and Heidmann, J. D., 2011, “Turbulence and Heat Transfer Measurements in an Inclined Large Scale Film Cooling Array – Part I, Velocity and Turbulence Measurements,” Proceedings of ASME Turbo Expo 2011, GT2011-46491.

Eriksen, V.L., and Goldstein, R.J., 1974, “Heat Transfer and Film Cooling Following Injection Through Inclined Circular Tubes,” ASME Journal of Heat Transfer, Vol. 96, pp. 239-245.

Fric, T.F., and Roshko, A., 1994, “Vortical Structure in the Wake of a Transverse Jet”, Journal of Fluid Mechanics, Vol. 279, pp. 1-47.

Gambit, 2008, Software Package, Version 2.3.16, ANSYS Inc., USA.

Germano, M., Piomelli, U., Moin, P., and Cabot, W. H., 1991, “A Dynamic Subgrid-Scale Eddy Viscosity Model,” Phys. Fluids, Vol. 3, pp. 1760-1765.

Ghosal, S., Lund, T. S., Moin, P., Akselvoll, K., 1995, “A Dynamic Localization Model for Large-Eddy Simulation of Turbulent Flows,” J. Fluid Mech., Vol. 286, pp. 229-255.

Goldstein, R.J., 1971, “Film Cooling,” *Advances in Heat Transfer*, Academic Press, San Diego, CA, **7**, pp. 312-379.

Goldstein, R.J., Eckert, E.R.G., and Ramsey, J.W., 1968, “Film Cooling with Injection Through Holes: Adiabatic Wall Temperatures Downstream of a Circular Hole,” ASME Journal of Engineering for Power, Vol. 90**,** pp. 384-395.

Goldstein, R.J., Eckert, E.R.G., Eriksen, V.L., and Ramsey, J.W., 1970, “Film Cooling Following Injection Through Inclined Circular Tubes,” Israel Journal of Technology, Vol. 8, pp. 145-154.

Goldstein, R.J., Eckert, E.R.G., and Burggraf, F., 1974, “Effects of Hole Geometry and Density on Three-Dimensional Film Cooling,” International Journal of Heat and Mass Transfer, Vol. 17, pp. 595-607.

Goldstein, R.J., and Jin, P, 2001, “Film Cooling Downstream of a Row of Discrete Holes with Compound Angle,” ASME Journal of Turbomachinery, Vol. 123, pp. 222-230.

Gritsch, M., Schulz, A., and Witting, S., 1998a, “Adiabatic Wall Effectiveness Measurements of Film Cooling Holes With Expanded Exits,” ASME Journal of Turbomachinery, Vol. 120, pp. 549-556

Gritsch, M., Schulz, A., and Witting, S., 1998b, “Discharge Coefficient Measurements of Film Cooling Holes With Expanded Exits,” ASME Journal of Turbomachinery, Vol. 120, pp. 557-563

Gritsch, M., Schulz, A., and Witting, S., 1998c, “Heat Transfer Coefficient Measurements of Film Cooling Holes With Expanded Exits,” Proceedings of Turbo Expo 1998, 98-GT-28.

Gritsch, M., Saumweber, C., Schulz, A., and Witting, S., 2000, “Effect of Internal Coolant Crossflow Orientation on the Discharge Coefficient of Shaped Film Cooling Holes,” ASME Journal of Turbomachinery, Vol. 122, pp.146-153.

Guo, X., Schroder, W., Meinke, M., 2006, “Large-eddy Simulations of Film Cooling Flows,” Comp. & Fluids, Vol. 35, pp. 587-606.

Harrison, K.L., and Bogard, D.G., 2008, "Comparison of RANS Turbulence Models for Prediction of Film Cooling Performance," Proceedings of the ASME Turbo Expo 2008, Berlin, Germany, GT2008-51423.

Haven, B.A., and Kurosaka, M., 1997, “Kidney and Anti-Kidney Vortices in Crossflow Jets,” Journal of Fluid Mechanics, Vol. 352, pp. 27-64.

Hay, N., and Lampard, D., 1995, “The Discharge Coefficient of Flared Film Cooling Holes,” Proceedings of Turbo Expo 1995, 95-GT-15.

Heidmann, J., and Ekkad, S. V., 2007, “A Novel Anti-Vortex Turbine Film Cooling Hole Concept,” ASME Turbo Expo 2007, GT2007-27528, Montreal, Canada.

Hoda, A., and Acharya, S., 2000, "Predictions of a Film Coolant Jet in Crossflow With Different Turbulence Models," ASME Journal of Turbomachinery, Vol. 122, pp.558-571.

Hyams, D.G., and Leylek, J.H., 2000, “A Detailed Analysis of Film-Cooling Physics: Part III – Streamwise Injection with Shaped Holes,” ASME Journal of Turbomachinery, Vol. 122, pp. 122-132.

Iourokina, I.V., and Lele, S.K., 2006, “Large Eddy Simulation of Film-Cooling Above the Flat Surface with a Large Plenum and Short Exit Holes,” Proceedings of the AIAA Aerospace Sciences Meeting and Exhibit, 2006, Reno, Nevada, USA.

Iourokina, I.V., and Lele, S.K., 2006, “Large Eddy Simulation of Film Cooling Flow Above a Flat Surface from Inclined Cylindrical Holes,” Proceedings of the ASME Joint U.S.-European Fluids Engineering Summer Meeting, 2006, Miami, Florida, USA.

Jeong, J., and Hussain, F., 1995, “On the Identification of a Vortex,” J. Fluid Mech., Vol. 285, pp. 69-94.

Jewkes, J., Yongmann, M. , and Carpenter, P. W., 2011, “Modifications to a Turbulent Inflow Generation Moethod for Boundary-Layer Flows,” AIAA J., Vol. 49, pp. 247-250.

Johnson, D. A., and King, L. S., 1985, “A Mathematically Simple Turbulence Closure Model for Attached and Separated Turbulent Boundary Layers,” AIAA J., Vol. 23, pp. 1684-1692.

Kaszeta, R.W., and Simon, T.W., 2000, “Measurement of Eddy Diffusivity of Momentum in Film Cooling Flows With Streamwise Injection," ASME Journal of Turbomachinery, Vol. 122, pp. 178-183.

Kiesow, 2008, “Turbines for Sustainable Power,” University of Central Florida course lecture.

Kim, W.-W., and Menon, S., 1997, “Application of the Localized Dynamic Subgrid-Scale Model to Turbulent Wall-Bounded Flows,” 35th AIAA Aerospace Sciences Meeting, AIAA-97-0210.

Kelso, R.M., Lim, T.T., and Perry, A.E., 1996, “An Experimental Study of Round Jets in Cross-flow,” Journal of Fluid Mechanics, Vol. 306, pp. 111-144.

Lakehal, D., 2002, “Near-Wall Modeling of Turbulent Convective Heat Transport in Film Cooling of Turbine Blades With the Aid of Direct Numerical Simulation Data,” ASME Journal of Turbomachinery, 124, pp. 485-498.

Launder, B. E., and Sharma, B. I., 1974, “Application of the Energy Dissipation Model of Turbulence to the Calculation of Flow near a Spinning Disc,” *Letters in Heat and Mass Transfer*, Vol. 1, No. 2, pp. 131-138.

Launder, B. E., Reece, G. J., and Rodi, W., 1975, “Progress in the Development of a Reynolds-Stress Turbulence Closure,” J. Fluid Mech., Vol 68, pp. 537-566.

Leedom, D.H., and Acharya, S., 2008, “Large Eddy Simulations of Film Cooling Flow Fields From Cylindrical and Shaped Holes,” GT2008-51009, Proceedings of ASME Turbo Expo 2008, Berlin, Germany, GT2008-51009.

Leylek, J.H., and Zerkle, R.D., 1994, “Discrete-jet Film Cooling: A Comparison of Computational Results With Experiments,” Journal of Turbomachinery, Vol. 116, pp. 358-368.

Li, Xianchang, 2010, "Numerical Simulation on Fluid Flow and Heat Transfer of Film Cooling with Backward Injection," Proceedings of the 14th ASME International Heat Transfer Conference, IHTC14-22995.

Liakopoulos, A., 1984, “Explicit Representations of the Complete Velocity Profile in a Turbulent Boundary Layer,” AIAA J., Vol. 22, pp. 844-846.

Ligrani, P.M., Wigle, J.M., Ciriello, S. and Jackson, S.W., 1994, “Film-Cooling from Holes with Compound Angle Orientations: Part I – Results Downstream of Two Staggered Rows of Holes with 3d Spanwise Spacing,” ASME Journal of Heat Transfer, Vol. 116, pp. 353-362.

Ligrani, P.M., Wigle, J.M., and Jackson, S.W., 1994, “Film-Cooling from Holes with Compound Angle Orientations: Part II – Results Downstream of a Single Row of Holes with 6d Spanwise Spacing,” ASME Journal of Heat Transfer, Vol. 116, pp. 353-362.

Lilly, D. K., 1992, “A Proposed Modification of the Germano Subgrid-Scale Closure Method,” Phys. Fluids, Vol. 4, pp. 633-635.

Lu, Y., Nasir, H., Ekkad, S.V., 2005, “Film Cooling from a Row of Holes Embedded in Transverse Trenches,” Proceedings of the ASME Turbo Expo 2005, Reno, Nevada, USA, GT2005-68598.

Lumley, J. L., 1970, “Toward a Turbulent Constitutive Relation,” J. Fluid Mech., Vol. 41, pp. 413-434.

Marusic, I., McKeon, B J., Monkewitz, P. A., Nagib, H. M., Smits, A. J., and Sreenivasan, K. R., 2010, “Wall-bounded Turbulent Flows: Recent Advances and Key Issues,” Phys. Fluids, Vol. 22, 065103

McGovern, K.T., and Leylek, J.H., 2000, “A Detailed Analysis of Film-Cooling Physics: Part II – Compound-Angle Injection with Cylindrical Holes,” ASME Journal of Turbomachinery, Vol. 122, pp. 113-121.

Meinke, M., Schroder, W., Krause, E., Rister, Th., 2002, “A Comparison of Second- and Sixth-Order Methods for Large Eddy Simulations”, Computers & Fluids, Vol. 31, pp. 695-718.

Menter, F. R., 1992, “Improved Two-Equation k-ω Turbulence Models for Aerodynamic Flows,” NASA TM-103975.

Minitab, 2007, “Minitab 15 Statistical Software English”, USA, Minitab Inc.

Moin, P., Squires, K., Cabot, W., and Lee, S., 1991, “A Dynamic Subgrid-Scale Model for Compressible Turbulence and Scalar Transport,” Phys. Fluids, Vol. 3, pp. 2746-2757.

Myers, R. H., Montgomery, D.C., and Anderson-Cook, C.M. 2009. Response Surface Methodology: Process and Product Optimization Using Designed Experiments, 3rd ed., John Wiley & Sons, New Jersey, Chapter 7, Section 4.

Nagib, H. M., and Chauhan, K. A., 2008, “Variations of von Karman Coefficient in Canonical Flows,” Phys. Fluids, Vol. 20, 101518.

Natsui, G., Johnson, P.L., Ricklick, M, and Kapat, J.S., 2011, “The Effect of Transpiration on Discrete Injection for Film Cooling,” ASME Turbo Expo, Vancouver, Canada, June 2011, GT2011-46138.

Nguyen, C. Q., 2010, “Interaction Between Secondary Flow and Film Cooling Jets of a Realistic Annular Airfoil Cascade (High Mach Number),” Ph.D. dissertation, University of Central Florida.

Orszag, S. A., Yakhot, V., Flannery, W. S., Boysan F., Choudhury, D. Maruzewski, J., and Patel, B., 1993, “Renormalization Group Modeling and Turbulence Simulations, *International Conference on Near-Wall Turbulent Flows*, Tempe, Arizona.

Patankar, S. V., *Numerical Heat Transfer and Fluid Flow*, Taylor and Francis, 1980.

Pedersen, D.R., Eckert, E.R.G., and Goldstein, R.J., 1977, “Film Cooling with Large Density Differences Between the Mainstream and the Secondary Fluid Measured by the Heat-Mass Transfer Analogy,” ASME Journal of Heat Transfer, Vol. 99, pp.620-627.

Peet, Y.V., and Lele, S.K., 2008, “Near Field of Film Cooling Jet Issued Into a Flat Plate Boundary Layer: LES Study” GT2008-50420, Proceedings of ASME Turbo Expo 2008, Berlin, Germany.

Peric, M., and Ferziger, J., *Computational Methods for Fluid Dynamics*, Springer-Verlag, 1996.

Pietrzyk, J.R., Bogard, D.G., and Crawford, M.E., 1990, “Effects of Density Ratio on the Hydrodynamics of Film Cooling,” ASME Journal of Turbomachinery, Vol. 112, pp. 437-443.

Pope, S. B., 1975, “A More General Effective-Viscosity Hypothesis,” J. Fluid Mech., Vol. 72, pp. 331-340.

Pope, S. B., *Turbulent Flows*, Cambridge University Press, 2000.

Prandtl, L., 1925, “Bericht Uber Untersuchungen Zur Ausgebildete Turbulenze,” Nachr. Akad. Wiss. Gollingen, pp. 6-19.

Renze, P., Schroder, W., Meinke, M., 2008a, “Large-Eddy Simulation of Film Cooling Flows at Density Gradients,” International Journal of Heat and Fluid Flow, Vol. 29, pp. 18-34.

Renze, P., Schroder, W., Meinke, M., 2008b, “Large-Eddy Simulation of Film Cooling Flows with Variable Density Jets,” Flow Turbulence and Combustion, Vol. 80, 119-132.

Renze, P., Schroder, W., and Meinke, M., 2008c, “Large-Eddy Simulation of Film Cooling Flow Ejected in a Shallow Cavity,” Proceedings of the ASME Turbo Expo 2008, Berlin, Germany, GT2008-50120.

Renze, P., Schroder, W., and Meinke, M., 2009, “Large-Eddy Simulation of Interacting Film Cooling Jets,” Proceedings of the ASME Turbo Expo 2009, Orlando, Florida, USA, BT2009-59164.

Rodriguez, S., 2008, “Effect of Pressure Gradient and Wake on Endwall Film Cooling Effectiveness,” Ph.D. dissertation, University of Central Florida, Orlando, FL

Rotta, J. C., 1951, “Statistische Theorie Nichthomogener Turbulenz,” Zeitschrift fur Physik, Vol. 129, pp. 547-572.

Rozati, A., and Tafti, D.K., 2007a, "Large Eddy Simulation of Leading Edge Film Cooling Part I: Computational Domain and Effect of Coolant Pipe Inlet Condition," Proceedings of ASME Turbo Expo 2007, Montreal, Canada, GT2007-27689.

Rozati, A., and Tafti, D.K., 2007b, "Large Eddy Simulation of Leading Edge Film Cooling Part II: Heat Transfer and Effect of Blowing Ratio," Proceedings of ASME Turbo Expo 2007, Montreal, Canada, GT2007-27690.

Rozati, A., and Tafti, D.K., 2008, "Large Eddy Simulations of Leading Edge Film Cooling: Analysis of Flow Structures, Effectiveness, and Heat Transfer Coefficient," International Journal of Heat and Fluid Flow, 29, pp. 1-17.

Rydholm, H.A., 1998, “An Experimental Investigation of the Velocity and Temperature Fields of Cold Jets Injected Into a Hot Crossflow,” ASME Journal of Turbomachinery, Vol. 120, pp. 320-326.

Saumweber, C., Schulz, A., and Wittig, S., 2003, “Free-Stream Turbulence Effects on Film Cooling With Shaped Holes,” ASME J. Turbomachinery, Vol. 125, pp. 65-73.

Schmidt, D.L., Sen, B., and Bogard, D.G., 1996, “Film Cooling with Compound Angle Holes – Adiabatic Effectiveness,” ASME Journal of Turbomachinery, Vol. 118, 807-813.

Scorer, R.S., 1958, *Natural Aerodynamics*, Pergamon Press, Oxford, pp. 193-195.

Sen, B., Schmidt, D.L., and Bogard, D.G., 1996, “Film Cooling with Compound Angle Holes – Heat Transfer,” ASME Journal of Turbomachinery, Vol. 118, pp. 800-806.

Shih, T. H., and Lumley, J. L., “Remarks on Turbulent Constitutive Equations,” Math. Comp. Modeling, Vol. 18, pp. 9-16.

Shih, T. H., Liou, W. W., Shabbir, A., Yang, Z., and Zhu, J., 1995, “A New k-ε Eddy-Viscosity Model for High Reynolds Number Turbulent Flows – Model Development and Validation,” *Computers and Fluids*, Vol. 24, No. 3, pp. 227-238.

Shih, T.-H., Liou, N.-S., and Chen, K.-H., 1998, “A Non-Linear k-epsilon Model for Turbulent Shear Flows,” 34th AIAA/ASME/SAE/ASEE Joint Propulsion Conference & Exhibit, AIAA-1998-3983.

Shih, T. H., personal communication, July 2011.

Shyam, V., personal communication, July 2011.

Sinha, A.K., Bogard, D.G., and Crawford, M.E., 1991, “Film-Cooling Effectiveness Downstream of a Single Row of Holes with Variable Density Ratio,” ASME Journal of Turbomachinery, Vol. 113, pp. 442-449.

Smagorinsky, J., 1963, “General Circulation Experiments with the Primitive Equations: I. The Basic Equations,” Mon. Weather Rev., Vol. 91, pp.99-164.

Smith, A. M. O., and Cebeci, T., 1967, “Numerical Solution of the Turbulent Boundary-Layer Equations,” Douglas Aircraft Division Report DAC 33735.

Smits, A. J., McKeon, B. J., and Marusic, I., 2011, “High-Reynolds Number Wall Turbulence,” Ann. Rev. Fluid Mech., Vol. 43, pp. 353-375.

Spalart, P. R., 1988, "Direct Simulation of a Turbulent Boundary Layer up to R_θ=1410," J. Fluid Mech., Vol. 187, pp. 61-98.

Spalart, P. R., and Allmaras, S. R., 1992, "A One-Equation Turbulence Model for Aerodynamic Flows," AIAA Paper 92-439.

Spalart, P. R., Deck, S., Shur, M. L., Squires, K. D., Strelets M. Kh., and Travin, A., 2006, "A New Version of Detached-Eddy Simulation, Resistant to Ambiguous Grid Densities," Theoret. Comp. Fluid Dyn., Vol. 20, pp. 181-195

Tannehill, J. C., Anderson, D. A., and Pletcher, R. H., *Computational Fluid Mechanics and Heat Transfer*, Taylor and Francis, 1997.

Taslim, M.E., and Ugarte, S., 2004, "Discharge Coefficient Measurements for Flow Through Compound-Angle Conical Holes with Cross-Flow," International Journal of Rotating Machinery, Vol. 10, pp. 145-153.

Tennekes, H., and Lumley, J. L., 1972, *A First Course in Turbulence*, MIT Press, Cambridge, MA.

Thole, K., Sinha, A., Bogard, D.G., and Crawford, M.E., 1992, "Mean Temperature Measurements of Jets with a Crossflow for Gas Turbine Film Cooling Application," Rotating Machinery Transport Phenomena, J.H. Kim and W.J. Yang, eds., Hemisphere Pub. Corp., New York.

Thole, K., Gritsch, M., Schulz, A., and Wittig, S., 1998, "Flowfield Measurements for Film Cooling Holes With Expanded Exits," ASME Journal of Turbomachinery, 120, pp. 327-336.

Thurman, D. R., El-Gabry, L. A., Poinsatte, P. E., and Heidmann, J. D., 2011, "Turbulence and Heat Transfer Measurements in an Inclined Large Scale Film Cooling Array – Part II,

Temperature and Heat Transfer Measurements," Proceedings of ASME Turbo Expo 2011, GT2011-46498.

Tyagi, M., and Acharya, S., 2003, "Large Eddy Simulation of Film Cooling Flow From and Inclined Cylindrical Jet," ASME Journal of Turbomachinery, Vol. 125, pp. 734-742.

van der Bos, F., and Guerts, B. J., 2005, "Commutator Errors in the Filtering Approach to Large-Eddy Simulation," Phys. Fluids, Vol. 17, 035108.

Vreman, B., Geurts, B., and Kuerten, H., 1997, "Large-Eddy Simulation of the Turbulent Mixing Layer," J. Fluid Mech., Vol. 339, pp. 357-390.

Walters, J.D.K., and Leylek, J.H., 1997, "A Systematic Computational Methodology Applied to a Three-Dimensional Film-Cooling Flowfield," Journal of Turbomachinery, Vol. 119, pp. 777-785.

Walters, D.K., and Leylek, J.H., 2000, "A Detailed Analysis of Film-Cooling Physics: Part I – Streamwise Injection with Cylindrical Holes," ASME Journal of Turbomachinery, Vol. 122, pp. 102-112.

Wang, L., Tsang, H., Simon, T., and Eckert. E.R.G., 1996, "Measurementes of Mean Flow and Eddy Transport Over a Film Cooling Surface," Proceedings of the 31st National Heat Transfer Conference.

Waye, S.K., and Bogard, D.G., 2006, "High Resolution Film Cooling Effectiveness Measurements of Axial Holes Embedded in a Transverse Trench with Various Trench Configurations," Proceedings of the ASME Turbo Expo 2006, Barcelona, Spain, GT2006-90226.

Wieghardt, K., 1946, "Hot Air Discharge for De-icing," AAF Translation F-TS-919-RE.

Wilcox, D. C., 2006, *Turbulence Modeling for CFD*, 3rd ed., DCW Industries, Inc., La Canada, CA.

Yakhot, V., and Orszag, S. A., 1986, "Renormalization Group Analysis of Turbulence: 1. Basic Theory," *Journal of Scientific Computing*, Vol. 1, pp. 3-51.

Yakhot, V., Orszag, S. A., Thangam, S., Gatski, T. B., and Speziale, C. G., 1992, "Development of Turbulence Models for Shear Flows by a Double Expansion Technique," Phys. Fluids, Vol. 4, p. 1510-1520.

Yu, Y., Yen, C.-H., Shih, T. I.-P., Chyu M. K., and Gogineni, 2002, "Film Cooling Effectiveness and Heat Transfer Coefficient Distributions Around Diffusion Shaped Holes," ASME Journal of Heat Transfer, Vol. 124, pp.820-827.

Zuniga, H.A., 2006, "Study of Discharge Coefficient and Trends in Film Cooling Effectiveness of Conical Holes with Increasing Diffusion Angles," M.S. Thesis, University of Central Florida.

Zuniga H. A., Krishnan, V., and Ling, J. P. C. W., 2007, "Trends in Film Cooling Effectiveness Caused by Increasing Angle of Diffusion Through a Row of Conical Holes," ASME Proceedings of Turbo Expo 2007, Montreal, Canada, Paper GT2007-28287.

Zuniga, H.A., 2009, "Study of Film Cooling Effectiveness: Conical, Trenched, and Asymmetrically Shaped Holes," Ph.D. Dissertation, University of Central Florida.